Leonid A. Kosyachenko, *editor*

Solar Cells

New Approaches and Reviews

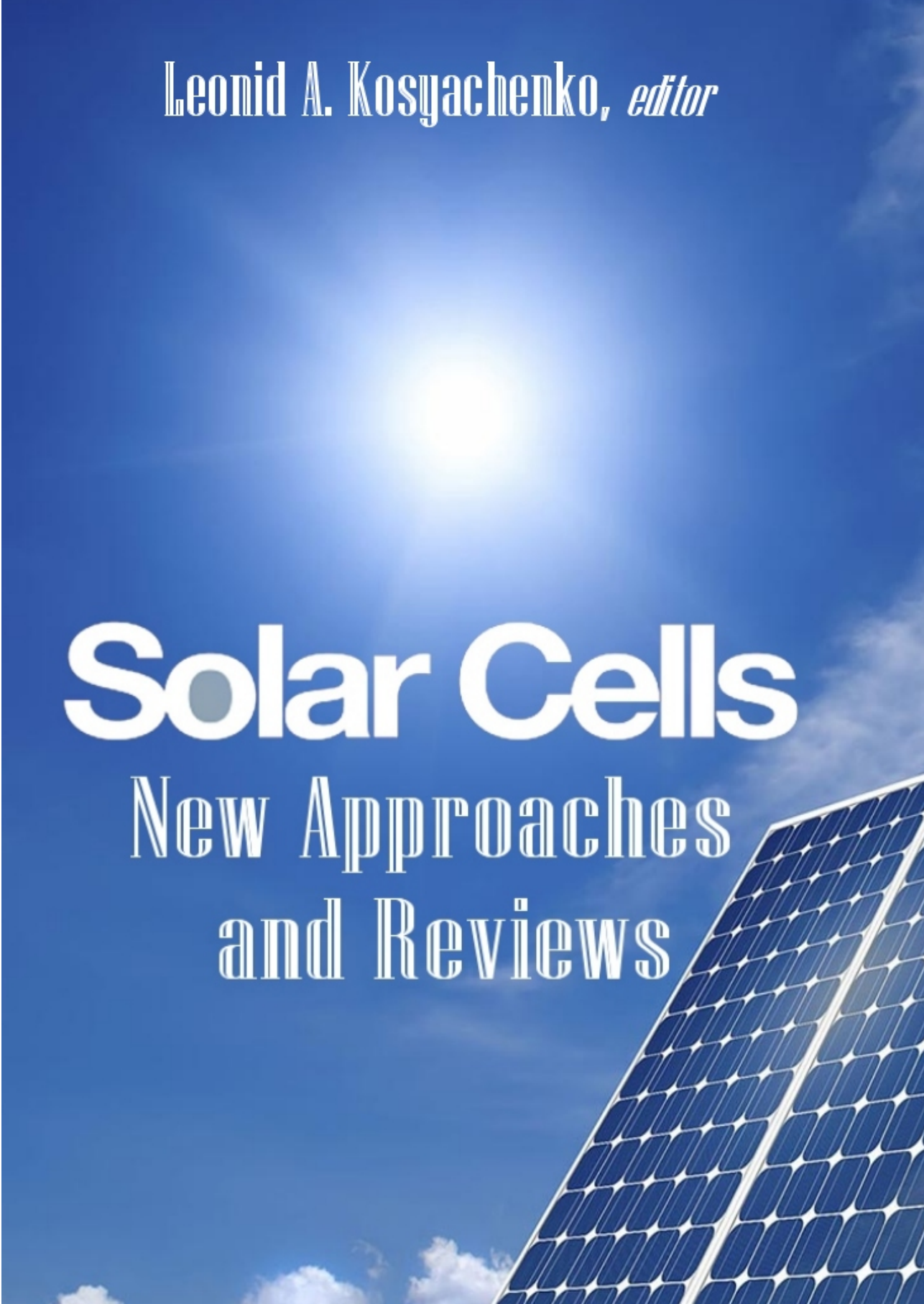

Solar Cells
New Approaches and Reviews

Edited by Leonid A. Kosyachenko

Solar Cells: New Approaches and Reviews

Edited by Leonid A. Kosyachenko

Published by AvE4EvA

Publishing Process Manager
Technical Editor
Cover Designer AvE4EvA MuViMix Records

Published: 22 October, 2015

ISBN-10: 953-51-2184-7
ISBN-13: 978-953-51-2184-8

Contents

Preface

This book contains chapters in which the problems of modern photovoltaics are considered.

The majority of the chapters provide an overview of the results of research and development of different types of solar cells. Such chapters are completed by a justification for a new solar cell structure and technology. Of course, highly effective solar energy conversion is impossible without an in-depth examination of the solar cell components as physical materials.

The relations between structural, thermodynamic, and optical properties of the physical material without addressing the band theory of solids are of both theoretical and practical interest. Requirements formulated for the material are also to be used for maximally efficient conversion of solar radiation into useful work.

Chapter 1

A Theoretical Description of Thin-Film $Cu(In,Ga)Se_2$ Solar Cell Performance

Leonid A. Kosyachenko

Additional information is available at the end of the chapter

http://dx.doi.org/10.5772/59363

1. Introduction

For a long time, solar cells based on $CuIn_{1-x}Ga_xSe_2$ ($Cu(In,Ga)Se_2$, CIGS), similar to CdTe-based devices, keep a stable position in thin-film photovoltaics as an alternative to solar modules based on mono- and poly-silicon wafers. The I-III-VI CIGS alloy is a solid solution of copper indium diselenide (CIS) and copper gallium diselenide (CGS). This alloy is tolerant in terms of material stability and miscibility in a wide range of x, when the semiconductor bandgap varies continuously from about 1.0 eV for CIS to about 1.65 eV for CGS. Irrespective of the material composition, CIGS is a direct-bandgap semiconductor and strongly absorbs sunlight. Because of its high optical absorption coefficient, a much thinner film is required compared to many other semiconductor materials (1–2 μm is enough to absorb most of the sunlight).

To date, mass production of cost-effective thin-film polycrystalline and monolithically interconnected CIGS-based modules has been achieved by many companies worldwide. Since 2007, one Japanese company Solar Frontier, alone for example, delivered over 1 GW CIGS modules. The CIGS devices demonstrate excellent long-term stability; can be fabricated on lightweight and flexible substrates that are desirable for portable, building-integrated photovoltaics and many other applications when solar panels are used to replace conventional building materials in parts of the roof or facades. It should also be noted that the CIGS modules, in addition to their long-term stability, have shown higher resistance to ionizing radiation compared to crystalline Si and III-V solar cells, i.e., such devices are promising for space application [1].

The energy conversion efficiency of CIGS modules is in the range of 12-15%, but for small area laboratory cells, the efficiency milestone of > 20% was achieved in 2010 [2]. In 2014, Solar Frontier has achieved 20.8% energy conversion efficiency for small area CIGS cells and Zentrum für Sonnenenergie-und Wasserstoff-Forschung Baden-Württemberg (ZSW) shortly

improved the cell efficiency to 20.9% [3,4]. Since the efficiency of CIGS modules lie in the 12-15% range (except for a 16.6 % world record [5]), which is about half of the theoretical limit 28-30%, there are plenty of opportunities to contribute towards the scientific and technological advancement of CIGS PV technology.

The device architecture of CIGS and CdTe solar cells are alike, similar to other p-n heterojuctions. In both cases, the CdS/absorber heterostructure is the key element in determining the electrical and photoelecnric characteristics of the device. In CIGS solar cells, the heterojunction is formed between the p-CIGS and n-CdS. The conductivity of CIGS is determined to a large degree by intrinsic defects, while the n-CdS is doped to a much larger extent by donors. This asymmetric doping causes the space charge region (SCR) to extend much further into the CIGS. As in CdTe solar cell, a thin layer of CdS serves as "window", through which radiation penetrates into the absorber.

The difference between these devices lays in their popular superstrate (CdTe) and substrate (CIGS) configurations. In superstrate configuration devices, the sunlight enters the absorber through the glass substrate and transparent conductive oxide layer (TCO, usually SnO_2:F) while only through the TCO layer (usually ZnO:Al) in substrate configuration. These design features are not of fundamental importance from the point of view of the physical processes taking place, but demand different device fabrication technologies. The physical models used for the interpretation of the CdTe solar cell characteristics has been successfully applied with some modifications to the CIGS devices [6,7].

Based on the above reasoning, in this chapter a detailed analysis of the optical and recombination losses in CIGS devices are presented, which are important causes of poor quantum efficiency (QE), leading to low solar-to-electric energy conversion efficiency in solar cells. A quantitative determination of the losses is presented and some possible pathways to reduce them are identified. Calculations of the optical losses are carried out using the optical constants, refractive indices and extinction coefficients, of the materials used. Equally important are the recombination losses, which are determined using the continuity equation considering the drift and diffusion components of the photocurrent and all possible recombination losses. In order to discuss the influence of the electrical parameters of the heterojunction on the photoelectric conversion efficiency of the device, an analysis of the current-voltage characteristics recorded in dark and under illumination is also included in this chapter. It seems that the analysis of the physical process involved in the photoelectric conversion is useful from a practical point of view since undoubted successes in the development of efficient CIGS solar cells have been achieved mainly empirically [8].

2. Optical constants and related material parameters

Three typical cases, with distinct bandgaps for the CIGS absorber E_g=1.02–1.04 eV (x=0), E_g=1.14–1.16 eV ($x \approx 0.3$) and E_g=1.36–1.38 eV (x=0.6 – 0.65) are considered for the analysis. The absorber with bandgap in the range 1.14-1.16 eV is widely utilized in the industry for the mass

http://dx.doi.org/10.5772/59363

production of solar modules, however, material with bandgap in the range 1.36 – 1.38 eV is promising to achieve the theoretically optimal value for maximum efficiency 28–30%.

Fig. 1 shows the schematic representation of a typical CIGS solar cell architecture, where the notations corresponding to the optical constants n_i and κ_i and the reflection coefficients R_{ij} at the interfaces used in the calculations are indicated.

Photoelectric conversion in these solar cells occurs in the CIGS absorber with a thickness of about 2 μm, while a thin n-type CdS buffer layer (20–50 nm) serves as the heterojunction partner and the window through which the radiation penetrates into the absorber. The Al doped ZnO layer serves as TCO with a thickness of 100–500 nm. Application of an undoped high-resistivity i-ZnO layer with thickness in the range 20–50 nm between TCO and CdS is very common in both substrate and superstrate configuration devices. In efficiency solar cells, an antireflection layer MgF_2, generally of ~ 100 nm thick is also deposited onto the front surface of ZnO.

In the QE calculations of CdS/CIGS cell, one needs to know the optical transmission of the ZnO/CdS structure $T(\lambda)$, which is determined by reflections from the interfaces air/ZnO, ZnO/CdS and CdS/CIGS and absorption in the ZnO and CdS layers. For estimating the transmission $T(\lambda)$, it is necessary to know the refractive indices n_i and extinction coefficients κ_i of ZnO, CdS and CIGS. According to the Fresnel equations, when the light is at near-normal incidence, the reflection coefficients (reflectances) from three interfaces R_{12}, R_{23} and R_{34} (see Fig. 1) can be calculated as

$$R_{ij} = \frac{\left| n_i^* - n_j^* \right|^2}{\left| n_i^* + n_j^* \right|^2} = \frac{(n_i - n_j)^2 + (\kappa_i - \kappa_j)^2}{(n_i + n_j)^2 + (\kappa_i + \kappa_j)^2}, \quad (1)$$

where n_i^* and n_j^* are the refractive indices of the materials, which account for light absorption containing imaginary parts and are written as $n_i^* = n_i - i\kappa_i$ and $n_j^* = n_j - i\kappa_j$.

Fig. 2 shows the spectral dependences of n and κ for ZnO taken from [8] and [10], CdS from [11] and CIGS from [12] (in some cases the extinction coefficient was determined using the relation $\kappa = \alpha\lambda/4\pi$, where α is the absorption coefficient).

It is worth to note the fact that for CIGS, the extinction coefficient in the photon energy range $h\nu < E_g$ ($\lambda > \lambda_g$) has a value of 0.04-0.05, which corresponds to an absorption coefficient $\alpha = 4\pi\kappa/\lambda = (4\text{-}5)\times10^3$ cm^{-1} [12]. With such values of α, a fairly high efficiency should be obtained for the solar cell, but, in fact, this is not observed. At $\lambda > \lambda_g = hc/E_g$, the quantum efficiency decreases quite rapidly with wavelength up to zero within a range about 120-150 nm above λ_g.

This extended QE response can be explained by the presence of so-called 'tails' of the density of states in the bandgap of the semiconductor with strong doping or/and disordered crystal structure. In this case, the electron wave functions and force fields of impurity atoms overlap,

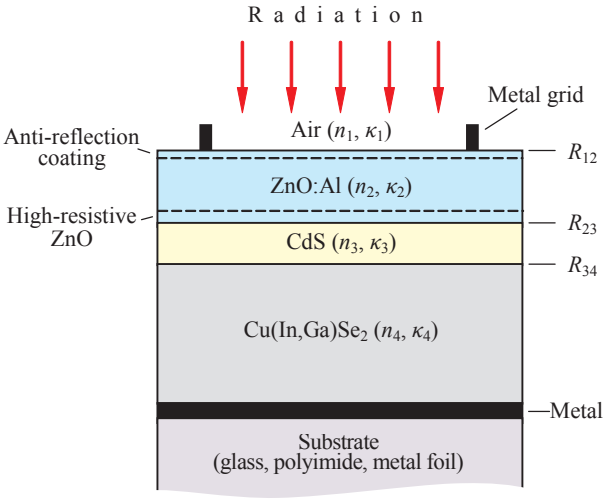

Figure 1. Schematic representation of a typical CIGS solar cell [9].

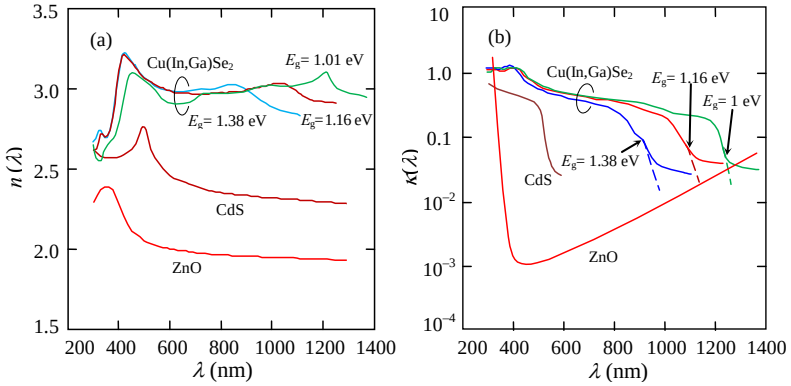

Figure 2. Wavelength dependences of the refractive indices (a) and extinction coefficients (b) of ZnO, CdS, $CuInSe_2$, $CuIn_{0.69}Ga_{0.31}Se_2$ and $CuIn_{0.34}Ga_{0.66}Se_2$.

whereby the discrete impurity levels are broadened and transformed into an impurity band. At a certain critical impurity (defect) concentration, this band joins with the conduction (valence) band, i.e., the tails of the density of states appear. The absorption coefficient in the range of tail depends exponentially on the photon energy, i.e., $\alpha(h\nu) \propto \exp[-(E_g - h\nu)/E_o)$, where E_o is a spectral independent value. Such spectral dependence is sometime called the Urbach rule (E_o can be proportional to kT at sufficiently high T). In this case, in order for the electron to make an interband transition and take part in the formation of the photocurrent, the electron must get the energy, which is equal to or greater than E_g. In the case of the tail

absorption at $h\nu < E_g$ this transition occurs because part of the energy, equal to $h\nu$, electron gets from photon, while the deficit ($E_g - h\nu$) is covered by phonons (the so-called multiphonon transitions). The probability of the multiphonon process decreases exponentially with lowering the $h\nu$, reproducing the spectral curve of photocurrent but with a stronger dependence on $h\nu$ compared with the density of states and the absorption curve (in the tails of state density some of the transitions occur without phonon participation) [13]. It is important to mention that an electron excited due to the absorption of a photon with energy $h\nu < E_g$ takes part in the photocurrent formation just as in the case of absorption of a photon with energy $h\nu \geq E_g$.

Based on the above comments, it is valid to use the $\kappa(\lambda)$ curves of CIGS corrected in the long-wavelength region as shown in Fig. 2b by dashed lines. Anticipating the tail effect, it can be noted that the spectrum at $h\nu < E_g$ makes a relatively small contribution to the photocurrent in solar cells: 1.0 % (0.5 mA/cm^2), 1.1% (0.4 mA/cm^2) and 1.9% (0.6 mA/cm^2) respectively for the absorber bandgaps 1.04, 1.16 and 1.38 eV.

In the range $h\nu \geq E_g$, the absorption coefficient follows the law for a direct-gap semiconductor:

$$\alpha = \alpha_o (h\nu - E_g)^{1/2} / h\nu \ . \tag{2}$$

The above correction of the spectral curves (Fig. 2b) does not exclude the possibility of determining the bandgaps of the samples by using Eq. (2) and the experimental values of α as illustrated in Fig. 3.

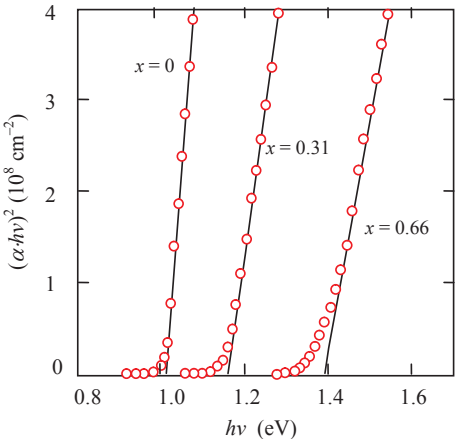

Figure 3. Dependence of the absorption coefficient α of $CuIn_{1-x}Ga_xSe_2$ on the photon energy $h\nu$ in accordance with Eq. (2).

The intercept of the extrapolated straight line portions on the photon energy $h\nu$ axis corresponds to the bandgaps of the discussed materials. The estimated bandgaps are 1.02, 1.16 and

1.38 eV for $CuInSe_2$, $CuIn_{0.69}Ga_{0.31}Se_2$ and $CuIn_{0.34}Ga_{0.66}Se_2$, respectively. The wavelengths corresponding to these bandgaps are indicated on the extinction coefficient data in Fig. 2b by arrows.

3. Optical losses caused by reflection and absorption

The optical transmission $T(\lambda)$ through the multilayer ZnO/CdS/CIGS structure shown in Fig. 1 can be written as

$$T(\lambda) = T_{gr}(1 - R_{12})\exp(-\alpha_2 d_2)(1 - R_{23})\exp(-\alpha_3 d_3)(1 - R_{34}). \quad (3)$$

Here R_{12}, R_{23} and R_{34} are the reflection coefficients at the interfaces air/ZnO, ZnO/CdS and CdS/CIGS respectively, whereas the absorption in ZnO and CdS are represented by $\exp(-\alpha_2 d_2)$ and $\exp(-\alpha_3 d_3)$, where α_2 and α_3, d_2 and d_3 are the absorption coefficients and thicknesses of the ZnO and CdS layers, respectively.

In order to minimize current losses in PV module, thin metal grids are deposited onto the front surface of ZnO, which serve as lateral current collectors. But these grids cause shadowing and a factor T_{gr} is included in Eq. (1) to take care of this effect. In practical modules, the grids are made very narrow and thin such that it shades only about 4–5% of the front area of the ZnO layer. The T_{gr} value can be set to 0.95 without introducing much loss [8].

The effect of an antireflection coating is not considered in Eq. (3), which can significantly reduce the reflectance of the front surface R_{12}. The commonly used antireflection coating for ZnO is MgF_2 which has the refractive index n_{arc} close to the theoretical optimal value $(n_2)^{1/2}$, where n_2 is the refractive index of ZnO. Fig. 4 compares the refractive indices n_{arc}, n_2 and $(n_2)^{1/2}$ in the wavelength region 300 to 1100 nm.

The reflection coefficient R_{arc} of a material with an antireflection coating can be written as [14]:

$$R_{arc} = \frac{r_f^2 + r_b^2 + 2r_f r_b \cos(2\beta)}{1 + r_f^2 r_b^2 + 2r_f r_b \cos(2\beta)}, \quad (4)$$

where r_f and r_b are the Fresnel coefficients, which are the amplitude values of reflectivity from the front and back surfaces of the antireflection material:

$$r_f = \frac{n_{arc} - n_1}{n_{arc} + n_1}, \quad (5)$$

http://dx.doi.org/10.5772/59363

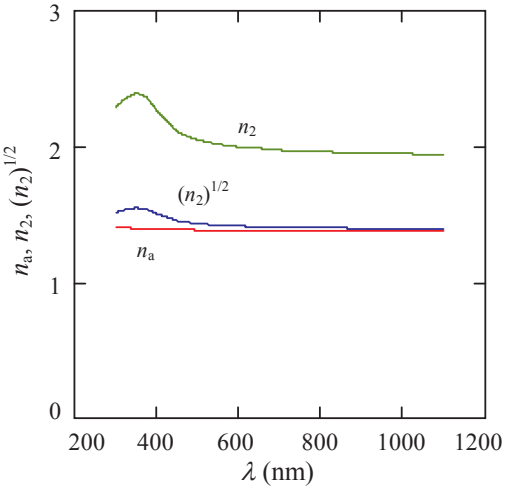

Figure 4. Comparison of the spectral dependences of the refractive indices for ZnO (n_2), MgF_2 (n_{arc}) and $(n_2)^{1/2}$ [9]

$$r_b = \frac{n_2 - n_{arc}}{n_2 + n_{arc}}, \tag{6}$$

and

$$\beta = \frac{2\pi}{\lambda} n_{arc} d_{arc}. \tag{7}$$

Fig. 5a shows a comparison of the reflectance of the bare ZnO surface (curve *1*) and that coated with a 100 nm thick MgF_2 (curve *2*). A comparison of the two curves reveals a significant decrease in reflection in the 500-800 nm region due to the antireflection coating. The observed peak in reflectance at $\lambda < 500$ nm does not produce a significant effect in solar cell performance since the intensity of solar radiation decreases at short wavelength $\lambda < 400$ nm. In addition, the region below 500 nm is dominated by absorption in the CdS film and the ZnO layer. On the contrary, increase in the reflectance at $\lambda > 600$ nm affect the solar cell performance significantly.

So, for taking into account antireflective coating, the reflection coefficient R_{12} in Eq. (3) for the transmission should be replaced by the coefficient R_{arc}, which is determined by Eq. (4):

$$T(\lambda) = T_{gr}(1 - R_{arc})\exp(-\alpha_2 d_2)(1 - R_{23})\exp(-\alpha_3 d_3)(1 - R_{34}). \tag{8}$$

Fig. 5b illustrates the impact of antireflective coating on the transmission property of ZnO/CdS layers in CIGS solar cells.

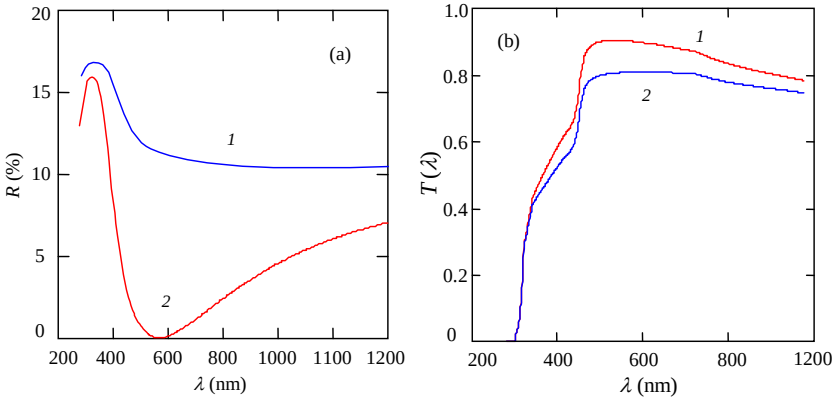

Figure 5. (a) Comparison of the reflectivity of bare ZnO surface (curve *1*) and that coated with MgF_2 (curve 2). (b) The optical transmission through the ZnO/CdS layers; curve *1* corresponds to ZnO with MgF_2 coating, and curve 2 in the absence of MgF_2 [9].

3.1. Reflection and absorptive losses

From a practical point of view, it is important to assess the various types of losses due to reflections from the interfaces and absorption in the ZnO and CdS layers.

Reflection loss at an interface can be determined using Eq. (8) as the difference between the photon flux that incident on the interface and that passed through it. Absorptive losses can be found from the difference between the photon flux entered the layer and that reached the opposite side.

An estimate of the decrease in solar cells performance due to the optical losses can be obtained by calculating the photocurrent density *J*. The value of *J* for the spectral distribution of AM1.5 global solar radiation is calculated using the Table of International Organization for Standardization ISO 9845-1:1992 [15]. Taking Φ as the incident spectral radiation power density and $h\nu$ the photon energy, then the spectral density of the incident photon flux is $\Phi/h\nu$ and one can write *J* as

$$J = q\sum_i T(\lambda_i)\frac{\Phi_i(\lambda_i)}{h\nu_i}\Delta\lambda_i, \tag{9}$$

where q is the electron charge, $\Delta\lambda_i$ is the interval between the neighboring values of λ_i in the ISO table.

Assuming that the solar radiation is negligible for $\lambda < 300$ (> 4.1 eV), the summation in Eq. (9) should be made over the spectral range from λ=300 nm to $\lambda=\lambda_g=hc/E_g$. The corresponding upper limits of the wavelength λ_g for CIGS solar cell with the bandgap of the absorber E_g=1.02–1.04, 1.14–1.16 and 1.36–1.38 eV are ~ 1200, 1080 and 900 nm respectively.

http://dx.doi.org/10.5772/59363

Analyzing the optical losses, we assume that the QE of the solar cell η=1, therefore Eq. (9) does not contain η. If the transmission through ZnO/CdS are also taken as 100%, then the photocurrent density J for the $CuInSe_2$, $CuIn_{0.69}Ga_{0.31}Se_2$ and $CuIn_{0.34}Ga_{0.66}Se_2$ solar cells would be equal to J_o=47.1, 42,0 and 33.7 mA/cm^2, respectively. However, for real situations where there are reflection and absorption losses even with antireflection coating the J value becomes equal to 38.4, 33.9 and 27.5 mA/cm^2 respectively and if there is no antireflection coating the corresponding values are 35.0, 30.8 and 24.8 mA/cm^2. It follows that the antireflection coating increases the photocurrent density J by 3.4, 3.1 and 2.7 mA/cm^2, respectively for the CIGS absorbers discussed above.

It is convenient to report the optical and other types of losses in percentage. Below, all the losses in percentage we will determine relatively to the photocurrent generated by the photon flux incident on the solar cell J_o, i.e., to the above values 47.1, 42,0 and 33.7 mA/cm^2 for the solar cells with the absorber bandgap 1.02–1.04, 1.14–1.16 and 1.36–1.38 eV, respectively. The calculations show that the antireflection coating increases the photocurrent density J by 7.1, 7.4 and 8.0%, for these solar cells, respectively.

Fig. 5a shows that the zero reflectance of ZnO with an antireflection coating takes place at the wavelength of 570 nm for a 100 nm thick layer of MgF_2 that corresponds approximately to the maximum of the solar radiation under the AM1.5 conditions. According to Eq. (4) and (7), the position of the reflectance minimum of the curve *2* depends on the thickness of antireflection coating d_{arc}.

It is interesting to see how the photocurrent density J (which takes into account the spectral distribution of solar radiation) depends on the thickness of the layer d_{arc}. The calculated dependences of decrease in $\Delta J/J_o$ on d_{arc} are shown in Fig. 6 for three samples of the studied solar cells. As seen, the losses are minimal when the thickness of the MgF_2 film is in the range of 105–115 nm that is close to the thickness commonly used of MgF_2 film but the losses become significant when the MgF_2 thickness is below or above the 105-115 nm range. Note that the reflection losses reach the range 9.3–12.4% in the absence of antireflection coating while with coating it is only 1.4–1.9%.

Next the results of calculations of the reflection losses at all interfaces and the absorptive losses in the ZnO and CdS layers are given for solar cells under study.

The losses due to reflection from the front surface of ZnO with an antireflection coating of a 100 nm thick MgF_2 layer in $CuInSe_2$, $CuIn_{0.69}Ga_{0.31}Se_2$ and $CuIn_{0.34}Ga_{0.66}Se_2$ solar cells are equal to 1.9, 1.5 and 1.4%, respectively. Using Eqs. (8) and (9) the calculated values of the reflection loss at the ZnO/CdS interface are 0.9, 0.9 and 1.0% respectively for these solar cells, whereas for the CdS/CIGS interfaces in the three cases the corresponding losses are 1.3, 1.2 and 1.1%, respectively.

Low reflection losses at the interfaces are due to the close values of the optical constants of different layers. This is illustrated in Fig. 7 by plotting the calculated values of the reflectance for ZnO, CdS and $CuIn_{0.33}Ga_{0.67}Se_2$ in the air and in optical contacts with each other. As seen, at the 700 nm region the reflection coefficients at the interfaces (air/MgF_2)/ZnO, ZnO/CdS and CdS/CIGS are 10–17 times smaller than those at the interfaces air/ZnO, air/CdS and air/CIGS.

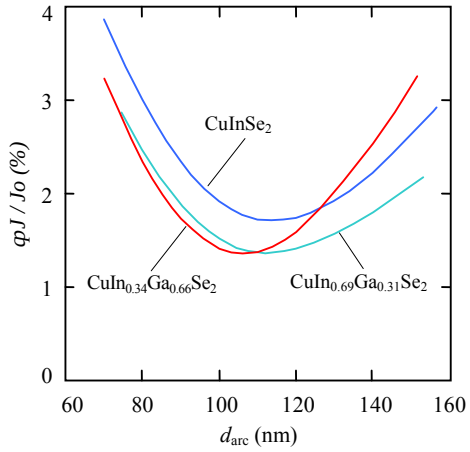

Figure 6. Relation between percentage photocurrent loss and thickness of antireflection coating applied on the ZnO surface for $CuInGaSe_2$, $CuIn_{0.69}Ga_{0.31}Se_2$ and $CuIn_{0.34}Ga_{0.66}Se_2$ solar cells.

The sharp increase in reflectance at $\lambda < 500$ nm for the (air/MgF_2)/ZnO interface does not produce a significant effect, which is discussed above.

Absorption losses in the 300 nm thick ZnO and 40 nm thick CdS layers are larger as compared to reflection losses and equal respectively to 2.9 and 5.2% for $CuInSe_2$, 2.2 and 5.6% for $CuIn_{0.69}Ga_{0.31}Se_2$ and 1.9 and 7.7% for $CuIn_{0.34}Ga_{0.66}Se_2$ solar cell. The difference in losses for the three types of samples is due to the difference in their bandgaps.

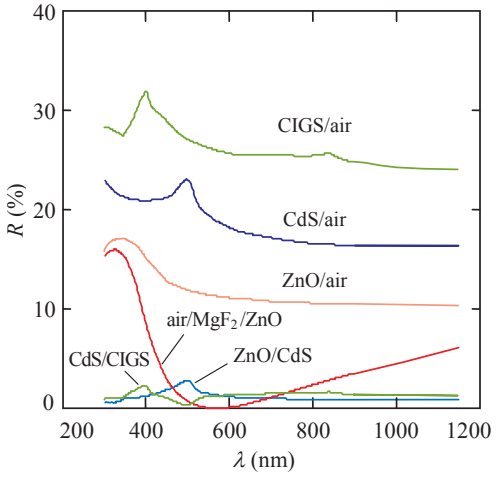

Figure 7. Reflectivity spectra of (MgF_2)ZnO, CdS and $CuIn_{0.34}Ga_{0.66}Se_2$ films in contact with air and other materials [9].

http://dx.doi.org/10.5772/59363

It seems that reflection losses cannot be reduced by virtue of their nature whereas the absorption losses can be reduced by thinning the CdS and ZnO layers. The data in Fig. 8 give some indication of a possible way of lowering these absorption losses. As seen, for d_{CdS}=40 nm, the loss is about 1-3% when the ZnO layer thickness is in the range of 100-500 nm, and when the layer is thinner (100-200 nm) the loss reduces to ~ 1%. The loss due to absorption in CdS layer (Fig. 8b) is higher, 4-5%, even at its lowest thickness of 20-30 nm. It seems that by thinning the CdS and ZnO layers the absorption losses may be limited to 2–3%.

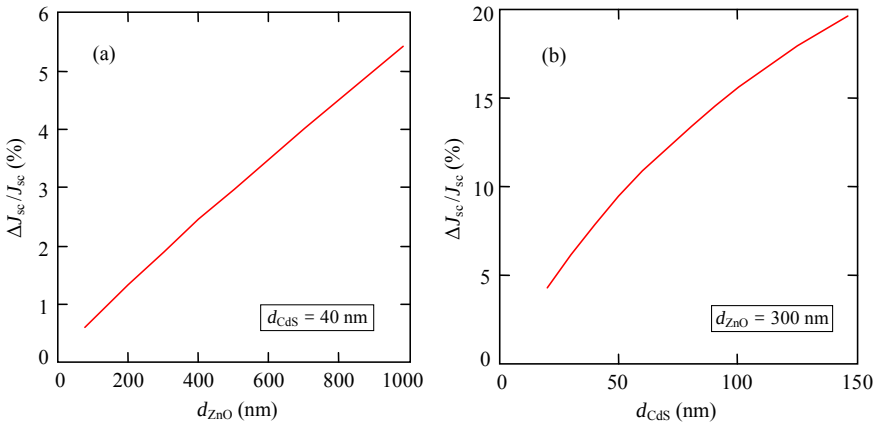

Figure 8. Dependences of the losses caused by absorption in the CdS and ZnO layers on their thicknesses [9].

The calculated values of optical losses along with the corresponding decrease in the photocurrent *J* given in brackets are summarized in Table 1. Note that the calculated data of optical losses are largely in agreement with the results reported in literature, but there are exceptions also. For example, according to our calculations, the reflection losses in $CuIn_{0.69}Ga_{0.31}Se_2$ solar cell (without shading from grid) is equal to 4.0 mA/cm^2 and in reference [8] it amount to 3.8 mA/cm^2, indicating similarity. However, the absorption losses in the CdS film for $CuIn_{0.69}Ga_{0.31}Se_2$ and $CuIn_{0.34}Ga_{0.66}Se_2$ solar cells in our calculations are equal to 2.6–2.9 A/cm^2 and only 0.8 mA/cm^2 in [8]. The losses due to insufficient absorptivity of the CIGS absorber also differ considerably being equal to < 0.1 and 1.9 mA/cm^2, respectively.

Origin of optical losses	Losses in solar cell		
	$CuInSe_2$	**$CuIn_{0.69}Ga_{0.31}Se_2$**	**$CuIn_{0.34}Ga_{0.66}Se_2$**
Reflection losses			
Air/ZnO interface with ARC	2.5% (0.8 mA/cm^2)	1.9% (0.6 mA/cm^2)	1.4% (0.5 mA/cm^2)
ZnO/CdS interface	0.9% (0.4 mA/cm^2)	0.9% (0.4 mA/cm^2)	1.0% (0.4 mA/cm^2)
CdS/CIGS interface	1.3% (0.7 mA/cm^2)	1.2% (0.6 mA/cm^2)	1.1% (0.4 mA/cm^2)

Origin of optical losses	Losses in solar cell		
	$CuInSe_2$	$CuIn_{0.69}Ga_{0.31}Se_2$	$CuIn_{0.34}Ga_{0.66}Se_2$
Total reflection losses	4.7% (1.9 mA/cm^2)	4.0% (1.6 mA/cm^2)	3.5% (1.3 mA/cm^2)
Absorption losses			
Absorption in ZnO	2.9% (1.5 mA/cm^2)	2.2% (1.1 mA/cm^2)	1.9% (0.7 mA/cm^2)
Absorption in CdS	5.2% (2.7 mA/cm^2)	5.6% (2.9 mA/cm^2)	7.7% (2.6 mA/cm^2)
Insufficient absorptivity	0.6% (0.1 mA/cm^2)	0.2% (0.1 mA/cm^2)	0.4% (0.1 mA/cm^2)
Total absorption losses	8.1% (4.3 mA/cm^2)	7.8% (4.1 mA/cm^2)	9.6% (3.4 mA/cm^2)
Total optical losses with grid shading	17.4% (9.4 mA/cm^2)	16.0% (9.0 mA/cm^2)	17.5% (7.3 mA/cm^2)

Table 1. Optical and the corresponding photocurrent losses in CIGS solar cells

3.2. Effect of multiple reflection in ZnO and CdS layers

In the calculations outlined in Section 3.1, we omitted the multiple reflections and interference effects in the ZnO and CdS layers, although they occur like those in antireflection coating (oscillations in CIGS are suppressed by strong absorption of the material). It should be noted that the periodic oscillations in the quantum efficiency spectra of the CIGS solar cells, originating from the interference effects, in many cases are not observed. To explain this fact, we calculated the optical transmission of the ZnO/CdS layered structure taking into consideration multiple reflections [9] and using the formula for the double-layer antireflection coatings [16]:

$$R_{\mathrm{dl}} = \frac{r_1^2 + r_2^2 + r_3^2 + r_1^2 r_2^2 r_3^2 + 2r_1 r_2 (1 + r_3^2)\cos(2\,\beta_1) + 2r_2 r_3 (1 + r_1^2)\cos(2\beta_2) + 2r_1 r_3 \cos(2\beta_1 + 2\beta_2)}{1 + r_1^2 r_2^2 + r_2^2 r_3^2 + r_1^2 r_3^2 + 2r_1 r_2 (1 + r_3^2)\cos(2\beta_1) + 2r_2 r_3 (1 + r_1^2)\cos(2\beta_2) + 2r_1 r_3 \cos(2\beta_1 + 2\beta_2)}, \tag{10}$$

where r_1, r_2, and r_3 are the amplitude reflection coefficients for the air/ZnO, ZnO/CdS and CdS/CIGS interfaces:

$$r_1^2 = \frac{(1 - n_2)^2 + (\kappa_2)^2}{(1 + n_2)^2 + (\kappa_2)^2}, \tag{11}$$

$$r_2^2 = \frac{(n_2 - n_3)^2 + (\kappa_2 - \kappa_3)^2}{(n_2 + n_3)^2 + (\kappa_2 + \kappa_3)^2}, \tag{12}$$

$$r_3^2 = \frac{(n_3 - n_4)^2 + (\kappa_3 - \kappa_4)^2}{(n_3 + n_4)^2 + (\kappa_3 + \kappa_4)^2}, \tag{13}$$

http://dx.doi.org/10.5772/59363

n_2, n_3, n_4 and n_2, n_3, n_4 are the refractive indices and extinction coefficients of ZnO, CdS and CIGS, respectively,

$$\beta_1 = \frac{2\pi}{\lambda} n_2 d_{\mathrm{ZnO}}, \tag{14}$$

$$\beta_2 = \frac{2\pi}{\lambda} n_3 d_{\mathrm{CdS}}. \tag{15}$$

Considering a grid contact at the front surface of the ZnO layer and using Eq. (10), one can write the expression for the transmission of the ZnO and CdS layers:

$$T(\lambda) = T_{\mathrm{gr}}(1 - R_{\mathrm{dl}}), \tag{16}$$

where T_{gr} takes into account the shadowing by grid on the front surface of ZnO.

The curve labeled *1* in Fig. 9 shows the calculated transmittance using Eq. (10) and (16) for $CuIn_{0.7}Ga_{0.3}Se_2$ solar cell, and the used parameters are T_{gr}=0.95, d_{ZnO}=300 nm, d_{CdS}=40 nm. The oscillations in the transmission spectrum are clear though the amplitude is small. The small amplitude may be due to the low reflectance from the interfaces since the refractive indices of the contacting layers are close to each other. This is confirmed by the fact that the amplitude of oscillations increases almost twice when the transmission is calculated without antireflective layer on the ZnO front surface.

Eq. (10) describes the oscillations in the reflection spectra due to interference effects in the ZnO and CdS layers, however it does not take into account absorption in these layers. When extinction coefficient κ is small the oscillations due absorption in the layers are visible, but for higher κ the oscillations cannot be observed at all. We can take into account the absorption of solar radiation for one passage in the ZnO and CdS layers by entering in the right side of Eq. (16) the exponential factors appearing in Eqs. (3) and (8):

$$T(\lambda) = T_{\mathrm{gr}}(1 - R_{\mathrm{dl}})\exp(-\alpha_2 d_2)\exp(-\alpha_3 d_3). \tag{17}$$

The results of calculations using Eq. (17) are shown in Fig. 9 as curve *2*. As seen, the oscillation amplitude in the spectral range $\lambda > 500$ nm, where the absorption in ZnO and CdS is weak has remained almost unchanged, but in the range of the interband transitions in CdS at $\lambda < 500$ nm, the amplitude decreased significantly.

The spectrum *3* in Fig. 9 was obtained by using Eq. (3) with $R_{\mathrm{arc}}=R_{12}$, i.e., without considering the multiple reflections in the ZnO and CdS layers. As it is clear from figure, when multiple reflections are considered (spectrum 2) only minor periodic deviations occur from spectrum

3. When calculating the photocurrent density of a solar cell, which is the sum of the current over the entire spectral range, ignoring multiple reflections should not cause significant errors. In fact, photocurrent density calculated using Eqs. (8) and (17) for $T(\lambda)$ shows only a difference less than 0.5% for the studied solar cells.

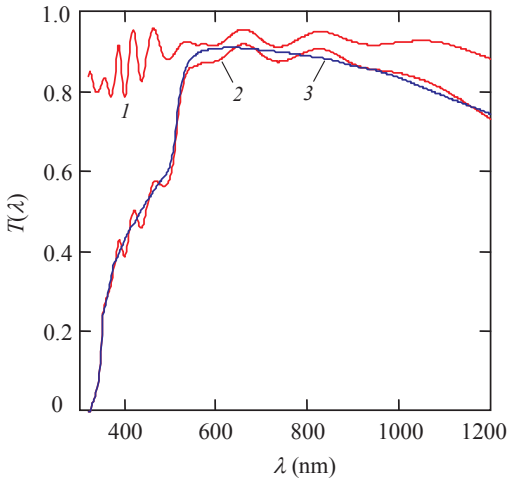

Figure 9. Transmission spectra of ZnO/CdS layers calculated by taking into account the multi-reflections but without considering absorption (line *1*), line 2 is the spectrum when the absorption in the ZnO and CdS layers is taken into account, and line 3 corresponds to case when multi-reflections are neglected [9].

It should also be borne in mind that the Eq. (17) has been deduced for flat, perfect and parallel interfaces air/ZnO, ZnO/CdS and CdS/CIGS. But real interfaces will be far away from the ideal conditions; hence the oscillations in the transmission spectra can be less than 0.5% or even not visible. In contrast, if the interfaces are perfect as mentioned above, the periodic variations in the transmission and photoresponse spectra of the devices will be clear [17].

3.3. Absorptive capacity of the CIGS absorber layer

In the previous sections while discussing the photocurrent, we assumed 100% light-to-electric conversion in the CIGS layer. However, there are losses related to the incomplete absorption of light in this layer. Considering this fact, while estimating the exact values of *integrated* absorptive capacity of the CIGS layer the spectral distribution of solar radiation and absorption coefficient of the material must be taken into account rather than determining the absorptive capacity for one wavelength in the range $h\nu > E_g$.

It should be noted that in the photon energy range from E_g to 4.1 eV electron-hole pairs arise independently of the energy absorbed. In other words, the energy needed for the band to band transition is less than the absorbed energy. So while considering the dependence of the absorptivity of solar radiation power A_Φ (rather than photon flux $A_{h\nu}$) on the thickness of the semiconductor this fact must be considered. For this reason, the number of electron-hole pairs,

http://dx.doi.org/10.5772/59363

and hence the photocurrent generated in the solar cell, is not proportional to the power of solar radiation. Hence, the dependences of A_{hv} and A_{Φ} on the thickness of the semiconductor are different and for calculation of the photocurrent, the absorptivity of photon flux A_{hv} should be used.

The *integrated* absorptive capacity of the semiconductor layer depends on two factors: (i) the spectral distribution of solar radiation, and (ii) the optical transmission of the ZnO and CdS layers that affect the spectral distribution of solar radiation reaching the absorber. With this consideration the integrated absorptivity can be taken as the ratio of the number of photons absorbed in the CIGS layer to the number of photons penetrated through the ZnO and CdS layers [18]:

$$A_{hv}(d) = \frac{\sum_i T(\lambda)\frac{\Phi_i}{h\nu_i}[1-\exp(-\alpha_i d)]\,\Delta\lambda_i}{\sum_i T(\lambda)\frac{\Phi_i}{h\nu_i}\Delta\lambda_i}. \quad (18)$$

Here summation is for the spectral range starting from λ=300 nm and the upper limit depends on the E_g of the material, which corresponds to λ=1200, 1080 or 900 nm respectively for $CuInSe_2$, $CuIn_{0.69}Ga_{0.31}Se_2$ and $CuIn_{0.34}Ga_{0.66}Se_2$ solar cells.

According to Eq. (18) for $CuInSe_2$, $CuIn_{0.69}Ga_{0.31}Se_2$ and $CuIn_{0.34}Ga_{0.66}Se_2$ solar cells, 99.4, 99.6 and 99.8% photon absorption happens for a layer thickness of 2 μm. But with a layer thickness of 1 μm the photon absorptivity values for these solar cells are equal to 97.0, 98.3 and 97.7% respectively, i.e., optical losses become noticeable. On the other hand, in another direct-gap semiconductor CdTe the photon absorptivity of 99.4–99.8% takes place at a thickness of about 30 μm [18].

It should also be borne in mind that CIGS solar cell is a substrate configuration device having metallic substrate as one of the electrodes. This implies that long wavelength radiation with low absorption coefficient can reflect back from the rear surface. In the event of 100% reflectance from the back surface, the absorptivity is the same as for the double thickness of the absorber layer, i.e., the $A_{hv}(d)$ value in such a solar cell can be found by doubling the thickness d in Eq. (18). This means that 99.4–99.8% photon absorption in CIGS takes place at a thickness of 1 μm rather than 2 μm.

4. Recombination losses

Electrons and holes (electron-hole pairs) created as a result of photon absorption in the space charge region (SCR) of CdS/CIGS heterostructure move apart under the influence of the junction built-in voltage. The electrons move towards to CdS side and reach the front metal grid contact after passing through the ZnO layer, while holes move to the neutral part of the CIGS layer and reach the Mo back contact. Not all the photogenerated carriers contribute to

the current; some of the carriers recombine in the SCR before reaching the contacts. Recombination can also occur at the front surface of the absorber contacting with the CdS film. Minority carriers (electrons), which are generated outside the SCR, also take part in the formation of the photocurrent, when electrons reach the SCR as a result of diffusion. This process competes with the recombination of electrons with the majority carriers (holes) in the neutral part of the absorber. Finally, recombination of electrons can occur on the back surface of the absorber, i.e., at the CIGS/metal interface.

For a given thickness of the absorber, the recombination losses depend mostly on the carrier lifetime and the width of the SCR, which in the case of a semiconductor containing both acceptor and donor type impurities are determined by the concentration of uncompensated acceptors $N_a - N_d$. Therefore, investigating the influence of the material parameters on the recombination losses, we will calculate the dependence of photocurrent J on $N_a - N_d$ for several values of carrier lifetimes.

Consideration of the statistics in a nonequilibrium state leads to the conclusion that the lifetimes of electrons τ_{no} and holes τ_{po} in the SCR are approximately equal to the lifetime of minority carriers in heavily doped respectively p-and n-type materials [19]. We assume that in the CIGS solar cell, the absorber is a heavily doped semiconductor (hole concentration is about 10^{15}–10^{16} up to 10^{17} cm^{-3} [8, 21].

The recombination losses can be judged by the value of photocurrent density J using the formula:

$$J = q\sum_i \frac{\Phi_i(\lambda)}{h\nu_i}\, T(\lambda)\eta_{\text{int}}(\lambda)\Delta\lambda_i, \tag{19}$$

where $T(\lambda)$ is the optical transmission of the ZnO and CdS layers, and $\eta_{\text{int}}(\lambda)$ is the internal quantum efficiency of photoelectric conversion.

The CdS/CIGS solar cell is generally treated as an abrupt asymmetric p-n heterostructure, in which the SCR (depletion layer) is practically located in the p-CIGS and the photoelectric conversion takes place almost in this layer (see [8] and references therein). The potential and field distributions in abrupt asymmetric p-n junction are practically the same as in a Schottky diode, therefore, further consideration of the processes in CdS/CIGS solar cells can be studied on the basis of the concepts developed for Schottky diodes.

The exact expression for the photovoltaic quantum efficiency of a p-type semiconductor Schottky photodiode obtained from the continuity equation taking into account the recombination at the front surface has the form [21]:

$$\eta(\alpha) = \frac{1 + S_f / D_p \exp(-W^2 / W_o^2)\ \ [A(\alpha) - D_p \Delta n / \Phi]}{1 + (S_f / D_p)\ \exp(-W^2 / W_o^2)\ B} - \frac{\exp(-\alpha W)}{1 + \alpha L_n} - \frac{D_n}{L_n}\frac{\Delta n}{\Phi}, \tag{20}$$

http://dx.doi.org/10.5772/59363

where α is the absorption coefficient, S_f is the recombination velocity at the front surface, D_n and D_p are the diffusion coefficients of electrons and holes, respectively, L_n is the diffusion length of electrons, Δn is the excess concentration of electrons at x=W, which is equal to

$$\Delta n = \Phi \frac{F_5}{D_p}. \tag{21}$$

In Eqs. (20) and (21)

$$F_5 = \frac{F_4 - F_3 \exp(-\alpha W)/(1+\alpha L_n)}{1 + F_3 / L_n}, \tag{22}$$

$$F_3 = \int_o^W \exp\{-[(x-W)/W_o]^2\}dx, \tag{23}$$

$$F_4 = \int_o^W \exp\{-\alpha x - [(x-W)/W_o]^2\}dx, \tag{24}$$

and the following notations are used:

$$W_o = \sqrt{\frac{2\varepsilon\varepsilon_o kT}{q^2(N_a - N_d)}}, \tag{25}$$

$$F_4 = \int_o^W \exp\{-\alpha x + [(x-W)/W_o]^2\}dx, \tag{26}$$

$$B = \int_0^W \exp[(x-W)/W_o]^2 dx, \tag{27}$$

where the $W_o / 2^{1/2}$ value is the Debye length.

In a CIS or CIGS with both acceptor and donor impurities, the SCR width W given in the above equations is determined by the expression [22]:

$$W = \sqrt{\frac{2\varepsilon\varepsilon_o(\varphi_{bi} - qV)}{q^2(N_a - N_d)}}, \tag{28}$$

where ε is the relative permittivity of CIGS (ε=13.6), ε_o is the permittivity of vacuum, and $N_a - N_d$ is the concentration of uncompensated acceptors (not the free hole density).

For the convenience in analyzing the dependence of η on the parameters of the diode structure, the expression (20) can be simplified.

In a solar cell, CIS or CIGS, with the barrier height from the semiconductor side φ_{bi} is of the order of 1 eV and the width of the SCR is about 1 μm, i.e., the electric field is close to 10^4 V/cm. At the boundary between the depletion layer and the neutral region (x=W), the photogenerated electrons are pulled into the SCR by strong electric field, and without causing error, one can assume that Δn=0 and disregard the terms containing Δn in Eq. (20) [21].

The integrand $f(x)$ in Eq. (24) decreases exponentially as x increases. Therefore, we can replace the integration by the multiplication of the maximum value of the function $\exp(W/W_o)^2$ by its "half-width", which is determined by the value of x_2 at the point where the value of $f(x)$ is smaller than the peak value by a factor e=2.71.

Thus, we can find the value of x that satisfies this condition from the equality:

$$\exp\{-\alpha x_2 + [(x_2 - W)/W_o]^2\} = \exp(W/W_o)^2 e^{-1} = \exp\left[(W/W_o)^2 - 1\right], \tag{29}$$

which is reduced to the quadratic equation

$$x_2^{\,2} - (\alpha W_o^2 + 2W)x_2 + W_o^2 = 0 \tag{30}$$

with the solution

$$x_2 = \frac{\alpha W_o^2 + 2W}{2}[1 - \sqrt{1 - 4W_o^2/(\alpha W_o^2 + 2W)^2}]. \tag{31}$$

Since the second term under the square root is much less than unity, $\sqrt{1-x} \approx 1 - x/2$,

$$x_2 \approx [\alpha + 2W/W_o^2]^{-1} = [\alpha + 2(\varphi_{bi} - qV)/2kTW]^{-1}. \tag{32}$$

Similarly, by replacing the integration in Eq. (23), we can obtain the expression for x_2 in the form

$$x_2 \approx [2(\varphi_{bi} - qV)/2kTW]^{-1}. \tag{33}$$

http://dx.doi.org/10.5772/59363

So, considering all the simplifications made for the photoelectric quantum yield it is possible to substitute Eq. (20) with the following expression:

$$\eta_{\text{int}} = \frac{1 + S_f / D_p \ [\alpha + (2/W)(\varphi_{bi} - qV) / kT]^{-1}}{1 + S_f / D_p \ [(2/W)(\varphi_{bi} - qV) / kT]^{-1}} - \frac{\exp(-\alpha W)}{1 + \alpha L_n}. \quad (34)$$

As an example comparison of the curves $\eta_{\text{int}}(\lambda)$, calculated using the exact Eq. (20) and Eq. (34) is shown in Fig. 10 in the case of the spectrum of $CuInSe_2$ solar cell.

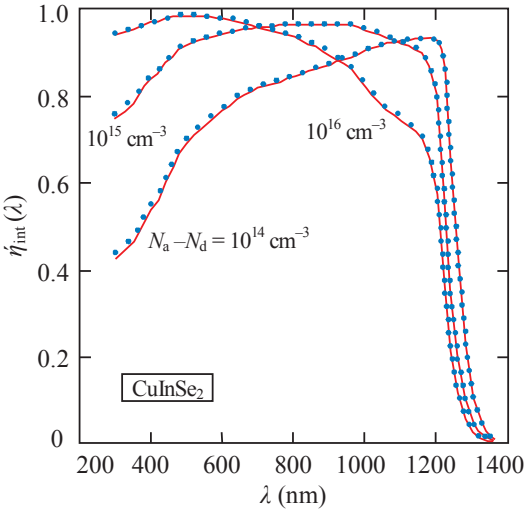

Figure 10. The quantum efficiency spectra of $CuInSe_2$ solar cell calculated by the exact formula (20) (solid line) and the simplified formula (34) (dotted line).

In the calculations we used the absorption curve $\alpha(\lambda)$ and typical parameters for this cell (see Table 2): barrier height φ_{bi}, the diffusion coefficients of electrons D_n and holes D_p, their mobility μ_n and μ_p, the electron lifetime τ_n (L_n=($\tau_n D_n$)$^{1/2}$), the surface recombination velocity S_f, and the concentration of uncompensated acceptors $N_a - N_d$ which varied in the range 10^{14}-10^{16} cm^{-3}. As seen, variation of $N_a - N_d$ modifies the shape of the $\eta_{\text{int}}(\lambda)$ spectra, but in all cases the curves calculated by Eqs. (20) and (34) are very close, i.e., Eq. (34) represents well the results of the exact calculation.

It should be bear in mind that Eq. (34) takes into consideration both the drift and diffusion components of the quantum efficiency but does not take into account recombination at the back surface of the absorber layer [21] which can result in significant losses in the case of a thin-film solar cell. In the case of CdS/CdTe cell, for example, it is possible to neglect the recombination at the back surface if the thickness of the absorber exceeds 4–5 μm. However,

solar cells with thinner layers are also of considerable interest. In this case, Eq. (34) is not valid, and the drift and diffusion components of the quantum efficiency should be separated.

To find an expression for the drift component of the photoelectric quantum yield one can use Eq. (34). Indeed, the absence of recombination at the front surface (S_f=0) transforms this equation into the known Gartner formula:

$$\eta = 1 - \frac{\exp(-\alpha W)}{1 + \alpha L_n}. \tag{35}$$

The above equation also ignores recombination at the back surface of the absorbed layer. Eq. (34) does not take into account recombination inside the SCR, therefore, subtracting the absorptive capacity of the SCR layer $1 - \exp(-\alpha W)$ from the right side of Eq. (34), we obtain the expression for the diffusion component of the quantum yield for a thick solar cell $\exp(-\alpha W)$ $\alpha L_n/(1+\alpha L_n)$ which ignores recombination at the back surface. Upon eliminating the diffusion component from the right side of Eg. (34) we come to the expression for the drift component of the quantum efficiency which take into account the surface recombination at the front surface of the absorber:

$$\eta_{drift} = \frac{1 + S_f / D_p \left(\alpha + 2(\varphi_{bi} - qV)/WkT\right)^{-1}}{1 + S_f / D_p \ \left(2(\eta_{ext}\varphi_{bi} - qV)/WkT\right)^{-1}} - \exp(-\alpha W). \tag{36}$$

For the diffusion component of the photoelectric quantum efficiency taking into account surface recombination at the back surface of the absorber layer, one can use the exact expression obtained for the p-layer in a solar cell with p-n junction [22]:

$$\eta_{dif} = \frac{\alpha L_n}{\alpha^2 L_n^2 - 1} \exp(-\alpha W) \times \\ \times \left\{ \alpha L_n - \frac{S_b L_n / D_n \left[\cosh[(d-W)/L_n] - \exp\left(-\alpha(d-W)\right) \right] + \sinh[(d-W)/L_n] + \alpha L_n \exp(-\alpha(d-W))}{(S_b L_n / D_n)\sinh[(d-W)/L_n] + \cosh[(d-W)/L_n]} \right\}, \tag{37}$$

where d is the thickness of the absorber layer and S_b is the recombination velocity at the back surface.

The internal quantum efficiency of photoelectric conversion in the absorber layer is the sum of the two components:

$$\eta_{int} = \eta_{drift} + \eta_{dif}, \tag{38}$$

whereas the external quantum efficiency can be written in the form

http://dx.doi.org/10.5772/59363

$$\eta_{ext} = T(\lambda)(\eta_{drift} + \eta_{dif}), \tag{39}$$

where $T(\lambda)$, as mentioned previously, is the optical transmission of the ZnO and CdS layers determined by Eq. (8).

Fig. 11 shows a comparison of the measured quantum efficiency spectra of $CuInSe_2$, $CuIn_{0.69}Ga_{0.31}Se_2$ and $CuIn_{0.34}Ga_{0.66}Se_2$ solar cells taken from [8] with the results of calculations using Eq. (39). Note that the data on the extinction coefficients (and hence the absorption coefficient α) used in this and following calculations were measured for E_g=1.02, 1.16 eV and E_g=1.38 eV [12] rather than 1.04, 1.14 and 1.36 eV, respectively [8] that explains the slight blue shift (10-20 nm) in the calculated long-wavelength edge of the spectra in Fig. 11.

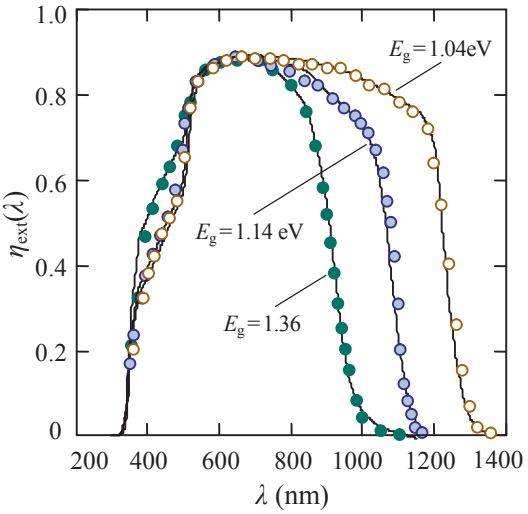

Figure 11. Comparison of the measured (circles) [8] and calculated (solid lines) quantum efficiency spectra of $CuInSe_2$ (E_g=1.04 eV), $CuIn_{0.76}Ga_{0.24}Se_2$ (E_g=1.14 eV) and $CuIn_{0.39}Ga_{0.61}Se_2$ (E_g=1.36 eV) solar cells.

According to the data in the above reference [8], in the calculations, the thicknesses of the CIGS, ZnO, CdS and MgF_2 layers were assumed to be 2000, 300, 20–50 and 100 nm, respectively. The parameters of the absorber layer were varied within the limits reported in the literature. It should be noted that for polycrystalline CIGS, there is a large spread in mobility values of electrons and holes. At room temperature, the values of the hole mobility are most often indicated in the range from 1–5 to 30–50 cm^2/(Vs) and from 1 to 100 cm^2/(Vs) for the electron mobility [23–25]. Unlike this, it was found in [26] that the electron and hole mobilities in $Cu(In,Ga)Se_2$ are much lower than 1 cm^2/(Vs). As mentioned in Section 2, we believe that such low mobilities refer to the charge transport in the sub-band joined with the conduction band (valence band) due to high doping or/and disorder in the crystal lattice. In contrast, electrons and holes arising as a result of absorption of photons with the energy $h\nu \geq E_g$ and involving in

the photocurrent formation are moving in the conduction and valence band, where their mobilities are much higher.

The lifetime of minority carriers (electrons), determining their diffusion length $L_n=(\tau_n D_n)^{1/2}$ has also a significant impact on the efficiency of solar cells. As reported back in 1996 [27], the lifetimes of electrons in $CuInSe_2$ are in the range of tens of picoseconds to a few nanoseconds, which was subsequently confirmed in [23, 28]. Lifetime of minority carriers affects the diffusion component of photocurrent and therefore reveals itself in the long-wavelength range ($\lambda >$ 600-700 nm) of the spectrum.

Yet another important parameter determining the quantum efficiency spectra of solar cells is the concentration of uncompensated acceptors $N_a - N_d$ in the absorber, which according to Eq. (28) determines the width of the SCR. At high $N_a - N_d$, the width of the SCR amounts to a small portion of the absorber thickness. With decreasing $N_a - N_d$, the efficiency of cell increases since more and more part of the radiation is absorbed in the SCR, where the photogenerated electrons and holes move apart in the opposite directions by the electric field and reach the contacts without recombination. However, an increase of the quantum efficiency due to expansion of the SCR occurs only to a certain extent, because with increasing W, the electric field in the SCR is weakened and, therefore, recombination at the front surface of the absorber layer is intensified. As a result, the quantum efficiency in the low wavelength region reduces.

The velocity of recombination at the front surface S_f affects the efficiency in a wide range of wavelengths (excluding the long wavelength part) and more stronger in a wider SCR.

Our calculations in section 4.3 show that recombination at the rear surface of 2 μm thick absorber layers of $CuInSe_2$, $CuIn_{0.76}Ga_{0.24}Se_2$ and $CuIn_{0.39}Ga_{0.61}Se_2$ manifests itself very weakly and only for long lifetimes of electrons.

It follows that the main parameters of the absorber layer affect the QE spectrum of the solar cell *differently* [29]. This facilitates the choice of the parameter values for better agreement between the calculated and experimental data and virtually eliminates getting the same spectral curve for different combinations of parameters. The data of calculations presented in Fig. 12 confirm the above statement showing how the spectrum of $CdS/CuInSe_2$ solar cell is modified when one of the parameters is varied.

As can be seen, a deviation upward or downward from the optimum value of the minority carrier lifetime (τ_n=2 ns) substantially affect the spectral distribution of the quantum efficiency only at wavelengths longer than ~ 700 nm. In contrast, the deviation of the recombination velocity at the front surface of the $Cu(In,Ga)Se_2$ layer from the value $S_f=2\times10^5$ cm/s results in significant changes in the short wavelength region (shorter than ~ 800 nm). Judging the curves in Fig. 12b, it might give the impression that the recombination at the front surface has more or less the same effect on the quantum efficiency over the entire spectrum, and it can induce doubt in the correctness of the physical model used. However, this is not so, a simple calculation shows that for $S_f=10^7$ cm/s in the spectral range 600-800 nm, surface recombination reduces the quantum efficiency only by 2-4% but as high as ~ 22% in the range 350-400 nm.

The concentration of uncompensated acceptors $N_a - N_d$ impacts the entire spectrum, and is more appreciable. Moreover, when concentration of $N_a - N_d$ is deviated by an order from the

http://dx.doi.org/10.5772/59363

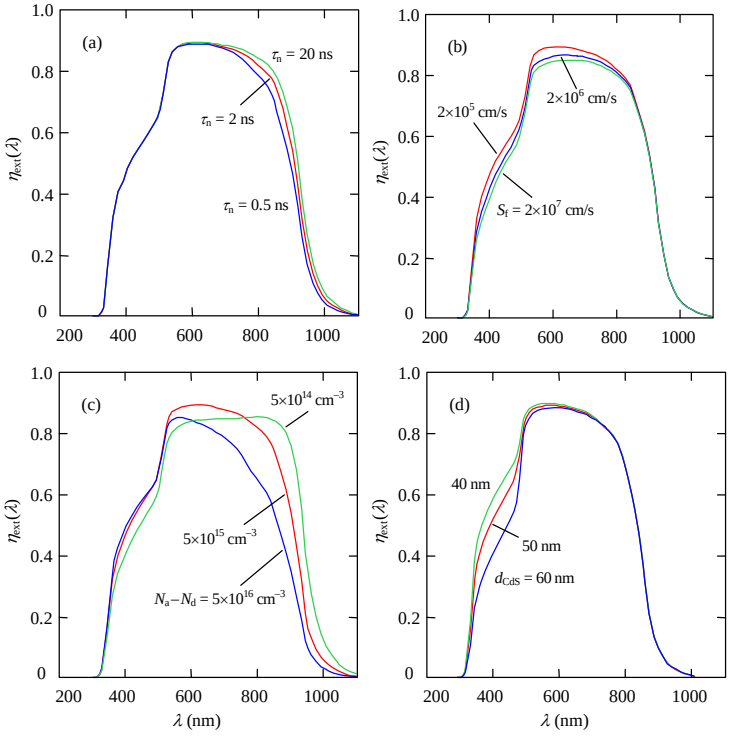

Figure 12. Effect of the electron lifetime τ_n (a), the surface recombination velocity S_f (b), the concentration of uncompensated acceptors $N_a - N_d$ (c) and the thickness of the CdS film (d) on the spectral distribution of the quantum efficiency of $CuInSe_2$ solar cell.

optimum value 5×10^{15} cm^{-3}, qualitative changes are observed in the spectrum, notably in the range λ=550-850 nm, increasing the efficiency with wavelength is replaced by its decay when $N_a - N_d$ is increased.

Finally, the variation of the CdS layer thickness manifests itself only in the range of the fundamental absorption of this semiconductor, i.e., when $\lambda < 500$ nm.

Parameters giving best match for the spectral distribution of calculated and experimental QE of the studied cells are summarized in Table 2. Notice that in the investigated solar cells, the SCR width (0.4–0.6 μm) amounts to a small part of the thickness of the absorber layer and the recombination velocity S_f is equal to $\sim 10^5$ cm/s, i.e., S_f is low as compared to thin-film CdS/CdTe heterostructure. This is explained by the known peculiarity of CdS/CIGS heterojunction.

Back in the late 1980s, it was shown that the CIGS solar cells are insensitive to defects caused by a lattice mismatch or impurities at the CdS/CIGS interface. In fact, the lattice mismatch is rather small for CdS and $CuInSe_2$ ($\sim$ 1%) and weakly increases with the Ga content. In addition, the deposition of CdS on the treated and cleaned surface of the CIGS layer is characterized by

pseudo-epitaxial growth, and the intermixing of the heterojunction constituents is observed even at relatively low-temperature processes [30, 31].

Solar cell	E_g (eV)	φ_{bi} (eV)	τ_n (ns)	$N_a - N_d$ (cm^{-3})	S_f (cm/s)	d_{CdS} (nm)
$CuInSe_2$	1.04	0.60	5	2×10^{15}	1×10^{5}	45
$CuIn_{0.3}Ga_{0.7}Se$	1.14	0.75	20	9×10^{15}	5×10^{5}	50
$CuIn_{0.67}Ga_{0.3}Se$	1.36	0.95	2	5×10^{15}	2×10^{5}	40

Table 2. Parameters of $CuInSe_2$, $CuIn_{0.76}Ga_{0.24}Se_2$ and $CuIn_{0.39}Ga_{0.61}Se_2$ solar cells giving better match between measured and calculated data

A comparison of measured and calculated results presented in Fig. 11 shows that the theoretical model describes in detail the spectral distribution of the quantum efficiency of CIGS solar cells, which is important for further analysis of recombination losses. But the question arises, how this model can be applicable in polycrystalline material, with its inhomogeneity, recombination at the grain boundaries, etc. A possible explanation for the applicability of the model in question to efficient solar cells based on polycrystalline CIGS is that during the growth of the absorber layer and post-growth processing, recrystallization leading to grain growth and their coalescence occur. Also no less important is the fact that a structure in the form of ordered columns oriented perpendicular to the electrodes is created in the CIGS layer (see reviews [32] and references therein). One can assume that in a layer of columnar structure, collection of photogenerated charge occurs without crossing the grain boundaries. In addition, the scattering and recombination on the lateral surfaces of the columns also have no significant effect due to the strong electric field in the barrier region.

Indeed, the width of the SCR in the studied solar cell is about 0.5 μm, and the electric field at a barrier height φ_{bi} of about 1 eV is higher than 10^4 V/cm. Under such conditions, the drift length of charge carriers with the mobility of 20-30 $cm^2/(Vs)$, and lifetimes 10^{-9} s is several microns which is significantly greater than the width of SCR and makes recombination improbable. Outside the SCR, where the diffusion component of photocurrent is formed, the electric field does not exist, but due to the high absorption capacity of CIGS the vast majority of solar radiation is absorbed in the SCR. This is illustrated in Fig. 13 with the example of $CuIn_{0.39}Ga_{0.61}Se_2$ (E_g=1.36 eV) solar cell, where the quantum efficiency spectra along with the drift and diffusion components are shown. As expected, the diffusion component falls mostly on the long-wavelength part of spectra (λ longer than ~ 600 nm) and its contribution to the quantum efficiency is quite insignificant.

Calculation given by Eq. (39) shows that for the parameters listed in Table 2, the contributions of the diffusion component in the photocurrent of $CuInSe_2$, $CuIn_{0.76}Ga_{0.24}Se_2$ and $CuIn_{0.39}Ga_{0.61}Se$ solar cells is about 2, 4 and 8%, which are far inferior to the drift component. This significantly weakens the role of recombination at the grain boundaries.

http://dx.doi.org/10.5772/59363

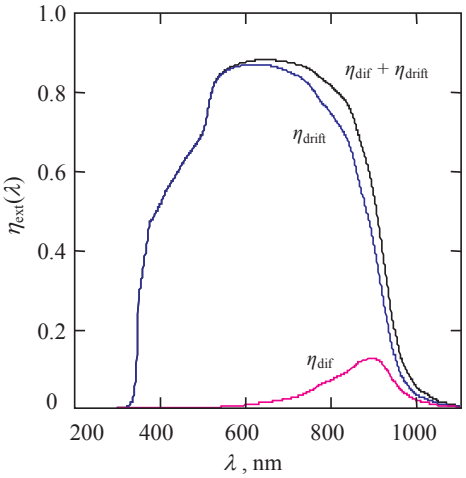

Figure 13. Drift and diffusion components of the quantum efficiency of $CuIn_{0.39}Ga_{0.61}Se_2$ solar cell and their sum.

4.1. Recombination losses at the absorber front surface

To determine the recombination losses, we will calculate the photocurrent density by varying the parameters of solar cells such as the recombination velocity at the absorber surface, concentration of uncompensated acceptors and carrier lifetimes in the material, as well as the thickness of the absorber. Photocurrent density will be calculated by Eq. (19) using for $T(\lambda)$ Eq. (39).

Until now, the internal quantum efficiency was calculated under zero bias, since it was necessary for comparison with the spectra measured at V=0. However, recombination losses should be calculated in the operating mode of the solar cell, i.e., at the voltage V_m, which maximizes the generated electrical power. As will be shown in Section 5.3, these voltages V_m are 0.36, 0.46 and 0.63 V for $CuInSe_2$, $CuIn_{0.76}Ga_{0.24}Se_2$ and $CuIn_{0.39}Ga_{0.61}Se_2$ solar cells, respectively.

Consider how the photocurrent density J varies depending on the concentration of uncompensated acceptors at different recombination velocities at the front surface of the CIGS absorber. Note that according to Eq. (36), the recombination does not depend on the carrier lifetime in this case. Fig. 14 shows for $CuIn_{0.39}Ga_{0.61}Se_2$ solar cell the dependences of J on $N_a - N_d$ in the range 5×10^{14}–10^{18} cm^{-3} and S_f in the range 10^4–10^7 cm/s and also at S_f=0. The lower range of $N_a - N_d$ is limited to 5×10^{14} cm^{-3}, because at this values the width of the SCR becomes greater than the thickness of the absorber layer d=2 μm.

As seen in Fig. 14a, if the concentration of uncompensated acceptors exceeds 10^{17} cm^{-3}, surface recombination does not reveals itself, but at lowering the $N_a - N_d$, the decrease in J becomes appreciable. At $S_f=10^4$ cm/s, recombination practically does not reduce the current and slightly lowers it at the real values of $N_a - N_d=5\times10^{15}$ cm^{-3} and $S_f=2\times10^5$ cm/s for this solar cell. As our calculations show in Fig. 14b, for $CuIn_{0.39}Ga_{0.61}Se$ solar cell, surface recombination reduces J by

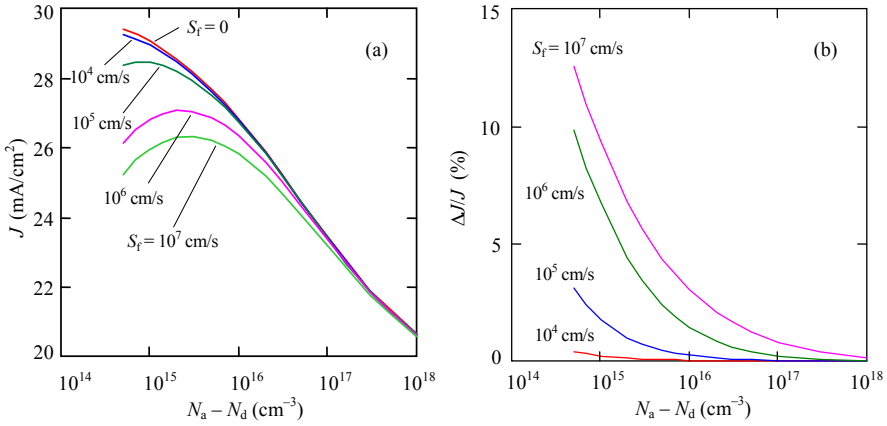

Figure 14. (a) Photocurrent density J as a function of the concentration of uncompensated acceptors $N_a - N_d$ at different recombination velocities S_f at the front surface of the CIGS absorber in $CuIn_{0.39}Ga_{0.61}Se$ solar cell. (b) Reduction in the photocurrent density, expressed as in percentage.

1.8% for $N_a - N_d = 5\times10^{15}$ cm^{-3}. Similar calculations carried out for $CuInSe_2$ and $CuIn_{0.76}Ga_{0.24}Se_2$ solar cells show that recombination losses for them are equal to 2.1% and 1.9%, respectively. Relatively small recombination losses are explained by the above mentioned fact that the CIGS solar cells are insensitive to defects at the CdS/CIGS interface due to pseudo-epitaxial growth of the CIGS and the intermixing of the heterojunction constituents.

4.2. Recombination losses in the SCR

Recombination of photogenerated charge carriers in the SCR can be taken into account, using the well-known Hecht equation [33]:

$$\eta_H(x) = \frac{\lambda_n}{W}\left[1-\exp\left(-\frac{x}{\lambda_n}\right)\right] + \frac{\lambda_p}{W}\left[1-\exp\left(-\frac{W-x}{\lambda_p}\right)\right], \tag{40}$$

where x is the coordinate (x is measured from the CdS/CIGS interface), λ_n and λ_p are the drift lengths of electrons and holes in the SCR:

$$\lambda_n = \mu_n F \tau_{no}, \tag{41}$$

$$\lambda_p = \mu_p F \tau_{po}, \tag{42}$$

F is the electric field strength; τ_{no} and τ_{po} are the lifetimes of electrons and holes in the SCR, respectively, which we will accept to be equal to τ_n assuming that the CIGS absorber is a highly doped semiconductor.

http://dx.doi.org/10.5772/59363

In CdS/CIGS heterostructure, the electric field is not uniform, but the problem of the nonuniformity is simplified, since the field strength F decreases in a Schottky diode linearly with the x coordinate. In this case, F in the expressions (41) and (42) can be replaced by the average values of F in the sections $(0,x)$ and (x,W) for electrons and holes, respectively, i.e.,

$$F(0,x) = \frac{\varphi_{bi} - qV}{qW}\left(2 - \frac{x}{W}\right), \tag{43}$$

$$F(x,W) = \frac{\varphi_{bi} - qV}{qW}\left(1 - \frac{x}{W}\right). \tag{44}$$

Evidently, charge collection efficiency in the dx interval of the SCR is $\eta_H \alpha \exp(-\alpha x)dx$ and then the charge-collection efficiency for the wavelength λ_i is determined by expression:

$$\eta_H(\lambda_i) = \int_0^W \eta_H(x)\alpha_i \exp(-\alpha_i \cdot x)dx. \tag{45}$$

Fig. 15 shows the photocurrent density J in $CuIn_{0.39}Ga_{0.61}Se_2$ as a function of the concentration of uncompensated acceptors $N_a - N_d$ at different carrier lifetimes given by the equation:

$$J = q\sum_i \frac{\Phi_i(\lambda_i)}{h\upsilon_i} T(\lambda_i)\eta_H(\lambda_i)\Delta\lambda_i. \tag{46}$$

As can be seen in Fig. 15a, when $N_a - N_d > 3\times10^{16}$ cm^{-3} ($W < 0.2$-0.3 μm), the curves calculated for different lifetimes of charge carriers $\tau_n = \tau_{no} = \tau_{po}$ coincide, but as the SCR width increases, the curves diverge and become more pronounced when τ_n is less. The reduction of J due to recombination can be found by subtracting the current at a given τ_n from the value of current j_o when recombination does not occur. The latter is possible for a sufficiently large lifetime of charge carriers. A simple calculation shows that when $\tau_n > 500$-600 ns, the current becomes independent of τ_n, therefore the values of j_o at different $N_a - N_d$ were found for τ_n=1000 ns (the curve j_o vs. $N_a - N_d$ is also shown in Fig. 15a).

Fig. 15b shows the reduction in J due to recombination in the SCR and its dependence on the $N_a - N_d$ and τ_n. As seen, when $N_a - N_d < 10^{16}$ cm^{-3} ($W > 1$ μm), the recombination losses increase rapidly up to 60% with decreasing $N_a - N_d$ and τ_n. The data presented in this figure allow determining the recombination losses for any values of $N_a - N_d$ and τ_n. For the real carrier lifetime of 2 ns and $N_a - N_d = 5\times10^{15}$ cm^{-3}, which are characteristic of $CuIn_{0.39}Ga_{0.61}Se$ solar cell, the recombination losses amount to 1.0%, whereas for $CuIn_{0.76}Ga_{0.24}Se_2$ solar cell the losses is

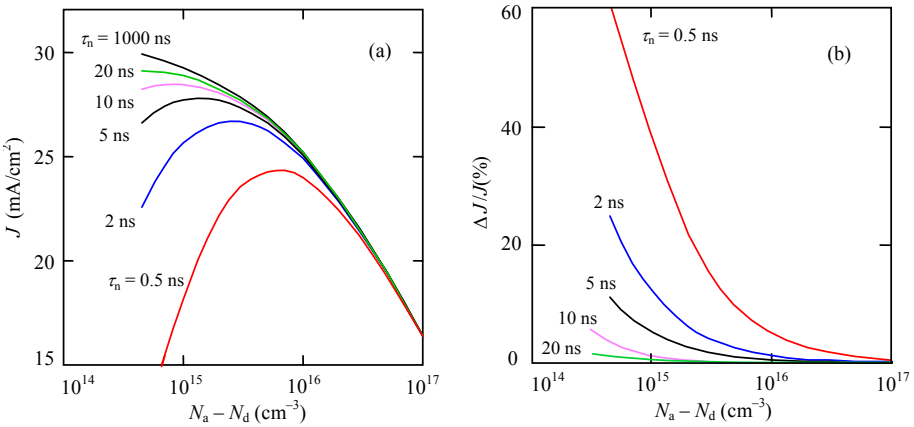

Figure 15. (a) Photocurrent density J as a function of the concentration of uncompensated acceptors $N_a - N_d$ for different carrier lifetimes τ_n in the $CuIn_{0.39}Ga_{0.61}Se_2$ absorber. (b) Reduction of the photocurrent density expressed in percentage.

only 0.1% because of higher values τ_n=20 ns and $N_a - N_d$=9×10^{15} cm^{-3}. For $CuInSe_2$ solar cell, the recombination losses due to recombination in the SCR amount to 0.7%.

4.3. Recombination losses at back surface and neutral part of absorber

Useful information about the effect of recombination at the back surface of the solar cell and the neutral part of the absorber on the photocurrent J can be obtained by studying the dependence of J on the absorber thickness d. If d is large, the effect of recombination at the back surface is imperceptible, but when the rear surface is close to the SCR by a distance comparable to the diffusion length of electrons, the role of recombination increases. This leads also to a decrease in the diffusion component of the photocurrent.

Subtracting the currents calculated for the recombination velocity S_b=10^7 cm/s and S_b=0, one can obtain the change of J due to recombination at the back surface. Obviously, for longer minority-carrier lifetime, recombination at the back surface of the absorber is intensified and manifests itself also at larger absorber thickness.

Fig. 16a shows the dependences of photocurrent J on the thickness d of the $CuIn_{0.39}Ga_{0.61}Se_2$ absorber calculated for S_b=10^7 cm/s and S_b=0 and at different lifetimes of electrons. As it is shown by dashed lines, when the $CuIn_{0.39}Ga_{0.61}Se_2$ layer becomes thinner, the photocurrent for S_b=0 first slightly grows and then rapidly decreases. The observed current growth can be explained by the fact that the diffusion component of the photocurrent is determined by the derivative of the excess concentration of photogenerated electrons $\Delta n/dx$ [22]. The derivative may be larger than that in the absence of recombination at the surface, but when d approaches the cross section x=W, the diffusion component eventually decreases due to reduced the Δn absolute value and next Δn=0 when x=W. This also explains why the dependence of ΔJ / J on d shown in Fig. 16b is described by a curve with a maximum.

http://dx.doi.org/10.5772/59363

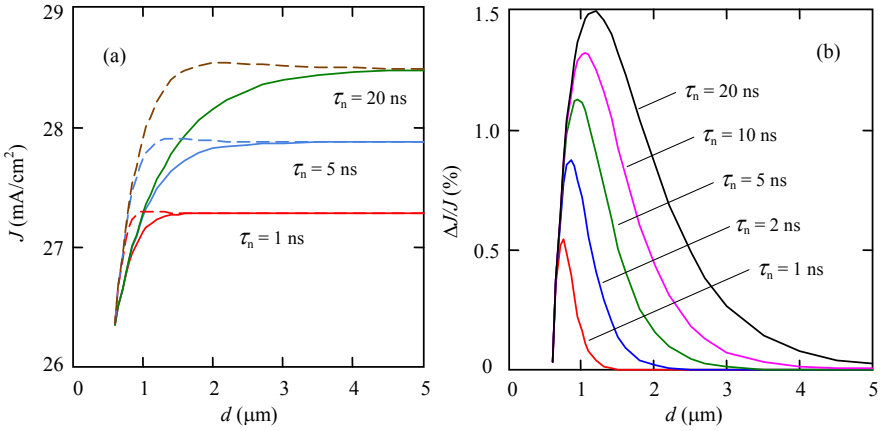

Figure 16. (a) Dependences of the photocurrent density on thickness of the $CuIn_{0.39}Ga_{0.61}Se_2$ layer calculated for different electron lifetimes with and without taking into account recombination at the back surface of the absorber (solid and dashed lines, respectively), (b) Decrease in photocurrent density due to recombination at the back surface calculated for different electron lifetimes.

As can be seen from Fig. 16b, the decrease in photocurrent does not exceed 1.5% even with lifetimes of electrons 20 ns. With such low recombination losses, the creation of a heavily doped layer adjacent to the back contact as it is proposed in CdS/CdTe solar cells [7] or to form a bandgap gradient outside the SCR in the CIGS absorber [8] to reduce the negative impact of recombination at the rear surface of the absorber seems to be unreasonable. As previously mentioned, a very small fraction of carriers taking part in the photocurrent formation (2–8%) falls on the neutral part of the studied CIGS solar cells that also should be borne in mind.

Of course, recombination of photogenerated carriers happens not only at the back surface of the absorber, but also in whole neutral part (outside the SCR). The losses due to such recombination can be found as the difference between photocurrent at: (i) real electron lifetime and recombination velocity at the rear surface and (ii) large value of the electron lifetime when recombination can be ignored (τ_n=1000 ns) and S_b=0. As the calculations show, such losses are 2.5, 5.0 and 2.9% for $CuInSe_2$, $CuIn_{0.76}Ga_{0.24}Se_2$ and $CuIn_{0.39}Ga_{0.61}Se_2$ solar cells, respectively. It is necessary to emphasize that recombination in the neutral part of the absorber and at the rear surface are not additive. But the calculation results for the neutral part, for example, with and without recombination at the rear surface of the absorber differ slightly. Nevertheless the determination of the combined influence of recombination in the neutral part of the absorber and at its rear surface is more correct.

The calculated values of *all types of recombination losses* along with the corresponding decrease in the photocurrent J (given in brackets) are summarized in Table 3. Analysis of obtained results allows us to formulate some recommendations to improve the photoelectric conversion efficiency in the solar cells studied.

The total recombination losses in $CuInSe_2$, $CuIn_{0.76}Ga_{0.24}Se_2$ and $CuIn_{0.39}Ga_{0.61}Se_2$ solar cells amount to 5.4, 7.0 and 4.1%, respectively. It can be assumed that the charge collection efficiency of the photogenerated charge in the absorber is 94.6, 93.0 and 95.9%, respectively. Having these data, it is worth to analyze the possibility of reducing the recombination losses and improving the charge collection efficiency that we will make with an example of $CuIn_{0.76}Ga_{0.24}Se_2$ solar cell.

Origin of recombination losses	Losses in solar cell		
	$CuInSe_2$	**$CuIn_{0.76}Ga_{0.24}Se_2$**	**$CuIn_{0.39}Ga_{0.61}Se_2$**
Front surface	2.2% (0.9 mA/cm^2)	1.9% (0.7 mA/cm^2)	0.2% (< 0.1 mA/cm^2)
Space-charge region	0.7% (0.4 mA/cm^2)	0.1% (< 0.1 mA/cm^2)	1.0% (0.3 mA/cm^2)
Neutral part of absorber and back surface	2.5% (1.0 mA/cm^2)	5.0% (1.8 mA/cm^2)	2.9% (1.0 mA/cm^2)
Only back surface	0.2% (< 0.1 mA/cm^2)	1.0% (0.4 mA/cm^2)	0.1% (< 0.1 mA/cm^2)
Total recombination losses	5.4% (2.3 mA/cm^2)	7.0% (2.5 mA/cm^2)	4.1% (1.4 mA/cm^2)

Table 3. Recombination and the corresponding *J* losses in CIGS solar cells

According to Eq. (36), the recombination losses at the front surface can be lowered by increasing the hole diffusion coefficient $D_p=kT\mu_p/q$, i.e., increasing the mobility of holes μ_p. The results of calculation from Eq. (19) show that increasing the hole mobility from 30 to 300 cm^2/(Vs) (this is real according to the literature data) reduces such losses from 1.9 to 0.3%.

Significant improvement of the charge collection efficiency can be achieved by increasing the lifetime of electrons, which is equivalent to an increase of electron mobility since the diffusion length L_n is equal to $(\tau_n D_n)^{1/2}$. Increase in electron mobility also by an order of magnitude from 20 to 200 cm^2/(V s) leads to a reduction of the recombination losses in the neutral part of the absorber and at its rear surface from 5.0 to 1.1%.

The recombination losses in the SCR 0.1% at large electron and holes mobilities approach to zero since the drift lengths of carries are proportional to the their mobilities. Thus, due to a real increase of the mobility of electrons and holes by one order of magnitude the charge collection efficiency improves from 93.0 to 98.6%.

An even greater improvement of the charge collection efficiency can be achieved by extending the SCR, which leads to absorption of a greater part of the radiation in the SCR and hence the better collection of the photogenerated charge. However, one should keep in mind that when the electron lifetime and mobility increase, the diffusion length becomes longer than the absorber thickness. This weakens the desired effect and in fact the charge collection efficiency for d=2 μm is 96.2%.

There is also a positive impact for a higher carrier lifetime and expanded SCR since it leads to a decrease in the forward recombination current. Analyzing the electrical characteristics of the

http://dx.doi.org/10.5772/59363

solar cell, it is not difficult to show that this causes enhancing the open circuit voltage (see the next sections).

Some useful information can be obtained from the spectral distribution of the reflection, absorption and recombination losses. Fig. 17 shows the distribution of these losses over the whole spectrum for $CuIn_{0.76}Ga_{0.24}Se_2$ solar cell obtained from the results given above.

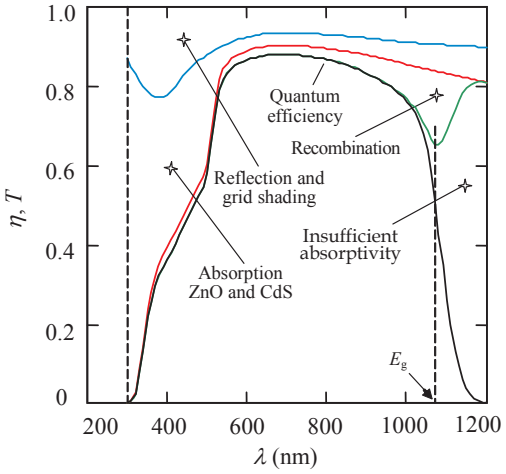

Figure 17. Illustration of spectral distribution of the reflection, absorption and recombination losses for $CuIn_{0.76}Ga_{0.24}Se_2$ solar cell (E_g=1.14 eV).

As clearly seen, the recombination losses are considerably less than those caused by reflection and absorption in the ZnO layer and especially in the CdS layer. The radiation in the range $h\nu < E_g$ gives a small contribution to the solar cell efficiency due to insufficient absorptivity of CIGS in this range, whereas at $h\nu > E_g$ slight decrease of the absorptivity compared to 100% takes place only when the photon energy is very close to E_g.

5. Electrical characteristics of CIGS solar cells

The electrical properties of CIGS solar cells are presented in many publications, but their *dark J–V* characteristics are practically absent and not discussed *analytically* in the literature with a few exceptions. This is despite the fact that the dark *J–V* relationship along with the quantum efficiency spectrum are the two key characteristics that determine substantially the performance of solar cells.

In this section we analyze the dark *J–V* characteristics of CIGS solar cells (x=0 – 0.61) extracted from the data under cell illumination reported in [8,34]. It is shown that the dark *J–V* curves are described by the theory of generation–recombination of charge carriers in the SCR

developed for the linearly graded silicon p-n junction in [19] and modified and adapted to a thin-film CdS/CdTe heterostructure taking into account peculiarities of the distribution of the electric potential and the concentrations of free electrons and holes in the SCR [29]. This is valid for CIGS solar cells taking into account the effect of the shunts at low forward voltages and the voltage drop across the series resistance at high forward currents. It is also shown that knowing the short–circuit current density (which can be obtained from spectra of the quantum efficiency and solar radiation), it is possible to calculate the *J–V* curves under illumination and find the open–circuit voltage, the fill factor and eventually the energy conversion efficiency. The electric losses caused by the presence of the shunts and series resistances of the bulk part of the CIGS absorber are also determined.

5.1. Experimental results and discussion

The *J–V* characteristics of CIGS solar cells having bandgaps of the absorber E_g=1.04, 1.14 and 1.36 eV under standard AM1.5 illumination taken from [8] are shown in Fig. 18a. The voltage dependences of the dark current derived from the difference between the short-circuit current density J_{sc} and the current density under illumination J_{IL} at each voltage are shown in Fig. 18b by solid (closed) circles, squares and triangles. At $V < 0.2$ V, the values of J_{IL} and J_{sc} are very close to each other, therefore the dark current cannot be determined with a proper accuracy.

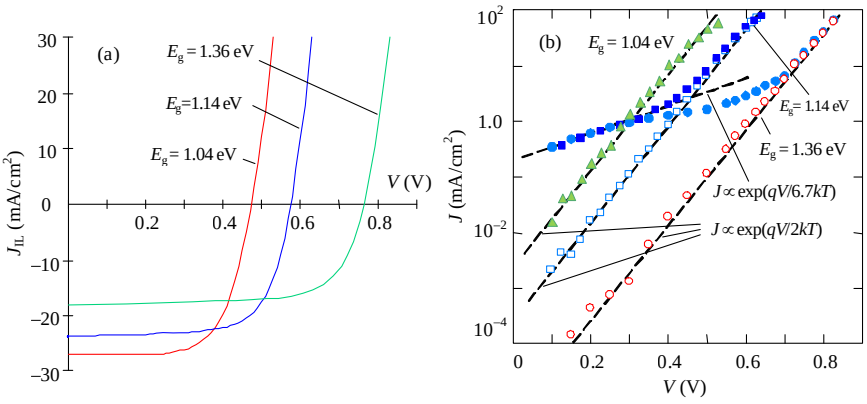

Figure 18. a) Voltage dependences of the current density in CIGS solar cells under illumination [8], (b) Dark currents (solid circles, squares, triangles) and currents obtained by subtracting the current through the shunt from the dark current in the absorber bandgaps 1.14 and 1.36 eV (open circles, squares).

As seen in Fig. 18b, the dark current in solar cell with the bandgap of the absorber 1.04 eV follows quite well the voltage dependence $J \propto \exp(qV/2kT)$ (dashed lines) in the range of almost four order of magnitude that confirms the recombination mechanism of charge transport suggested in [8, 34]. However, for the absorbers with the bandgap of 1.14 and 1.36 eV the *J–V* curves have a complicated form. As seen, the dependences $J \propto \exp(qV/2kT)$ are observed only at $V > 0.5$ and 0.7 V for the samples with E_g=1.14 (solid squares) and 1.36 eV (solid circles),

http://dx.doi.org/10.5772/59363

respectively. At lower voltage the *J–V* relationship deviates from such dependence for some reason. Note that, despite the significant difference of currents at higher voltages, the dark currents in these two cells at low voltages practically coincide and the *J–V* relationship can be interpolated by the expression $J \propto \exp(qV/AkT)$ with enormous large value of the ideality factor A=6.7.

Useful information about the electrical properties of the diode can be obtained from the analysis of the voltage dependence of the differential resistance $R_{dif}=dV/dI$ [22]. These dependences for three samples are shown in Fig. 19. It is known that the differential resistance of a semiconductor diode decreases exponentially with increasing forward voltage in a wide range including the lowest voltage as shown in Fig. 19 by dashed oblique straight lines. Such behavior of the differential resistance is observed only for $CuInSe_2$ diode (E_g=1.04 eV). For other two diodes, when a low forward voltage is applied, the dependence of R_{dif} on V deviates downward from the exponent and an invariance of R_{dif} takes place at the level of 0.3-0.4 Ω for diode area of 0.4 cm^2. It is quite realistic to assume that at low voltages, the current through the shunt rather than through the diode is dominant and only when bias is above 0.4 and 0.6 V respectively for devices with CIGS bandgaps E_g=1.14 and 1.36 eV, the diode currents are higher than that through the shunts (for CIS cell with bandgap E_g=1.04 the shunt is absent).

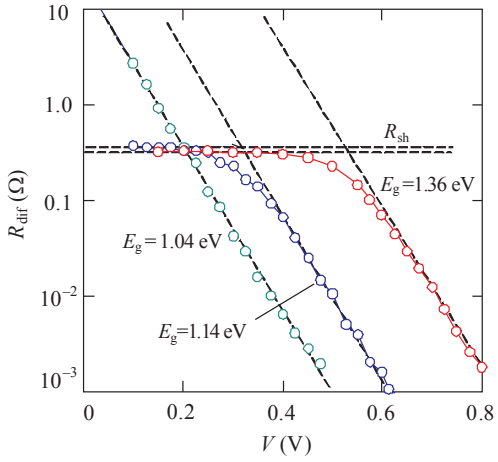

Figure 19. Voltage dependences of the differential resistance of the studied CIGS solar cells.

One can assume that shunting in the studied solar cells is caused by pin-holes and defects associated with a thin film of CdS (20–30 nm) used in the layered structure. In high efficiency CIGS solar cells, a thin intrinsic i-ZnO layer is applied which is capped by a thicker Al-doped ZnO layer. It is believed that the i-ZnO layer reduces the shunt paths by forming a thin high resistive transparent film (HRT), thin enough to promote tunneling, which is proven to enhance the device performance. However, ZnO is usually deposited by sputtering which is known as a damaging process [35]. Seemingly the damages at the CdS/CIGS interface pro-

duced by i-ZnO sputtering leads also to the occurrence of shunts. However, in the case of i-ZnO, the value of the shunt resistance is much larger compared to ZnO:Al due to high resistivity of i-ZnO and the shunting reveals itself only at relatively low voltages.

The voltage-independent differential resistance at $V < 0.2$ and 0.4 V for the two samples (Fig. 19) means that the shunt is a *linear* element of the electric circuit. Therefore, the effect of the shunt can be taken into account by subtracting the current through the shunt V/R_{sh} from the measured current J. The results of such manipulations for cells with the absorber bandgaps 1.14 and 1.36 eV are shown in Fig. 18b by open squares and circles, respectively, whereas the J–V curves without accounting for the shunt and series resistances are shown by solid circles and squares.

As seen in Fig. 18b, *qualitative* changes in the forward J–V characteristic of cells with the absorber bandgaps 1.14 and 1.36 eV occur after subtracting the current through the shunt resistance. In the range $V < 0.45$ V for the first cell (E_g=1.14 eV) and $V < 0.65$ V for the second cell (E_g=1.36 eV), the forward current rapidly decreases with decreasing the voltage by three and five orders of magnitude, respectively, continuing the same trend of the curves $J(V)$ as at the higher voltages. It is important to note that after subtracting the current through the shunt the current in the cells with the absorber bandgaps 1.14 and 1.36 eV as well as the measured current in a cell with the bandgap 1.04 eV ($CuInSe_2$) without shunting are proportional to $\exp(qV/AkT)$ at $A \approx 2$.

The obtained results can create the impression that the occurrence of shunt is due to the introduction of Ga into the $CuInSe_2$ crystal lattice in order to widen the semiconductor bandgap for increasing the efficiency of solar cells. However, some results reported in the literature indicate that the shunting in solar cells with wide bandgap can be avoided by modifying the fabrication technology, in particular by increasing the temperature of CIGS deposition and post-growth processing [36].

Soda-lime glass is a common substrate material used in CIGS solar cells due to its low cost and good thermal expansion match to $CuInSe_2$. In addition, the soda-lime glass supplies sodium to the growing CIGS layer by diffusion through the Mo back contact, leading to enhanced grain growth with a higher degree of preferred orientation.

It is known that the CIGS deposition requires a substrate temperature at least 350°C and efficient cells have been fabricated at the maximum temperature ~ 550°C, which the glass substrate can withstand without softening. In these temperature ranges, CIGS solar cells are typically made with low Ga content ($x \leq 0.3$) resulting in an absorber bandgap value of 1.1-1.2 eV. However as suggested by the theory, for optimum conversion efficiency it is desirable to open the bandgap up to E_g=1.4-1.5 eV.

It was shown in [36] that the growth and post-growth processing at temperature higher than 550°C leads to significant improvements of the performance of CIGS solar cells with bandgaps up to 1.4–1.5 eV. For this purpose, borosilicate glasses have been used in CIGS research even though it has non-optimum thermal coefficient of expansion and no sodium in it. Nevertheless the solar cells with a wide bandgap for CIGS absorber, fabricated on borosilicate glass at the substrate temperatures in the range of 600 to 650°C had a rather high efficiency.

http://dx.doi.org/10.5772/59363

In addition to improving efficiency, the shunting of heterostructure in the device fabricated at an elevated temperature can be eliminated. This is illustrated by Fig. 20 where the data obtained for solar cells with the absorber bandgap 1.5 eV fabricated using standard technology $T < 550$°C (sample #1) and at elevated temperature 600–650°C (sample #2) are shown by solid and open circles, respectively. The J–V curves for recombination current $J=J_o[\exp(qV/2kT) - 1]$ are also shown in Fig. 20a by solid lines *2* and *6*.

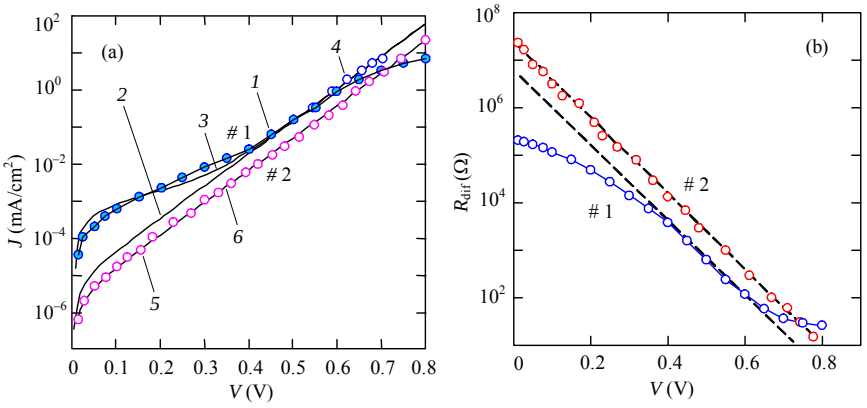

Figure 20. Voltage dependence of dark current density [36] (a) and differential resistance (b) of CIGS solar cells with absorber bandgap ~ 1.5 eV fabricated at standard temperature ≤ 550°C (sample #1) and elevated temperature 650°C (sample #2).

As can be seen in Fig. 20a, for solar cells fabricated using standard technology, the J–V relationship at $V < 0.4$ V deviates from the expression $J \propto [\exp(qV/2kT) - 1]$ (curve *#1*) that is caused by the effect of shunting. This observation is confirmed by the dependence of the differential resistance R_{dif} of this sample shown in Fig. 20b. As expected, the $R_{dif}(V)$ relationship deviates from the exponential decrease at low voltages in the range $V < 0.4$ V. However, the R_{dif} value does not become constant when the voltage approaches zero as it is observed in samples with the absorber bandgaps 1.14 and 1.36 eV in Fig. 19. Therefore, the shape of a measured curve cannot be accurately calculated by adding the current through the shunt V/R_{sh} to the recombination current. An approximate description of the measured curve is possible by taking the average value of the shunt resistance $R_{sh}=1.3\times10^5$ Ω. (line *3* in Fig. 20a).

The J–V relationship shown in Fig. 20a for sample #1 (solid circle) also deviates downward from the exponential increase at $V > 0.6$ V due to voltage drop across the series resistance R_s of the neutral part of the absorber layer. If this voltage drop is subtracted from V, a good agreement of theory with experiment can be achieved (curve *3* at $V > 0.6$ V).

As seen in Fig. 20a, the data obtained for solar cells fabricated at elevated temperature of 650°C is in good agreement with the expression $J=J_o[\exp(qV/2kT) - 1]$ over the whole voltage range. Thus, by growth and post-growth processing of the film at higher temperatures, CIGS solar

cells with wide bandgap for the absorber (up to 1.5 eV) can be fabricated without shunting at low voltages and the voltage drop across the series resistance at high currents.

5.2. Generation–recombination in space–charge region theory

As mentioned previously, the theory of generation–recombination of charge carriers in the space-charge region (SCR) was developed for the linearly graded silicon p-n junction by Sah et al. [19] and modified and adapted to a Schottky diode taking into account the distribution of the potential and free carrier concentrations in the SCR [37,38].

The generation–recombination rate through a single level trap for nonequilibrium but steady-state conditions in the cross section x of the SCR at voltage V is determined by the Shockley-Read-Hall statistics:

$$U(x,V)=\frac{n(x,V)p(x,V)-n_{\mathrm{i}}^{2}}{\tau_{\mathrm{po}}[n(x,V)+n_{1}]+\tau_{\mathrm{no}}[p(x,V)+p_{1}]}, \tag{47}$$

where $n(x,V)$ and $p(x,V)$ are the carrier concentrations in the conduction and valence bands within the SCR, respectively; n_{i} is the intrinsic carrier concentration in the semiconductor; $\tau_{\mathrm{no}}=1/\sigma_{\mathrm{n}}\upsilon_{\mathrm{th}}N_{\mathrm{t}}$ and $\tau_{\mathrm{po}}=1/\sigma_{\mathrm{p}}\upsilon_{\mathrm{th}}N_{\mathrm{t}}$ are respectively the effective lifetimes of electrons and holes in the SCR (τ_{no} and τ_{po} are the *shortest* lifetimes for given N_{t} and carrier capture cross sections of electrons and holes σ_{n} and σ_{p}, respectively [19]); υ_{th} is the charge-carrier thermal velocity; N_{t} is the concentration of generation–recombination centers. The quantities n_1 and p_1 in Eq. (47) are determined by the ionization energy of the generation–recombination center E_{t}: $n_1=N_{\mathrm{c}}\exp[-(E_{\mathrm{g}}-E_{\mathrm{t}})/kT]$ and $p_1=N_{\mathrm{v}}\exp(-E_{\mathrm{t}}/kT)$, where $N_{\mathrm{c}}=2(m_{\mathrm{n}}\kappa T/2\pi\hbar^{2})^{3/2}$ and $N_{\mathrm{v}}=2(m_{\mathrm{p}}\kappa T/2\pi\hbar^{2})^{3/2}$ are the effective densities of state in the conduction and valence band, m_{n} and m_{p} are the effective electron and hole masses, respectively.

The expressions for the electron and hole concentrations in the SCR of Schottky diode involved in Eq. (47) in the chosen reference system take the form [39]

$$n(x,V)=\mathrm{N_{v}}\exp\left[-\frac{E_{g}-\Delta\mu-\varphi\left(x,V\right)-qV}{kT}\right], \tag{48}$$

$$p(x,V)=N_{\mathrm{v}}\exp\left[-\frac{\Delta\mu+\varphi(x,V)}{kT}\right], \tag{49}$$

where $\Delta\mu$ denotes the energy difference between the Fermi level and the top of the valence band in the bulk part of the CIGS layer, $\varphi(x,V)$ is the potential distribution in the SCR at voltage V, given by the expression:

http://dx.doi.org/10.5772/59363

$$\varphi(x,V) = (\varphi_{bi} - qV)\left(1 - \frac{x}{W}\right)^2, \tag{50}$$

φ_{bi} is the height of the potential barrier in equilibrium for holes from the CIGS side related to the built-in (diffusion) voltage V_{bi} by the equality $\varphi_o = qV_{bi}$, W is the width of the SCR given by Eq. (28).

The recombination current density under forward bias and the generation current under reverse bias are found by the integration of $U(x,V)$ throughout the entire depletion layer

$$J = q\int_0^W U(x,V)dx. \tag{51}$$

From the above equations one can obtain the exponential voltage dependence of the recombination current under forward bias.

Substitution of Eqs. (48)–(50) into Eq. (47) and simple manipulation yield the following expression for the generation–recombination rate:

$$U = \frac{n_i(\tau_{no}\tau_{po})^{-1/2}\sinh(qV/2kT)}{\exp(-qV/2kT)\cosh[(E_g^* - 2E_t)/2kT] + \cosh\{[(E_g^* - 2\Delta\mu - qV - 2\varphi(x,V)]/2kT\}}, \tag{52}$$

where $E_g^* = E_g + kT\ln[(\tau_{po}N_c)/(\tau_{no}N_v)]$.

We assume that CIGS contains a lot of shallow and deep impurities (defects) of donor and acceptor types. According to the Shockley-Read-Hall statistics the most effective generation–recombination centers are those whose levels are located near the middle of bandgap. Taking into account this, one can neglect the first term in the denominator of Eq. (52) and obtain the following expression for the current density using Eq. (51):

$$J = qn_i\sinh(qV/2kT)\int_0^W f(x,V)dx. \tag{53}$$

where

$$f(x,V) = \{\cosh[(E_g^* - 2\Delta\mu - qV - 2\varphi(x,V)]/2kT]\}^{-1}. \tag{54}$$

The function $f(x,V)$ has a symmetric bell-shaped form, therefore without incurring noticeable errors, the integration in Eq. (53) may be replaced by the product of the maximum value of the

integrand $f(x,V)$ and its half-width $\Delta x_{1/2}$. By calculating $\Delta x_{1/2}$ as the difference of the values for which $f(x,V)$ is equal to ½, one can obtain under conditions that qV approaches not very close to $E_g - 2\Delta\mu$:

$$\Delta x_{1/2} \approx W\left(\frac{E_g - 2\Delta\mu - qV}{2(\varphi_{bi} - qV)}\right)^{1/2} \cdot \frac{2\,\mathrm{arccosh}2}{E_g - 2\Delta\mu - qV} = W\frac{2kT}{\sqrt{(\varphi_{bi} - qV)(E_g - 2\Delta\mu - qV)}}. \quad (55)$$

So Eq. (53) in the integral form yields the exponential dependence of the recombination current on the applied voltage ($\sinh(qV/2kT)=\exp(qV/2kT)/2$) [37, 38]:

$$J \approx \frac{qn_iW}{\sqrt{\tau_{no}\tau_{po}}}\frac{kT}{\sqrt{(\varphi_{bi} - qV)(E_g - 2\Delta\mu - qV)}}\left[\exp\left(\frac{qV}{2kT}\right) - 1\right]. \quad (56)$$

Fig. 21 shows a comparison of the voltage dependence of the recombination currents in CIGS solar cell, for example, with E_g=1.14 eV calculated using Eq. (51) and (56).

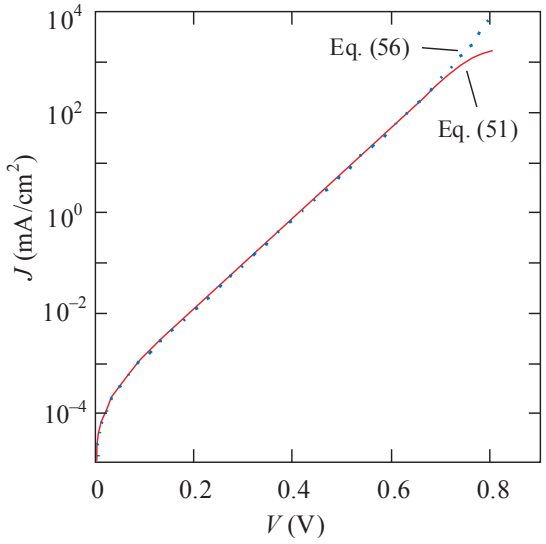

Figure 21. Comparison of the recombination currents in CIGS solar cell with 1.14 eV bandgap calculated from Eqs. (51) and (56).

As seen in Fig. 21, the *J–V* curves practically coincide. Currents calculated from the exact Eq. (51) exceeds those calculated from Eq. (56) by no more than 5–6% at low voltages and no more than 8–10% at higher voltages. When $V > 0.7$ V the curves are separated from one another

http://dx.doi.org/10.5772/59363

because in deriving Eq. (56) the effect associated with V approaching to φ_{bi}/q did not take into account. Thus, when analyzing the J–V characteristic at higher voltages, only exact Eq. (51) should be applied.

In addition to the results shown in Fig. 21, it is appropriate to draw attention to the rather important fact. If we express the voltage dependence of the recombination current as $J=J_o\exp(qV/AkT)$, the ideality factor A turns out to be slightly different from 2, close to 1.9. It is also appropriate to note that as early as the mid-1990s, the well-known scientists and experts came to the conclusion that the forward current in efficient thin-film CdS/CdTe solar cells is caused by recombination in the SCR of the absorber layer and it was shown that the ideality factor A in these devices coincides with the value 1.9 [40]. Comprehensive analysis and generalization of the experimental results obtained over many years confirm these results [41].

The difference of A from 2 is explained by the fact that according to Eq. (56), the dependence of the recombination current on the voltage is determined not only by the exponent $\exp(qV/2kT)$ but also by the pre-exponential factor $(E_g - 2\Delta\mu - qV)^{-1/2}$, which somewhat accelerates an increase in current with V, and thus lowers the ideality factor.

5.3. Finding the photoelectric characteristics of solar cells

First consider an applicability of the above theory of generation–recombination in the SCR to the experimental data discussed in Section 5.2.

The dark J–V curves (circles) along with the calculated results (solid lines) using Eq. (51) are shown in Fig. 22. In the calculations, we used the exact Eq. (51) in order to reflect the deviation of the forward current from the expression $J \propto \exp(qV/2kT)$, when qV approaches φ_{bi}. For CIS solar cell (E_g=1.04 eV) the experimentally obtained data is shown without modification (shunting is virtually absent), whereas for CIGS with the absorber bandgaps 1.14 and 1.36 eV the presented experimental data is obtained by subtracting the current through the shunts R_{sh} and taking into account the voltage drop across the series resistance R_s. As mentioned previously, at $V < 0.1$–0.2 V, the values of current under illumination J_{IL} and the short-circuit current J_{sc} are very close to each other, therefore the dark current cannot be determined with a proper accuracy and the experimental points are not shown for low voltages for the three solar cells. For solar cell with bandgap of the absorber E_g=1.5 eV fabricated at elevated temperature the measured data of the dark current is shown for low voltages as well.

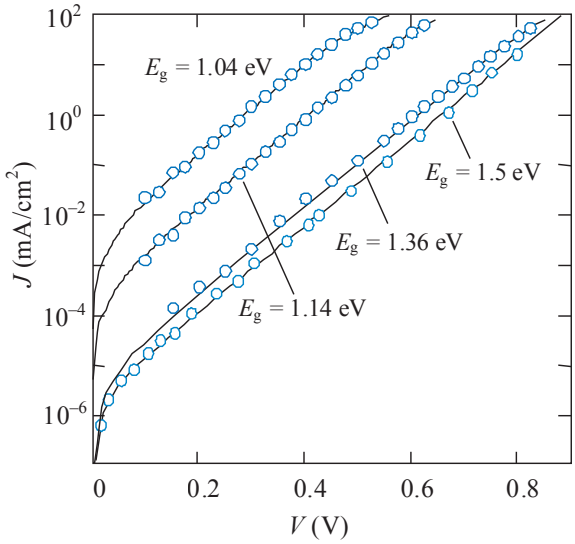

Figure 22. Comparison of the dark forward characteristics of CIGS solar cells extracted from the *J–V* curves under illumination [8] and the generation current (solid lines) calculated from Eq. (51).

As seen in Fig. 22, the calculated results agree well with the experimental data for all solar cells. One point to be mentioned is that in order to obtain a fit with the experimental data of solar cell with E_g=1.5 eV fabricated at elevated temperature, the effective carrier lifetime in the SCR was taken about an order of magnitude less than that for other solar cells. This explains why the curves with so much different bandgaps, E_g=1.36 and 1.5 eV, are located close to each other. It should also be emphasized that reducing the carrier lifetime results in the lowering of open-circuit voltage by ~ 0.06 V, which apparently is one of the negative aspects of the growth and post-growth processing at elevated temperature [36].

Knowing the dark *J–V* characteristics and the short-circuit current densities, it is not difficult to calculate the *J–V* curves under illumination as the dependences of $J_{IL}=J-J_{sc}$ vs. V, which are shown in Fig. 23a by bashed lines. For the short-circuit current densities we use the data given in Fig. 18a, although they can be obtained using the spectral distribution of the quantum efficiency and solar radiation (for the studied samples the discrepancy between the J_{sc} values calculated by these two methods does not exceed 3–4%). Also shown in Fig. 23a by circles are the measured results of the *J–V* curves for the samples with the absorber bandgaps 1.04, 1.14 and 1.36 eV.

Fig. 23b shows the dependences of the electrical power in the solar cell circuit $P=(J-J_{sc})V$ as a function of voltage V. The solid lines in both figures are the calculated results corresponding to the presence of shunts in cells, whereas dashed lines are the results obtained by subtracting the current through the shunt from the measured current.

http://dx.doi.org/10.5772/59363

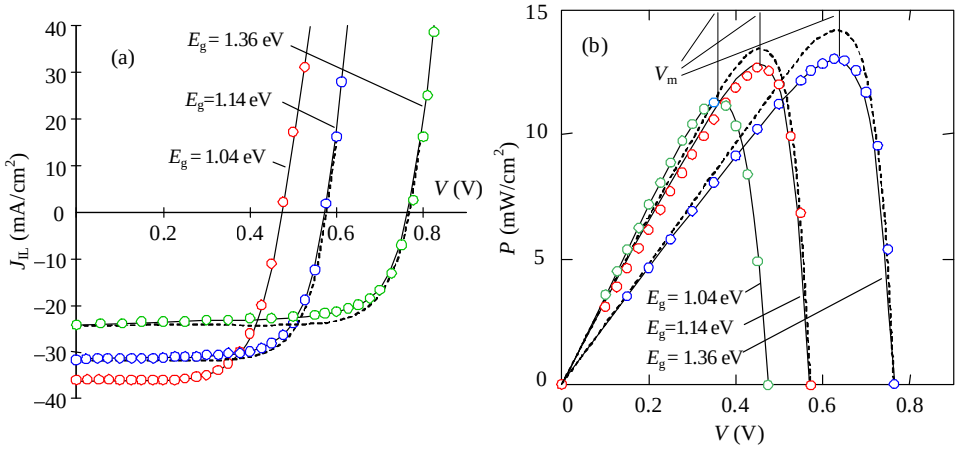

Figure 23. Comparison of voltage dependences of the measured current in CIGS solar cells under illumination I_{IL} (a) [8], and the electrical power P in the circuit of solar cell (b). The measured results are shown by circles, the results of calculations considering the presence of shunts and without them are shown by solid and dashed lines, respectively.

As seen in Fig. 23a, the calculated curve for sample with the bandgap 1.04 eV practically coincides with experimental curve, but in the cases of the absorbers with bandgaps 1.14 and 1.36 eV the calculations give overestimated values of the current. However, if the shunts are taken into account, the calculated and experimental curves for all samples practically coincide. It follows that a comparison of the theory and experiment gives the *quantitative* information on the electrical losses in solar cells. These losses manifest themselves clearly on the voltage dependences of the electrical power P produced by solar cell, $P=(J-J_{sc})V$ shown in Fig. 23b (as in Fig. 23a, the solid lines are the calculated results with the presence of a shunt in cell, whereas dashed line are the results obtained by subtracting the current through the shunts from the measured currents.).

As seen in Fig. 23, the calculated results agree well with the experimental data and indicate a noticeable negative effect of shunting in the studied cells. The effect of shunting is higher when the bandgap of the CIGS absorber is large (shunting does not reveal itself in CIS solar cell). As expected, the shunting does not practically vary the open circuit voltage but reduces the fill factor and the energy conversion efficiency. For the cell with absorber bandgap 1.14 eV, shunting leads to decreasing the fill factor from 0.73 to 0.70 and the efficiency from 13.3 to 12.7%. For cell with the absorber bandgap 1.36 eV, these values are 0.77 to 0.70 and 14.3 to 13.0%, respectively. The fill factor and efficiency of $CuInSe_2$ solar cell are equal to 0.67 and 11.3%, respectively.

Note that the efficiency of studied CIGS solar cells is in the range of 11-14% which is comparable with the efficiency of the modules produced in large volume, but much inferior to record efficiency of small area CIGS solar cells achieved so far.

6. Conclusions

The optical losses in $Cu(In,Ga)Se_2$ solar cells caused by reflections from the interfaces and absorption in the ZnO and CdS layers have been calculated using the optical constants of the materials. When calculating the integral photoelectric characteristics of a solar cell, ignoring the multiple reflections and interference effects in the ZnO and CdS layers cannot cause remarkable errors. (i) The losses due to reflection (reducing the short-circuit current density) from the front surface of ZnO with an antireflection coating in $CuInSe_2$, $CuIn_{0.69}Ga_{0.31}Se_2$ and $CuIn_{0.34}Ga_{0.66}Se_2$ solar cells are equal to 2.5, 1.9 and 1.4%, respectively (antireflection coating increases the photocurrent by 7.1%, 7.4% and 8.0%). The reflection losses at the ZnO/CdS interface are equal to 1.0, 0.9 and 0.9% for these cells, respectively, whereas for the CdS/CIGS interface the losses are 1.3, 1.2 and 1.1%, respectively. The total reflection losses for typical parameters of these solar cells are equal to 4.7, 4.0 and 3.5%, respectively (excluding shading by grid). (ii) The losses caused by absorption in the ZnO and CdS layers amount to 8.1, 7.8 and 9.6% for these solar cells, respectively. The losses due to insufficient absorptivity of the CIGS absorber are 0.6, 0.2 and 0.4%, respectively. The *total optical losses* with the antireflection coating amount to 17.4, 16.0 and 17.5% for solar cells with absorber bandgaps 1.04, 1.14 and 1.36 eV, respectively.

The recombination losses in the studied solar cells have been determined by comparing the measured quantum efficiency spectra with the calculation results. This approach allowed determining the real main parameters of the devices such as: lifetimes of charge carriers, concentration of uncompensated acceptors in the absorber, recombination velocity at the front and back surfaces, the thickness of the CdS film. (i) Recombination at the front surface of the absorber reduces the short-circuit current density by 2.2, 1.9 and 0.2% in solar cells with the CIGS bandgap 1.04, 1.14 and 1.36 eV, respectively. (ii) Recombination in the space-charge region causes a reduction of the short-circuit current density by 0.7, 0.1% and 1.0% for these devices, respectively. (iii) The losses in the neutral part of the absorber and the back surface amount to 2.5, 5.0 and 2.9%, respectively. (iv) Recombination only at the back surface of solar cells cause a decrease in the short-circuit current by no more than 0.2, 1.0 and 0.1%, respectively. *Total recombination losses* in the studied CIGS solar cells with bandgap of absorber 1.04, 1.14 and 1.36 eV are equal to 5.4, 7.0 and 4.1%, respectively. The recombination losses, which degrade the charge collection efficiency of solar cells, can be lowered by increasing the mobility and lifetime of electrons and holes within the literature data. Even greater improvement of the charge collection efficiency can be achieved by extending the SCR. However, positive impact of these measures is limited by the fact that the diffusion length of electrons and the SCR width can become larger than the absorber thickness, which for 100% charge collection efficiency should be increased.

Knowing the short-circuit current density and the dark *J–V* characteristic of $CuIn_{1-x}Ga_xSe_2$ solar cell, the *J–V* curve under illumination can be accurately calculated along with the fill factor, open-circuit voltage and energy conversion efficiency. A comparison of the calculated and measured *J–V* curve under illumination gives the quantitative information on the electrical losses in solar cells indicated a significant impact of shunting, which increases

http://dx.doi.org/10.5772/59363

with increasing the absorber bandgap. If to take into account the effect of shunts, the *J–V* curves of all samples are described by the theory of generation-recombination of charge carriers in the space-charge region. For a cell with the absorber bandgap 1.14 eV, shunting leads to decreasing the fill factor from 0.73 to 0.70 and the efficiency from 13.3 to 12.7%, whereas for cell with the absorber bandgap 1.36 eV the efficiency loss amounts to 1.3%. In $CuInSe_2$ solar cell there are no electric losses, the fill factor and efficiency are equal to 0.67 and 11.3%, respectively. Fabrication technology of CIGS solar cell at elevated temperature (600 – 650°C) allows eliminating the effect of shunting in solar cells with the absorber bandgaps up to 1.4–1.5 eV, but this is accompanied by shortening the carrier lifetime and results in lowering the open-circuit voltage.

Acknowledgements

Author would like to thank Xavier Mathew (Instituto de Energias Renovables, UNAM, Mexico) for his valuable suggestions and support in compiling this chapter.

Author details

Leonid A. Kosyachenko*

Chernivtsi National University, Chernivtsi, Ukraine

References

[1] Bailey S., Raffaelle R. (2011) Space Solar Cells and Arrays. In: Handbook of Photovoltaic Science and Engineering, Luque A. and Hegedus S., editors, 2nd ed. West Sussex, UK: John Wiley & Sons, pp. 365-401.

[2] Green M.A., Emery K., Hishikawa Y., Warta W. (2011) Solar cell efficiency tables (version 37), Prog. Photovolt: Res. Appl. 19: 84-92.

[3] Jackson P., Hariskos D., Wuerz R., Wischmann W. and Powalla M. (2014) Compositional investigation of potassium doped Cu(In,Ga)Se_2 solar cells with efficiencies up to 20.8%. Phys. Status Solidi (RRL) 8: 219–222.

[4] <http://www.pv-magazine.com/services/press-releases/details/beitrag/first-solar-sets-world-record-for-cdte-solar-cell-efficiency_100014340/#axzz2zdlNoCPE>.

[5] < http://www.avancis.de/en/cis-technology/cis-world-records/>

[6] Kosyachenko L.A., Grushko E.V., Mathew X. (2012) Quantitative assessment of optical losses in thin-film CdS/CdTe solar cells, Solar Energy Materials and Solar Cells 96: 231–237.

[7] Kosyachenko L.A., Mathew X., Roshko V.Ya., Grushko E.V. (2013) Optical absorptivity and recombination losses: The limitations imposed by the thickness of absorber layer in CdS/CdTe solar cells, Solar Energy Materials and Solar Cells 114: 179-185.

[8] Shafarman W.N., Siebentritt S. and Stolt L. (2011) Cu(InGa)Se_2 Solar Cells. In: Handbook of Photovoltaic Science and Engineering, Luque A. and Hegedus S., editors, 2nd ed. West Sussex, UK: John Wiley & Sons, pp. 546-599.

[9] Kosyachenko L.A., Mathew X., Paulson P.D., Lytvynenko V.Ya., Maslyanchuk O.L. (2014) Optical and recombination losses in thin-film Cu(In,Ga)Se_2 solar cells. Solar Energy Materials and Solar Cells. 120: 291–302.

[10] Dai Z.-H., Zhang R.-J., Shao J., Chen Y.-M., Zheng Y.-X., Wu J.-D., Chen L.-Y. (2009) Optical properties of zinc-oxide films determined using spectroscopic ellipsometry with various dispersion models. J. Korean Phys. Soc. 55: 1227–1232.

[11] Ninomiya S., Adachi S. (1995) Optical properties of wurtzite CdS. J. Appl. Phys. 78: 1183– 1190.

[12] Paulson P.D., Birkmire R.W., and Shafarman W.N. (2003) Optical characterization of $CuIn_{1-x}Ga_xSe_2$ alloy thin films by spectroscopic ellipsometry. J. Appl. Phys. 94: 879–888.

[13] Bonch-Bruevich V.L. (1970) Interband optical transitions in disordered semiconductors Phys. Status Solidi (b). 42: 35–39.

[14] Born M., Wolf E. (1999) Principles of Optics, 7th ed., Cambridge: University Press, p. 65.

[15] Reference Solar Spectral Irradiance at the Ground at Different Receiving Conditions. Standard of International Organization for Standardization ISO 9845-1:1992.

[16] Wang E.Y., Yu F.T.S., Sims V.L., Brandhorst E.W., Broder J.D., Optimum design of anti-reflection coating for silicon solar cells. 10th IEEE Photovoltaic Specialists Conference. November 13-15, 1973, Palo Alto, California, pp. 168-171.

[17] Pern F.J., L. Mansfield, DeHart C., Glick S.H., Yan F., and Noufi R.. Thickness effect of Al-doped ZnO window layer on damp heat stability of $CuInGaSe_2$ solar cells. Presented at the 37th IEEE Photovoltaic Specialists Conference, Seattle, Washington June 19-24, 2011. Conference Paper NREL/CP-5200-50682.

[18] Kosyachenko L.A., Grushko E.V., Mykytyuk T.I. (2012) Absorptivity of semiconductors used in the production of solar cell panels, Semiconductors. 46: 466-470.

[19] Sah C., Noyce R., Shockley W. (1957) Carrier generation and recombination in p-n junctions and p-n junction characteristics, Proc. IRE 46: 1228–1243.

[20] Schroeder D., Rockett, A, J. (1997) Electronic effects of sodium in epitaxial $CuIn_{1-x}Ga_xSe_2$. Appl. Phys. 82: 4982–4985.

[21] Lavagna M., Pique J.P., Marfaing Y. (1977) Theoretical analysis of the quantum photoelectric yield in shottky diodes. Solid State Electronics 20: 235-242.

[22] Sze S.M., Ng K.K. (2006) Physics of Semiconductor Devices, 3rd ed., New Jersey: Wiley-Interscience.

[23] Brown G., Faifer V., Pudov A., Anikeev S., Bykov E., Contreras M., Wu J. (2010) Determination of the minority carrier diffusion length in compositionally graded Cu(In,Ga)Se_2 solar cells using electron beam induced current. Appl. Phys. Lett. 96: 022104.

[24] Kodigala S.R, (2011) $Cu(In_{1-x}Gax)Se_2$ Based Thin Film Solar Cells. Burlington. USA: Academic Press.

[25] Chien-Chen Diao, Hsin-Hui Kuo, Wen-Cheng Tzou, Yen-Lin Chen, Cheng-Fu Yang. (2014) Fabrication of CIS absorber layers with different thicknesses using a non-vacuum spray coating method, Materials. 7: 206–217.

[26] Dinca S.A., Schiff E.A., Shafarman W.N., Egaas B., Noufi R., Young D.L. (2012) Electron drift-mobility measurements in polycrystalline $CuIn_{1-x}Ga_xSe_2$solar cells, Appl. Phys. Lett. 100: 103901.

[27] Puech K., Zott S., Leo K., Ruckh M., Schock H.-W. (1996) Determination of minority carrier lifetimes in $CuInSe_2$ thin films. Appl. Phys. Appl. Phys. Lett. 69: 3375-3377.

[28] Repins I., Contreras M., Romero M., Yan Y., Metzger W., Li J., Johnston S., Egaas B., DeHart C., Scharf J., McCandless B.E., Noufi R. (2008) Characterization of 19.9%-efficient CIGS absorbers, 33rd IEEE Photovoltaic Specialists Conference, San Diego, California, May 11–16,, Paper NREL/CP-520-42539.

[29] Kosyachenko L., Toyama T. (2014) Current–voltage characteristics and quantum efficiency spectra of efficient thin-film CdS/CdTe solar cells, Solar Energy Materials and Solar Cells 120: 512–520.

[30] Wada T. (1997) Microstructural characterization of high-efficiency Cu(In,Ga)Se_2 solar cells, Solar Energy Materials and Solar Cells 49: 249–260.

[31] Nakada T., Kunioka A. (1999) Direct evidence of Cd diffusion into Cu(In,Ga)Se_2 thin films during chemical-bath deposition process of CdS films, Appl. Phys. Lett. 74: 2444–2446.

[32] Birkmire R.W., Eser E. (1997) Polycrystalline thin film solar cells: Present Status and Future Potential. Annu. Rev. Mater. Sci. 27: 625-53.

[33] Hecht K. (1932) Zum Mechanismus des lichtelektrischen Primärstromes in isolierenden Kristallen, Zeits. Phys. 77: 235-243.

[34] Shafarman W.N., Klenk, W.N., McCandless, R.B.E. (1996) Device and Material Characterization of Cu(InGa)Se_2 Solar Cells with Increasing Band Gap. J. Appl. Phys. 79(9): 7324-7328.

[35] Cooray N.F., Kushiya, K., Fujimaki, A., Sugjyama, I., Miora, T., Okumura, D., Sato, M., Ooshita, M., Yamase, O. (1997) Large area ZnO films optimized for graded bandgap Cu(InGa)Se_2-based thin-film mini-modules. Solar Energy Materials and Solar Cells. 49: 291–297.

[36] Contreras M.A., Mansfield L.M., Egaas B., Li J., Romero M., Noufi R., Rudiger-Voigt E., Mannstadt W. (2012) Wide bandgap Cu(In,Ga)Se_2 solar cells with improved energy conversion efficiency. Progress in Photovoltaics: Research and Applications. 20: 843–850.

[37] Kosyachenko L.A., Maslyanchuk O.L., Motushchuk V.V., Sklyarchuk V.M. (2004) Charge transport generation-recombination mechanism in Au/n-CdZnTe diodes. Solar Energy Materials and Solar Cells. 82(1-2): 65-73.

[38] Kosyachenko L.A. (2006) Problems of efficiency of photoelectric conversion in thin-film CdS/CdTe solar cells. Semiconductors. 40(6): 710-727.

[39] Kosyachenko L.A., Savchuk A.I., Grushko E.V. (2009) Dependence of efficiency of thin-film CdS/CdTe solar cell on parameters of absorber layer and barrier structure. Thin Solid Films. 517: 2386–2391.

[40] Phillips J.E., Birkmire R.W., McCandless B.E., Meyers P.V., Shafarman W.N. (1996) Polycrystalline heterojunction solar cells: A device perspective, Phys Status Solidi B 194: 31–39.

[41] McCandless B.E., Sites J.R. (2011) Cadmium telluride solar cells. In: Handbook of Photovoltaic Science and Engineering. Eds. A. Luque, S. Hegedus, 2nd ed., John Wiley & Sons, Ltd., Hoboken, NJ, pp. 600–641.

Chapter 2

Theoretical Calculation of the Efficiency Limit for Solar Cells

Abderrahmane Belghachi

Additional information is available at the end of the chapter

http://dx.doi.org/10.5772/58914

1. Introduction

In recent years there has been intense research work into the development of high efficiency solar cells relying on emerging novel materials and structures. All this has lead to a continuous record breaking of highest achievable efficiencies using different technologies. Since the first photovoltaic devices were developed the most prevalent concern is to hem in all sorts of efficiency losses preventing from reaching the physical limits [1-3]. To overcome this impediment, thorough investigations have been carried out to control and unearth their origins in order to identify potential efficiency advantages. Numerous thermodynamic approaches were employed to calculate solar cell efficiency limit, starting from the ideal Carnot engine to the latest detailed balance with its improved approach.

The aim of this chapter is to present a review of the techniques used to calculate the energy conversion efficiency limit for solar cells with detailed calculation using a number of numerical techniques. The study consists of analyzing the solar cell intrinsic losses; it is these intrinsic losses that set the limit of the efficiency for a solar energy converter. Several theoretical approaches were used in order to obtain the thermodynamic limit for energy conversion.

In the first place a solar cell could be considered as a simple energy converter (engine) able to produce an electrical work after the absorption of heat from the sun. In this fundamental vision the solar cell is represented by an ideally reversible Carnot heat engine in perfect contact with high temperature reservoir (the sun) and low temperature reservoir representing the ambient atmosphere. If the sun is at a temperature of *6000K* and the ambient temperature is *300K*, the maximum Carnot efficiency is about *95%* this value constitutes an upper limit for all kind of solar converters.

When the solar cell is supposed a blackbody converter absorbing radiation from the sun itself a blackbody, without creating entropy, we obtain an efficiency of about 93 % known as the Landsberg efficiency limit, which is slightly lower than Carnot efficiency.

Whilst a solar cell is assumed as an endoreversible system [4], the energy conversion efficiency is limited to 85.7% this figure is obtained where the sun is assumed fully surrounding the cell (maximum concentration). If we bear in mind that in a real situation the solar cell does not operate always in maximum concentration and the solid angle under which the cell sees the sun is in fact only a minute fraction of a hemisphere, the maximum efficiency is not larger than 12.79%, which is actually lower than most recently fabricated solar cells. However, we can conclude that solar cell is a quantum converter and cannot be treated as a simple solar radiation converter [5].

Semiconductor *pn* junction solar cell is a quantum converter where the energy band-gap of semiconductor material is the most important and critical factor controlling efficiency. Incident photons with energy higher than the energy gap can be absorbed, creating electron-hole pairs, while those with lower energy are not absorbed, either reflected or transmitted.

In the ideal model of a monochromatic cell incident photons are within a narrow interval of energy, while the cell luminescence outside this range is prevented. The overall resulting efficiency upper limit for an infinite number of monochromatic cells is 86.81% for fully concentrated sun radiation.

The ultimate efficiency of a single band gap *pn* junction for an AM1.5 G solar spectrum gives a value of 49%, this maximum efficiency, if compared to Carnot efficiency limit, is substantially lower. Therefore in quantum converters it is obvious that more than 50% of the solar radiation is lost because of spectral mismatch.

To represent a more realistic picture of a solar cell, three other fundamental factors should be taken into account, namely; the view factor of the sun seen from the solar cell position, the background radiation which could be represented as a blackbody at ambient temperature, and losses due to recombination, radiative and non-radiative.

In the detailed balance efficiency limit calculation first suggested in 1961 by Shockley and Queisser (SQ) in their seminal paper [6]. It is assumed that illumination of semiconductor *pn* junction by a blackbody source creates electron-hole pairs due to the fundamental absorption of photons with energies greater than the band-gap. These pairs either recombine locally if they are not separated and extracted along different paths to perform work in an external circuit. They assumed that recombination in the semiconductor is partly radiative and the maximum efficiency is attained when radiative recombination in dominant. The Shockley-Queisser model has been extended and completed to account for more physical phenomena [7-13]. For instance, the generalised Planck radiation law introduced by Würfel [7], the effect of background radiation has been included and elaborate numerical techniques has been used in order avoid mathematical approximations which would yield erroneous results.

The currently achieved short-circuit current densities for some solar cells are very close to predicted limits [14]. Nevertheless, further gain in short-circuit current can therefore still be

http://dx.doi.org/10.5772/58914

obtained, mainly by minimising the cell surface reflectivity, while increasing the thickness, so as to maximize the photons absorption. For thin film solar cells gain in photocurrent can be obtained by improving light trapping techniques to enhance the cell absorption.

Radiative recombination and the external fluorescence efficiency have a critical role to play, if the created photons are re-emitted out of the cell efficiently, which corresponds to low optical losses, the open circuit voltage and consequently the cell efficiency approach their limits [15]. Concentrating solar radiation onto a solar cell improves remarkably its performance. Comparable effect could be obtained if the solar cell emission and acceptance angles were made equal.

2. Solar cell as a heat engine

2.1. Solar cell as a reversible heat engine

Thermodynamics has widely been used to estimate the efficiency limit of energy conversion process. The performance limit of solar cell is calculated either by thermodynamics or by detailed balance approaches. Regardless of the conversion mechanism in solar cells, an upper efficiency limit has been evaluated by considering only the balances for energy and entropy flux rates. As a first step the solar cell was represented by an ideally reversible Carnot heat engine in perfect contact with high temperature T_s reservoir (the sun) and low temperature T_a reservoir representing the ambient atmosphere. In accordance with the first law of thermodynamics the extracted work, the cell electrical power output, is represented as the difference between the net energy input from the sun and the energy dissipated to the surrounding environment. The model is illustrated in figure 1. Where Q_1 is the incident solar energy impinging on the cell, Q_2 is the amount of energy flowing from the converter to the heat sink and W is the work delivered to a load in the form of electrical energy ($W=Q_1-Q_2$). The efficiency of this system is defined using the first thermodynamic law as:

$$\eta_c = \frac{W}{Q_1} = \frac{Q_1 - Q_2}{Q_1} = 1 - \frac{Q_2}{Q_1} \tag{1}$$

for a reversible engine the total entropy is conserved, $S = S_1 - S_2 = 0$, then;

$$\frac{Q_1}{T_1} - \frac{Q_2}{T_2} = 0 \tag{2}$$

Hence the Carnot efficiency could be represented by:

$$\eta_c = 1 - \frac{T_a}{T_s} \tag{3}$$

This efficiency depends simply on the ratio of the converter temperature, which is equal to that of the surrounding heat sink, to the sun temperature. This efficiency is maximum ($\eta_c=1$) if the converter temperature is *0 K* and the solar energy is totally converted into electrical work, while $\eta_c=0$ if the converter temperature is identical to that of the sun T_s the system is in thermal equilibrium so there is no energy exchange. If the sun is at a temperature of *6000K* and the ambient temperature is *300K*, the Carnot efficiency is *95*% this value constitutes an upper limit for all solar converters.

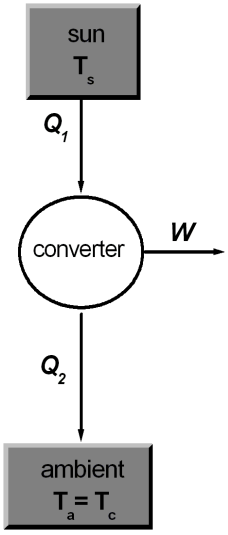

Figure 1. A schematic diagram of a solar converter represented as ideal Carnot engine.

Another way of calculating the efficiency of a reversible heat engine where the solar cell is assumed as a blackbody converter at a temperature T_c, absorbing radiation from the sun itself a blackbody at temperature T_s, without creating entropy, this efficiency is called the Landsberg efficiency[16].

Under the reversibility condition the absorbed entropy from the sun S_{abs} is given off in two ways one is emitted back to the sun S_{emit} and the second part goes to the ambient thermal sink S_a. Under this condition, the solar cell is called reversible if:

$$S_{abs} - S_{emit} - S_a = 0 \tag{4}$$

In accordance with the Stefan–Boltzmann law of black body, the absorbed heat flow from the sun is:

http://dx.doi.org/10.5772/58914

$$Q_{abs} = \sigma T_s^4 \tag{5}$$

For a blackbody radiation, the absorbed density of entropy flow is:

$$S_{abs} = \frac{4}{3}\sigma T_s^3 \tag{6}$$

The energy flow emitted by the converter at a temperature T_c is:

$$Q_{emit} = \sigma T_c^4 \tag{7}$$

And the emitted entropy flow is:

$$S_{emit} = \frac{4}{3}\sigma T_c^3 \tag{8}$$

In this model the blackbody source (sun) surrounds entirely the converter at T_c which is assumed in a contact with a thermal sink at T_a then T_c=T_a. Therefore the entropy transferred to the thermal sink is:

$$S_a = S_{abs} - S_{emit} = \frac{4}{3}\sigma(T_s^3 - T_c^3) \tag{9}$$

And the transferred heat flow is:

$$Q_a = T_c S_a = \frac{4}{3}\sigma T_c (T_s^3 - T_c^3) \tag{10}$$

The entropy-free, utilizable work flow is then:

$$W = Q_{abs} - Q_{emit} - Q_a \tag{11}$$

Therefore the Landsberg efficiency can be deduced as:

$$\eta_L = \frac{W}{Q_{abs}} = 1 - \frac{4}{3}\frac{T_c}{T_s} + \frac{1}{3}\left(\frac{T_c}{T_s}\right)^4 \tag{12}$$

The actual temperature of the converter T_c depends on the operating point of the converter and is different from the ambient temperature T_a, ($T_c \neq T_a$). To maintain the same assumption as the Landsberg efficiency calculation, the entropy transferred to the ambient thermal sink is rewritten as:

$$Q_a = T_a S_a = \frac{4}{3}\sigma T_a (T_s^3 - T_c^3) \tag{13}$$

We arrive to a more general form of the Landsberg efficiency η':

$$\eta'_L = 1 - \left(\frac{T_c}{T_s}\right)^4 - \frac{4}{3}\frac{T_a}{T_s}\left(1 - \frac{T_c^3}{T_s^3}\right) \tag{14}$$

Both forms of Landsberg efficiency (η_L and η'_L) are plotted in Figure 2, Carnot efficiency curve is added for comparison. At $300K$ η_L and η'_L coincide at 93.33 % which is slightly lower than Carnot efficiency. When the temperature of the converter is greater than the ambient temperature ($T_c > T_a$) there is less heat flow from the converter to the sun (in accordance with Landsberg model). This means that much work could be extracted from the converter leading to a higher efficiency. As T_c approaches the sun temperature, the net energy exchange between the sun and the converter drops, therefore the efficiency is reduced and finally goes to zero for T_c=T_s.

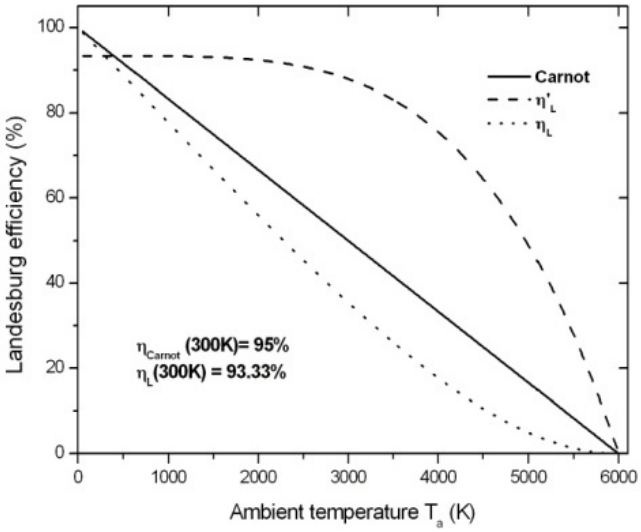

Figure 2. Landsberg and Carnot Efficiency limits of a solar converter versus ambient temperature.

http://dx.doi.org/10.5772/58914

In the Landsberg model the blackbody radiation law for the sun and the solar cell has been included, unlike the previous Carnot engine.

This figure represents an upper bound on solar energy conversion efficiency, particularly for solar cells which are primarily quantum converters absorbing only photons with energies higher or equal to their energy bandgap. On the other hand in the calculation of the absorbed solar radiation the converter was assumed fully surrounded by the source, corresponding to a solid angle of 4π.

Using the same approach it is possible to split the system into two subsystems each with its own efficiency; the Carnot engine that include the heat pump of the converter at T_c and the ambient heat sink at T_a, with an efficiency η_c (ideal Carnot engine).

$$\eta_c = 1 - \frac{T_a}{T_c} \tag{15}$$

The ambient temperature is assumed equal to 300 *K*, therefore high efficiency is obtained when the converter temperature is higher then the ambient temperature.

The second part is composed of the sun as an isotropic blackbody at T_s and the converter reservoir assumed as a blackbody at a temperature T_c. The energy flow falling upon Q_{abs} and emitted by the solar converter Q_{emit} are given by:

$$Q_{abs} = C\, f\, \sigma T_s^4 \text{ and } Q_{emit} = \sigma T_c^4 \tag{16}$$

In which *f* is a geometrical factor taking into account the limited solid angle from which the solar energy falls upon the converter. In accordance with the schematic representation of figure 3, where the solar cell is represented as a planar device irradiated by hemisphere surrounding area and the sun subtending a solid angle ω_s at angle of incidence θ, *f* is defined as the ratio of the area subtended by sun to the apparent area of the hemisphere:

$$f = \frac{\int_{\omega_s} \cos\theta \, d\omega}{\int_{2\pi} \cos\theta \, d\omega} = \frac{\omega_s}{\pi} \tag{17}$$

ω_s being the solid angle subtended by the sun, where ω_s=6.85×10^{-5} sr. The concentration factor *C* (*C* > 1) is a measure of the enhancement of the energy current density by optical means (lens, mirrors…).The maximum concentration factor is obtained if we take T_s=6000°*K*:

$$\sigma T_s^4 = C_{\max}\, f\, \sigma T_s^4 \tag{18}$$

Then

$$C_{max} = 1/f \approx 46200$$

The case of maximum concentration also corresponds to the schematic case where the sun is assumed surrounding entirely the converter as assumed in previous calculations.

Similar situation can be obtained if the solid angle through which the photons are escaping from the cell (emission angle) is limited to a narrow range around the sun. This can be achieved by hosing the cell in a cavity that limits the angle of the escaping photons.

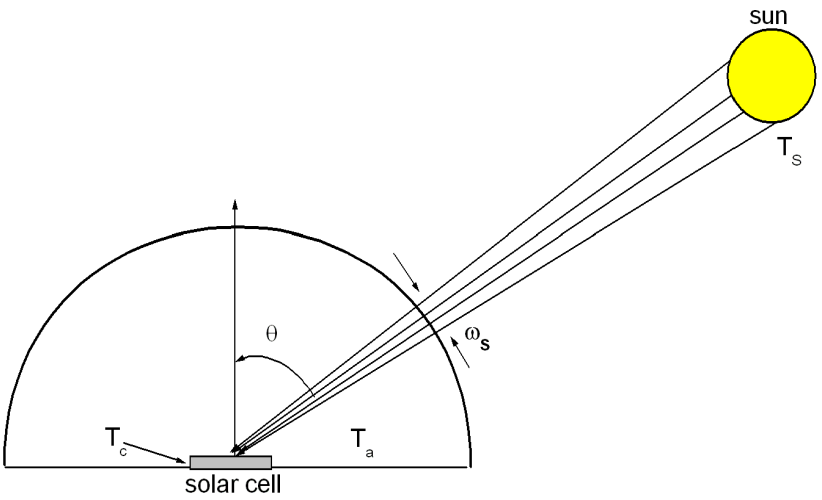

Figure 3. A schematic representation of a solar converter as a planar cell irradiated by the sun subtending a solid angle ω_s at angle of incidence θ.

The efficiency of this part of the system (isolated) is given by:

$$\eta_{abs} = 1 - \frac{Q_{emit}}{Q_{abs}} \tag{19}$$

the resulting efficiency is simply the product:

$$\eta_{ac} = \eta_c . \eta_{abs} = \left(1 - \frac{T_c^4}{C\, f\, T_s^4}\right)\left(1 - \frac{T_a}{T_c}\right) \tag{20}$$

This figure represents an overall efficiency of the entropy-free energy conversion by blackbody emitter-absorber combined with a Carnot engine. The temperature of the surrounding ambient

http://dx.doi.org/10.5772/58914

T_a is assumed equal to 300*K*. When *f* is taken equal to ω_s/π=2.18×10^{-5} and without concentration (*C*=1) we obtain a very low efficiency value (about 6.78%), as shown in figure 4. The efficiency for concentrations of 10, 100 and full concentration (46200) is found respectively 31.36, 53.48 and 85.38%. In this model the solar cell is not in thermal equilibrium with its surrounding ($T_c \neq T_a$), then it exchanges radiation not only with the sun but also with the ambient heat sink. Therefore, energy can be produced or absorbed from the surrounding acting as a secondary source. Neglecting this contribution naturally decreases the efficiency of the converter, particularly at *C*=1. The second explanation of the low efficiency value is the under estimation of the re-emitted radiation from the cell, at operating conditions the solar cell re-emits radiation efficiently especially at open circuit point.

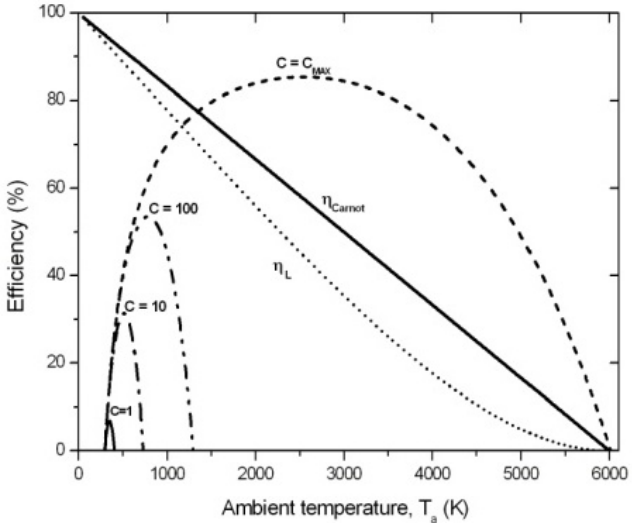

Figure 4. Efficiency η_{ac} for different concentration rates (*C*=1, 10, 100 and C_{max}) with Landsberg and Carnot Efficiency limits of a solar converter as a function of ambient temperature.

2.2. Solar cell as an endoreversible heat engine

A more realistic model has been introduced by De Vos et al. [8] in which only a part of the converter system is reversible, endoreversible system. An intermediate heat reservoir is inserted at the temperature of the converter T_c, this source is heated by the sun at T_s (blackbody radiation) and acting as a new high temperature pump in a reversible Carnot engine. In this system the entropy is generated between the T_s reservoir and the converter, the temperature T_c is fictitious and is different from the ambient temperature T_a. The effective temperature T_c depends on the rate of work production. In this model the solar converter is assumed to behave like the Müser engine, itself a particular case of the Curzon-Ahlborn engine, as shown in Fig. 5, the sun is represented by blackbody source at temperature T_1=T_s the solar cell includes a heat reservoir assumed as blackbody at T_3=T_c (the converter temperature) and an ideal Carnot

engine capable of producing utilizable work (electrical power), however T_c is related to the converter working condition. This engine is in contact with an ambient heat sink at T_2 representing the ambient temperature T_2=T_a. In addition to the absorbed energy from the sun, the converter absorbs radiation from ambient reservoir assumed as a blackbody at T_a.

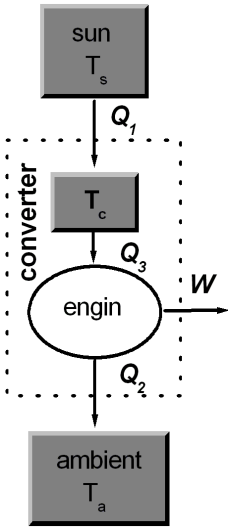

Figure 5. A schematic diagram of a solar converter represented as an endoreversible system.

The net energy flow input to the converter, including the incident solar energy flow $f\,\sigma\,T_s^4$, the energy flow $(1-f)\,\sigma\,T_a^4$ from the surrounding and the energy flow emitted by the converter is then:

$$Q_1 = f\sigma T_s^4 + (1-f)\sigma T_a^4 - \sigma T_c^4 \tag{21}$$

The Müser engine efficiency (Carnot engine):

$$\eta_M = \frac{W}{Q_1} = 1 - \frac{T_a^4}{T_c^4} \tag{22}$$

The converter temperature can be extracted from η_M:

$$T_c = \frac{T_a}{1-\eta_M} \tag{23}$$

http://dx.doi.org/10.5772/58914

And the solar efficiency is defined as ratio of the delivered work to the incident solar energy flux:

$$\eta_S = \frac{W}{f\sigma T_s^4} \tag{24}$$

hence

$$\eta_S = \eta_M \left[1 + \frac{(1-f)(1-\eta_M)^4 - 1}{(1-\eta_M)^4} \frac{T_a^4}{f T_s^4} \right] \tag{25}$$

The maximum solar efficiency is then a function of two parameters; the Müser efficiency and the surrounding ambient temperature. From the 3d representation at figure 6 of the solar efficiency (η_s) against Müser efficiency η_M and the surrounding temperature T_a, the efficiency is high as the temperature is very low and vanishes for very high temperature (as T_a approaches the sun temperature). For T_a=289.23K the efficiency is 12.79% if the sun's temperature is 6000°*K*.

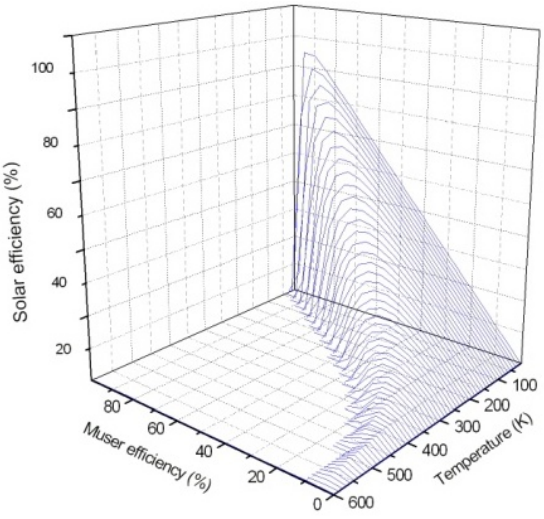

Figure 6. The solar efficiency surface η_s (η_M, T_a), the sun as a blackbody at T_s=6000°*K*.

A general expression of solar efficiency of the Müser engine is obtained when the solar radiation concentration factor *C* is introduced:

$$\eta_S = \eta_M \left[1 + \frac{(1 - C f)(1 - \eta_M)^4 - 1}{(1 - \eta_M)^4} \frac{T_a^4}{C f T_s^4} \right] \tag{26}$$

Compared to Carnot efficiency engine the Müser engine efficiency, even when C is maximal, remains low.

If the ratio $T_a^4 / f\ T_s^4$ is fixed to 1/4, as in [5], which gives a good approximation for ambient temperature, T_a=289.23K, with T_s=6000K.

Hence, the corresponding η_S becomes:

$$\eta_S = \eta_M \left[1 + \frac{(1 - C f)(1 - \eta_M)^4 - 1}{4(1 - \eta_M)^4} \right] \tag{27}$$

In the assumption of T_a=289.23K the maximum efficiency without concentration, i.e. the solar cell sees the sun through a solid angle ω_s is 12.79% which is better than the predicted value of Würfel [7] but still very low, as shown in figure 8. For concentration equal to 10, 100 and C_{MAX}, the efficiency reaches 33.9, 54.71 and 85.7% respectively.

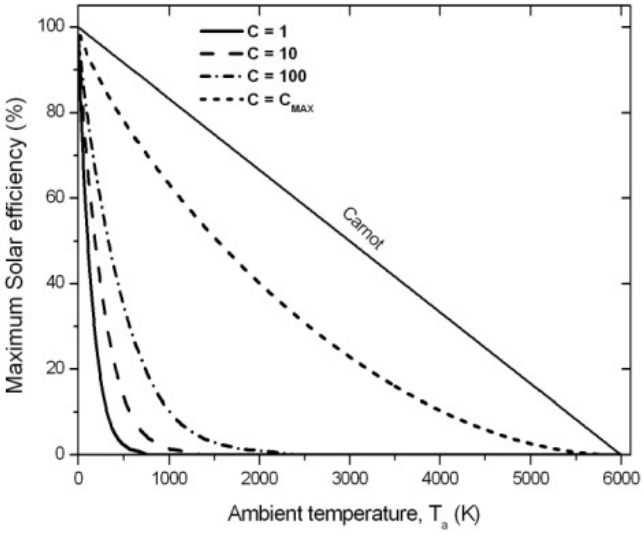

Figure 7. The maximum solar efficiency using Müser engine for different concentration rates (C=1, 10, 100 and C_{max}) with Carnot Efficiency limit as a function of ambient temperature.

http://dx.doi.org/10.5772/58914

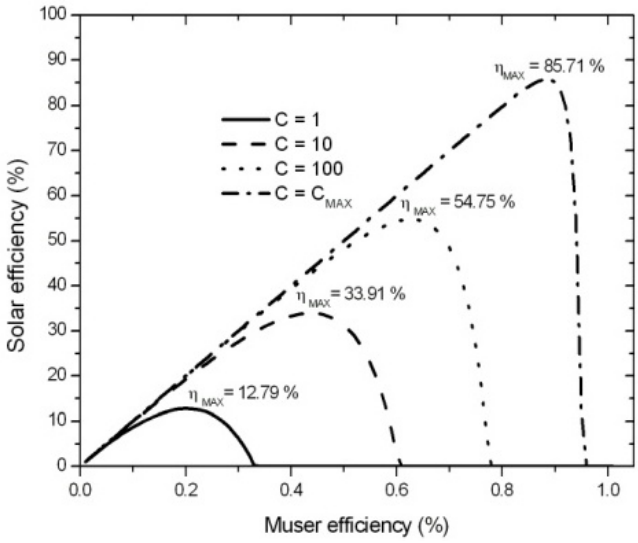

Figure 8. The solar efficiency using Müser engine for different concentration rates (C=1, 10, 100 and C_{max}) as a function of Müser efficiency.

3. Solar cell as a quantum converter

3.1. Introduction

In a quantum converter the semiconductor energy band-gap, of which the cell is made, is the most important and critical factor controlling efficiency losses. Although what seems to be fundamental in a solar cell is the existence of two distinct levels and two selective contacts allowing the collection of photo-generated carriers [2].

Incident photons with energy higher than the energy gap can be absorbed, creating electron-hole pairs, while those with lower energy are not absorbed, either reflected or transmitted. The excess energy of the absorbed energy greater than the energy gap is dissipated in the process of electrons thermalisation, resulting in further loss of the absorbed energy. Besides, only the free energy (the Helmholtz potential) that is not associated with entropy can be extracted from the device, which is determined by the second law of thermodynamics.

3.2. Monochromatic solar cell

It is interesting to examine first an ideal monochromatic converter illuminated by photons within a narrow interval of energy around the bandgap $h\nu_g = E_g$. In the ideal case each absorbed photon yields an electron-hole pair. This cell also prevents the luminescent radiation of energy outside this range from escaping. According to the blackbody formula of the Plank distribu-

tion, the number of photons incident from the sun within an interval of frequency $d\nu$ per unit area per second is:

$$dN_S = \frac{2\pi}{c^2} \frac{\nu_g^2}{\exp\left(\frac{h\nu_g}{kT_s}\right) - 1} d\nu \tag{28}$$

The number of created electron-hole pairs, in the assumption that each absorbed photon yields an electron-hole pair, could be simply represented by: $C\, f\, A_c d N_S$, where C is the solar radiation concentration factor, f is a geometrical factor, taking into account the limited angle from which the solar energy falls upon the solar converter and A_c is the converter projected area. In monochromatic cell only photons with proper energy are allowed to escape from the cell ($h\nu_g \approx E_g$) as a result of recombination. To obtain the efficiency of monochromatic ideal quantum converter we assume that only radiative recombination is allowed. Using the generalised Planck radiation law introduced by Würfel [7], the number of photons emitted by the solar cell per unit area per second within an interval of frequency $d\nu$ is:

$$dN_c = \frac{2\pi}{c^2} \frac{\nu_g^2}{\exp\left(\frac{h\nu_g - \mu_{eh}}{kT_c}\right) - 1} d\nu \tag{29}$$

Where μ_{eh} is the emitted photon chemical potential, with $\mu_{eh}=F_n-F_p$, (F_n, F_p are the quasi Fermi levels of electrons and holes respectively). The cell is assumed in thermal equilibrium with its surrounding ambient, then $T_c=T_a$.

This expression describes both the thermal radiation (for $\mu_{eh}=0$) and emission of luminescence radiation (for $\mu_{eh} \neq 0$). The number of emitted photons from the cell is then: $f_c\, A_c d N_c$, f_c is a geometrical factor depending on the external area from which the photons are leaving the solar converter and is equal to 1 if only one side of the cell is allowed to radiate and 2 if both sides of the cell are luminescent (f_c is chosen equal to one in the following calculation). For a spatially constant chemical potential of the electron-hole pairs $\mu_{eh}=Const.$, the net current density of extracted electron-hole pairs, in the monochromatic cell, dJ, (the area of the cell is taken equal to unity, $A_c=1$) is:

$$dJ = q\frac{2\pi}{c^2}\left(\frac{C\, f}{\exp\left(\frac{h\nu_g}{kT_s}\right) - 1} - \frac{1}{\exp\left(\frac{h\nu_g - \mu_{eh}}{kT_c}\right) - 1}\right)\nu_g^2 d\nu \tag{30}$$

http://dx.doi.org/10.5772/58914

This equation allows the definition of an equivalent cell temperature T_{eq} from:

$$\frac{h\nu_g - \mu_{eh}}{kT_c} = \frac{h\nu_g}{kT_{eq}} \Rightarrow \mu_{eh} = h\nu_g\left(1 - \frac{T_c}{T_{eq}}\right) \tag{31}$$

When a solar cell formed by a juxtaposition of two semiconductors *p*- and *n*-types is illuminated, an electrical voltage *V* between its terminals is created. This voltage is simply the difference in the quasi Fermi levels of majority carriers at Ohmic contacts for constant quasi Fermi levels and ideal Ohmic contacts, this voltage is equal to the chemical potential: $qV=\mu_{eh}=F_n-F_p$.

At open circuit condition, the voltage V_{oc} is given by a simple expression (deduced from (31)):

$$V_{oc} = \frac{E_g}{q}\left(1 - \frac{T_c}{T_{eq,oc}}\right) \tag{32}$$

The density of work delivered to an external circuit (density of extracted electrical power) *dW* is:

$$dW = dJ.V = \frac{2\pi}{c^2}\left(\frac{Cf}{\exp\left(\frac{h\nu_g}{kT_s}\right)-1} - \frac{1}{\exp\left(\frac{h\nu_g}{kT_{eq}}\right)-1}\right)\nu_g^2 d\nu\ h\nu_g\left(1 - \frac{T_c}{T_{eq}}\right) \tag{33}$$

The incoming energy flow from the sun can be written as:

$$dQ_1 = \frac{2\pi}{c^2}\left(\frac{Cf}{\exp\left(\frac{h\nu_g}{kT_s}\right)-1}\right)\nu_g^2 d\nu\ h\nu_g \tag{34}$$

The emitted energy density from the solar cell in a radiation form (radiative recombination) is:

$$dQ_2 = \frac{2\pi}{c^2}\left(\frac{1}{\exp\left(\frac{h\nu_g}{kT_{eq}}\right)-1}\right)\nu_g^2 d\nu\ h\nu_g \tag{35}$$

The efficiency of this system is:

$$\eta = \frac{dW}{dQ_1} = \frac{dQ_1 - dQ_2}{dQ_1} = \left(1 - \frac{T_c}{T_{eq}}\right) \tag{36}$$

The work extracted from a monochromatic cell is similar to that extracted from a Carnot engine. The equivalent temperature of this converter is directly related to the operating voltage. At short-circuit condition it corresponds to the ambient temperature (μ_{eh}=0 then $T_{eq,sc}$=T_c=T_a) whereas at open circuit condition and for fully concentrated solar radiation, the equivalent temperature is that of the sun, (dJ=0 then $T_{eq,oc}$=T_s). For non-concentrated radiation ($C \neq C_{Max}$) at open circuit voltage $T_{eq,oc}$ is obtained by solving the equation dJ =0, neglecting the 1 compared to the exponential term, we find then:

$$\frac{1}{T_{eq,oc}} = \frac{1}{T_s} - \frac{k}{h\nu_g} \ln(C.f) \tag{37}$$

It is therefore possible to consider a monochromatic solar cell as reversible thermal engine (Carnot engine) operating between $T_{eq,oc}$ and T_a.

We can see that an ideal monochromatic cell, which only allows radiative recombination, represents an ideal converter of heat into electrical energy.

In order to find the maximum efficiency of such a cell as a function of the monochromatic photon energy ($h\nu_g$), the dW=dJ×V versus V characteristic is used. We search for the point (dJ_{mp}, V_{mp}) corresponding to the maximum extracted power. The maximum chemical energy density (dW_{mp}=dJ_{mp}× V_{mp}) is divided by the absorbed monochromatic energy gives the efficiency $\eta_{mono}(E_g)$ as a function of the bandgap.

The monochromatic efficiency is considerable, particularly in the case of fully concentrated radiation (C=C_{Max}), and rises with the energy bandgap, as shown in figure 9. In theory the connection of a large number of ideal monochromatic absorbers will produce the best solar cell for the total solar spectrum. To calculate the overall efficiency numerically, a fine discretization of the frequency domain is made; the sum of the maximum power density over the solar spectrum divided by the total absorbed energy density. The efficiencies resulting from this calculation are respectively 67.45% and 86.81% for non-concentrated and fully concentrated radiation.

To cover the whole solar energy spectrum an infinite number of monochromatic absorbers, each for a different photon energy interval, are needed. Each absorber would have its own Carnot engine and operate at its own optimal temperature, since for a given voltage the cell equivalent temperature depends on the photon energy ($h\nu_g$). Finally this model can not be directly used to describe semiconductor solar cells where the electron-hole pairs are generated in bands and not discrete levels, besides if the cell is considered as a cascade of tow-level

http://dx.doi.org/10.5772/58914

converters; the notion of effective or equivalent temperature is no longer valid, since for each set of levels a different equivalent temperature is defined.

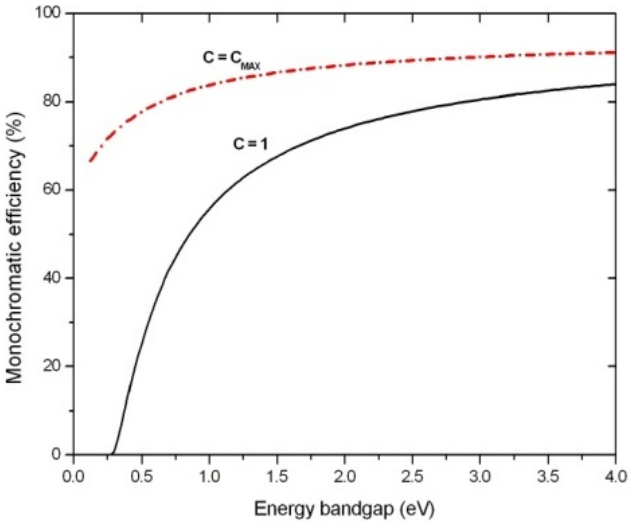

Figure 9. The monochromatic efficiency against the photon energy corresponding to the energy band-gap of the cell for non-concentrated (C=1) and fully concentrated (C=C_{max}) solar spectrum.

3.3. Ultimate efficiency

The total number of photons of frequency greater than ν_g (E_g=$h\nu_g$) impinging from the sun, assumed as a blackbody at temperature T_s, in unit time and falling upon the solar cell per unit area N_s is given by:

$$N_s = \left(2\pi / c^2\right)\int_{\nu_g}^{\infty} \frac{\nu^2 d\nu}{\exp(h\nu / kT_s) - 1} \tag{38}$$

This integral could be evaluated numerically.

In the assumption that each absorbed photon will produce a pair of electron-hole, the maximum output power density that could be delivered by a solar converter will be:

$$P_{out} = h\nu_g \times N_s \tag{39}$$

The solar cell is assumed entirely surrounded by the sun and maintained at T_c=0K as a first approximation and to get the maximum energy transfer from the sun. The total incident energy density coming from the sun at T_s and falling upon the solar cell, P_{in} is given by

$$P_{in} = \left(2\pi / c^2\right)\int_0^\infty \frac{\nu^3 d\nu}{\exp(h\nu / kT_s) - 1} = 2\pi(kT_s)^4 / h^3c^2 \int_0^\infty \frac{x^3 dx}{\exp(x) - 1} \tag{40}$$

$$P_{in} = 2\pi^5(kT_s)^4 / 15h^3c^2 \tag{41}$$

In accordance with the definition of the ultimate efficiency [6, 17], as the rate of the generated photon energy to the input energy density, its expression can be evaluated as a function of E_g as follows:

$$\eta_u(\nu_g) = \frac{h\nu_g N_s}{P_{in}} \tag{42}$$

This expression is plotted in figure 10, so the maximum efficiency is approximately 43.87% corresponding to E_g=1.12 eV, this energy band-gap is approximately that of crystalline silicon. Similar calculation of the ultimate efficiency taking the solar spectrum AM1.5 G (The standard global spectral irradiance, ASTM G173-03, is used [18]) is shown in figure 10 gives a slightly higher value of 49%. If one compares this efficiency to the aforementioned thermodynamic efficiency limits, most of them approach the Carnot limit for the special case where the converter's temperature is absolute zero, this ultimate efficiency limit is substantially lower (44% or 49%) than the Carnot limit (95%). In quantum converters it is obvious that more than 50% of the solar radiation is lost because of the spectral mismatch. Therefore, non-absorption of photons with less energy than the semiconductor band-gap and the excess energy of photons, larger than the band-gap, are the two main losses.

3.4. Detailed balance efficiency limit

The detailed balance limit efficiency for an ideal solar cell, consisting of single semiconducting absorber with energy band-gap E_g, has been first calculated by Shockley and Queisser (SQ) [6]. The illumination of a *pn* junction solar cell creates electron-hole pairs by electronic transition due to the fundamental absorption of photons with $h\nu > E_g$, which is basically a quantum process. The photogenerated pairs either recombine locally or circulate in an external circuit and can transfer their energy. Their approach reposes on the following main assumptions; the probability that a photon with energy $h\nu > E_g$ incident on the surface of the cell will produce a hole-electron pair is equal to unity, while photons of lower energy will produce no effect, all photogenerated electrons and holes thermalize to the band edges (photons with energy greater than E_g produce the same effect), all the photogenerated charge carriers are collected at short-

http://dx.doi.org/10.5772/58914

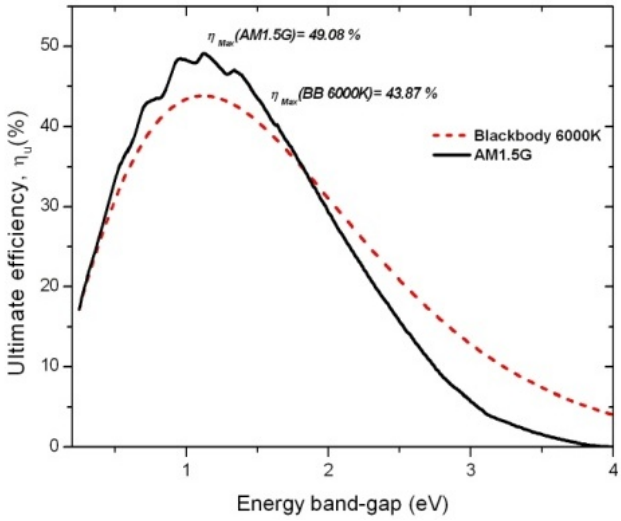

Figure 10. The ultimate efficiency against the energy band-gap of the solar cell, using the AM1.5G spectrum with the blackbody spectrum at T_s=6000°*K*.

circuit condition and the upper detailed balance efficiency limit is obtained if radiative recombination is the only allowed recombination mechanism.

The model initially introduced by SQ [6] has been improved by a number of researchers, by first introducing a more exact form of radiative recombination. The radiative recombination rate is described using the generalised Planck radiation law introduced by Würfel [7], where the energy carried by emitted photons turn out to be the difference of electron-hole quasi Fermi levels. While for non-radiative recombination the released energy is recovered by other electrons, holes or phonons.

In the following sub-section the maximum achievable conversion efficiency of a single band-gap absorber material is determined.

3.4.1. Short-circuit current density (J_{sc}) calculation

Now we consider a more realistic situation of a solar cell, depicted in figure 3. Three factors will be taken into account, namely; the view factor of the sun seen from the solar cell, the background radiation is represented as a blackbody at ambient temperature T_a, and losses due to recombination (radiative and non-radiative).

In steady state condition the current density $J(V)$ flowing through an external circuit is the algebraic sum of the rates of increase of electron-hole pairs corresponding to the absorption of incoming photons from the sun and the surrounding background, in addition to recombination (radiative and non-radiative). This leads to a general current voltage characteristic formula:

$$J(V) = q(2\pi / c^2)\Big[C f \times \int_{\nu_g}^{\infty} \frac{\nu^2 d\nu}{\exp(h\nu / kT_s) - 1} + (1 - C f) \times \int_{\nu_g}^{\infty} \frac{\nu^2 d\nu}{\exp(h\nu / kT_a) - 1} - \frac{1}{f_{RR}} \times \int_{\nu_g}^{\infty} \frac{\nu^2 d\nu}{\exp((h\nu - qV) / kT_c) - 1}\Big] \tag{43}$$

with reference to the solar cell configuration shown in figure 3, T_s, T_a and T_c are the respective temperatures of sun, ambient background and solar cell. As defined previously, C and f are the concentration factor and the sun geometrical factor, while f_{RR} represents the fraction of the radiative recombination rate or radiative recombination efficiency. If U_{NR} and U_{RR} are the non-radiative and radiative recombination rates respectively, f_{RR} is defined by:

$$f_{RR} = \frac{U_{RR}}{U_{RR} + U_{NR}} \tag{44}$$

The current density formula (43) can be rewritten in a more compact form as follows:

$$J(V) = qCf\phi_s + q(1 - C f)\phi_a - \frac{q}{f_{RR}}\phi_c(V) \tag{45}$$

With:

$$\varphi_s = (2\pi / c^2)\int_{\nu_g}^{\infty} \frac{\nu^2 d\nu}{\exp(h\nu / kT_s) - 1} \quad \text{a}$$

$$\varphi_a = (2\pi / c^2)\int_{\nu_g}^{\infty} \frac{\nu^2 d\nu}{\exp(h\nu / kT_a) - 1} \quad \text{b} \tag{46}$$

$$\varphi_c(V) = (2\pi / c^2)\int_{\nu_g}^{\infty} \frac{\nu^2 d\nu}{\exp((h\nu - qV) / kT_c) - 1} \quad \text{c}$$

Under dark condition and zero bias the current density must be null, then:

$$J(0) = 0 \Rightarrow \varphi_a = \frac{1}{f_{RR}}\varphi_c(0) \tag{47}$$

Therefore the current density expression becomes:

$$J(V) = qCf(\phi_s - \phi_a) - \frac{q}{f_{RR}}\big(\phi_c(V) - \phi_c(0)\big) \tag{48}$$

http://dx.doi.org/10.5772/58914

From the above *J (V)* expression we can obtain the short-circuit current density (J_{sc}=$J_{(V=0)}$) as follows:

$$J_{sc} = qCf(\phi_s - \phi_a) \tag{49}$$

In the ideal case the short-circuit current density depends only on the flux of impinging photons from the sun and the product *Cf*, recombination has no effect. The term φ_a in J_{sc}, representing the radiation from the surrounding ambient is negligible. The total photogenerated carriers are swept away and do not recombine before reaching the external circuit where they give away their electrochemical energy. Figure 11 illustrates the maximum short-circuit current density to be harvested against band-gap energy according to (49) for a blackbody spectrum at T_s=6000°*K* normalised to a power density of 1000W/m^2 and a spectral photon flux corresponding to the terrestrial AM1.5G spectrum. Narrow band-gap semiconductors exhibit higher photocurrents because the threshold of absorption is very low, therefore most of the solar spectrum can be absorbed. For power extraction this is not enough, the voltage is equally important and more precisely, the open circuit voltage.

The currently achieved short-circuit current densities for some solar cells are very close to predicted limits. Nevertheless, further gain in short-circuit current can therefore still be obtained, mainly by minimising the cell surface reflectivity, while increasing its thickness, so as to maximize the photon absorption. For thin film solar cells the gain in J_{sc} can be obtained by improving light trapping techniques to enhance the cell absorption.

For instance crystalline silicon solar cells with an energy band-gap of 1.12 eV at 300K has already achieved a J_{sc} of 42.7 mA/cm^2 compared to a predicted maximum value of 43.85 mA/cm^2 for an AM1.5 global spectrum (only 39.52 mA/cm^2 for a normalised blackbody spectrum at 6000°*K*), while for GaAs with E_g=1.43eV a reported maximum J_{sc} of 29.68 mA/cm^2 compared to 31.76 mA/cm^2 (only 29.52 mA/cm^2 for a normalised blackbody spectrum at 6000°*K*) [14].

	J_{sc}(mA/cm^2)		V_{oc}(V)		η (%)	
	Limit	record	limit	record	limit	record
Si	43.85	42.7	0.893	0.706	34.37	25.0
GaAs	31.76	29.68	1.170	1.122	33.72	28.8

Table 1. Summary of the reported records [14] and the calculated limits of Si and GaAs solar cells performances under the global AM1.5 spectrum.

3.4.2. Open-circuit voltage (V_{oc}) calculation

At open circuit condition electron-hole pairs are continually created as a result of the photon flux absorption, the only mechanism to counter balance this non-equilibrium condition is

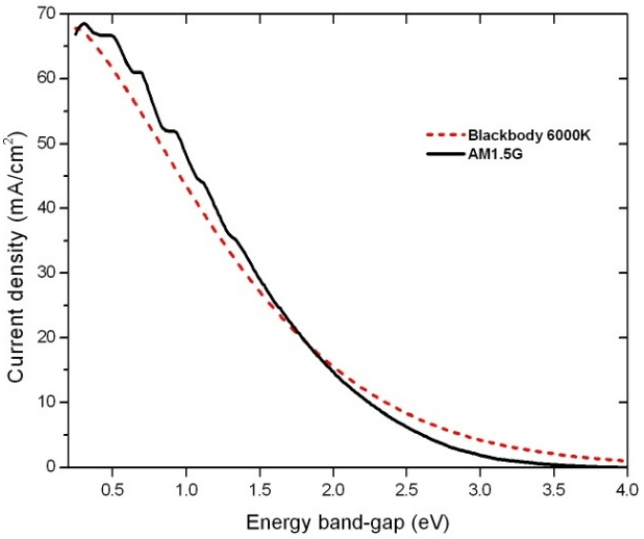

Figure 11. The maximum short-circuit current density against the energy band-gap of the solar cell, using the AM1.5G spectrum with the blackbody spectrum at T_s=6000°*K*.

recombination. Non-radiative recombination could be eliminated, whereas radiative recombination has a direct impact on the cell efficiency and particularly on the open circuit voltage. The radiative current as the rate of radiative emission increases exponentially with the bias subtracts from the current delivered to the load by the cell. At open circuit condition, external photon emission is part of a necessary and unavoidable equilibration process [15]. The maximum attainable V_{oc} corresponds to the condition where the cell emits as many photons as it absorbs. The open circuit voltage of a solar cell can be found by taking the band gap energy and accounting for the losses associated with various sources of entropy increase. Often, the largest of these energy losses is due to the entropy associated with radiative recombination.

In the case where qV is several kT smaller than $h\nu_g$, $\varphi_c(V)$ could be approximated by:

$$\phi_c(V) \cong (2\pi / c^2)\left(\int_{\nu_g}^{\infty} \frac{\nu^2 d\nu}{\exp((h\nu)/kT_c)-1}\right)\exp\left(\frac{qV}{kT_c}\right) = \phi_c(0)\exp\left(\frac{qV}{kT_c}\right) \tag{50}$$

The current density expression becomes then:

$$J(V) = qCf(\phi_s - \phi_a) - \frac{q}{f_{RR}}\phi_c(0)\left(\exp\left(\frac{qV}{kT_c}\right)-1\right) \tag{51}$$

The open circuit voltage can be deduced directly from this expression as:

http://dx.doi.org/10.5772/58914

$$0 = Cf(\phi_s - \phi_a) - \frac{1}{f_{RR}}\phi_c(0)\left(\exp\left(\frac{qV_{oc}}{kT_c}\right) - 1\right) \tag{52}$$

$$V_{oc} = \frac{kT_c}{q}\ln\left(\frac{Cf(\phi_s - \phi_a)}{\phi_c(0)}f_{RR} + 1\right) \tag{53}$$

The open circuit voltage is determined entirely by two factors; the concentration rate of solar radiation C ($C \geq 1$) and radiative recombination rate f_{RR} ($f_{RR} \leq 1$).

$$\begin{aligned} V_{oc} &\approx \frac{kT_c}{q}\ln\left(\frac{Cf(\phi_s - \phi_a)}{\phi_c(0)}f_{RR}\right) \\ &= \frac{kT_c}{q}\ln\left(\frac{f(\phi_s - \phi_a)}{\phi_c(0)}\right) - \frac{kT_c}{q}\ln\left(\frac{1}{C}\right) - \frac{kT_c}{q}\ln\left(\frac{1}{f_{RR}}\right) \end{aligned} \tag{54}$$

Radiative recombination has a critical role to play, if the created photons are re-emitted out of the cell, which corresponds to low optical losses, the open circuit voltage and consequently the cell efficiency approach the SQ limit. Therefore the limiting factor for high V_{oc} (efficiency) is the external fluorescence efficiency of the cell as far as radiative recombination is concerned. Since the escape cone is in general low, efficient external emission involves repeated escape attempts and this is ensured by perfect light trapping techniques. In this case the created photons are allowed to be reabsorbed and reemitted again until they coincide with the escape cone, reaching high external fluorescence efficiency [15, 18-19].

So dominant radiative recombination is required to reach high V_{oc} and this is not sufficient to reach the SQ limit, the other barrier is to get the generated photons out of the cell and this is limited by the external fluorescence efficiency η_{fex}. Hence, the external fluorescence efficiencyη_{fex}, is introduced in the expression of V_{oc} and f_{RR} is multiplied by η_{fex}, ($\eta_{fex} \leq 1$) then:

$$V_{oc} = \frac{kT_c}{q}\ln\left(\frac{f(\phi_s - \phi_a)}{\phi_c(0)}\right) - \frac{kT_c}{q}\ln\left(\frac{1}{C}\right) - \frac{kT_c}{q}\ln\left(\frac{1}{f_{RR}\eta_{fex}}\right) \tag{55}$$

If we define a maximum ideal open circuit voltage value $V_{oc,max}$ for fully concentrated solar radiation (C=C_{max}=1/f) and when the radiative recombination is the only loss mechanism with maximum external fluorescence efficiency (i.e, $f_{RR}\eta_{fex}$=1), then:

$$V_{oc} = V_{oc,\max} - \frac{kT_c}{q}\ln\left(\frac{C_{\max}}{C}\right) - \frac{kT_c}{q}\ln\left(\frac{1}{f_{RR}\eta_{fex}}\right) \tag{56}$$

It is worth mentioning that (56) is not an exact evaluation of V_{oc}. As shown in figure 12.b equation (56) for narrow band-gap semiconductors yields wrong values of $V_{oc,max}$ (above E_g/q line), acceptable values are obtained only for E_g greater than 2 eV, where it coincides with the result obtained when solving numerically (45) for $J(V)=0$.

From this figure one can say that taking $V_{oc,max}=E_g/q$ is a much better approximation; thus, instead of (56) we can use the following approximation:

$$V_{oc} = \frac{E_g}{q} - \frac{kT_c}{q}\ln\left(\frac{C_{\max}}{C}\right) - \frac{kT_c}{q}\ln\left(\frac{1}{f_{RR}\eta_{fex}}\right) \tag{57}$$

A more accurate value of V_{oc} is obtained after numerical resolution of equation (45) for $J(V)=0$, the results are plotted in figure12a and 12.b.

The other type of entropy loss degrading the open-circuit voltage is the photon entropy increase due to isotropic emission under direct sunlight. This entropy increase occurs because solar cells generally emit into 2π steradian, while the solid angle subtended by the sun is only 6.85×10^{-5} steradian.

The most common approach to addressing photon entropy is a concentrator system. If the concentration factor C of sun radiation is increased, this is generally achieved by optical means, a significant increase of V_{oc} is obtained (as shown in figure 12.b). The calculation is carried out assuming a dominant radiative recombination and with maximum external fluorescence efficiency ($f_{RR}\eta_{fex}=1$). In this case we can notice that as C is increased V_{oc} approaches its ultimate value E_g/q, for example GaAs (E_g=1.43 eV) for $C=C_{Max}$ we get $V_{oc}=0.99\times E_g/q=1.41$ V, which corresponds to an efficiency limit of approximately 38.5% (blackbody spectrum at 6000K). This theoretical limit shows the importance of dealing with entropy losses associated with angle of acceptance of photons from the sun and emission of photons from the cell efficiently. This value is well above the predicted SQ limit, where the concentration factor was considered.

With reference to table 1 we can clearly see that the record open circuit voltage under one-sun condition (C=1) of gallium arsenide solar cell (1.12 V) is already close to the SQ limit (1.17 V) while silicon solar cell is still behind with a record V_{oc} of 0.706 V compared to a limit of 0.893 V, this difference is due to the fact that GaAs has a direct band gap, which means that it can be used to absorb and emit light efficiently, whereas Silicon has an indirect band gap and so is relatively poor at emitting light. Although Silicon makes an excellent solar cell, its internal fluorescence yield is less than 20%, which prevents Silicon from approaching the SQ limit [20]. On the other hand It has been demonstrated that efficiency in Si solar cells is limited by Auger recombination, rather than by radiative recombination [20-22].

3.4.3. The efficiency calculation

Energy conversion efficiency η is usually known as the most relevant figure for solar cell performance. Solar cell efficiency is calculated by dividing a cell's electrical power output at its maximum power point by the input solar radiation and the surface area of the solar cell.

http://dx.doi.org/10.5772/58914

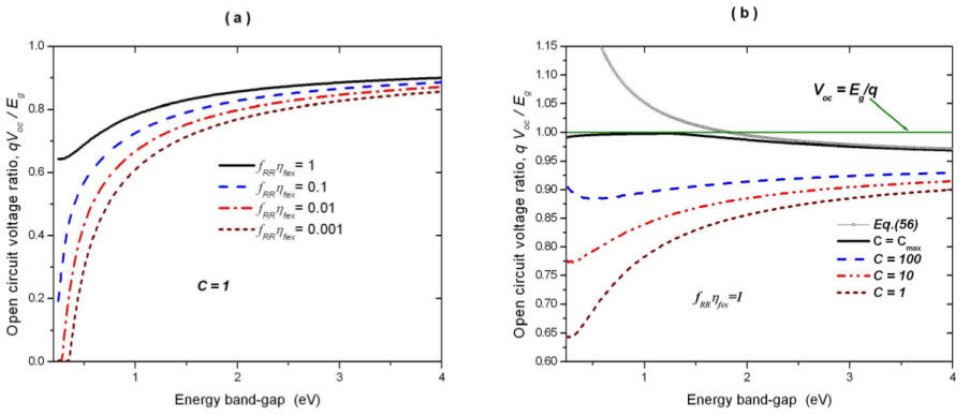

Figure 12. The V_{oc}/E_g against energy band-gap of the solar cell, using a blackbody spectrum at T_s=6000°*K*; a)-for different radiative recombination rates, b)-for different solar concentrations and a plot of (56) for $C=C_{max}$.

The maximum power output from the solar cell is obtained by choosing the voltage V so that the product current-voltage (IV) is a maximum. This point corresponds to the situation where a maximum power is extracted from the cell. Using equation 45 we can define the power delivered by a cell as:

$$P(V) = (qCf\phi_s + q(1-Cf)\phi_a - \frac{q}{f_{RR}}\phi_c(V)) \times V \tag{58}$$

The maximum power $P_M = J_M \times V_M$ is obtained numerically from (58) and the efficiency η (if the sun is assumed a blackbody at T_s) is then calculated as:

$$\eta(\%) = \frac{P_M}{P_{in}} = \frac{P_M}{2\pi^5 (kT_s)^4 / 15h^3c^2} \times 100 \tag{59}$$

For AM1.5G solar spectrum P_{in} is replaced by 1000.

Figure 13 illustrates efficiency against energy band-gap of a solar cell, using the AM1.5G spectrum and the blackbody spectrum at T_s=6000°*K* for one sun and full concentration ($C=C_{Max}$), the only recombination mechanism is radiative and 100% external fluorescence efficiency, which means that all emitted photons from the cell (issue from radiative recombination) are allowed to escape. The maximum efficiency is 34.42% for AM1.5G corresponding to a gap of 1.34 eV, for a blackbody spectrum normalized to 1000 W/m^2 the maximum efficiency is 31.22% at 1.29 eV, while for a full solar concentration the maximum is 40.60% at 1.11 eV, this confirms the fact that the optimal band gaps decrease as the solar concentration increases.

In figure 14 the product of radiative recombination rate and the external fluorescence efficiency ($f_{RR} \times \eta_{fex}$) is decreased from 1 to 10^{-3} to illustrate the effect radiative recombination and the external fluorescence on the cell efficiency. The maximum efficiency limit dropped from 34.42% to 28.58%.

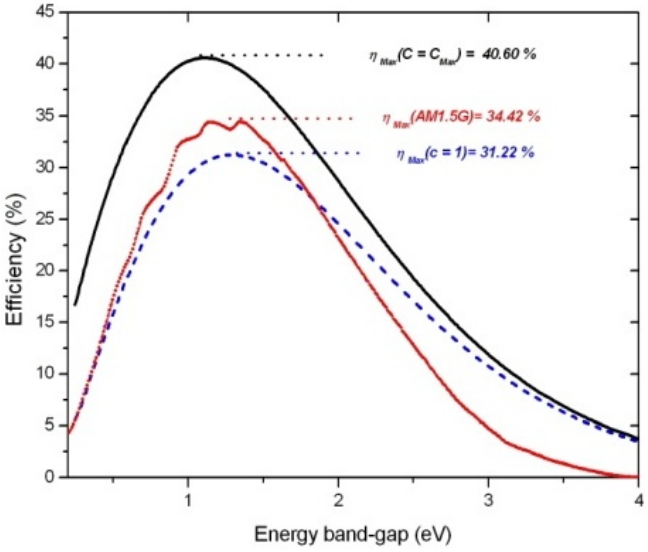

Figure 13. The maximum efficiency against the energy band-gap of the solar cell, using the AM1.5G spectrum with the blackbody spectrum at T_s=6000°K for one sun and full concentration (C=C_{Max}).

Since the power output of the cell is determined by the product of the current and voltage, it is therefore imperative to understand what material properties (and solar cell geometries) boost these two parameters. Certainly, the short-circuit current in the solar cell is determined entirely by both the material absorption property and the effectiveness of photo-generated carriers collection at contacts. As previously mentioned (section 2.4.1), the manufactured solar cells with present technologies and materials have already achieved short-circuit currents close to predicted limits. Therefore the shortfall in efficiency could be attributed to the voltage. We show here that the key to reaching the highest possible voltages is first to have a recombination predominantly radiative with a maximal external emission of photons from the surface of the solar cell. Secondly we need a maximum solar concentration. The second condition could be achieved either by using sun concentrators, there are concentrators with concentration factor from ×2 to over ×1000 [23] or by non-concentrating techniques with emission and acceptance angle limited to a narrow range around the sun [24-26].

At this level we can conclude that the efficiency limit of a single energy gap solar cell is bound by two intrinsic limitations; the first is the spectral mismatch with the solar spectrum which retains at least 50% of the available solar energy. The best known example of how

http://dx.doi.org/10.5772/58914

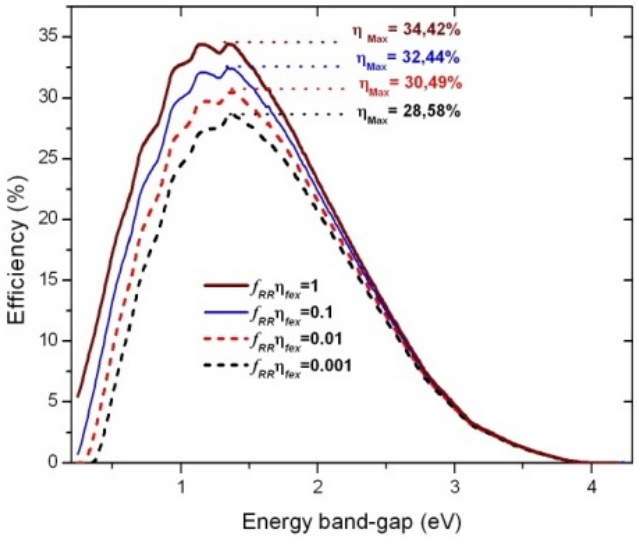

Figure 14. The maximum efficiency against the energy band-gap of the solar cell, using the AM1.5G spectrum with the blackbody spectrum at T_s=6000°K for one sun and full concentration (C=C_{Max})

to surmount such efficiency restraint is the use of tandem or stacked cells. This alternative will become increasingly feasible with the likely evolution of materials technology over the decades to 2020 [27].

The second intrinsic loss is due to the entropy associated with spontaneous emission. To overcame this limitation three conditions should be satisfied, that is: a) – prevailing radiative recombination (to eliminate the non-collected electro-hole pairs), b)-efficient external fluorescence (to maximise the external emission of photons from the solar cell) and c)-using concentrated sun light or restricting the emission and acceptance angle of the luminescent photons to a narrow range around the sun.

4. Conclusion

For single junction cell the record at present is 28.8% (GaAs) [14] compared to the SQ limit of 33.7% which is a significant accomplishment and little room has been left for improvement. Immense experimental research is now directed towards maximizing the external emission of photons from the solar cell. One way of getting beyond the SQ limit for a single junction is the use of concentrated radiation, the current record for concentrator cell is only 29.1% (GaAs) under 117 suns [14], this technology has a number of challenging problems (such as tracking and cooling systems) and there is still a long way to go. The same goal is accomplished by matching the angles under which light impinges from the sun and into which light is emitted from the solar cell. Recently it has been demonstrated that light trapping GaAs solar cell with

limited emission angle efficiencies above 38% may be achievable with a single junction solar cell [25].

To overcome the restrictions of a single junction solar cell several directions were investigated during the last decades (i.e. hot carrier cells, carrier multiplication and down-conversion, impurity photovoltaic and multiband cells, thermophotovoltac and thermophotonic conversion…).

The most widely explored path has been tandem or stacked cells; they provide the best known example of how such high efficiency might be achieved. The present efficiency record for a triple junctions cell (InGaP/GaAs/InGaAs) is 37.9% compared to a predicted value of over 51% for an optimised set of three stacked cells [28, 29]. The major technological challenge with tandem solar cells is to find materials with the desired band gaps and right physical properties (i.e. lattice constant and thermal parameters). The ultimate efficiency target for this kind of configuration is 86.81% (for a set of an infinite number of stacked monochromatic cells under maximum solar concentration) which constitutes an arduous target, corresponding to an infinite number of stacked junctions radiated by a maximum solar concentration. The best performance that the present technology can offer is 44.4% using a triple junction GaInP/GaAs/GaInAs cell under 302 suns [14].

Acknowledgements

The author would like to thank Professor Helmaoui A. for his valuable and helpful discussions throughout the preparation of this work.

Author details

Abderrahmane Belghachi*

Address all correspondence to: abelghachi@yahoo.fr

Laboratory of Semiconductor Devices Physics, University of Bechar, Algeria

References

[1] Michael Y. Levy (2011). Maturity of Photovoltaic Solar-Energy Conversion, Solar Cells-Silicon Wafer-Based Technologies, Prof. Leonid A. Kosyachenko (Ed.), ISBN: 978-953-307-747-5, InTech, DOI: 10.5772/20023. Available from: http://www.intechopen.com/books/solar-cells-silicon-wafer-based-technologies/maturity-of-photovoltaic-solar-energy-conversion.

[2] Hegedus S, Luque A. (2003). Theoretical Limits of Photovoltaic Conversion, Handbook of photovoltaic science and engineering, Luque A., Hegedus S. (Ed.), John Wiley & Sons Ltd, The Atrium, Southern Gate, Chichester, England,1-41.

[3] Luque A, Hegedus S. (2003). Status, trend, challenges and the bright future of solar electricity from photovoltaics, Handbook of photovoltaic science and engineering, Luque A., Hegedus S. (Ed.), John Wiley & Sons Ltd, The Atrium, Southern Gate, Chichester, England,113-49.

[4] Navarrete-Gonzalezy T D, Rocha-Martınezy J A, Angulo-Brownz F. A Muser–Curzon–Ahlborn engine model for photothermal conversion. J. Phys. D: Appl. Phys. 1997; 30:2490–96.

[5] Baruch P, De Vos A, Landsberg P T, Parrott J E. On some thermodynamic aspects of photovoltaic solar energy conversion. Solar Energy Materials and Solar Cells 1995; 36:201-22.

[6] Shockley W, Queisser H J. Detailed balance limit of efficiency of p-n junction solar cell. Journal of Applied Physics1961; 32 (3):510-19.

[7] Würfel P. Physics of Solar Cells: From Basic Principles to Advanced Concepts. Wiley-Vch Verlag GmbH & Co. KGaA, Weinheim (2005).

[8] De Vos A. Thermodynamics of photochemical solar energy conversion. Solar Energy Materials and Solar Cells 1995; 38:11-22.

[9] Sahin A D, Dincer I, Rosen M A. Thermodynamic analysis of solar photovoltaic cell systems. Solar Energy Materials and Solar Cells 2007; 91:153–59.

[10] Joshi A S, Dincer I, Reddy B V. Thermodynamic assessment of photovoltaic systems. Solar Energy 2009;83:1139-49.

[11] Markvart T, Landsberg PT. Thermodynamics and reciprocity of solar energy conversion, Physica 2002; E14:71 – 7.

[12] Queisser H J. Detailed balance limit for solar cell efficiency. Materials Science and Engineering 2009; B159–160: 322–8.

[13] Henry C H. Limiting efficiencies of ideal single and multiple energy gap terrestrial solar cells. J. Appl. Phys. 1980;51:4494-500.

[14] Green M A, Emery K, Hishikawa Y, Warta W, Dunlop E D. Solar cell efficiency tables (version 42). Prog. Photovolt: Res. Appl. 2013; 21:827–37.

[15] Miller O D, Yablonovitch E, Kurtz S R. Intense Internal and External Fluorescence as Solar Cells Approach the Shockley-Queisser Efficiency Limit. IEEE Journal of Photovoltaics 2 2012; 303-11.

[16] De Vos A, Landsberg P T, Baruch P, Parrott J E. Entropy fluxes, endoreversibility, and solar energy conversion. J. Appl. Phys. 1993; 74:3631-37.

[17] Chen C. J. Semiconductor Solar Cells. Physics of Solar Energy. Hoboken, New Jersey: John Wiley & Sons Inc.;2011.

[18] American Society for Testing and Materials (ASTM) (http://www.astm.org/) (accessed 10 July 2014).

[19] Smestad G, Ries H. Luminescence and current-voltage characteristics of solar cells and optoelectronic devices. Solar Energy Materials and Solar Cells 1992;25:51-71.

[20] Yablonovitch E, Gmitter T. Auger recombination in silicon at low carrier densities. App. Phys. Lett. 1986;49:587-9.

[21] Araujo L G, Marti A. Limiting Efficiencies of GaAs Solar Cells. IEEE Trans. Electron Devices1990; 37(5):1402-5.

[22] Tiedje T, Yablonovitch E, Cody G D, Brooks B G. Limiting Efficiency of Silicon Solar Cells. IEEE Trans. Electron Devices 1984;31(5):711-6.

[23] Andrea Antonini (2010). Photovoltaic Concentrators-Fundamentals, Applications, Market & Prospective, Solar Collectors and Panels, Theory and Applications, Dr. Reccab Manyala (Ed.), ISBN: 978-953-307-142-8, InTech, Available from :http://www.intechopen.com/books/solar-collectors-and-panels--theory-and applications/photovoltaic-concentrators-fundamentals-applications-market-prospective.

[24] Markvart T. Solar cell as a heat engine: energy–entropy analysis of photovoltaic conversion. physica status solidi (a) 2008;205(12):2752-6.

[25] Kosten E D, Atwater J H, Parsons J, Polman A, Atwater H A. Highly efficient GaAs solar cells by limiting light emission angle. Light: Science & Applications 2013;2e45.

[26] Kostena ED, Atwater H A. Limiting acceptance angle to maximize efficiency in solar cells.: In: Winston R., Gordon J. M. (eds.) Nonimaging Optics: Efficient Design for Illumination and Solar Concentration VIII: Proceedings of SPIE Vol. 8124 (2011) 81240F1-6.

[27] Green M.A. Third Generation Photovoltaics: Advanced Solar Energy Conversion. In: Springer Series in Photonics 12, Kamiya T., Monemar B., Venghaus H., Yamamoto Y. (Ed.), Springer-Verlag Berlin Heidelberg 2003.

[28] Brown A. S., Green M. A. Detailed balance limit for the series constrained two terminal tandem solar cell. Physica E: Low-dimensional Systems and Nanostructures 2002; 14(1–2):96–100.

[29] Bremner S. P., Levy M. Y., Honsberg C. B. Rapid detailed balance calculations for multiple energy gap solar cells 2007. In: Proceedings of 22nd European Photovoltaic Solar Energy Conference; 2007 Sep 3-7; Milano, Italy; 2007.P.75-8.

Chapter 3

Crystal Structures of $CH_3NH_3PbI_3$ and Related Perovskite Compounds Used for Solar Cells

Takeo Oku

Additional information is available at the end of the chapter

http://dx.doi.org/10.5772/59284

1. Introduction

Recently, organic-inorganic hybrid solar cells with perovskite-type pigments have been widely fabricated and rapidly studied [12, 8, 11]. Solar cells with a perovskite structure have high conversion efficiencies and stability as the organic solar cells. Since a photoconversion efficiency of 15% was achieved [2], higher efficiencies have been reported for various device structures and processes [13, 23], and the photoconversion efficiency was increased up to 19.3% [27]. The photovoltaic properties of solar cells are strongly dependent on the fabrication process, hole transport layers, electron transport layers, nanoporous layers, interfacial microstructures, and crystal structures of the perovskite compounds. Especially, the crystal structures of the perovskite-type compounds, strongly affect the electronic structures such as energy band gaps and carrier transport, and a detailed analysis of them is mandatory.

In the present article, crystal structures of perovskite-type compounds such as $CH_3NH_3PbI_3$ $CH_3NH_3PbCl_3$, $CH_3NH_3PbBr_3$, $CsSnI_3$, $CH_3NH_3GeCl_3$, and $CH_3NH_3SnCl_3$, are expected for solar cell materials, are reviewed and summarized. Since these perovskite-type materials often have nanostructures in the solar cell devices, summarized information on the crystal structures would be useful for structure analysis on the perovskite-type crystals. The nanostructures of the solar cell devices are often analysed by using X-ray diffraction (XRD) and transmission electron microscopy (TEM), and the diffraction conditions are investigated and summarized. Transmission electron microscopy, electron diffraction, and high-resolution electron microscopy are powerful tools for structure analysis of solar cells [18] and perovskite-type structures in atomic scale [17, 19].

2. Synthesis of methylammonium trihalogenoplumbates (II)

There are various fabrication processes for the methylammonium trihalogenoplumbates (II) ($CH_3NH_3PbI_3$) compound with the perovskite structures. Two typical synthesis methods for the $CH_3NH_3PbI_3$ ($MAPbI_3$) were reported [1]. $MAPbI_3$ could be synthesised from an equimolar mixture of CH_3NH_3I and PbI_2 using the reported method [8]. CH_3NH_3I was synthesised at first by reacting a concentrated aqueous solution of hydroiodic acid with methylamine, and the cleaned precipitant was mixed with PbI_2 in gamma-butyrolactone to obtain the $MAPbI_3$ product. Crystalline $MAPbI_3$ was obtained by drop-casting the solutions on glass substrates, and annealed at 100 °C. Polycrystalline $MAPbI_3$ could be also prepared by precipitation from a hydroiodic acid solution [22]. Lead(II) acetate was dissolved in a concentrated aqueous HI and heated. An HI solution with CH_3NH_2 was added to the solution, and black precipitates were formed upon cooling from 100 °C.

A typical fabrication process of the $TiO_2/CH_3NH_3PbI_3$ photovoltaic devices is also described here [28]. The details of the fabrication process is described in the reported paper [2] except for the mesoporous TiO_2 layer [16]. The photovoltaic cells were fabricated by the following process. F-Doped tin oxide (FTO) substrates were cleaned using an ultrasonic bath with acetone and methanol and dried under nitrogen gas. The 0.30M TiO_x precursor solution was prepared from titanium diisopropoxide bis(acetyl acetonate) (0.11 mL) with 1-butanol (1 mL), and the TiO_x precursor solution was spin-coated on the FTO substrate at 3000 rpm for 30 s and annealed 125 °C for 5 min. This process was performed two times, and the FTO substrate was sintered at 500 °C for 30min to form the compact TiO_2 layer. After that, mesoporous TiO_2 paste was coated on the substrate by a spin-coating method at 5000 rpm for 30 s. For the mesoporous TiO_2 layer, the TiO_2 paste was prepared with TiO_2 powder (Aerosil, P-25) with poly(ethylene glycol) in ultrapure water. The solution was mixed with acetylacetone and triton X-100 for 30min. The cells were annealed at 120 °C for 5min and at 500 °C for 30min. For the preparation of pigment with a perovskite structure, a solution of CH_3NH_3I and PbI_2 with a mole ratio of 1:1 in γ-butyrolactone (0.5 mL) was mixed at 60 °C. The solution of CH_3NH_3I and PbI_2 was then introduced into the TiO_2 mesopores by spin-coating method and annealed at 100 °C for 15min. Then, the hole transport layer (HTL) was prepared by spin coating. As the HTLs, a solution of spiro-OMeTAD (36.1 mg) in chlorobenzene (0.5 mL) was mixed with a solution of lithium bis(trifluoromethylsulfonyl) imide (Li-TFSI) in acetonitrile (0.5 mL) for 12 h. The former solution with 4-tert-butylpyridine (14.4 μL) was mixed with the Li-TFSI solution (8.8 μL) for 30min at 70 °C. Finally, gold (Au) metal contacts were evaporated as top electrodes. Layered structures of the photovoltaic cells were denoted as $FTO/TiO_2/CH_3NH_3PbI_3$/HTL/Au.

3. Crystal structures of $CH_3NH_3PbX_3$ (X=Cl, Br, or I) compounds

The crystals of methylammonium trihalogenoplumbates(II) ($CH_3NH_3PbX_3$, X=Cl, Br, or I) have perovskite structures and provide structural transitionsupon heating [24], 22]. The crystal

http://dx.doi.org/10.5772/59284

systems and transition temperatures are summarized in Table 1, as reported in the previous works [22, 21]. Atomic sites were indicated from the space group table [6]. Although the $CH_3NH_3PbX_3$ perovskite crystals have a cubic symmetry for the highest temperature phase, the CH_3NH_3 ion is polar and has C_{3v} symmetry, which should result in disordered cubic phase [14]. In addition to the disordering of the CH_3NH_3 ion, the halogen ions were also disordered in the cubic phase, as shown in Figure 1(a) and Table 2 [14]. Site occupancies were set as 1/4 for I and 1/12 for C and N. The CH_3NH_3 ion occupies 12 equivalent orientations of the C_2 axis, and hydrogen atoms have two kinds of configurations on the C_2 axis. Then, the total degree of freedom is 24 [21].

As the temperature decreases, the cubic phase is transformed in the tetragonal phase, as shown in Figure 1(b) and Table 3 [10]. The isotropic displacement parameters B were calculated as $8\pi^2 U_{iso}$. For the tetragonal phase, I ions are ordered, which resulted in the lower symmetry from the cubic phase. Site occupancies were set as 1/4 for C and N for the tetragonal $CH_3NH_3PbI_3$. As the temperature decreases lower, the tetragonal phase is transformed in the orthorhombic systems, which is due to the ordering of CH_3NH_3 ions in the unit cell, as shown in Figure 1(c) and Table 4 [1].

Energy gaps of the $CH_3NH_3PbI_3$ were also measured and calculated [1], as summrized in Table 5. The energy gap increases with increasing temperature from the *ab-initio* calculation, and the measured energy gap of ~1.5 eV is suitable for solar cell materials.

Material	**$CH_3NH_3PbCl_3$**	**$CH_3NH_3PbBr_3$**	**$CH_3NH_3PbI_3$**
Crystal system	Cubic	Cubic	Cubic
Transition temperature (K)	177	236	330
Crystal system	Tetragonal	Tetragonal	Tetragonal
Transition temperature (K)	172	149~154	161
Crystal system	Orthorhombic	Orthorhombic	Orthorhombic

Table 1. Crystal systems and transition temperatures of $CH_3NH_3PbX_3$ (X=Cl, Br, or I).

Atom	**site**	***x***	***y***	***z***	***B* (Å²)**
Pb	1*a*	0	0	0	3.32
I	12*h*	0	0.0435	0.5	8.68
N	12*j*	0.413	0.413	0.5	5.82
C	12*j*	0.578	0.578	0.5	7.05

Table 2. Structural parameters of cubic $CH_3NH_3PbI_3$. Space group *Pmm* (Z=1), *a*=6.391 Å at 330 K. B is isotropic displacement parameter.

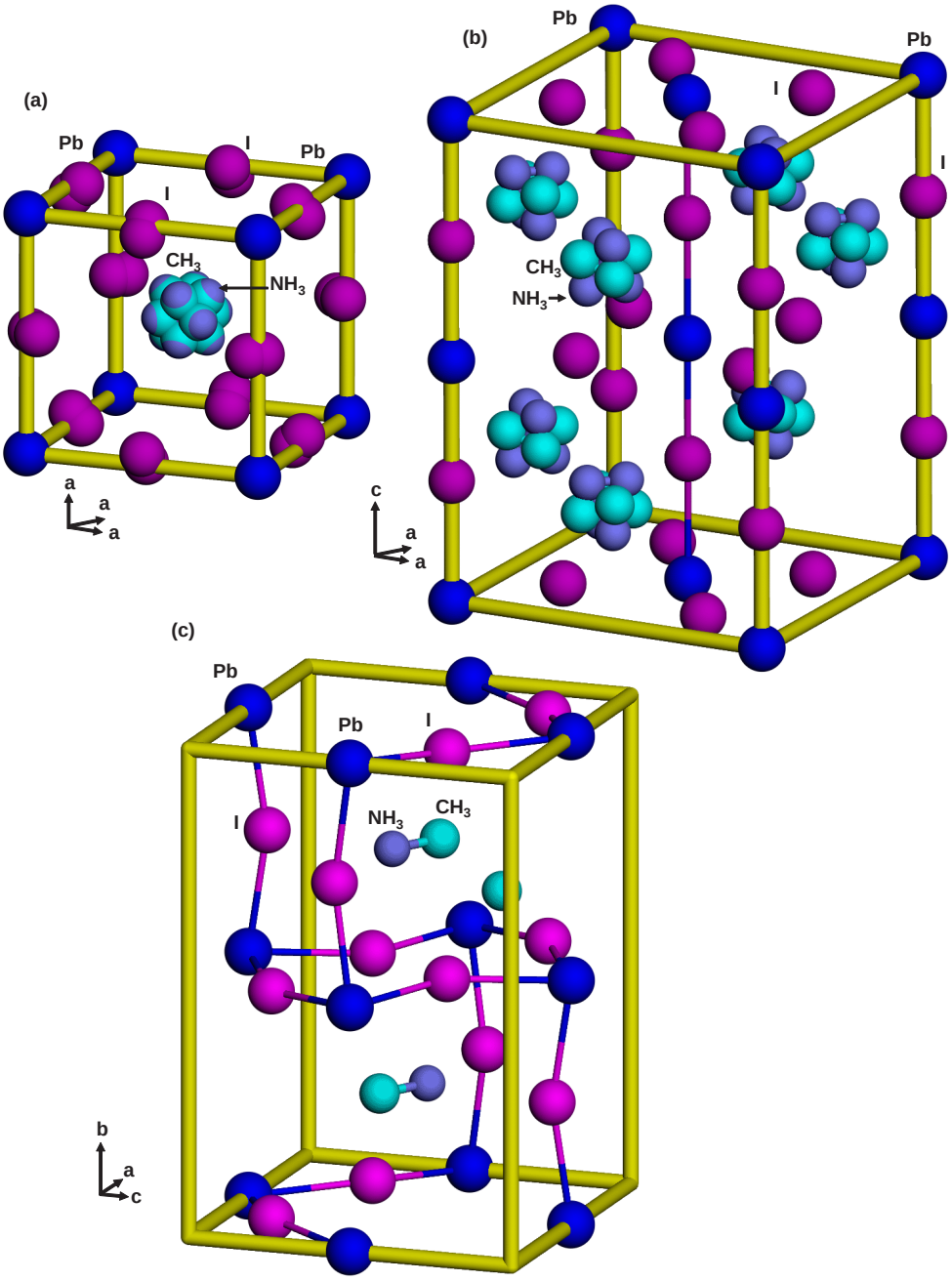

Figure 1. Structure models of $CH_3NH_3PbI_3$ with (a) cubic, (b) tetragonal and (c) orthorhombic structures.

http://dx.doi.org/10.5772/59284

Atom	site	*x*	*y*	*z*	*B* (Å²)
Pb	4*c*	0	0	0	1.63
I(1)	8*h*	0.2039	0.2961	0	4.38
I(2)	4*a*	0	0	0.25	4.11
N	16*l*	0.459	0.041	0.202	4.60
C	16*l*	0.555	–0.055	0.264	3.19

Table 3. Structural parameters of tetragonal $CH_3NH_3PbI_3$ at 220 K. Space group *I4/mcm* (Z=4), *a*=8.800 Å, *c*=12.685 Å. *B* is isotropic displacement parameter.

Atom	site	*x*	*y*	*z*	*B* (Å²)
Pb	4*b*	0.5	0	0	4.80
I(1)	4*c*	0.48572	0.25	–0.05291	1.03
I(2)	8*d*	0.19020	0.01719	0.18615	1.33
N	4*c*	0.932	0.75	0.029	2.37
C	4*c*	0.913	0.25	0.061	1.50

Table 4. Structural parameters of orthorhombic $CH_3NH_3PbI_3$ at 100 K. Space group *Pnma* (Z=4), *a*=8.8362 Å, *b*=12.5804 Å, *c*=8.5551 Å. All occupancy factors 1.0. B is isotropic displacement parameter.

Material	$CH_3NH_3PbI_3$	$CH_3NH_3PbI_3$	$CH_3NH_3PbI_3$
Crystal system	Cubic	Tetragonal	Orthorhombic
Measured energy gap (eV)		1.51	
Calculated energy gap (eV)	1.3	1.43	1.61

Table 5. Energy band gaps of $CH_3NH_3PbI_3$.

Atom	*x*	*y*	*z*	B (Å²)
Pb	0	0	0	1.13
Cl	0	0.0413	0.5	6.73
N	0.413	0.409	0.5	8.1
C	0.578	0.583	0.5	5.8

Table 6. Structural parameters of cubic $CH_3NH_3PbCl_3$. Space group *Pm3m* (Z=1), *a*=5.666 Å at 200 K. B is isotropic displacement parameter.

Structural parameters of cubic $CH_3NH_3PbCl_3$ and $CH_3NH_3PbBr_3$ are summarized as Table 6 and 7, respectively [14, 15]. They have similar structure parameters compared with the cubic

$CH_3NH_3PbI_3$, except for the lattice constants. Lattice parameters of these compounds are strongly depedent on the size of halogen ions, as shown in Figure 2. As summarized in Table 8, ion radii of halogen elements increase with increasing atomic numbers, which affect the lattice constants of $CH_3NH_3PbX_3$, as observed in Figure 2.

Atom	*x*	*y*	*z*	B (Å²)
Pb	0	0	0	1.61
Br	0	0.0413	0.5	5.41
N	0.413	0.417	0.5	6.02
C	0.578	0.582	0.5	6.05

Table 7. Structural parameters of cubic $CH_3NH_3PbBr_3$. Space group *Pm3m* (Z=1), *a*=5.933 nm at 298 K. B is isotropic displacement parameter.

Hologen element	F-	Cl^-	Br^-	I^-
Ion radius (Å)	1.33	1.81	1.96	2.20
14 group element		Ge^{2+}	Sn^{2+}	Pb^{2+}
Lattice parameters		0.73	0.93	1.18

Table 8. Ion radii of halogen and 14 group elements.

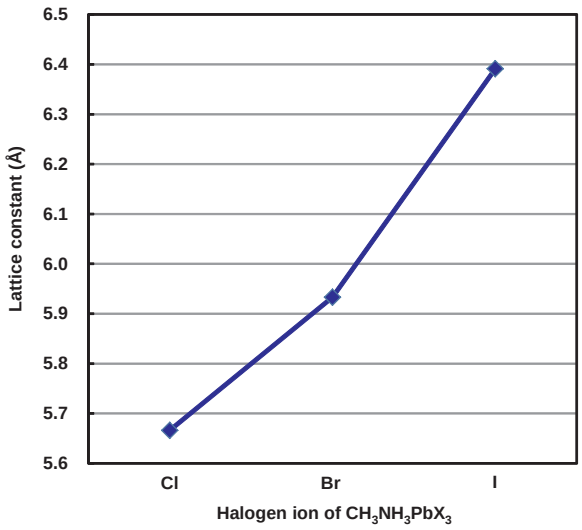

Figure 2. Lattice constants of $CH_3NH_3PbX_3$ (X=Cl, Br, or I).

http://dx.doi.org/10.5772/59284

4. X-ray diffraction of $CH_3NH_3PbI_3$

Microstructure of the perovskite phases can be investigated by X-ray diffraction (XRD). The XRD will indicate that the sample is a single phase or mixed phase. If the sample consists of nanoparticles or nanocrystals, the crystallite size can be estimated from the full width at half maximum (FWHM). From the XRD data, analyses of high-resolution TEM image and electron diffraction would become easier. If the sample is a known material, plane distances (d) and indices can be clarified from the diffraction peaks of XRD. When the sample has an unknown structure, the values of the plane distances can be obtained by the XRD, which will effectively stimulate the structure analysis.

Calculated X-ray diffraction patterns on the $CH_3NH_3PbI_3$ with cubic, tetragonal and orthorhombic structures is shown in Figure 3, and calculated X-ray diffraction parameters of cubic, tetragonal and orthorhombic $CH_3NH_3PbI_3$ are listed in Table 9, 10, and 11, respectively. For the cubic phase, site occupancies were set as 1/4 for I and 1/12 for C and N. Structure factors were averaged for each index. Site occupancies were set as 1/4 for C and N for the tetragonal $CH_3NH_3PbI_3$. Figure 4 is an enlarged calculated X-ray diffraction patterns of $CH_3NH_3PbI_3$. Reflection positions of 211 and 213 inconsistent with cubic symmetry for tetragonal structure are indicated by asterisks, which would be helpful for the distinction between the cubic and tetragonal phase [1].

Index	2θ (°)	*d-spacing (Å)*	|*F*|	Relative intensity (%)	Multiplicity
1 0 0	13.8449	6.3910	107.1	100	6
1 1 0	19.6279	4.5191	46.3	18	12
1 1 1	24.0990	3.6898	29.4	3	8
2 0 0	27.8973	3.1955	164.3	55	6
2 1 0	31.2695	2.8581	93.4	56	24
2 1 1	34.3423	2.6091	44.4	10	24
2 2 0	39.8633	2.2596	136.0	35	12
2 2 1	42.3942	2.1303	84.0	23	24
3 0 0	42.3942	2.1303	76.0	5	6
3 1 0	44.8082	2.0210	35.9	4	24
3 1 1	47.1237	1.9270	8.6	0.2	24
2 2 2	49.3555	1.8449	116.1	10	8
3 2 0	51.5149	1.7725	69.5	10	24
3 2 1	53.6114	1.7081	35.9	5	48
4 0 0	57.6458	1.5978	100.9	4	6
4 1 0	59.5956	1.5500	66.8	13	48

Table 9. Calculated X-ray diffraction parameters of cubic $CH_3NH_3PbI_3$. Equivlent indices were combined. Space group *Pm3m* (Z=1), *a*=6.391 Å at 330 K. *F* is structure factor.

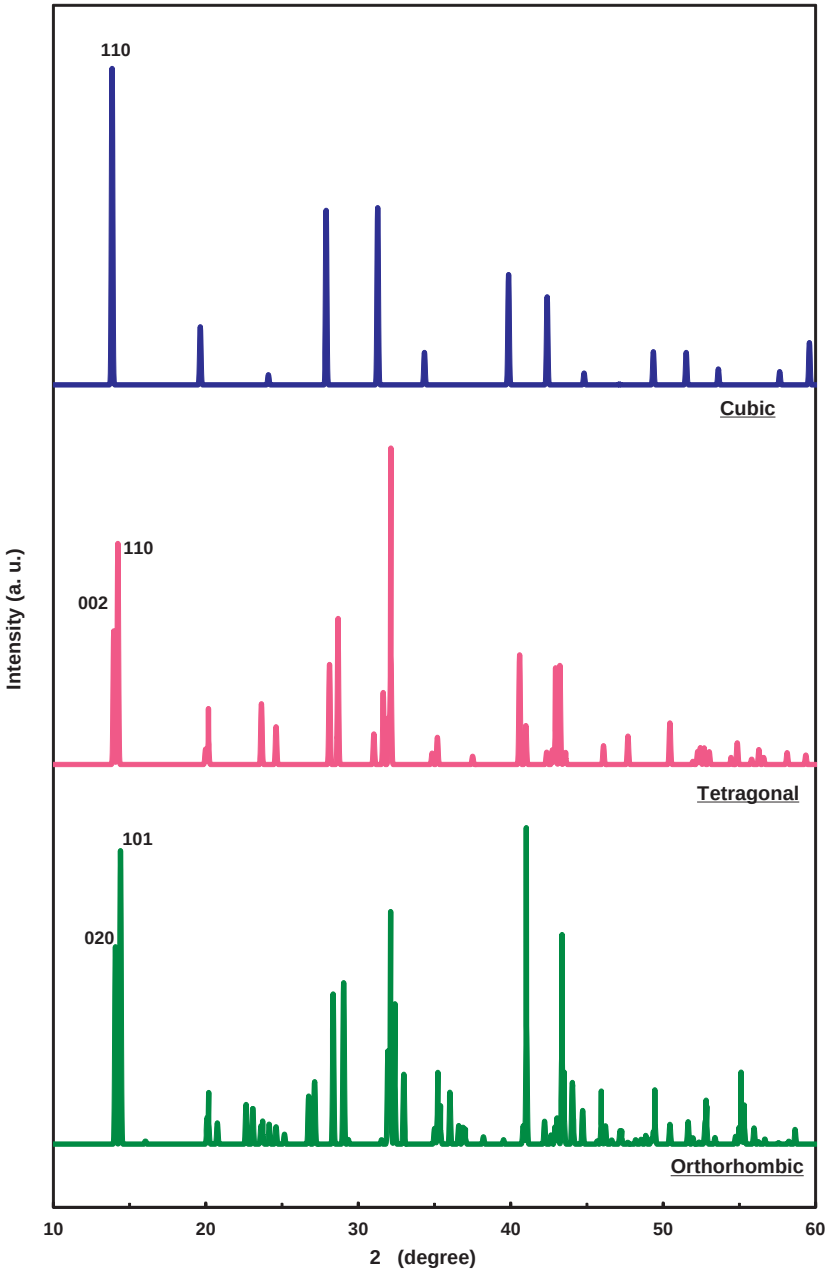

Figure 3. Calculated X-ray diffraction patterns of $CH_3NH_3PbI_3$ with cubic, tetragonal and orthorhombic structures.

http://dx.doi.org/10.5772/59284

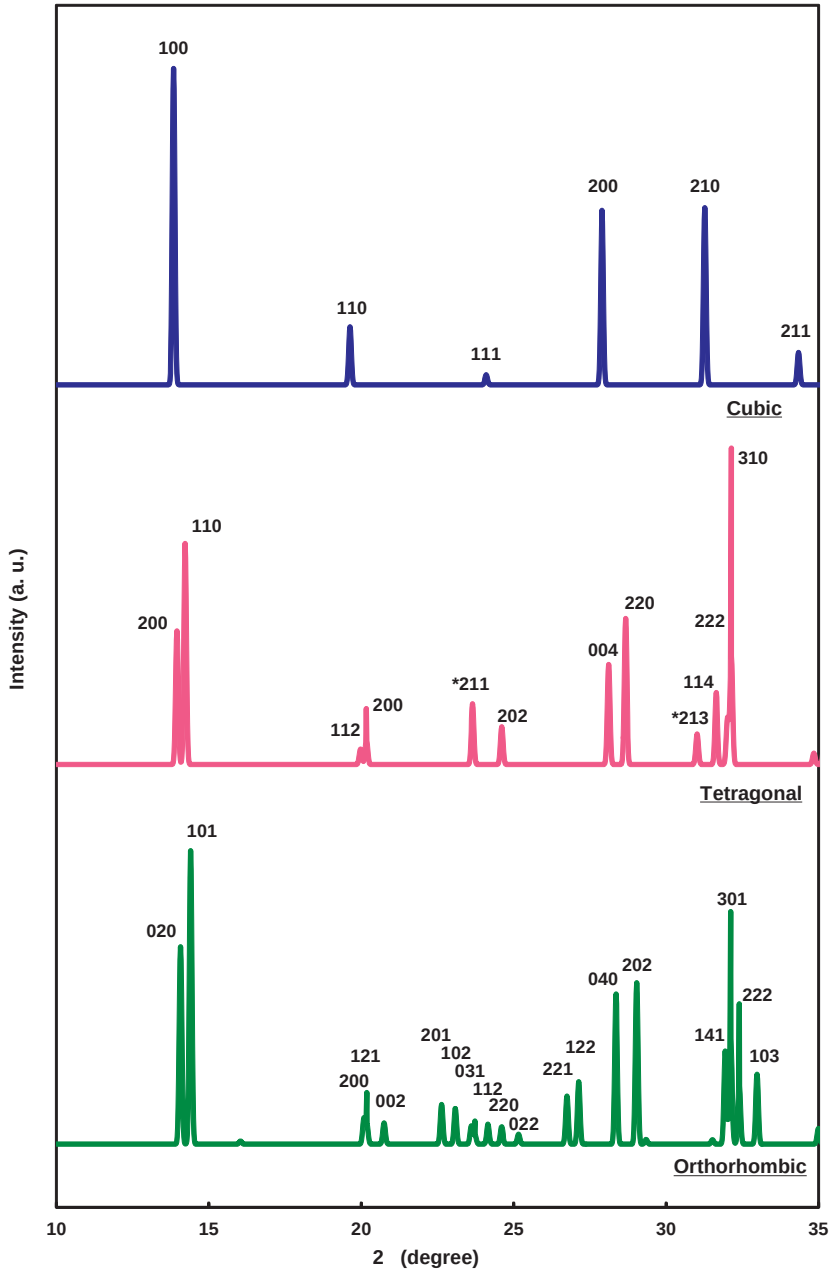

Figure 4. Enlarged calculated X-ray diffraction patterns of $CH_3NH_3PbI_3$ with cubic, tetragonal and orthorhombic structures. *Reflection positions inconsistent with cubic symmetry for tetragonal structure.

Index	2θ (°)	*d-spacing (Å)*	$\|F\|$	Relative intensity (%)	Multiplicity
0 0 2	13.9513	6.3425	477.0	60	2
1 1 0	14.2216	6.2225	442.5	100	4
1 1 2	19.9730	4.4418	116.8	7	8
2 0 0	20.1647	4.4000	211.6	11	4
2 1 1	23.6509	3.7587	195.7	27	16
2 0 2	24.6041	3.6152	227.6	17	8
0 0 4	28.1149	3.1713	852.4	45	2
2 2 0	28.6684	3.1113	744.0	66	4
2 1 3	31.0176	2.8808	184.5	14	16
1 1 4	31.6405	2.8255	410.3	33	8
2 2 2	32.0148	2.7933	331.7	21	8
3 1 0	32.1387	2.7828	511.0	49	8
2 0 4	34.8441	2.5727	180.5	5	8
3 1 2	35.1881	2.5483	199.6	12	16
3 2 1	37.4940	2.3967	117.9	4	16
2 2 4	40.5874	2.2209	665.6	50	8
4 0 0	40.9903	2.2000	566.6	18	4
2 1 5	42.3526	2.1323	165.5	6	16
0 0 6	42.7343	2.1142	415.0	4	2
3 2 3	42.7418	2.1138	109.2	2	16
4 1 1	42.9354	2.1047	277.8	15	16
3 1 4	43.2169	2.0917	479.9	45	16
4 0 2	43.5043	2.0785	222.4	5	8
3 3 0	43.5998	2.0742	225.3	2	4
4 2 0	46.0901	1.9677	317.2	8	8
2 0 6	47.6844	1.9056	155.2	2	8
4 1 3	47.6913	1.9053	265.2	11	16
4 0 4	50.4445	1.8076	523.0	19	8
3 2 5	51.9446	1.7589	106.0	1	16
2 2 6	52.2716	1.7487	303.6	6	8
4 3 1	52.4442	1.7433	171.5	4	16
3 3 4	52.6864	1.7359	218.2	3	8
5 1 0	53.0165	1.7258	307.9	6	8
3 1 6	54.4599	1.6834	165.0	3	16
4 2 4	54.8632	1.6720	294.6	10	16
2 1 7	55.8045	1.6460	149.8	2	16

http://dx.doi.org/10.5772/59284

4 1 5	56.2804	1.6332	250.9	7	16
4 3 3	56.5963	1.6249	171.4	3	16
0 0 8	58.1285	1.5856	657.6	5	2
4 4 0	59.3600	1.5556	423.9	4	4
1 1 8	60.1739	1.5365	353.3	6	8

Table 10. Calculated X-ray diffraction parameters of tetragonal $CH_3NH_3PbI_3$. Space group *I*4/*mcm* (Z=4), *a*=8.800 Å, c=12.685 Å at 220 K.

Index	2θ (°)	*d-spacing (Å)*	|*F*|	Relative intensity (%)	Multiplicity
0 2 0	14.0679	6.2902	462.7	67	2
1 0 1	14.3989	6.1463	408.5	100	4
1 1 1	16.0356	5.5225	32.8	1	8
2 0 0	20.0813	4.4181	238.7	9	2
1 2 1	20.1828	4.3961	106.9	7	8
0 0 2	20.7483	4.2775	225.2	7	2
2 0 1	22.6324	3.9255	239.3	14	4
1 0 2	23.0816	3.8501	231.4	12	4
0 3 1	23.6082	3.7654	168.3	6	4
2 1 1	23.7239	3.7473	86.8	3	8
1 1 2	24.1539	3.6816	128.7	7	8
2 2 0	24.6029	3.6154	172.8	6	4
0 2 2	25.1559	3.5372	132.9	3	4
2 2 1	26.7471	3.3302	221.7	16	8
1 2 2	27.1323	3.2838	256.6	21	8
0 4 0	28.3536	3.1451	834.3	51	2
2 0 2	29.0316	3.0732	627.4	55	4
2 3 0	29.3402	3.0415	108.2	2	4
1 3 2	31.5191	2.8361	80.9	2	8
1 4 1	31.9379	2.7998	373.2	32	8
3 0 1	32.1130	2.7850	560.5	35	4
0 1 3	32.1584	2.7811	155.6	3	4
2 2 2	32.3965	2.7612	304.2	20	8
1 0 3	32.9780	2.7139	473.6	24	4
2 4 0	34.9912	2.5622	239.4	5	4

3 2 1	35.2135	2.5465	244.8	11	8
0 4 2	35.3949	2.5339	225.2	5	4
1 2 3	36.0126	2.4918	317.4	18	8
2 4 1	36.5799	2.4545	193.6	6	8
1 4 2	36.8717	2.4357	185.8	6	8
3 0 2	37.0262	2.4259	145.8	2	4
2 1 3	38.2065	2.3536	127.4	3	8
1 3 3	39.5204	2.2784	101.4	1	8
4 0 0	40.8148	2.2091	432.0	6	2
2 4 2	41.0283	2.1980	555.9	41	8
4 0 1	42.2164	2.1389	281.7	5	4
0 0 4	42.2189	2.1388	305.7	3	2
2 5 1	42.6467	2.1183	161.0	3	8
1 5 2	42.9036	2.1062	142.9	2	8
3 3 2	43.0398	2.0999	157.9	3	8
0 6 0	43.1073	2.0967	330.6	3	2
3 4 1	43.3616	2.085	506.1	30	8
4 2 0	43.3783	2.0843	145.8	1	4
2 3 3	43.4643	2.0803	157.5	3	8
1 0 4	43.4991	2.0787	318.3	6	4
1 4 3	44.0352	2.0547	429.7	21	8
1 1 4	44.1197	2.0509	140.7	2	8
4 2 1	44.7146	2.0250	292.5	9	8
0 2 4	44.7169	2.0249	202.1	2	4
1 6 1	45.6801	1.9844	100.8	1	8
1 2 4	45.9414	1.9738	258.0	7	8
4 0 2	46.2136	1.9628	352.1	6	4
3 2 3	46.5832	1.9481	73.0	1	8
2 5 2	46.6144	1.9468	93.9	1	8
2 0 4	47.1728	1.9251	308.8	5	4
3 4 2	47.2817	1.9209	124.0	1	8
0 5 3	48.1925	1.8867	181.8	2	4
4 2 2	48.5489	1.8737	135.7	2	8
1 3 4	48.8598	1.8625	183.1	3	8

2 6 1	49.2266	1.8494	148.3	2	8
1 5 3	49.3503	1.8451	124.9	1	8
1 6 2	49.4567	1.8414	175.3	3	8
2 2 4	49.4736	1.8408	218.7	4	8
4 4 0	50.442	1.8077	403.4	7	4
4 4 1	51.6367	1.7686	236.3	4	8
0 4 4	51.6388	1.7686	287.3	3	4
0 7 1	51.9470	1.7588	234.2	2	4
4 0 3	52.3451	1.7464	135.0	1	4
2 5 3	52.7109	1.7351	82.5	1	8
1 4 4	52.7410	1.7342	270.6	5	8
2 6 2	52.8123	1.7320	242.3	4	8
5 0 1	52.8555	1.7307	280.3	3	4
4 1 3	52.8858	1.7298	121.2	1	8
3 1 4	53.3946	1.7145	162.9	2	8
3 6 1	54.7548	1.6751	197.8	3	8
3 2 4	54.9839	1.6686	176.9	2	8
4 4 2	55.1098	1.6651	333.9	8	8
2 7 0	55.1235	1.6647	160.7	1	4
4 5 0	55.2931	1.6600	194.8	1	4
1 6 3	55.3226	1.6592	258.8	4	8
2 4 4	55.9564	1.6419	290.5	5	8
1 2 5	56.6693	1.6229	166.9	2	8
2 1 5	58.2395	1.5829	131.8	1	8
0 8 0	58.6587	1.5726	586.0	5	2
4 0 4	60.1713	1.5366	266.9	2	4

Table 11. Calculated X-ray diffraction parameters of orthorhombic $CH_3NH_3PbI_3$. Space group *Pnma* (*Z*=4), *a*=8.8362 Å, *b*=12.5804 Å, *c*=8.5551 Å at 100 K. B is isotropic displacement parameter. All occupancy factors 1.0.

Calculated X-ray diffraction patterns of $CH_3NH_3PbI_3$ with various FWHM values are shown in Figure 5. When the crystallite sizes decrease, the FWHM values increase, and different peak intensities are observed in Figure 5.

Figure 6 is an enlarged calculated X-ray diffraction patterns of $CH_3NH_3PbI_3$. With increasing FWHM values, the diffraction peaks of 200 and 110 seem to be combined, which should be very careful for the XRD structure analysis.

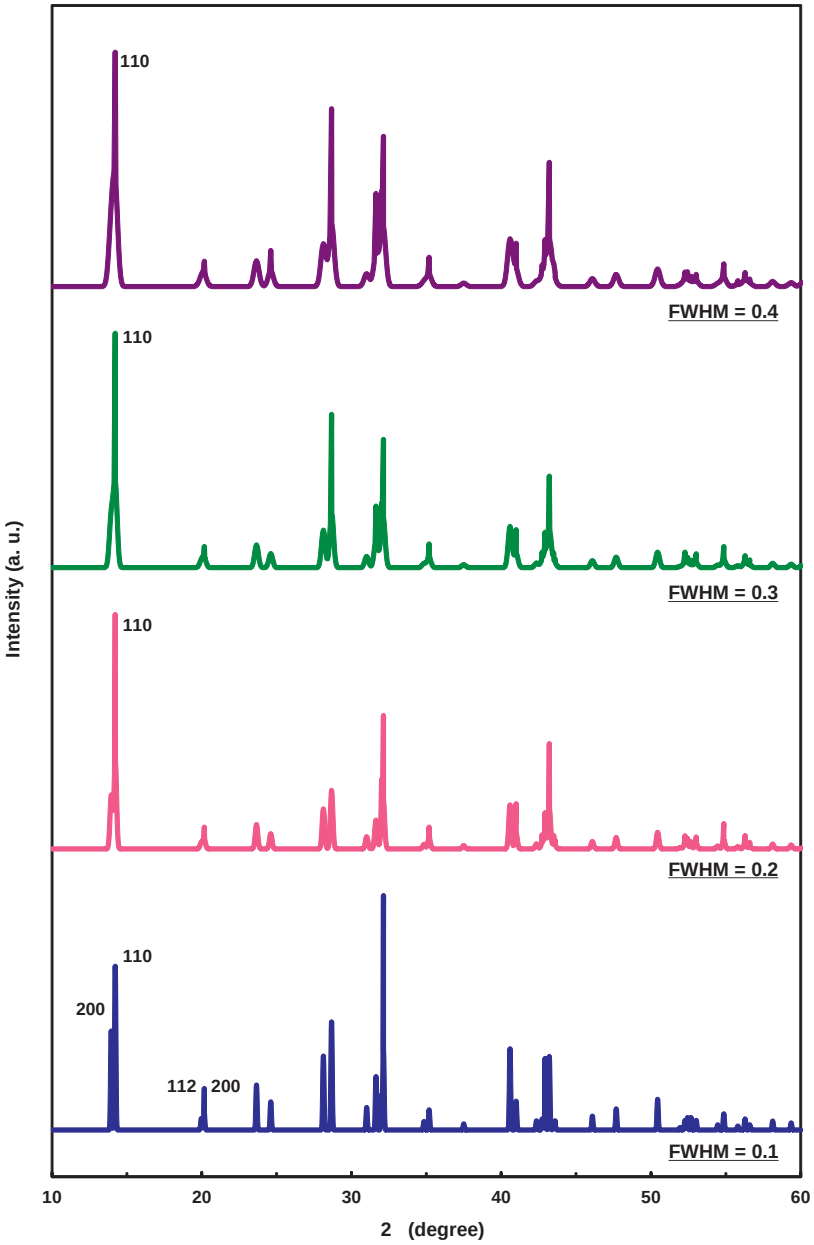

Figure 5. Calculated X-ray diffraction patterns of $CH_3NH_3PbI_3$ with various FWHM values.

http://dx.doi.org/10.5772/59284

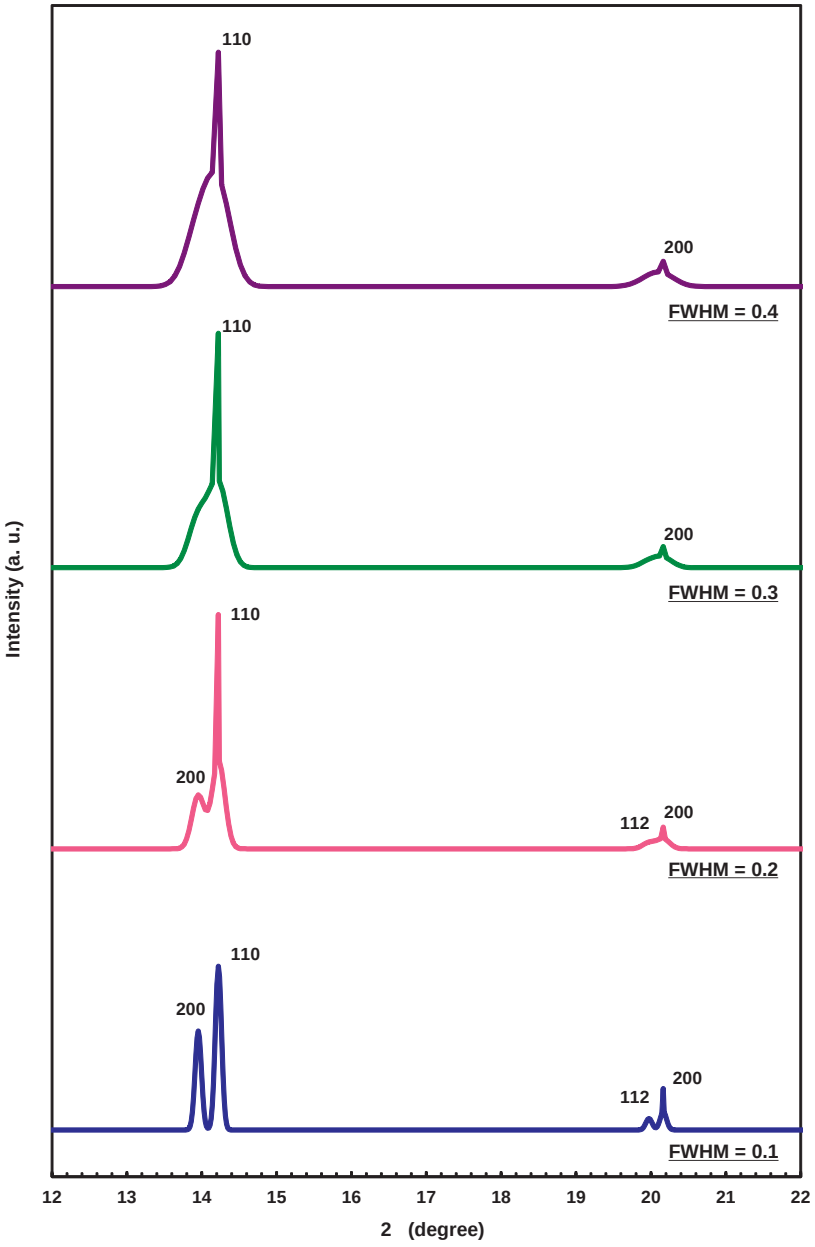

Figure 6. Enlarged calculated X-ray diffraction patterns of $CH_3NH_3PbI_3$ with various FWHM values.

5. Electron diffraction of $CH_3NH_3PbI_3$

When the sample amount, sample area or film thickness is smaller, it is difficult to obtain the necessary diffraction amplitude by XRD. Since the amount is enough for the TEM observation, only TEM observation may be applied to obtain the structure data. To obtain the information on the fundamental atomic arrangements, electron diffraction patterns should be taken along the various directions of the crystal, and the fundamental crystal system and lattice constants may be estimated. Then, high-resolution TEM observation and composition analysis by energy dispersive X-ray spectroscopy are performed, and the approximate atomic structure model is constructed. Most of the materials have similar structures to the known materials, and the structures will be estimated if the database on the known structures is available. For example, lots of new structures were found for high-Tc superconducting oxides, which have basic perovskite structures, and the approximate atomic structure models can be constructed from the high-resolution TEM images, electron diffraction patterns, and composition analysis of the elements [17, 19].

If a structure of the TEM specimen is known, observation direction of the crystal should be selected, and electron diffraction pattern along the direction should be estimated. Any regions selected by the selected area aperture can be observed in electron diffraction patterns, and the structure can be easily analyzed by comparing TEM images with electron diffraction patterns. When electron diffraction pattern is observed in the selected area, the diffraction pattern is often inclined from the aimed direction, which is noticed from the asymmetry of the electron diffraction pattern. The sample holder can be usually tilted along two directions, and the specimen should be tilted as the diffraction pattern shows center symmetry. Atomic structure models of cubic $CH_3NH_3PbI_3$ observed along varioius directions are shown in Figure 7. Note that the atomic positions of CH_3, NH_3 and I are disordered as observed in the structure models. Corresponding electron diffraction patterns of cubic $CH_3NH_3PbI_3$ calculated along the [100], [110], [111] and [210] directions are shown in Figure 8.

Atomic structure models of tetragonal $CH_3NH_3PbI_3$ observed along [001], [100], [021], [221] and [110] are shown in Figure 9, which correspond to [001], [110], [111], [210] and [100] of cubic phase in Figure 8, respectively. Atomic positions of I are fixed for the tetragonal phase, and only atomic positions of CH_3 and NH_3 are disordered. For the tetragonal phase, the crystal symmetries are lowered as indicated by arrows in Figure 9(c) and 9(e). Several diffraction spots in Figure 9 have different diffraction intensities compared with Figure 8, which would be due to the different crystal symmetry of the $CH_3NH_3PbI_3$ compound.

High-resolution TEM observations have been performed for the perovskite materials [20], and the nanostructures were discussed. Although TEM is a powerful tool for nanostructured materials, sample damage by electron beam irradiation should be avoided, because the $CH_3NH_3PbI_3$ are known to be unstable during annealing at elevated temperatures. Several TEM results have been reported for the $CH_3NH_3PbI_3$ and $CH_3CH_2NH_3PbI_3$, and the structures were discussed by electron diffraction and high-resolution images in these works [1, 9, 28].

http://dx.doi.org/10.5772/59284

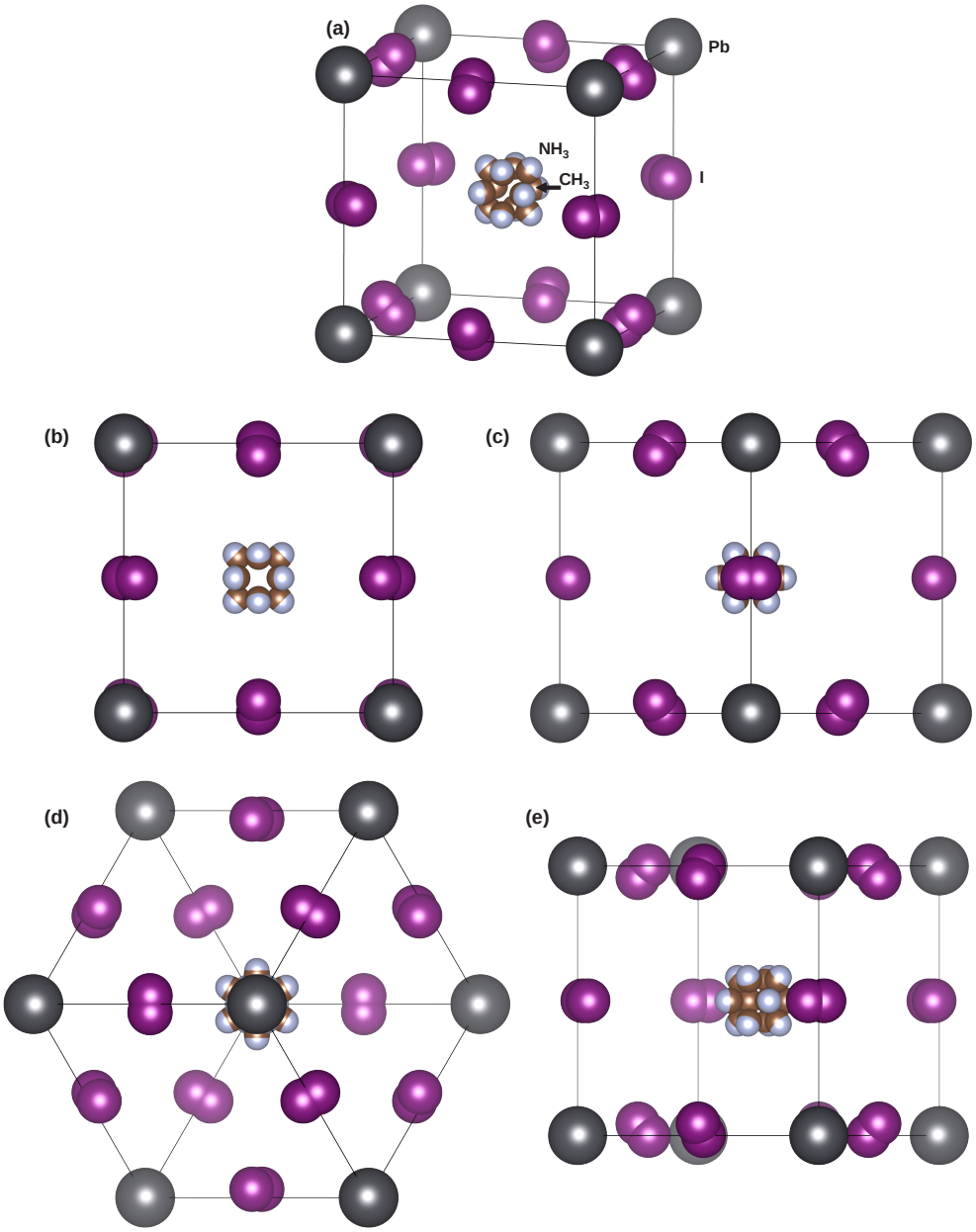

Figure 7. Atomic structure models of cubic $CH_3NH_3PbI_3$ observed along (a) perspevtive view, (b) [100], (c) [110], (d) [111] and (e) [210].

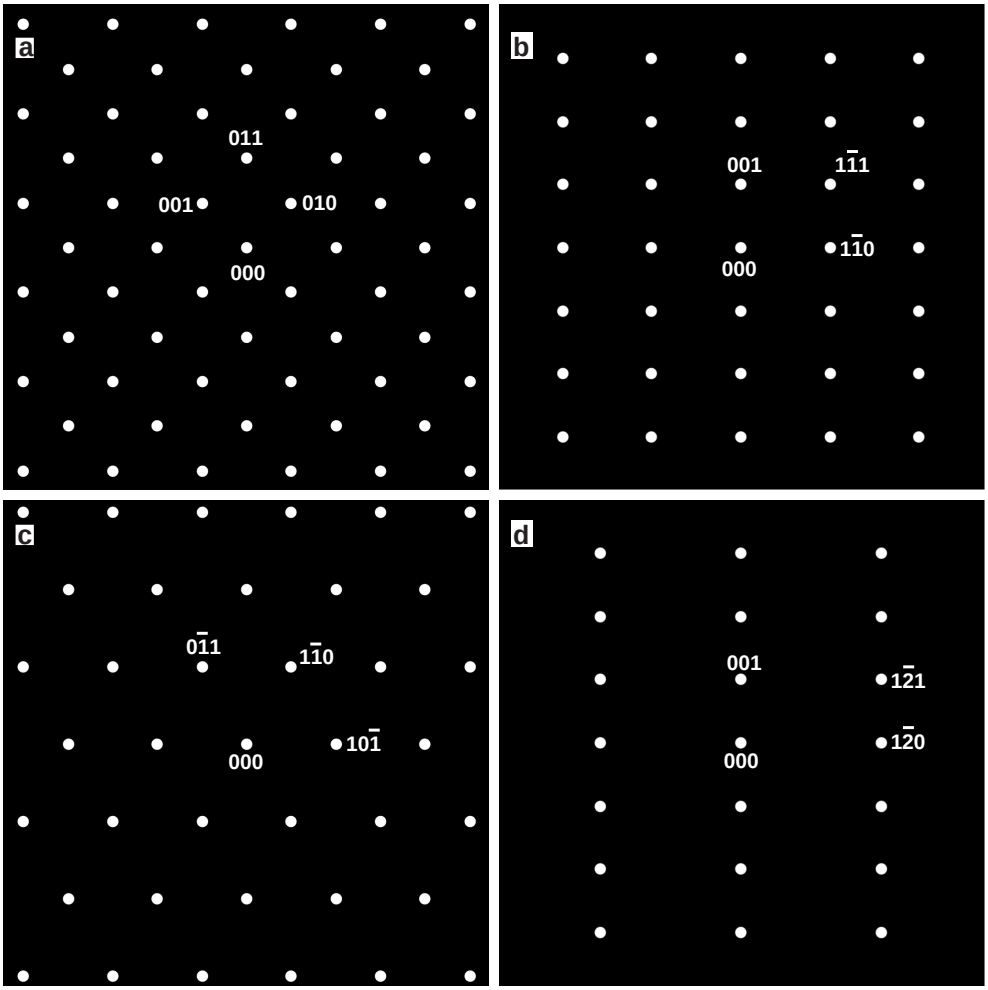

Figure 8. Calculated electron diffraction patterns of cubic $CH_3NH_3PbI_3$ along (a) [100], (b) [110], (c) [111] and (d) [210].

http://dx.doi.org/10.5772/59284

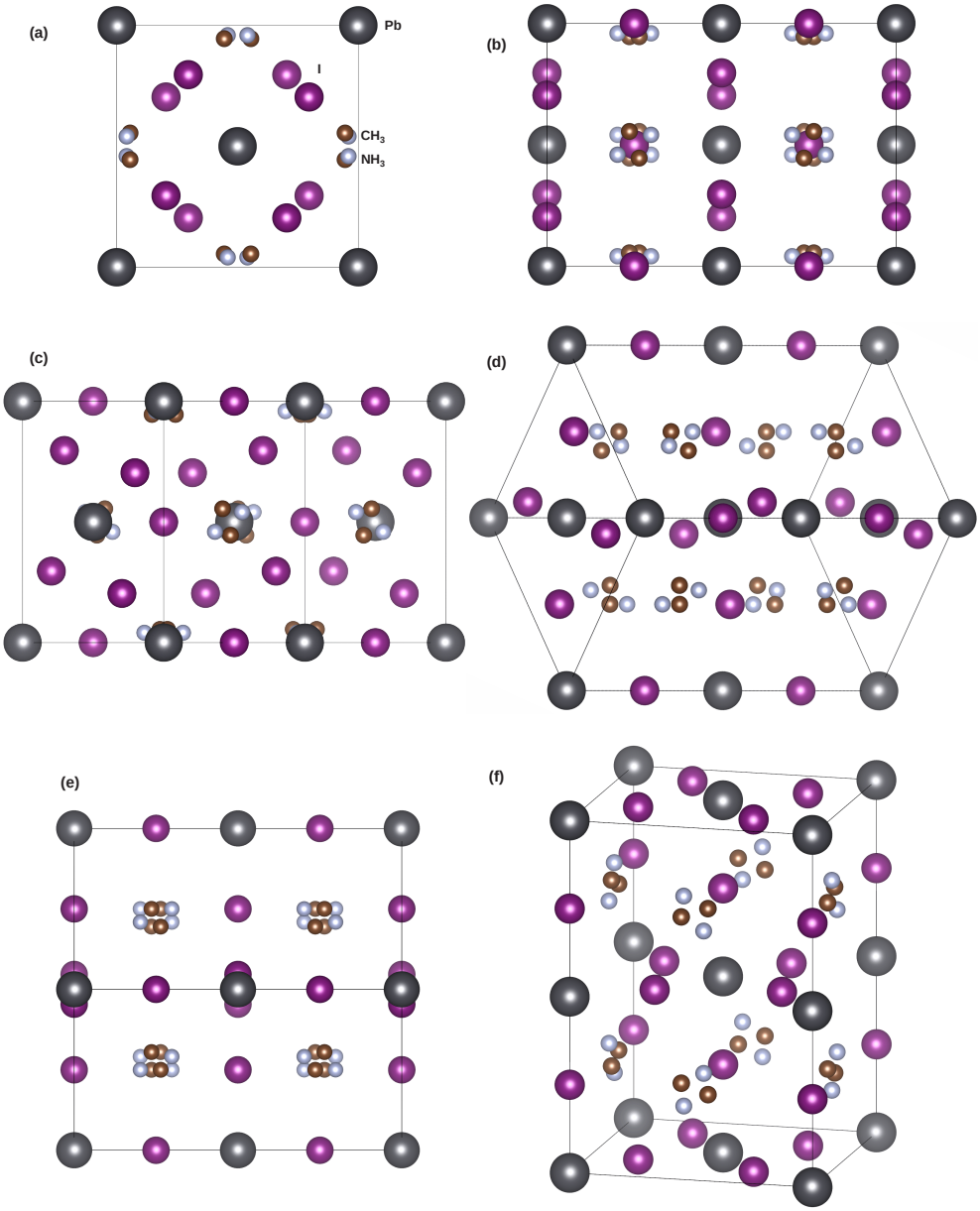

Figure 9. Atomic structure models of tetragonal $CH_3NH_3PbI_3$ observed along (a) [001], (b) [100], (c) [021], (d) [221] and (e) [110] and (f) perspevtive view.

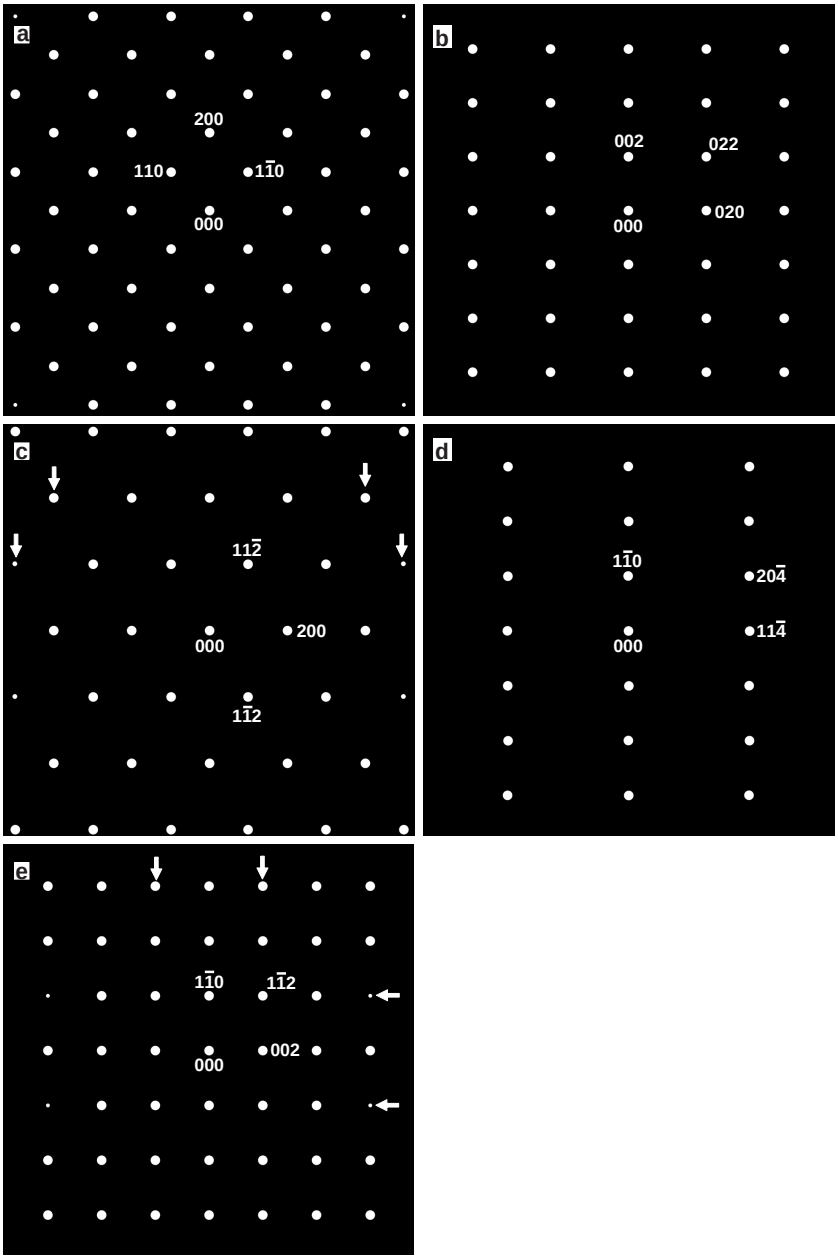

Figure 10. Calculated electron diffraction patterns of tetragonal $CH_3NH_3PbI_3$ along (a) [001], (b) [100], (c) [021], (d) [221] and (e) [110].

http://dx.doi.org/10.5772/59284

6. Other compounds with perovskite structures for solar cells

In addition to $CH_3NH_3PbX_3$ (X=Cl, Br, or I) compounds, various perovskite compounds with perovskite structures for solar cells have benn reported and summarized [1]. Crystal systems and temperatures of $CsSnI_3$ are listed in Table 12, which has very similar structures and phase transitions [3] compared with the $CH_3NH_3PbX_3$. Solar cells with F-doped $CsSnI_{2.95}F_{0.05}$ provided an photo-conversion efficiency of 8.5% [4].

Temperature (K)	300	350	478
Crystal system	Orthorhombic	Tetragonal	Cubic
Space group	*Pnma*	*P4/mbm*	*Pmm*
Z	4	2	1
Lattice parameters	*a* = 8.6885 Å *b* = 12.3775 Å *c* = 8.3684 Å	*a* = 8.7182 Å *c* = 6.1908 Å	*a* = 6.1057 Å

Table 12. Crystal systems and temperatures of $CsSnI_3$.

Temperature (K)	2	250	370	475
Crystal system	Monoclinic	Orthorhombic	Trigonal	Cubic
Space group	$P2_1/n$	*Pnma*	*R3m*	*Pmm*
Z	4	4	1	1
Lattice parameters	*a* = 10.9973 Å *b* = 7.2043 Å *c* = 8.2911 Å α = 90.470°	*a* = 11.1567 Å *b* = 7.3601 Å *c* = 8.2936 Å	*a* = 5.6784 Å α = 90.945°	*a* = 5.6917 Å

Table 13. Crystal systems and temperatures of $CH_3NH_3GeCl_3$.

Similar structures of $CH_3NH_3GeCl_3$ and $CH_3NH_3SnCl_3$ are shown in Table 13 and 14, respectively [28, 26]. Ion radii of Ge and Sn ions are listed in Table 8, and they can be substituted for the Pb atoms in $CH_3NH_3PbX_3$. Lead-free $CH_3NH_3SnI_3$ solar cells were developed, which provided 5.7% efficiency [7]. $(CH_3CH_2NH_3)PbI_3$ with a 2H perovskite structure was reported, which privided 2.4% efficiency [9]. Perovskite oxides such as $[KNbO_3]_{0.9}[BaNi_{0.5}Nb_{0.5}O_{3-x}]_{0.1}$ were found to have an energy gap of ~1.4 eV, which would also be expected as solar cell materials [5].

Temperature (K)	297	318	350	478
Crystal system	Triclinic	Monoclinic	Trigonal	Cubic
Space group	*P*1	*Pc*	*R3m*	*Pmm*
Z	4	4	1	1
Lattice parameters	a = 5.726 Å b = 8.227 Å c = 7.910 Å α = 90.40° β = 93.08° γ = 90.15°	a = 5.718 Å b = 8.236 Å c = 7.938 Å β = 93.08°	a = 5.734 Å α = 91.90°	a = 5.760 Å

Table 14. Crystal systems and temperatures of $CH_3NH_3SnCl_3$.

7. Conclusion

Crystal structures of perovskite-type $CH_3NH_3PbI_3$ compounds with cubic, tetragonal and orthorhombic structures were reviewed and summarized, and X-ray diffraction parameters and diffraction patterns were calculated and presented. Electron diffraction patterns were also calculated along various crystal directions and discussed. Other perovskite compounds such as $CH_3NH_3PbCl_3$, $CH_3NH_3PbBr_3$, $CH_3NH_3GeCl_3$, $CH_3NH_3SnCl_3$, and $CsSnI_3$ were also reviewed, which are expected as next generation, organic-inorganic hybrid solar cells with high photo-conversion efficiencies.

Acknowledgements

The author would like to acknowledge M. Zushi and A. Suzuki for fruitful discussion on the perovskite materials for solar cells.

Author details

Takeo Oku*

Address all correspondence to: oku@mat.usp.ac.jp

The University of Shiga Prefecture, Japan

http://dx.doi.org/10.5772/59284

References

[1] Baikie, T.; Fang, Y,; Kadro, J. M.; Schreyer, M.; Wei, F.; Mhaisalkar, S. G.; Grätzel, M. & Whitec, T. J. (2013). Synthesis and crystal chemistry of the hybrid perovskite $(CH_3NH_3)PbI3$ for solid–state sensitised solar cell applications, *Journal of Materials Chemistry A*, Vol. 1, pp. 5628–5641.

[2] Burschka, J.; Pellet, N.; Moon, S.–J.; Humphry–Baker, R.; Gao, P.; Nazeeruddin, M. K. & Grätzel, M. (2013). Sequential deposition as a route to high–performance perovskite–sensitized solar cells. *Nature*, Vol. 499, pp. 316–320.

[3] Chung, I.; Song, J. H.; Im, J.; Androulakis, J.; Malliakas, C. D.; Li, H.; Freeman, A. J.; Kenney, J. T. & Kanatzidis, M. G. (2012A). CsSnI3: semiconductor or metal? High electrical conductivity and strong near–infrared photoluminescence from a single material. High hole mobility and phase–transitions. *Journal of the American Chemical Society*, Vol. 134, pp. 8579–8587.

[4] Chung, I.; Lee, B.; He, J.; Chang, R. P. H. & Kanatzidis, M. G. (2012B). All–solid–state dye–sensitized solar cells with high efficiency. *Nature*, Vol. 485, pp. 486–489.

[5] Grinberg, I.; West, D. V.; Torres, M.; Gou, G.; Stein, D. M.; Wu, L.; Chen, G.; Gallo, E. M.; Akbashev, A. R.; Davies, P. K.; Spanier J. E. & Rappe A. M. (2013). Perovskite oxides for visible–light–absorbing ferroelectric and photovoltaic materials. *Nature*, Vol. 503, pp. 509–512.

[6] Hahn, T. (1995). *International tables for crystallography, Volume A*. Kluwer Academic Publishers, The Netherland.

[7] Hao, F.; Stoumpos, C. C.; Cao, D. H.; Chang, R. P. H. & Kanatzidis M. G. (2014). Lead–free solid–state organic–inorganic halide perovskite solar cells. *Nature Photonics*, Vol. 8, pp. 489–494.

[8] Im, J.–H.; Lee, C.–R.; Lee, J.–W.; Park, S.–W. & Park, N.–G. (2011). 6.5% efficient perovskite quantum–dot–sensitized solar cell. *Nanoscale,* Vol. 3, pp. 4088–4093.

[9] Im, J.–H.; Chung, J.; Kim S.–J. & Park N.–G. (2012). Synthesis, structure, and photovoltaic property of a nanocrystalline 2H perovskite–type novel sensitizer $(CH_3CH_2NH_3)PbI3$. *Nanoscale Research Letters*, Vol. 7, 353–1–7.

[10] Kawamura, Y.; Mashiyama, H. & Hasebe, K. (2002). Structural study on cubic–tetragonal transition of CH3NH3PbI3. *Journal of the Physical Society of Japan*, Vol. 71, pp. 1694–1697.

[11] Kojima, A.; Teshima, K.; Shirai, Y. & Miyasaka T. (2009). Organometal halide perovskites as visible–light sensitizers for photovoltaic cells. *Journal of the American Chemical Society*, Vol. 131, pp. 6050–6051.

[12] Lee, M. M.; Teuscher, J.; Miyasaka, T.; Murakami, T. N. & Snaith, H. J. (2012). Efficient hybrid solar cells based on meso–superstructured organometal halide perovskites. *Science*, Vol. 338, pp. 643–647.

[13] Liu, D. & Kelly, T. L. (2014). Perovskite solar cells with a planar heterojunction structure prepared using room–temperature solution processing techniques. *Nature Photonics*, Vol. 8, pp. 133–138.

[14] Mashiyama, H.; Kurihara, Y. & Azetsu T. (1998). Disordered cubic perovskite structure of CH3NH3PbX3 (X=Cl, Br, I). *Journal of the Korean Physical Society*, Vol. 32, pp. S156–S158.

[15] Mashiyama, H.; Kawamura, Y.; Magome, E. & Kubota Y. (2003). Displacive character of the cubic–tetragonal transition in $CH_3NH_3PbX_3$. *Journal of the Korean Physical Society*, Vol. 42, pp. S1026–S1029.

[16] Oku, T.; Kakuta, N.; Kobayashi, K.; Suzuki, A. & Kikuchi, K. (2011). Fabrication and characterization of TiO2–based dye–sensitized solar cells. *Progress in Natural Science: Materials International*, Vol. 21, pp. 122–126.

[17] Oku, T. (2012). Direct structure analysis of advanced nanomaterials by high–resolution electron microscopy. *Nanotechnology Reviews*, Vol. 1, pp. 389–425.

[18] Oku, T.; Takeda, A.; Nagata, A.; Kidowaki, H.; Kumada, K.; Fujimoto, K.; Suzuki, A.; Akiyama, T.; Yamasaki, Y. & Ōsawa, E. (2013). Microstructures and photovoltaic properties of C60 based solar cells with copper oxides, CuInS2, phthalocyanines, porphyrin, PVK, nanodiamond, germanium and exciton diffusion blocking layers. *Materials Technology*, Vol. 28, pp. 21–39.

[19] Oku, T. (2014). Structure analysis of advanced nanomaterials: nanoworld by high–resolution electron microscopy. Walter De Gruyter Inc. Germany.

[20] Oku, T. (2014). High–resolution electron microscopy and electron diffraction of perovskite–type superconducting copper oxides. *Nanotechnology Reviews*, Vol. 3, 413–444.

[21] Onoda–Yamamuro, N.; Matsuo, T. & Suga, H. (1990). Calorimetric and IR spectroscopic studies of phase transitions in methylammonium trihalogenoplumbates (II). *Journal of Physics and Chemistry of Solids*, Vol. 51, pp. 1383–1395.

[22] Poglitsch, A. & Weber, D. (1987). Dynamic disorder in methylammonium trihalogenoplumbates (II) observed by millimeter–wave spectroscopy. *The Journal of Chemical Physics*, Vol. 87, pp. 6373–6378.

[23] Wang, J. T.–W.; Ball, J. M.; Barea, E. M.; Abate, A.; Alexander–Webber, J. A.; Huang, J.; Saliba, M.; Mora–Sero, I.; Bisquert, J.; Snaith, H. J. & Nicholas, R. J. (2014). Low–temperature processed electron collection layers of graphene/TiO2 nanocomposites in thin film perovskite solar cells. *Nano Letters*, Vol. 14, pp. 724–730.

http://dx.doi.org/10.5772/59284

[24] Weber, D. (1978). $CH_3NH_3PbX_3$, ein Pb(II)–system mit kubischer perowskitstruktur *Zeitschrift für Naturforschung B*, Vol. 33, pp. 1443–1445.

[25] Yamada, K.; Kuranaga, Y.; Ueda, K.; Goto, S.; Okuda, T. & Furukawa, Y. (1998). Phase transition and electric conductivity of ASnCl3 (A = Cs and CH3NH3). *Bulletin of the Chemical Society of Japan*, Vol. 71, pp. 127–134.

[26] Yamada, K.; Mikawa, K.; Okuda, T. & Knight, K. S. (2002) Static and dynamic structures of CD3ND3GeCl3 studied by TOF high resolution neutron powder diffraction and solid state NMR. *Journal of the Chemical Society, Dalton Transactions*, pp. 2112–2118.

[27] Zhou, H.; Chen, Q.; Li, G.; Luo, S.; Song, T.–B.; Duan, H.–S.; Hong, Z.; You, J.; Liu, Y. & Yang, Y. (2014). Interface engineering of highly efficient perovskite solar cells. *Science*, Vol. 345, pp. 542–546.

[28] Zushi, M.; Suzuki, A.; Akiyama, T. & Oku T. (2014). Fabrication and characterization of TiO_2/$CH_3NH_3PbI_3$–based photovoltaic devices. Chemistry Letters, Vol. 43, pp. 916–918.

Chapter 4

New Approaches to Practical High-Effective Solar Energy Conversion

Viktor I. Laptev and Halyna Khlyap

Additional information is available at the end of the chapter

http://dx.doi.org/10.5772/58935

1. Introduction

High-effective solar energy conversion is impossible without deep examination of solar cell'components as physical materials. Studies of structure of matter, its optical and thermodynamic properties belong to the scope of several disciplines. The concept of generalized formula units is of particular importance. For example, a category of crystal lattice is the result of crystal's mathematical modeling, while the regularity of the crystal structure represents the basis of its zone structure, which, in turn, is the model for description of energy states of the electrons. It is clear that after all chemical bonds are broken and crystal is evaporated there will be no crystal lattice and its inherent energy bands. Only particles of the crystal remain. However, the band theory considers only energy states of the electrons. Therefore, studies of the relations between structural, thermodynamic and optical properties of material without addressing to the band theory of solids are of both theoretical and practical interest. Here we show that such relations can be found by presenting the sequence of ground and excited states of primitive and non-primitive crystal cells as a thermodynamic process. Calculation of frequencies at which maximal useful work can be produced by a crystal cell and radiation is presented by the example of magnesium. The number of such frequencies increases in the row diamond-graphite-soot. On the example of silicon it is suggested that objects can be comparable with ideal radiator, or black body, in terms of their property to absorb radiation energy if they are composed of nanoparticles, i.e. clusters with small number of atoms. Requirements formulated for such objects are to be used for maximally efficient conversion of solar radiation into useful work. At the same time, current-voltage characteristics of solar cells are of special interest. We report experimental results and data of their numerical simulation showing novel features of common silicon-based solar cells with metallic Cu/Ag-nanoclustered contacts.

2. StructuI and formula units of crystalline substance

2.1. History of the problem

Atomic-molecular theory of matter structure is a basis of our understanding various properties of substances. Laws of Kirchhoff, Win, Stephan-Boltzmann and the Planck formula build a simplest model of optical, structural, thermal and chemical characteristics of substances: these laws are valid for any solids, liquids, gases, plasmas and radiation in the state of absolute black body. Our interest is focused on unity of these properties as a tool for introducing Formula Units or preventing a movement of solids to the state of black body.

This chapter presents a crystal-chemical model of unity of structural and optical properties and chemical and thermal characteristics for real solids. Self-consistence of their actions causes various departures of solid from the black body. Knowledge of these departures is necessary for proper choice of the object of investigation and working body under solving science-technological tasks, in particular, for predicting and calculating efficiency of transformation solar heat → useful work.

The simplest Kirchhoff-Planck model gives identity of the optical properties of solids. Otherwise, the optical properties of real solids may belong to two groups according to sensing their atomic structure. Structural sensitivity of optical properties depends on atomic structure of the solid; absence of this sensitivity depends principally on electronic structure of the atom, ion, and other atomic particles. The fundamental absorption of UV-radiation is an example for the first case. The own color of solids and absorption of visual and IR-radiation are an example for the second case.

The first set of optical properties is defined by chemical composition of the light absorber; the second one is defined by mechanism of interaction between light and matter. A number of original works and reference editions summarize data on optical properties of solids in various aggregate and structural states. Here we will use one of them [30, 31, 56, 61].

Thermal properties of solids are characterized by melting heat, evaporation heat, sublimation heat, and by the energy of decaying chemical bonds. They are not so sensible to atomic structure as the optical properties. Sensing optical properties to structural changes is negligible in some cases.

Thermal and chemical properties of substances are subjected to the thermo-chemistry examinations. They are defined by the laws of thermodynamics and are studied well enough. Numerous data are reported in many reference books, for example, in [70]. Correlations of thermal and chemical properties of substances are considered in chemical thermodynamics. We should note the general theory of comparative calculating thermal properties proposed by Karapetjanz M.Ch. and Kireev V.A. in [37].

Crystals are presenting the limit case of regular and periodic locations of atomic particles in space. In non-crystalline solids there are micro-and nano-parts where the regular (partially periodical or completely crystal-like) distribution of atomic particles is also realized. Thus we

http://dx.doi.org/10.5772/58935

will below consider the crystal as an ideal case of regular and periodical location of atomic particles.

After finding chemical individuality the crystal becomes a formula unit. The formula unit (FU is identical to the molecular unit of the substance in symbols of chemical elements. In a period for the X-ray analysis the mineralogy had a false opinion that the minerals are built from molecules, therefore, the mathematical crystallography did not need separating categories “structural unit of the crystal” and “formula unit of the crystal”. Fedorov’s crystallographic analysis made it possible to define the type of crystal lattice and, using his tables of mutual arrangement of the crystal facets gave a possibility to find out the chemical composition of the mineral, i.e. the formula unit [1]. However, the Fedorov’s crystal-chemical analysis did not allow determining the particles which are to be located in the sites of the crystal lattice.

Invention of X-ray analysis made it possible to highlight the formula unit from the set of many structural units of the crystal. The modern crystallography and crystal chemistry consider atoms, ions, and their groups located at the sites of the crystal lattice as structural units. The contemporary X-ray structural analysis revealed a great number of structural units of the crystal which build a hierarchy. These data are described in various publications.

We have to note here that the first separation of categories "structural unit" and "formula unit" took place not in mineralogy, but in molecular theory worked out by Avogadro. It was appeared as a tool for describing chemical interaction of gases. At beginning of 50th years of 19th century it was further developed by A. M. Butlerov in theories of chemical structure, valence and coordination compounds. At the same time Kirchhoff investigations led to optical identification of structural units of the substance-to the atom and molecule.

Spectral analysis is not a decisive tool for determining structural unit and formula unit of the crystal. For example, in the crystal of magnium oxide (periclas) one can differ atoms' groups Mg, O, Mg_4O_4, MgO_6, Mg_6O, and many others. The first two ones are filling in the primitive crystal cell. The third structural unit symbolizes a formula unit of the substance; the next ones present the content of the elementary cell and coordination groups of atoms. All these units are the most important parts of crystal structure of periclas. Optical identification of the crystal does not consider its formula unit as one of the structural units. Modern hierarchy of these categories had been formed in crystallography and mineralogy as a consequence of neutron, electron, X-ray, and other structural analytical methods only.

Laue M., Friedrich W. and Knipping P. in 1913 made it possible to find out a function between experimentally observed diffraction patterns from dark points at one side and real locations of atoms in crystals and X-ray wave length from the other side. Scientific achievements of Bragg W. G. and Bragg W. L. reduced the analysis of simple crystals to the standard technique. It was a beginning of a new method of crystallographic analysis called X-ray crystallography. Laue M., Bragg W. G. and Bragg W. L. were awarded by Nobel Preis (1914, 1915).

Fedorov E.S. understood for the first time that only the atoms but not molecules are to be located periodically in the space at the sites of crystal lattice [17]. It was his explanation of false attempting to connect the molecule geometry with the form of crystal [16]. Further Fedorov E. S. carefully analyzed and discussed [18] works of Bragg W. G. and Bragg W. L. [11] and had

found out that in chemical sense inorganic crystals are not built from separate atomic groups [18], he has correctly assumed existence of molecules in crystals of organic compounds [118].

[23, 36, 71] showed that the crystal structure is determined not only by the energy of particles interaction, relationship of their dimensions, polarization, but also by their number. So that the choice and numbering structural units of the crystal are of special importance for describing correlations between optical and thermal properties of crystal in dependence on the atomic structure.

X-ray structural analysis of simple crystals and complex chemically crystals allowed finding out geometric parameters of elementary cell, i.e. there is a cell of minimal dimension which keeps symmetry of atomic structure of the crystal. The relation between the volume of the structure cell V_{cell} and density of crystal ρ is as follows:

$$V_{cell} = M_0 Z / (\varrho N_A),$$

where M_0 is mass of one mole of molecules, and N_A is the Avogadro constant. Letter Z denotes a number of formula units in the cell of the crystal. After substituting a picknometry density of the crystal in this relation it became clear that the parameter Z is a rational constant of the crystal structure and elemental cells of various crystals can have one, two, three, or more formula units.

2.2. State-of-the-art of the problem

In this chapter the formula unit of the crystal is a group of atomic particles corresponding to the molecule of the substance. The formula unit gives information about chemical elements and their relationship in the crystal. Thus writing the formula unit of the crystal as a set of chemical elements' symbols coincides with an analogical denote of chemical molecule. In crystal of organic compounds the formula unit of the crystal corresponds to the molecule, but its elemental cell may be formed by different molecules. The formula unit of the inorganic crystal may correspond to the real object, namely, to the molecule of substance, but its elemental cell can also not correspond to the formula unit or molecule of the substance.

Despite the evidences of ionic structure of minerals they were further called "molecules". Thus, the crystal was called "a giant molecule" [21], p.128, which is not correct. In 50th years of XX century the international crystal-chemistry literature started using the category "formula unit" as an alternative to the category "molecule". Authors [7] have critically analyzed the situation. At present time the category "formula unit" is practically usable in crystal-chemistry literature regardless the absence of its official formulation.

A long discussion how is the ionic crystal to be presented: single macromolecule or a set of any structural units was ended by separation of categories "formula unit, cell, individuum, and crystal habitus" and establishment of hierarchical relationships between them.

If using categories "formula unit" and "cell of the crystal structure" is now doubtless, the category "individual of crystal" is still attractive for researchers. This topic is almost completely

http://dx.doi.org/10.5772/58935

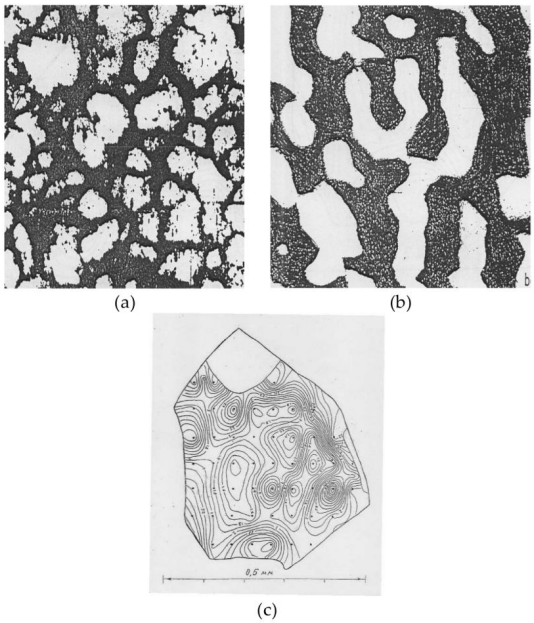

Figure 1. Kathodoluminescence image (a) of polished diamond surface (size 300 μm²) [32, 41];.auger-electron image (b) of polycrystalline lead sulphide surface [60] and the map (c) of isolines of concentration of Fe^{2+}ions in the wafer of olivine [2].

worked-out by G. B. Bokii with using an example of individuals in mineralogy [9]. Vesnin Yu. I. wrote in his preprint [73] about "elemental unit of the crystal" principally corresponding to the category of individual. At present time one considers a monograin or monocrystal with a surface of phase separation as an individual. A separate crystal block with sizes of $10^{-5} \div 10^{-6}$ cm is called sub-individual if dangle chemical bonds, linear and screw dislocation, and other defects of crystalline structure are concentrated along the boundaries of this crystalline block. These blocks are relatively disoriented in 1 – 3°, sometimes up to 5°. Namely, the sub-individuals of the crystal are regions of coherent X-ray dispersion [9].

The crystal sub-individuals may be identified by tunnel electron microscopy. Fig. 1a shows an electron image of diamond surface obtained in mode of the cathodoluminescence of the sample [32, 41]. White fields can be considered as images of sub-individuals, and the black ones are images of their boundary regions. Fig. 1b plots Auger-electron image of the polycrystalline PbS film [60]. The seed of the crystal is also may be considered as its sub-individual.

Results [2] are also present identification of olivine sub-individual by method of optical spectroscopy. Fig. 1c illustrates a map of isolines built for distribution of arbitrary concentration of Fe^{2+}ions in the wafer of olivine crystal.

The distance between the closest isolines is significantly larger than the measurement error. Points show regions of photometry. Authors [2] suppose microblock-like structure of the

olivine crystal. The blocks are of submicron sizes but they have practically same crystallographic orientation which is highlighted by simultaneous turning-off of the entire crystal in crossed Nicole prisms under microscopic examination. These properties of olivine and absence of interruptions in isolines are allowing to assume that identificated blocks of the crystal are sub-individuals of olivine.

Modern X-ray analysis has no difficulties in giving principal information about geometry of crystal cells. There is a big data set on numbers and multiplicity of regular point systems, and on numbers of formula units in cells of many crystal structures. There is no doubt that these properties are affecting the facets of the crystal. Many outside forms of crystals are studied and identified. As an example one can use Fedorov's crystal-chemical analysis allowing determination of the crystal formula unit from its macro-and microsymmetry.

Habitus (facets working-out) is a visual level of structure organization of any crystal. It was found out that the facets are to be described by simple forms: by a single form or by a combination. The simple form is a set of facets defining by elements of symmetry of point group satisfying the Hauyi law. If the crystal visuallyoutside presents the same and symmetrical facets, it can be described by a simple form. If the facets are differing by shape and size the crystal habitus may be presented by a combination of simple forms. Now we know47 geometrically different simple forms, 146 physically different simple forms [5], and 1403 structural-cry stallographic differentiations [68]. The number of facets is not countable. For example, in [23, 24] are presented more than 30000 images of the crystals.

Atoms coordination in the crystal is caused by their spatial localization. The complex of symmetry location elements does not multiply the symmetry. However, the plane out of this location will be cloned and will create one of the simple forms (shapes) depending on its placement relative to the elements of symmetry for a chosen location. When all peaks of the simple form or part of them will belong to equivalent positions relative to the chosen one, the symmetry of the simple form should be bound with symmetry of coordination polyhedron [51, 52].

2.3. The atom and nanovoid as structural units of an ideal crystal

A number of types of coordination polyhedra is limited. Creating an image of one of them reveals voids in polyhedral models of the crystal [58]. There are no sites of crystal lattice in these voids. Thus, the appearance of the voids is assumed to be explained by the category of coordination simple forms which are building the coordination polyhedron [45]. In this case the voids in polyhedral models of the crystal are explained as coordination vacancies due to partial incomplete population of peaks in coordination simple forms. From outside it can be seen as reduce of peaks in the coordination polyhedron proposed by Belov N. V. as a geometrical puzzle. In reality the coordination polyhedron is a matter image of coordination simple forms or their combinations with taking into account the population of the peaks.

It was found a mathematical relation between the number of atoms in the formula unit, coordination number of the atom, number of the facets, and the populations of peaks in simple forms [45, 46]. This relation shows that the interaction of inside structure and outside shape of the crystal is to be extended by a statement saying the following: the ideal crystal structure

http://dx.doi.org/10.5772/58935

there are coordination nanovoids forbidden for self-population. These nanovoids are functionally and periodically located in the crystalline structure [3, 51, 52, 65]. For example, they form well-known throughout-pipelines (channels) in diamond.

So that, the crystal has a level hierarchy of its organization as a system. The first level shows chemical composition and relationships of atomic particles. The second one presents a function of their inter-location in the space. The level presents an organization of the crystal as a physical object. Categories „ formula unit", „cell", and „crystal individuum"build the basis of every level. The habitus of the crystal is supposed to be a fourth level of its structural organization.

The coordination nanovoids are to be considered as the special (zero) level of the system organization of the crystal. They reflect the fact that the empty space before its substance population is a same participant (as the atoms) in the process of crystal formation. Namely the kept primary space is built from coordination voids which may be called relic nanovoids.

The category „coordination nanovoid"is important in other scientific fields. The nanovoids may be populated by other particles, for example, by photons, electrons, positrons, atoms or molecules. In this case the description of the particles absorber is to be started from characterizing the rest of primary space which is forbidden to the self-population by crystal substance. For example, describing the structure of periclas as a photon absorber should begin from stating the relic tetrahedral voids, and than one can highlight the atoms groups Mg, O, MgO, Mg_4O_4, MgO_6, Mg_6O and others. Further we present description of interaction between periclas and UV-radiation [49, 51, 54].

3. Amount of a substance as key category for thermodynamic and chemical description of photon absorber

The concept of "amount of substance" arose from corpuscular knowledge about the structure of matter. Dalton based his hypothesis on the number of atoms, Avogadro counted molecules. The number of substances had not differ fundamentally from the masses until the moment, when the quantum theory and the theory of relativity have shown that the mass of the atoms and molecules of the same substance in different energy states and with various total mass is not proportional to their number. For chemists, this difference of masses is minor, metrologists take it into account. The fundamental difference between the concepts of "amount of substance" and the „mass" was relatively recently justified in Metrology. In 1971 XIV General Conference on weights and measures in its decision confirmed a fundamental difference between the mass and volume of a substance: in the International system of units was entered the seventh basic unit, which is designed to measure the amount of a substance. Its name-mol, marked with the symbol ν.

3.1. Mole and kilogram: Apart and forever?

The definition is common: the mole is the amount of substance of a system which contains as many elementary entities as there are atoms in 0.012 kilogram of carbon – 12. When the mole

is used, the elementary entities must be specified and may be atoms, molecules, ions, electrons, other particles, or specified groups of such particles [33, 34]. The number of specified structural elements in one mole of a substance is called Avogadro constant (Avogadro's number), usually denoted as N_A. Thus, the carbon-12 of mass 0,012 kg contains N_A atoms. Physical value "amount of substance" should not be called a "number of moles", as it is impossible to name the physical size of the "mass" as "the number of pounds" or “number of kilograms” [12].

The current definition of the mole depends on the definition of the kilogram. The XXIV [22] adopted a resolution [22] which had proposed to re-define a mole as a category. Mol should remain a unit of amount of substance; but its value will be determined not by the fixed mass 0,012 kg of carbon-12, but by the numerical value of the Avogadro constant. On the opinion of *Bureau International des Poids et Mesures, BIPM*, «Redefining the mole so that it is linked to +an exact numerical value of the Avogadro constant N_A would have the consequence that it is no longer dependent on the definition of the kilogram even when the kilogram is defined so that it is linked to an exact numerical value of *h*. This would thereby emphasize the distinction between the quantities "amount of substance" and "mass"» [4].

Indeed, mass is a physical characteristic of matter, which expresses and simultaneously measures the gravitational and inertial properties of the matter. The amount of matter is the number of atoms, molecules, ions and other structural units that build the matter. One value of the mass of a substance can correspond to a series of numerical values of quantities of the substance. For example, the mass of the Universe is constant, but the amount of matter in it can be calculated differently if its structure is considered as a set of Galaxies, star systems, molecules and atoms, protons and electrons, photons or other atomic particles. The difference between mass and amount of a substance can serve as the physical basis of the existence in Nature of the right of choice. The bearer of this right is the man as a part of the Universe. The observer in the theory of relativity proofs it.

3.2. Velues derived from amount and mass of substance

When building a system of units derived from number of substances the first values should be the values that are expressed only through the basic units of the system. The diagram below illustrates this requirement.

Mass, m	Amount of the substance, ν
Mole mass, M = m/ ν	Specific amount of substance, ν / m
Density, ρ = m/ V	?
Specific volume, v = V/ m	Mole volume, V_{mol} = V / ν

This scheme shows that its logical completion needs entering another derived value. This may be the density of the amount of substance, which is proposed to be denoted by symbol σ.

The density of substance quantity σ is a physical value equal to ratio of the amount of a substance to its volume. The equation determining σ is as follows:

http://dx.doi.org/10.5772/58935

$$\sigma=\nu/ V. \quad (1)$$

According to this equation the dimension of σ is expressed by the ratio of L^{-3} N, where L and N are symbols of the dimension of length and amount of substance. Unit of measure for σ is "mol per cubic meter", which is in SI units equal to the density of the amount of substance, under condition: if the volume of amount of substance is one cubic meter, then the amount r of substances is one mol.

3.3. Amount of substance for some matters

Method of measuring the amount of substance is count. Direct counting atoms and molecules does not seem reason-nable. Even the number of galaxies in the Universe is already not countable. For example, one of proposed models of the Universe considers it as an ideal gas, containing galaxies. Therefore, the amount of substance is calculated by measurement of volume or mass. Relations between the density of amount of substance σ with density ϱ, specific volume v and molar V_{mol} volume of substance are revealed by joint solution of equations defining these values:

$$\sigma=\rho/ M = 1 / vM= 1 / V_{mol} \quad (2)$$

Under calculating σ it is necessary to identify the structural element of the matter.

3.3.1. Gases

Molecule can be accepted a a structural element of gas. Table 1 lists values of densities of amount of substance σ for some matters calculated according to eq. (2). Density of amount of substance for gaseous simple matters under normal conditions does not depend on chemical nature of gas and is equal 44.6 mole molecules/m^3. Gas of molecules of chemical compounds has the same value of σ. The Avogadro law says that all gases in the same states have a constant value of σ. The ratio ν/σ for any matters is equal to the volume of substance and does not depend on the choice of structural element.

The number of molecules determines the volume ratios of gases; the number of atoms determines weight ratios. Therefore, the density of gaseous matters has fundamentally different functional dependences: the ratio ϱ / σ is equal to the mass of a mole of a substance and depends on choice of structural element, chemical nature and it is proportional to the ordinal number of the element.

3.3.2. Small particles

Atomic structure of bodies in general theory of systems supposes availability of atomic aggregates between gases and condensed bodies with properties which are fundamentally

differ or are intermediate between the properties of isolated atoms of gas and bounded atoms of bulks. Usually aggregates from two to several hundred atoms are called clusters, and the larger aggregates are called small or microparticles [13]. The clusters as well as particles can have linear size more than 1 nm. At present time they are called nano-clusters and nanoparticles that expect different dimension effects. There are no general criteria for type definition of small particles on the number of atoms. In paragraph X of this chapter we propose to consider crystalline nanoparticles the particles which have no translation in the atomic arrangement. These groups contain from 27 to 63 atoms of one chemical element, depending on the type of syngony of a bulk crystal [48, 51, 52].

It is seemed to be reasonable to identify the structural element as the formula unit in calculations of the number of substances of small particles. In the case of simple substances the mass of mole of formula units is equal to the mass of the mole of atoms; in the case of chemical compounds it is equal to the mass of the mole of molecules. Characters of these molar quantities are marked with lower index "0". Therefore, the values σ_0 may describe the density of amount of substance of nanoscaled bodies and they will be useful in examining features of dimension effects.

The principle of construction of physical quantities "density of matter and density of amount of the substance" is the same for all bodies: the ratio of the corresponding main unit to the volume as a value derived from the length. However, their functional relationships principally differ from the linear dimension. For example, the density of the bodies ϱ depends on the chemical composition. The diversity of chemical composition can be expressed through the radius of the atom. In Fig. 2a these densities p of chemical elements are compared with the radius of the atom: any correlation between the density of small particles and the radius of the atom is not observed.

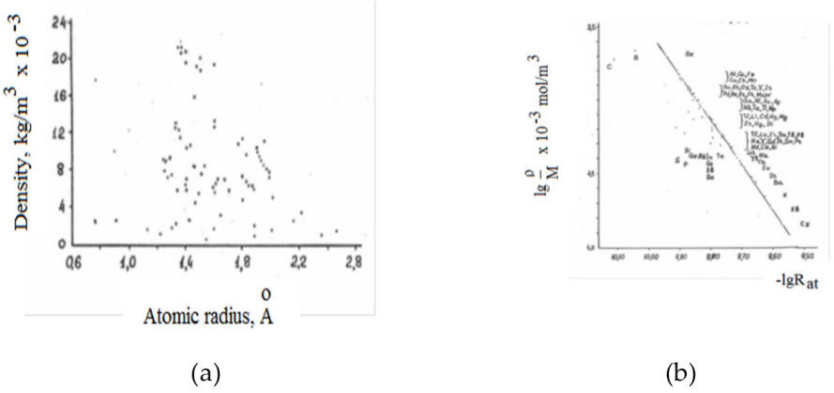

Figure 2. (a)-uncorrelative density ϱ and radius of the atom in crystals of simple solids: metals, semiconductors, dielectrics. Points of gases densities are coinciding with abscissa axes; (b)-correlation between the density of amount of substance σ or ratio ϱ/M_0 of the density to the mole weight and the radius of atom in simple solid. lg ϱ/M=1.65 for all gases under normal conditions.

http://dx.doi.org/10.5772/58935

If we take into account the chemical identity of atoms through the mass of the mole, there is a linear correlation of the amount of substance σ of the small particle from the radius of the atom. For example, the density of the amount σ of any gaseous substances under the same conditions is constant. Therefore, the boundary between the molecule, nanocluster, nanoparticle and a bulk of the given substance can be found according to the nature of the dependence of the density of amount σ_0 of the substance on the radius of atom or molecule. Let's consider a simple example.

The sizes of the atoms are in a periodic dependence on the number of the chemical element in the Periodic system. The density of amount σ_0 of gaseous substance does not depend on the size of atom or molecule. For example, for all gases under normal conditions $lg\sigma_0$ is equal to 1.65. If $lg\sigma_0$ of the gaseous system exceeds this value, one should consider a body consisting of small particles. The more $lg\sigma_0$ differs from 1.65, the smaller particle differs from the molecule. Molecular associates in gases can be an example. The density of small particles in aerosols and gels is higher; the deviation $lg\sigma_0$ from 1.65 will be significant.

3.3.3. Amorhous and dispersive bodies

In extreme cases of aggregation of atoms or molecules the density of small particle can reach the density of solid phase, in particular, of the crystalline phase. When the aggregation of atoms is completed by formation of micro-particles, the formation of a massive body is possible, and Fig. 2a can be considered as an illustration of the mass distribution in amorphous body, which represents the fine system of ultramicroparticles. Chaotic arrangement of points disappears if the value of density of substance in each point of Fig. 2a will be divided by the mass of one mole of atoms. The result is presented in Fig. 2b.

The ordinate in Fig. 2brepresents the logarithm of the density of amount of substance, expressed per mole of molecules/m^3. It is seen that the lowest values of σ have alkaline and alkaline-earth metals; the highest values σ have boron, beryllium and carbon. Other solid substances have intermediate values of the density of amount of substance under specification of their structural elements as formula unit.

The dependence p/M_0-R_{at} for gases can be shown in Fig. 2b by the horizontal line $lg\ p/M_0$=1.65. Points between straight lines for gases and solids can be characterized the structure of small particles: from molecules, nano, nano-particles, small particle to microparticle, bulk liquid and solid body. Table 1 shows values of the density of amount σ for number of simple substances calculated by equation (2). Under calculating σ the structural element of the substance has corresponded to the chemical formula of the compound. In condensed phases the structural element in exceptional cases corresponds to a molecule or atom. The data show that the lowest values of σ have alkaline and alkaline-earth metals; the highest values of σ have boron, beryllium and carbon. It should be noted that the liquid hydrogen has maximum σ. Other solid and liquid substances have intermediate values of the density of the amount of substance under specification of their structural elements as formula unit.

substance	Atom radius R_{at}		Density of the amount of substance σ_0 or mole mass M_0, 10^3 кg/mol	Density of substance ϱ, кg/ m^3
	10^{-10} m	$-lgR_{at}$		
H_2, gas	2.22 / 1.1	9.654 / 9.559	2,0158	0,08987
H_2, liq.	0.3707	10.43	2,0158	708*
He, gas	1.82	9.740	4,0026	0,1785
He, liq.	0.53	10.276	4,0026	126*
N_2, gas	3.22 / 1.5	9.492 / 9.824	28,0134	1,2506
N_2, liq.	0.547	10.262	28,0134	808
Li	1.520	9.823	6,94	534
Cs	2.655	9.576	132,91	1900
Mg	1.599	9.796	24,31	1740
Ba	2.174	9.663	137,34	3760
Al	1.432	9.844	26,98	2699
W	1.371	9.863	183,85	19320
Hg, liq.	1.503	9.823	200,59	13600
Br_2, liq.	1.1415	9.943	159,81	3102
B	0.795	10.10	10,81	2340
Be	1.113	9.953	9,01	1850
C	0.771	10.11	12,01	1880

*Density of substance at boiling point.

Table 1. Values of density and density of amount of substance for some simple matters

According to Fig. 2b and Table 1, the points showing the density of amount of substance of liquids and radii of the atoms are arranged between straight lines for solids and gases. The position of these points allows giving a qualitative characteristic of the structure bodies. So that, liquid bromine and liquid mercury with their structure are similar to solids. In opposite, liquid helium and liquid nitrogen are maximally removed from the line of correlation. Absence of own correlation among them confirms the fact that liquids are the transitional state in condensation of gas to solid. Therefore, one should not expect the existence of a universal equationof state for liquids. These states should be described by special solutions of the equation of state of the real gas and solid body. An example is the equation of van der Waals describing condensation of gas to liquid, and a chain of equations by Bogoliubov-Born-Green-Kirkwood-Yvon (BBGKY) which describes the melting of a solid body.

3.3.4. CrystalsAmorhous and dispersive bodies

The radii of atoms can be associated with periods of their location in the crystal space. In Table 2, for example, the cubic lattice provides relationships between the lattice period *a* and radius of atoms in the dense packing, number Z of atoms in the elemental cell of the crystal.

http://dx.doi.org/10.5772/58935

Lattice type	Atomic radius	Coordination number	Dense packing	Number of atoms in the elemental cell of the crystal
Primitive	$a/2$	6	0.52	1
Volume-centered	$(a\sqrt{3})/4$	8	0.68	2
Face-centered	$(a\sqrt{2})/2$	12	0.74	4

Table 2. Correlation between atoms of the dense packing with parameters of cubic lattices.

There are other relationships for crystals of another syngonies. So that, there is a possibility to move from the dependence of density ϱ to the density of the amount of substance σ as a function of the volume of elemental cell of the crystal V_{cell} and number Z of formula units of substance in the cell.

The upper part of Fig. 3 presents points linking based (picknometry) density p and volume V_{cell} of elemental cells of the crystal determined from x-ray structural analysis data. Each point corresponds to the crystal of certain chemical composition. Chaotic arrangement of points gives place of their correlation, if the density of the crystal will be divided by the mass of the mole of formula units. It is shown in the middle part of Fig. 3. The ratio ϱ/M_0 is the density of a standard amount of substance σ_0 or density of standard amount of crystal substance. It was calculated by the formula (1)

$$\sigma_0=\rho/ M_0.$$

If chemical identity of the crystal was registered by the mass of mole of formula units M_0, the structural identity of the crystal can be taken into account by the number Z of formula units of the substance in the cell of the crystal. Lower part of Fig. 3 shows a linear correlation between the volume of the unit cell and the density of amount of crystalline substance $\sigma=\varrho / (Z M_0)$. It corresponds to the formula

$$V_{cell}= M_0Z / (\varrho N_A),$$

which is known in X-ray structural analysis for calculating Z. The join solution is

$$\sigma= 1 / (V_{cell}N_A),$$

showing that the tangent of the slope of the straight line is numerically equal to the reverse value of the Avogadro number N_A.

Note some features of gradual transition from the density of the crystal p to its relation to molecular weight M_0 and density of amount of crystalline substance $\sigma=\rho / (Z M_0)$.

First, in Fig. 3 the properties correlation (or absence of it) completes within the error of measurement of density of substance about 400 chemical compounds of different classes.

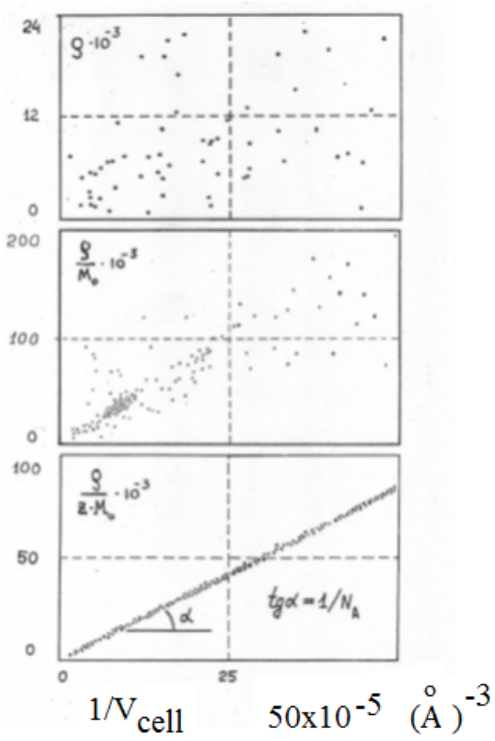

Figure 3. Evolution of correlation between the volume of unit cell of the crystal in series of properties „density – mole mass – number of formula units in the cell of the crystal".

Electrical properties present here conductors, semiconductors and dielectrics. Chemical composition except for simple substances presents here oxides, halides, chalcogenides, oxidocompounds, nitrates, nitrites, sulphates, carbonates, iodates, bromates, chlorates, wolframites, carbides, nitrides, hydrides, hydroxides and other chemical compounds. Optical properties present here transparent and colored crystals, as well as metals. On structural properties here are the crystals of all systems (syngonies). By type of chemical bond here are presented crystals with metallic, ionic and covalent bond, and molecular crystals.

Second, the density of amount of substance $\sigma=\rho / (Z M_0)$ and the volume of the elementary cell was calculated from the experimental data. We used tables of molecular weights of chemical compounds that are defined with sufficient precision, tables of densities found by picknometry method, the cell sizes of the crystals were determined by X-ray structural analysis of crystals.

Third, the tangent of the slope of a line is numerically equal to the inverse value of Avogadro's number N_A. This result obtained in 1997 [43, 44, 51, 52] corresponds to the Resolution XXIV of the General conference on weights and measures (General Conference on Weights and

http://dx.doi.org/10.5772/58935

Measures, 2011), which proposed in the future to determine mol by fixation of the numerical value of the Avogadro constant.

These features allow stating that following expressions for calculation

$$\sigma_0=\rho/ M_0,$$
$$\nu_{m0}= (M_0)^{-1},$$

and the standard density of amount of substance of crystalline σ_0 as well as its specific amount $\nu_{m,0}$ are corresponding each other (Table 3).

Natural or artificial crystal	Density of mass ϱ, kg/m³	Specific density of standard amount of substance ν_{m0}, mole/kg
Cu	8950	15,74
NaCl	2170	17,11
CsCl	3980	5.940
Diamond C	3470*	83,26
Lonsdeylite C	3510	83,26
Double-layer α-graphite (C-2H)	2090*	83,26
Three-layer β-graphite (C-3R)	2090*	83,26
Wurtzite ZnS	4087	10,26
Sphalerite ZnS	4090	10,26
CdJ_2	5670	2,731

* The lowest density of natural diamonds and carbons (graphite)

Table 3. Density of standard amount of substance for some chemical elements and compounds.

Opposite, the calculation expressions

$$\sigma = \varrho/ (Z M_0),$$
$$\nu_m= \nu/ m = (Z M_0)^{-1}$$

correspond to the density σ of real amount of crystal substances and its specific amount ν_m. Table 4 shows comparison of the calculation results σ and ν_m of diamonds, graphite, copper, and other compounds. These crystals are found in nature, and they are grown artificially.

One can see from Tables 3, 4 that specific amount of crystal substances of four carbon structures varies, although one kg of each allotropic form of carbon contains an equal number of atoms. However, a unit mass of a diamond and lonsdeylite, two-layer α-graphite (2H) and three-layer

β-graphite (3R) has a different number of cells. Therefore, the change in the amount of crystalline substances illustrates kinetic difference in polymorphic transformations of carbon (Table 5).

Natural or artificial crystal	Density of mass ϱ, kg/m³	Z	density of amount of crystalline substance	
			Specific density ν_{m0}, mole/kg	Volume density σ, mole/m³
Cu	8950	4	3.935	35220
NaCl	2170	4	4.278	9280
CsCl	3980	1	5.940	26640
Diamond C	3470*	8	10.41	36110
Lonsdeylite C	3510	4	20.82	73050
Bilayer α-graphite (C-2H)	2090*	4	20.82	43500
Trilayer β-graphite (C-3R)	2090*	6	13.88	29000
Wurtzite ZnS	4087	2	5.132	20970
Sphalerite ZnS	4090	4	2,566	10490
CdJ_2	5670	1	2.730	15480

* The lowest density of natural diamonds and graphite

Table 4. Density of amount of crystalline substance of some chemical elements and compounds

Traditional form of writing phase transition	Change $\Delta\nu_0$ of standard amount of substance, mole	Crystal-chemical form of writing phase transition (short)	Change Δν of amount of crystalline substance, mole
Diamond → α-graphite 2H	0	$C_8 \rightarrow 2\,C_4$	2
Diamond → β-graphite 3R	0	$3\,C_8 \rightarrow 4\,C_6$	1
Diamond → lonsdeylite	0	$C_8 \rightarrow 2\,C_4$	2
β-graphite → α-graphite	0	$2C_6 \rightarrow 3C_4$	1
Diamond → C_{gas}	0	$C_8 \rightarrow 8\,C_{gas}$	8
α-graphite → C_{gas}	0	$C_4 \rightarrow 4\,C_{gas}$	4
β-graphite → C_{gas}	0	$C_6 \rightarrow 6\,C_{gas}$	6
Lonsdeylite → C_{gas}	0	$C_4 \rightarrow 4\,C_{gas}$	4

Table 5. Balance of amounts of standard and crystalline substances in polymorphic transformations and sublimation of carbon.

http://dx.doi.org/10.5772/58935

Crystal-chemical formulation of phase transitions of graphite is given in Table 5 in short form. It does not reflect the difference in structures of α-graphite and lonsdeylite if writing ithem as the form C_4. The full form takes into account the number of regular systems of points (the equivalent of locations) in the crystal structures of carbon. So, in 2H cell of double-layer α-graphite four atoms are located at the points of two regular systems. In 3R cell of β-graphite six carbon atoms are arranged on two points of regular systems. Full form of polymorphic transformations in graphite is given in Table 6. Atoms of diamond and lonsdeylite are located on the same system of equivalent points. Therefore, the forms of their entries are given in Tables 5, 6.

Traditional and full crystal-chemical forms of writing phase transitions		Change of specific density of standard amount of substance $\Delta\nu_{m0}$, mole/kg	Change of specific density of amount of crystalline substance $\Delta\nu_m$, mole/kg	Increase of amount of crystalline substance per phase transition, mole/ 0.012 kg
Diamond → α-graphite 2H	$C_8 \rightarrow 2\,C_2C_2$	0	10.41	1/8
Diamond → β-graphite 3R	$3\,C_8 \rightarrow 4\,C_3C_3$	0	3.47	1/24
Diamond → lonsdeylite	$C_8 \rightarrow 2\,C_4$	0	10.41	1/8
β-graphite → α-graphite	$2\,C_3C_3 \rightarrow 3\,C_2C_2$	0	6.94	1/12
Diamond → C_{gas}	$C_8 \rightarrow 8\,C_{gas}$	0	72.9	7/8
α-graphite → C_{gas}	$C_2C_2 \rightarrow 4\,C_{gas}$	0	62.5	3/4
β-graphite → C_{gas}	$C_3C \rightarrow 6\,C_{gas}$	0	69.4	5/6
Lonsdeylite → C_{gas}	$C_4 \rightarrow 4\,C_{gas}$	0	62.5	3/4

Table 6. Change of specific amounts of standard and crystalline substance under polymorphic transformations and sublimation of carbon

Suppose that 0.012 kg of α-graphite 3R turn on the β-graphite 2H. The initial amount of crystalline substances is 1/6 mole, as Z=6, and in 3R cell of β-graphite six carbon atoms are arranged on points of two regular systems. The amount of crystalline substance obtained from the phase transition 3R → 2H, will be ¼ mole, because Z=4, and in 2H cell of α-graphite four atoms are located at the points of two regular systems. So, 0.012 kg of graphite from a form 3R turns into 2H with decrease of crystalline substance 1/4-1/6=1/12 mole. The increase in the amount of crystalline substance for other phase transitions is shown in Table 6.

Suppose now that 0.012 kg of diamond turned into Lonsdeylite. The initial amount of crystalline substances is 1/8 mole, as Z=8, and eight carbon atoms are arranged by points of one regular system. The amount of crystalline substance obtained for the phase transition diamond → lonsdeylite will be 1/8 mole, because four atoms in the cell of lonsdeylite are located on the points of one regular system. Table 5 shows the changes in the amount of crystalline substances in all possible polymorphic transformations of diamond and graphite.

3.3.5. Crystal twinnings

Natural graphite is a cluster of two modifications of carbon 2H and 3R: the content of rhombohedral modifications may reach 30%. Therefore, calculating the specific amount of crystalline substance

$$\nu_m=\nu/ m$$

of the whole crystal requires knowledge of the part of one of the structures. If the part of two-layer packaging of graphite is equal to x, then its mass will be equal xm, and the weight of three-layer packaging of graphite shall be equal to (1-x)m, where m is the mass of the entire crystal. The number n of all cells of graphite is

$$n = N_A[x m /4M_0+ (1-x)m /6M_0],$$

where M_0=0.012 kg/mol. We denote the ratio mN_A/M_0 by symbol n_0. Then the ratio $n_0/n=\beta$ will express the ratio of the number of carbon atoms to the number of all cells of the crystal, and the equation written above can be reduced to $\beta=12 / (2+x)$.

The value of x for mechanical mixtures of pure graphite 2H and 3R is determined by weighing components. If case of clusterization it is necessary to calculate β with knowledge of x which can be determined by the spectrophotometric method, comparing the absorption intensity of UV radiation at wavelengths 219Å and 418Å, the principle of which is described below in the section 6.1. If intensities of these peaks of absorption of UV-radiation in Fig. 8 identified by the symbol h, then the value of x can be calculated from the equation

$$h_1/ h_2=x/(1 -x)$$

Having determined the value of x from the spectral experiment, one can calculate the specific amount of crystalline substance in the cluster of graphite by the formula

$$\nu_m=\nu/ m = (\beta M_0)^{-1}$$

and density of crystalline substance of graphite by the expression

$$\sigma=\nu/ V =\varrho(\beta M_0)^{-1},$$

where ϱ is the density of graphite. Let in Fig. 8 x=0.8. Then the value β of is 12/ (0.8+2)=4.29, and specific quantity of crystal substance of crystal is 1/ (4.29x0.012)=19.44 mol/kg. If the density of graphite is taken to be equal 2090 kg/m^3, then the desired density of the amount of crystalline substance which is to be found for the graphite cluster will be 19,44 x 2090=40640 mol/m^3.

http://dx.doi.org/10.5772/58935

3.3.6. Solid solutions

Mixtures are homogeneous, uniform, multi-component systems that have no separation surface between any parts. The properties of all the parts of such systems are the same. So we can assume that the structural element of the substance of the solution of given composition is the same throughout the volume of solution. Properties of solutions are a function of composition. Consider one of these functions for two cases of specification of the structural elements: formula unit and their number Z in the unit cell of the crystal.

According to formula (2), for one mole of amount of crystalline substance of solid solutions equality is valid:

$$\varrho / M = 1 / \left(v N_A \right), \tag{3}$$

where ϱ is the density of a substance, M is the mass of one mole of a structural element of substance of solid solution, v is a volume of a structural element, N_A is the Avogadro constant. The mass M of the mole of structural elements will be expressed through mass M_0 of mole of formula units of solid solution, and the value of Z which is the number of formula units in structural cell of crystalline material:

$$M = Z M_0 \tag{4}$$

The mass of mole of formula units we express by the sum

$$M_0 = \Sigma M_i N_i, \tag{5}$$

where M_i is a mass of mole of formula unit of i-component of the solution, and N_i is its mole part. Multiply the left and right parts of the solution of equations (3)-(5) by the multiplier M_i N_i. We get ratio

$$Z M_i N_i / (\rho v N_A) = M_i N_i / \Sigma M_i N_i. \tag{6}$$

We denote the left part of this ratio as H/N_A and the right part we denote by k symbol. The value of k is a dimensionless and it corresponds to the fraction of total mass by way of expression of the concentration of a solution. Therefore, the value of H has the same dimensionality [the number of particles/mol] that the Avogadro constant. For i-component of the solution we obtain the expression

$$H_i = k_i N_A. \tag{7}$$

Experimentally determined values of p, v, Z and M_{0i} building the amount H_i, are connected with it by a linear dependence with mass fraction k_i of i-component of solid solution. The relation (7) is interesting because empirical rules of L. Vegard and Rutgers are particular cases of demonstration of the function found above according to (7).

Indeed, L. Wegard had found out an additivity of sizes for the elementary cell of solid solution:

$$a = N_1a_1 + N_2a_2,$$

where N_1 and N_2 are the molar fractions, a_1 and a_2 are any parameters of a cell of pure components or any average interatomic distance. Additivity of the cell volumes is set by the rule of Rutgers, which is written as

$$V = N_1V_1 + N_2V_2,$$

where V, V_1 and V_2 are the molar volumes of solid solution and pure components. However, there are quite common deviations from these rules. Examples are solid solutions of NaCl-KCl [71]. Deviations from the rules of L. Vegard and Rutgers can have alternating nature. An example is solid solution Ni-Al.

It should be noted that the additivity of the parameters of a cell does not mean additivity of the cell volume. The equality (6) allows avoiding this contradiction and using parameters and the volume of the cell of the crystal as an example of simple linear function (7) in systems with deviations from the rules of Vegard and Rutgers.

Dependences of lattice constants and densities of solid solution Ni-Al on the structure are presented in Fig. 4a [38]. Solid solutions Ni-Al crystallize in the structural type of cesium chloride and have region of homogeneity between 45 and 60 at.% nickel. The curve of dependence of the lattice parameter on the composition has a maximum, and density curve has a sharp bend. Such curves indicate that in the region of low concentrations of Nickel we have solid solutions of subtraction: the structure has defects, and a part of places for Nickel atoms remain empty. These voids are statistically distributed throughout the volume of the crystal. Solutions with a Nickel content of more than 50 at.% are normal solutions of substitution, in which the atoms of Nickel are statistically replaced by atoms of aluminium.

Let us transform the diagram "property-structure" in Fig. 4a in the diagram “H-k" of solid solutions Ni-Al as an illustration of the function (7). To do this, we calculate the values of H and k for Nickel. The symbols characterizing its properties will be denoted with footnote index 1. Solid solutions Ni-Al have a cubic cell with a parameter *a*. Therefore, the volume of their structural element is equal to a^3. Then

$$\begin{aligned} H_1 &= Z\, M_1N_1/(\rho a^3), \\ H_2 &= Z\, M_2N_2/(\rho a^3), \\ H_1/H_2 &= M_1N_1/\left(M_2N_2\right) \end{aligned} \qquad (8)$$

The value of the Z of solid solutions of substitution is equal to 2 (body-centered cube), and for solutions of subtraction Z is less than two, even though the cell structure is also a body-centered

http://dx.doi.org/10.5772/58935

cub. Assume Z equal to $4N_1$, as at N_1=0.5 solid solutions of subtraction become normal solid solutions of substitution with Z=2. Values of density of crystals p and lattice parameters *a* of solid solutions remain unchanged.

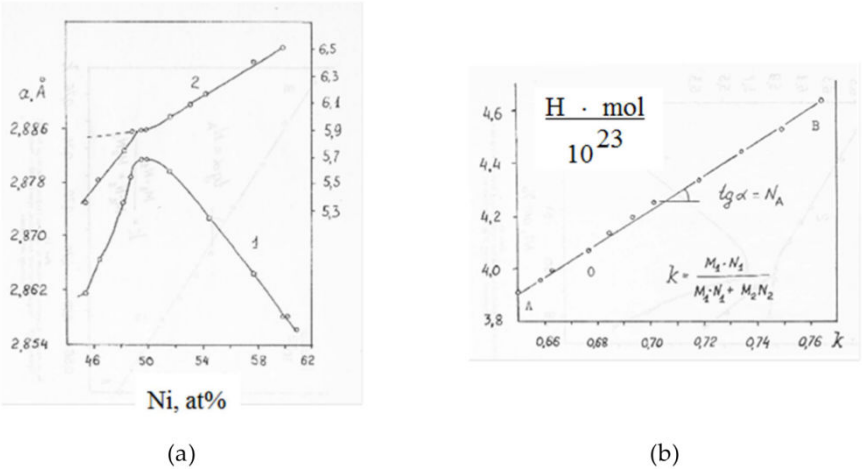

Figure 4. (a)-lattice constant (line 1) and density (line 2) for solid solutions Ni – Al as functions of Ni concentration in at.% [38]; (b)-diagram «H – k» of solid solutions Ni – Al as dependence of the value H_1 on Ni concentration in mass parts of k. Straight line AO corresponds to solid solutions of subtraction, straight line OB corresponds to solid solutions of substitution.

Values k_1 of nickel were calculated according to (6) – (7) by the expression

$$k_1 = M_1N_1/\left(M_1N_1 + M_2N_2 \right), \tag{9}$$

where M_2 and N_2 are the mass of mole of aluminium atoms and its molar fraction in solution. Calculated by formulas (8), (9) the values of k_1, N_1 for Nickel are presented in Table 7. Fig. 4b shows a diagram "H-k" for solid solution Ni-Al, which presents the relation (7) as line AOB. Part of the line AO corresponds to solid solutions of subtraction, the section OB corresponds to solid solutions of substitution.

Now suppose that the atom as formula unit is chosen as a structural element of crystalline substance of solid solution Ni-Al. Then the amount per structural element of the substance of solid solution equals to $a^3/Z=a^3/2$ for solutions of substitution as well as for solutions of subtraction. Symbols of values related to the mole of formula units we denote by lower index 0. To show that the value of H_0, referred to mole of formula units of crystal, has no universality of the values of H_1 found above, we divide both sides of (3) by a molar part Ni of the component. Taking into account the relation (5)

$$M_0=\Sigma M_iN_i,$$

Mole part of Ni, N_1	Mass part of Ni, k_1	Lattice parameter, a/Å	Density of solution ϱ, kg /m³	Number of formula units in the cell, Z	H_1 mol / 10^{23}	H_{01} mol / 10^{23}
0.46	0.650	2.864	5430	1.84	3.895	2.998
0.47	0.659	2.868	5550	1.88	3.962	3.008
0.48	0.668	2.873	5700	1.92	4.002	2.998
0.49	0.676	2.880	5900	2	4.081	2.957
0.50	0.685	2.882	5920	2	4.142	3.023
0.51	0.694	2.881	5960	2	4.201	3.089
0.52	0.702	2.879	6000	2	4.264	3.158
0.54	0.719	2.875	6140	2	4.345	3.265
0.56	0.735	2.869	6250	2	4.454	3.395
0.58	0.750	2.864	6400	2	4.529	3.501
0.60	0.765	2.858	6500	2	4.642	3.639

Table 7. Structure parameters of solid solution Ni – Al [38] and values of k_i, H_1 for Ni calculated according to (8), (9).

we obtain the following expression for mole parts of Ni or Al:

$$\begin{aligned} H_{01} &= N_1\left(M_1N_1 + M_2N_2 \right) / (\rho v) = N_1N_A, \\ H_{02} &= N_2\left(M_1N_1 + M_2N_2 \right) / (\rho v) = N_2N_A, \\ H_{01} &= H_{02}\left(N_1 / N_2\right) \end{aligned} \tag{10}$$

Denoting left parts of equations as H_{0i}, we reduce it to a general form

$$H_{0i} = N_iN_A, \tag{11}$$

Which formally coincides with (7), but with different form of expressing the concentration: the mole fraction N instead of the mass part k, i.e.

$$H_i / H_{0i} = k_i / N_i.$$

Values H_{01} for Ni are calculated according to the expression

$$H_{01} = N_1\left(M_{01}N_1 + M_{02}N_2 \right) / \left(\rho a^3/2\right) = N_1N_A, \tag{12}$$

http://dx.doi.org/10.5772/58935

they are presented in table. 7. Fig. 5 shows that diagram "H_{01}-N_1" in region of homogeneity of solid solutions Ni-Al represents two curves instead of one curve; these two curves are broken on the border of two types of solid solution. The line has a tangent of slope angle $6x10^{23}$ close to the numerical value of Avogadro constant. Thus, equation (11) is valid only for the region of solid solutions of substitution with some deviation, value H_{01} of solid solutions of subtraction does not depend on the concentration.

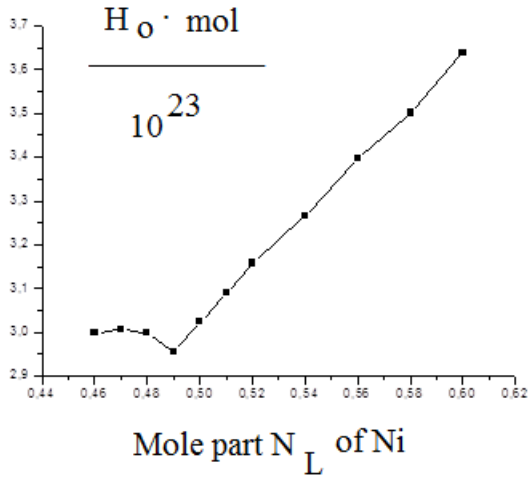

Figure 5. Dependence of the value H_0 on the mole part Ni for solid solutions Ni – Al. Horizontal line corresponds to solid solutions of subtraction, the slope line corresponds to solid solutions of substitution. Structural element of crystalline substance is specified as atom of Ni or Al.

Comparing Figs. 7, 8 and 9 shows the three representations of the experimental data on density and parameters of a crystal cell. Two of them are based on the idea of a structural element of the crystal in the form of formula unit. In this case it is an atom of Nickel or aluminium. Curves have maximum, break and other geometrical features. A third way to view ρ and a of crystals of solid solutions is based on the specification of the structural element of crystalline substance in the form of elementary cell. In this case, there is a linear function $H_{i\ of}$ chemical composition for the whole range of homogeneity of solid solutions regardless of the type of structure and its defectiveness. Compactness, simplicity and universality of diagram presentation of the experimental data on density and the crystal unit cell parameters in dependence on mass fraction show its advantage over other methods of presentation of the concentrations of solid solutions.

The value H has dimension [the number of particles/mol]. When the mass of solid solutions remains constant, the value of H indicates a change in the number of crystalline substance of solid solutions with concentration. The range of homogeneity and cell parameters of solid solutions depend on temperature and pressure. Therefore, the amount of crystalline substance of solid solutions is also dependent on temperature and pressure.

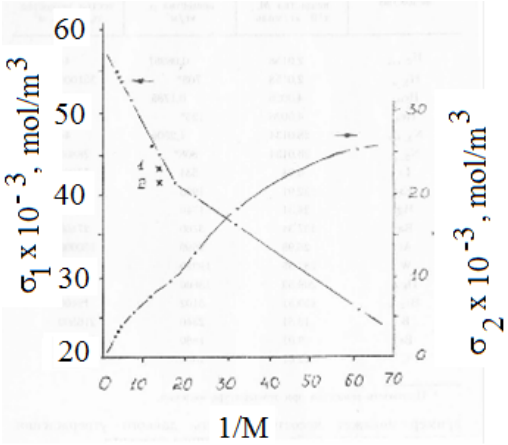

Figure 6. A change of density of amount of matter in series of liquid alkanes from methane to eicosane as a function of reciprocal mass of mole of molecules. The lower curve corresponds to the specification of the structural element of a liquid substance in the form of molecule, straight lines and points 1, 2 correspond to the specification in form of groups of hydrogen atoms with one atom of carbon.

3.3.7. Liquid alcanes

We calculate the density of a standard amount of substance in a series of liquid alkanes from methane to eicosane by the formula

$$\sigma_0 = \varrho / M_0$$

where ϱ is the density of the fluid, M_0 is the mass of the mole of molecules. The dependence of the density of the amount of liquid alkanes on chemical composition is presented in Fig. 6 as a function σ_0 from the reciprocal mass of mole of molecules M_0. It is seen that σ_0 decreases in a series of alkanes from methane to eicosane, and the nonlinearity of the function is explained by the different densities of alkanes, which depends on the length of the carbon chain of the molecule and hydrogen environment of the carbon atom.

Remember that on the Butlerov's theory properties of organic compounds are sufficiently determined by the number and spatial position of carbon atoms in the chain of the molecule. So we give up on the structural element of liquid alkanes in the form of molecules and choose the structural element of a liquid substance in a series of alkanes in the form of groups of hydrogen atoms with one atom of carbon. In this case, the density of the amount of substance must be calculated by the formula

$$\sigma_n = n\varrho / M_0,$$

where n is the number of carbon atoms in the molecule. Function σ n-1/ M_0 is also presented in Fig. 6. In this case this function is linear and is explained by features of building a carbon

http://dx.doi.org/10.5772/58935

chain of alkanes molecules. The fracture of the line can be explained by the different amount of hydrogen associated with the given carbon atom. Indeed, among methane and butane prevails group CH_3 (bottom line), in the rest of alkanes prevails the group CH_2 (upper line). As

$$\nu_0/\sigma_0=\nu_n/\sigma_n= V,$$

the different volumes of atomic groups explain various slope of straight lines in Fig. 6.

In a series of molecules of isoalkanes one can choose groups S, CH, CH_2 and CH_3. The value σ of normal pentane C_5H_{12} or

$$CH_3– CH_2– CH_2– CH_2– CH_3$$

corresponds to the top line in Fig. 6, as in its molecule the group CH_2 dominates. The value σ of isopentane (CH_3) CH_2CH belongs to the bottom line (point 1), as in its molecule the group CH_3 is predominant. The value σ of neopentane $(CH_3)_4C$ does not belong to these lines (point 2), as in the molecule, one carbon atom is not bound with hydrogen. As pentane isomers with equal chemical composition have a different density of amount of substance, the phenomenon of isomerism is characterized not only by different geometry of molecules, but a different amount of substance. Kinetic equations of chemical reactions are determined by the number of reacting substances. Therefore, the characteristics of the reaction of pentane isomers can be described with the values of the density of the amount of substance in the kinetic equation.

3.4. Summary

The diversity of the aggregate state and structural bodies are shown in the diagrams called "state diagrams" for one-, two-, and three-component systems. Phase boundaries are depicted graphically in the coordinates of temperature and pressure, temperature and composition. We have shown above that the intersection of the phase boundaries is accompanied by changes in the amount of substance under given mass of this substance. Therefore, the authors of this Chapter argue that *the amount of substance is a function of temperature, pressure and composition.*

Presented here and previously received the knowledge of the amount of substance [42, 43, 51] corresponds to the resolution of XXIV the General conference on weights and measures, which proposes in future to link determinations of theamount and mass of the substance [22].

4. The nanovoid of an ideal crystal

This section shows that crystallographic nanovoids, which are not defects of the crystal structure, may be limited to atom filling. It is suggested that we consider coordination polyhedra as simple forms or consider their combinations. The relation between the multiplicity, the number of regular point systems, the coordination number, and the number of

formula units per unit cell is obtained in the form of algebraic equations. On the basis of these equations, it has been shown that for all 14 Bravais lattices there are 146 corresponding coordination spheres with an arrangement of atoms inside these spheres that is consistent with both space and point groups of symmetry. The shapes of the coordination polyhedra inscribed into these spheres correspond (with due regard for the vertex occupancies) to 146 crystallographic types for 47 simple forms.

4.1. Atom and Nanovoids in the polyhedron model of an ideal crystal

The idea of providing the coordination polyhedron in a crystal belongs to L. Pauling. N. V. Belov identified more complex and less symmetric forms of coordination polyhedra than the octahedron and the tetrahedron. As a further development of the polyhedron method of presentation for the crystal, one can consider the idea of the image of the coordination polyhedron combinations of simple forms [45] because through these combinations it is possible to explain the role of voids in the polyhedral models of crystal structures.

Using examples of the structures of periclase, sphalerite, wurtzite, fluorite, rutile, anatase, brookite, nickeline, barite, stannum, hydrargyrum, copper, and magnesium the following regularity is found:

- if the forms of nanovoids correspond to the class of symmetry of the crystal, they are becoming the uninhabited vertices of simple forms that construct the coordination polyhedron and the nanovoids have coordination vacancies;
- if the forms of nanovoids do not correspond to the class of symmetry of the crystal, the vertices and faces of the coordination simple form are settled and the nanovoids have no coordination vacancies.

So, the concept regarding coordination vacancies that are unpopulated vertices and the faces of coordination simple forms is formulated. Coordination vacancy may coincide with the host lattice or it can be in the interstitial space. In the first case, the filling or the formation of coordination vacancies leads ultimately to a change in the symmetry of the structure. As an example, we can look at the structural transition in the system Ni-As. In the second case, coordination vacancies can be populated with impurity atoms (diamond) or extra electrons of π-bound (graphite) and unattributed electron pairs (litharge).

4.2. Crystallochemical vacancy in the nanovoid of an ideal crystal

One of the most important properties of a crystal is the coordination of the constituent atoms. The coordination polyhedron in a crystal was isolated for the first time by [58]. Then the method of coordination polyhedra was successfully developed by [3]. The coordination of atoms in crystals was also considered in recent publications by Urusov, O'Keeffe, Parthe, and Grekov [26, 55, 57, 71]. The present study is developed toward the establishment of the relation between the number (Z) of the formula units per unit cell of the crystal and the coordination number (c.n.). As far as we know, there are no other publications addressing this particular topic.

The number Z of the formula units per unit cell of a real crystal is usually determined by the formula

http://dx.doi.org/10.5772/58935

$$Z = V_{cell} \rho N_A / M_0,$$

where V_{cell} is the cell volume unit, ρ is the measured density, N_A is the Avogadro constant, and M_0 is the molar weight. The value of Z for an ideal crystal can also be calculated without this formula by invoking the concept of a regular point system. With this aim, we denote the total number of atoms in the unit cell with P, the number of regular point systems with n, and the multiplicity of an regular point system with k. According to the [69], we obtain the dependence of the form

$$Z = (q+1)s(p_i)^{-1}\Sigma_n(1/S_i) \ / \Sigma_m(1/S_i^*). \tag{13}$$

where q is the number of additional translations equal to unity for A, B, C, and I cells. S_i is the factor that characterizes the symmetry of the position in regular point system. The symmetry factor S_i is a numerical indicator of the position symmetry that indicates the order of the point group for the special position [75]. S_i^* is the symmetry factor of the subgroup characterizing the position of a face of the particular simple form in the point group, which, in turn, characterizes the symmetry of the simple form itself. Here s is the number of the faces of several simple forms (see in detail in [45]. The characteristics of the space and point groups are borrowed from [27] and the description of the structure is borrowed from [8, 39, 59].

In particular, Eq. (13) establishes the relation between the number of the formula units in the unit cell of a crystal and the number of faces of the coordination polyhedron. The relation between the convex coordination polyhedron and the coordination number is described by the Euler-Descartes formula [39] in the following form

$$s + v = e + 2, \tag{14}$$

where s and e are the number of faces and edges of the coordination polyhedron, respectively. The number of the coordination-polyhedron vertices is denoted by v and is equal to the coordination number if all the vertices are occupied by atoms. Relationship (14) is invalid for monohedra and pinacoids that are characterized by s=1 and s=2, respectively. Their faces may have one or several regular point system positions forming various figures.

The separation of coordination polyhedra and the determination of the coordination numbers of atoms is not always unique. The simplicity and clear representation of these concepts for cubic structures is partly lost for more complicated structures with low symmetry. For more details see e.g. [8, 71]. Here, we should like to note only that the coordination polyhedra do not necessarily look like simple forms or their combinations. In this case, some vertices may be unoccupied and can be considered crystallochemical vacancies with occupancy δ. Therefore Eq. (14) takes the form

$$s + c.n./\delta = e + 2.$$

The reduction of the coordination polyhedra to simple forms or their combinations is similar to a certain normalization procedure leading to self-consistent coordination numbers and is somewhat analogous to the representation of a crystal structure by Bravais lattices or their combinations.

4.3. The atom and nanovoid as two entities of an antenna processin a crystal

Thus, the action of the photon antenna in the crystal may be considered a reversible movement of the particle from its equilibrium position (for example, the lattice's site) into a nanovoid, and this nanovoid is forbidden from being steadily filled in by the symmetry of placement of the neighbor particles. This nanovoid pushes out the particle resulting in photon absorption in the initial position. If this cycled process is accompanied by the absorption and radiation of the photon, it may be considered an antenna process.

5. The nanovoid and predissociation of an ideal crystal cell

The sublimation, dissociation, or destruction of a crystal is the process of destroying those chemical bonds that place atomic particles in the space periodically. This section examines the crystal predissociation as a state of its particles that follows after the breaking of the chemical bonds of the crystal cell and directly precedes their scattering. A description of the crystal predissociation is missing in the literature, but it is similar to the predissociation of molecules in gas, which has been studied well enough. In this section, we consider the fragments of an ideal crystal. These fragments are restricted based on the number of atomic particles. The elemental cell of the crystal serves as an example of such a fragment.

5.1. The molecule predissociation in a void

The predissociation of molecules is a non-radiant transition of the excited molecule with a stable electronic state to an unstable one with the same energy, accompanied by the dissociation of the molecule [62]. The phenomenon of the molecule predissociation is explained on the basis of curves of potential energy. They are presented in Fig. 7a.

Under interaction with a photon, the molecule moves from the basic electron state (curve in Fig. 7a) into the excited one (curve 2); here the vibrational motion of the molecule enables the non-radiant transition to the repulsion curve (curve 3), which leads to the dissociation of the molecule. Being in the predissociation state, the molecule dissociates if its full energy exceeds the energy of separated particles that diverge along the potential curve of repulsion. Particles scatter with a kinetic energy

$$\varepsilon_{kin}=\varepsilon_{pr}- D_0 \tag{15}$$

where ε_{pr} is the predissociation energy and D_0 is the energy of molecule dissociation. In the case of a gently sloping repulsion curve, D_0 can have a smaller departure from ε_{pr}. If there is no separation then from Eq. (15) it follows that

$$\varepsilon_{pr}= D_0, \tag{16}$$

because in this case ε_{kin}=0. Therefore, the energy of molecule predissociation, ε_{pr} is a limit for the energy of dissociation, D_0.

http://dx.doi.org/10.5772/58935

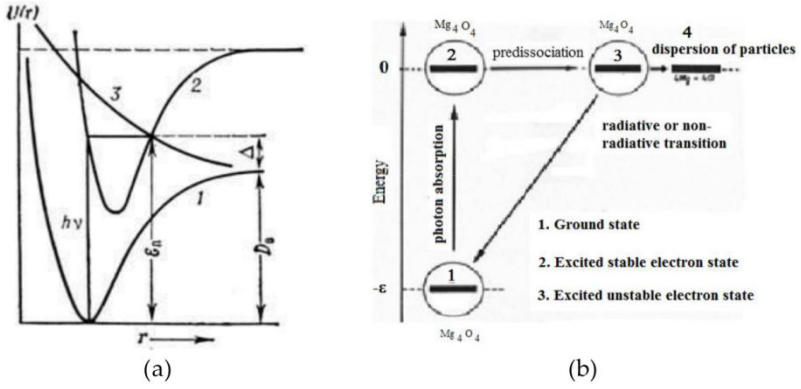

Figure 7. (a)-predissociation scheme under molecule transition to the repulsion curve: 1 and 2 are attraction curves in the basic electronic state and in the excited electronic state, respectively; 3 is the repulsion curve; ε_n and D_0 are energies of predissociation and dissociation, respectively; D is the kinetic energy of the scattered atoms [62]. (b)-Predissociation in the scheme of energy states in the cell of a periclase crystal after the resonance absorption of a photon with energy $Z\Delta H_{subl}/N_A$. The particles are in the sites of the crystal lattice (states 1 and 2); in state 3 the particles are displaced in the nanovoids of the crystalline structure of the crystal as a solid system.

5.2. The photopredissociation in a void of an ideal crystal

According to the Frank-Kondon principle, the transition corresponding to the crossing attraction and repulsion curves is the most probable. From (Fig. 7a) one can suppose that Eq. (17):

$$\varepsilon_{pr}=\varepsilon \tag{17}$$

is correct, where ε is the energy of the absorbed photon. Joining Eq. (16) and (17) we obtain

$$\varepsilon_{pr}= D_0=\varepsilon \tag{18}$$

There are no molecules in ionic and covalent crystals, or in amorphous and liquid solids. However, we can write equations similar to Eq. (16)– (18) for the condensate state of the matter.

In laser technology, the film's solid target is under the action of a powerful radiation flux. If this power is over 10^9 W/m^2, the sublimation of the target occurs. The expression for the kinetic energy of the i-particles can be written by analogy with Eq. (15) in this form:

$$\varepsilon_{kin}=\varepsilon_{pr}- f(D_{subl}, Z),$$

where ε_{pr} is the energy of cell predissociation consisting of Z chemical formula units, giving birth to i-particles, and D_{subl} is the energy of sublimation of a mole of chemical formula units.

When the laser radiation power is less than 10^9 W/m^2, a crystal melts. At still lower radiation capacities, for example, in the spectral experiment, the destruction of the crystal does not take place, i.e. the value ε_{kin}=0. Assume also that

$$\varepsilon = f(D_{subl}, Z, \varepsilon_{pr}),$$

describes the interaction of radiation with the solid in regards to which predissociation states may be realized.

As an example, we consider the cell of periclase (Mg_4O_4), while Z=4. The cell can increase its potential energy through the resonance absorption of a photon with energy ε. Then, according to Fig. 7 we can write

$$\left(Mg_4O_4\right)^0 = \left(Mg_4O_4\right)^* + \varepsilon, \tag{19}$$

where $(Mg_4O_4)^0$ is the basic state of the cell and $(Mg_4O_4)^*$ is an excited state. We can write

$$Mg_4O_4\left(\text{crystal}\right) = 4\ MgO\ \left(\text{quasi-gas}\right) + Z\Delta H_{subl}/N_A, \tag{20}$$

Comparing Eq. (19) and (20) one can acknowledge that if the states

$$(Mg_4O_4)^0 \text{and } Mg_4O_4(\text{crystal})$$

are energetically identical, the predissociation of the crystal cell in Fig. 7 may be presented as a transition

$$(Mg_4O_4)^* \rightarrow 4\ MgO\ (\text{quasi-gas})$$

between energetically identical states if $\varepsilon = Z\Delta H_{subl}/N_A$.

Shown below are the particles filling the crystallographic cells; this process is accompanied by the formation of nanovoids in the space of an ideal crystal. Filling in these nanovoids can damage the cells' symmetry. If the particles can temporarily move into these nanovoids after photon absorption, we have a prerequisite for the particles' predissociation as a stage of the antenna process without any damage to the symmetry of the crystal as a whole.

5.3. The atom and nanovoid as two entities of a crystal

The destruction of the crystal does not take place in the spectral experiment. Assume ε is the absorption photon energy, ε_{pr} is the predissociation energy and D_{subl} is the energy of crystal dissociation. If that is true, then the function

http://dx.doi.org/10.5772/58935

$$\varepsilon = f(D_{subl}, Z, \varepsilon_{pr}),$$

describes the interaction of radiation with the crystal where the predissociation states may be realized (see §4 in this chapter). Value Z in this function makes it possible supposing that the nanovoids between atoms of Z formula units are providing the space necessary for predissociation of particles belonging to the crystal cell. Let's show a role of nanovoids in predissociation of particles using an example of crystals with three diferent structures.

1. As an example, we consider the cell of periclase, Mg_4O_4, while Z=4. The cell can increase its potential energy through the resonance absorption of a photon with energy ε. Then, according to Fig. 7b we can write

$$(Mg_4O_4)^0 = (Mg_4O_4)^* + \varepsilon,$$

where $(Mg_4O_4)^0$ is the basic state of the cell and $(Mg_4O_4)^*$ is an excited state.

The anions of oxygen form cubic close packing [65]. There are octahedral and tetrahedral voids. All the octahedral voids are filled in with cations; all the tetrahedral voids are empty. If four tetrahedral voids are temporarily filled in due to photon excitement, the part of the solid (4MgO) will lose the particles' placement symmetry, and we will write

$$Mg_4O_4(\text{crystal}) = 4\ MgO\ (\text{non-crystal}) + Z\Delta H / N_A,$$

Comparing those states one can acknowledge that if the states

$$(Mg_4O_4)^0 \text{and } Mg_4O_4(\text{crystal})$$

are energetically identical, the predissociation of the crystal cell in Fig. 7b may be presented as a transition of the particle into the nanovoid with the following dispersion in the crystal

$$(Mg_4O_4)^* \rightarrow 4\ MgO\ (\text{non-crystal}) \rightarrow 4\ MgO\ (\text{quasi-gas})$$

between energetically identical states if $\varepsilon = 4\Delta H_{subl}/N_A$. Thus, in Mg_4O_4 cell of magnium oxide crystal there are 2Z=8 tetrahedral voids providing their space to 4 Mg atoms at the moment of pre-dissociation of Mg-O chemical bonds in spectral experiment.

2. As an example we consider the cell of sphalerite, Zn_4S_4, while Z=4. The cell can increase its potential energy through the resonance absorption of a photon with energy ε. Then, according to Fig. 7b we can write

$$\left(Zn_4S_4\right)^0 = \left(Zn_4S_4\right)^* + \varepsilon, \quad (21)$$

where $(Zn_4S_4)^0$ is the basic state of the cell and $(Zn_4S_4)^*$ is an excited state.

Sulfur anions form cubic close packing with tetrahedral voids [65]. Half of them are filled in with zinc cations, while the second half is empty. When four tetrahedral voids are temporarily filled in due to photon excitement, the part of the solid (4ZnS) will lose the particles' placement symmetry, and we will write

$$Zn_4S_4\left(\text{sphalerite}\right) = 4\ ZnS\ \left(\text{non-crystal}\right) + 4\Delta H / N_A, \tag{22}$$

Comparing states (21) and (22), one can acknowledge that if the states

$$(Zn_4S_4)^0 \text{and } Zn_4S_4(\text{crystal})$$

are energetically identical, the predissociation of the crystal cell in Fig. 7b may be presented as a transition

$$(Zn_4S_4)^* \rightarrow 4\ ZnS\ (\text{non-crystal}) \rightarrow 4\ ZnS\ (\text{quasi-gas})$$

between energetically identical states if $\varepsilon=4\Delta H_{subl}/N_A$. So, in the cell Zn_4S_4 of sphalerite there are 2Z=8 tetrahedral voids, half of which is populated by 4 zinc atoms. Remaining 4 voids can provide their space to Zn atoms at the moment of pre-dissociation of no more than 4 chemical bonds Zn-S in spectral experiment.

3. Following this example, we consider the cell of wurtzite, Zn_2S_2, while Z=2. The cell can increase its potential energy through the resonance absorption of a photon with energy ε. Then, according to Fig. 7b we can write

$$(Zn_2S_2)^0 = (Zn_2S_2)^* + \varepsilon,$$

where $(Zn_2S_2)^0$ is the basic state of the cell and $(Zn_2S_2)^*$ is an excited state.

Sulfur anions form cubic close packing with tetrahedral voids [65]. Half of them are filled in with zinc cations, while the second half is empty. When four tetrahedral voids are temporarily filled in due to photon excitement, the part of the solid (4ZnS) will lose the particles' placement symmetry, and we will write

$$(Zn_2S_2)^* \rightarrow 2\ ZnS\ (\text{non-crystal}) \rightarrow 2\ ZnS\ (\text{quasi-gas})$$

between energetically identical states if $\varepsilon=2\Delta H_{subl}/N_A$. Thus, in Zn_2S_2 of wurtzite there 2Z=4 tetrahedral voids half of which is populated by 2 atoms of zinc. Remaining 2 nanovoids can provide their space to Zn atoms at the moment of pre-dissociation of no more than 2 chemical bonds Zn-S in spectral experiment.

http://dx.doi.org/10.5772/58935

These examples of crystal-chemical description of spectral experiment allow explaining that the atom transition from one terahedral void to another is the principal essence of crystal predissociation under photons' action. Suppose that among absorbed photons there are photons which are satisfying the condition $\varepsilon=\varepsilon_{pr}$. Then the original function $\varepsilon=f(D_{subl,} Z, \varepsilon_{pr})$ may be presented as follows:

$$1/\lambda = \text{const} Z \Delta H_{subl}$$

that relates the wavelength λ of the ultraviolet radiation absorbed by the crystal to its sublimation and dissociation enthalpies ΔH [10, 43].

6. Crystal-chemical symbolism and system theory

In the general theory of systems, the category of "emergence" is used as an effective tool for studying natural, economic, and social objects. The system has emergent properties, i.e. properties that are not inherent in its subsystems and modules as well as the ensemble of its elements without system-forming bounds. System properties are not reduced to the sum of the properties of its components. In solid-state physics, the emergence can be expressed as follows: one particle is not a body. For example, the symmetry of the body is not applicable to the individual particle. The photon is a particle that is not subjected to disassembling in elements or subsystems. The system consisting of photons has emergent properties. For example, the photon gas, unlike the unique photon, is characterized by its temperature and entropy. In the solar cell, the photon is one of the components of the system "crystal — radiation". In this chapter, we consider one of the changes in the system emergence as an antenna process. In crystallography and crystal chemistry, the emergence is the appearance of new functional unities of crystal that are not reduced to a simple rearrangement of particles.

In the system classification, the emergence can be the basis of their systematics, representing the criterion feature of the system. Let us consider the single crystal as a set of interrelated atomic particles located in the respective specific order, i.e. as a system, and denote it with **S**. It has emergent properties. For example, a crystal system is characterized by the symmetry of the external shape as well as by the symmetry of the spatial location of atomic particles.

Authors of [9] define the crystal system **S** as a set of individuals belonging to a mineral species that are, in turn, present in the crystalline formations of the atoms of corresponding chemical elements; these sets of atoms can independently exist with further growth.

In crystalline systems, the crystallinity and size limit can serve as the unifying community feature. Work [9] describes the elements of such systems. Their reality makes it possible, for example, to measure the amount of substance in the initial stage of crystallization by the mole of seeds, the number of cosmic dust particles by the mole of dust, the amount of substance in real crystal by the mole of blocks that are broken by line and screw dislocations, nuclear, and other macroscopic defects. The substance of colloidal solutions may be measured by the mole of colloidal particles that they contain. Let us denote such elements with the letter **b**.

In this chapter we will consider the element **b** as a crystal system **S*** and characterize it by the element that corresponds to the symmetry of the crystal. Note that this element is denoted as **a**. In the first approximation, the element **a** is formed in an ideal crystal environment and is defined as a set of atoms of chemical elements; the number of these elements is limited and is equal to the multiplicity of regular point systems. The element **a**, that keeps the chemical composition of the crystal does not exist independently.

In connection with the definition of the element **a**, the special procedure for defining the substance quantity of a crystal consists of disassembling systems **S** and **S*** into new subsystems, i.e. into such systems where the internal laws correspond to the geometric theory of the structure of crystals. Such subsystems are identified by us with the element **a** and are identified as the structural elements of matter (elementary entity).

The practical value of disassembling such crystal systems is that for the first time we have an opportunity to relate the quantitatively geometrical properties of the crystal with the density of the matter and the mass of the atoms, and to describe other characteristics through these features.

This relation is based on the individuality of the ratio value of the regular points systems of crystalline space. That is why the ratio of the amount of element a present in relation to the crystal volume is its characteristic value. This value will be called the "density of substance quantity" with the measurement unit of a mole. It characterizes the number of structural elements of substance in the crystal volume. It is necessary to clarify that the other physical quantity, "density," is characterized not by quantity, but by weight. Therefore, it is obvious that the values of the "density of matter" and the "density of the amount of a substance" differ in terms of their physical nature.

The density of the amount of a substance was introduced into scientific practice only recently in [42] as a derived quantity stated in SI and marked with the letter σ. The unit σ represents the "moles per cubic meter." The crystal as a system is characterized by the ratio of the volume, ν, of the amount of a substance to its volume, V. Therefore, the equations defining and linking it with other physical values are the following:

$$\sigma=\nu/ V =\varrho/ M, \tag{23}$$

where M is the mass of a mole of a structural element of the substance or a structural element **a** of the subsystem **S*** in the system **S**; ρ is the density of matter.

The values σ for gases do not depend on the chemical nature. For example, according to Avogadro's law, σ is a gas under normal conditions equal 44.6 moles of molecules per cubic meter. The values σ for crystals are individualized and are determined by the formula derived from Eq. (23)

$$\sigma=\varrho/ \Sigma^{n}_{i=1} \left(k_i M_i\right), \tag{24}$$

http://dx.doi.org/10.5772/58935

where k_i is the multiplicity of a regular points system for atoms of i-sort; M_i is the mass of moles for atoms of i-sort. For example, the denominator of the ratio (24) for CaF_2 equals

$$4M_{Ca}+ 8M_F,$$

because the multiplicity of the regular points system for calcium atoms equals 4 and for fluorine atoms it equals 8. Taking into account the density of matter, the σ value for CaF_2 equals 10.2 kmol of element **a** in a cubic meter, and the mole of element **a** corresponds to the mole of elementary Bravais cells in the crystal.

In this chapter, we calculated σ values for simple substances and chemical compounds that are crystallizing in differently spaced symmetry groups. The multiplicity of regular points systems may differ from each other under calculation, so that the amount of element **a** in a given crystal system may vary by the number of included atoms. In this case, a unit mass of a substance will contain a different number of elements **a**. In other words, we can say that the phenomenon of polymorphism is a reflection of the state of a unit mass of a crystal with a different number of substances. For example, the multiplicity of a regular points system of carbon-12 in a diamond equals 8 and in graphite it equals 2. Thus, 0.012 kg of carbon-12 corresponds to either an 1/8 mole of diamond or a 1/4 mole of graphite. Let us explain the value of a mole of graphite. There are two sorts of carbon atoms with the same multiplicity of regular points systems in graphite. Thus, the denominator of relation (24) equals

$$2M_{C1}+ M_{C2}= 4M_{graphite}$$

because $M_{C1}=M_{C2}$. The values σ are equal to 36.6 and 47.0 moles of elements **a** in a cubic meter of diamond and graphite, respectively.

The use of a multiplicity of a regular points system in calculations of substance amounts in crystals allows us to reveal completely unexpected correlations in numerous known experimental data. For example, the enthalpy values of gas-crystal phase transitions related to the mole of elements **a** correlate to the wavelengths of the absorption of substances in the ultraviolet region of the electromagnetic spectrum. The description of this correlation is presented in the next section, in which the element **a** of the crystal system is presented through the Bravais cell.

6.1. The photon and the crystal cell as elementary entities of matter

The mole is a unit of measure of an amount of substance, i.e. the number of atoms, molecules, ions, or other elementary entities of a substance (EES). We are adopting a definition of the mole that was presented at the 14th General Conference on Measures and Weights in 1971: "mole is equal to the amount of substance of a system containing in carbon-12 with a mass of 0.012 kg. In application of the mole, the elementary entities must be specified: they may be atoms, molecules, ions, electrons, or other particles or specified groups of particles" [12, 67], IUPC, 1988).

The mole is applied to a gas without any difficulty. In a liquid, the specification of elementary entities often creates difficulties. In the application of the mole to a crystal, we propose specifying the elementary entities in accordance with the basic indicator of a crystal—its three-dimensional periodic structure.

The elementary cell will correspond to such an elementary entity. In this case, the elementary entity will be characterized by the number of formula units Z. For example, the formula of the elementary entity of fluorite is written as Ca_4F_8; Z will be equal to 4. Here it has been shown that the elementary entity corresponding to an elementary cell of the crystal is an object that is capable of absorbing a quantum of energy.

Let us examine this in the example of copper, for which the formula of the elementary entity is written as Cu_4. Through the symbol ΔE we will denote the change in the energy of the crystal upon the dissociation of a mole of Cu_4 into an ideal atomic gas. The value of ΔE can be calculated based on Hess' law:

$$Cu_4(\text{crystal}) \leftrightarrow 4\ Cu\ (\text{gas}).$$

Under isobaric conditions, the heat of this reaction is equal to the enthalpy change ΔH. Then ΔE will be equal to the product of Z and the ΔH of the sublimation of copper:

$$\Delta E = Z\ \Delta H_{subl}$$

For copper at 1 atm and 25^0 C, according to [70], $\Delta E = 4 \cdot 80.7 = 323$ kcal/mol.

Let us assume that one of the mechanisms of radiation absorption by a crystal is resonance absorption by an elementary entity of a quantum of energy, $\varepsilon = \Delta E/N_A$, where N_A is the Avogadro number. After resonance absorption, the transition of the elementary entity from a stable electronic state to an unstable state is possible without any change in energy. Such a transition is called "predissociation." It may also end in the dissociation of an elementary entity.

If the probability of absorption of an energy quantum ε makes it possible for the intensity of absorption to exceed the background level, an individual peak in the absorption spectrum of the crystal, or possibly a shelf, wing, or shoulder on a peak of a different nature can occur. Their positions on the absorption curve can be calculated from the generally known relationship between the wavelength and the energy of the quantum. In the present case, it is written as

$$\lambda = chN_A/\Delta E, \tag{25}$$

where h is the Planck constant and c is the speed of light. For copper, the value of λ is 887 Å. In the absorption spectrum of copper [56], this wavelength corresponds to a shelf in the 885–950 Å interval (Fig. 8).

http://dx.doi.org/10.5772/58935

From this standpoint, let us examine graphite, for which there are two modifications with the number of formula units *Z*: 4 and 6. Calculations of λ are 418 Å for Z=4 and 219 Å for Z=6. Since natural graphite is a concretion of these two modifications, the absorption curve of graphite should have two maximums corresponding to the values of ΔE for these two kinds of elementary entities. In fact, in spectrum [28] there are two such peaks that are not observed on amorphous samples of carbon (see Fig. 8).

Eq. (24) and (25) offer a means for predicting the positions of the absorption peak maximum for another modification of carbon, namely diamond, the structure of which, according to [27, 70], is characterized by a single Z=8 and ΔHatom of atomization 1364 kcal/mol. The maximum of the sought peak should lie in the 210 Å region. This absorption band of diamond has not been investigated [56], but it can be obtained in principle. Germanium and silicon have a structure analogous to that of diamond. The values of λ calculated for these elementary entities, 395 and 331 Å, respectively, practically coincide with the maximum at 395 Å on the germanium absorption curve and the wing at 330 Å for the silicon [56].

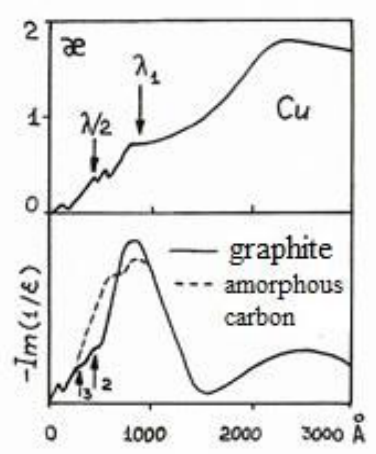

Figure 8. Absorption spectra (the absorptivity to the wavelength) of copper, graphite, and amorphous carbon [28, 56].

7. Metallic nano-cluster open new ways to enhancement of solar cell' efficiency

Novel high ecfective solar devices are based not only on semiconductors (bulk or thin films), but also on nano-scaled clusterized structures. These structures are fabricated using various chemical technologies.

For example, Chen et al. describe synthesis of silver particles on copper substrates using ethanol-based solution (Chen et al., 2014). Previously we have reported success of wet chemical

technology in manufacture of Ag/Co-nanocluster wires forming the contact grid for common silicon-based solar cells with enhanced efficiency [54].

Along with structural and morphological analysis the interpretation of experimental electrical measurements is also of great importance. Basing on our analysis of manufactured solar devices we should note that semi-classical theories widely used for interpreting properties of semiconductor-based devises are not always applicable for end-description of characteristics observed experimentally. In particular, role of semiconductor channel carrier concentration is analysed by [72]. Carrier escape mechanisms can also play a significant role in effective function of solar devices [66].

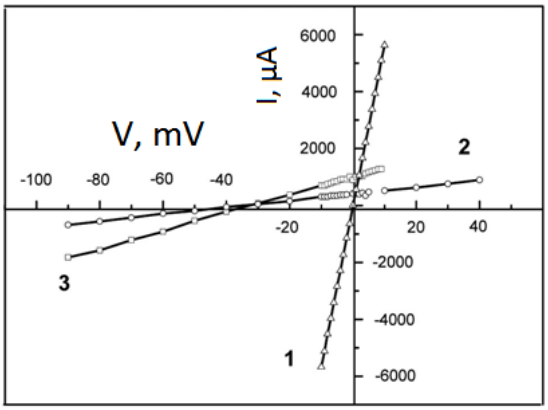

Figure 9. Current–voltage dependences for (1) a contact SGE (Stripe-Geometry Element) made of silver, (2) a contact SGE with copper clusters positioned in the silver pores, and (3) SGE with a copper layer positioned on the surface and with copper clusters positioned in the silver pores.

Current-voltage characteristics are of special importance and interest. Their analysis is helpful for estimation of efficiency limitations in solar cells [29]. Open-circuit voltage and the driving force of charge separation in solar cells based on different junctions are particular features defining efficiency of the device (Hara et al., 2013).

Below we report our experimental results and first attempts to model them.

The experimental setup was described in detail previously [54]. The measurements were performed for two specimens placed in a box with black walls and a solar simulator. The main part of the experimental equipmen was a tungsten contact-needle. Its role is explained below. The experimental results are presented in Figs. 9-10.

As we can see, the curve 1 is the current–voltage dependence for the initial silver contact SGEs (Stripe-Geometry Element) arranged at a wafer surface. Other curves in Fig. 9 are the current–voltage dependences for contacts obtained after copper deposition. All the curves support the metallic conduction of the contact SGEs. The distinction between them resides in the fact that, in the case of contacts with copper clusters, these curves do not pass through the origin for

http://dx.doi.org/10.5772/58935

either the forward current or for the back one. The phenomenon of a current flowing through a metal in the absence of an applied electric field is not outlined in the literature. In our experiment, the luminous current of 450 μA flows along the contact with copper clusters disposed only in silver pores and that of 900 μA flows along the contact with copper clusters disposed in the pores and at the silver surface.

Of fundamental importance is the fact that, in the absence of an applied electric field, the electric current continues to flow along the same samples when a solar simulator was taken out of service. The luminous and dark currents flowing along the contact SGEs are presented in Fig. 10. As can be seen, under the zero bias, in the case of darkness, the generation of charge carriers is kept constant in the duration of the experiment. In the silver contact, the dark current is associated with charge carriers generated in the contact itself. The silver clusters positioned in pores and at the silver surface serve as a source of charge carriers for the dark current.

We should note that various nanoscaled solar devices are proposed for high-effective photon harvesting [40, 74, 76, 77]. Now let us describe our results and first attempts of their numerical simulation.

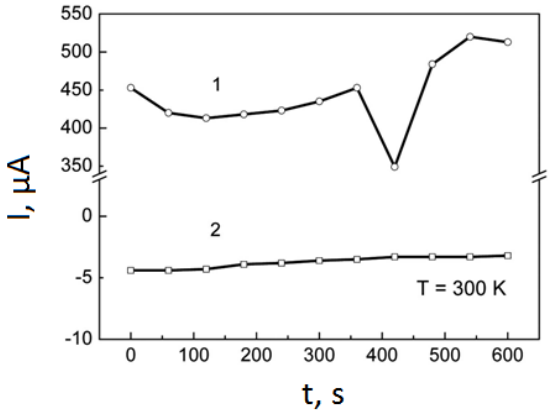

Figure 10. Time dependencies of dark and luminous currents in the absence of applied bias at contact SGEs (Stripe-Geometry Element) with copper clusters positioned in silver pores.

As we have shown previously [53], the first attempting for explanation is to consider a Si-based p-n-junction with Ag/Cu-contacts with different heights of barriers formed at the metal-semiconductor interfaces: $¢_{Beff}=¢_{Bn}+¢_{Bp}$ ~ 0.05 eV (this value characterizes the effective barrier heights for electrons and holes, respectively) [53] and Refs. therein) and, on the other side, the barrier may be formed due to the difference of work functions of the contact metals: $\varphi_B=\varphi_{Cu}-\varphi_{Ag}$=0.17 eV [53] and Refs. therein). Remembering how the solar cell operates (under illumination the device harvests generated carriers and in darkness our active element produces practically no work, therefore, it should be no current!), we tried to calculate possible currents according to the semi-classical theory of semiconductor devices [53] and Refs. therein):

$$I_{Cu} = A_{el} A^{**} T^2 T_{tun} \exp(-e\phi_{Beff} / k_B T) \exp(eV_a / k_B T), \quad (26)$$

where I_{Cu} denotes the current producing by illumination of the sample where Cu-atoms are in Ag-pores and on the surface of the Ag-finger, A_{el} is an electrical area of the contact, A** is the effective Richardson constant, T_{tun} is a coefficient of the barrier tunneling transparency, k_B is the Boltzmann constant, V_a is an applied voltage.

What can we obtain for a dark current, when only the deformation of clusters in the contact stripe due to difference between the lattice constants of silver and copper can change the work function and the barrier height, respectively?

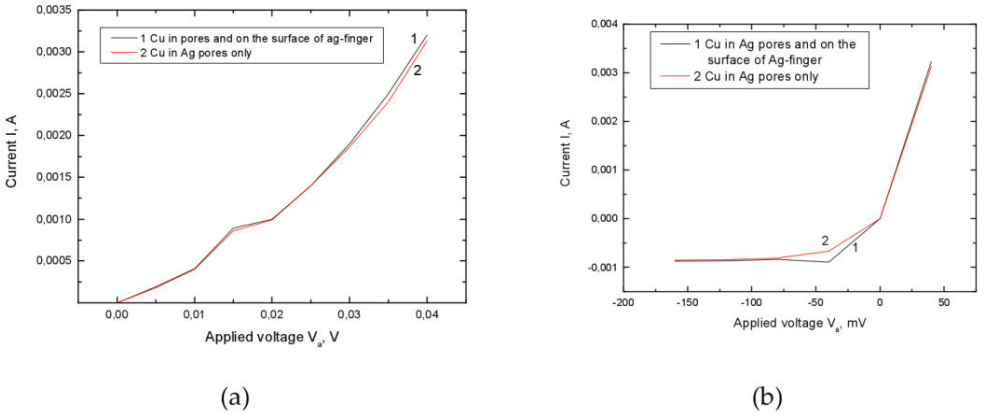

(a) (b)

Figure 11. (a)-current-voltage characteristics (numerical experiment!) of the Cu/Ag-cluster contacts of the Si-based solar cell: the calculation is performed according to the expressions (65)-(66): (a)-"forward" sections of the experimental dependencies, (b)-both sections of the experimental dependencies.

The expression is as follows:

$$I_{Cu1} = A_{el} A^{**} T^2 T_{tun} \exp(-e\phi_{B1f} / k_B T) \exp(eV_a / k_B T), \quad (27)$$

where I_{Cu1} denotes the current observed under illumination of the sample with cu-atom in Ag-pores of the Ag-finger only; we should note that values of the tunneling transparency coefficient are in the range $10^{-7} - 10^{-5}$ (they are determined numerically basing on the experimental data). Fig. 11 show results of the numerical experiment.

As one can see, the numerical experiment performed in the region of very small applied bias (up to 40 mV) produces only a qualitative agreement with the measurements. First, there is no a "solar-cell feature" (calculated IVCs are beginning from zero unlike that of the illuminated solar cells), second, the values of experimental and calculated currents are also different. The semi-classical approximation (we introduced it by using the tunneling transparency coeffi-

http://dx.doi.org/10.5772/58935

cient) does not take into account all features of the conductivity of nanoscaled cluster structures. Before we discuss the further results we would like to say some words about current-voltage dependencies of nanostructures. The overlap energy between different sites is related to the width of the energy bands. The second factor is disorder-induced broadening of the energy levels. If the ratio of these values is small, it is hard to match the width of the energy level on one site with that of a neighboring site to that the allowed energies do not overlap and there is no appreciable conductivity through the sample. On the other hand, if the ratio is large, the energy levels easily overlap and we have bands of allowed energy, so that there are extended wave functions and a large conductance through the sample [53] and Refs. therein).

The current flowing along a silver contact with copper clusters is induced by charge carriers generated in the semiconductor section of the wafer when the solar cell is illuminated. The density of carriers generated within the *p*–*n* junction is two orders of magnitude higher than that which occurred in the copper clusters, because the luminous current is two orders of magnitude larger than the dark one (Fig. 10).

Depositing copper onto silver does not result in the formation of the silver–copper solid solution. The contact between the crystal structures assures the electrical potential difference. The difference is inadequate to generate the charge carriers. However, the contact between the silver–copper crystal structures may result in the compressive deformation of a metallic SGE and in a decrease in the electron work function for copper clusters.

It is our opinion that, in darkness, charge carriers generated by copper clusters within a contact SGE (Stripe-Geometry Element), which is the component part of the solar cell, are governed by the deformation of the SGE [25]. It is known [63] that the deformation of metal cluster structures may also result in high temperature superconductivity. On the other hand, the experimental measurements are made with special needles which are mechanically contacting with the investigated structure. We have to account additional "external" mechanical deformation which, in turn, may cause appearance of additional external electric field without any voltage source. Going back to Chapter 5 of our book [54], see the scenarios about positive and negative pressures!) we should note that this "needle"-caused deformation brings the system "metallic Cu/Ag-cluster contact-Si-semiconductor surface" to the state with different local pressures, for example, negative pressure under the needle on the front side of the structure ($-F_{1el}$) and positive pressure under clusters on the semiconductor surface ($+F_{2el}$). Thus, we have no zero resultant force (F_{1el}-F_{2el}) acting between the electrons localized in the clusters. We suppose that these local pressures are of different values, and the resultant stress is $\sigma=(F_1-F_2)/A_{cluster,}$ where $A_{cluster}$ is a cross-sectional area of the Cu/Ag-cluster. The second possibility to observe the dark current is the effect of nanovoids introduced as the first level of the structural organization of the crystal (see text above) serving as drains and sources for charge carriers. More detailed: the nanovoids play one of principal roles in the processes of pre-dissosiation of atoms building basic semiconductors for photovoltaics: Si, ZnSe, ZnTe, and other wide-gap materials. Experimental current-voltage characteristics of the structures can only be approximately described by different theoretical models, while the charge carriers moving from the left contact to the right one (direct current) and in opposite direction (reverse current) are experiencing not only the barrier effects but they dissipate and exchange their energy in and with nanovoids.

Acknowledgements

Dr. Sc. V. I. Laptev is very grateful to Bokii G. B. and Urusov V. S. and for their interest in this study, useful remarks, discussions, and help, as well as to D. Yu. Pushcharowsky and colleagues from the department of crystal chemistry and crystallography of Lomonosov Moscow State University and to colleagues from the department of general and inorganic chemistry of D. Mendeleev University of chemical technology, Russian Federation.

Dr. H. Khlyap is very grateful to her unforgettable teacher Dr. M. G. Andrukhiv and supervisor Dr. L. V. Bochkariova for their interest in studies, fruitful discussions and help.

Author details

Viktor I. Laptev[1*] and Halyna Khlyap[2]

*Address all correspondence to: viktor.laptev@yahoo.com

1 Russian New University, Moscow, Russia

2 Kaiserslautern University, Kaiserslautern, Germany

References

[1] Artemiev, D.& Fedorov, E.S. (1920). *Das Krystallriech: Tabellen zür krystallochemicher Analyse*, 2 Bande, Petrograd, Russland.

[2] Bakhtin, A.I.; Denisov, I.G. & Lopatin O.N. (1996). *Crystallography Reports*. Vol. 41, № 6, pp. Особенности кристаллохимического строения пророднух оливинов. *Кристаллография.* Т. 41, № 6. С. 1041-1043. *ISSN PRINT: 1063-7745, ISSN ONLINE: 1562-689X*

[3] Belov, N.V. (1947). *Struktura ionnykh kristallov i metallicheskikh faz (Structure of Ionic Crystals and Metal Phases)*; Akad. Nauk SSSR: Moscow.

[4] BIPM. (2011). Bureau International des Poids et Mesures [BIPM], http://www.bipm.org/en/si/new_si/why.html.

[5] Bokii, G.B. (1938). *Dokl. Akad. Nauk SSSR.* Vol. 21, no. 5, p. 244-245.

[6] Bokii, G.B. (1940). Tr. Lab. Crystallogr. *Akad. Nauk SSSR*. No. 2, p. 13.

[7] Bokii, G.B. (1954). *Vvedeniee v Kristasllokhimiyu (Introduction to Crystal Chemistry)*; Mosk. Gos. Univ. Moscow.

[8] Bokii, G.B. & Batzanov, S.S. (1954). К вопросу о понятии «молекула». *Вестник МГУ*, 1954, т. 9, № 5, с.71-74.

[9] Bokii, G.B. (1985). Individuals of mineral species in the framework of the General theory of systems. In: *Metodological problems of crystallography*, pp. 267-273, Nauka: Moscow, Russia.

[10] Bokii, G.B.& Laptev, V.I. (1991). *Zh. Strukt. Khim*. Vol. 32, no. 3, p. 8.

[11] Bragg, W.H. & Bragg W.L. (1916). *Ренгеновские лучи и строение кристаллов*. Пер. с англ. – М.: Космос, 1916, 233 с.

[12] Braslavsky, S.F. & Horek, K.N. Eds. (1987). *Glossary of Terms Used in Photochemistry*, IUPAC Commission on Physicochemical Symbols, Terminology, and Units; Organic Chemistry Division on Photochemistry; Scientific Units and Symbols in Phys. Chemistry; Mills, I., Ed. Oxford: *Blackwell Scientific Publications*.

[13] Castleman, A.W.& Bowen, K.H. (1996). Clusters: Structure, Energetics, and Dynamics of Intermediate States of Matter. *J. Phys. Chem*. 100, 12911-12944.

[14] Chen, L.; Zhang, Z.; Gang, C.; Chunhong, L. & Hui, Z. (2014). *Synthesis of silver particles on copper substrates using ethanol-based ssolution for surface-enhanced Raman spectroscopy*. AIP Advances 4, 031324-1-9.

[15] Fedorov, E.S. (1891). *Zap. Mineral.* O-va. Ser. 2. Vol. 28, p.6.

[16] Fedorov, E.S. (1913). Кристаллы кубической сингонии. Записки Горного института Императрицы Екатерины II. Т. 4. Вып. 4. С. 312-320.

[17] Fedorov, E.S. (1914). Die erste experimentelle Feststellung eines asymmorphen regelmäßigen Punktsystem, *Zeitschrift für krystallographie und mineralogy*, B.54. H 2, s. 163-165.

[18] Fedorov, E.S. (1916). Результаты первой стадии экспериментального исследования структур кристаллов. Известия Императорской Академии Наук. 1916. Сер.6. № 5. С. 359-389.

[19] Fedorov, E.S. (1916a). Основной закон кристаллохии. Известия Императорской Академии Наук. 1916. Сер 6. № 17. С. 435-454.

[20] Fedorov, E.S. (1916b). Новый пример особого структурного изоморфизма. Записки Горного института Императрицы Екатерины II. Т. 6. Вып. 1. С. 65-66.

[21] Fermi, E. (1934). *Molecole e cristalli*, Zanichelli, Bologna: N. Italian. OCLC 19918218.

[22] General Conference on Weights and Measures. (2011). 24th Meeting of the General Conference on Weights and Measures. On the possible future revision of the International System of Units, the SI. Resolution 1.

[23] Goldschmidt, V. (1923—27). *Geochemische Verteilungsgesetze der Elemente*, Bd 1—8, Kristiania.

[24] Goldschmidt, V. (1913-1923) *Atlas der Krystallformen*, 9 books, Verlag Winters, Heidelberg.

[25] Greenwood, M. A. (2007). Solar Cells, Array Films Constructed from Nanotubes, *Photonics Spectra* 41 (9), 114–116.

[26] Grekov, E.E. (1995). *Geologiya. 2 {Programma "Universitety Rossii" [Geology. 2 (The Russian Universities Program)]}*; *Mosk.* Gos. Univ.: Moscow.

[27] Hahn, T., Editor. (1989). *International Tables for Crystallography*; 3rd ed. Vol. A. Kluwer Acad.: Dordrecht.

[28] Hagemann, H.-J.; Gudat, W. & Kunz, C. (1974). Optical Constants from the Far Infrared to the X-ray Region: Mg, Al, Cu, Ag, Au, Bi, C and Al2O3. *DESY-report SR-74/7*.

[29] Hages, S.J.; Carter, N.J.; Agrawal, R. & Unold, T. (2014). Generalized current-voltage analysis and efficiency limitations in non-ideal solar cells: Case of Cu2ZnSn (SxSe1x) and Cu2Zn (SnyGe1y) (SxSe1x)4. J. Appl. Phys. 115, 234504-1-15.

[30] Handbook of optical properties. (1995). Vol.I. Thin Films for optical coating. Edited by R.E.Hummel, P.Wißmann. CRC Press, Boca Raton.

[31] Handbook of optical properties. (1997). Vol.II. Optics of small particles. Edited by R.E.Hummel, K.H.Guenther. CRC Press, Boca Raton.

[32] Hanley, P.L., Kiflawi, I. & Lang, A.R. (1977). *Phill. Trans. R. Soc*, Lond, A.284, p. 329-368.

[33] IUPAC. (1988). *Quantities, Units and Symbols in Physical Chemistry*, Blackwell, London.

[34] IUPAC. (1997). *Compendium of Chemical Terminology*. 2nd Edition.

[35] IUPAC, (1988a). *IUPC Nomenclature of Chemistry; Moscow*. Vol. 6; *Physical Chemistry and Photochemistry.*

[36] Kapustinsky, A.F. (1933). Über das zweite Prinzip der Kristallchemie, *Z. Krist*., v. 86, p. 359 – 369, Russland.

[37] Karapetjanz, M.Ch. (2014). *Методы сравнительного расчета физико-химических свойств*. Изд.2, испр. 2014, 408 с.

[38] Konobeevskii, S.T. (1943). *Уч. Зап. МГУ*, 24, 13.

[39] Kostov, I. (1987). *Kristallografiya (Crystallography)*; 3rd ed. Nauka i Iskustvo: Sofiya.

[40] Kuznetsov, A. S.; Tikhomirov, V. K. ; Shestakov, M. V. & Moshchalkov, V. V. (2013). Ag nanocluster functionalized glasses for efficient photonic conversion in light sources, solar cells and flexible screen monitors. *Nanoscale* 5, 10065–10075.

[41] Lang, A.R. (1979). *Internal Structure- The Properties of Diamond*; Edited by J.E.Field. Academic Press, London, New-York, San-Francisco, p. 434

[42] Laptev, V.I. (1986). About density of amount of substance. Amount of Substance; Moscow. *Dep. VIMI*, № D06732 at 25.03.1986, ser. IM.

[43] Laptev, V.I. (1989). *Kolichestvo veshchestva v gazovykh i nekotorykh kondensirovannykh sredakh (Amount of Substance in Gaseous and Some Condensed Media)*; Moscow.

[44] Laptev, V.I. (1989a). *Kolichestvo veshchestva v gazovykh i nekotorykh kondensirovannykh sredakh (Amount of Substance in Gaseous and Some Condensed Media)*; Moscow. 2nd. ed.

[45] Laptev, V.I. (1995). *Crystallography Reports, vol*. 40, *no*. 5, p. 1. *ISSN PRINT: 1063-7745, ISSN ONLINE: 1562-689X*.

[46] Laptev, V.I. (1995a). Regular point systems and coordination of atoms in some crystals, *Crystallography Reports, vol*. 40, *no*. 5, pp. 713 – 718, *ISSN PRINT: 1063-7745, ISSN ONLINE: 1562-689X*.

[47] Laptev, V.I. & Urusov, V.S. (1995b). Симметрия бинарного кристалла и связь между координационными числами, стехиометрическими коэффициентами и числом формульных единиц. 7-е совещание по кристаллохимии, Петербург.

[48] Laptev, V.I. (1996). Shot-Range Order in Bravais Lattices, *Crystallography Reports, vol*. 41, *no*. 4, pp. 669 – 673, *ISSN PRINT: 1063-7745, ISSN ONLINE: 1562-689X*.

[49] Laptev, V.I. & Bokii, G.B. (1996). Crystallographic Aspect of Selective Absorption and Emission of the Ultraviolet Radiation in MgO Crystals, *Crystallography Reports, vol*. 41, *no*. 2, pp. 287 – 291, *ISSN PRINT: 1063-7745, ISSN ONLINE: 1562-689X*.

[50] Laptev, V.I. & Bokii, G.B. (1996a). Crystallochemical mechanism in the fundamental absorption of MgO Crystal. *Journal of Structural Chemistry, vol*. 37, *no*. 5, pp. 247-251.

[51] Laptev, V.I. (1997). Автореферат докторской диссертации. МХТИ им. *Д.И.*Менделеева, Москва.

[52] Laptev, V.I. (1997a). Кристаллохимическая модель единства структурных, термических, оптических свойств и химического состава бинарных неорганических кристаллов. Докторская диссертация, МХТИ им. *Д.И.*Менделеева, Москва.

[53] Laptev, V. I. & Khlyap, H. (2008). High-effective solar energy conversion: thermodynamics, crystallography and clusters. In: Solar Cell Research Progress (Ed. Josef A. Carson), Nova Science Publishers, New York. Pp. 181-204.

[54] Laptev, V. I. & Khlyap, H. (2014). Technological prerequisires for the energy and raw materials independence of state and corporate economies. Nova Science Publishers, New York. ISBN: 978-1-63117-703-3.

[55] O'Keeffe, M. (1991). *Z Kristallogr*. Vol. 196, no. 1–4, p.21.

[56] Palik, E.D. (1985). *Handbook of Optical Constant of Solid,*. Academic Press, ISBN-10: 0125444206, ISBN-13: 978-0125444200, New York, USA.

[57] Parthe, E. (1990). *Elements of Inorganic Structural Chemistry*. A Course on Selected Topics.

[58] Pauling, L. (1929). The principles determining the structure of complexe ionic crystals, *J. Amer. Chem. Soc*, vol. 51, pp.1010-1026. Print Edition ISSN: 0002-7863, Web Edition ISSN: 1520-5126.

[59] Penkala, T. (1972). *Zarys Krystalochemi*; Panstwowe Wydavnictwo Naukowe. Warszawa.

[60] Petrov, V.I. (1992). Cathodoluminescence Scanning Microscopy, *Phys. Stat. Sol. (a)*, v. 133, p. 189 – 230.

[61] Phillips, J. (1968). *Optical Spectra of Solids in Fundamental Absorption Region* [*Russian translation*]; Mir: Moscow.

[62] Physics Enciklopaedia. (1994). In 5 v. Moscow. Vol. 4.

[63] Pillai, S.; Catchpole, K. R.; Trupke, T. & Green, M. A. (2007). Surface Plasmon Enhanced Silicon Solar Cells, *J. Appl. Phys.* 101 (9), 093105.1–093 105.8.

[64] Rinke,T.J.; Bergmann, R.B.; Brüggemann, R & Werner, J.H. (1999). Ultrathin Quasi-Monocrystalline Silicon Films for Electronic Devices. *Solid State Phenomena*. V.67-68, 229-234.

[65] Schaskolskay, M.P. (1976). *Kristallografiya*. Bisschay Schkola: Moscow.

[66] Sellers, D.G.; Polly, S.; Hubbard, S.M. & Doty, M.F. (2014). Analyzing carrier escape mechanisms in InAs/GaAs quantum-dot p-i-n-junction photovoltaic cells. *Appl. Phys. Lett*. 104, 223903-1-3.

[67] Sena, L.A. (1972). *Units of Physical Quantities and Their Dimensions*; *Mir:* Moscow.

[68] Shafranovskii, I.I. (1957). *Кристаллы минералов*. *Л*енинград, изд-во *Л*ГУ, 222 с.

[69] Shubnikov, A.V. (1922). *Izv. Ross. Akad. Nauk.* Vol. 16, p. 515.

[70] Thermal Constants of Substances. (1999). 8 Volume Set, Vol.7, part IX. V. S. Yungman (Editor), Begel Hous, Inc. And John Wiley and Sons, Inc., ISBN-10: 0471315273, ISBN-13: 978-0471315278, New York, USA.

[71] Urusov, V.S. (1987). *Teoreticheskaya Kristallokhimiya (Theoretical Crystal Chemistry)*; *Mosk. Gos.* Univ: Moscow, p. 276. Теоретическая кристаллохимия. М.: изд-во МГУ, 276 с.

[72] Vagadia, M.; Ravalia, A.; Solanski, P.S.; Pandey, P.; Asokan, K. & Kuberkar, D. G. (2014). *Electrical properties of BaTiO3-based MFIS-heterosructures: Role of semiconductor channel carrier concentration*. AIP Advances 4, 057131-1-8.

[73] Vesnin, J.I. (1994). *Вторичная структура кристаллов*. Новосибирск, 1994, 31 с.

http://dx.doi.org/10.5772/58935

[74] Wang, Qi; Li, Y.; Yan, X.; Rathi, M.; Ropp, M.; Galipeau, D. & Jiang, J. (2008). Organic photovoltaic cells made from sandwich-type rare earth phthalocyaninato double and triple deckers. Appl. Phys. Lett. 93 (7), 073303.1-073303-3.

[75] Zagal'skaya, Yu.G.; Litvinskaya, G.P. & Egorov-Tismenko, Yu.K. . (1983). *Rukovodstvo k Prakticheskim Zanyatiyam po Kristallokhimii (The Guidebook for Practical Studies of Crystal Chemistry)*; Belov, N. V., Ed. *Mosk. Gos. Univ.:* Moscow.

[76] Zatirostami, A. (2011). Analysis Parameters And Waste Output In Nano Structured Solar Cells. Journal of Applied Sciences Research, 7 (11), p. 389.

[77] Zhang, D.; et al. (2013). Al-TiO2 Composite Modified Single-Layer Graphene. Nano-Letters.

Chapter 5

Towards 50% Efficiency in Solar Cells

Luis M. Hernández, Armando Contreras-Solorio, Agustín Enciso, Carlos I. Cabrera, Maykel Courel, James P. Connolly and Julio C. Rimada

Additional information is available at the end of the chapter

http://dx.doi.org/10.5772/59616

1. Introduction

High-efficiency solar cells are of interest to further decrease the cost of solar energy. Conventional solar cells are based on single junction semiconductor structures and its efficiency limit is constrained by the Shockley-Queisser limit [1] to 31%. Among the several concepts for ultra-high-efficiency photovoltaic cells, in this chapter will be presented two: quantum well solar cell and superlattice solar cells.

These approaches consist of a p-i-n solar cell of wider bandgap semiconductor (called barrier or host material) with several very thin layers of another semiconductor of lower bandgap inserted into the intrinsic region, which constitutes multiple quantum well or superlattice system. The photon absorption is then enhanced to lower energies than the bandgap of the host material, adressing one of the fundamental losses of single-junction solar cells, improving the spectral response of the solar cell in the energy region below the absorption edge of host material.

This idea was pioneered by Barnham and Duggan in 1990 [2] when they proposed the quantum well solar cell (QWSC). The superlattice solar cell (SLSC) is a more recent proposal [3], which extends the QWSC concept to the case when tunneling probability of photogenerated carriers of adjacent wells is greatly increased, and the carriers are no longer localized in individual wells. Both approaches are based on the use of nanotechnology, by the exploiting of the quantum effects of the nanostructures presented, therefore the proper understanding and calculation of the quantum effects on the solar cell operation parameters is of crucial importance.

Improving the spectral response of the cell by absorbing low energy photons from the solar spectrum is important in order to obtain extra photocurrent and therefore an increment in the short-circuit current. Nevertheless, a drop in open circuit voltage (V_{OC}) of the device has been observed, due to carrier losses caused by inclusion of lower bandgap material and the interfaces, but this voltage loss could be overcompensated by the increased short-circuit current (I_{SC}) from the quantum wells as has benn demonstrated by Nelson et al[4].

In the quantum well solar cell, as the quantum wells are inserted in the intrinsic region, the built-in electric field of the depletion layer drives to an efficient collection of carriers photo-generated in the wells. Quantum efficiency (QE) modeling showed that escape efficiency from the wells is practically unity[5], leading to an enhanced photo-current. In the case of SLSC, as the spuperlattice is obtained by tuning the quantum well width in order to maximise the tunnel probability between adjacent wells, the carriers are spreaded out through the whole superlattice via continuous minibands [6] and as a consequence obtain high conductivity and delocalisation of photogenerated carriers in the minibands decreasing the recombination. QWSC or SLSC can also be tuned, playing with material structure and compositions, in order to diminish the mistmatch between the incident spectrum and the spectral absorption properties of the device.

GaAs solar cells currently hold the world efficiency record for single-junction solar cells [7], hence the improvement of GaAs based solar cell could be important to enhance solar cell performance. The use of GaAs as host material for the design of a QWSC or SLSC would be, then, the best option. However, lattice mismatch issues place an upper limit on the quantity of quantum wells that can be contained in the intrinsic region before strain relaxation takes place, compromising the open circuit voltage. The first attempts included strained GaAs/InGaAs QWSCs, but they shown not enough quantum well absorption to increase the short-circuit current in order to overcome the loss in the Voc resulting from dislocations [8].

As a solution to the lattice mismatch problem was the insertion of strain-balanced GaAsP/InGaAs quantum wells and barriers into the intrinsic region [9]. The GaAsP/InGaAs strain-balanced quantum well solar cell (SB-QWSC) has shown an impressive performance, achieving 27% conversion efficiency at 320 suns concentration [10]. Furthermore, the SB-QWSC can offer some other advantages if used in a tandem, in the substitution of the current-limited GaAs cell in the design of high-concentration triple-junction cells which potentially could exceed the performance over the conventional metamorphic approach. These include: the absence of dislocations, dark-current dominated by radiative recombination at high incident light concentration, and so the possibility of using radiative recycling to enhance efficiency and the ability to optimize the middle cell absorption edge of the tandem for different spectral conditions.

Another novel material system proposed is the dilute nitride (GaIn)(NAs) lattice matched to GaAs. This compound is obtaining growing interest in recent years due to its very unique physical properties and a wide range of possible device applications. The band gap of GaAs decreases rapidly with the addition of small atomic fractions of nitrogen [11], besides the addition of In to GaNAs does not only provide a lattice matched material to GaAs and also decreases the band gap. A approach, using GaInNAs subcells, has been formulated to enhance the efficiency of existing triple and quadruple junction solar cells [12]. Nonetheless, so far, the poor minority carrier properties and doping issues specific to bulk dilute nitrides have frustrated the success of this approach. A different strategy has been published by Freundlich et al [13], where multiple quantum wells of GaNAs are growth inside the intrinsic region of conventional GaAs p-i-n solar cells. The authors showed a short-circuit current about 25 A/m^2 without anti-reflection coating (ARC) and open circuit voltages approximately 0.6 V, although much smaller than those reported for conventional GaAs solar cells, certainly due to high interface recombination as consequence of the lattice mismatch between GaAs and GaNAs layers.

http://dx.doi.org/10.5772/59616

In this chapter, we examine a general theoretical model for QWSC, which is applied to p-i(QW)-n QWSC of different material systems. Firstly we will apply it to an AlGaAs/GaAs QWSC, and will show that conversion efficiencies are significantly enhanced when compared with the corresponding AlGaAs baseline solar cell. Open circuit voltage, current densities, I-V curves and conversion efficiencies are calculated as function of the well and barrier band gaps, the width and depth of the wells, the number of the wells in the intrinsic region. We will take into account the light absorption by the energy levels in the quantum wells, and we show that for certain values of the studied parameters, the conversion efficiencies of the quantum well solar cell are higher than that of the corresponding homogenous p-i-n solar cell.

This theoretical model when applied to the study of AlGaAs/GaAs SLSC, also allows the determination of performance parameters (short-circuit current density, open-circuit voltage, and conversion efficiency) behavior as a function of absorption and recombination mechanisms. We present a comparative study between AlGaAs/GaAs SLSC and QWSC, which could predict the possible advantages for the use of the SLSC. A variably spaced semiconductor super-lattice was optimized to enhance the resonant tunneling between adjacent wells following the method reported by Reyes-Gómez et al. [14]. A discussion about the conditions where the SLSC performance overcomes that of QWSC is addressed. Our approach will be focused on examining the viability of the SLSC for its possible use and to clarify if they present advantages over QWSC.

Following, the model is then applied to a GaAsP/InGaAs/GaAs SB-QWSC, demostrating that high efficiency devices are feasible. Our model takes into account the influence of the strain over the energy bands of the material. The impact of tensile and compressive strain on the band structure for both conduction band and valence band are calculated in order determine the electron and hole dispersion relation $E(\mathbf{k_B})$. Similarly, the optical transitions in quantum well and barriers as a function of tensile and compressive strain are evaluated to calculate the quantum efficiency, dark current and photo-current and compared with experimental data. The broken degeneracy of the valence band due to the effect of the strain is also studied, which causes the suppression of a transition that contributes to photon emission from the edge of the quantum wells. We study both, the emission light polarized in the plane perpendicular (TM) to the quantum well which couples exclusively to the light hole transition and the emission polarized in the plane of the quantum wells (TE) which couples mainly to the heavy hole transition. It is found that the spontaneous emission rates TM and TE increase when the quantum wells are deeper. The addition of a distributed Bragg reflector can substantially increase the photocurrent while decreasing the radiative recombination current. We examine the impact of the photon recycling effect on SB-QWSC performance. Then, GaAsP/InGaAs/GaAs solar cell is optimized to reach the maximum performance by evaluating the current-voltage curves under illumination. Our model was used to determine the highest efficiencies for cells containing quantum wells under varying degrees of strain, but it could also allow the optimization of the photocurrent or the open circuit voltage in a triple-junction concentrator cell based on a SB-QWSC middle cell.

Another approach, where GaAs/GaInNAs multiple quantum wells and superlattice are added within the intrinsic region of conventional GaAs p-i-n solar cells is also presented. First, the model is applied to GaAs/GaInNAs QWSC in order to study the conversion efficiency as a function of nanostructure parameters as wells width and depth. On the other hand, a variably spaced superlattice structure was designed to enhance the resonant tunneling between adjacent wells after the method reported [3, 14] and J-V characteristic

for this devices is obtained. The effect of the superlattice characteristics on the conversion efficiency is discussed. The SLSC conversion efficiency is compared with the maximum conversion efficiency obtained for the QWSC. Finally, we present GaAs/ GaInNAs SLSC conversion efficiency as a function of solar concentration, showing an clear increment in its performance.

2. Model details

In this section, we will develop the model, starting with the QWSC, whose structure is shown in figure 1. The make use of the common assumptions of homogeneous composition in the doped and intrinsic layers, the depletion approximation in the space-charge region, and total photogenerated carrier collection, assuming an equal carrier temperature in all regions. Transport and Poisson equations were used to compute the quantum efficiency in the charge-neutral layers while the quantum efficiency of the intrinsic region is determined taking into account the absorption coefficient of the nanostructure involved. The overall photocurrent is simply expressed in terms of superposition, adding photocurrent, obtained form the calculated quantum efficiency, to the dark current in order to find out the illuminated current-voltage characteristic.

2.1. Modelling the Quantum Well Solar Cell

The derived current-voltage relationship of a QWSC with N_W wells each of length L_W into the intrinsic region of length W, with barrier band gap Eg_B and well band gap Eg_W is given by equation 1, after [15, 16];

$$J(V) = J_0(1 + r_R\beta)\Big[\exp(\frac{qV}{\mathbf{k_B}T}) - 1\Big] + (\alpha r_{NR} + J_S)\Big[\exp(\frac{qV}{\mathbf{2k_B}T}) - 1\Big] - J_{PH} \tag{1}$$

where q is the electron charge, V is the terminal voltage of the device, $\mathbf{k_B}T$ the thermal energy, $\alpha = qWA_Bn_{iB}$ and $\beta = \frac{qWB_Bn_{iB}^2}{J_0}$ are parameters defined following Anderson [17]. J_0 is the reverse saturation current density; A_B is the nonradiative coefficient for barriers in the depletion region, which is related to barrier non-radiative lifetime τ_B by $A_B = \frac{1}{\tau_B}$; B_B is the radiative recombination coefficient of the host material; n_{iB} is the equilibrium intrinsic carrier concentration for the host material; r_R and r_{NR} are the radiative enhancement ratio and non-radiative enhancement ratio respectively given by the equations 2 and 3.

$$r_R = 1 + f_W\left[\gamma_B\gamma_{DOS}^2\exp\left(\frac{\Delta E - qFz}{\mathbf{k_B}T}\right) - 1\right] \tag{2}$$

$$r_{NR} = 1 + f_W\left[\gamma_A\gamma_{DOS}\exp\left(\frac{\Delta E - qFz}{\mathbf{2k_B}T}\right) - 1\right] \tag{3}$$

Those enhancement ratios represent the fractional increase in radiative and non-radiative recombination in the intrinsic region, due to the influence of quantum wells. In the

http://dx.doi.org/10.5772/59616

equations 2 and 3, $\Delta E = Eg_B - Eg_W$, f_W is the fraction of the intrinsic region volume substituted by the quantum well material, $\gamma_{DOS} = \frac{g_W}{g_B}$ is the density of states enhancement factor, g_W and g_B are the effective density of states for the wells and barriers, and γ_B and γ_A are "oscillator enhancement factor" and "lifetime reduction factor", respectively [17]. The built-in field is denoted by F and z is the position in the wells, so r_R and r_{NR} are position dependent. The photocurrent J_{PH} is calculated from the quantum efficiency of the cell. The p-region and n-region contribution to QE was classically evaluated solving the carrier transport equations at room temperature within the minority carrier and depletion approximations. The quantum efficiency (QE) is calculated by the expression:

$$QE(\lambda) = [1 - R(\lambda)] \exp\left(-\sum_{i=1}^{3} \alpha_i z_i\right) [1 - \exp(-\alpha_B W - N_W \alpha_W^*)] \tag{4}$$

where $R(\lambda)$ is the surface reflectivity of the antireflection layer. The first exponential factor is due to the attenuation of light in the precedent layers to the depletion layer as showed in Figure 1. The layers numbered in Figure 1, are: (1) antireflection coating, (2) emitter and (3) space-charge region of the emitter; α_i is the the absorption coefficient of each layer and z_i its corresponding width, α_B is the absorption coefficient of the bulk barrier material, and α_W^* is the dimensionless quantum well absorption coefficient, used for energies below the barrier band gap.

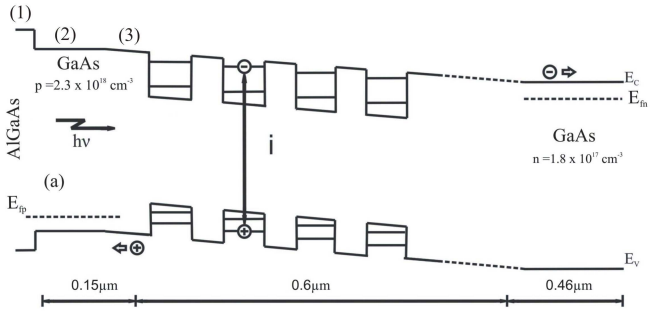

Figure 1. Sketch of energy band diagram of a GaAs p-i-n solar cell with quantum wells inserted within the intrinsic region.

When mixing between light and heavy valence sub-bands is neglected, the absorption coefficient can be calculated as follows[18]

$$\alpha_W^* = \alpha_W \Lambda \tag{5}$$

$$\alpha_W(E) = \sum \alpha_{e_n - hh_m}(E) + \sum \alpha_{e_n - lh_m}(E) \tag{6}$$

where $\sum \alpha_{e_n - hh_m}(E)$ and $\sum \alpha_{e_n - lh_m}(E)$ are sums over well states n and m, which numbers depend on the quantum wells width and depth, $\alpha_{e_n - hh_m}(E)$ and $\alpha_{e_n - lh_m}(E)$ are the absorption coefficients due to electron-heavy hole and electron-light hole transitions to conduction band, respectively; α_W is the well layer absorption coefficient and Λ is called "quantum thickness of the heterostructure" [18].

The exciton absorption is taken into account in the theoretical calculation and exciton binding energies are analytically evaluated in the framework of fractional-dimensional space developed by Mathieu et al [19]. Once the total QE is calculated, by using the AM1.5 incident solar spectrum represented by $F(\lambda)$, the photocurrent is then determined by integration following equation 7:

$$J_{PH} = q \int_{\lambda_1}^{\lambda_2} F(\lambda) QE_{TOTAL}(\lambda) d\lambda \tag{7}$$

where λ_1 and λ_2 are limits of the taken solar spectrum. Then, equation (1) is completely determined and conversion efficiency η can be evaluated.

2.1.1. Including the effect of strain in the nanostructure of QWSC

As mentioned previously, the best host material for a QWSC should be GaAs. However is very difficult to grow high quality quantum wells in a GaAs p-i-n solar cell because there are no high quality, lattice matched materials with a lower band-gap than GaAS. Therefore is required to use strained materials for that goal, but, once a critical thickness of strained material is deposited, it relaxes and causes the formation of misfit dislocations, which serve as centres for non-radiative recombination [20].

The increase in average strain can be limited by including tensile and compressively strained layers alternatively, choosing appropriately alloy composition and layer thickness, and taking into account each elastic constant. This way is possible to obtain structures which are locally strained, but exert no net force on the substrate or neighbouring repeat units. Such strain-balanced structures have demonstrated great photovoltaic performance, and the strain-balanced quantum well solar cell (SB-QWSC) is currently the most efficient QWSC [21].

One of the methods to reach the strain balance condition is the average lattice method [22]. If we considered L_B as the barrier thickness, L_W as the well thickness, and we denote a_B and a_W as the respective well and barrier lattice constants; its defined as:

$$a_{GaAs} \equiv \langle a \rangle = \frac{L_B a_B + L_W a_W}{L_B + L_W} \tag{8}$$

The total strain in the layer may be separated into a hydrostatic component and an axial component. In the case of unstrained bulk material, the heavy hole (hh) and light hole (lh) bands are degenerate at the Brillouin zone centre. The hydrostatic component of strain acts on the band edges changing the band gaps. On the other hand, the axial strain component acts on degeneration of bands. In the valence band, the axial component broken the degeneracy that exists at the band edge (Γ point).

http://dx.doi.org/10.5772/59616

Under compressive strain, the bottom energy of the conduction band is shifted to higher energies and the valence band splits, with the light hole band moving further away from the conduction band than the heavy hole band, suppressing the lh transition [23]. In contrast, under tensile strain the material band gap is reduced and the higher energy valence band is the light hole band.

During strained growth, the lattice constant of the epitaxial layer is forced to be equal to the lattice constant of the substrate. Then, there is an biaxial in-plane strain $\varepsilon_{i,j}$, where i, j = x, y, z. In the case of biaxial strain in (001) plane, the values along [001] direction are $\varepsilon_{xx} = \varepsilon_{yy} \neq \varepsilon_{zz}$. The strain causes changes of the band edges as explained above at Γ point, which are given by [24]:

$$E^{\varepsilon}_{hh} = a_v(2e_{xx} + e_{zz}) - b(e_{xx} - e_{zz}) \tag{9}$$

$$E^{\varepsilon}_{lh} = a_v(2e_{xx} + e_{zz}) + b(e_{xx} - e_{zz}) - b^2\frac{(e_{xx} - e_{zz})^2}{\Delta_{SO}} \tag{10}$$

$$E^{\varepsilon}_{c} = Eg + a_c(\varepsilon_{xx} + \varepsilon_{yy} + \varepsilon_{zz}) \tag{11}$$

where E^{ε}_{hh}, E^{ε}_{lh} and E^{ε}_{c} are the energy level values under strain for heavy holes, light holes and electrons, respectively, Eg is the band gap, a_v and a_c are the hydrostatic deformation potentials, b is the shear deformation potential and Δ_{SO} is the spin-orbit splitting of the valence band at Γ point. The separation of the total hydrostatic deformation potential in conduction (a_c) and valence band (a_v) contributions is important at heterointerfaces.

The band structure dispersion relations for strained InGaAs and GaAsP, are shown in Figure 8. Note that due to strains, the $In_{0.2}Ga_{0.8}As$ layer experiences a band increment of 121 meV, while for $GaAs_{0.7}P_{0.3}$ layer a decrease up to 176 meV is obtained. When the In and P compositions and layer widths are changed, such that the condition given by the definition (8) is satisfied, the strain is changed in the well and barrier layers, causing in both layers a variation in the absorption threshold.

The envelope function approximation is here assumed to determine QW energy levels in the conduction band. The electron energy E_e and wave function ψ_e can be then calculated within effective mass approximation. Then, the shift of the conduction band electron in the QW is described by Schrödinger equation. In order to obtain the QW energy levels in the hh and lh bands under varying compressive strain, a 4×4 $k \cdot p$ Kohn-Luttinger Hamiltonian was used:

$$H^{\varepsilon}_{KL} = H_{KL} + H^{\varepsilon} \tag{12}$$

where H_{KL} is the Kohn-Luttinger Hamiltonian without strain and H^{ε} is the strain Hamiltonian for epilayers grown in [001] direction, which is given by:

$$H^{\varepsilon} = \begin{bmatrix} E^{\varepsilon}_{hh} & 0 & 0 & 0 \\ 0 & E^{\varepsilon}_{lh} & 0 & 0 \\ 0 & 0 & E^{\varepsilon}_{lh} & 0 \\ 0 & 0 & 0 & E^{\varepsilon}_{hh} \end{bmatrix} \tag{13}$$

In a QW system, some splitting of the confined valence band levels takes place due to the differences in effective mass, which can be greatly enhanced if the QW is strained. When the well material is strained we have the confinement effects, but in addition we have the consequences of the non-degenerate bulk band edges. For example under (001) biaxial compressive strain the lh band is shifted further energetically from the conduction band.

In a sense, compressive strain acts in the same way as the effect of confinement. Then, biaxial strain, in well and barriers layers, lifts the degeneracy in the valence band such that it is possible to consider independently the hh and lh bands. Under above approximations, the QW energy levels for hh and lh bands where found. The Schrödinger equation corresponding to Hamiltonian is not separated so it is assumed that the "off-diagonal" terms, which lead to valence band mixing, are small enough that they can be neglected. With this assumption the Schrödinger equation becomes separable:

$$\left[-\frac{h^2}{2m_0}\left(\gamma_1 - 2\gamma_2\right)\frac{d^2}{dz^2} + U(z) + E^{\varepsilon}_{hh} - E_{hh}\right]\Psi^{\uparrow}_{hh}(z) = 0 \tag{14}$$

$$\left[-\frac{h^2}{2m_0}\left(\gamma_1 + 2\gamma_2\right)\frac{d^2}{dz^2} + U(z) + E^{\varepsilon}_{lh} - E_{lh}\right]\Psi^{\uparrow}_{lh}(z) = 0 \tag{15}$$

where $\Psi^{\uparrow}_{hh}$ and $\Psi^{\uparrow}_{lh}$ are the envelope functions with spin direction. The equations (14) and (15) are solved in barrier and well regions with the corresponding $U(z)$ potential and Konh-Luttinger parameter values (γ_1 and γ_2) in each layer. Computed the E_e, E_{hh} and E_{lh} values the optical transitions are calculated by Fermi's golden rule and the equation (7) is evaluated to determine the absorption in the quantum wells. Then, the procedure to calculate the photocurrent is analogous to that described in 2.1.

Compressive strain results in lower thermal occupancy of the *lh* band relative to the *hh* band, and radiative transitions from the conduction to the *hh* band are favored over those to the *lh* band. If the splitting becomes greater than a few $\mathbf{k_B}T$, *lh* transitions could be suppressed almost entirely[23]. In order to examine this behavior, the anisotropic radiative recombination and gain, as consequence of the strain in the quantum wells, is investigated in order to determinate their influence in the SB-QWSC performance.

As a result of the dislocation-free material, the radiative recombination dominates in SB-QWSCs at high current levels bringing the structure close to the radiative limit. This allows the exploitation of radiative photon recycling by means of the growth of distributed Bragg reflectors (DBRs) between the active region and the substrate of the cell, increasing the efficiency of the SB-QWSC.

This observed increase in solar cell efficiency due to DBRs is due to first to the reduction of the dark current via radiative photon recycling, and second to an increase in photocurrent. The first is due to the reflection of radiative emission back into the cell, reducing the net radiative emission and there-fore, the radiative dark current which, as we have seen, dominates in these structures. The second is the product of the reflection of photons back into the cell of photons which would otherwise have been absorbed in the substrate, leading

http://dx.doi.org/10.5772/59616

to decreased photon loss to the substrate, and increasing the photocurrent, equivalent to a net increase in the quantum well absorption.

We will discuss the theoretical background to radiative recombination, gain and photon recycling. The electron and hole quasi-Fermi separation was calculated in order to determine the spontaneous TE and TM emission rate from QW and gain as a function of In composition. Similarly, the optical transitions in quantum well are evaluated to calculate the QW absorption coefficient. Then, we present the results of simulations of the SB-QWSC that it takes account of DBR and anisotropic effects. We calculate quantum and conversion efficiencies and observe an increment in the SB-QWSC performance, particularly under solar concentration.

The radiative recombination current could be suppressed in SB-QWSC devices with deep QWs relative to the prediction of the generalized Planck formula assuming isotropic emission. Following Adams et al [23], emission can be defined as TE, which is polarized in the plane of the QWs, and TM, which is polarized perpendicular to the plane of the QWs. It is therefore possible for TE-polarized light to be emitted either out of the face or the edge of the QWs, whereas TM polarized light can only be emitted out of the edge of the QWs. The *hh* transition couples solely to TE-polarized emission, and the lh band couples predominantly to TM-polarized emission with a minor TE-polarized contribution.

The spontaneous emission rates, R_{spon}, were calculated by ab-initio methods, where the transition from bulk to quantum wells structures was carried out by converting the 3D density of states to the 2D density states. Calculations of TE and TM emission out of the faces and edges of a quantum well include the strain modifications to the spontaneous emission rate resulting from varying the In and P compositions and their layer widths such that the condition given by equation (8) is satisfied.

The emission spectrum from a solar cell depends on the absorption coefficient and the carrier density through the quasi-Fermi-level separation, ΔE_f. To model the emission from either sample at a given generated strain, we first calculated the absorption coefficient using a quantum-mechanical model above mentioned. We assumed that the number of photogenerated carrier pairs is equal to the total emitted photo flux. In the absence of any photon density, the emission rate is the spontaneous emission rate, provided a state $\overrightarrow{k}$ is occupied by an electron and a hole is present in the same state $\overrightarrow{k}$ in the valence band. The rate depends on the occupation probability functions for electrons, f_e, and holes, f_h, with the same $\mathbf{k_B}$-value. The occupation probability function for electrons and holes depends on the corresponding quasi-Fermi level. The spontaneous emission rate expression for quantum well structures is obtained be integration over all possible electronic states

$$R_{spon} = \int d(\hbar\omega) A\hbar\omega \sum_{n,m} \left[\frac{d^2k}{(2\pi)^2} |\hat{a} \cdot \overrightarrow{p}_{if}|^2 \delta \left(E_n^e(\overrightarrow{k}) - E_m^h(\overrightarrow{k}) \right) \times f_e(E_n^e(\overrightarrow{k})) f_h(E_m^h(\overrightarrow{k})) \right] \tag{16}$$

The integral over $d(\hbar\omega)$ is to find the rate for all photon emitted and the integration over d^2k is to get the rate for all the occupied electron and hole subband state. Equation (16) summarizes the discrete energy states of the electrons (index n) and the heavy holes (index

m) in the well. $E_n^e(k')$ and $E_m^h(k')$ denote the QW subbands of the electrons and heavy holes and δ denotes the Dirac delta function. The factor $A = \frac{2q^2 n_r}{m_0^2 c^3 h^2}$ is a material dependent constant, where n_r is the refractive index of the well material. The first term inside the element $|\widehat{a} \cdot \overrightarrow{p}_{if}|$ represents the polarization unit vector, $\widehat{a}$, while the second term represents the momentum matrix element, $\overrightarrow{p}_{if}$. The spontaneous emission rate of the QWs was calculated using the above formula.

In a semiconductor in nonequilibrium condition, the total electron concentration n and the total hole concentration p are described to be the, respectively, electron and hole quasi-Fermi levels. If detailed balance is applied when each photon produces one electron-hole pair and all recombination events produce one photon, the electrons and hole quasi-Fermi levels in the quantum well structure were calculated by solving the following system of equations [28]:

$$n(E_{F_c}) = p(E_{F_h}); \qquad \Delta E_f = E_{F_c} - E_{F_h} \tag{17}$$

Determining ΔE_f is essentially a matter of normalizing the emission spectrum to the generation rate. If detailed balance applies, the number of photogenerated carrier pairs is equal to the total emitted photon flux, and the gain (G) is defined is defined as the number of photogenerated carrier pairs per unit area and time:

$$G = \int_0^\infty \int G(\lambda, z) dz d\lambda = \int_0^\infty L(\hbar\omega) d(\hbar\omega) \tag{18}$$

where $G(\lambda, z)$ is the electron-hole pair generation rate at z depth from the surface in the growth direction and is given by the expression:

$$G(\lambda, z) = [1 - R(\lambda)]\, \alpha(\lambda, z) F(\lambda) \exp\left[- \int_0^z \alpha(\hbar\omega, z') dz' \right] \tag{19}$$

The exponential factor is due to the attenuation of light in the layers between the surface of the cell and the depletion layer. The layers considered in our calculus are antireflection layer, emitter layer, and space-charge region from to the emitter layer (see Figure 7). The emitted flux density $L(\hbar\omega)$, of photons of energy $\hbar\omega$, is given by:

$$L(\hbar\omega) = \frac{2n_r^2}{h^3 c^2} \frac{\alpha(\hbar\omega)(\hbar\omega)}{e^{\frac{\hbar\omega - \Delta E_f}{k_B T}} - 1} \tag{20}$$

At low enough carrier density, where ΔE_f is much smaller than the effective band gap, the Boltzmann approximation is used, and Eq. (20) is simplified, then the dependence on ΔE_f is an explicit function. From Eqs. 18 and 20, we found:

http://dx.doi.org/10.5772/59616

$$\Delta E_f = -\mathbf{k_B} T \ln \left[\frac{1}{G} \int_0^{\infty} \frac{2n_r^2}{(2\pi\hbar)^3 c^2} \alpha(\hbar\omega)(\hbar\omega)^2 \exp - \frac{\hbar\omega}{\mathbf{k_B} T} d(\hbar\omega) \right] \tag{21}$$

The total electron concentration is determined by:

$$n = \int_{E_{W_e}}^{E_{B_e}} g_e^{QW}(E) f_e(E) dE + \int_{E_{B_e}}^{\infty} g_e^{Bulk}(E) f_e(E) dE \tag{22}$$

where E_{W_e} and E_{B_e} are the conduction valence band edge energy for quantum well and barrier material respectively, $g_e^{QW}(E)$ is the electron quantum well density of state and $g_e^{Bulk}(E)$ is the electron bulk density of state in the quantum well material. The calculation of the total hole concentration is analogous. Then the equation system (17) may be solved and the quasi-Fermi level is determined. The spontaneous emission rate from QW region was then calculated according to Eq. (16).

2.2. Modelling the Superlattice Solar Cell

In contrast with a QWSC where the different quantum wells are considered independent and there is no coupling between neighboring quantum wells, in the superlattice solar cell an interaction exist between neighboring wells and the wave function becomes extended over the whole nanostructure. Therefore the discrete levels in isolated quantum wells spread into a miniband, as it can be seen in Figure 2.

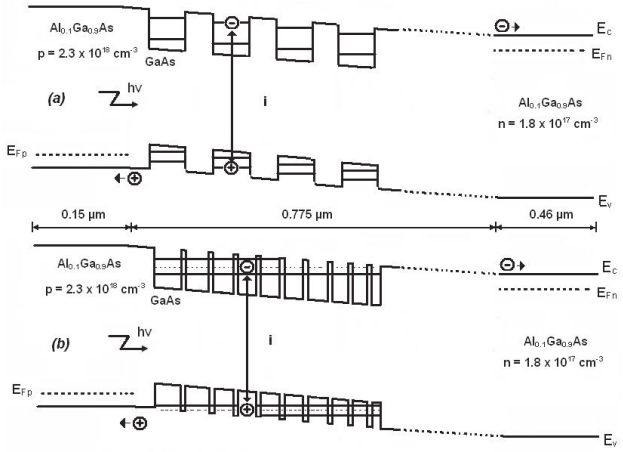

Figure 2. Sketch of energy band diagram of a typical $Al_{0.1}Ga_{0.9}As$ p-i-n solar cell with inserted quantum wells (a) and superlattices (b) in the intrinsic region

In order to achieve the quantum well coupling in the intrinsic region, which is inside an electric field, a variable spaced superlattice is proposed. In this case is necessary that each well width changes in the way that electron levels of the wells are resonant at the operating bias. Then the conditions are fullfilled for resonant tunneling of carriers in the whole nanostructure for a specific value of the electric field, which depends of the doping of the p- and n- regions.

From the theoretical point of view, the advantages of an SLSC over an QWSC are the following: (i) provides quantum levels for electrons and holes within specific eigen-energies (minibands), (ii) improves the miniband photon absorption, (iii) cancels deep-level recombination between single and double heterojunction, (iv) the carriers are able of tunneling along the growth direction through thin barriers while they are essentially free along the transverse direction, and (v) allows an efficient escape rate of carriers out of quantum wells, which are collected in the emitter and base regions [25].

In order to extend the model to the SLSC, the coefficients r_R and r_{NR} (Eqs. (2) and (3)) and the photocurrent J_{PH} should be related to superlattice structure. Now, the f_W factor is the intrinsic region fraction replaced by superlattices, with g_{SL} and g_B as the effective density of states for superlattices and barriers, $\gamma_B = B_{SL}/B_B$ and $\gamma_A = A_{SL}/A_B$ are the radiative and non radiative recombination coefficients referred to superlattices and barriers respectively. The photocurrent is evaluated using absorption coefficients of the transitions of the minibands. The effective density of states for electrons in the superlattice was found [3]:

$$\begin{aligned} g_{SLe} = & \frac{m_e}{\pi\hbar^2 d_{SL}} \int_0^{\Gamma_e} \left(\frac{1}{2} + \frac{1}{2} \arcsin\left(\frac{E - \frac{\Gamma_e}{2}}{\frac{\Gamma_e}{2}} \right) \right) \exp\left(-\frac{E + E_e}{\mathbf{k_B} T} \right) dE \\ & + \frac{m_e}{\pi\hbar^2 d_{SL}} \mathbf{k_B} T \left[\exp\left(-\frac{E_e + \Gamma_e}{\mathbf{k_B} T} \right) - \exp\left(-\frac{\Delta E_c}{\mathbf{k_B} T} \right) \right] \\ & + 2 \left(\frac{2\pi m_e \mathbf{k_B} T}{\hbar^2} \right)^{\frac{3}{2}} \left[2\sqrt{\frac{\Delta E_c}{\pi \mathbf{k_B} T}} \exp\left(-\frac{\Delta E_c}{\mathbf{k_B} T} \right) + erfc\sqrt{\frac{\Delta E_c}{\mathbf{k_B} T}} \right] \end{aligned} \tag{23}$$

where E_e is the electron miniband bottom, $erfc$ is the complementary error function, m_e is the electron effective mass, $\Delta E_c = Q_c(Eg_B - Eg_W)$ is the well depth in the conduction band, Q_c is the band offset factor, d_{SL} is the superlattice period and Γ_e is the miniband width in the conduction band. Analogous expressions are obtained for heavy hole and light hole effective density of states ($g_{SL_{hh}}, g_{SL_{lh}}$). Then the total superlattice effective density of states was calculated as:

$$g_{SL} = \sqrt{g_{SLe}(g_{SL_{hh}} + g_{SL_{lh}})} \tag{24}$$

The absorption coefficient for the transitions between light hole and electron minibands was also determined as a function of their widths, Γ_{lh} and Γ_e which we will use in our model as

http://dx.doi.org/10.5772/59616

a parameter:

$$\alpha_{lh-e}(E) = \frac{q^2}{cm_e^2\varepsilon_0 n_r d_{SL}\hbar^2\omega}|\hat{a}\cdot\overrightarrow{p}_{if}|^2 \times \frac{m_{lh}m_e}{m_{lh}+m_e}\left\{\frac{1}{2}+\frac{1}{\pi}\arcsin\left[\frac{E-Eg_0-\frac{\Gamma_e+\Gamma_{lh}}{2}}{\frac{\Gamma_e+\Gamma_{lh}}{2}}\right]\right\} \quad (25)$$

where $|\hat{a}\cdot\overrightarrow{p}_{if}|$ is the optical matrix element between the initial i and the final f transition states, a is an unit vector in the direction of propagation, p is the momentum, n_r is refraction index of the heterostructure, ε_0 is the vacuum dielectric constant, ω is the angular frequency of radiation, m_{lh} is the light hole effective mass, $Eg_0 = Eg_W + E_e + E_{lh}$ and E_{lh} is the light hole miniband top energy. An analogous expression for the absorption coefficient of the transitions between heavy hole and electron minibands ($\alpha_{hh-e}(E)$) is also found. The total superlattice absorption coefficient can be expressed by:

$$\alpha(E) = \alpha_{lh-e}(E) + \alpha_{hh-e}(E) \quad (26)$$

According to the detailed balance theory, the radiative recombination coefficient is expressed by:

$$B = \frac{8\pi n_r^2}{c^2h^3n_0p_0}\int_{E_1}^{E_2}\frac{\alpha_{SL}E^2dE}{\exp\left(\frac{E}{\mathbf{k_B}T}\right)-1} \quad (27)$$

Now the quantum efficiency the intrinsic region is calculated by the expression 28, considering the absorption of photons through a miniband and not by quantum well levels:

$$QE(\lambda) = [1-R(\lambda)]\exp\left(-\sum_{i=1}^{3}\alpha_i z_i\right)[1-\exp\left(-\alpha_B W - N_{SL}L_{SL}\alpha_{SL}^*\right)] \quad (28)$$

where L_{SL} is the superlattice width. This superlattice could be considered an structural unit and we can repeat several of this superlattice units as much as they fit inside the intrinsic region. So, let's define this superlattice units as a cluster. Then, N_{SL} is the number of clusters or superlattice units that we insert in the intrinsic region of the p-i-n solar cell.

Once the expressions for the effective density of states, the absorption coefficient, the radiative recombination coefficient, and photocurrent were found for SLSC, we are able to determine the J-V characteristic from equation (1) and then it is possible to calculate the conversion efficiency.

3. Results and Discussion

3.1. AlGaAs/GaAs multiple quantum well and superlattice solar cell

As a test of our model, we compare the QE calculated with the experimental values of G951 QWSC sample ($Al_{0.33}Ga_{0.67}As/GaAs$) from the Quantum Photovoltaics Group at Imperial College London [26]. Table 1 displays the pertinent features of several solar cells that were

used to compare our model with experimental parameters. The absorption coefficient of $Al_xGa_{1-x}As$ bulk solar cell was determined from the GaAs spectrum $\alpha(\lambda)$, using the same nonlinear shift of the energy axis reported by M. Paxman et al. [5].

The expressions for the generation of the bulk absorption coefficient and the values of AlGaAs parameters used in the calculation are obtained from reference [15]. The internal quantum efficiency for G951 QWSC is calculated as function of energy and is compared to experimental curve shown in Figure 3, where is shown a good agreement between experimental and modeled spectra. In the calculations only the QWSC growth and material parameters were used, without any fitting parameter. The deconvolved spectra in Figure 3 clearly show that the absorption edge of the QWSC is shifted to lower energies due to the existence of quantum wells in the intrinsic region, and increases the QE values in the short wavelength region and consequently the short-circuit current will increase.

Cell	Cap (μm)	p layer (μm)	p doping (cm^{-3})	n layer (μm)	n doping (cm^{-3})	i layer (μm)	well number	well width (μm)
G946	0.017	0.15	1.3×10^{18}	0.46	1.3×10^{18}	0.51	50	8.5
QT76	0.02	0.3	7.0×10^{17}	0.6	3.0×10^{17}	0.48	30	8.7
G951	0.02	0.15	1.3×10^{18}	0.46	1.3×10^{18}	0.81	50	8.5
QT468A	0.04	0.15	9.0×10^{17}	0.6	2.5×10^{17}	0.48	30	8.4
QT229	0.045	0.5	2.0×10^{18}	0.5	6.0×10^{18}	0.80	50	10.0
QT468B	0.02	0.15	9.0×10^{17}	0.6	2.5×10^{17}	0.48	0	0
CB501	0.02	0.15	9.0×10^{17}	0.6	9.0×10^{17}	0.31	1	5.0

Table 1. Details of cells structures

Good fit between modeled and experimental QE spectra was also observed for all solar cells reported in Table 1. The photocurrent calculated by equation (7) is compared with the experimental values in Table 2 and also show good agreement as the difference between theoretical and experimental values did not exceed 10%.

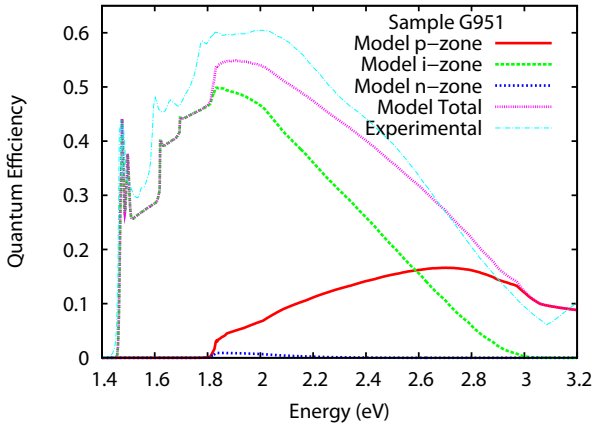

Figure 3. Experimental and modeled IQE for G9551 QWSC. The contributions from p, i, and n layers are separated.

http://dx.doi.org/10.5772/59616

We also compared the calculated open-circuit voltages with experimental shown in table 3 for four QWSCs, showing a good agreement between experimental and calculated values.

The influence of the quantum well width and the barrier band gap energy upon the normalized efficiency η^* is shown in Figure 4. We define the η^* as the ratio between $Al_xGa_{1-x}As/GAs$ QWSC efficiency and baseline p-i-n solar cell efficiency. The best values for η^* are obtained for shallow and wider wells with an efficiency enhancement of about 15%. Increasing the quantum well thickness also increases the normalized efficiency until saturation. For high barrier Al concentration the normalized efficiency grows more quickly with the increase of L_W. The η^* have a maximum value for 15 wells of 15 nm width using $Al_{0.1}Ga_{0.9}As/GaAs$ QWSC, with and approximately 20% of efficiency enhancement between the QWSC and its equivalent baseline cell. On the other hand, the increase of Al composition in the barrier, that means deeper wells, is detrimental for η^*.

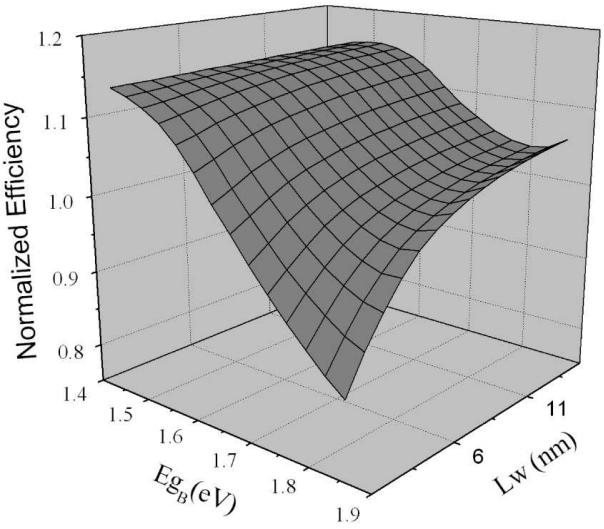

Figure 4. AlGaAs/GaAs QWSC normalized efficiency as a function of the quantum well width and the barrier band gap energy for $N_W = 20$.

On the other hand, the expected high efficiency of the SLSC not only depends on the material and structure quality, ensuring minimum non-radiative recombination losses at the bulk and the interfaces, but it also depends on the escape rate of photogenerated carriers out of the clusters into the n and p-regions having minimum radiative losses within minibands.

We looked for recombination mechanisms in an SLSC and compared them with the same mechanisms in an QWSC. Using Equations (2)-(3) , we calculated radiative enhancement ratio, non-radiative enhancement ratio, and the interface recombination current for the SLSC (Figure 2(b)). These coefficients are function of the effective density of states and the absorption coefficient, which depend on the electron miniband width. Similar calculations were carried out for an QWSC with 15-nm well width and 24 wells in the intrinsic region (Figure 2(a)) where the efficiency reaches a maximum, which is always higher to the

corresponding homogeneous p-i-n cell without quantum wells, as it was shown in a previous study [3].

Sample	Photocurrent (A/m^2)	
	calculated	experimental
G946	87.8	82.2
QT76	76.0	81.5
G951	112.0	132.8
QT468A	76.8	77.0
QT229	18.9	20.6

Table 2. Experimental and calculated photocurrent of AlGaAs QWSCs.

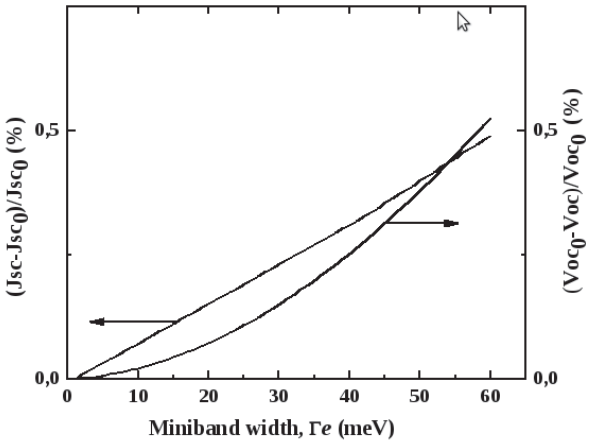

Figure 5. $(Jsc - Jsc_0)/Jsc_0$ and $(Voc_0 - Voc)/Voc_0$ as a function of electron miniband width. Jsc_0 and Voc_0 were calculated for Γe = 1 meV.

In the case of the AlGaAs/GaAs SLSC, the effective density of states and the absorption coefficient were calculated using the AlGaAs parameters reported in Table 2 of reference [15]. The short-circuit current density J_{SC} and the open-circuit voltage V_{OC} were determined using Equation (1) and showed in Figure 5, as a function of the miniband width Γ_e. In this figure, J_{sc_0} and V_{oc_0} were calculated at $\Gamma_e = 1meV$ and it can be observed that an increment in the electron miniband width causes a light increase in the J_{sc_0} and the V_{oc_0} does not decrease significantly. This result suggests that changing the width of the miniband does not influence

Sample	$V_{OC}(V)$	$V_{OC}(V)$
	experiment	theory
QT468A	0.99	0.99
QT229	1.02	0.97
CB501	1.10	1.16
QT468B	1.18	1.28

Table 3. Experimental and calculated open-circuit voltage for three AlGaAs QWSCs.

http://dx.doi.org/10.5772/59616

too much the photon absorption, which could be because solar photon density in that spectral region is not high. The linear dependence of J_{SC} is a confirmation of this assumption. The very small decrease in V_{OC} is a consequence of the weak increment of the interface recombination current with the miniband width.

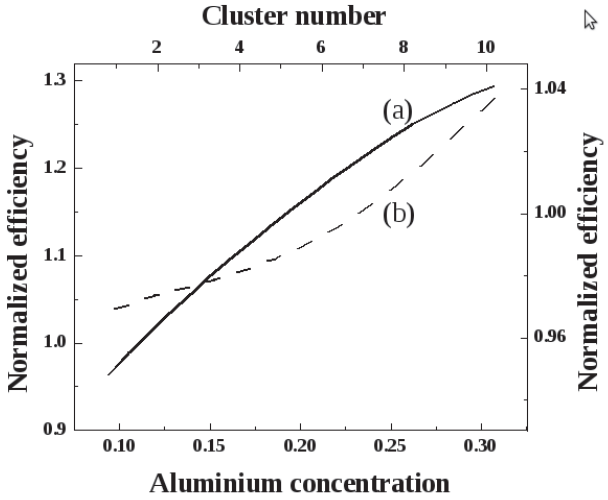

Figure 6. The normalized efficiency versus cluster number (a) and Al composition (b). The normalized efficiency is defined as the ratio between SLCS efficiency and its equivalent QWSC efficiency

If we increase the electric field in the intrinsic region, the number of quantum wells in the superlattice period should be smaller in order to obtain the resonant tunneling conditions. Therefore, a larger amount of cluster should be inserted to enhance the absorption, but then the interfaces and non-radiative recombination will increase. Great reduction of the electric field is not good in the p-i-n solar cells because it requires a low doping level in the p- and n-regions or an increase of the intrinsic region width.

After aplying the model proposed to the case of AlGaAs/GaAs SLSC, it was obtained that the three studied recombination mechanisms show independence with electron miniband width, remaining constant the heavy and light-hole miniband width, 35 and 15 meV, respectively. This is a significant result because the photocurrent could be improved in SLSC, and open-circuit voltage does not change. The values of the SLSC radiative recombination are almost smaller by two orders of magnitude than those obtained for the QWSC.

This result suggests that photogenerated carriers can escape out of the clusters more efficiently in SL structures because transport of carriers is enhanced via tunneling through thin potential barriers. In fact, the electrons in the minibands have high probability of tunneling assisted by electric field, through thin barriers and are recollected in n-AlGaAs region. An advantage of an SL barrier over a bulk barrier is the elimination of deep-level recombination between single and double heterojunctions, therefore, a non-radiative recombination reduction is expected in SLSC. This assumption is supported by our calculations, which show a drop in the non-radiative recombination value. The interface recombination current is greater for SLSC as a consequence that there are more interfaces,

in particular, when 10 clusters of superlattices are inserted in the intrinsic region. Therefore, this mechanism becomes the most relevant for SLSC.

We researched the AlGaAs/GaAs SLSC efficiency, which was compared with the AlGaAs/GaAs QWSC efficiency. Figure 6 illustrates the normalized efficiency versus Aluminium composition and cluster number in the QWSC. The normalized efficiency in this figure is defined as the ratio between the efficiencies of SLSC and its corresponding QWSC for the graph versus Aluminium concentration. In the case of the graph in function of the cluster number the QWSC efficiency in the ratio is the highest. The SLSC efficiency is better than the highest QWSC efficiency for five or more clusters of superlattices in the intrinsic region which meas that under these conditions the photocarrier generation in the SLSC overcome the recombination. However, the best SLSC efficiency is just 4% better than the QWSC efficiency because the increase of SLSC photocurrent does not increase enough. This suggest that the miniband absorption and the absorption of wide quantum wells are comparable. On the other hand, normalized efficiency was plotted versus Al concentration in the QWSC, for 10 clusters in the SLSC intrinsic region, 15 nm well width, and 24 wells in the QWSC intrinsic region and in this case Figure 6 exhibits that SLSC efficiency is always higher than the QWSC efficiency, and become larger as the well barrier height increases. Because of the results that our model predictions are neither compared nor confirmed experimentally, it would be interesting to see if future experiments will corroborate our findings.

3.2. Strain-balanced GaAsP/InGaAs/GaAs SB-QWSC

The SB-QWSC is a GaAs p-i-n solar cell with quantum well layers incorporated into the i-region with InGaAs as well material and GaAsP as barrier material. Figure 7 shows the band-structure of the GaAsP/InGaAs/GaAs SB-QWSC modeled by C. I Cabrera et al. [27].

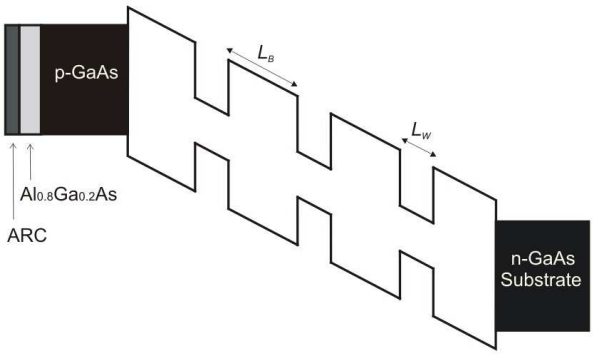

Figure 7. The band-structure of the SB-QWSC. The QW stack is embedded within the depletion zone of the GaAs cell and extends the absorption edge of the cell beyond that of a classical GaAs solar cell.

The compressive strain in the InGaAs QW is matched by tensile strain in GaAsP barriers, overcoming the lattice-mismatch limitation. The GaAsP and InGaAs layer widths were chosen to ensure the average lattice parameter across the i-region was equal to that of GaAs following equation 8, where the barrier material is GaAsP and well material InGaAs.

http://dx.doi.org/10.5772/59616

Elastic constants were considered to evaluate the tensile and compressive strain in GaAsP and InGaAs layers and examine the effect on the band structure of both materials under strain. Consequently, when the In an P compositions are varied, the strains in the barrier and well layers modify absorption threshold in both layers.

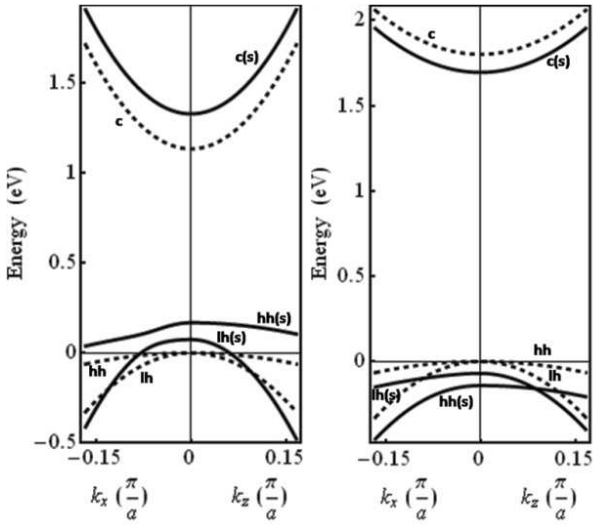

Figure 8. Representation of the effect of strain on band structure of $In_{0.2}Ga_{0.8}As$ and $GaAs_{0.7}P_{0.3}$ around of the first Brillouin zone center compared with unstrained bulk material (dashed line) which is degenerate degenerate at the zone centre for valence band. $c(s)$ is the strained conduction bands, $lh(s)$ and $hh(s)$ are the strained light and heavy hole bands, respectively (straight lines). The vertical axes give the energy in eV, the lateral axes give the wave number k_x and k_z, respectively. (a) Shift and deformation of $In_{0.2}Ga_{0.8}As$ energy bands for compressive strain, $\varepsilon_{xx} = -0.014$, $\varepsilon_{zz} = 0.013$, (b) of $GaAs_{0.7}P_{0.3}$ energy bands for tensile strain, $\varepsilon_{xx} = 0.019$; $\varepsilon_{zz} = -0.010$.

The p- and n- regions were designed with 200 and 500 nm width respectively, with a 40 nm $Al_{0.8}Ga_{0.2}As$ window layer before the p-region to reduce front surface recombination, with a MgF: SiN layerfor anti-reflective coating (ARC) of 70 nm width. The electron and hole concentrations are $n = 10^{18}cm^{-3}$ and $p = 10^{18}cm^{-3}$, respectively. Finally a passivation layer in the solar cell rear was assumed with 200 cm/s surface recombination velocity.

Figure 9 depicts TE and TM spontaneous emission rates and the ratio TM/TE as a function of In fraction. The discontinuous steps at approximately 6% In are due to the emergence of QW energy levels, $e_2 - hh_2$ and $e_2 - lh_2$ transitions as the well depth increases. It is evidenced that as the In fraction increases, the QWs influence a higher compressive strain. As a result of this, radiative transitions from the conduction band to *hh* band (TE) are favoured over those to *lh* band (TM). However, both polarized emissions increase with well depth, indicating that biaxial compressive strain does not suppresses a mode of radiative recombination in the plane of the QWs, although certainly the TM/TE ratio is reduced. We, consequently, observe that increasing the In composition leads to larger radiative recombination that increases the total recombination dark current.

In Figure 10, spontaneous emission rates and gain are presented as a function of In fraction, where is important emphasize the great difference between the values of the spontaneous

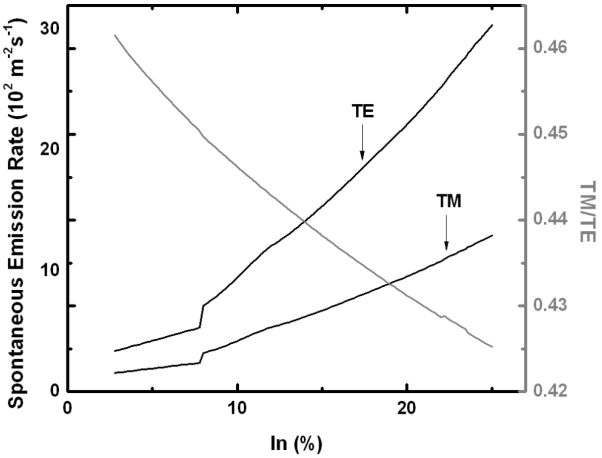

Figure 9. Modeled spontaneous emission rate for TE and TM modes and TM/TE ratio versus In composition for 10 well embedded within i-region of the SB-QWSC. Well width, L_W =15 nm and P composition, y = 0.05. The TE mode is favored over TM mode, but both polarized emissions increase with well depth.

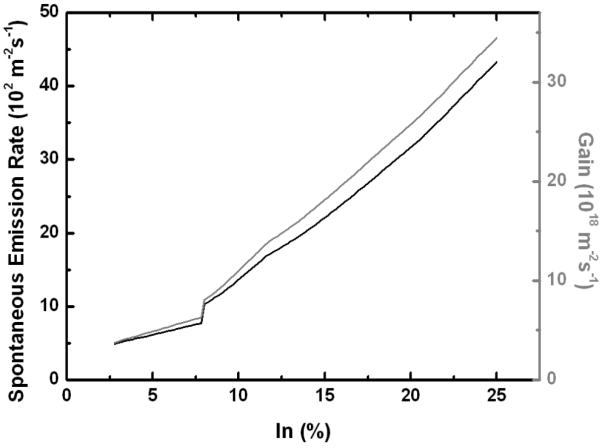

Figure 10. Spontaneous emission rate and gain versus In composition for 10 well embedded within i-region of the SB-QWSC. Well width, L_W =15 nm and P composition, y =0.05. Gain is several orders greater than radiative recombination

emission rates evidenced in the ratio TM/TE. The results of this study indicate that the generation of electron-hole pairs in the QWs is much higher than the radiative recombination, and if we add to this the influence of transverse electric field in the depletion region, which favors thermally assisted tunneling, then the carriers escape from the QWs with unity efficiency.

A distributed Bragg reflector (DBR) is a region consisting of layers of alternating refractive indices optimized for a specific wave-length such that each layer is a quarter wavelength

http://dx.doi.org/10.5772/59616

thick. As a result, partial reflections from each interface interfere constructively and the reflectivity is high over a narrow wavelength band.

Photon-recycling is the generation of an electron-hole pair via the absorption of a photon emitted elsewhere in the cell. The increased absorption is due to the reflection of incident solar radiation which has not been absorbed on its first pass through the cell and may then be reabsorbed on its second pass. It is equivalent to say that a DBR doubles the optical path length of a SB-QWSC without altering the length over which minority carriers must travel. The photons emitted by recombination into quantum wells were also considered.

The net solar incident radiation flow on front surface of a solar cell was modeled as a Fabry-Perot cavity. We derived an expression to calculate the contribution of the multiple internal reflections inside the device and then the net spectrum, $F_{net}(\lambda)$, which takes into account all contributions and the incident AM1.5 solar spectrum $F(\lambda)$ is given by:

$$F_{net}(\lambda) = F(\lambda)\left[1 + \frac{r_B\left(r_A + e^{\alpha_T^*}\right)}{e^{2\alpha_T^*} - r_B r_A}\right] \tag{29}$$

$$\alpha_T^* = \sum_j \alpha_j(\lambda) l_j \tag{30}$$

where $\alpha_j(\lambda)$ are the absorption coefficients of each layer of Fabry-Perot cavity structure, where the exciton effect in the quantum well was taken into account, l_j are layer widths, and r_A, r_B are the internal reflectivity from the front and back surface of the cell, respectively.

The photocurrent J_{PH} is calculated from the total quantum efficiency (QE_{TOTAL}) of the cell:

$$J_{PH} = q\int_{\lambda_1}^{\lambda_2} F(\lambda)\left[1 + \frac{r_B\left(r_A + e^{\alpha_T^*}\right)}{e^{2\alpha_T^*} - r_B r_A}\right] QE_{TOTAL}(\lambda)d\lambda \tag{31}$$

where $\lambda_1 = 400nm$ and λ_2 is the effective absorption threshold determined by the fundamental electron and hole confinement states.

Figure 11 shows modeled and experimental quantum efficiency (QE) versus wavelength for qt1897b sample from the Quantum photovoltaics Group of Imperial College. The cell is a p-i-n diode with an i-region containing five QWs that are 9.6 nm wide of compressively strained $In_{0.16}Ga_{0.84}As$ inserted into tensile-strained $GaAs_{0.91}P_{0.09}$ barriers at strain-balance condition. The extra absorption is displayed in the inset of Figure 11, at wavelengths in excess of the GaAs band gap where the increase in quantum efficiency in the 880 nm is readily apparent. Figure 11 also shows the computed QE spectrum with DBR, using $r_A = 0.1$ and $r_B = 0.95$. The main feature of this plot is that for a highly reflecting mirror, nearly all photons absorbed contribute to the QE. This is clearly a desirable feature as it implies that carrier collection from the QWs is very efficient allowing the increase in short circuit current. It is a good indicator that the QE of an QWSC could well approach that of a bulk cell with

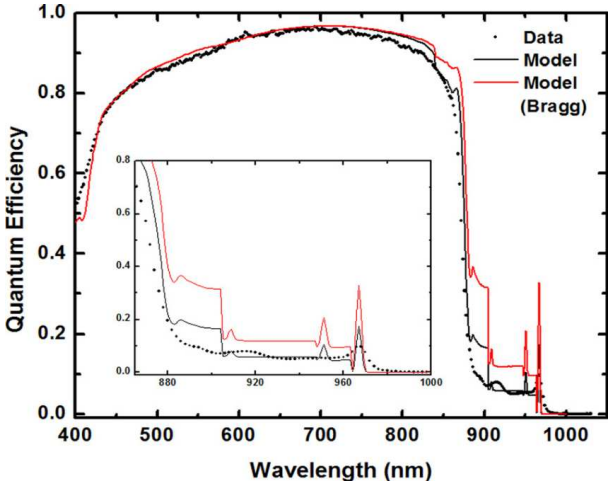

Figure 11. Modelled and experimental quantum efficiency versus wavelength for 5 well qt1897b sample from the Quantum photovoltaics Group of Imperial College. The inset shows the wavelength range dominated by the QW absorption with and without influence of DBR.

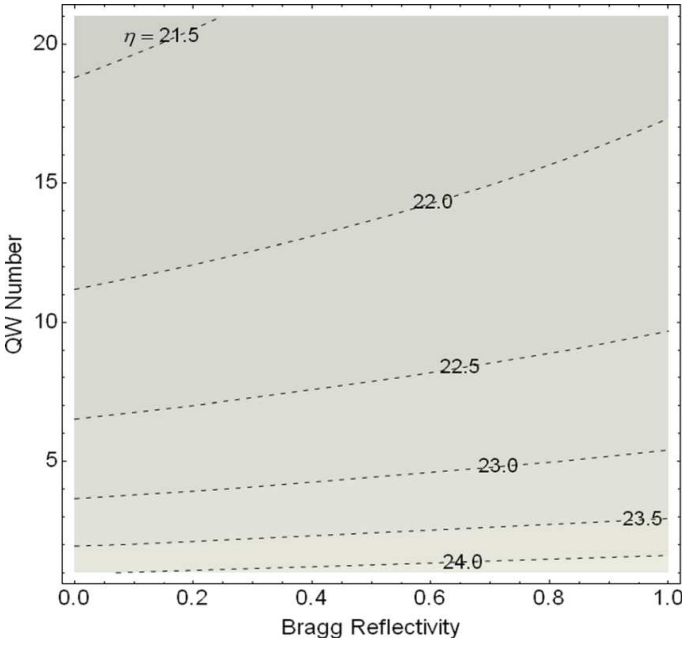

Figure 12. Contour plot for conversion efficiency as function of Bragg reflectivity and quantum well number. P composition y = 0.09, In composition x = 0.17 and L_W = 9.6 nm

http://dx.doi.org/10.5772/59616

a similar band-gap if the light could be confined inside the cell until it was completely absorbed.

For qt1897b solar cell, the dependence of conversion efficiency on back mirror reflectivity and quantum well number (N_W) is examined in Figure 12. This plot suggests that with the addition of a DBR in the device, fewer quantum wells are required to grow in the i-region in order to achieve high performance. In fact, low energy photons from the radiative recombination in the QWs can be reflected back into i-region and reabsorbed, lowering the radiative recombination current and improving the open-circuit voltage

It can be expected that SB-QWSC under concentration will be operating in a regime where recombination is dominated by radiative processes. Therefore, photon recycling effect is favoured under solar concentration when photons emitted from radiative recombination are subsequently reabsorbed by the solar cell. This can be explained as an increase in minority carrier lifetime or reduction in dark-current.This behavior is shown in Figure 13, where we have examined the conversion efficiency as a function of solar concentration for optimized $GaAs_{0.96}P_{0.04}/In_{0.03}Ga_{0.97}As/GaAs$ solar cell with 20 nm quantum well width. We used $r_A = 0.1$, $r_B = 0.95$ and resistive effects were neglected. It can be observed how the conversion efficiency should increase with solar concentration up to 1000 suns. In any concentration range, the DBR cell efficiency improvement over the non-DBR cell which is explained by the fact of the lower dark current in the DBR cell. This effect also causes that the net increase in conversion efficiency is lower with increasing N_W, as it can be noted in Figure 13.

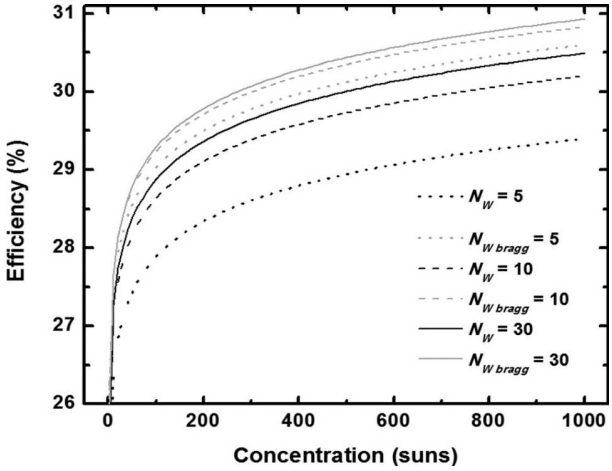

Figure 13. Conversion efficiency as a function of solar concentration for several $GaAs_{0.96}P_{0.04}/In_{0.03}Ga_{0.97}As/GaAs$ SB-QWSC which differ in the number of QW embedded within the i-region with and without influence of DBR.

3.3. GaAs/GaInNAs QWSC and SLSC

A recent alloy able to be used as well material in GaAs p-i-n solar cell is the GaInNAs. In order to investigate the $GaAs/Ga_{1-x}In_xN_yAs_{1-y}$ QWSC conversion efficiency, small nitrogen concentrations were considered to modify the quantum well depth. The lattice

matching condition to GaAs is met if the Indium and Nitrogen concentrations satisfy the relation $x = 2.85y$. The electron and hole concentrations, in GaAs base and emitter regions are $1.8 \times 10^{17} cm^{-3}$ and $2.3 \times 10^{18} cm^{-3}$, respectively, while their widths are $0.15 \mu m$ (p-region), $0.60 \mu m$ (i-region), and $0.46 \mu m$ (n-region). A 40 nm $Al_{0.8}Ga_{0.2}As$ window layer was incorporated into the p- region to reduce front surface recombination and a 70 nm MgF:SiN layer as ARC was used.

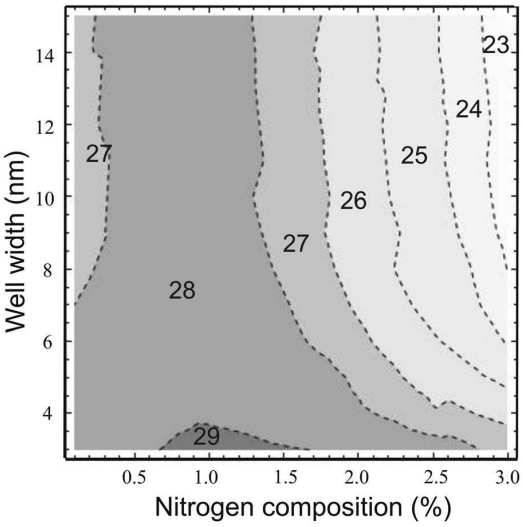

Figure 14. Contour plot of GaAs/GaInNAs QWSC efficiency as a function of the quantum well width and the nitrogen composition.

GaInNAs parameters were taken from reference [29]. High values of conversion efficiency are reached up to 3% N composition [30, 31], as depicted in Figure 14. The maximum values of efficiency are obtained for a narrow region around 1% of nitrogen composition and narrow quantum well widths. These N compositions correspond to shallow quantum wells, where the carrier generation overcomes the recombination. Also, for these N fractions a second quantum level appears in the heavy hole band slightly increasing photon absorption.

When the quantum wells are deeper (nitrogen percent increases) the carrier recombination increases and the conversion efficiency drops. In Figure 14 is shown the conversion efficiency as function of quantum well width. For 1% nitrogen composition, the conversion efficiency is almost insensitive to quantum well width due to a compensation effect, as there is a trade-off between quantum well width and quantum well number. Wider quantum wells absorbs more photons, but the amount quantum wells in the intrinsic region ($0.6 \mu m$) is smaller. On the other hand, narrow quantum wells have small photon absorption but it is possible to insert more of them in the intrinsic region. For other nitrogen compositions higher than 1%, the efficiency drops when the quantum well width increases because the carrier recombination is higher.

To study the case of GaAs/GaInNAs SLSC, keeping the other device parameters identical as it was defined for QWSC, the condition for resonant tunneling were calculated by the

http://dx.doi.org/10.5772/59616

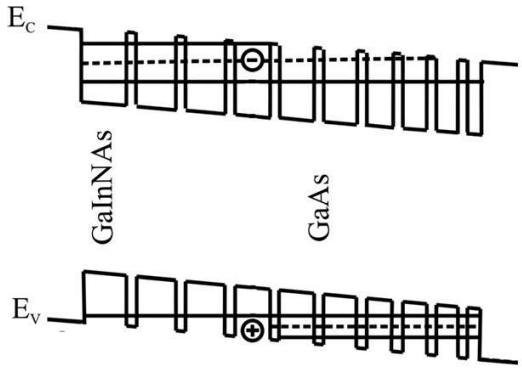

Figure 15. A variably spaced multiple quantum well (cluster) which enhances the resonant tunneling between adjacent wells.

well-known transfer matrix method without back-scattered wave. A variably spaced multiple quantum well or superlattice was considered. Figure 15 illustrates this particular superlattice unit that we have been refering as a cluster, in which the resonant tunneling character were obtained. The resonance takes place for an electric field of 12 kV/cm, which was obtained accounting uniform doping levels at the p- and n-regions, and intrinsic region width $0.60\mu m$. We have used a fixed field, which is a parameter in our model.

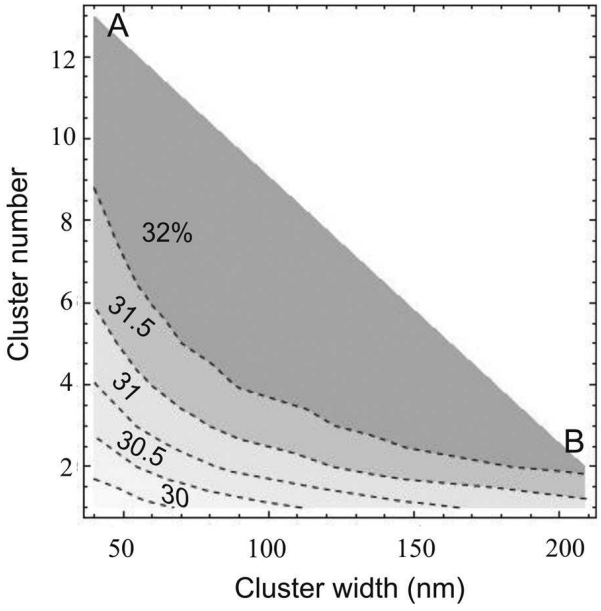

Figure 16. Contour plot of GaAs/GaInNAs SLSC efficiency as a function of the cluster width and number.

To study the GaAs/GaInNAs SLSC performance, it was considered a cluster composed of ten variably spaced multiple quantum wells optimized to maximise the resonant tunneling between adjacent wells. The GaInNAs quantum wells contains of 1% nitrogen composition and the GaAs barriers are 1 nm wide. A series of clusters are inserted in the intrisic region, independent from each other, in such a way that there is no coupling between neighboring clusters.

Figure 16 exhibits a contour plot of the conversion efficiency for the SLSC as a function of the cluster width and the number. If we compare these results with Figure 15 is evidenced that maximum SLSC conversion efficiencies are higher than those of QWSC by 3%. The AB contour in Figure 16 represents highest conversion efficiency obtained in the calculations. It can be also evidenced that the conversion efficiency rises as the width and the number cluster also increase, due to higher photon absorption.

4. Conclusions

A model for quantum well and superlattice solar cells was presented and applied to theoretically study qualitative trends in quantum well and superlattice solar cell performances. The findings from this study enhance our understanding of these devices and could provide a suitable guide for its designing. The model allows optimization the solar cell performance as a function of several of its parameters. The well and barrier band gaps, the width and depth of the wells, the amount of the wells in the intrinsic region are considered in the model to attain the best conversion efficiency.

We have shown theoretically that the insertion of multiple quantum wells into the intrinsic region of a p-i-n $Al_xGa_{1-x}As$ solar cell can enhance the conversion efficiency compared with its baseline cell. The quantum efficiency and the photocurrent for the AlGaAs/GaAs QWSC was calculated and compared with experimental results obtaining good agreement. These results, together with the agreement of the calculated open-circuit voltage with experimental values confirm the reliability of the model presented in this chapter.

GaAsP/InGaAs/GaAs strain-balanced solar cell was presented and studied. The effect of the electric field and the tensile and compressive stress, were carefully considered. The results of the modeling of SB-QWSC were also compared with experimental measurements successfully, validating again the suitability of the model. Following the model was used to determine the highest possible efficiencies for SB-QWSC containing quantum wells under varying degrees of strain. The strain-balanced multiple quantum well solar cells show a high conversion efficiency that makes it very attractive for their use in multijunction solar cells for space applications or concentrator photovoltaics based on a GaAsP/InGaAs/GaAs middle cell. Solar cells containing strain balanced QWs in a multijunction solar cell allow the absorption edge of each subcell to be independently adjusted.

We have shown a new type of photovoltaic device, the superlattice solar cell (SLSC), where coupled quantum wells or superlattices are inserted into the intrinsic region. The aim of this approach is the possibility of better tailor the photon absorption improving, at the same time, the transport of photogenerated carriers due to the tunneling along the nanostructure. The model adjusted to the superlattice solar cell case was then applied to GaAs/AlGaAs and GaAs/GaInNAs material systems. For the GaAs/AlGaAs case, was found photocurrent increase, and slight increments in the conversion efficiency over the QWSC. When applied the

model to GaAs/GaInNAs, was obtained the dependence of conversion efficiency as function of nitrogen composition and quantum well width, which allowed determining the range of these parameters where higher conversion efficiencies than in QWSC of the same material system are reached.

Besides, the GaAs/GaInNAs QWSC or SLSC show high conversion efficiency. That make them very attractive for space applications or for a triple-junction concentrator cell based on a GaAs/GaInNAs bottom cell that could reach 50% conversion efficiency. Because of the results that our model predicts haven't been compared nor confirmed experimentally, it would be interesting to see if future experiments will corroborate our findings.

Solar cell efficiency potential remains far greater than actual solar cell efficiencies, including those achieved in research laboratories. New approaches are necessary in order to increase the conversion efficiency and the quantum based solar cells could be a road to reach this goal.

5. Acknowledgments

Thanks to COZCYT for the partial financial support for this chapter.
J.C. Rimada acknowledges the International Centre for Theoretical Physics (ICTP) for partial funding under the TRIL programme.

Author details

Luis M. Hernández[1], Armando Contreras-Solorio[2], Agustín Enciso[2], Carlos I. Cabrera[2], Maykel Courel[3], James P. Connolly[4] and Julio C. Rimada[5*]

*Address all correspondence to: jcrimada@fisica.uh.cu; jcrimada@gmail.com

1 Faculty of Physics, University of Havana, Colina Universitaria, La Habana, Cuba

2 Academic Unit of Physics, Autonomous University of Zacatecas, Zacatecas, Mexico

3 Higher School in Physics and Mathematics, National Polytechnic Institute, Mexico, Mexico

4 Nanophotonics Technology Center, Polytechnic University of Valencia, Valencia, Spain

5 PV Laboratory, Institute of Materials Science and Technology (IMRE)- Faculty of Physics, University of Havana, La Habana, Cuba

References

[1] W Shockley, HJ Queisser (1961) Detailed balance limit of ef- ficiency of p-n junction solar cells. J. Appl. Phys; 32 510âĂŞ519. doi:10.1063/1.1736034

[2] K.W.J. Barnham, C. Duggan (1990) A new approach to high-efficiency multi-bandgap solar cells. J. Appl. Phys. 67 (7) 3490-3493

[3] M. Courel, J. C. Rimada, L. Hernández (2011) AlGaAs/GaAs superlattice solar cells. Progress in Photovoltaics: Res. Appl. 21 276-282 doi: 10.1002/pip.1178

[4] J. Nelson, M. Paxman, K. W. J. Barnham, J. S. Roberts and C. Button (1993) Steady-State Carrier Escape from Single Quantum Wells. IEEE Journal of Quantum Electronics, Vol. 29, No. 6 1460-1465. doi:10.1109/3.234396

[5] M. Paxman, J. Nelson, K. W. J. Barnham, B. Braun, J. P. Connolly, C. Button, J. S. Roberts and C. T. Foxon (1993) Modeling the Spectral Response of the Quantum Well Solar Cell. Journal of Applied Physics, Vol. 74, No. 1 614-621. doi:10.1063/1.355275

[6] T. Aihara, A. Fukuyama, Y. Yokoyama, M. Kojima, H. Suzuki, M. Sugiyama, Y. Nakano, and T. Ikari (2014) Detection of miniband formation in strain-balanced InGaAs/GaAsP quantum well solar cells by using a piezoelectric photothermal spectroscopy. Journal of Applied Physics, 116, 044509 doi: 10.1063/1.4887443

[7] Green, Martin A. and Emery, Keith and Hishikawa, Yoshihiro and Warta, Wilhelm and Dunlop, Ewan D. (2015) Solar cell efficiency tables (version 46). Progress in Photovoltaics: Research and Applications 23 (7) 805–812 doi: 10.1002/pip.2637

[8] P. R. Griffin, J. Barnes, K. W. J. Barnham, G. Haarpaint-ner, M. Mazzer, C. Zanotti-Fregonara, E. Grunbaum, C. Olson, C. Rohr, J. P. R. David, J. S. Roberts, R. Gray and M. A. Pate (1996) Effect of Strain Relaxation on Forward Bias Dark Currents in GaAs/InGaAs Multiquantum Well p-i-n Diodes. Journal of Applied Physics, Vol. 80, No. 10 5815-5820. doi:10.1063/1.363574

[9] N. J. Ekins-Daukes, K. W. J. Barnham, J. P. Connolly, J. S. Roberts, J. C. Clark, G. Hill and M. Mazzer (1999) Strain-Balanced GaAsP/InGaAs Quantum Well Solar Cells. Applied Physics Letters, Vol. 75, No. 26 495-497. doi:10.1063/1.125580

[10] D. C. Johnson, I. Ballard, K. W. J. Barnham, M. Mazzer, T. N. D. Tibbits, J. Roberts, G. Hill and C. Calder (2006) Optimisation of Photon Recycling Effects in Strain-Balanced Quantum Well Solar Cells. Proceedings of the 4th World Conference on Photovoltaic Energy Conversion, Hawaii, 7-12 May 2006 26-31

[11] M. Kondow, K. Uomi, A. Niwa, T. Kitatani, S. Watahiki and Y. Yazawa (1996) GaInNAs: A Novel Material for Long- Wavelength-Range Laser Diodes with Excellent High-Temperature Performance. Japanese Journal of Applied Physics, Vol. 35 1273-1275. doi:10.1143/JJAP.35.1273

[12] D. J. Friedman and S. R. Kurtz (2002) Breakeven Criteria for the GaInNAs Junction in GaInP/GaAs/GaInNAs/Ge Four-Junction Solar Cells. Progress in Photovoltaics, Vol. 10, No. 5 331-344. doi:10.1002/pip.430

[13] A. Freundlich, A. Fotkatzikis, L. Bhusal, L. Williams, A. Alemu, W. Zhu, J. A. H. Coaquira, A. Feltrin and G. Rad- hakrishnan (2007) III-V Dilute Nitride-Based Multi-Quantum Well Solar Cell. Journal of Crystal Growth, Vol. 301- 302, 993-996. doi:10.1016/j.jcrysgro.2006.11.256

[14] E. Reyes-Gómez, L. E. Oliveira and M. de Dios-Leyva (2005) Quasi-Bond States and Intra-Band Transition Energies in GaAs-(Ga,Al)As Variably Spaced Semiconductor Super- lattices. Physica B, Vol. 358, No 1-4, 269-278. doi:10.1016/j.physb.2005.01.462

[15] J. C. Rimada, L. Hernández, J. P. Connolly and K. W. J. Barnham (2007) Conversion Efficiency Enhancement of AlGaAs Quantum Well Solar Cells. Microelectronics Journal, Vol. 38, No. 4-5 513-518. doi:10.1016/j.mejo.2007.03.007

[16] J.C. Rimada, L. Hernández (2001) Modeling of ideal AlGaAs quantum well solar cells. Microelectronics Journal. Vol. 32, 719-723

[17] N.G. Anderson (1995) Ideal theory of quantum well solar cells. J. Appl.Phys. 78 (3) 1850 - 1861

[18] G. Bastard (1988) Wave Mechanics Applied to Semiconductor Heterostructures. Editions de Physique, Paris

[19] H. Mathieu, P. Lefebre, P. Christol (1992) Simple analytical method for calculating exciton binding energies in semiconductor quantum wells. Phys. Rev. B 46 (1) 4092-4101

[20] Petroff, P. M. and Logan, R. A. and Savage, A. (1980) Nonradiative Recombination at Dislocations in III-V Compound Semiconductors. Phys. Rev. Lett., 44(4),287–291, doi: 10.1103/PhysRevLett.44.287

[21] B. Browne, A. Ioannides, J. Connolly, K. Barnham, J. Roberts, R. Airey, G. Hill, G. Smekens and J. Van Begin (2008) Tandem quantum well solar cells. Proceedings of 33rd IEEE Photovoltaic Specialists Conference, San Diego, CA. USA.

[22] N. J. Ekins-Daukes, K. Kawaguchi, and J. Zhang (2002) Strain-Balanced Criteria for Multiple Quantum Well Structures and Its Signature in X-ray Rocking Curves. Crystal Growth and Design 2 (4) 287–292

[23] Adams, J. G. J. and Browne, B. C. and Ballard, I. M. and Connolly, J. P. and Chan, N. L. A. and Ioannides, A. and Elder, W. and Stavrinou, P. N. and Barnham, K. W. J. and Ekins-Daukes, N. J (2011) Recent results for single junction and tandem quantum well solar cells. Progress in Photovoltaics: Research and Applications 19 (7) 865-877 doi:10.1002/pip.1069

[24] P. Harrison (2005) Quantum Wells, Wires, and Dots. John Wiley & Sons, Ltd., 219-230

[25] Varonides AC (2004) Tunneling photoconductivity computations of multi-quantum well p-i(nano)-n photovoltaic nanostructures by means of the causal Green's function. Thin Solid Films 451-452: 393-396

[26] J. C. Rimada , L. Hernández, J. P. Connolly and K. W. J. Barnham (2005) Quantum and conversion efficiency calculation of AlGaAs/GaAs multiple quantum well solar cells. Physica Status Solidi 242, 1842

[27] CI Cabrera, JC Rimada, JP Connolly, L Hernández (2013) Modelling of GaAsP/InGaAs/GaAs strain-balanced multiple-quantum well solar cells. Journal of Applied Physics 113, 024512

[28] C. I. Cabrera, J. C. Rimada, L. Hernández, J. P. Connolly, A. Enciso, and D. A. Contreras-Solorio (2014) Anisotropic emission and photon-recycling in strain-balanced quantum well solar cells. Journal of Applied Physics 115, 164502

[29] Sheng-Horng Yen, Mei-Ling Chen, Yen-Kuang Kuo (2007) Gain and threshold properties of InGaAsN/GaAsN material system for $1.3\mu m$ semiconductor lasers. Optics & Laser Technology, Volume 39, Issue 7 1432-1436 doi:10.1016/j.optlastec.2006.10.003.

[30] M.Courel, J.C.Rimada, L.Hernández (2012) GaAs/GaInNAs quantum well and superlattice solar cells. Appl. Phys. Lett. 100, 073508.

[31] M.Courel, J.C.Rimada, L.Hernández (2012) An approach to high efficiencies using GaAs/GaInNAs multiple quantum well and superlattice solar cell. J. Appl. Phys. 112, 054511.

Chapter 6

Solar Cell Efficiency Increase at High Solar Concentration, by Thermionic Escape via Tuned Lattice-Matched Superlattices

A.C. Varonides

Additional information is available at the end of the chapter

http://dx.doi.org/10.5772/59039

1. Introduction

General p-i-n solar cell structures are suitable hosts for regions where quantum effects might occur; excess photo-carriers can be developed in quantum traps (quantum wells) grown along the direction of the cell (from p to n region). The cell absorbs at two different wavelengths (a) the host **($E_{host}=hc/\lambda_{host\ band\text{-}gap}$)** and (b) the optical gap wavelength (**$E_{solar\text{-}photon}=hc/\lambda_{optical\ gap}$**). The optical gap of the superlattice can be tuned to desired solar photon energy values (e.g. 1eV photons, Figure-1), with optical gap matching the desired solar photon flux (Figure 1) [1].

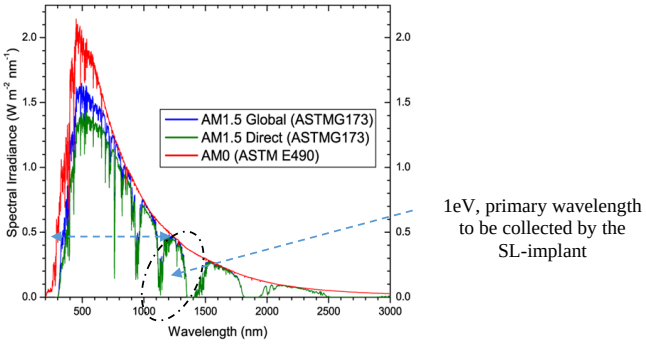

Figure 1. Solar spectrum (AM1.5 Direct) and the region of interest at primary wavelength 1240nm.

Superlattices (large number of periods with thin quantum wells) in the intrinsic region of p-i-n cells provide photo-carrier separation (electron-hole pairs or EHP's) via carrier drifting, leading to effective mass separation of photo-carriers and recombination loss reduction; the advantage of using quantum wells in the intrinsic region of the host material (here GaAs) is the widening of the gap of low-gap material (here Ge); the optical gap ($E_{e1} - E_{hh1}$) [4] caused by the narrow gap layer in the cell, can in essence be tuned to equal-energy incident solar wavelengths. This means that excess carriers may be trapped in quantum wells and thus thermionic escape will lead to *excess* currents in the cell. A cell design that could lead to excess current may occur in an all-GaAs p-i-n cell with a lattice-matched GaAs-Ge superlattice, grown in the middle of the intrinsic region (Figure 2b), and where excess photo-electrons are *thermionically* reaching the conduction band and are swept away by the built-in electrostatic field. In this chapter we provide a first-principles derivation of excess thermionic current, after radiative recombination losses are taken into account. We propose a short superlattice implanted in the middle of a bulk p-i-n solar cell (Figure 2a), with the expectation of excess current generation via concentrated optical illumination. Such a superlattice will be expected to trap photo-carriers with the chance of overcoming the potential barrier. Once such carriers are out of the quantum traps, they will be likely to join the flux of bulk currents in the p-i-n device. These carriers will essentially be swept away by the built-in electrostatic field, especially in the mid-region of the structure.

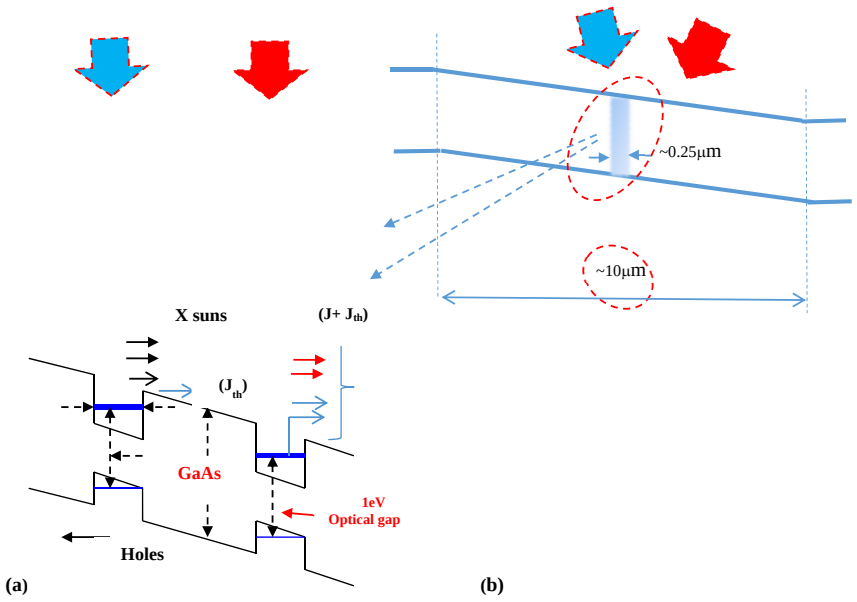

Figure 2. a) A portion of a superlattice embedded in the intrinsic region and illuminated at X suns. Carriers are excited in the quantum wells and thermionically escape to the conduction band (b) Bird's eye view of the intrinsic region with the SL (0.5 μm) portion illuminated at concentrated light.

http://dx.doi.org/10.5772/59039

2. Theory

In this section we derive thermionic currents for a single quantum well. The model as shown in Figure 1 includes a double heterostructure with a quantum well formed by a low-gap medium. According to this figure, electrons may be trapped in eigen-states in the quantum wells under both dark or illumination conditions (as long as incident photons have sufficient energy to excite carriers from the valence band to the conduction band). Once in the quantum well, electrons may thermionically acquire energy to overcome the potential barrier ΔE_c, formed by the wide-gap medium. The potential barrier is the conduction band difference $E_{c2} - E_{c1}=\Delta E_c$ (Fig-2) of the two layers that are in contact. Standard thermionic emission models [2, 3] describe thermal currents due to electrons having sufficient kinetic energy (KE) to overcome the highest conduction band edge E_{c2} (KE=E-E_{c2} ≥ ΔE_c) [3]. Thermionic currents can be described by integrating over all energies above E_{c2} through the following expression:

$$J = q\int dE g(E) f(E) v(E) \tag{1}$$

Where q is the electronic charge, g(E) is the electronic density of states (DOS) (eV^{-1} cm^{-3}) of the two-dimensional system (here a quantum well of width L_w), f(E) is the Fermi-Dirac distribution function, and v(E) is the velocity acquired by the escaping electrons to overcome the barrier potential. Expression (1) is usually re-written as

$$J = q\int_{Ec2}^{\infty} dE\left(\frac{m^*}{\pi\hbar^2 L_W}\right)\left(e^{-(E-E_F)/kT}\right)\left(\frac{2}{m^*}\right)^{1/2}(E-E_{C2})^{1/2} \tag{2}$$

Where the two-dimensional DOS was used for quantum wells of width L_w [3], and where the Fermi-Dirac distribution was replaced with a Maxwell-Boltzmann ($E-E_{c2} >> 3kT$). Expression (2) can be written as:

$$\begin{aligned} J &= \frac{q\sqrt{2m^*}}{\pi\hbar^2 L_W} e^{-(E_{C2}-E_F)/kT}\int_{E_{C2}}^{\infty} dE(E-E_{C2})^{1/2} e^{-(E-E_{C2})/kT} \\ &= \frac{q\sqrt{2m^*(kT)^3}}{\pi\hbar^2 L_W} e^{-(E_{C2}-E_F)/kT} \end{aligned} \tag{3}$$

The latter expression can be written in a more familiar form, in terms of the barrier height ΔE_c, which is a distinct property of the superlattice geometry. The exponential term does not change if we add and subtract the lower conduction band E_{C1}. Since

E_{C2}-E_F=(E_{C2}– E_{C1})+(E_{C1}–E_F), we can repeat (3) as follows:

$$J = \frac{q\sqrt{2m^*(kT)^3}}{\pi\hbar^2 L_W} e^{-(E_{C2}-E_{C1})/kT} \times e^{-(E_{C1}-E_F)/kT} \tag{4}$$

The last term in (4) is directly related to the total carrier concentration of electrons n_{tot} in region 1 which is the low-gap medium, hence it can be expressed via the conduction band effective density of states N_c (cm^{-3}) and the carrier density according to the standard relation

$$n_{tot} = N_C e^{(E_{C1}-E_F)/kT},$$

with

$$N_C = 2\left(\frac{2\pi m^* kT}{h^2}\right)^{3/2}$$

Implementing the latter in the current, as in (4), we obtain a finalized form of thermionic current due to thermally escaping electrons from individual quantum wells:

$$\begin{aligned} J &= \frac{q\sqrt{2m^*(kT)^3}}{\pi\hbar^2 L_W} e^{-(E_{C2}-E_{C1})/kT} \times \left(\frac{n_{tot}}{N_C}\right) \\ &= \left(\frac{qh}{m_o}\right)\left(\frac{n_{tot}}{\mu L_W}\right) e^{-\Delta E_C/kT} \end{aligned} \tag{5}$$

Where we replaced the effective mass m* with the product of rest electron's mass m_o and a numerical factor μ [$m_c=(9m_l m_t^2)^{1/3}$, the DOS effective mass] that differs from material to material [4]. The prefactor (qh/m_o) in (5) is a constant (q for the electronic charge, h for Planck's constant and m_o for the electron's rest mass) equal to 1.1644×10^{-22} ($A \cdot m^2$); the current becomes:

$$J = 1.1644 \times 10^{-22} \times \left(\frac{n_{tot}}{\mu L_W}\right) \times e^{-\Delta E_C/kT} (A/m^2) \tag{6}$$

Expression (6) describes thermionic current produced from a quantum well; this current is a strong function of (a) quantum well width (b) barrier height and (c) total carrier density in the well-layer. Total carrier concentration in the well is the sum of (a) dark carrier concentration in the quantum well n_{qu} and of (b) excess photo-carrier concentration in the miniband under illumination, δn_{ph}: $n_{tot}=n_{qu}+\delta n_{ph}$.

Hence,

$$J = \frac{1.1644 \times 10^{-22}}{\mu L_W} \times (n_{qu} + \delta n_{ph}) \times e^{-\Delta E_C/kT} (A/m^2) \tag{7}$$

http://dx.doi.org/10.5772/59039

The term n_{qu} represents carriers trapped in quantum wells [6]:

$$n_{qu} = \frac{m^*(kT)}{\pi\hbar^2 L_W} \ln\left(1 + \exp(-\frac{E_1 - E_F}{kT}\right) \tag{8}$$

E_1 is the lowest eigen-state included (suitably thin layers will provide only one eigen-solution in the wells). If the energy difference ($E_1 - E_F$) is much greater than kT, the dark quantum well contribution is essentially (numerically) negligible compared to excess photo-concentration, as seen from (8). The n_{qu} term would become significant if the Fermi level stays near the conduction band edge of the low-gap semiconductor; however this would require relatively high n-type doping levels of the quantum trap material, and hence scattering and increased absorption losses. The goal here is to embed a superlattice region in the intrinsic part of the p-i-n cell, with undoped (or low doping level) quantum well layer to reduce scattering. On the other hand, illumination would excite electrons from the valence to the conduction band at wavelengths near the gap of the layer. The quantum-well semiconductor is tuned to photons of equal energy and tuned photo-excitation populates the energy band with excess electrons δn_{ph}; these electrons can be found from the form:

$$\delta n_{ph} = n_o e^{-x/L_n} + \sqrt{\frac{\Phi_\lambda}{B}} e^{-\alpha x/2} \tag{9}$$

Relation (9) is the solution of the diffusion equation [7], describing minority photo-electrons induced in quantum wells under illumination (through Φ_λ). The first term in (9) is a diffusion term in the x direction, with electron diffusion length L_n (the solution of the homogeneous diffusion equation) and the second term includes directly the absorption coefficient in the exponential term and indirectly through the generation rate term Φ_λ; B is the coefficient of radiative recombination B respectively. More specifically, if the solar photon flux ($cm^{-2}\ s^{-1}$) is $F_{ph}(\lambda)$, the photon generation rate ($cm^{-3}\ s^{-1}$) is taken to be: $\Phi_\lambda(cm^{-3}s^{-1})\_\alpha\ (1\text{-}R)F_{ph}(\lambda)$, where R is the reflectivity of the surface and α is the absorption coefficient. At high solar concentration (e.g. X=400 or for X ≥100)), n_o, $n_{qu} << \sqrt{\frac{X\,\Phi_\lambda}{B}}$ (by at least two orders of magnitude: n_o, n_{qu} ~10^{11}-10^{12} cm^{-3}, $(X\Phi/B)^{1/2}$=10^{14} cm^{-3}), expression (7) becomes:

$$J_{ph}(A/m^2) \cong \frac{1.1644 \times 10^{-13}}{\mu L_W(nm)} \sqrt{X} \sqrt{\frac{\Phi_\lambda}{B}} (e^{-\alpha x/2} e^{-\Delta E_C/kT}) \tag{10}$$

Where both n_{qu} and n_o terms have been removed as negligible compared to X-sun photo-generation. On the other hand, B represents the cross section of radiation recombination losses (radiation coefficient); we use a nominal value of the order of $10^{-10}\ cm^3s^{-1}$=$10^{-16}m^3s^{-1}$ [8]. Currents in (10) depend on (a) width L_w of quantum wells (b) carrier effective mass $m^*=\mu\ m_o$ (c) solar concentration X (# of suns) (d) carrier photo-generation Φ_λ and (e) conduction band discontinuity ΔE. The formula above describes thermionic escape current from an illuminated

quantum well of width L_w (nm), with one mini-band and tuned to a specific solar wavelength λ_o. Such a choice creates favorable conditions for absorption of photons at energy E_o(eV)=1.24/λ_o(μm); one can deduce the value of carrier generation rate Φ_λ by dividing the irradiance I_{rr}(W/m^2) at the specific wavelength $\lambda_{o,}$ by the energy of the corresponding photon of energy E_o. In other words, the solar photon flux F_{ph} (m^{-2} s^{-1}) is the ratio $I_{rr} / E(\lambda_o)$. By tuning a quantum well at 1eV (see Figure-1), we increase the prospects of photon absorption at λ_o=*1.24μm* (note also that E (λ_o=*1.24μm*)=1.24/1.24=1eV), and hence the solar photon flux at λ_o is (see also Figure-1):

$$F_{ph}(\lambda_o) = \frac{I_{rr}}{E(\lambda_o)} = \frac{I_{rr}(W/m^2/nm)}{E(\lambda_o)(J/nm)} = 3.12\times10^{18} m^{-2}s^1 \tag{11}$$

Where the irradiance I_{rr} *at* a primary wavelength λ_o=*1,240.00 nm* is taken equal *to 0.5W/m*^{2} [1]. The carrier generation rate (absorption coefficient is assumed to be ~ 10^4 cm^{-1}=10^6 m^{-1}) is:

$$\Phi_{\lambda o} = \alpha(1-R)F_{ph}(\lambda_o) \cong (10^4\times10^2)\times3.13\times10^{18} m^{-3}s^1 = 3.13\times10^{24} m^{-3}s^1$$

[Note also the approximation: a 1240nm photon, impinging on a 5nm quantum well, suffers negligible reflection, hence *R negligible*]. The conduction bandgap term ΔE, is the energy discontinuity between GaAs and Ge layers. Numerical values of ΔE are strongly dependent on fabrication conditions and crystal orientation. We compromise with a well-balanced value 350 meV for ΔE [9]. Based on numerical values of the relevant parameters, the composite cell will generate excess thermionic currents at X suns and with N superlattice periods:

$$J_{ph} = 1.557N\sqrt{X}(mA/cm^2) \tag{12}$$

The exponential term $e^{-\alpha x/2}$ in (10) refers to absorbed radiation within the span of single quantum well (several nanometers), while the absorption coefficient is taken to near 10,000 cm^{-1} [10]. This means that this exponential term will be very close to 1 within the span of one quantum well (~ 0.998) and it is not a significant term in computing expression (10). Expression (12) is now a finalized result of thermionic current density due to electrons escaping from a Ge-quantum well illuminated at a primary wavelength λ_o. Note also that we assumed no losses of thermionic carriers once they are above E_{C2} (work in progress; see also expression (3) above, in relation with Figure 2a).

To summarize, we have developed a thermionic current formula based on the following assumptions:

a. Electrons are assumed to have kinetic energy $KE \geq E_{c2} - E_{c1}$

b. Electrons occupy *2-D* states in quantum wells

c. Total current is calculated from *dj=q g(E) f(E) v(E) dE*

http://dx.doi.org/10.5772/59039

d. Fermi-Dirac statistics is approximated to Maxwell-Boltzmann's

e. Thermal currents are strong functions of incident *concentrated* solar photon radiation

f. the quantum wells are tuned at their optical gap; high concentrations of excess photo-electrons are expected to accumulate in the mini-bands and hence significant thermionic currents are expected

g. Currents depicted here, are in accordance with thermionic patterns $J \sim J_o\, e^{-q\Phi/kT}$ (Φ the potential barrier) and given by (10) as a strong function of solar concentration and number of periods.

h. We use 5nm quantum well widths (GaAs/Ge/GaAs), tuned at 1eV; the current density is

$J_{ph} = 1.557\sqrt{X}\,(mA/cm^2)$; Per low-gap layer

The figure below indicates solar thermal current dependence on solar concentration (from (11), N=1).

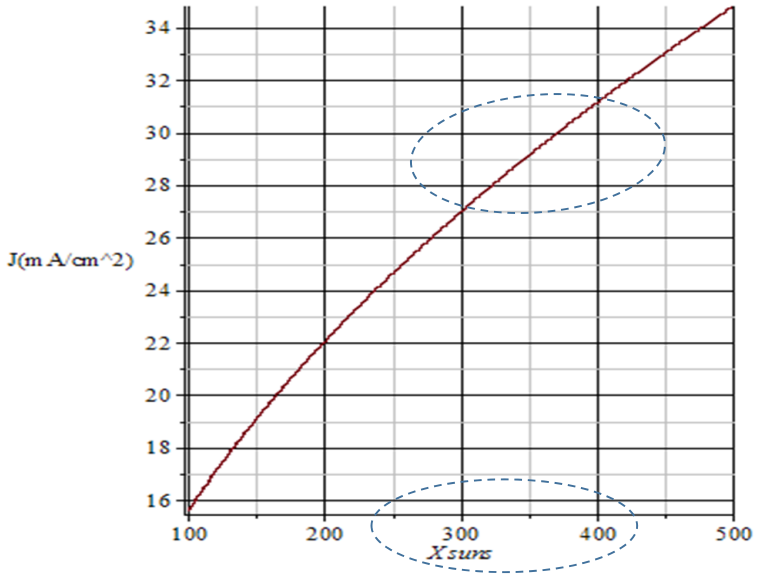

Figure 3. Thermionic current density dependence on solar concentration. 31mA/cm^2 excess thermal current is generated per quantum well at 400 suns (tuned at 1eV, $N=1$, $J \sim 1.557X^{1/2}$).

From Figure-3, we see that highly illuminated quantum well layers at specific wavelengths produce high currents (for instance, 31mA/cm^2 at 400 suns). Excess short circuit current J_{ph} increases drastically with photo-concentration as seen from Figure-3. Such rapid rise is expected (the higher the irradiance the more carriers available for thermal escape from the wells). However, drastic increase in current does not (a) affect open circuit voltage and (b) total

efficiency. Open-circuit voltage remains near the one-sun value (X=1), while fill factors reduce. As a result, the efficiency of the hybrid cell will be affected accordingly. The next section deals with the collection efficiency of the hybrid cell (bulk plus superlattice cell).

3. Device design

Incorporating a superlattice-layer GaAs/Ge, with 5nm-thick quantum wells, embedded in the middle of the intrinsic region of the bulk cell, will increase the current dramatically but not the open circuit voltage. This current will add to the bulk GaAs-related current of the PV cell, and will affect the open-circuit voltage as well. The bulk cell illuminated at X suns will produce an open-circuit voltage V_{oc}^{ph} given by the standard formula:

$$V_{oc}^{'} = V_t \ln(\frac{XJ_L}{J_o} + 1) \cong V_t \ln(\frac{XJ_L}{J_o}) = V_{oc} + V_t \ln(X) \tag{13}$$

Where the photo-current has been multiplied by the X (suns) factor [1]. Based on the above, net *OC*-voltage will increase by 15mV: V_t *ln* (X)=0.025 ln (400)=0.150V (with V_t=kT/q) and hence $V_{oc}^{(ph)}$=1.051+0.15=1.201V. We simulate a GaAs p-i-n cell with the following geometry [11]:

a. Total device 14μm)

b. Length of p-region 2 μm

c. Length of intrinsic region 10 μm

d. Longer intrinsic region provides excess photo-carriers swept away from the junctions; excess minority carriers are developed in both p-and n-regions

e. Total current is essentially the sum of minority and off-intrinsic region currents

f. Length of n-region 2 μm

g. GaAs/Ge multilayer in the intrinsic region (Ge layers at 5nm): total length of SL region for 100 periods, 100 x 5=500 nm=0.5 μm

h. Illumination of the whole device (including intrinsic region) at X suns (e.g. X=400)

i. PC1D simulations of a host-GaAs p-i-n host cell, (steps (a) through (d)) lead to J_{sc}=J_L=25.73 mA/cm^2, V_{oc}=1.051V, FF=0.94, at X=1, P_{in}=100mW/cm^2); efficiency η=(0.94) (25.73) (1.051) / P_{in}=25.42%

j. Illumination of the composite cell at X-suns will affect the collection in two ways (i) short-circuit photo-currents and input power will increase by a factor X (ii) OC-voltage will increase as indicated by (12).

k. The fill factor FF is $FF = 1 - \frac{V_t}{V_{oc}^{total}} \ln(1 + \frac{V_m}{V_t}) - \frac{V_t}{V_{oc}^{total}}$ [12]

http://dx.doi.org/10.5772/59039

1. Host (bulk) GaAs-cell (no superlattice, X=400) shows 26.26%, through FF and V_m computation

$$V_m = V_{oc}^{total} - V_t \ln(1+\frac{V_m}{V_t}) = (V_{oc} + V_t \ln X) - V_t \ln(1+\frac{V_m}{V_t}) \tag{14}$$

$$\eta = (0.85)\frac{(400\times 25.73)\times(1.201)}{400} = 26.26\,\%$$

Note that open-circuit voltage is $V_{oc}^{(X=400)}=V_{oc}^{(X=1)}+V_t \ln(400)=1.201V$

The efficiency of the hybrid (bulk+superlattice) device is:

$$\begin{aligned} &\eta = (FF)\frac{(XJ_L + J_{ph})}{XP_{in}}V_{oc}^{'} = (FF)\frac{J_L + (\frac{J_{ph}}{X})}{P_{in}}V_{oc}^{'} \\ &Or \\ &\eta = (FF)\frac{J_L + (1.557NX^{-1/2})}{P_{in}}V_{oc}^{'} \end{aligned} \tag{15}$$

We re-write (15) by splitting it in two parts containing bulk and superlattice regions:

$$\begin{aligned} &\eta = (FF)\frac{J_L + (1.557NX^{-1/2})}{P_{in}}V_{oc}^{'} \\ &= (FF)\frac{J_L V_{oc}^{'}}{P_{in}} + (FF)\frac{1.557X^{-1/2}V_{ov}^{'}}{P_{in}} \equiv \eta_{bulk}^{X} + \delta\eta \end{aligned} \tag{16}$$

The first term of (16) is the bulk-cell efficiency at X suns, and the second one is the excess collection efficiency due to the superlattice region. Rewriting (16) we get:

$$\eta = \eta_{bulk} + \delta\eta = \left(FF\frac{J_L V_{ov}^{'}}{P_{in}}\right) + \left(FF\frac{1.557V_{oc}}{P_{in}}N\right)(1+\frac{V_t}{V_{oc}}\ln X)X^{-1/2} \tag{17}$$

From (16), we predict total efficiency $\eta = 26.26\% + 0.079N(\%) = 28.63(\%)$ (with FF=0.85, X=400, V_{oc}=1.051V, V_t=0.025eV, N=30). On the other hand, collection efficiency at 400 suns for 50 periods will increase efficiency to 30.21%. The advantage of higher efficiency, at greater N values, is depicted in Figure 4 below:

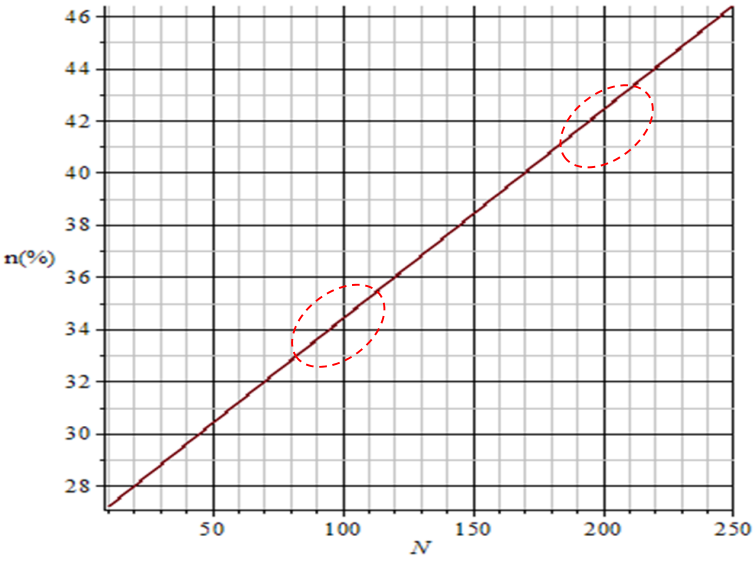

Figure 4. Collection efficiency vs number N of 5nm-Ge layers in the intrinsic region of a GaAs p-i-n cell. Note that 42% is feasible with 200 periods at 400 suns (XP_{in}=400mW/cm^2).

Note from Figure 4, that 42% collection efficiency can be expected at 400 suns and at large number of superlattice periods (N ~ 200). By using (11) in (17) we propose the total efficiency as the sum of two conclude by re-writing as the sum of two factors bulk efficiency and excess efficiency:

$$\eta(\%) = \eta_{bulk} + \delta\eta = \eta_{bulk} + (1.557FF) \times \frac{NX^{-1/2}V_{oc}^{'}}{P_{in}} \tag{18}$$

Expression (17) essentially predicts excess efficiency $\boldsymbol{\delta\eta}$ of a cell, enriched with an embedded N-period superlattice, under concentrated power equivalent to X suns. We would also like to see excess efficiency against X at a fixed N: (17) can be re-written:

$$\eta = \eta_{bulk} + \delta\eta = 26.26 + \frac{1.323(N)}{P_{in}\sqrt{X}}(V_{oc} + V_t \ln X)) \tag{19}$$

Note however from (18) that the excess efficiency δη strongly depends on $X^{-1/2}$ and N. High X "slows down" excess efficiency as shown from Figure-5:

Note from Figure-5 that high X does not necessarily mean better performance; at 100 and 400 suns, 30 SL layers in the intrinsic region will provide 30.88% and 28.63% collection respectively;

http://dx.doi.org/10.5772/59039

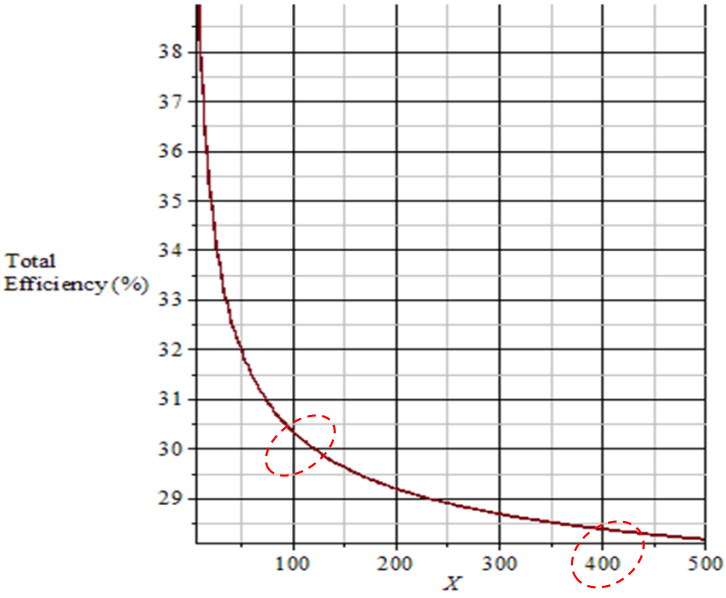

Figure 5. Efficiency vs number of suns X, with 30 superlattice layers in the intrinsic region. Excess efficiency decreases with X (see (18)). Note higher efficiencies at lower irradiances.

this is because excess efficiency gains (δη) drop quickly with X (Fig. 5 and expression (18)); high concentration does not increase the second term of (17) or (18). For instance, compromising with N=50 periods, 100 suns would suffice for excess efficiency δη=7.7% (or total efficiency of 25.50+7.7=33.20% according to (18). As the concentration increases, the excess term decreases down to the bulk cell's efficiency. On the other hand, as long as the concentration is kept between 100 and 500 suns, considerable increase in efficiency is plausible as seen in Figure 5. A summary of cell performance improvement is shown below (Table 1) where (i) bulk cell at one sun (ii) bulk cell at 400 suns and (iii) hybrid cell at 400 suns is depicted.

Table-1 summarizes some results predicted at 1 and 400 suns respectively; note (a) ideal efficiency at 400 suns with varying period number N.

Cell properties & conditions	**GaAs p-i-n cell**	**GaAs p-i-n cell (no SL)**	**Hybrid cell with GaAs/Ge superlattice (SL)**
J_L (mA/cm^2)	25.73	$400J_L$	31.14 (X = 400, N = 1)
V_{oc} (V)	1.051	1.201	1.201
FF	0.94	0.85, **[(FF) = 0.85, X > 100]**	0.85

Cell properties & conditions	GaAs p-i-n cell	GaAs p-i-n cell (no SL)	Hybrid cell with GaAs/Ge superlattice (SL)
X (suns)	1	400	400
η (%)	25.42	26.26	28.63 (N =30) 30.21 (N= 50)[16] 32.58 (N = 80) 38.11 (N 150) 42.06 (N = 200) 52.33 (N = 330)

Table 1. Bulk and hybrid cell at 1 and 400 suns (P_{in}=100mW/cm^2, X=1); The bulk p-i-n GaAs cell is simulated as a standard 1-cm^2 PV device.

Notice improvements in the efficiency of the bulk pin GaAs cell: from 25.42% (X=1) to 26.25% (X=400) and 28.63% at X=400, N=30, and 30.21% at X=400, N=50 (compare with Fig-16 of reference [16] good agreement in overall efficiency for p(GaAs)-I(quantum well)-n(GaAs) strained-layer cell).

Table-2 below summarizes improvements on cell performance:

Hybrid cell OC-voltage $V'=V_{oc}+V_t \ln X$	X(suns)	δ/N	Excessefficiency δη (%)	Bulk cell Efficiency,	Hybrid cell Efficiency [b]
1.166	100	0.154	7.70	25.50	33.20
1.183	200	0.111	5.55	25.87	31.42
1.194	300	0.091	4.55	26.11	30.66
1.201	400	0.079	3.95	26.26[a]	30.21
1.206	500	0.071	3.55	26.37	29.92

[α]: (25.73) ($V_{oc}+V_t$ lnX) (0.85)=26.26%; [b]: N=50.

(Where $\delta = \frac{1.323 V'_{OC}}{P_{in}\sqrt{X}}$ (see (18)), and V_{OC} (bulk, one sun)=1.051V).

Table 2. Comparison between bulk and hybrid cell at various solar concentrations

Note that 50% efficiency is feasible by posing the question: what is the N value in the intrinsic region of the host cell at a given X? Table 3 below summarizes device design for high performance; for instance, 50% efficiency is feasible with a 1.5 μm superlattice at 400 suns. Table 3 summarizes and compares bulk and hybrid cell performance at different concentration levels. For instance, note that 50% efficiency is feasible under 300 suns with 260 Ge layers. Of course, cost reduction and high efficiency levels would lead to the obvious choice (Table-3)

http://dx.doi.org/10.5772/59039

with 100 suns illuminating a 160-period superlattice in a p-i-n GaAs cell with 10 um-long intrinsic region.

X (solar concentration)	Bulk η(%) GaAs pin cell	δη(%) GaAs-Ge (SL)	η + δη (%) Hybrid cell combined efficiency	N Number of SL periods	L_{SL}(μm) Total length of SL region	L_{SL}/L_i SL region vs i-region of control cell
100	25.50	24.50	50.00	160	0.800	8%
200	25.87	24.13	50.00	220	1.100	11%
300	26.11	23.89	50.00	260	1.300	13%
400	26.26	23.74	50.00	300	1.500	15%
500	26.37	23.63	50.00	330	1.650	16.5%
600	26.48	23.40	50.00	360	1.800	18%

Table 3. Choice of number N periods for 50% total ideal efficiency at different solar concentrations X; the last column indicates the length of the SL region (length of intrinsic region L_i=10μm); last column compares superlattice vs intrinsic region widths. We set a lowest limit of X=100 to ensure negligible dark carrier concentration (see also expression (7)). High X increases current but not necessarily the efficiency.

Table-3 above is an extrapolation to higher efficiencies, feasible through the proposed structure (Figure 6). We set a limit at 50% and simulate the feasibility of the structure proposed. The latter is a p-i-n cell with a superlattice in the middle of the intrinsic region; the superlattice is illuminated at X-suns and produces excess thermionic current density from two-dimensional systems (quantum wells). The most reasonable choice is indicated by the first row of Table-3, where 50% can be reached (X=100, N=160; η=50%). Such designs and high efficiency options are perfectly suited for concentration photovoltaics (CPV); note also that maturity of (a) current light-concentrating systems and (b) device enrichment via routine MBE growth-techniques make the proposed design reasonable for production. On the other hand, three junction cells (MJ) are equally complicated structures because they include three cells in series with highly doped AlGaAs/GaAs tunnel-junctions linking them. Our proposed cell is a bulk GaAs cell enriched with a matched N-period superlattice and without the need of any tunnel junction. The proposed device relies on the bulk properties of a GaAs cell which in turn is enriched with an implanted superlattice strip that provides excess current under X > 100. Its twofold-advantage over current multi-junction (MJ) cells is (a) absence of top cell (hence no photon shadowing effects) and (b) absence of tunnel junctions (TJ). Such a superlattice grown in the mid-intrinsic region of an all-GaAs p-i-n solar cell illuminated at X suns is depicted in Figure-6 below. Light is supposed to be focused on the interior of the device covering the superlattice where 1eV photons are expected to be strongly absorbed and from where photo-carriers are expected to thermionically escape.

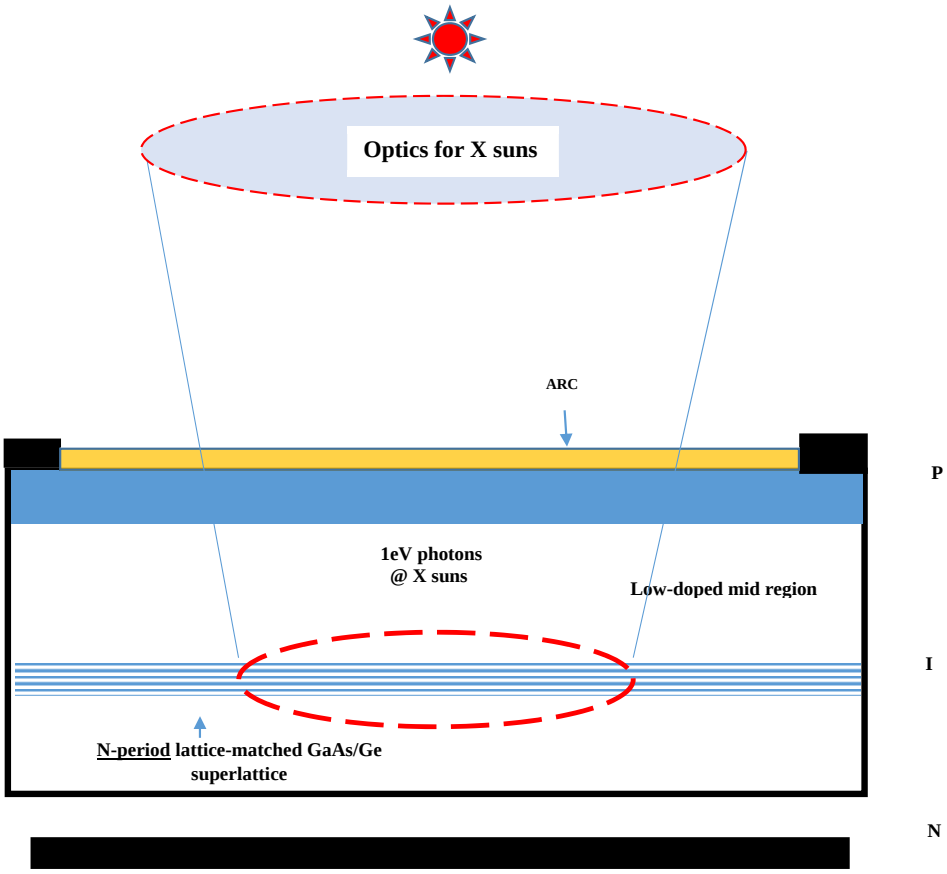

Figure 6. Concentrated solar radiation incident on a 1-cm² GaAs p-i-n cell with a GaAs/Ge lattice-matched superlattice (SL) in its intrinsic region. Total efficiency of the hybrid cell is the sum of bulk cell efficiency η and excess efficiency. Implanted SLs in the bulk are feasible based on routine MBE techniques [15]. Details of the optical system and the spot covering most of the SL region are under study.

As seen from Figure 6, a superlattice can become the source for excess carriers in the conduction band if light can be concentrated on it inside the pin cell. This is an immediate advantage: the SL region generates excess carriers and causes efficiency increase δη as seen in expression (18):

$\delta\eta = \frac{1.323(N)}{P_{in}\sqrt{X}}(V_{oc} + V_t \ln X)$; (No losses due to excess carrier scattering are assumed, see also [12])

Figure-6 presents the main concept: a lattice-matched superlattice in the middle of the bulk GaAs i-layer of the control cell and illuminated at X suns improves cell performance through thermionic escape of photo-electrons from individual quantum wells. In our analysis we

http://dx.doi.org/10.5772/59039

assume 100% escape rate of these electrons from their quantum traps [12] and an ideal device performance in terms of quality factors and shunt resistance.

4. Conclusions

A different type of multijunction cell structure is proposed in this chapter. The multijunction term refers to a proposed lattice-matched superlattice, grown in the bulk of the intrinsic region of a p-i-n cell; current high efficiency cells are basically designed as a top-cell/bottom-cell tandem arrangement, on GaAs or Ge. These cells are in-series connected via tunnel junctions and the whole structure is illuminated at high solar irradiance [13, 14, and 16]. We demonstrate the case for higher efficiencies achievable in GaAs p-i-n solar cells through embedded lattice-matched superlattices in the intrinsic region. Our model is based on thermionically escaping carriers from individual quantum wells of the superlattice in the intrinsic region of the p-i-n control cell. The total carrier concentration in quantum wells is the sum of (a) photo-excited carriers and of (b) carriers that occupy eigen-energy levels under dark. The total population in each quantum well is dominated by photo-carries at highly concentrated incident solar light. The latter has been the major approximation in our model, namely, the photocarrier population is much greater than the bulk and quantum well populations respectively in each and every quantum trap in the cell. We then proposed a p-i-n device that includes a superlattice structure in the middle of its intrinsic region, a superlattice layer composed of GaAs/Ge units (the low gap material is in essence the quantum well: Ge). The advantages of such a proposal are (a) concentrated light on the cell (X=400 suns) produces excess thermionically escaping carriers (b) these carriers may overcome the potential barriers of the superlattice region and contribute excess photo-current that depends strongly on concentration level X and on the number of superlattice (SL) periods N and (c) the SL region is only a small fraction of the total device length. Our results stand in good agreement with efficiency improvements of standard designs of tandem/multijunction cells. We simulate a GaAs control/reference device hosting a superlattice embedded in its intrinsic region that can generate appreciable currents at 400 suns. Specifically, a 26.26% efficient all-GaAs control solar cell (X=400) increases its efficiency to 30.21% when a 50-period GaAs/Ge-superlattice is grown in its intrinsic region. Excess collection efficiency depends on the period number of the superlattice and the concentration level. We claim that 50% efficiency levels are feasible for p(GaAs)-i(GaAs/Ge-SL)-GaAs cells with either 330 periods at 400 suns or 160 period under 100 suns. The sequence of steps for high cell performance is outlined in the figure below:

The sequence shown above describes the steps undertaken in this chapter. The control cell is the primary choice that provides the fundamental efficiency of the cell. The superlattice unit, which is a small fraction of the mid-region of the control cell, can be implanted in the cell as a lattice-matched layer. Generalizing we show that cell efficiency may increase by means of a superlattice implanted in the mid of a p-i-n GaAs cell according to the formula:

$$\eta(\%) = 26.26 + \left[(N)(W) \frac{1.323(V_{OC} + V_T \ln(X))}{P_{in}\sqrt{X}} \right]; X \geq 100 suns$$

Where N is the superlattice number of periods, W is the probability of excess carriers being collected [12], P_{in} is the incident solar power, V_T is the thermal voltage. The proposed design is ideal for concentrated photovoltaics (CPV): small size cells (therefore reduced material costs) and low-cost optics.

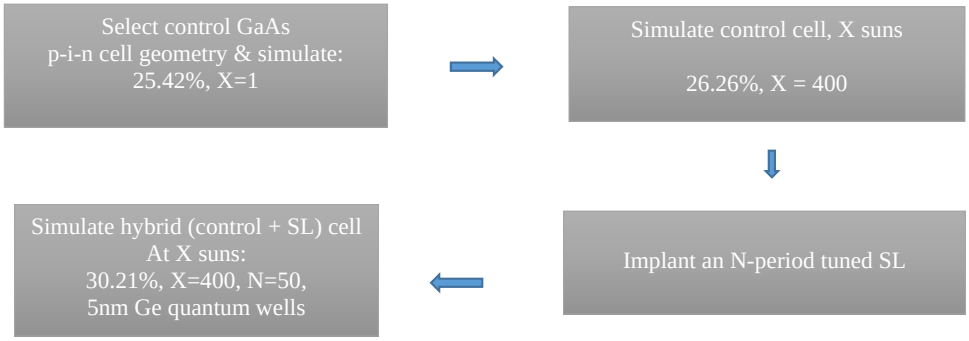

Figure 7. Four steps for hybrid cell simulation

Author details

A.C. Varonides

Physics & Electrical Engineering Dept. University of Scranton, USA

References

[1] www.pveducation.org/pvcdrom/appendices/standard-solar-spectra

[2] RK Pathria, Statistical Mechanics, Pergamon Press, 1972

[3] van der Ziel, Solid State Physical Electronics, Prentice Hall, 1968

[4] O Manasreh, Semiconductor Heterojunctions and Nanostructures, McGraw Hill

[5] S Dimitrijef, Principles of Semiconductors, Oxford U Press 2012

[6] M Shur, GaAs Devices and Circuits, Plenum 1987

http://dx.doi.org/10.5772/59039

[7] AC Varonides, work in progress

[8] H Unlu, A Nussbaum, Band discontinuities as Heterojunction Device Design Parameters, IEEE Transactions on Electron Devices, Vol. ED 33, No 5, May 1986

[9] Capasso/Margaritondo, Heterojunction Band Discontinuities, North Holland 1987

[10] Sze and Lee, Semiconductor Devices, John Wiley, 3d Ed, 2010

[11] PC1D, Version 5.0 (1997) University of New South Wales, Serial # 5034

[12] AC Varonides, Escape rate of thermionic electrons from highly illuminated superlattices, work in progress (EMRS 2015, 30th European PV, 2015)

[13] JM Olson, DJ Friedman, S Kurz, High Efficiency III-V Multijunction Solar Cells, Handbook of Photovoltaic Science and Engineering, Ed. A Luque and S Hegedus, 2003, John Wiley & Sons, Ltd ISBN: 0-471-49196-9

[14] C Algora, Next generation photovoltaics: high efficiency through full spectrum utilization, Marti & Luque editors, Institute of Physics Publ. (Bristol) 2004

[15] DK Ferry, Editor-in-Chief, Gallium Arsenide Technology, Vol II, Howard W. Sams & Company, 1990.

[16] JG Adams, BC Browne et al, Recent results for single-junction and tandem quantum well solar cells, Progress in Photovoltaics Res. Appl., pp 865-877, 2011.

Chapter 7

Deep Level Transient Spectroscopy: A Powerful Experimental Technique for Understanding the Physics and Engineering of Photo-Carrier Generation, Escape, Loss and Collection Processes in Photovoltaic Materials

Aurangzeb Khan and Yamaguchi Masafumi

Additional information is available at the end of the chapter

http://dx.doi.org/10.5772/59419

1. Introduction

Deep Level Transient Spectroscopy (DLTS) is an efficient and powerful method used for observing and characterizing deep level impurities in semiconductors. The method was initially introduced by D. V. Lang [1] in 1974. DLTS is a capacitance transient thermal scanning technique, operating in the high frequency (Megahertz) range. It uses the capacitance of a p-n junction or Schottky barrier as a probe to monitor the changes in charge state of a deep centre. The capacitance techniques [2-10] used before DLTS lacked either in sensitivity, speed, range of observable trap depths, or the spectroscopic nature, thus rendering the techniques inadequate for a complete characterization of a deep level. DLTS has the advantage over all the techniques used to-date in that it fulfils almost all the requirements for a quick and complete characterization of a deep centre. DLTS is a technique, which is sensitive enough, rapid and easy to analyze. It is able to distinguish between majority- and minority-carrier traps [2]. DLTS can also give the concentrations, energy and capture rates of both kinds of traps. It is spectroscopic in the sense that it can also resolve signals due to different traps. In the many variants of the basic DLTS technique the deep levels are filled with free carriers by electrical or optical methods. Subsequent thermal emission processes give rise to a capacitance transient. The transient is analyzed by signal processing while the temperature is varied at a constant rate. This results in a full spectroscopic analysis of the semiconductor band-gap.

For a complete understanding of DLTS we must have some basic knowledge of capacitance transients arising from the depletion region of a p-n junction. The use of capacitance transients for studying the properties of defect centers is well known [4-6]. These transients provide

information about an impurity level in the depletion region by observation of the capacitance transient originating from the return to thermal equilibrium after a perturbation is applied to the system. A brief description of the capacitance change due to the change in occupancy of the deep levels in the depletion region is given below.

2. p-n junction capacitance

When voltage across a p-n junction is changed, there is a corresponding change in the depletion region width. This change in width causes a change in the number of free charge carriers on both sides of the junction, resulting in a change in the capacitance. This change has two contributions; a) the contribution due to change in depletion width known as the junction capacitance and b) the contribution due to change in minority carrier concentration called the diffusion capacitance. Junction capacitance is dominant under reverse biased conditions while diffusion capacitance is dominant under forward biased conditions.

Consider a p-n junction with a deep level present having its energy as E_T. In steady state there is no net flow of charge carriers across the trap. Also the electron and hole densities within the depletion region are negligible. Thus from Shockley and Reed [11] and Hall [12] the relationship between the total density of deep sates N_T and density of filled traps is given by

$$e_p n_T = \left(e_n + e_p\right) N_T \tag{1}$$

where e_p is the hole emission rate, e_n is the electron emission rate, n_T is the density of filled traps, and N_T is the total density of deep sates.

or

$$n_T = \left(\frac{e_p}{e_n + e_p}\right) N_T \tag{2}$$

which gives the density of filled traps n_T under steady state conditions.

Now if the system is perturbed, this number changes and will thus cause the total charge in the depletion region to increase or decrease, leading to a corresponding change in the capacitance. This change is only due to deep levels.

For a simple analysis of the response of the diode and interpretation of results, the junction is assumed to be asymmetric. An asymmetric diode is one in which one side of the junction is much more heavily doped than the other, implying that the space charge region is almost exclusively on the low doped side as shown in Figure. 1(a). Here we will consider a p^+n diode with an electron emitting level. The depletion region is thus on the n-side. Figure 1 (b)

http://dx.doi.org/10.5772/59419

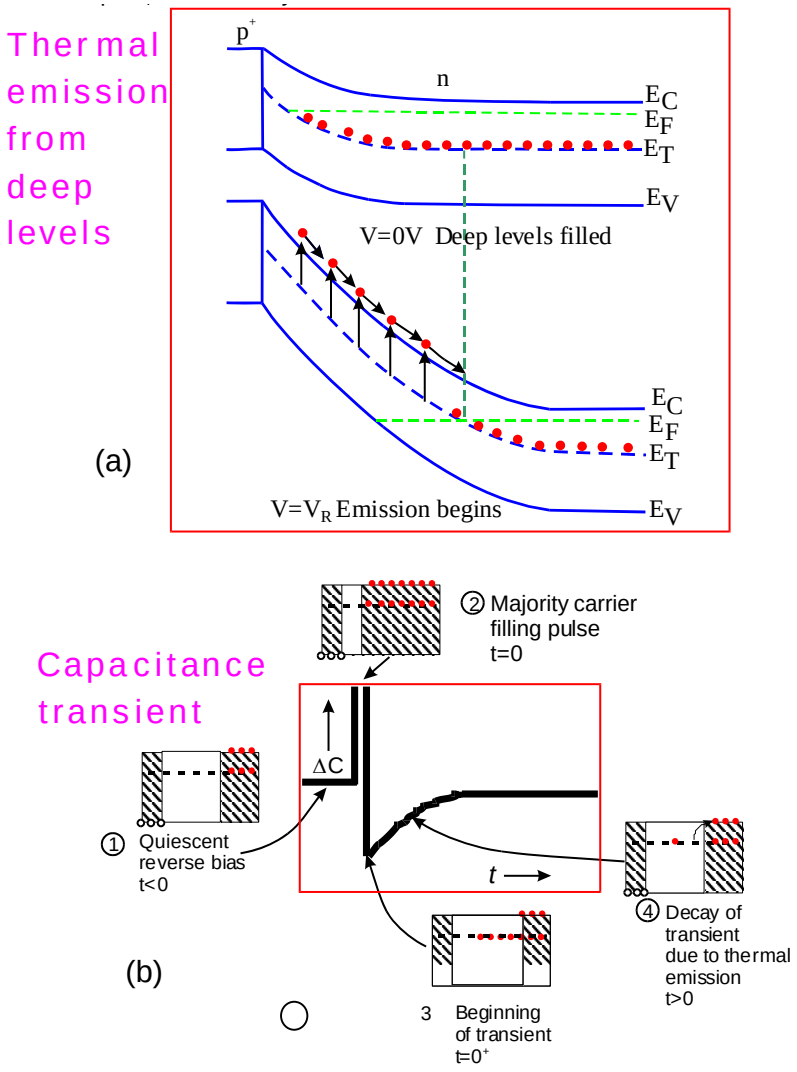

Figure 1. Basic concept of thermal emission from a deep level and capacitance transient (a) energy band diagram of a p^+n junction with an electron trap present at energy E_T at zero applied bias and at steady reverse bias V_R, (b) isothermal capacitance transient for thermal emission of the majority carrier traps. The condition for the trap occupation and free carrier concentration during various phases 1-4 of the transient are also shown. The part not shaded in the insets 1-4 shows space charge width (after Lang [1]).

schematically shows four processes of generating a capacitance transient due to majority carrier level.

Process (1) shows the diode in the quiescent reverse bias condition. Traps in the space charge region are empty because no free carriers are available for capture (t<0). Process (2): reverse

bias is reduced to zero by a majority carrier pulse. The electrons are capture in the deep levels (t=0). The sharp raise in capacitance is due to the collapse of the depletion region. Process (3): when the reverse bias is restored, the capacitance drops to a minimum value because the electrons are trap in the depletion layer ($t=0^+$). Process (4): decay of the transient due to thermal emission of the trapped electrons (t>0).

Suppose we have a reverse bias V_R applied to the sample and it is decreased for a short time to zero. Then electrons will flow into what was previously the depletion region and the levels in this volume will capture electrons (Figure. 1[a]). Neglecting the re-emission of electrons (i.e. temperature is low enough) we get:

$$\frac{dn_T}{dt} = c_n\left(N_T - n_T\right) \tag{3}$$

where c_n is the capture time constant of electrons

Now if bias pulse is long enough i.e. $t_p >> \frac{1}{c_n}$, all levels will be filled and $n_T = N_T$. Next the sample is returned to quiescent reverse bias V_R and thus the depletion region is again depleted of free carriers. The electron emitting traps now start to emit and n_T will vary with time. This variation is given by with n= p= 0 i.e.

$$\frac{dn_T}{dt} = e_p N_T - \left(e_n + e_p\right)n_T \tag{4}$$

The solution to this is given by

$$\begin{aligned} n_T(t) &= \left[\frac{e_p}{e_n + e_p}N_T + \frac{e_n}{e_n + e_p}N_T \exp\left(-\left(e_n + e_p\right)t\right)\right] \text{for } t > 0 \\ &= N_T \text{ for } t < 0 \end{aligned} \tag{5}$$

Thus n_T decreases exponentially with a time constant:

$$\tau = 1/\left(e_n + e_p\right) \tag{6}$$

Now for an electron emitting centre $e_n \gg e_p$. Equ. (5) then reduces to:

$$n_T(t) = N_T \exp\left(-e_n t\right) \tag{7}$$

Thus the amplitude of the transient describing the filled level population gives the measure of trap concentration, while the time constant gives the emission rate of electrons:

http://dx.doi.org/10.5772/59419

$$\tau = 1/e_n \tag{8}$$

The variation of occupancy with time gives information about the emission rate but it is not possible to measure the occupancy directly. The simplest indirect method is to measure the capacitance changes of the p-n junction associated with the occupancy changes.

The equation governing the capacitance of a p-n junction is the same as that of a parallel plate capacitor i.e.

$$C = \frac{\varepsilon A}{W} \tag{9}$$

where

$$W^2 = \frac{2\varepsilon\left(V_b - V\right)\left(N_D + N_A\right)}{qN_D N_A} \tag{10}$$

ε is the relative permittivity of the material, V_b is the built-in voltage, V is the applied voltage, q is the electronic charge, N_D and N_A are the donor and acceptor concentrations, W is the depletion region width and A is the junction area.

For a p^+n junction, including the contribution of the filled traps in the depletion region, this becomes:

$$W^2 = \frac{2\varepsilon\ \left(V_b - V\right)}{qN_D^*} \tag{11}$$

where $N_D^* = N_D - n_T$

Now for n_T « N_D one can expand and get the following result:

$$C = C_0\left(1 - \frac{n_T}{2N_D}\right) \tag{12}$$

where C_0 is the capacitance at reverse bias (V_R).

By taking into consideration the time variation of n_T, we get:

$$C(t) = C_0\left[1 - \frac{N_T}{2N_D}\exp\left(-\frac{t}{\tau}\right)\right] \tag{13}$$

Thus the emission rates and trap concentrations can be determined from the changes in the capacitance of a p-n junction due to bias pulses. These changes are in the form of capacitance transients.

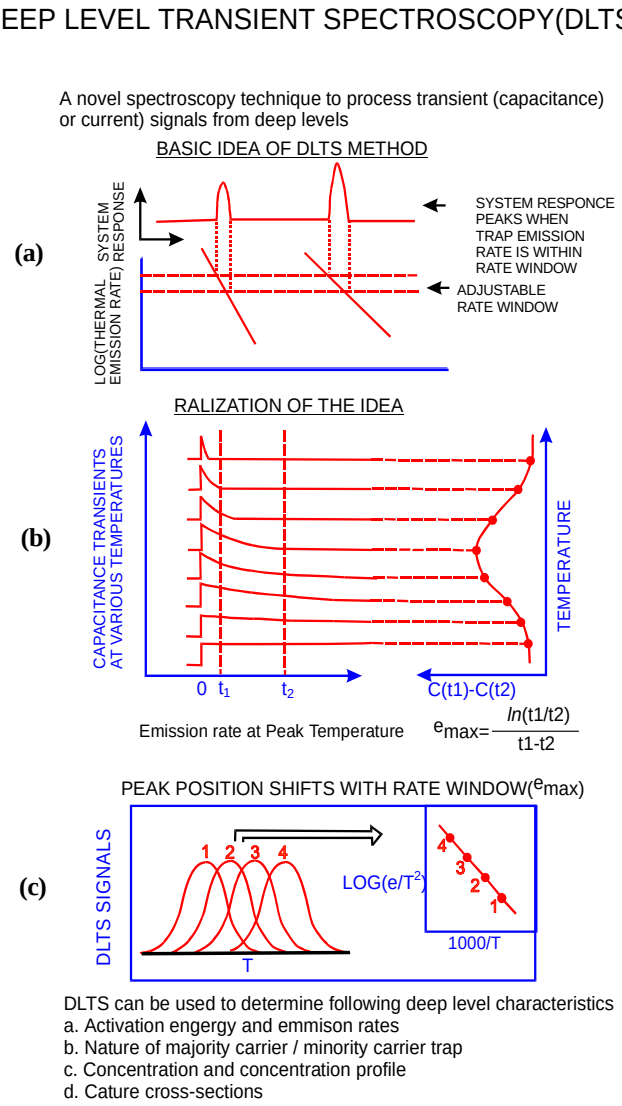

Figure 2. Diagram illustrating the basic principles of DLTS (a) the rate window concept (after Lange [1]), (b) application of the rate window concept using a time filter such as dual-gate box car shown here (after Lange [1]), (c) showing the shift of the peak positions in temperature with the rate window and the Arrhenius plot obtained from the peak positions ([31].

http://dx.doi.org/10.5772/59419

3. Basic methodology of DLTS

The capacitance transients of Eq. 13 can be obtained by holding the sample at constant bias and temperature and applying a single filling pulse. The resultant isothermal transient can then be analyzed to obtain the emission rate of the carriers at that particular temperature. For obtaining a wide range of emission rates, this is a time consuming technique. Also if a lot of deep levels are present, the experiment and its analysis become difficult. This is where DLTS has a major edge over the conventional techniques.

The essential feature of DLTS [1] is its ability to set up a *rate window* so that the measuring apparatus gives an output only when a transient occurs with a rate within the window. This concept is illustrated in Figure 2 (adopted with permission from IEEE Proc. of WCPEC-4, 2006, p. 1763).Thus if the sample temperature is varied at a constant rate, causing the emission rate of carriers from defect center(s) present in it to vary, the measuring instrument will give a response peak whenever the defect center emission rate is within the window. Instead of talking about rate window, we can say that the DLTS technique uses a time filter, which gives an output signal only when the transient has a time constant coinciding with the center of the time window of the filter. A very important property of such a filter (time or rate) is that the output is proportional to the amplitude of the transient. Thus we can excite the diode repeatedly while the temperature is varied and by scanning over a large temperature interval we can directly get information as to which levels are present, what are their concentrations and by using different time/rate windows we can obtain the thermal activation energies of the levels.

There are many ways of constructing a time filter. One of the widely used methods is one in which a variation of the dual-gate boxcar integrator is employed. It precisely determines the emission rate window and provides signal-averaging capabilities to enhance the signal-to-noise ratio, making it possible to defect center having very low concentrations. The use of a double boxcar for rate window selection is illustrated in Figure 2b. The capacitance transients are observed on a fast-response capacitance bridge. A series of transients for a typical defect center are shown on the left-hand side of Fig. 2.8b. These transients are fed into the double boxcar with gates set at t_1 and t_2. The boxcar measures the capacitance at the two times t_1 and t_2. The difference $C(t_1)$ - $C(t_2)$ = ΔC is calculated. It is clear from the figure that this ΔC goes through a maximum. This ΔC after going through some filtering is converted into the DLTS output S(T) given by (assuming an exponential transient):

$$S(T) = \Delta C_0 \left[\exp(-t_1 / \tau) - \exp(-t_2 / \tau) \right] \tag{14}$$

where ΔC_o is the capacitance change due to the pulse at time t = 0.

It can easily be seen that S(T) really has a maximum for a certain time constant τ_{max}. First consider a transient that is very rapid. Then it has already finished before the first gate opens and hence $C(t_1) = C(t_2)$, and S(T) =0. Similarly when the transient is too slow, it will not change much between the two gates and so again S(T) =0. Thus there will be an output with some maximum value S_{max} only for transients having time constants in between these two.

We can get τ_{max} by differentiating S with respect to t and setting the derivative equal to zero. This gives:

$$\begin{aligned}\tau_{max} &= (t_1 - t_2)/\ln(t_1/t_2) \\ &= (x-1)t_1/\ln(x)\end{aligned} \tag{15}$$

where $x = t_2/t_1$

Substituting this value in the expression for S gives S_{max} as:

$$S_{max} = \Delta C_0\left[\exp(-\ln(x)/(x-1)) - \exp(-x\ln(x)/(x-1)\right] \tag{16}$$

Thus it is seen that the peak height is independent of the absolute value of t_1 and t_2, rather it depends upon their ratio. Moreover, it is seen that S_{max} is proportional to ΔC_o and therefore to the defect centre concentration N_T. Therefore, the DLTS peak height can directly give the defect centre concentration.

4. Parameters characterizing deep levels by DLTS technique

Below are described some of the ways in which the DLTS technique can be used to study defect centers in semiconductors and to obtain their different characteristic parameters.

4.1. Deep level concentration

As mentioned in the previous section the DLTS signal S is proportional to the magnitude of the capacitance transient ΔC. Equation (12) can be rewritten as

$$\frac{\Delta C}{C_0} = \frac{N_T}{2N_D}$$

where it is assumed that all the traps have been filled.

4.1.1. Transition Distance, λ

The DLTS peak height gives a direct measure of the deep level concentration. Here it must be remarked that in obtaining Eq. (12) the edge region contribution has been neglected. Figure 3 illustrates the edge region in a p-n junction under zero and reverse bias. The distance between the edge of the depletion layer and the point where the Fermi level crosses the trap level is referred to as the transition distance, λ, given by.

http://dx.doi.org/10.5772/59419

$$\lambda = \sqrt{\frac{2\varepsilon\ \varepsilon_0(E_F - E_T)}{q^2 N_D}} \tag{17}$$

where ε_0 and ε are the permittivity of vacuum and of the material, E_f is the Fermi level, E_T is the trap energy level above the valence band, q is the electronic charge and the carrier concentration p is essentially equal to the acceptor concentration, N_a.

In the absence of deep levels and when the doping is uniform, plots of $1/C^2$ vs V are straight lines. However, if the criterion $N_T << N_a$ is not met then the additional capacitance of the charge trapped by deep levels within the distance λ contributes to the measured depletion capacitance. This produces a shoulder in the $1/C^2$ vs V plot at low reverse bias. Also the apparent carrier concentration, $N_{measured}$, as a function of distance, x, deduced from the derivative dC \dV from the same C-V data becomes approximately (for a *uniform* distribution of a single compensating trap level) [13].

$$N_{measured}(x) = N_a(x) - \frac{\lambda}{w} N_T(x) \tag{18}$$

DLTS monitors the capacitance transient associated with the gradual emission of charge from trap centers when the depletion layer is abruptly widened by increasing the applied reverse bias (e. g. switching from V=0 as in Figure. 3a) to V=-V as in Figure 3b)). The calculation of the trap concentration must take into account the fact that the volume within which the charge state of the traps is changed upon the increase of reverse bias and which therefore contributes to the DLTS signal (corresponding to the interval x_2-x_1 in Figure 3) is different to the volume by which the depletion layer is increased (w_2-w_1 in Figure 3).

For exponential transients, this leads to the approximate expression for the trap concentration,

$$N_T = 2\frac{\Delta C}{C} N_a \left(\frac{w_2^2}{x_2^2 - x_1^2} \right) \tag{19}$$

where

$$x_1 = w_1 - \lambda \tag{20}$$

and

$$x_2 = w_2 - \lambda \tag{21}$$

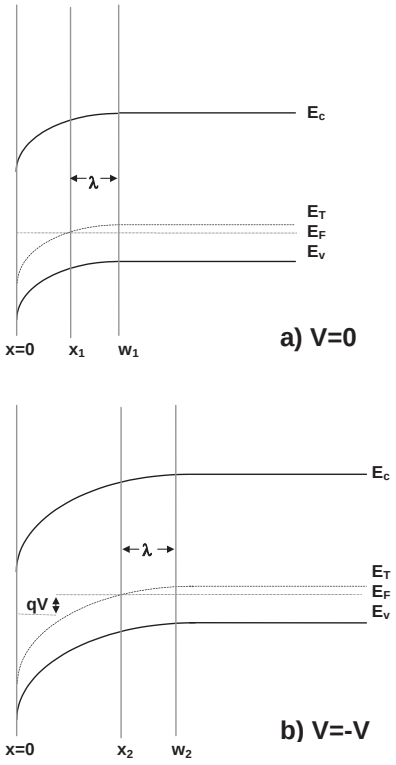

Figure 3. Band diagram of p-type material close to an n+\p junction indicating a deep level at energy E_T above the valence band a) with zero applied bias and b) with applied reverse bias of -V.

The activation energy for emission and the capture cross section of the trap are deduced from an Arrhenius plot of the DLTS maxima as a function of temperature.

As an example of the importance of the inclusion of the transition distance in the calculations, in the case of a sample irradiated with 3 x 10^{16}e /cm^2, p=4 x 10^{14} /cm^3, E_f=0.09 eV at 125K and thus for the di-vacancy with E_T=E_V+0.18 eV, E_f - E_T =0.011 eV. Application of Eq. (17) gives λ=0.48 μm. The Fermi function is of the order of 10^{-3} and to a close approximation the trap is filled with holes. During a fill pulse from -2V to 0V, the depletion region is collapsed from a width of 3 μm at a quiescent bias of -2V to 1.6 μm at zero bias. Thus application of Eqs. (18) to (21) results in an increase of a factor 1.9 in the calculated trap concentration in comparison with the value obtained if the transition distance is ignored.

4.1.2. Non exponential transients

When the condition $N_T << N_a$ is not fulfilled, there is a significant probability that emitted charge will be recaptured before it can be swept out of the depletion region, leading to a non-exponential capacitance transient. In this case, Eq. (19) is no longer appropriate. Several

http://dx.doi.org/10.5772/59419

analyses of this situation exist [1,14] and we have considered the method of Stievenard et al. [13] to calculate a non-exponential transient analysis. In this case, if the transition region is negligibly small then the capacitance transient can be written as

$$\frac{\Delta C}{C} = 1 - \sqrt{1 - \frac{z}{1+z}\exp(-et)} \tag{22}$$

where $z=N_T/N_a$

4.2. Majority carrier emission rates

The simplest way in which the DLTS technique can be used is the measurement of majority carrier emission. The pulse sequence used is shown in Figure 1b, along with the band diagram and the capacitance transient resulting from such a sequence. The bands have been assumed to be flat for simplicity. The method consists of employing a sufficiently large bias over the sample so as to overcome the edge effects and at the same time be small enough to of lesser value than the break down voltage of the semiconductor. The sample is cooled below the starting measurement temperature. Now bias pulses close to zero volt are repeatedly applied while the sample is reheated. During the pulses, the levels are filled with majority-carriers. As soon as the sample returns to the quiescent reverse bias, the levels start emitting resulting in a transient. During the transient, the capacitance is measured at the pre-set rate window and the DLTS output is plotted as a function of the temperature. Thus we get a peak for each level which has an emission rate within the pre-set time window in the temperature range of scan. The temperature dependence of the emission rate is determined by observing the peak position for several different time windows.

4.3. Minority carrier emission rates

For the observation of minority carrier emission, we have to first fill the level with minority carriers. This is accomplished through minority carrier injection by forward biasing the diode so that a current flows. After the end of the bias pulse, as the sample returns to the quiescent reverse bias, the deep level will emit minority carriers giving rise to a transient. Thus the DLTS measurement is the same as for the majority carrier emission except that the sign of the peak (transient) is now opposite.

4.4. Activation energy

Under thermodynamic equilibrium, the emission rates and the capture coefficients of a deep level are related according to the following equations:

electron emission,

$$e_n = \sigma_n \langle v_n \rangle_{th} N_C \exp\left(-\frac{E_C - E_T}{kT}\right) \tag{23}$$

where σ_n is the capture cross-section and $\langle v_n \rangle_{th}$ the average thermal velocity of the electron, and N_c is the effective density of states in the conduction band.

hole emission,

$$e_p = \sigma_p \left\langle v_p \right\rangle_{th} N_V \exp\left(-\frac{E_T - E_V}{kT} \right) \tag{24}$$

where σ_p is the capture cross-section and $\langle v_p \rangle_{th}$ the average thermal velocity of the hole, and N_V is the effective density of states in the valence band.

Thus the emission rate variation with temperature is given by

$$e_{n,p} \propto \exp(-1/T) \tag{25}$$

Hence a plot of log(e) versus $1/T_{pk}$, where T_{pk} is the temperature position of the peak in the corresponding time window, gives a straight line with the slope $-E_A/kT$, where E_A is the activation energy of the level. Such a plot is known as an Arrhenius Plot. From the intersection of the plotted line with 1/T = 0, the capture cross-section $\sigma_{n,p}$ at T = ∞ can be calculated.

One may often encounter plots of $\log(e/T^2)$ versus 1/T instead of log(e) versus 1/T. The factor T^2 comes in because of the temperature dependence of $\langle v_{th} \rangle$ and effective density of states $N_{C,V}$. The activation energy thus obtained may still not be the true activation energy because in some cases, the capture cross-section is found to be temperature dependent. Thus the true thermal activation energy in such cases would be obtainable if the temperature dependence of capture cross-section is first determined independently and then the relevant correction is applied to the apparent activation energy.

4.5. Measurement of capture cross-section

The third important parameter for identifying a defect centre is the capture cross-section $\sigma_{n,p}$. One can extrapolate the Arrhenius plot to 1/T = 0 and obtain the capture cross-section at T = ∞ from the intercept. But this usually leads to a far from true value of the capture cross-section because of the following two reasons: a) $\sigma_{n,p}$ may be temperature dependent and hence the extrapolation is not valid; b) a slight error in extrapolation may lead to several orders of magnitude difference in values of capture cross-section. Hence, the capture cross-section must be directly measured whenever possible and over as long a range of temperatures as possible.

Measurement of majority carrier capture cross-section is relatively simple as compared to minority carrier capture cross-section measurements. A fixed emission rate is chosen and DLTS scans carried out while the filling pulse-width is varied from scan to scan. As the pulse width increases from a small value so does the peak height until for a certain value of pulse width, it reaches a maximum i.e. at this value all defect centers are completely filled during a single

http://dx.doi.org/10.5772/59419

saturation pulse. The peak height is related to the filling pulse width t_p via the following equation:

$$1-S/S_{\infty} = \exp(-t_p / \tau) \tag{26}$$

where S is the peak height for any pulse width t_p and S_∞ the saturated peak height.

The slope of $\ln(1-S/S_\infty)$ versus t_p gives $1/\tau$.

now

$$\sigma_n = 1/(\tau n \langle V_{th} \rangle) \tag{27}$$

Thus capture cross-section is known if n and $<v_{th}>$ are known.

The calculation of capture cross-sections for minority carriers is complicated due to the difficulty in determining the concentration of electrons/holes, which is a function of the current during the injection pulse.

5. Application of DLTS technique on photovoltaic materials

5.1. Radiation-induced recombination centers in Si

In order to clarify the origins of radiation-induced defects in Si and correlation between their behavior and Si solar cell properties, DLTS analysis has been carried out. DLTS measurements were made using a quiescent bias of -2V and a saturating fill pulse of 2V, 1 ms duration. Figure. 4 shows both the majority- and minority-carrier DLTS spectra of some of the same Si diode as a function of 1 MeV electron fluence. A large concentration of a minority carrier trap with an activation energy of about E_C-0.18 eV has been observed, as well as the majority carrier traps at around E_v+0.18eV and E_v+0.36eV.

A comparison of the total majority carrier defect concentration observed by DLTS with the measured change in carrier concentration for all the diodes is made in Figure 5. The compensation observed in the C-V profile is mainly caused by the minority carrier trap E_C-0.18 eV shown in Figure 4. The total concentrations of these majority-carrier traps and the minority-carrier trap at around E_c-0.18eV have been found to be nearly equal to the change in carrier concentrations. The concentration of the minority carrier trap at around E_c-0.18eV, was high enough to be responsible for most of the observed compensation and subsequently type conversion of the base layer from p to n-type. The E_v+0.36eV defect is thought to be responsible for minority-carrier lifetime (diffusion length) deg radiation according to the annealing experiments in the higher temperature range as will be described below. This means that the E_v+0.36eV is thought to act as a recombination center, in addition to a role as a majority-carrier trap center.

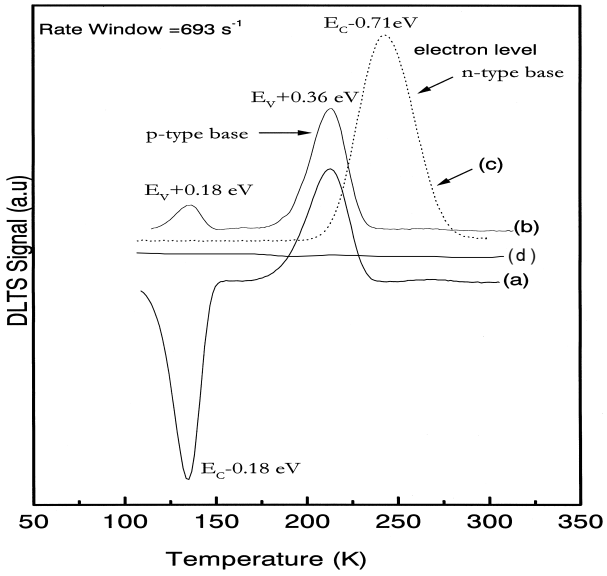

Figure 4. DLTS spectra of p-type Si before and after 1 MeV electron irradiation: (d) before irradiation, (b) and (a) majority and minority carrier signals after 1 x 10^{16} cm^{-2} fluence, respectively and (c) majority carrier signal after 1 x 10^{17} cm^{-2} fluence. The base of the diode irradiated with 1 x 10^{17} cm^{-2} electrons was n-type and required a correction to the spectrum to account for the effects of series resistance.

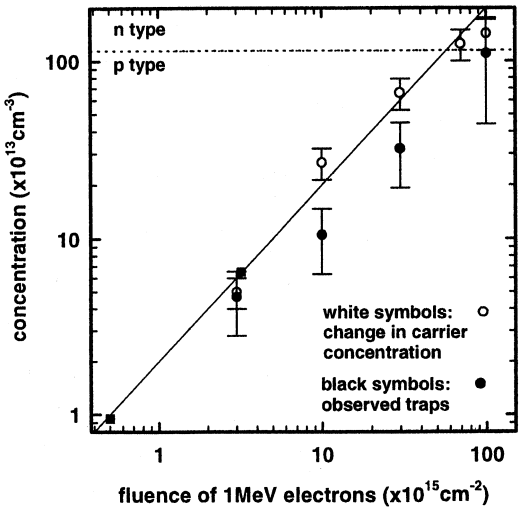

Figure 5. Total trap concentration observed by DLTS in comparison with the change in carrier concentration observed by C-V measurements at 300 K as a function of 1 MeV electron fluence.[15]

http://dx.doi.org/10.5772/59419

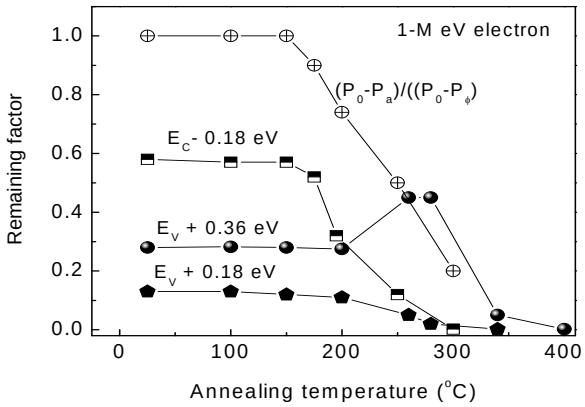

Figure 6. Comparison of isochronal annealing of densities of E_c-0.18eV, E_v+0.18eV and E_v+0.36eV defect centers measured by DLTS with that of carrier concentration of p-type Si irradiated with 1-MeV electrons. Each annealing step duration was 20 min.[15].

It is important to note that after annealing at 250°C, although the carrier concentration had recovered substantially, the observed concentration of the E_v+0.36eV defects had increased as shown in the Figure 6. This suggests that the E_v+0.36eV defects are not principally responsible for carrier removal.

We were able to confirm that the degradation of lifetime (diffusion length) is likely to be caused by the introduction of dominant hole level E_v+0.36eV and annealing behavior of this level govern the diffusion length recovery [15]. Figure 7 compares isochronal annealing of density of the majority-carrier trap at E_v+0.36eV measured by DLTS and that of recombination center determined by solar cell properties in p-type Si irradiated with 1-MeV electrons. Changes in the relative recombination center density N_r with annealing were also estimated by changes in short-circuit current density J_{sc} of the solar cell according to the following equation:

$$\frac{N_{ra}}{N_{r\varphi}} = \frac{\Delta(1/L_a^2)}{\Delta(1/L_\varphi^2)} = \frac{\left[1/L_a^2 - 1/L_0^2\right]}{\left[1/L_\varphi^2 - 1/L_0^2\right]} \sim \frac{\Delta(1/J_{sca}^2)}{\Delta(1/J_{sc\varphi}^2)} = \frac{\left[1/J_{sca}^2 - 1/J_{sco}^2\right]}{\left[1/J_{sc\varphi}^2 - 1/J_{sco}^2\right]} \tag{28}$$

Features of the E_v+0.36eV majority-carrier trap center with reverse annealing stage at 200^0 C~300^0 C and a recovery stage at around 350^0 C are similar to the changes in minority-carrier diffusion length L determined from the solar cell properties. This implies that the E_v+0.36eV majority-carrier trap center may also act as a recombination center.

As shown in Figure 6 the estimated initial concentration of the trap at approximately E_C-0.18eV is about 60% of the change in carrier concentration and therefore populous enough to be the dominating influence. Furthermore, the recovery of the carrier concentration after annealing occurs over roughly the same temperature range as disappearance of the minority trap signal.

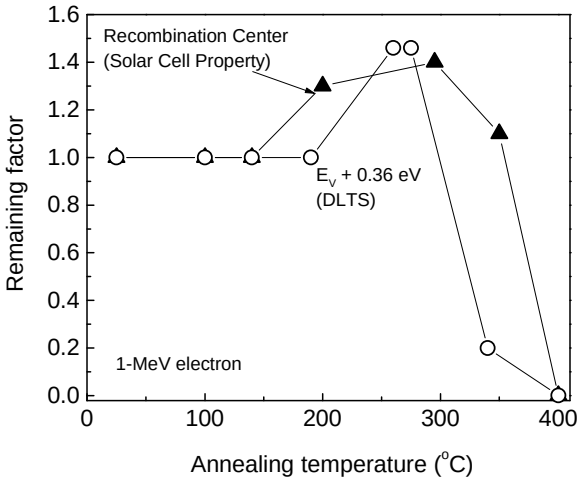

Figure 7. Comparison of isochronal annealing of the majority-carrier trap at E_v+0.36eV measured by DLTS with that of the dominant recombination center determined by solar cell properties in p-type Si irradiated with 1-MeV electrons [15].

This evidence is, therefore, coherent with the hypothesis that the E_c-0.18 eV center is mainly responsible for the compensation of the base layer. The radiation-induced traps, which play an important role regarding the carrier removal and conduction type conversion of the base region, should be principally deep-level donors, which must be positively charged before electron capture.

$$X^+ + e^- \leftrightarrow X^0 \tag{29}$$

5.2. Role of boron on compensator center

Interestingly, the introduction rate of the E_C-0.18eV electron level in B-doped samples is strongly boron concentration dependent. Comparison of introduction behavior, annealing kinetics and the strong relation to boron and oxygen contents, supports correlation of this level (E_C-0.18eV) with the B_i-O_i (Figure 8).

5.3. Role of gallium on compensator center

One of the most interesting and technological important feature of our work was the disappearance of the dominant donor like electron level E_C-0.18 eV in Ga-doped CZ- grown samples [17] (Figure 9). As we have discussed above this level acts as a compensator center, which is positive charge before electron capture. The concentration of this level is about 60% of the change in carrier concentration after heavy fluences and therefore populous enough to be the dominating influence on device performance. This implies that carrier removal effects can be

http://dx.doi.org/10.5772/59419

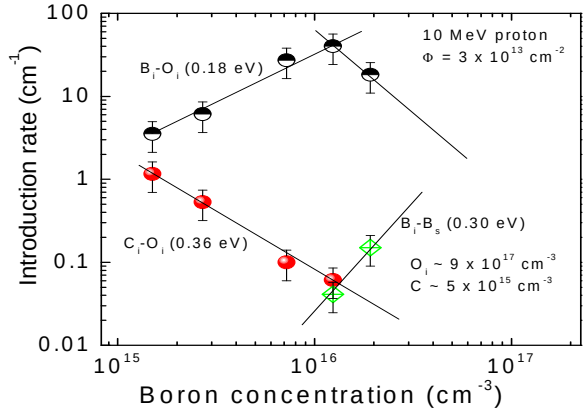

Figure 8. Introduction rates of the interstitial related defects in 10 MeV proton irradiated p-Si as a function of background impurity concentration [16].

partially offset by using Ga as dopant instead of boron. The absence of this level in Ga-doped Si gives support that this center in B-doped Si is related to B_i-O_i [18-20] complex.

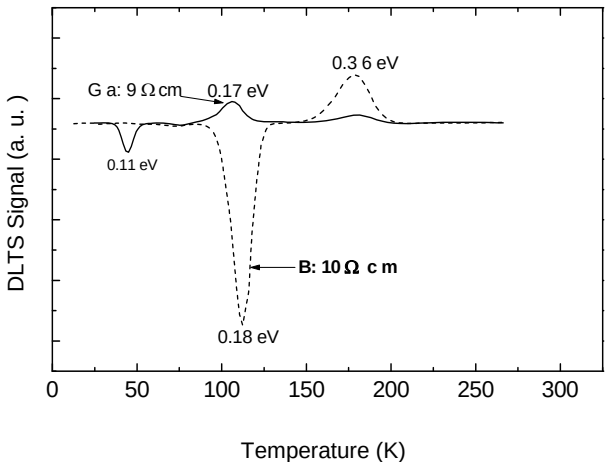

Figure 9. Comparison of the minority carrier DLTS spectra measured for boron-or gallium –doped CZ-grown Si irradiated with 1-MeV 3 x 10^{16} electrons/cm^2. The spectra were acquired using a reverse bias of 2 V, a pulse voltage of -1.5V, a pulse width of 1x 10^{-3} s and period width of 200 ms. [17].

5.4. Superior radiation resistance of InGaP solar cells

In this section, we present the direct observation of minority-carrier injection annealing of the dominant 1 MeV electron irradiation-induced hole trap labeled H2 located at 0.50-0.55 eV

above the valence band in p-InGaP by Deep Level Transient Spectroscopy (DLTS). Furthermore, an evidence of a large minority carrier capture cross section for this hole trap has been obtained by double-carrier pulse DLTS which demonstrate the important role of this trap as an recombination center. The one aim of present study was to clarify the mechanism involved in minority-carrier injection-enhanced annealing of the radiation-induced defect H2 in p-InGaP [22-27].

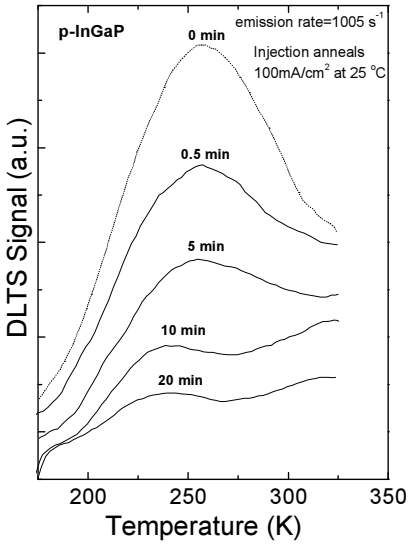

Figure 10. Changes of the DLTS spectrum of trap H2 with various time of injection at 25°C with an injection density of 0.1 A cm^{-2} [21].

The important result of this study is the influence of minority-carrier injection on the annealing kinetics of dominant hole level H2 [21]. In order to clarify the recovery of the solar cells properties following minority-carrier injection annealing, we carried out a systematic study of the variation of the concentration of the hole level H2 using a constant amplitude of forward bias injection (0.1 A/cm^2) at various temperatures for 0.5, 1, 2, 5, 10 and 20 min. The majority-carrier emission DLTS scans taken after different forward bias injection steps show a pronounced reduction in the H2 amplitude as shown in Figure. 10, which is correlated with a recovery of the maximum power output of the solar cells. It should be noted that the H2 peak; is rather broad and after pronounced reduction following forward bias, exhibits a double structure, indicating that this peak consists of more than one closely spaced peaks; one on the high temperature side appear to anneal relatively slowly

Figure 11 presents the temperature dependence of the annealing rate A^* of the hole trap H2 by minority-carrier injection-enhanced processes, determined from DLTS.

A comparison is given with the injection-enhanced annealing rates estimated by changes in short-circuit current density J_{sc} of the solar cells according to the following:

http://dx.doi.org/10.5772/59419

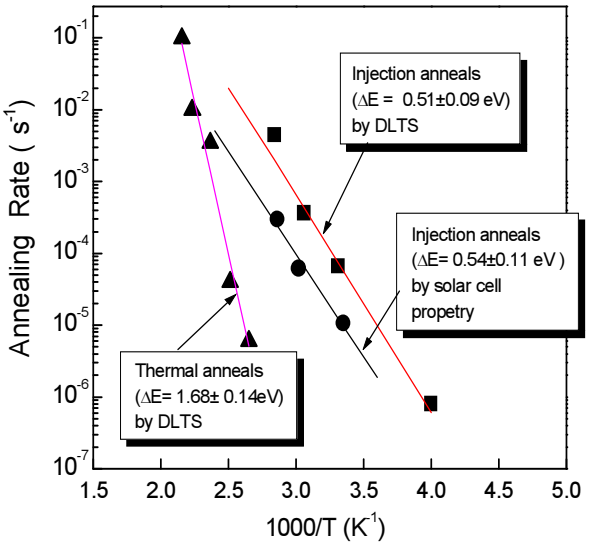

Figure 11. Temperature dependence of the thermal and injection annealing rates of the radiation-induced defects in p-InGaP, determined from solar cells property (J_{sc} or L) and for H2 trap observed by DLTS [21].

$$\frac{N_{TI}}{N_{T\varphi}} = \frac{L_{\varphi}^2(L_0^2 - L_I^2)}{\left[L_I^2(L_0^2 - L_{\varphi}^2)\right]} \sim \frac{J_{sc\varphi}^2(J_{sc0}^2 - J_{scI}^2)}{\left[J_{scI}^2(J_{sa0}^2 - J_{sc\varphi}^2)\right]} \tag{30}$$

where suffixes 0, φ, and I correspond to before and after irradiation, and after injection, respectively. The important result of this study is the direct relationship between the annealing rates, the solar cells properties and the H2 trap.

A close agreement between activation energy for recovery of radiation-induced defects, determined by solar cell properties and for the hole traps H2, demonstrates that this trap controls the minority-carrier lifetime. This result demonstrates that the dominant majority hole level H2 (E_V+0.5–0.55 eV) is the recombination center, which governs the minority-carrier lifetime in n^+–p InGaP solar cells.

5.5. Superior radiation resistance of AlInGaP solar cells

Figure 12 presents the temperature dependence of the annealing rate A of the trap H1, in p-AlInGaP determined by DLTS. The annealing activation energy of electron irradiation-induced defect H1 in p-AlInGaP is evaluated to be 0.50eV. A comparison is provided with the injection-enhanced annealing rates estimated for the defect H2 in p-InGaP. It is to be noted that the minority carrier injection annealing properties of the defect H2 in p-InGaP observed in the previous 1 MeV electron study are almost the same as those observed in the present study of H1 defect in p-AlInGaP after 1 MeV electron irradiation, which identified that the defect H1

observed in p-AlInGaP has the same nature of the defect H2 previously observed in P-InGaP and H4 in InP [28,29].

The recovery of the radiation damage due to minority carrier injection under forward bias is thought to be caused by an energy release mechanism in which enhancement is induced by the energy released when a minority carrier is trapped on the defect site. According to this mechanism, a change of charge states due to capture of carriers can result in electron phonon coupling. That is, vibration relaxation occurs, which may activate various reactions of the defect such as its migration or destruction, and ultimately decays to heat the lattice. The detailed analysis of this mechanism was previously studied in case of defects in InP, GaAs, and InGaP by the authors and others.

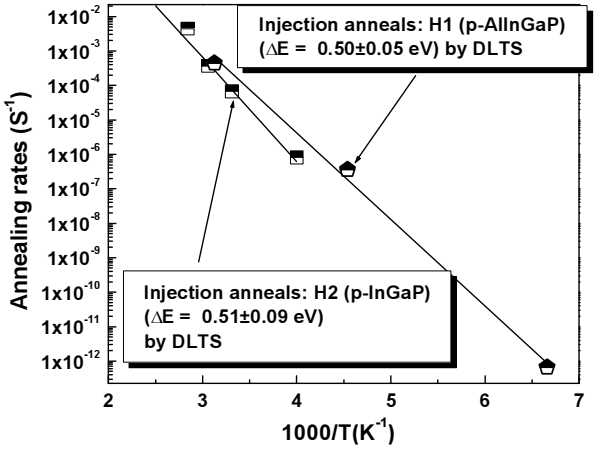

Figure 12. Comparison of the temperature dependence of injection annealing rates of the radiation-induced defect H1 (E_V+0.37eV) in p-AlInGaP and H2 (E_V+0.55eV) in p-InGaP [29].

5.6. Self-annihilation of electron irradiation induced defects in $InAs_xP_{1-x}$/InP multiquantum well solar cells

In this study, the authors demonstrated the direct observation of majority and minority carrier defects in $InAs_xP_{1-x}$/InP diodes and solar cells structures before, and after 1MeV electron irradiation by double-correlation deep level transient spectroscopy (DDLTS) in order to further evaluate the potential use of this material for space applications [30].

In order to electrically characterize radiation-induced deep center in InAsxP1-x/InP quantum well structure, the DDLTS technique is used to explore the recombination characteristics of deep levels in $InAs_xP_{1-x}$/InP multiquantum well solar cell structures.

The activation energy and apparent capture cross sections are determined to be 0.65 eV and 4.3×10^{-14} cm^2. The apparent high capture cross section of E1, suggests that this level might act as a strong recombination center.

http://dx.doi.org/10.5772/59419

We observed an unexpected and interesting reduction in the strength of the peak E1 in our deep level spectrum recorded subsequent to a room temperature storage of the irradiated device. Consequently, we carried out a detailed study of the room temperature isothermal annealing effects and carefully monitored the various deep-level peaks in our spectra as a function of sample storage time at room temperature (25°C). The dashed DLTS curve of Figure 13 represents a spectrum recorded after 90 days storage at room temperature and the significant reduction in the intensity of the E1 peak.

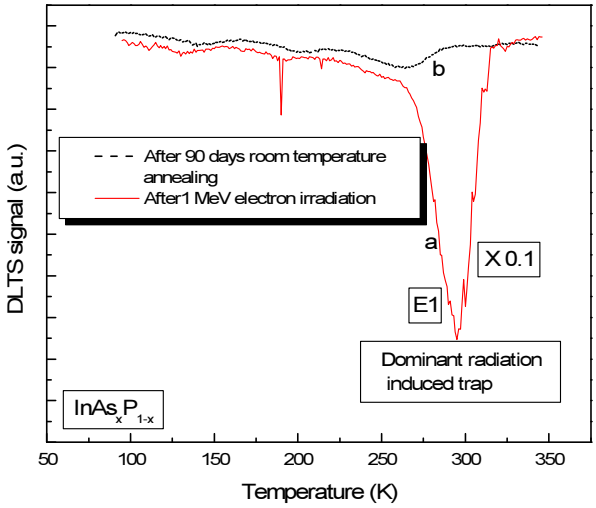

Figure 13. Room temperature annealing effects: (a) after irradiation (b) after 90 days storage at room temperature following irradiation [30].

The activation energy and apparent capture cross sections are determined to be 0.65eV and 4.3 x 10^{-14} cm^2. The apparent capture cross section of E1 is very high, which indicates that it may act as a strong recombination center. However, serendipitously long duration room temperature storage of the device yielded a total annihilation of E1. Although the detailed mechanisms at play are not fully understood, the serendipitous findings reported here clearly demonstrate the fact that insertion of QWs in the intrinsic region of an InP p-i-n solar cell results in a more radiation tolerant devices.

6. Summary

DLTS is an effective spectroscopy technique for processing transient (capacitance or current) from deep levels. This technique has proved to be an instrumental in determining most of the properties of the defects such as structure, introduction rates, introduction mechanism, thermal stability of the defects etc. DLTS is particularly attractive because it can be used to

characterize defects using various kinds of space charge based devices such as Schottky barrier diodes, and p-n junction to quantum well based complex devices. In addition, sensitivity of the DLTS for detecting defects in concentration of 10^9 cm^{-3} is superior to any other characterization technique. In this chapter we have reviewed the extensive work done by the authors, on the electronic properties of the recombination and compensator centers in Si and III-V compound materials for space and terrestrial solar cells.

Deep level transient spectroscopy (DLTS) is the best technique for monitoring and characterizing deep levels introduced intentionally or occurring naturally in semiconductor materials and complete devices. DLTS has the advantage over all the techniques used to-date in that it fulfils almost all the requirements for a complete characterization of a deep center and their correlation with the device properties. In particular the method can determine the activation energy of a deep level, its capture cross-section and concentration and can distinguish between traps and recombination centers.

In this chapter we provide an overview of the extensive R & D work that has been carried out by the authors on the identification of the recombination and compensator centers in Si and III-V compound materials for space solar cells. In addition, we present an overview of key problems that remain in the understanding of the role of the point defects and their correlation with the solar cell parameters.

Author details

Aurangzeb Khan[1*] and Yamaguchi Masafumi[2]

*Address all correspondence to: akhan@southalabama.edu

1 Department of Electrical and Computer Engineering, University of South Alabama, Mobile, AL, USA

2 Toyota Technological Institute, 2-12-1 Hisakata, Tempaku, Nagoya, Japan

This chapter is an expanded version of the authors' earlier proceedings paper [31] (© 2006 IEEE. Excerpts reprined with permission).

References

[1] D. V. Lang, J. Appl. Phys. 45, 3023 (1974).

[2] C. T. Sah and J. W. Walker, Appl. Phys. Lett. 22, 384 (1973).

[3] J. C. Carballes, J. Varon and T. Ceva, Solid State Commun. 9, 1627 (1971).

http://dx.doi.org/10.5772/59419

[4] D. L. Losee, Appl. Phys. Lett. 21, 54 (1972).

[5] R. Williams, J. Appl. Phys. 37, 3411 (1966).

[6] C. T. Sah L. Forbes, L. L. Rosier, and A. F. Tasch Jr., Solid State Electron. 13, 759 (1970).

[7] L. D. Yau and C. T. Sah, Phys. Status Solidi A 6, 561 (1971).

[8] C. H. Henry H. Kukimoto, G. L. Miller and F. R. Merritt, Phys. Rev. B 7, 2499 (1973).

[9] H. Kukimoto, C. H. Henry and F. R. Merritt, Phys. Rev. B 7, 2486 (1973).

[10] D. V. Lang, *Topics in Applied Physics - Thermally Stimulated Relaxation in Solids*, Vol. 37, ed. P. Bräunlich, Soringer Verlag, New York, (1979).

[11] W. Shockley and W. T. Read Jr., Phys. Rev. 87, 835 (1952).

[12] R. N. Hall, Phys. Rev. 83, 228 (1951).

[13] D. Stievenard, M. Lannoo and J. C. Bourgoin, Solid State Electronics 28, 485 (1985).

[14] L. C. Kimerling, J. Appl. Phys. 45, 1839 (1974).

[15] M. Yamaguchi, A. Khan, S. J. Taylor, K. Ando, T. Yamaguchi, S. Matsuda, and T. Aburaya, J. Appl. Phys. 86, 217 (1999).

[16] A. Khan, M. Yamaguchi, M. Kaneiwa, T. Saga T. Abe, O. Annzawa and S. Matsuda. J. Appl. Phys. 90, 1170(2001).

[17] A. Khan, M. Yamaguchi, M. Kaneiwa, T. Saga T. Abe, O. Annzawa and S. Matsuda. J. Appl. Phys. 87, 8389 (2000).

[18] A. Khan, M. Yamaguchi, S. J. Taylor, T. Hisamatsu and S. Matsuda, Jpn. J. Appl. Phys. 1, 38, 2679, (1999).

[19] A. Khan, M. Yamaguchi, T. Hisamatsu and S. Matsuda, J. Appl. Phys. 87, 2162 (2000).

[20] P. M. Mooney, L.J. Cheng, M. Sull, J. D. Gerson, and J. W. Corbett, Phy. Rev. B 15, 3836 (1977).

[21] A. Khan, M. Yamaguchi, J.C. Bourgoin and T. Takamoto., Appl. Phys. Lett. 76, 2550 (2000).

[22] J. C. Bourgoin and J. W. Corbett, Radiation Effects 36, 157 (1978).

[23] L. C. Kimerling, Solid State Electronics, 21, 1391 (1978).

[24] L. C. Kimerling and D. V. Lang, Inst. Phys.Conf. Ser. 23, 589 (1975).

[25] J. C. Bourgoin and J. W. Corbett, Phys. Lett. 83A, 135 (1972).

[26] J. C. Bourgoin and J. W. Corbett, Inst. Phys. Conf. Ser. 23, 149 (1975).

[27] D. V. Lang and L. C. Kimerling, Phys. Rev. Lett. 35, 22 (1975).

[28] A. Khan, Masafumi Yamaguchi, Jacques C. Bourgoin, and Tatsuya Takamoto. J. Appl. Phys. 89, 4263 (2001).

[29] A. Khan, S. Marupaduga, M. Alam, N. J. Ekins-Daukes, Appl. Phys. Lett. 85, 5218 (2004).

[30] A. Khan, A. Freundlich J. Gou, A. Gapud, M. Imazumi, and M.Yamaguchi, "Self-annihilation of electron-irradiation-induced defects in $InAs_XP_{1-X}$/InP multiquantum-well solar cells," *Applied Physics Letters*, vol. 90, p. 233111, 2007.

[31] A. Khan, Masafumi Yamaguchi, Hae-Seok Lee, Nicholas J. Ekins-Daukes, Tatsuya Takamoto, Mitsuru Imaizumi, Steve Taylor, in Proc. of 4th World Conference and Exhibition on Photovoltaic Solar energy Conversion (WCPEC-4), Hilton Waikoloa Village, Waikoloa, Hawaii, May 7-12, 2006, p. 1763.

Chapter 8

Inorganic–Organic Perovskite Solar Cells

Sohrab Ahmadi Kandjani, Soghra Mirershadi and Arash Nikniaz

Additional information is available at the end of the chapter

http://dx.doi.org/10.5772/58970

1. Introduction

The most of modern commercial optoelectronic devices such as Laser diodes, solar cells, light-emitting diodes (LEDs), and nonlinear optical devices are built on the basis of traditional inorganic semiconductors. However, a lot of progress has been made in producing devices based on organic electronic materials, in recent decades [1], but the current development prospects of organic materials are mostly limited in their scope to relatively low-performance areas. Low mobility of charge carriers in molecular materials, can be mentioned as one of import reason for this topic. Strong chemical interaction between organic molecules and metal electrodes can destroy the injection of charge carriers into the organic molecules [2].

A qualitatively different way of using organic electronic compounds can be *via* exploiting resonant interactions in organic-inorganic hybrid structures [3–5]. Within the same hybrid structure, one could combine high conductivity of the inorganic semiconductor component with the strong light-matter interaction of the organic component. However, this properties classified them as named organic-inorganic hybrid materials with large exciton binding energy (about several hundreds of meV) because of large dielectric confinement. These layered organic-inorganic perovskites with the general formula $(RNH_3)_2MX_4$ (R= C_nH_{2n+1}; M= Pb or Sn; X= halogen), can be regarded as semiconductor/insulator multiple quantum well systems consisting of lead halide semiconductor layers sandwiched between organic ammonium insulator layers [6–10]. Lead halide is well known as typical ionic crystals with a large exciton binding energy (a few tens of meV) [11]. Further, the organic layer has a larger band gap and lower dielectric constant than those of the inorganic layer. Therefore, the exciton binding energy is considerably amplified due to the quantum and dielectric confinement effects [12]. As a result, stable excitons are observed even at room temperature. Thus, the appropriate properties of both the organic and the inorganic materials can exploited to overcome their

limitations when used separately. The lead halide based organic-inorganic perovskites have potential applications in nonlinear optical devices [13,14] and novel luminescent devices [15,16]. Organometallic halide perovskites have recently emerged as a promising material for high-efficiency nanostructured devices [17]. Over the past several months, we have witnessed an unanticipated breakthrough and rapid progress in the field of developing photovoltaics, with the realization of highly efficient solar cells based on organometallic trihalide perovskite absorbers [18–21].

Simplified schematic representation of the crystal structure of the organic-inorganic hybrids as shown in Figure 1. The two-dimensional inorganic layers and an organic ammonium layer are stacked alternately. These layers is comprised of a two-dimensional sheet of [MX_6^{-4}] octahedra which are connected at the four corners with halide ions on the plane.

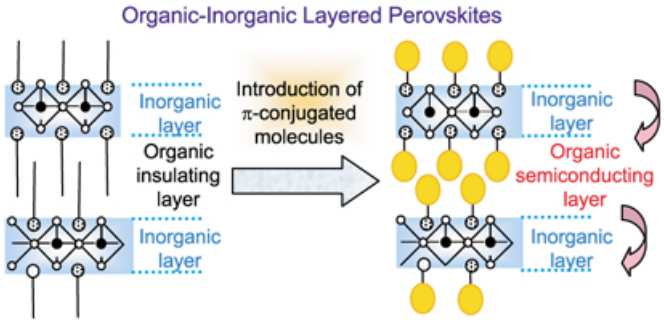

Figure 1. Schematic structure of the organic-inorganic hybrid crystal

As shown in Figure 2, the six halogen ions X^- surrounded M^{2+}, forming an octahedral [MX_6^{-4}] cluster. The inorganic layer has thickness of a few atomic layers. The $–NH_3^+$ ends of the cations bind to the anion layers of [MX_6^{-4}] in a specific orientation determined by hydrogen bonding with both equatorial and axial halide ions. A multi-layer structure is organized by neutralizing [MX_6^{-4}] with alkylammonium ions [24].

Also Perovskites Material use as solar cell in last few years as show in Figure 3. The reasons for make them as one of best candidate for photovoltaics is explain below:

1. Appropriate Material properties of high efficiency photovoltaics
2. High coefficient of optical absorption
3. Excellent charge carrier transportation
4. Promising device parameters
5. Stability for maintain more than 80% of its initial efficiency after 500 hours.
6. Lower manufacturing costs because of directly deposition from solution

http://dx.doi.org/10.5772/58970

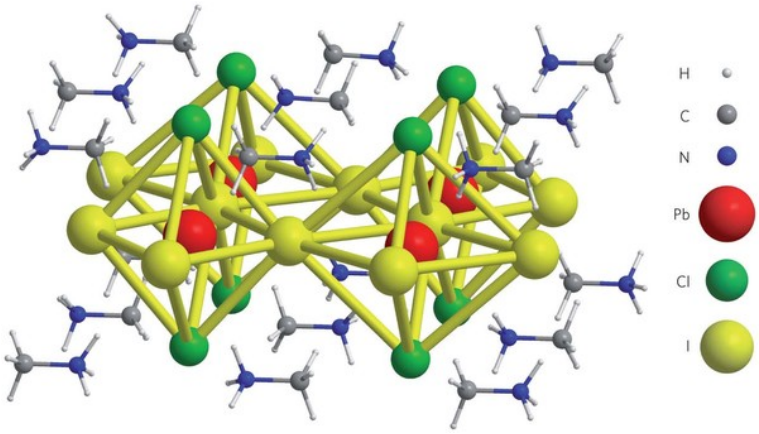

Figure 2. Schematic of the cluster structure of the organic-inorganic hybrid []

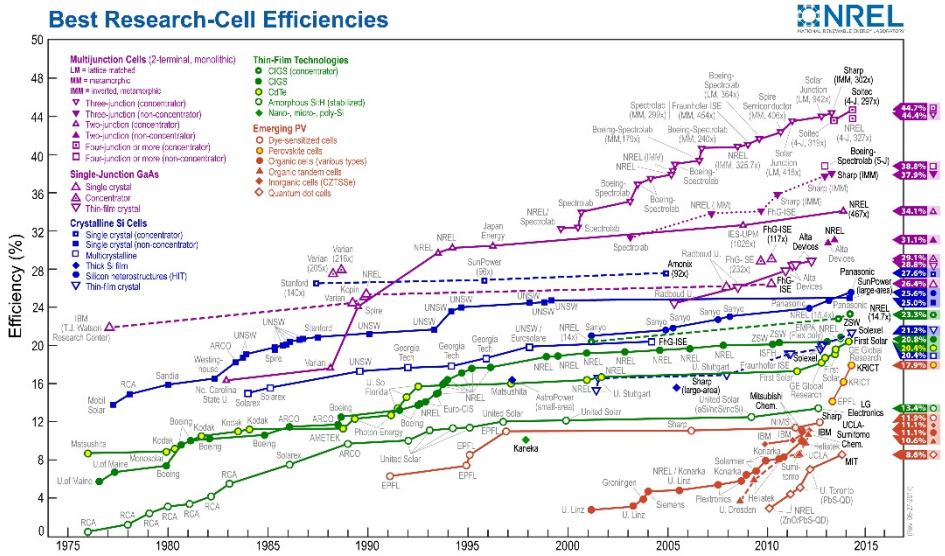

Figure 3. Best research cell efficiencies of all type of solar cells (NREL)

2. Synthesis of inorganic–organic solar cells materials

The synthesis of perovskites is the main and important procedure among perovskites study. Compared with the common semiconductors, the fabrication of perovskites samples is relatively easy. Because the crystals of perovskites molecules can form spontaneously via self-

assembly process and they need neither intricate equipment nor confined environment condition but can be synthesized and deposited simply by soft chemical methods at room temperature. Generally there are two steps for synthesis: synthesis of ammonium salts and preparation of perovskites solution.

In the first step, for the perovskites that are mainly in form of $(R\text{-}NH_3)_2MX_4$, the as-prepared amines transform to ammonium salts by reacting the amines with halogen acid. This neutralization reaction where the salts are generate is described in formula 1:

$$R\text{-}NH_2 + HX \rightarrow R\text{-}NH_2 . HX \tag{1}$$

The halogen acids used to produce corresponding ammonium salts are HI 57 wt%, HBr 48 wt % or HCl 37 wt% aqueous solution. After several days of drying in desiccator, the salts are dry. These dry ammonium salts are used to prepare perovskites solution. In this step, $R\text{-}NH_2 . HX$ ammonium salt is mixed with lead halide PbX_2 in stoichiometric amount in mole, and dissolved in solvent. This is a coordination reaction and it can be described by the chemical formula: 2:

$$2(R\text{-}NH_2 . HX) + MX_2 \rightarrow (R\text{-}NH_3)_2 MX_4 \tag{2}$$

The solution is then put under agitation or in ultrasonic bath until the solutes are totally dissolved and the solution appears limpid. From the perovskites solution, 2D crystals can be obtained by evaporation of solvent by self-organization process. The solvent containing $R\text{-}NH_2 . HX$ and MX_2 is first spin-coated on the substrate. 2D layered perovskites crystals are then obtained upon solvent evaporation. In the absorption spectra of 2D layered perovskites crystals, a sharp peak appears at room temperature, which is characteristic of the formation of 2D layered perovskites crystal structure [25].

Another method to synthesis of perovskites is two-step based on the layer-by-layer technique. For example, thin films of microcrystalline $(C_8H_{17}NH_3)_2PbBr_4$ are prepared by the two-step growth process by Kitazawa et.al as follows: (1) precipitation of nanometer-sized $PbBr_2$ particles on substrates by vapor deposition and then (2) growth of $(C_8H_{17}NH_3)_2PbBr_4$ films by exposing $PbBr_2$ particles to $C_8H_{17}NH_3Br$ vapor. A simple vacuum chamber is used as a deposition apparatus with about 8×10^{-6} Torr as Background pressure. This chamber is attached to a vacuum system, two-independent thermal evaporation sources, a shutter and a substrate holder. The thermal evaporation source consists of a quartz cell coiled with a tantalum wire. First of all, $PbBr_2$ particles are deposited on Si (100) substrates by vapor deposition. Next, $PbBr_2$ particles are exposed to $C_8H_{17}NH_3Br$ vapor for growing of $(C_8H_{17}NH_3)_2PbBr_4$ films. Exposure time is varied from 0 to 600 s. The substrate temperature is kept at room temperature during deposition. Thin films of microcrystalline that prepared by the two-step growth process and their optical properties are dependent on the exposure time [12].

Perovskites in form of luminescent nanoparticles are another remarkable kind of crystals which has attracted excessive attention recently. Between bulk materials and atomic or molecular structures, the nanoparticles show very specific properties with potential applica-

http://dx.doi.org/10.5772/58970

tions in various fields such as sensing or LEDs. Nanoparticles often have specific optical properties as they are small enough to confine their electrons and produce quantum effects. Thus, the fabrication method which chooses the size of nanoparticles is very vital. For the first time Audebert et al. have realized luminescent nanoparticles by a spray-drying method. In brief, the ammonium salts and $PbBr_2$ or PbI_2 semiconductors are firstly dissolved in DMF solvent and used for the nanoparticles spray drying. The experimental spray drier is composed of an aerosol generator and an evaporation chamber which is settled in an oven maintaining at 250 °C. (Figure 4)

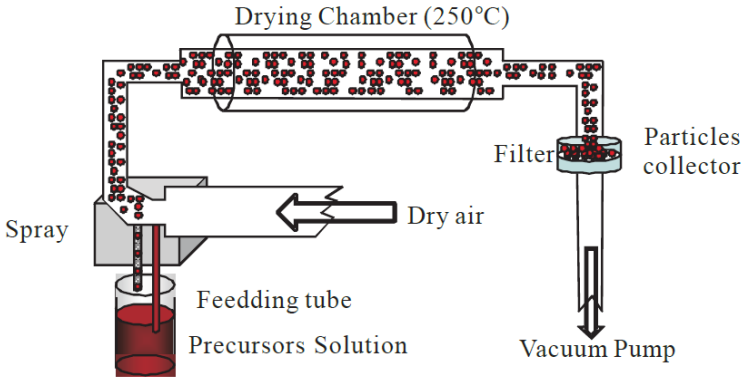

Figure 4. Schematic of the spray-drying method to preparation of organic-inorganic perovskite nanoparticles [25].

Droplets with initial mean diameter of 0.35 μm are carried by dry air from the aerosol generator to the evaporation chamber. Dried particles are collected onto a 0.2 μm cutoff Teflon filter and are stored at ambient temperature [25]. Transmission electron microscopy measurements show that these particles are spherical and their sizes are of the order of 50 to 500 nm.

2.1. Deposition techniques of inorganic–organic solar cells materials

The deposition technique is a quite important issue for perovskites studies, because many investigations and possible usages of organic-inorganic perovskite hybrids rely on the accessibility of simple and accurate thin film deposition method. But deposition of perovskite materials is often challenging because of the different chemical and physical property of the inorganic and organic portions [26]. For example, organic materials trend to be soluble in various solvents than inorganic section, this is causing chemical precursor solution preparation techniques (e.g., spin coating and dip coating) usually infeasible. For those reasons where the organic-inorganic hybrid is soluble, solution techniques are sometimes not suitable because of adverse wetting characteristics of some substrates, make deposition inhomogeneous. With respect to vacuum evaporation methods, the gradual heating of organic-inorganic compounds typically results in the decomposition or dissociation of the organic component at a lower

temperature or rapidly than that needed for evaporation of the metal halide component. Despite these evident difficulties, organic-inorganic perovskites represent a number of significant opportunities for thin film deposition or crystal growth of organic-inorganic hybrid perovskites, such as two-step dipping technique, spin coating, stamping, Langmuir-Blodgett (LB), two source thermal evaporation, solution evaporation and so on, which make possible the applications of perovskites as organic-inorganic electronic or photonic devices [27,28]. This section will offered a selected compilation of recent progress in this topic, demonstrating that a number of simple and effective methods can be utilized for the deposition of this considerable class of materials.

2.2. Spin-coating technique

Spin-coating is a very convenient technique widely applied to uniform thin film deposition. As it is shown in Figure 5, an amount of solution is dropped on the substrate which is fixed on the spin-coater, and then it is rotated at high speed in order to spread the fluid by centrifugal force. It can be considered as a special case of solution crystal growth, which allows the formation of highly oriented layered perovskites on a substrate, while the solvent is evaporating off. On the other hand, Spin-coating enables deposition of hybrid perovskites on various substrates, including glass, plastic, quartz, silicon and sapphire. Selection of the substrate, the solvent, the concentration of the hybrid in the solvent, the substrate temperature, and the spin speed are relevant parameters for this technique. In some cases, the wetting properties of the solution on the chosen substrate improved by pretreating the substrate surface with a suitable adhesion agent. In addition, post deposition low-temperature annealing ($T < 250^{o}C$) of the hybrid films is sometimes employed to improve crystallinity and phase purity. Mitzi et al. (2001b) comparing with the traditional deposition technique for inorganic semiconductors, spin-coating method doesn't require cumbersome equipment while it gives high-quality films in quite short time (several minutes) in room environment.

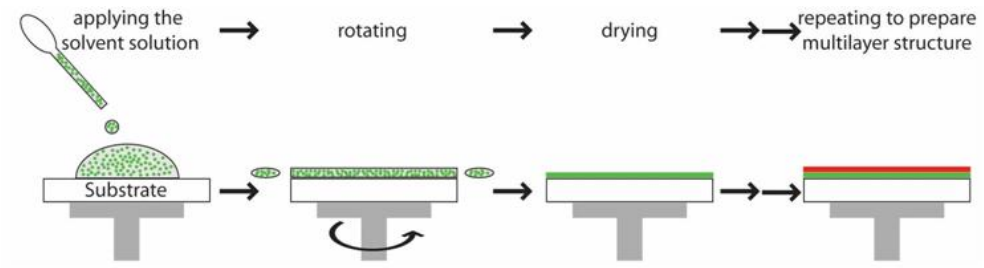

Figure 5. Schematic of the spin-coating process

Actually, in order to realize a layer with the desired thickness, can modify the concentration of perovskites solution and keep the other spin-coating parameters (spin speed, acceleration and spin duration) fixed. Generally, homogeneous 2D layered perovskites films with a thickness from 10 nm to 100 nm can be obtained by carefully selecting the parameters: less

http://dx.doi.org/10.5772/58970

concentrated solutions give thinner layers. The choice of the solvent is important because we need to consider the solubility for both the organic ammonium and the inorganic lead halide. Dimethylformamide (DMF) or Dimethyl sulfoxide (DMSO) are good solvents in which the perovskites usually have very high solubility. Some other solvents such as acetone, or acetonitrile can also be used. But solubility of perovskites in them is relatively poor (less than 5 wt%), and it takes too long to completely dissolve the solutes.

With the help of a profilemeter or an Atomic force microscopy to measure the layer thickness, can draw a calibration curve (thickness as a function of concentration) and adjust the concentration of solution in order to produce the desired thickness. The spin-coated 2D layered perovskites films are very reproducible, and therefore they are appropriate to be deposited on devices.

2.3. Two-step dip-coating

In a sequential deposition procedure, a metal halide film is first deposited by vacuum evaporation or spin-coated from solution. Subsequently this film is transformed into the perovskite by dipped into a solution including the organic cation. Proper selection of solvent for the dipping solution is important. So that the organic salt is soluble in it, but the starting metal halide and the final organic-inorganic perovskite are not soluble.

In this case, the organic cations in solution intercalate into and rapidly react with the metal halide on the substrate and form a crystalline film of the desired hybrid, as it is described in Figure 6.

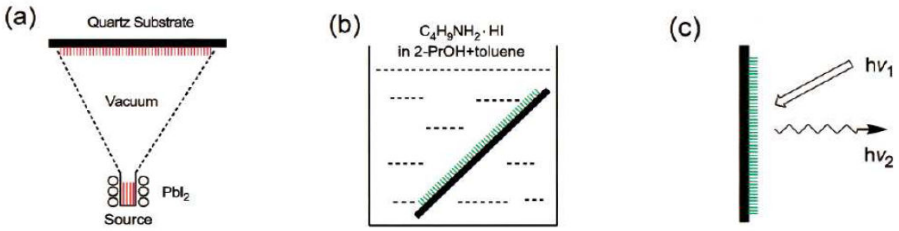

Figure 6. Schematic representation of the two-step dipping technique. In (a), a film of the metal halide is deposited onto a substrate using vacuum evaporation. The metal halide film is then (b) dipped into a solution containing the organic cation. The resulting film after dipping has the characteristic room temperature photoluminescence spectrum.

For the perovskite family, $(R\text{-}NH_3)_2 (CH_3NH_3)_{n-1} M_nI_{3n+1}$ (R = butyl or phenethyl; M = Pb or Sn; n = 1 or 2), toluene/2-propanol mixture is a suitable solvent for the organic salt. The dipping times are relatively short: several seconds to several minutes, depending on the system. For example, a film of $(C_4H_9NH_3)_2PbI_4$ was composed of a vacuum deposited film of PbI_2 (See figure 6 (a)) by dipping it into a butylammonium iodide solution, the reaction time was 1-3 min, which depends the PbI_2 film thickness (200-300 nm). After dip-coating, the films were instantly immersed in a rinse solution of the same solvent ratio as the initial dipping solution

without organic salt and dried in vacuum. Two-step dip-processing is a convenient method which can be used for a variety of organics and inorganics, even if they have incompatible solubility characteristics [26].

2.4. Thermal evaporation technique

The thermal evaporation method was firstly used by M. Era et al in 1997. They performed the dual-source vapor deposition by using lead iodide PbI_2 and organic ammonium iodide RNH_3I, in particular, the 2-phenylethylammonium iodide $C_6H_5C_2H_4NH_3I$.

As it is shown in Figure 7 organic and inorganic source were co-evaporated and deposited on fused quartz substrates. The pressure of evaporation chamber was about 10^{-6} Torr. In the preparation, the substrates were allowed to stand at room temperature. The spectrum of the vacuum deposited film corresponds well to those of single crystal and spin-coated films of the layered perovskite. Appearance of the strong exciton absorption and sharp exciton emission proves that the layered perovskite structure is organized in the vacuum deposited film [17].

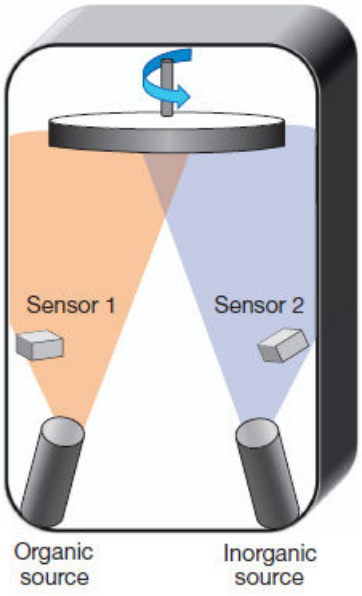

Figure 7. Schematic representation of the two-step dipping technique.

The benefits of this technique are that it is possible to precisely control the thickness and smoothness of the thin-film surfaces. However, this method has some disadvantage. It is often difficult to balance the organic and inorganic rates, an important criterion for achieving the correct compositions of the resulting perovskite films. Because each organic component easily contaminates the inside of the evaporation equipment is expected to limit the preparation of

http://dx.doi.org/10.5772/58970

various perovskites using different organic components. In addition, in some cases, the organic salt might not be thermally stable up to the temperatures required for evaporation, making this approach impracticable for a certain number of systems.

Furthermore, another method was developed to deposit perovskites thin films by using a single evaporation source. Mitzi et al. (1999). The apparatus for this single source thermal ablation (SSTA) technique consists of a vacuum chamber, with an electrical feed-through to a thin tantalum sheet heater, as shown in Figure 8.

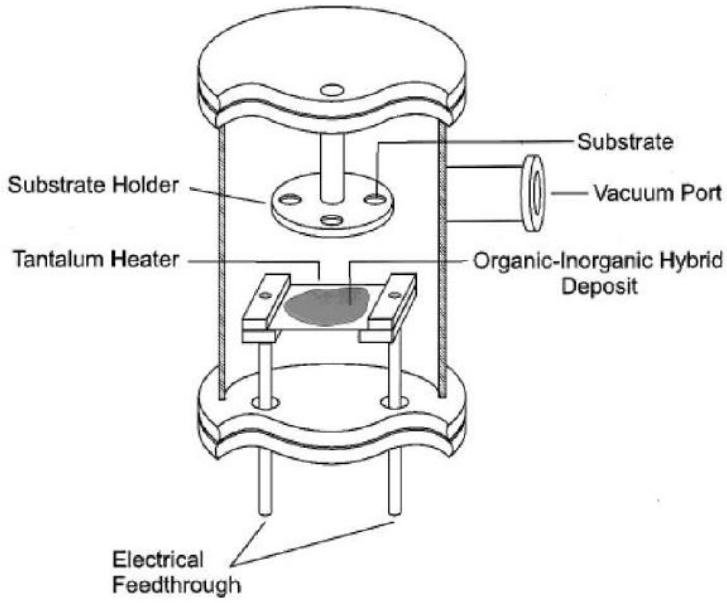

Figure 8. Schematic cross section of a single source thermal ablation chamber

Crystals, powder, or a concentrated solution of starting charge is placed on the heater. A suspension of insoluble powders in a quick-drying solvent are placed on the heater, because this enables the powder to be in better physical and thermal contact with, as well as more evenly dispersed across, the sheet. Under a suitable vacuum condition, the sheet temperature reaches approximately 1000 ^{o}C in 1-2 second, the entire starting charge ablates from the heater surface well before it incandesces. After ablation, the inorganic and organic parts reassemble on the substrates to produce optically clear films of the chosen product.

The key point to this procedure is that the ablation is quick enough for the inorganic and organic compounds to evaporate from the source at basically the same time and before the organic portion has had an opportunity to decompose. In many instances (particularly with

comparatively simple organic cations), the as-deposited films are crystalline and single phase at room temperature [26].

As show in Figure 9 Mingzhen Liu et al. compare the X-ray diffraction pattern of films of $CH_3NH_3PbI_{3-x}Cl_x$ both vapour-deposited and solution-cast onto compact TiO_2-coated FTO-coated glass. The main diffraction peaks, assigned to the 110, 220 and 330 peaks at 14.12 °, 28.44 ° and, respectively, 43.23°, are in same positions for both methods of films preparation, demonstrating that both techniques have produced the same organic-inorganic perovskite with an orthorhombic crystal structure [17]. Remarkably, focusing on the region of the (110) diffraction peak at 14.12 °, there is only a small peak at 12.65 ° (the (001) diffraction peak for PbI_2) and no observable peak at 15.68 ° (the (110) diffraction peak for $CH_3NH_3PbCl_3$), indicating a high level of phase purity.

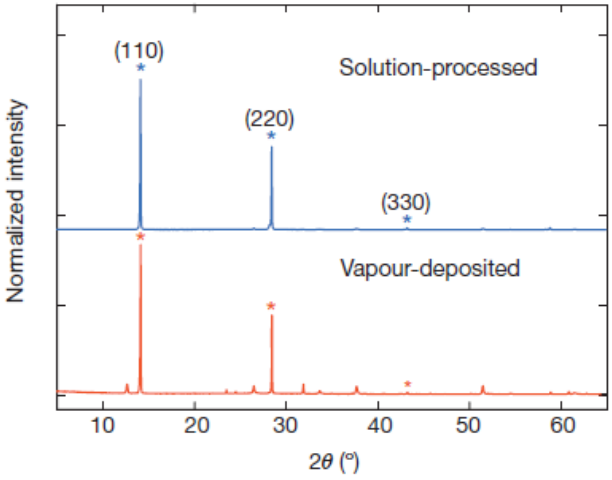

Figure 9. X-ray diffraction spectra of a solution-processed perovskite film (blue) and vapour deposited perovskite film (red) [17].

Figure 10 shows high-resolution scanning electron micrographs of $CH_3NH_3PbI_3$ perovskite film spin-cast on a glass/ITO/PEDOT:PSS substrate by Jun-Yuan Jeng et al. The crystal sizes in the cluster-domain regions of the perovskite are around 100–150 nm in $CH_3NH_3PbI_3$ perovskite film from butyrolactone solution and around 150–200nm in DMF solution [29].

Sanjun Zhang et al. performs atomic force microscopy (AFM) measurements for each spin-coated $(R\text{-}(CH_2)_nNH_3)_2PbX_4$ in order to examine the ability of the molecules to self-organize and define the surface roughness. Several examples of the obtained images are given in Figure 11.With the phenyl based semiconductor (2-phenylethanamine lead iodide), it was possible to cover the whole surface of the glass substrate; however, this was not the case for Cyclohexyl-methanamine lead iodide, Myrtanylamine lead iodide and Cyclohexanamine lead bromide. It is clear that the surface roughness of the 2D phenyl-based is lower than that of the others [30].

http://dx.doi.org/10.5772/58970

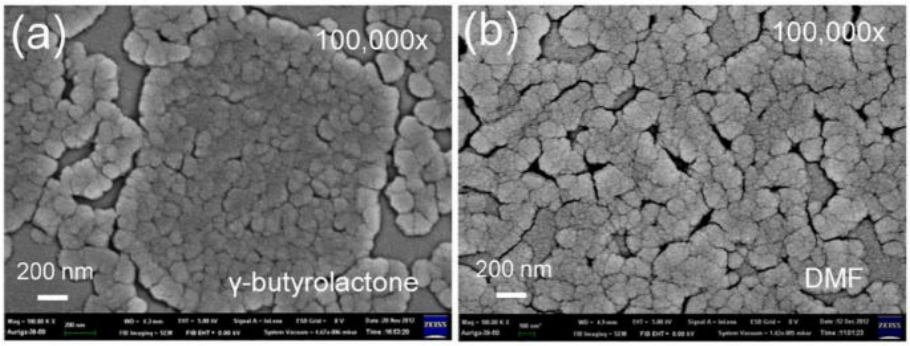

Figure 10. High-resolution scanning electron micrographs of CH3NH3PbI3 perovskite film from (a) butyrolactone solution and (b) DMF solution [29].

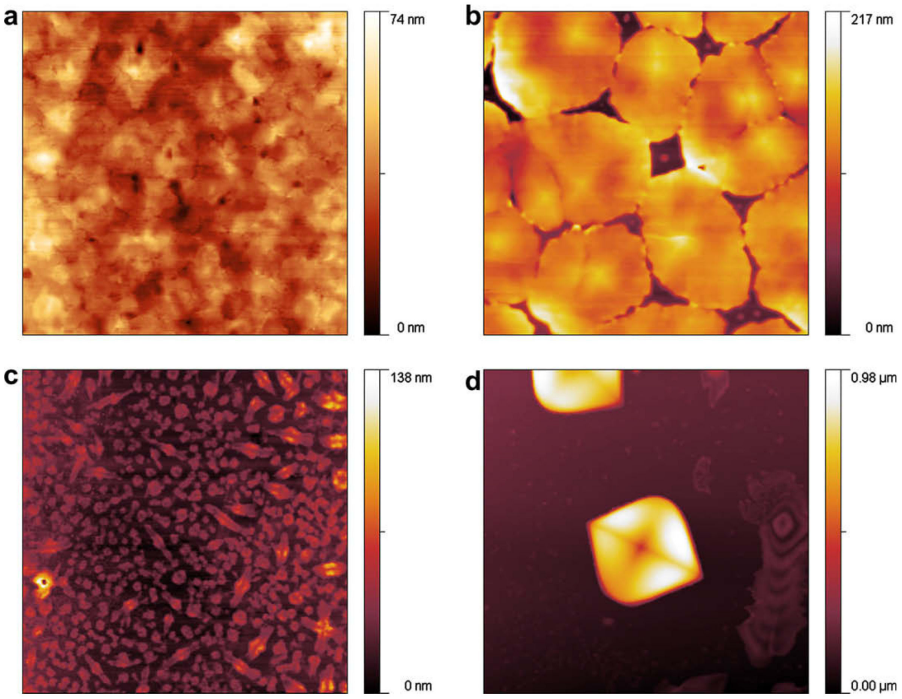

Figure 11. AFM images of 2D organic–inorganic semiconductor films: (a) 2-phenylethanamine lead iodide, (b) Cyclohexylmethanamine lead iodide, (c) Myrtanylamine lead iodide and (d) Cyclohexanamine lead bromide. The scales are 20 μm × 20 μm. Color coding of height is shown in the bar [30].

3. Electronic and optical properties of inorganic–organic solar cells materials

In the present decade organic-inorganic halide perovskite solar cells has been the most significant development in the field of photovoltaics for best bet at satisfying the need for high efficiencies while allowing for low cost manufacturing solutions. Since the first reports of stable solid state solar cells based on $CH_3NH_3PbI_3$ perovskite in middle of 2012, the power conversion efficiencies of the hybrid solar cells have already exceeded 17%, surpassing every other solar cells produced by solution-processing methods. The wide range of efficient perovskite solar cell device design indicated point towards a considerable semiconducting material with excellent electrical and optical properties. Early pioneering research [31] in organic-inorganic halides field has clearly shown that this hybrid materials are good candidates for low dimensional electronic systems with tunable properties, permitting for the development of newer perovskite materials for solar cells in addition to $CH_3NH_3PbI_3$. This section focuses on the recent progresses (*i.e.*, up to Feb 2014) in the area of perovskite solar cells as well as their electronic, optical properties and the dynamics of charge carriers [32]. We first review the electronic properties of this class of hybrid perovskites, followed by its progress as a solar cell material. Due to the rapid pace of research in this area, this section does not aim to be comprehensive but will highlight key work and findings.

Initial studies on the electronic band structures of organic-inorganic (3-D and low-dimensional) perovskites can be traced to the works as below, in 1996 koutselas and his team using band structure calculations by a semi-empirical method based on the extended Huckel theory and an *ab-initio* approach based on the Hartree-Fock theory [33]. Then T. Umebayashi *et. al*. using ultraviolet photoelectron spectroscopy and first principles density functional theory (DFT) band calculations for the room temperature cubic phase [34] and Chang team using first principles pseudopotential calculations in 2004 [35]. As shown in Figure 12 DFT calculations for the three dimensional $CH_3NH_3PbI_3$ crystal shown that the maxima of valence band consist of the Pb 6p - I 5p σ-anti-bonding orbital, while the minima of conduction band contains Pb 6p –I 5s σ anti-bonding and Pb 6p - I 5p π anti-bonding orbitals [34].

In line with respect to perovskite solar cells, interests in the DFT studies of 3D perovskites began renewed in earnest with the work of E. Mosconi together with F. De Angelis and their collaborators [37]. They calculated the band structure for $CH_3NH_3PbX_3$ (cubic phase) and the mixed halide $CH_3NH_3PbI_2X$ (tetragonal phase) (X = Cl, Br and I) with the surrounding $CH_3NH_3^+$, which were ignored in the earlier studies. Nevertheless, the organic component had little influence to the bandgap energy, of which is mainly determined by the $[PbI_4]^{6-}$ network. In addition, the authors highlight that their calculated bandgaps (by ignoring spin-orbit coupling (SOC)) are in good agreement with the experimental results. These findings are consistent with those in the later works by T. Baikie *et. al.*[37] and Y. Wang *et. al.* [38].

Figure 13 show the absorption spectra of the perovskite quantum well structures. Sharp resonance are due to the exciton state associated with the inorganic layers. So, by replacing different metal cations or halides in organic framework, the positions of the resonance can be manipulated[33, 39]. Room-temperature UV–vis absorption spectra for thin films of

http://dx.doi.org/10.5772/58970

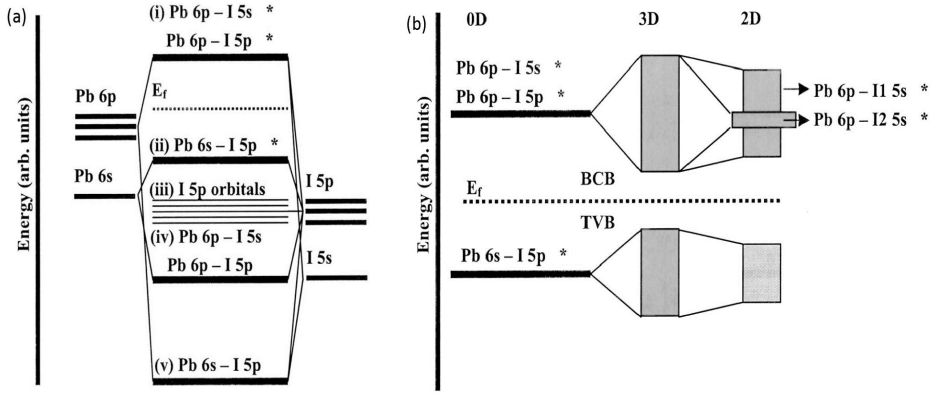

Figure 12. Bonding diagram of (a) [PbI6]4- cluster (0-D), (b) CH3NH3PbI3 (3-D) and (b) (C4H9NH3)2PbI4 (2-D) at the top of the valence band and the bottom of the conduction band [34].

$(C_4H_9NH_3)_2PbX_4$ with (a) X = Cl, (b) X= Br, (c) X = I are shown by Mitzi *et. al.* as shown in Figure 13. In each spectrum, the arrow demonstrates the position of the exciton absorption peak. The corresponding photoluminescence (PL) spectrum (λ_{ex} = 370 nm) is shown by the dashed curve in figure 13-c. A stokes shift of about 15nm between peaks of the absorption and emission peaks for the excitonic transition is notable.

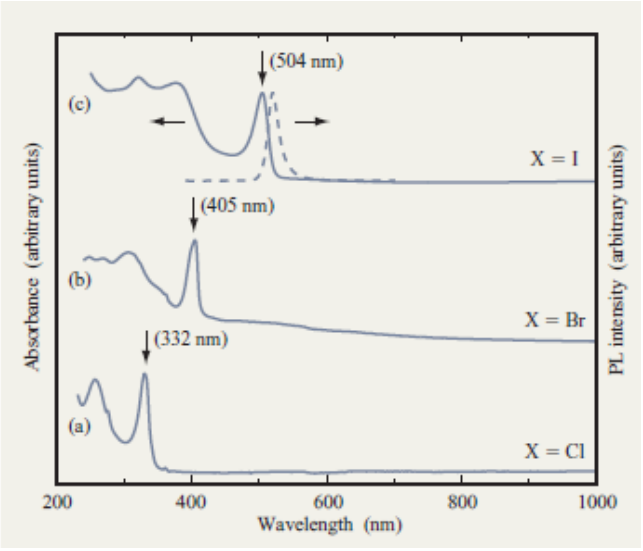

Figure 13. Room-temperature UV–vis absorption spectra for thin films of (C4H9NH3)2PbX4 with (a) X= Cl, (b) X= Br, (c) X = I [39].

Because of the two-dimensionality of the inorganic structure, coupled with the dielectric modulation between the organic and inorganic layers, the strong binding energy of the excitons arise, which enables the optical features to be observed at room temperature. Also strong photoluminescence, nonlinear optical effects and tunable polariton absorption arise from the large exciton binding energy and oscillator strength [39].

The excitonic absorption and light emission closely relate to the different metal halide in 2D perovskite. For instance, the absorption and photoluminescence of $(C_5H_4CH_2NH_3)_2PbX_4$ varied with substitution of different halogens. As show in Figure 14, the light emissions change by green to blue and blue to ultraviolet when X= I → Br → Cl [40]. The small FWHM of the peaks and very small Stokes shift between the UV-vis absorption and PL emission spectra are the signature of exciton.

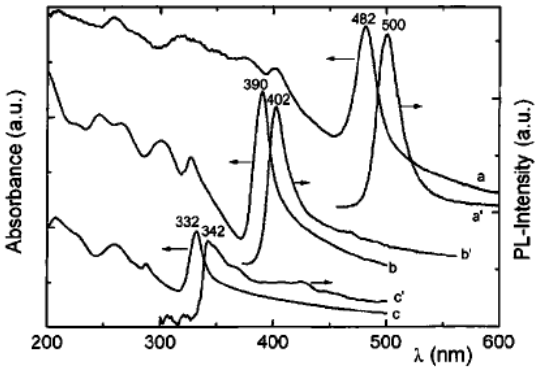

Figure 14. Optical absorption of (a, b, c) and photoluminescence (a′, b′, c′) spectra for $(C_5H_4CH_2NH_3)_2PbI4$ (a, a′), $(C_5H_4CH_2NH_3)_2PbBr4$ (b, b′) and $(C_5H_4CH_2NH_3)_2PbCl4$ (c,c′)

The noticeable feature of the exciton state in this system is the extremely large binding energy. For example, the binding energy in $(C_6H_5–C_2H_4NH_3)_2PbI_4$ are 220 meV. For comparison, the exciton state in bulk PbI_2 has a binding energy of only 30 meV. According to the other studies the larger binding energy is due to the unusual alternating organic–inorganic layered structure and the effect of dielectric confinement. The screening of carriers in organic layer is small due to lower dielectric constant of the inert organic molecules. Also lower dielectric constant of organic layer lead to enhancement of the coulomb interaction between electron and hole (higher exciton binding energy) [40].

As already pointed out in a lot of published works it is interesting to compare the luminescence and absorption properties of the organic–inorganic compounds. As revealed, extensive studies of the excitonic properties of lead halide based organic–inorganic materials $(R–NH_3)_2PbX_4$ have been performed. The measured absorption and photoluminescence wavelengths of $(R–NH_3)_2PbI_4$ and $(R–NH_3)_2PbBr_4$ reported in the literature are summarized in Table 1. Using different organic chains (e.g. simple saturated organic chains and unsaturated chains

including aromatic rings and delocalized p electrons) demonstrate enhancement of the photoluminescence and the binding energy of excitons. For the saturated alkylammonium chains organic layers, the length of organic chain and the width of the PbI_4 wells does not affect the excitonic properties. This is due to the small difference between the dielectric constants of the inorganic and organic layers which leads to a rather weak impact of the dielectric confinement (see, for instance, the work of Ishihara et al. on $(C_nH_{2n+1}NH_3)PbI_4$ with n = 4, 6, 8,..., 12). In contrast, when the organic chains consist of aromatic rings and delocalized p electrons, the binding energy of exciton is low because of the difference between the organic and inorganic dielectric constants (dielectric confinement effect) and the luminescence peak shows red shift [41-44]. This dependence of the saturated/unsaturated nature of the organic chains is summarized in Table 1.

Comparison of the absorption and photoluminescence peak wavelengths and the exciton binding energy of $(NH_3(CH_2)_6NH_3)PbBr_4$ with those of the homologous bromide and iodide compounds as shown in Table 1. It is clear that the exciton binding energy of compounds (I) and (II) containing saturated organic chains are almost the same (about 180 meV). On the other hand, compounds (III) and (IV) containing unsaturated organic chains, exhibit much lower exciton bending energy. The homologous iodide compound (V) with the same (saturated) organic chain as $(NH_3(CH_2)_6NH_3)PbBr_4$ shows strong photoluminescence at room temperature. The efficient emitted photoluminescence is observable by naked eyes

References	Stokes shift (exciton binding energy)	PL (nm)	Absorption (nm)	Compound
[41]	nm (181 mev) 22	402	380	**$(NH_3(CH_2)_6NH_3)PbBr_4$ (saturated chain)**
[42]	nm (177 mev) 25	430	405	**$(C_4H_9NH_3)_2PbBr_4$ (saturated chain)**
[41]	nm (107 mev) 17	436	419	**$(C_5H_7NH_3)PbBr_4$ (unsaturated chain)**
[43]	nm (127 mev) 15	417	399	**$(R–PhNH_3)PbBr_4$ (unsaturated chain)**
[44]	nm (330 mev) 56	555	–	**$(NH_3(CH_2)_6NH_3)PbI_4$ (saturated chain)**

Table 1. Absorption, photoluminescence wavelengths and Stokes shifts of some reported compounds.

4. Photovoltaic effect in inorganic–organic perovskite solar cells

Solar power is the one of the world's most abundant energy resource and daily input of this energy to the earth's surface is enough to cover our energy needs, but efficient and cost-effective ways of converting it to electricity, have remained as one of the scientist's challenges.

Photovoltaic cells are the most promising device for directly converting the photons to electricity and it has been extensively studied in the past 50 years using various combinations of inorganic semiconductors or organic sensitizers. For photovoltaic energy to become competitive with fossil fuels and to capture a worthy place at energy markets, it is necessary to reduce the total cost of solar energy conversion by increasing their power conversion efficiencies or by reducing the cost of photovoltaic cells.

Today there is a lot of material used in photovoltaic structure and installed around the world. The photovoltaic market is currently dominated by crystalline Si solar cells with efficiencies close to 20% that known as First Generation of Solar Cells. This generation that have more than 150 micrometer thick, have the highest efficiency in all type of Solar cells that manufactured, but take a lot of energy to produce and therefore the cost of manufacturing is too high.

As cost-effective devices, thin film solar cell those containing a few micrometers of inorganic materials that known as second generation can be introduced. With a thin photovoltaic film, optical management is an important key for harvesting light while ensuring high efficiency. Thin film solar cell often limit light-harvesting ability because of their materials low absorption coefficients and narrow absorption bands. At least, these flexible cells have lower material costs, but they are also less efficient.

Alternative "third generation" technologies such as dye sensitized solar cells, organic photovoltaics and quantum dot solar cells in both electrochemical and solid-state structures, assure low cost solar power because of low cost fabrication methods based on solution-processing techniques such as blade coating, screen printing and spraying, but high bandgap light absorption by these types has not allowed high performance in quantum conversion and photovoltaic generation.

The first observation of photocurrents in oxide perovskite material can date back to 1956 [1] that have been widely studied. David B. Mitzi in 1990 used organometal halide perovskites in LED [2] and thin-film field-effect transistors [3] and demonstrated its high efficiency as light emitters. Given that we know the good light emitter is a good light absorber, perovskites materials because of their light absorption efficiently over a broad spectrum is convenient option as photovoltaic materials.

Also, because perovskite can directly deposited from solution, manufacturing costs is lower than another type of solar cells. But it should be noted that manufacturing cost could rise due to encapsulation process. Therefore, perovskites could resolve the solar cell industry by matching the output of silicon cells at a lower price than that of thin film, because of their low-cost materials and manufacturing process.

For first time in 2009, perovskites were used as solar cell [4]. As show in Figure 15 this device are built upon the architectural basis for DSSCs and achieved 3.8% efficiencies in a liquid electrolyte configuration where the absorber was regarded as a QDs deposited on tio_2. The efficiency was further improved to 6.5% but the enormous drawback to this types, regardless of their low efficiency, were had dissolution of liquid electrolyte away the perovskite that cause short stability for device.

http://dx.doi.org/10.5772/58970

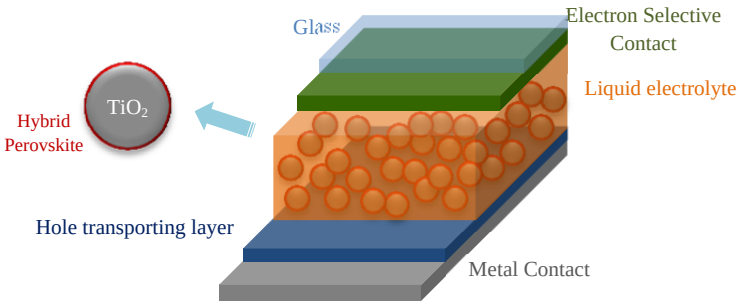

Figure 15. Schematic of first perovskites solar cell

Introducing of Solid Hole Transporting Layer (HTL) by Nam-Gyu Park and Gratzel [5], and replace liquid electrolyte by it, solve this problem in 2012 and rose the efficiency to 9%. (Figure 16)

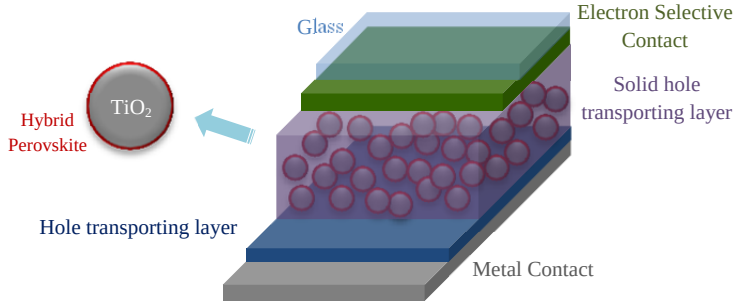

Figure 16. Nam-Gyu Park and Gratzel perovskites solar cell

In the late 2012s, research topics towards to materials engineering and switch structure by manufacturing methods to increase the Efficiency of these type of solar cells. Henry Snaith [6] in Oxford University Switched TiO_2 to an insulating Aluminum oxide scaffold in Gratzel perovskites solar cell that show in Figure 17. This switch, surprisingly increase efficiency to 10.9%.

Figure 17. Switching TiO_2 to an Al_2O_3 in Gratzel perovskites solar cell

On the other hand, Snaith and coworkers [17] demonstrated efficient planar solar cells of $CH_3NH_3PbI_{3-x}Cl_x$ formed by dual source evaporation of $PbCl_2$ and CH_3NH_3I. The film was evaporated on a compact TiO_2 layer (as an electron transport layer) and then a Spiro-OMeTAD layer (as a hole transport layer) was spin coated over it (Figure 18). The evaporated films containing crystalline structures on the length scale of hundreds of nanometers are enormously uniform [32].

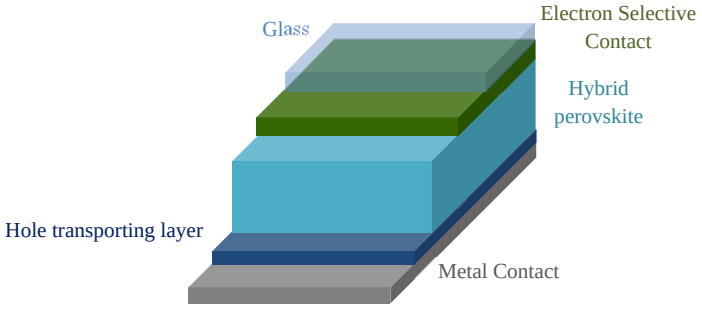

Figure 18. Schematic of Snaith hybrid perovskite solar cell

Finally they reported 15.4% efficiency for their device and another research in this area, reported the difference efficiency by using different material for example Pbl_2 that Graetzel and Bolink [7] used (device efficiency was 12.04 %) or difference evaporation method for example as show in Figure 19 employs both solution based deposition and vapor phase transformation by Graetzel [21] and coworkers, that report 12.1 % efficiency for their device.

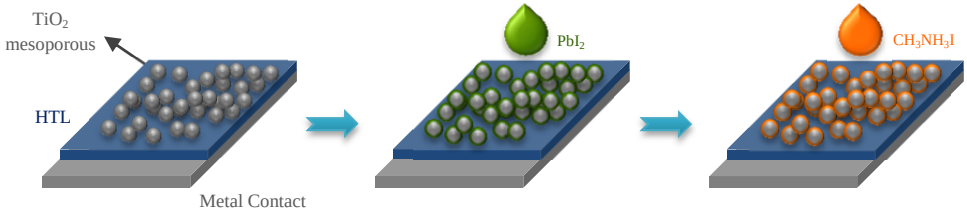

Figure 19. Gratzel sticks with the TiO_2 structure and tinkered with the deposition step.

These deposition techniques had two important drawbacks: first challenging for large-scale industrial production and second is that the all-solution process results in decreased film quality, and the vacuum process requires expensive equipment and uses a great deal of energy. Yang Yang [16] from UCLA university present new method named "Vapor-assisted solution process" that organic material infiltrates the inorganic matter and forms a compact perovskite film. These films is significantly more uniform than the films produced by the wet technique (Figure 20).

http://dx.doi.org/10.5772/58970

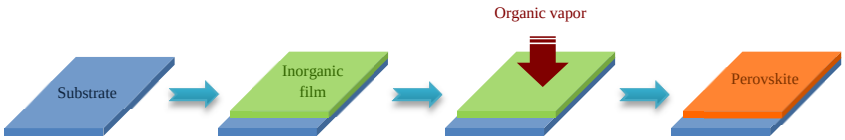

Figure 20. Vapor-assisted solution process

In conjunction with these exciting device-centric advancements, fundamental studies into the photoexcited species and their photogeneration and recombination dynamics in perovskites also began in earnest.

At least one of the remaining question is "Is the Solar Cell Excitonic?" Perovskite solar cell had similar diffusion lengths for electron and hole that average is about 100 to 300 nm [8] that put these cells in conventional solar cell class. On other hand either indicate similar mobilities for both holes and electrons [9] and this classify these cells in excitonic solar cell group (Figure 21).

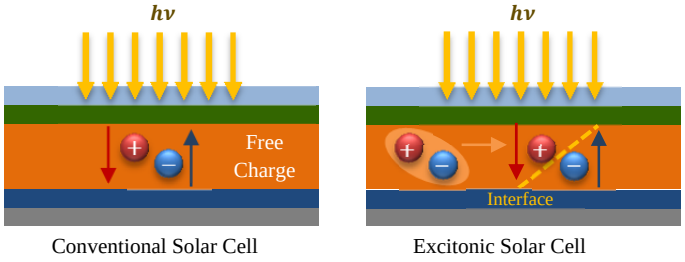

Figure 21. Schematic of conventional and excitonic solar cell

Accordingly, due to the common properties of these types of solar cells, between Conventional and excitonic solar cell, researchers cannot exactly determine whether the photoexcited species are excitons or free charges.

5. Conclusion

In this section we have presented the synthesis and characterization of organic-inorganic hybrid perovskite. Hybrid organic-inorganic materials represent an alternative to present materials as they guarantee improved optical and electronic properties by combining organic and inorganic components together. The unusual features and versatile characteristics of hybrid organic-inorganic perovskites open up promising applications in many fields such as electronics, optics, optoelectronics, mechanics, environment, medicine and biology. The application of these materials in the solar cells as a novel class of low-cost materials for high efficiency hybrid semiconductor photovoltaic cells has been explained in more detail.

Author details

Sohrab Ahmadi Kandjani*, Soghra Mirershadi and Arash Nikniaz

*Address all correspondence to: s_ahmadi@tabrizu.ac.ir

Research Institute of Applied Physics and Astronomy (RIAPA), University of Tabriz, Iran

References

[1] Agranovich V, Gartstein Y N, Litinskaya M. Hybrid Resonant Organic-Inorganic Nanostructures for Optoelectronic Applications. Chemical Reviews 2011; 111 5179–5214.

[2] Pope M, Kalmann H, Magnante P. Electroluminescence in Organic Crystals The Journal of Chemical Physics 1963; 38 2042–2043.

[3] Agranovich V, Atanasov R, Bassani F. Hybrid interface excitons in organic-inorganic quantum wells. Solid State Communications 1994; 92 295–301.

[4] Agranovich V, La Rocca G C, Bassani F. Efficient electronic energy transfer from a semiconductor quantum well to an organic material. JETP Letters 1997; 66 748–751.

[5] Agranovich V, Benisty H, Weisbuch C. Organic and inorganic quantum wells in a microcavity: Frenkel-Wannier-Mott excitons hybridization and energy transformation. Solid State Communications 1997; 102 631–636.

[6] Dammak T, Elleuch S, Bougzhala H, Mlayah A, Chtourou R, Abid Y. Synthesis, vibrational and optical properties of a new three-layered organic inorganic perovskite $(C_4H_9NH_3)_4Pb_3I_4Br_6$. Journal of Luminescence 2009; 129 893–897.

[7] Mitzi D, Field C, Harrlson W, Guloy A. Conducting tin halides with a layered organic-based perovskite structure. Nature1994; 369 467–469.

[8] Hong X, Ishihara T, Nurmikko A V. Photoconductivity and electroluminescence in lead iodide based natural quantum well structures. Solid State Communications 1992; 84 657-661.

[9] Cheng Z Y, Wang Z, Xing R B, Han Y C, Lin J. Patterning and photoluminescent properties of perovskite-type organic/inorganic hybrid luminescent films by soft lithography. Chemical Physics Letters 2003; 376 481–486.

[10] Tabuchi Y, Asai K, Rikukawab M, Sanuib K Ishigure K. Preparation and characterization of natural lower dimensional layered perovskite-type compounds. Journal of Physics and Chemistry of Solids 2000; 61 837–845.

[11] Kitazawa N, Watanabe Y. Optical properties of natural quantum-well compounds (C6H5-CnH2n-NH3)2PbBr4 (n=1–4). Journal of Physics and Chemistry of Solids 2010; 71 797–802.

[12] Kitazawa N, Yaemponga D, Aono M, Watanabe Y. Optical properties of organic–inorganic hybrid films prepared by the two-step growth process. Journal of Luminescence 2009; 129 1036–1041.

[13] Ema K, Ishi J, Kunugita H, Ban T, Kondo T. All-optical serial-to-parallel conversion of Tbits/s signals using a four-wave-mixing process. Optical and Quantum Electronics 2001; 33 1077–1087.

[14] Brehier A, Parashkov R, Lauret J S, Deleporte E. Strong exciton–photon coupling in a microcavity containing layered perovskites semiconductors. Applied Physics Letters 2006; 89 171110-1.

[15] Era M, Morimoto S, Tsutsui T, Saito S. Organic–inorganic heterostructure electroluminescent device using a layered perovskite semiconductor $(C_6H_5C_2H_4NH_3)_2PbI_4$. Applied Physics Letters 1994; 65 676–678.

[16] Shibuya K, Koshimizu M, Takeoka Y, Asai, K. Scintillation properties of $(C_6H_{13}NH_3)_2PbI_4$: exciton luminescence of an organic/inorganic multiple quantum well structure compound induced by 2.0 MeV protons. Nuclear Instruments and Methods B 2002; 194 207–212.

[17] Liu M, Johnston M B, Snaith H J. Efficient planar heterojunction perovskite solar cells by vapour deposition. Nature 2013; 501 395–398.

[18] Snaith H J. Perovskites: The Emergence of a New Era for Low-Cost, High- Efficiency Solar Cells. The Journal of Physical Chemistry Letters 2013; 4 3623−3630.

[19] Edri E, Kirmayer S, Cahen D Hodes G. High Open-Circuit Voltage Solar Cells Based on Organic−Inorganic Lead Bromide Perovskite The Journal of Physical Chemistry Letters 2013; 4 897−902.

[20] Heo J H, Im S H, Noh J H, Mandal T N, Lim C S, Chang J A, Lee Y H, Kim H J, Sarkar A, Nazeeruddin M K, Gratzel M, Seok S. Efficient inorganic–organic hybrid heterojunction solar cells containing perovskite compound and polymeric hole conductors. Nature photonics 2013; 7 486−491.

[21] Burschka J, Pellet N, Moon S J, Humphry-Baker R, Gao P, Nazeeruddin M K, Gratzel M. Sequential deposition as a route to high-performance perovskite-sensitized solar cells; Nature 2013. 499, 316− 319.

[22] Kitazawa N, Aono M Watanabe Y. Excitons in organic–inorganic hybrid compounds $(C_nH_{2n+1}NH_3)_2PbBr_4$ (n=4, 5, 7 and 12); Thin Solid Films 2010. 518 3199–3203.

[23] Liang L, Zhang J, Zhou Y, Xie J, Zhang X, Guan M, Pan B and Xie Y 2013 High-performance flexible electrochromic device based on facile semiconductor-to-metal transition realized by $WO_3.2H_2O$ ultrathin nanosheets; Scientific reports 2013. 1936 1-8.

[24] Tabuchi Y, Asai K, Rikukawa M, Sanui K Ishigure K. Preparation and characterization of natural lower dimensional layered perovskite-type compounds; Journal of Physics and Chemistry of Solids 2000. 61 837–845.

[25] Wei Y. Synthesis and optical properties of self-assembled 2D layered organic-inorganic perovskites for optoelectronics. PhD thesis. The Quantum and Molecular Photonics Laboratory, France 2012.

[26] Mitzi D B. Thin-Film Deposition of Organic-Inorganic Hybrid Materials; Chemistry of Materials 2001. 13 3283-3298.

[27] [27].Kitazawa N, Enomoto K, Aono M, Watanabe Y. Optical Properties of $(C_6H_5C_2H_4NH_3)_2PbI_{4-x}Br_x$ (x =0–4) mixed-crystal doped PMMA films; Journal of Materials Science 2004. 39 749–751.

[28] Dwivedi V K, Baumberg J, Vijaya Prakash G. Direct deposition of inorganic organic hybrid semiconductors and their template-assisted microstructures; Materials Chemistry and Physics 2013. 137 941–946.

[29] Jeng J Y, Chiang Y F, Lee M H, Peng S R, Guo T F, Chen F, Wen T C. Methylammonium lead iodide perovskite/fullerene-based hybrid solar cells; SPIE Newsroom 2014. 10.1117/2.1201307.005033.

[30] Zhang S, Lanty G, Lauret J S, Deleporte E, Audebert P, Galmiche L. Synthesis and optical properties of novel organic–inorganic hybrid nanolayer structure semiconductors; Acta Materialia 2009. 57 3301–3309.

[31] Mitzi D B. Progress in Inorganic Chemistry, John Wiley & Sons, Inc., 2007, DOI: 10.1002/9780470166499.ch1, pp. 1-121.

[32] Sum T C, Mathews N. Advancements in Perovskite Solar Cells: Photophysics behind the Photovoltaics; Energy & Environmental Science 2014. 7 2518-2534

[33] Koutselas I B, Ducasse L, Papavassiliou G C. Electronic properties of three- and low-dimensional semiconducting materials with Pb halide and Sn halide units ; Journal of Physics: Condensed Matter 1996. 8 1217-1227.

[34] Umebayashi T, Asai K, Kondo T, Nakao A. Electronic structures of lead iodide based low-dimensional crystals; Physical Review B 2003 67.....

[35] Chang Y H, Park C H, Matsuishi K. First-Principles Study of the Structural and the Electronic Properties of the Lead-Halide-Based Inorganic-Organic Perovskites $(CH_3NH_3)PbX_3$ and $CsPbX_3$ (X = Cl, Br, I) ; Journal of the Korean Physical Society 2004. 44 889-893.

[36] Mosconi E, Amat A, Nazeeruddin M K, Gratzel M, De Angelis F. First-Principles Modeling of Mixed Halide Organometal Perovskites for Photovoltaic Applications; The Journal of Physical Chemistry C 2013. 117 13902-13913.

[37] Baikie T, Fang Y N, Kadro J M, Schreyer M, Wei F X, Mhaisalkar S J, Graetzel M, White M T. Synthesis and crystal chemistry of the hybrid perovskite $(CH_3NH_3)PbI_3$ for solid-state sensitised solar cell applications; Journal of Materials Chemistry A 2013. 1 5628-5641.

[38] Wang Y, Gould T, Dobson J F, Zhang H, Yang H, Yao X, Zhao H. Density functional theory analysis of structural and electronic properties of orthorhombic perovskite $CH_3NH_3PbI_3$; Physical Chemistry Chemical Physics 2014. 16 1424-1429.

[39] Mitzi D B, Chondroudis K, Kagan C R. Organic–inorganic electronics; IBM Journal of Research and Development 2001. 45 29-45.

[40] Cheng Z, Lin J. Layered organic–inorganic hybrid perovskites: structure, optical properties, film preparation, patterning and templating engineering Crystal Engineer Community 2010. 12, 2646–2662.

[41] Dammak T, Fourati N, Boughzala H, Mlayah A, Abid Y. X-ray diffraction, vibrational and photoluminescence studies of the self-organized quantum well crystal $H_3N(CH_2)_6NH_3PbBr_4$; Journal of Luminescence 2007. 127 404- 408.

[42] Yamamoto Y, Oohata G, Mizoguchi K, Ichida H, Kanematsu Y. Photoluminescence of excitons and biexcitons in $(C_4H_9NH_3)_2PbBr_4$ crystals under high excitation density; physica status solidi (c) 2012. 9 2501-2504.

[43] Cheng Z Y, Wang H F, Quan Z W, Lin C K, Lin J, Han Y C, Layered organic–inorganic perovskite-type hybrid materials fabricated by spray pyrolysis route; Journal of Crystal Growth 2005. 285 352-357.

[44] Goto T, Ohshima N, Mousdis G A, Papavassiliou G C. Excitons in a single two-dimensional semiconductor crystal of $H_3N(CH_2)_6NH_3PbI_4$; Solid State Communications 2001. 117, 13-16.

[45] ChenF S, Optically induced changes in refractive index in $LiNbO_3$. Journal of AppliedPhyics 1969; 40 3389–3396.

[46] MitziD B, ChondroudisK. Electroluminescence from an Organic–Inorganic Perovskiteincorporating a quaterthiophenedye within lead halide perovskitelayers. Chemical Material 1999; 11 (11), pp 3028–3030.

[47] KaganC R, MitziD B, DimitrakopoulosC D. Organic-inorganic hybrid materials as semiconducting channels in thin-film field-effect transistors, Science 1999; 286 (5441), 945-947.

[48] Bulkin B. Perovskites: the future of solar power?, Theguardian 2014; http://www.theguardian.com/sustainable-business/perovskites-future-solar-power

[49] Gratzel M, Park NG. Lead iodide perovskite sensitized all-solid-state submicron thin film mesoscopic solar cell with efficiency exceeding 9%, Science Rep. 2012;2591.

[50] SnaithHJ, LeeMM. Efficient hybrid solar cells based on meso-superstructuredorgano-metal halide perovskites, Science 2012; 338(6107)643-7.

[51] MalinkiewiczO, YellaA, LeeY H, EspallargasG M, GraetzelM, NazeeruddinM K,BolinkH. Perovskite solar cells employing organic charge-transport layers, J. Nat Photonics2014; 8, 128-132.

[52] Stranks S, Eperon G, Grancini G, Menelaou C, Alcocer M, Leijtens T, Herz L, PetrozzaA, Snaith H. Electron-hole diffusion lengths exceeding 1 micrometer in an organometaltrihalideperovskite absorber, Science 2013; 342(6156)341-4.

[53] Gregg B A. Excitonic solar cells, J. Phys. Chem. B 2003; 107(20) 4688–4698.

Chapter 9

The Physics of High-Efficiency Thin-Film III-V Solar Cells

Roger E. Welser, Ashok K. Sood,
Ramesh B. Laghumavarapu, Diana L. Huffaker,
David M. Wilt, Nibir K. Dhar and Kimberly A. Sablon

Additional information is available at the end of the chapter

http://dx.doi.org/10.5772/59283

1. Introduction

Optically-thin absorber structures represent an interesting class of photovoltaic devices, both in terms of their performance characteristics and the economic advantages of employing thinner semiconductor material layers. This chapter reviews the underlying physics of high-efficiency optically-thin solar cells employing thin-film III-V materials. By combining thin III-V absorber structures with advanced light-trapping structures, single-junction devices can deliver high efficiency performance over a wide range of operating conditions at a fraction of the cost of multi-junction structures. Moreover, by leveraging hot carrier and/or optical up-conversion mechanisms to extend infrared absorption, the power conversion efficiencies in single-junction nano-enhanced solar cells can potentially exceed the Shockley-Queisser limit and outperform multi-junction devices. Experimentally, suppressed radiative recombination and high voltage operation have been observed in step-graded InGaAs quantum well structures. In addition, recent results from a novel InAs/AlAsSb quantum dot structure prove the validity of the intermediate band solar cell approach for infrared up-conversion, and underline the potential of thin-film III-V materials for realizing cost-effective, high-efficiency solar cells.

By minimizing semiconductor material content, optically-thin absorber structures provide a pathway to lower the manufacturing cost of high-performance photovoltaic (PV) devices. Thin-film solar cells are also an attractive source of portable and mobile power, as they can be integrated into flexible, lightweight photovoltaic modules that can operate in both terrestrial and space environments. Several different emerging technologies can be employed to fabricate flexible thin-film PV cells [1-2]. Although the deposition of copper indium gallium diselenide (CIGS) directly onto flexible substrates offers some advantages in terms of ease of manufacturing, the epitaxial lift-off (ELO) of III-V devices can provide much higher efficiency performance.

By stacking multiple p-n junctions of different III-V semiconductor materials into one two-terminal device, multi-junction solar cells have achieved record-high efficiency at converting solar power into electrical power. Under air mass zero (AM0) spectral conditions found in space, InGaP/GaAs/InGaAs inverted metamorphic (IMM) cells have been demonstrated with efficiencies in excess of 32% [3-4]. Even higher efficiencies exceeding 35% have been achieved under an air mass spectrum (AM1.5) typically used to characterize terrestrial performance [5]. However, changes in the solar spectrum can dramatically degrade the performance of multi-junction devices – changes that occur naturally throughout the day, from season to season, and from location to location as sunlight passes through the earth's atmosphere. As illustrated in Figure 1, the efficiency of a multi-junction device will decrease by more than a factor of two under higher air mass spectra. This reduction in efficiency is due to a decrease in the current output of the series-connected multi-junction device, which is limited by the subcell generating the least amount of photocurrent. Series-connected multi-junction cells can also degrade more rapidly than single-junction III-V cells upon irradiation, particularly as the current output of the limiting subcell fails. Moreover, multi-junction III-V cells require thick, complex epitaxial layers and are therefore inherently expensive to manufacture. Thus the inconsistent performance under changing environmental conditions and high manufacturing costs of multi-junction III-V cells severely hamper the application of this established high-efficiency technology.

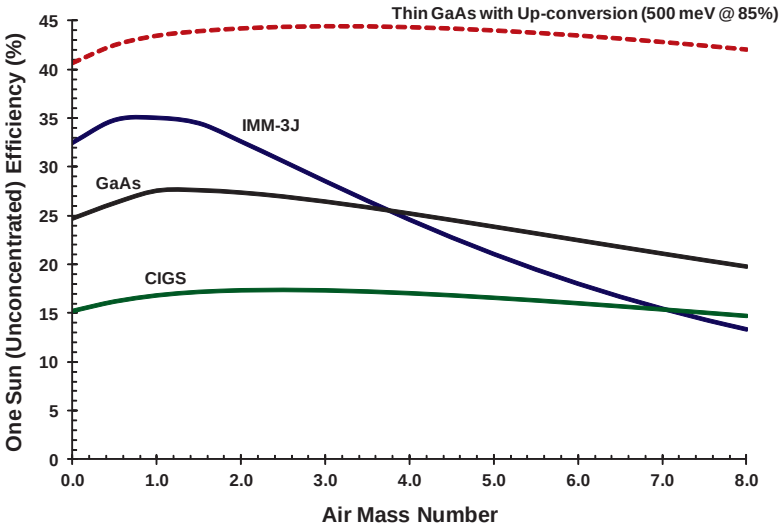

Figure 1. Projected un-concentrated efficiency versus air mass spectrum for several different types of solar cell structures, including a high-performance IMM triple-junction III-V structure, a single-junction CIGS cell, and a single-junction GaAs solar cell. Also shown is the theoretical performance of a thin GaAs-based device incorporating up-converting and light-trapping structures to harness a notable fraction of the available low energy photons. The calculations assume a Bird – Riordan model of the air mass spectrums and realistic spectral response and dark diode characteristics, as detailed in reference [6].

http://dx.doi.org/10.5772/59283

Thin-film single-junction III-V cells can potentially address the performance and cost limitations of multi-junction devices. By avoiding current matching constraints, single-junction structures can offer a more robust performance than multi-junction devices [6]. The efficiency of established single-junction CIGS and GaAs cell technologies is more stable to changes in the incident spectrum, and can actually outperform III-V multi-junction structures under higher air mass spectrums, as depicted in Figure 1. Moreover, the efficiency of single-junction III-V cells can be dramatically increased by employing additional structures that leverage optical up-conversion and/or hot carrier effects. Theoretically, both up-conversion and hot carrier mechanisms have been projected to increase the limiting one-sun efficiency of single-junction photovoltaic devices to over 50% [7-8]. By combining thin III-V absorber structures with advanced light-trapping structures, nano-enhanced III-V single-junction devices can potentially deliver high efficiency performance in a flexible format at a fraction of the cost of multi-junction structures. As illustrated in Figure 1, efficiencies of more than 40% over a wide range of spectrums are projected for an optically-thin GaAs-based device that can harness 85% of the infrared photons falling within 500 meV of the GaAs band edge [6].

In this chapter, the theoretical performance of optically-thin solar cells is first described using a generalized detailed balance model, specifically adapted for nano-enhanced absorbers. This model is then employed to describe the impact of both absorber thickness and effective optical path length on the performance of III-V photovoltaic devices, using data from GaAs-based structures to validate the approach. In later sections, recent experimental work focused on reducing the diode dark current (and hence increasing the operating voltage) and boosting the current output of nano-enhanced III-V solar cells is summarized. In particular, the combination of a thin optical absorber and advanced light trapping structures is shown to provide a means to increase the voltage of operation while maintaining current output in photovoltaic devices. However, if the absorber thickness is reduced too far, two-dimensional carrier confinement effects will in essence enhance radiative recombination and negate the voltage benefits of thin-absorber cells. In addition, optical losses in the high-doped contact layers and surface regions can limit some of the benefits of light-trapping on voltage in thin-absorber structures. There are, however, several other mechanisms for reducing radiative emissions in photovoltaic devices. For example, radiative emissions can be minimized and voltage enhanced by embedding thin-absorbers in lower refractive index material or employing step-graded structures to harness hot carrier effects. Finally, infrared up-conversion provides a pathway to enhance current output and thus increase efficiency.

2. Generalized detailed balance model applied to optically-thin nano-enhanced devices

The concept of detailed balance is often used to estimate the limiting efficiency of ideal photovoltaic devices. Since its introduction by Shockley-Queisser, detailed balance calculations have been generalized to include a continuous absorbance function and a variety of different cell geometries [9-11]. More recently, detailed balance concepts have been further generalized and applied to the analysis of experimental results from several different types of

functional photovoltaic devices [12-14]. In this section, a generalized detailed balance model is applied to optically-thin nano-enhanced photovoltaic absorber structures. A device geometry with negligible photon recycling is considered the starting point for the discussion because of the reduced absorption inherent to optically-thin structures. Experimental dark current and external quantum efficiency characteristics from a high-voltage InGaAs quantum well structure are then analyzed within the framework of this generalized detailed balance model.

By extending detailed balance concepts to include both carrier generation and carrier transport properties, Kirchartz and Rau have demonstrated that the photovoltaic external quantum efficiency, Q_e (E), measured at normal incidence, can be related to the radiative dark current and luminescent characteristics of photovoltaic (PV) and light emitting diode (LED) devices [13]. The radiative dark current (J_{rad}) follows an n=1 voltage dependence, β (V) = exp(qV/kT) – 1, that will fundamentally limit the operating voltage of a photovoltaic device, and that can be related to the experimentally measured external quantum efficiency:

$$J_{rad} = q \int Q_e(E)\, \phi_{bb}(E)\, \beta(V)\, dE \tag{1}$$

where q is the elementary charge, V is the applied bias voltage, and kT is the thermal energy. The relevant blackbody spectral photon density spectrum, ϕ_{bb} (E), in Equation (1) is contingent upon the cell geometry, but can be generalized here with the introduction of a dark current factor (F_{dc}) to characterize, among other things, the overall effective etendue of the photovoltaic device, such that:

$$\phi_{bb}(E) = \left(2\, F_{dc} \,/\, h^3 c^2\right) E^2 \,/ (\exp(E/kT) - 1) \tag{2}$$

In many detailed balance calculations, F_{dc} is often assumed to be as low as π, corresponding to the limit in which emitted photons are reabsorbed after perfect reflection off the back surface or total internal reflection off the front surface. However, such photon recycling effects, which effectively restrict the angular emissions of the device, may become negligible in optically-thin structures with low reflectance surfaces and/or high absorbing contact layers. In this limit of negligible re-absorption:

$$F_{dc} = 2\, \pi\, n_b^2 \tag{3}$$

where n_b is the refractive index of the barrier material surrounding the optically-thin absorber.

The external quantum efficiency of a photovoltaic device, Q_e (E), is also related to the short circuit current density (J_{sc}) via:

$$J_{sc} = q \int U_c(E)\, Q_e(E)\, \phi_{sun}(E)\, dE \tag{4}$$

where ϕ_{sun} (E) is the incident solar spectrum and U_c (E) is a correction factor to the photocurrent introduced here in order to account for optical up-conversion effects [15]. In

http://dx.doi.org/10.5772/59283

conventional PV devices, U_c (E) = 1. However, in some devices, including optically-thin nano-enhanced absorber structures, the presence of low-energy photons can enhance carrier generation beyond that measured in a typical photovoltaic external quantum efficiency measurement [16-18], resulting in an effective enhancement in the incident solar spectrum such that U_c (E) > 1.

The validity of the generalized detailed balance model for optically-thin photovoltaic devices described above has been confirmed by analyzing experimental results from a high-voltage InGaAs quantum well solar cell. The measured external quantum efficiency and current-voltage characteristics from a high-voltage GaAs-based diode with a single nearly-square 15 nm InGaAs well embedded within the junction depletion region are summarized in Figure 2. The baseline diode consists of an extended p-type wide band gap emitter, which minimizes non-radiative recombination, and a relatively thin (0.5 μm) GaAs base layer, similar to the high-voltage InGaAs well structures described in reference [19]. As-grown wafers were quartered and 0.25 cm^2 thin-film cells were fabricated using a substrate removal process at MicroLink Devices [20]. The measured external quantum efficiency characteristics summarized in Figure 2 (a) were taken from a cell employing a low reflectance two-layer anti-reflectance coating on the front surface and an absorbing Ge-based back metallization. Small, simple mesa test devices were also fabricated via standard wet etch chemistry and photolithography on a second quarter piece of the same wafer. For the dark I-V measurements reported in Figure 2 (b), a test structure consisting of a device with a junction area of 200 μm x 270 μm has been employed.

The measured dark current in Figure 2 (b) exhibits a non-ideal voltage dependence at lower bias, presumably due to non-radiative recombination within the depletion region. However, the voltage dependence of the dark current approaches unity as the bias approaches 1 V. Quantitatively, the measured dark current at higher bias nearly matches the radiative dark current calculated from Equations (1) – (3), assuming T = 25°C, n_b = 3.5 (refractive index of the GaAs surrounding the well), and the measured external quantum efficiency shown in Figure 2 (a). While the calculated n=1 component of the dark current shown in Figure 2 (b) assumes negligible re-absorption ($F_{dc} = 2\pi n_b^2$), we note that the dark current factor can be generalized further to account for non-radiative and non-equilibrium effects. Non-radiative recombination will result in higher effective F_{dc} values that can also vary with voltage if recombination occurs within the junction depletion region. On the other hand, lower F_{dc} values could be obtained if the overall angular emissions of the device are restricted, for example via photon recycling, or through non-equilibrium effects such as hot carrier extraction. Finally, we note that misleadingly high F_{dc} values could be obtained if the falloff in Q_e (E) is not accurately measured at longer wavelengths, as emissions from the Urbach tail region can have a significant impact on the dark current, as will be discussed in later sections.

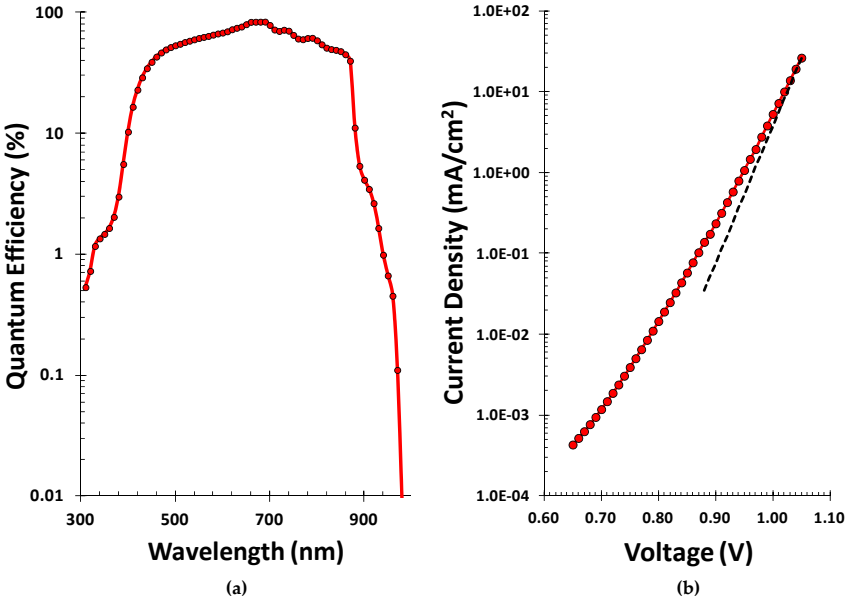

Figure 2. External quantum efficiency spectra (a) and dark current-voltage measurements (b) from a high voltage InGaAs quantum well solar cell structure employing an extended wide band-gap AlGaAs/InGaP emitter heterojunction. The dashed line in (b) is the calculated J_{rad} from equations (1) – (3) using the measured Q_e (E).

3. Dependence of radiative dark current on absorber thickness

Like conventional photovoltaic devices, the output voltage of optically-thin solar cells is governed by the underlying dark current. The dark current of typical III-V semiconductor diodes is composed of several different components involving both radiative and non-radiative processes. Non-radiative dark current processes can follow either an n=2 or n=1 voltage dependence, contingent upon the location of the recombination. Non-radiative defects within the junction depletion region contribute to the n=2 space charge recombination component of the dark current, while non-radiative defects in the quasi-neutral regions of the device contribute to the n=1 component. Radiative processes also follow an n=1 voltage dependence, and as discussed in the previous section, will ultimately limit the voltage performance of the best photovoltaic devices. In this section, the impact of absorber layer thickness on the radiative dark current is detailed after making some simplifying assumptions regarding absorption processes in GaAs-based devices.

In a previous section, we summarized how detailed balance considerations can be used to relate the radiative dark current to the external quantum efficiency – e.g. Equation (1). The external quantum efficiency is in turn proportional to the effective absorber layer width (W_{eff}) and the absorption coefficient α (E):

http://dx.doi.org/10.5772/59283

$$Q_e(E) = C(E)\,\alpha(E)\,W_{eff} \tag{5}$$

where C (E) is a correction factor which accounts for loss mechanisms, such as reflections off the front surface and photogenerated carrier recombination prior to collection. While the absorption coefficient of GaAs is arguably the most well-known of all the III-V compounds, the reported values can vary significantly with doping, particularly at energies close to and below the band gap. In this section, the GaAs absorption coefficient is modeled using a piecewise continuous function as described in Miller *et al.* [21] but calibrated using the experimental data from Kurtz *et al.* [22], as shown in Figure 3 (a).

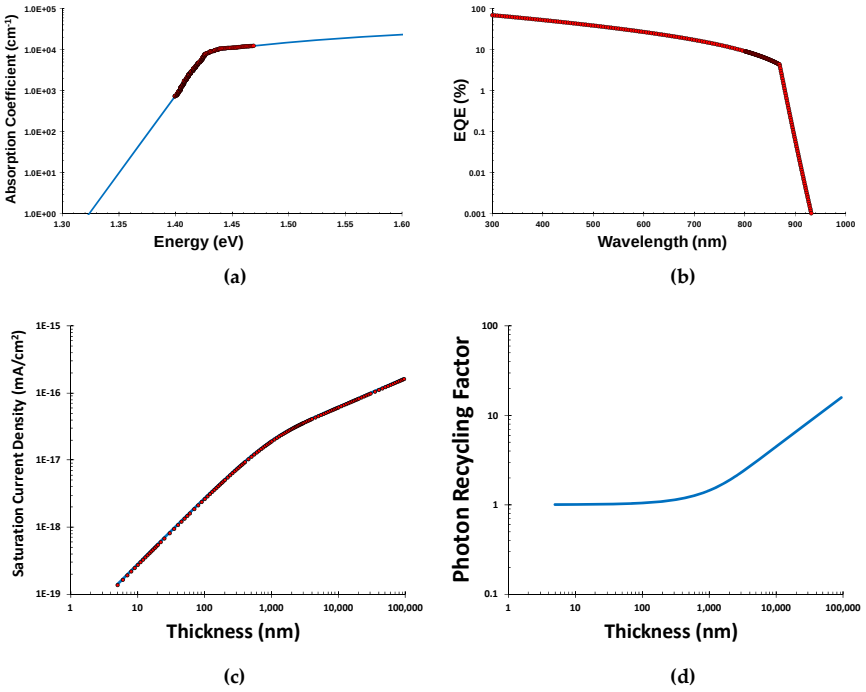

Figure 3. (a) Modeled (line) and measured (circles) absorption spectra of GaAs; (b) modeled external quantum efficiency spectra for a 50 nm GaAs absorber; (c) dependence of the radiative saturation dark current as a function of absorber layer thickness as calculated (circles) from detailed balance considerations and fit (line) to Equation (6); and (d) photon recycling factor as a function of absorber thickness, derived from the fit to Equation (6).

In the limit of negligible photon recycling, the effective absorber layer width can be equated to the physical absorber layer width ($W_{eff} = W_p$). Furthermore, in ideal structures, reflection losses are minimized and all of the absorbed photons are collected, e.g. C (E) = 1. With these simplifying assumptions, the external quantum efficiency can be calculated from equation (5) for any given thickness of an ideal GaAs absorber. For example, Figure 3 (b) depicts the calculated external quantum efficiency spectrum of a 50 nm GaAs layer. The Q_e (E) generated from Equation (5) can then be combined with equations (1) – (3) to calculate the dependence

of saturated radiative dark current on absorber thickness for GaAs, as summarized in Figure 3 (c). Clearly the radiative dark current can be reduced, and the operating voltage enhanced, by minimizing the absorber layer thickness.

Radiative recombination can also be described mechanistically in terms of carrier recombination via the use of a radiative recombination coefficient. With this mechanist approach, the radiative saturation current density ($J_{o1,rad}$) can be related to the intrinsic carrier density (n_i) and the physical absorber layer thickness (W_p) via a three-dimensional radiative recombination coefficient (B_{3D}):

$$J_{o1,rad} = q\, n_i^2\, (B_{3D} / \phi_r)\, W_p \tag{6}$$

where ϕ_r is Asbeck's photon recycling co-factor [23-24]. Figure 3 (d) summarizes the dependence of ϕ_r on thickness, as inferred from fitting Equation (6) to the radiative dark current derived from detailed balance calculations as described above and summarized in Figure 3 (c). Assuming $n_i = 2.1 \times 10^6$ cm^{-3}, a typical value quoted for GaAs, the fit also implies $B_{3D} = 3.9 \times 10^{-10}$ cm^3/s, reasonably in-line with previous estimates of the radiative recombination coefficient in GaAs [23].

4. Transition from 3D to 2D carrier confinement

Nano-enhanced III-V absorbers are a specific example of optically-thin photovoltaic device structures that are being investigated as a pathway to extend infrared absorption and increase photovoltaic power conversion efficiency. In a typical III-V nano-enhanced solar cell, quantum well and/or quantum dot layers are added to the depletion region of a PIN diode. In principle, the addition of narrow band gap material to the diode structure is expected to result in an increase in the fundamental radiative dark current. In practice, non-radiative recombination both in the narrow band gap material and underlying baseline diode often obscures the radiative dark current. However, nano-enhanced absorber structures with a novel material structure have recently achieved ultra-low dark currents by employing advanced band gap engineering to suppress non-radiative recombination and expose the limiting radiative component of the dark current [19]. As the thickness of the absorber layer decreases, quantum confinement effects can begin to play a role. In this quantum confinement limit, the variation of the radiative dark current with thickness will deviate from that implied in Equation (6), as derived in the previous section.

In this section, we describe the saturation in radiative recombination with decreasing well thickness observed in both photoluminescence and dark current measurements on high-voltage, single InGaAs well structures. The observed saturation in PL intensity and radiative dark current is consistent with a transition from a three-dimensional (3D) to a two-dimensional (2D) density of states as quantum confinement effects increase with decreasing well thickness. The dependence of the radiative dark current on well thickness is described mechanistically in terms of a transition from 3D to 2D carrier recombination.

http://dx.doi.org/10.5772/59283

Figure 4 compares the photoluminescence spectra and diode dark currents from a set of single, square InGaAs well structures with varying well thickness but the same effective well energy. These InGaAs quantum well structures have been synthesized on semi-insulating GaAs substrates via metal-organic chemical vapor deposition (MOCVD). To minimize the diode dark current, an extended wide band gap emitter heterojunction structure has been employed, consisting of wide energy-gap InGaP and AlGaAs materials in the emitter and in the depletion region adjacent to the emitter [19]. To ensure that photogenerated carriers can overcome potential energy barriers via field-assisted thermionic emission, the InGaAs quantum wells and the transitions to higher energy-gap materials are located within the built-in field of the junction depletion region [25].

The as-grown samples have been characterized by photoluminescence (PL) measurements generated with excitation from a 785 nm laser source. In Figure 4 (a), the PL intensity measured on each sample has been normalized to the peak GaAs base layer emissions near 1.42 eV. The PL emission peak from the InGaAs well is a function of both the well composition and thickness. In the set of structures discussed in this section, the indium composition in the well is higher in the thinner wells in order to maintain a peak PL emission near 1.32 eV. Interestingly, the relative PL intensity from the InGaAs layer clearly decreases as the well thickness decreases from 30 nm to 15 nm, but is only marginally lower for the structure with the thinnest well (2.5 nm).

The wafers were quartered after the PL measurements, and standard wet etch chemistry and photolithography were employed to define simple mesa test devices with junction areas as small as 75 μm x 75 μm. These devices were then characterized via illuminated current versus voltage, capacitance versus voltage, and dark current versus voltage measurements. For dark I-V measurements shown in Figure 4 (b), a test structure consisting of a device with a junction area of 200 μm x 270 μm has been employed. While some sample-to-sample scatter in the n=2 space charge recombination component of the dark current is observed, the magnitude of n=1 component of the measured dark current mimics the behavior of the relative PL intensity emitted by the InGaAs wells. Specifically, the n=1 component decreases with well thickness from 30 nm to 15 nm, but the 2.5 nm sample has a dark current that is nearly indistinguishable from the 15 nm sample. This observed near saturation in PL intensity and radiative dark current is consistent with a transition from a three-dimensional (3D) to a two-dimensional (2D) density of states as quantum confinement effects increase with decreasing well thickness.

Figure 5 compares the reverse saturation radiative current density, as derived by scaling the integrated PL spectra in Figure 4 (a), to the n=1 reverse saturation current density extracted directly from the measured dark diode current in Figure 4 (b). The comparison in Figure 5 indicates a very close correlation between the photoluminescence and dark current measurements in this sample set. By relating the radiative recombination rate to the intrinsic carrier density (n_i) via a bulk three-dimensional radiative recombination coefficient (B_{3D}), the radiative dark current in an optically thin absorber has previously been expressed in terms of the physical absorber layer thickness (W_p) – e.g. Equation (6). However, radiative emissions from quantum-confined structures can be more appropriately described in terms of a two-dimensional radiative recombination coefficient (B_{2D}) [26]. In particular, the rate of radiative recombination in a quantum-confined layer is proportional to the product of the electron and hole

densities within the quantum well. In the limit of evenly emitting wells in which the effective carrier densities are the same within each well, the radiative current density generated by a multiple quantum well structure can be expressed as:

$$J_{o1,rad} = q\, n_{qw}\, p_{qw}\, B_{2D} M_{qw} \tag{7}$$

where n_{qw} and p_{qw} are the effective quantum well electron and hole densities per unit area at zero bias and M_{qw} is the number of wells in the structure (M_{qw}=1in the set considered here). For any given effective well energy, equation (7) implies that the radiative component of the dark current will scale with the number of wells, independent of well thickness.

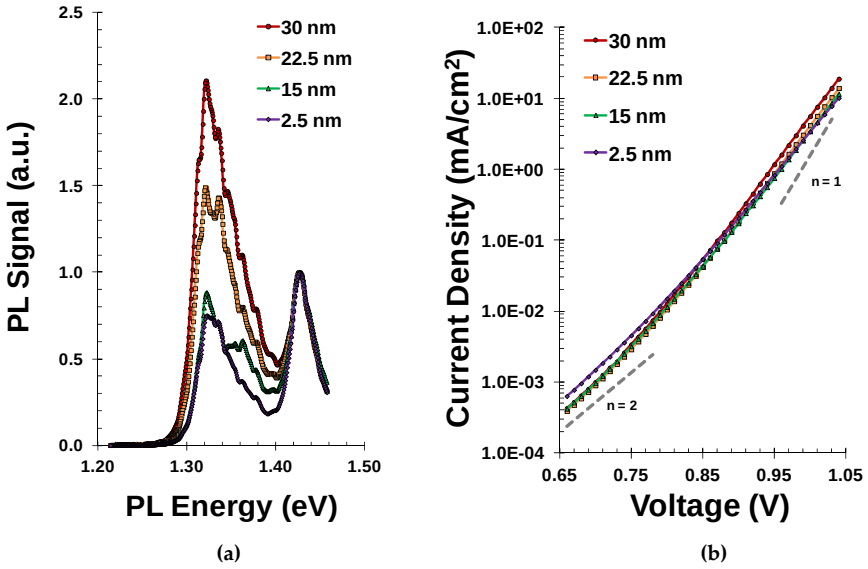

Figure 4. Normalized photoluminescence spectra (a) and dark current-voltage measurements (b) from a set of high-voltage InGaAs quantum well solar cell structures, all emitting at approximately 1.325 eV but with varying well thickness.

In Figure 5, the reverse saturation current density values inferred from both the dark diode current and photoluminescence measurements are compared to calculations using Equations (6) and (7). For the thicker samples, the variation in $J_{o1,rad}$ with absorber layer thickness is well fit by a 3D representation of the carrier recombination, as given by Equation (6), assuming the radiative recombination coefficient is independent of indium composition (B_{3D} = 3.9 x 10^{-10} cm^3/s) and that the intrinsic carrier combination scales inversely with the effective energy gap ($n_i = (N_c N_v)^{1/2} \exp(-E_g/2kT)$ = 1.57 x 10^7 cm^{-3}). On the other hand, for the thinner samples, the variation in $J_{o1,rad}$ with absorber layer thickness is well fit by a 2D representation of the carrier recombination as given by Equation (4), assuming $n_{qw} = p_{qw}$ = 0.37 cm^{-2} and B_{2D} = 1.3 x 10^{-3} cm^2/s.

http://dx.doi.org/10.5772/59283

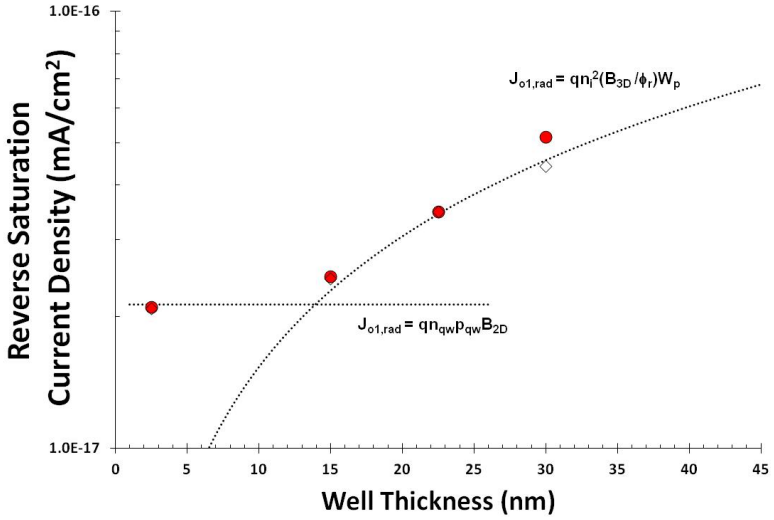

Figure 5. Reverse saturation current density of the n=1 component of the diode current as derived from the measured dark diode current (solid circles) and calculated from the measured PL spectra (open diamonds). Also shown is the expected variation in the radiative dark current in the 3D and 2D regimes using Equations (6) and (7).

5. Impact of enhanced optical path length

The application of light trapping structures to thin-film devices provides a means to both further suppress the radiative dark current via photon recycling and increase the current output via enhanced optical path lengths within the thin absorber structure. Figure 6 summarizes the current-voltage characteristics of a simple example of an optically-thin absorber structure employing a reflective back contact [6]. This uncoated test device employs a 30 nm GaAs absorber embedded within a wider energy-gap InGaP/AlGaAs heterojunction, and has been fabricated into a thin-film device using an epitaxial liftoff process at MicroLink Devices [20]. Record-low dark current characteristics for a GaAs-based device have resulted in an ultra-high open circuit voltage (V_{oc}) of 1.122 V at a short circuit current density (J_{sc}) of 14.7 mA/cm^2.

Equation (6) can be employed to estimate the expected impact of enhanced optical path length on the radiative dark current of a GaAs-based device. In particular, Figure 7 compares the calculated dependence of the radiative n=1 saturation current density as a function of absorber thickness for four different structures with varying optical path length (OPL) enhancements. Because photon emissions are omnidirectional in nature, the OPL enhancements assumed in Figure 7 represent angle averaged values. For these calculations, we further assume that B = 3.9 x 10^{-10} cm^3/s, n_i = 2.1 x 10^6 cm^{-3}, and that self- absorption effects – see ϕ_r dependence on thickness shown in Figure 3 (d) – scale with the OPL factor. Enhancements in the OPL due to reflections off the front and back surfaces of the device can result in the re-absorption of emitted

photons and thus a significant increase of self-absorption effects, particularly in thicker absorber structures.

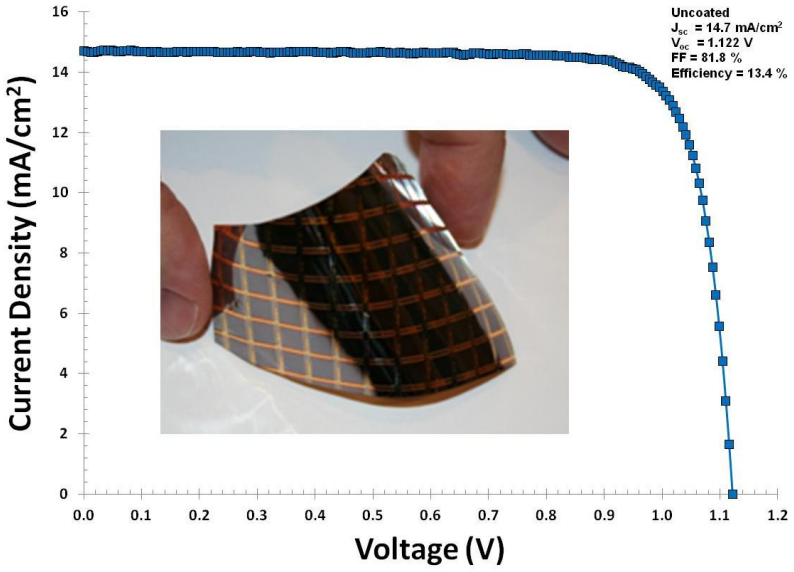

Figure 6. Illuminated current-voltage characteristics from a small area (0.25 cm²), optically-thin GaAs test device fabricated via epitaxial liftoff [19]. An optical photograph of the flexible test cells is shown inset.

For thin absorbers, such as the test device summarized in Figure 6, the impact of light trapping on radiative dark current is relatively small. However, the impact of light trapping on the short circuit current of thin-absorber structures can be quite significant. Figure 8 highlights the dependence of the short circuit current density on both the physical absorber layer thickness and the effective optical thickness due to enhancements in the optical path length. The OPL enhancements shown in Figure 8, unlike Figure 7, are not angle averaged but instead describe the average path length of normal incident photons. For these calculations, the GaAs absorption coefficient was modeled using a piecewise continuous function described in Miller *et al.* [21] but calibrated using the experimental data from Kurtz *et al.* [22], as shown earlier in Figure 3 (a). After accounting for reflection off the front surface of an uncoated device (R ~ 35%), it was further assumed that all absorbed incident low energy photons with wavelengths greater than 715 nm generated collectable electron-hole pairs. Higher energy photons are assumed to be absorbed in a wider energy gap matrix surrounding the GaAs layer, providing 13.1 mA/cm² of current under simulated AM1.5 illumination. The effective thickness in Equation (5) was then assumed to be the product of the physical thickness and the OPL factor. As seen in Figure 7, the application of light trapping structures which can enhance the optical path length of incident photons is projected to have a significant impact on the current output of thin absorber structures, but has minimal impact on thicker absorber structures.

http://dx.doi.org/10.5772/59283

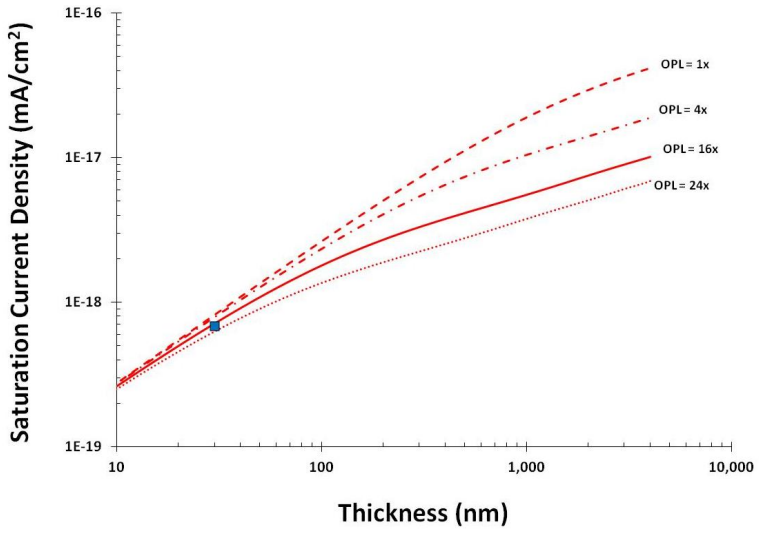

Figure 7. Projected dependence of the radiative saturation dark current as a function of GaAs absorber layer thickness assuming four different structures with varying degrees of light trapping, resulting in optical path length enhancements of 1x, 4x, 16x, and 24x. Also shown is the n=1 saturation dark current extracted from measurements on the optically-thin GaAs test device summarized in Figure 6 and described in more detail in reference [6].

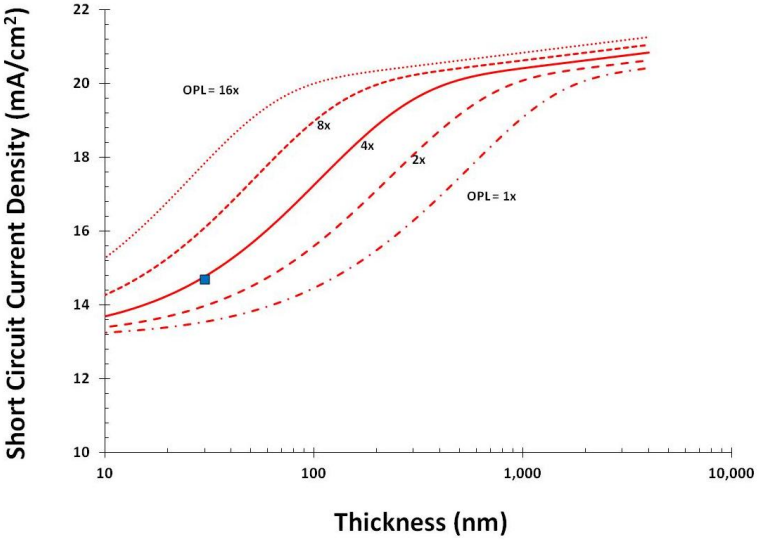

Figure 8. Projected dependence of the uncoated short circuit current as a function of GaAs absorber layer thickness under AM 1.5 illumination, assuming five different structures with varying degrees of light trapping, resulting in optical path length enhancements of 1x, 2x, 4x, 8x, and 16x. Also shown is the short circuit current density measured on the optically-thin GaAs test structure characterized in Figure 6 and described in more detail in reference [6].

6. High-voltage nano-enhanced devices with suppressed radiative recombination

In the last section, we saw that light trapping is not a particularly effective means to reduce the radiative dark current of optically-thin absorber structures. However, recent experimental work indicates that it may be possible to reduce radiative recombination in thin absorber structures by manipulating the compositional profile of quantum well absorbers [19]. In particular, a compositional step-grade design has been experimentally observed to enhance the performance of high-voltage InGaAs quantum well solar cells by reducing the overall diode dark current. A comparison of square and step-graded well structures with varying well thickness but comparable well emission energy suggests a 2x reduction in the radiative recombination coefficient. Theoretically, we will show that reducing either the Urbach tail or the refractive index environment can result in a notable reduction in the radiative dark current of optically-thin structures. In addition, non-equilibrium effects, partially hot-carrier effects, can lead to even more substantial reductions in the radiative dark current.

By embedding narrow energy-gap wells within a wide energy-gap matrix, quantum well solar cells seek to harness a wide spectrum of photons at high voltages in a single-junction device. Quantum well solar cells have the potential to deliver ultra-high efficiency over a wide range of operating conditions, avoiding the limitations of current matching inherent in multi-junction devices. Over the years, quantum well solar cells have been fabricated using a variety of different material systems, and the basic concept has been extended to include quantum dot absorber structures [27-29]. Clear enhancements in the infrared spectral response have been experimentally observed in both quantum well and quantum dot solar cells. Recently, GaAs-based quantum well solar cells with a novel material structure which minimizes non-radiative recombination have also achieved record-high open circuit voltages, in some cases exceeding 1 V at one-sun bias levels [19,30]. In this section, we detail the additional performance benefits resulting from the use of compositionally step-graded InGaAs well designs.

Figure 9 compares external quantum efficiency as derived from measured photoluminescence (PL) spectra and dark diode current-voltage characteristics from a single square InGaAs well photovoltaic device to a similar structure employing a compositionally step-graded well design. The baseline diode consists of an extended p-type wide band gap emitter, which minimizes non-radiative recombination, and a relatively thin (0.5 μm) GaAs base layer, synthesized on semi-insulating GaAs substrates via metal-organic chemical vapor deposition (MOCVD) [19]. In each structure the well is placed within the junction depletion region, as photogenerated carriers can then escape from the well via field-assisted thermionic emission [25]. A comparison of the simplified band structures of the square and step-graded wells is illustrated in Figure 10.

The indium content of the square and step-graded well structures compared in Figure 9 has been tuned to yield a nearly identical peak PL energy of approximately 1.325 eV. As a result, the forward emission and carrier collection characteristics are quite similar. However, the measured dark diode characteristics of the step-graded structure are notably lower than the square structure, with fits of the n=1 component yielding a factor of 2x reduction in the reverse

http://dx.doi.org/10.5772/59283

saturation current density. These results imply that the use of a composition step-graded profile in the quantum well results in a 2x reduction in the radiative recombination coefficient.

There are several possible mechanisms by which a step-graded well profile or other device designs may reduce the radiative recombination coefficient, and thus enhance the limiting operating voltage of photovoltaic devices. For example, any shifts in the absorption profile, and in particular the sub-band gap (e.g. Urbach tail) region, can impact radiative emissions. Figure 11 compares the calculated reverse saturation current density assuming two different Urbach tail energies. As in earlier sections, the absorption spectrum is modeled using a piecewise continuous function [21]. The absorption spectrum is then used to generate an external quantum efficiency spectrum, which is in turn used to calculate the radiative dark current based upon detailed balance concepts – e.g. Equations (5) and (1). Reducing the activation energy which describes the sub-bandgap absorption profile results in a reduction in the radiative dark current, but more so in thicker absorbers. Altering in the Urbach tail absorption characteristics may thus provide some benefits, but seems unlikely to account for the 2x reduction in the radiative recombination B-coefficient observed in thin step-graded well structures.

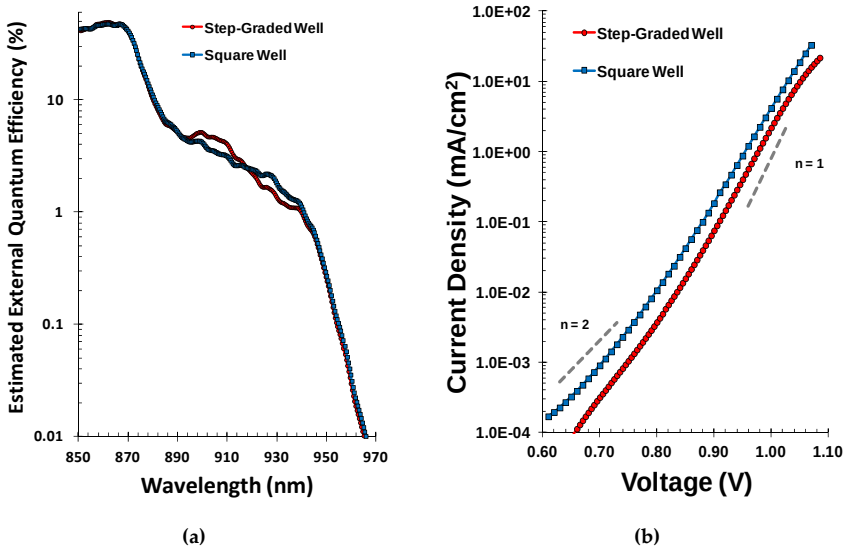

Figure 9. Estimated external quantum efficiency (a) and dark current-voltage measurements (b) from two high-voltage InGaAs quantum well structures, one employing a square well and the other a compositionally step-graded well. The external quantum efficiency was estimated from PL measurements assuming a reciprocity relationship between spectral response characteristics and luminescent emissions in PV and LED devices [12]. The dark current was measured on mesa test structures with a junction area of 500 μm x 500 μm fabricated via standard photolithography and wet etch chemistry. The dashed lines depict the slope of ideal n=1 and n=2 components of the dark current.

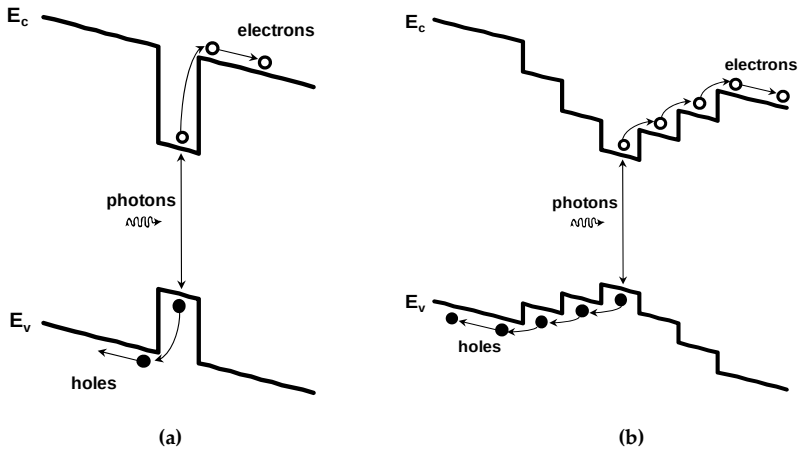

Figure 10. Simplified band structures of the (a) square and (b) step-graded well structures employed in the Figure 9 comparison, illustrating the field-assisted photogenerated carrier escape processes.

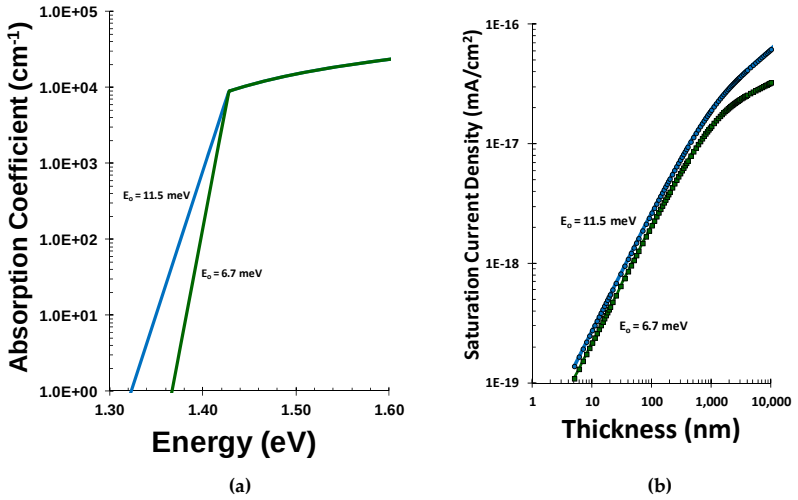

Figure 11. (a) Absorption spectra assuming two different activation energies (E_o) for the Urbach tail sub-band gap absorption, and (b) the resulting calculated radiative saturation current density as a function of absorber thickness.

Restricting the angular range of emissions provides another mechanism for reducing radiative dark current. The most direct means of restricting the range of angular emissions is to alter the refractive index environment in which the absorber layer is embedded. Figure 12 (a) summarizes the calculated radiative saturation dark current for several different refractive index values. Reducing the refractive index of the material above and below the absorber layer can

http://dx.doi.org/10.5772/59283

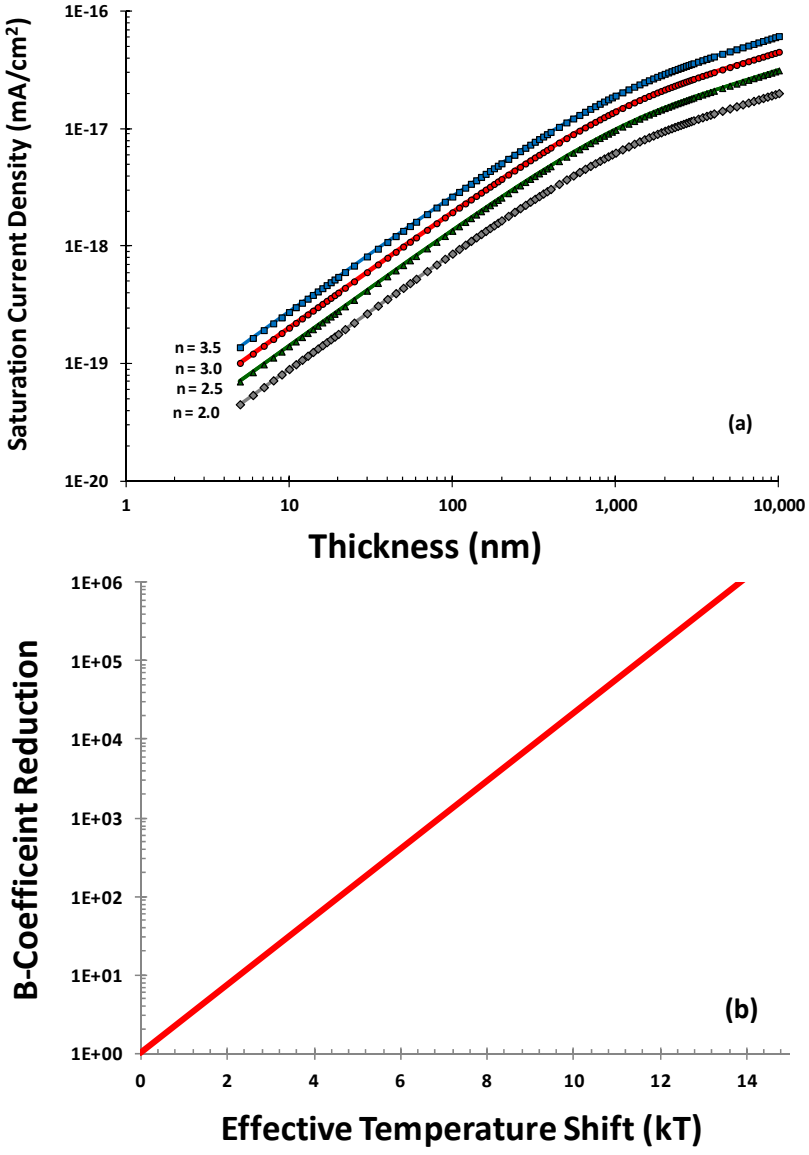

Figure 12. (a) Projected dependence of the radiative saturation dark current as a function of the refractive index of the material surrounding the absorber layer; and (b) Projected impact of hot carrier effects on the radiative recombination coefficient as a function of the effective carrier temperature difference between the barrier and wells.

effectively reduce the angular emissions, and lowering the refractive index from 3.5 to 2.5 can result in a 2x reduction in the radiative recombination coefficient. However, the changes in effective value of the refractive index in the step-graded structure are not expected to be this

large. Step-graded structures could also potentially alter the strain profile in the well, and strain in quantum wells has been found to result in a non-isotropic radiation profile that may reduce overall radiative recombination losses [31]. The non-isotropic radiation profile resulting from strain is in many ways similar to that resulting from a reduction in the refractive index of the barrier material, and while potentially beneficial, would seem unlikely to account for the 2x reduction in dark current observed in step-graded structures.

Step-graded structures may also provide a means of minimizing the overall recombination losses in quantum well solar cells. Faster escape rates can potentially be obtained by employing a step-graded compositional profile to allow photogenerated carriers to readily hop out of the InGaAs well [19], as illustrated in Figure 10. Enhanced extraction of hot carriers from the absorber region of a photovoltaic device has been suggested as a potential mechanism for reducing radiation losses and increasing efficiency [8]. Hot carrier effects can result in a large reduction in the radiative recombination, potentially reducing the B-coefficient by many orders of magnitude – see Figure 12 (b). Even a small effective carrier temperature difference of less than 1 kT is projected to result in more than a 2x reduction in the radiative dark current. Hot carrier effects can potentially be further enhanced by optimizing device design and employing optical concentration [8].

7. Intermediate band solar cells based on quantum dot nanostructures

In the previous section, we summarized how the operating voltage of nano-enhanced absorbers can be enhanced by suppressing the radiative dark current. In this section we will focus on the application of three dimensional quantum dot nanostructures in photovoltaics to increase the current output. Luque *et al*. [32] proposed that forming an intermediate band in a single junction photovoltaic cell can drastically enhance the energy conversion efficiency of the cell. The enhancement in efficiency is due to increased infrared light absorption via optical up-conversion. This type of internally up-converting PV device is known as an intermediate band solar cell (IBSC). Figure 13 shows the band diagram of a PV cell with an intermediate band. This configuration will enable the absorption of two additional sub-bandgap photons in addition to one above bandgap photon. With proper design, the ultimate open circuit voltage should not be affected by the insertion of the intermediate band. Instead, the open circuit voltage will be equal to the separation between valance and conduction band quasi Fermi levels of the wider bandgap host material, independent of the intermediate band material, i.e $V_{oc} = \mu_{CV}/q$. Based on the IBSC theory, a maximum efficiency is possible when the host material bandgap is 1.93 eV with an intermediate band located at 0.7 eV. Semiconductor quantum dots (QDs) are perhaps the best choice to create an intermediate band in a single-junction solar cell due to the inherent tunability of their shape, size, and quantum confinement properties. For an IBSC to work properly, the QD system being used must satisfy certain conditions in terms of bandgaps and band alignments [32].

Many attempts have been made to realize IBSCs based upon QD nanostructures. Initially, QD systems such as InAs, InGaAs, and GaSb dots with GaAs as host material have been studied.

http://dx.doi.org/10.5772/59283

InAs and InGaAs QDs in GaAs exhibit a type I band alignment, while GaSb QDs in GaAs have a type II band alignment. In type I QDs, both electrons in the conduction band and holes in the valence band are confined. In type II QDs, only one type of carriers is confined, for example, in GaSb QDs only holes are confined and electrons are delocalized. Compared to Type I QDs, Type II QD systems offer advantages with longer carrier life times. But in GaSb QDs the high effective mass of holes puts the hole energy levels close to each other and making it difficult to achieve an intermediate band. This makes InAs/GaAs system more appropriate to demonstrate the operation of IBSC. So far, QDs used for IBSC study have been grown using a self-assembly process known as the Stranski–Krastanov (S-K) growth method. Molecular beam epitaxy (MBE) and metal organic chemical vapor deposition (MOCVD) systems are generally used to synthesize such QDs. InAs QDs grown using on GaAs are typically 5-7 nm tall and 25-30 nm wide with QD density ranging from $10^{10} – 10^{11}$ cm^{-2}. Figure 14 shows the atomic force microscope (AFM) image of InAs QDs grown on GaAs and its distribution. The width of the intermediate band (ΔE_{IB}) formed by QD depends on the QD distribution. Larger QD distribution leads to higher ΔE_{IB}. Levy *et al*. calculated that highest cell efficiency results when ΔE_{IB} ~ 825 meV [33].

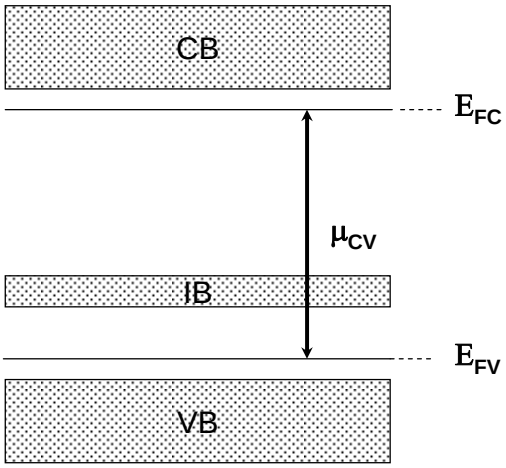

Figure 13. Schematic showing the bands involved in an intermediate band photovoltaic cell. The intermediate band is located between the conduction and valence bands of a barrier material. The open circuit voltage of this ideal cell is equal to the separation between the conduction and valence band quasi Fermi levels E_{FC} and E_{FV}. There are three transitions – valence band to conduction band, valence band to intermediate band, and intermediate band to conduction band – that contribute to the photocurrent.

A typical QD, due to its small size, has a small absorption cross section for incident photons. Due to this fact, a large number of QD layers need to be stacked together to provide sufficient sub-bandgap photon absorption. These layers are separated by a barrier material also known as a spacer. To accommodate a large number of dot layers in a given intrinsic region thickness, very thin spacers are used. However, the accumulated strain due to stacking the thin spacer

layers leads to the formation of defects and dislocations in the system. Figure 15 shows the high resolution TEM image of ten layers of InAs QDs on GaAs. A thin 15 nm spacer, which is not enough to de-couple strain between two successive dot layers, leads to dislocation formation. To avoid such effects due to QD stacking, a technique known as strain compensation has been adopted. In this technique, a tensile material with respect to both barrier and QD materials is inserted between two successive QD layers. GaP and GaAsN are widely used strain compensation materials for the InAs/GaAs system.

Figure 16 shows a schematic illustrating the strain compensation process in a multi-layer QD system. In order to compensate the strain accumulated during the stacking process, a material with smaller lattice constant with respect to the buffer layers is introduced between two successive QD layers. This process reduces the effects caused by the strain buildup. The strain compensation material and its thickness should be selected such that the total elastic strain in the system is less than a critical value. The total elastic strain (E_{total}) depends on the number of QD stacks (N), spacer thickness (t_{spacer}) and the average strain ($< \varepsilon_{\perp} >$) in each QD layer, i.e $E_{total} < N. t_{spacer.} < \varepsilon_{\perp} >$. For example, the use of a 4 monolayer (ML) thick GaP strain compensation layer relieves ~36% of the compressive strain in the InAs/GaAs material system [34]. To achieve good quality material, either the spacer should be thick enough so that the successive QD layers are strain de-coupled, or strain compensation layers must be employed. Strain compensation has been successfully implemented in photonic devices such as lasers and photovoltaic cells [29, 35-38].

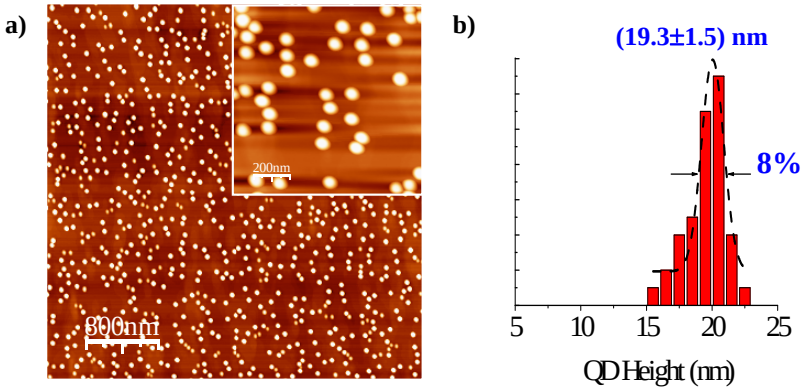

Figure 14. (a) Atomic force microscope image of InAs/GaAs QDs grown via the Stranski–Krastanov growth mode using MBE, and b) the resulting QD height distribution. As the formation of these QD is a strain driven process, a variation in QD size is expected. The FWHM of the distribution can be reduced with careful optimization of growth conditions.

http://dx.doi.org/10.5772/59283

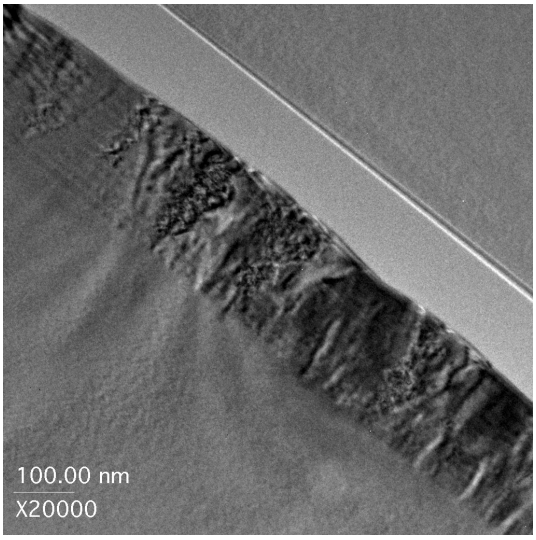

Figure 15. Cross-sectional TEM image of 10 stacks of InAs/GaAs QD grown by MOCVD with 15 nm spacers. In this structure, the use of thin spacer layers results in formation of unwanted dislocations [34].

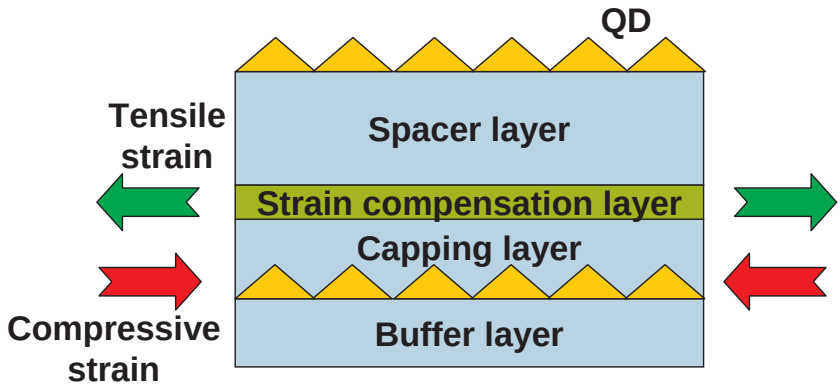

Figure 16. Schematic showing the implementation of strain compensation in a QD structure. Self-assembled QDs are formed due to compressive strain between QD and buffer materials. During the process of stacking QD layers, a material with smaller lattice constant (tensile with respect to buffer) is inserted between two successive QD layers to avoid strain induced effects.

Figure 17 shows a strain-compensated GaAs *p-i-n* photovoltaic cell in which 3 layers of InAs QD layers with a 29 nm GaAs spacer are inserted [38]. A 4 ML GaP strain compensation layer between two successive QD layers is also included here. One can easily study the affect of strain compensation by measuring PL from the stacked QD samples (transmission electron

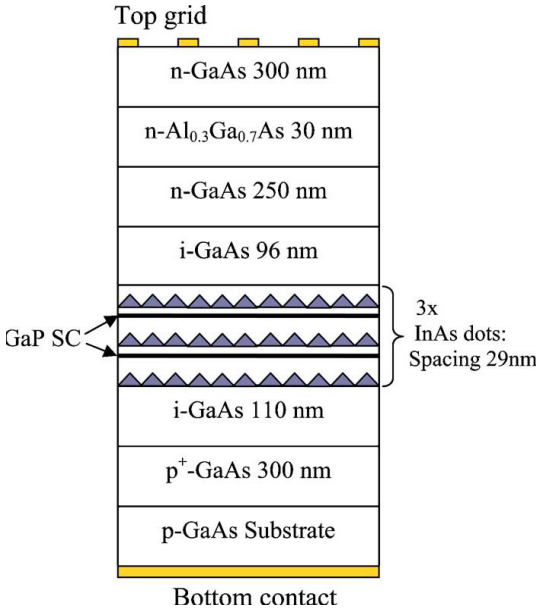

Figure 17. Schematic representation of an InAs/GaAs quantum dot photovoltaic device stucture with 3 QD layers that employ 4 ML GaP layers for strain compensation [38].

microscope and atomic force microscope also help in such study but are more destructive, expensive and time consuming). The PL measurements conducted on QDs alone are presented in Figure 18. The sample without GaP strain compensation has poor PL emission compared to that of the sample with strain compensation. This is indicative of poor material quality and increased defect density. PL from the sample without stain compensation also shows a bimodal distribution which indicates a large variation in dot size due to strain.

The electrical characteristics of QD photovoltaic cells with and without strain compensation have been studied via current-voltage (I-V) and quantum efficiency measurements. The I-V characteristics of InAs/GaAs QD PV cell structures (Figure 17) are compared in Figure 19. It is evident from the figure that the cell without strain compensation performs poorly when compared to other cells. In this study, three different GaP strain compensation schemes are chosen, i.e. 2 ML, 4 ML and 2ML+2ML (with 5 nm GaAs in between). It is observed from the data that both 4ML and 2ML+2ML samples behave in similar ways with the latter showing slightly better current. This observation is also supported by EQE data shown in Figure 20. The devices with QDs in their active regions show an extended photoresponse compared to the device without QDs. For a higher number of QD layers in the PV cell, a careful optimization of strain compensation layers is needed. Though this I-V data shows a drop in V_{OC} with the insertion of QDs in the PV cells, it is possible to develop QD cells with minimal voltage drop. Bailey *et al*. have demonstrated that by carefully tuning the QD and strain compensation material thicknesses, the V_{OC} can approach 1 V, comparable to that of the GaAs control cell [39].

http://dx.doi.org/10.5772/59283

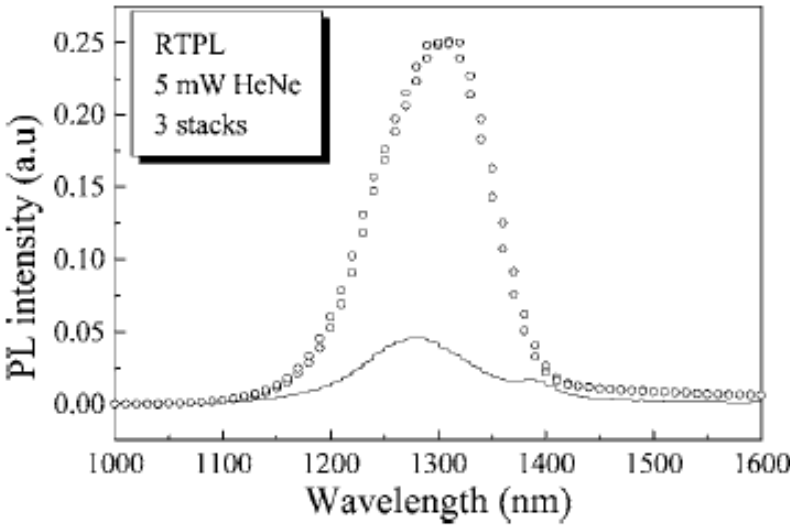

Figure 18. Photoluminescence spectra from 3 layers of stacked InAs QDs with (circles) and without (solid) strain compensation layers. It is obvious from these spectrums that including proper strain compensation layers improves the material quality.

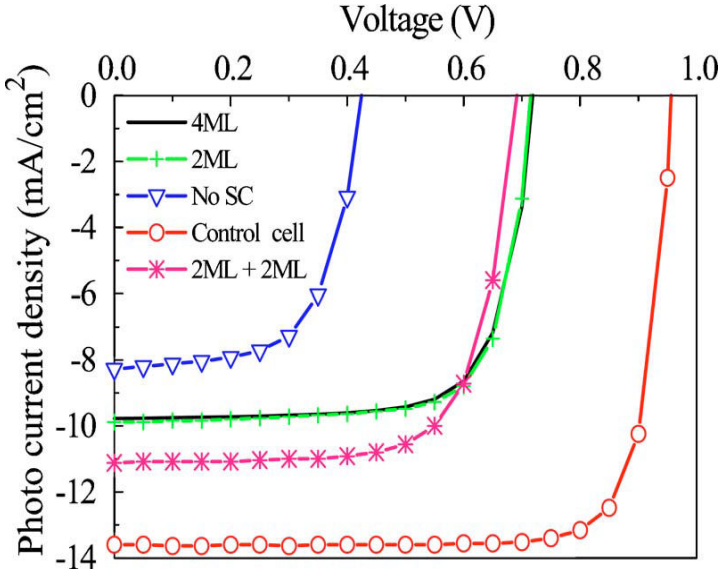

Figure 19. Current-voltage characteristics of InAs/GaAs QD photovoltaic cells with 3 QD layers. GaP has been used for compensating strain. A 2ML+2ML GaP with 5 ML separation provides best compensation.

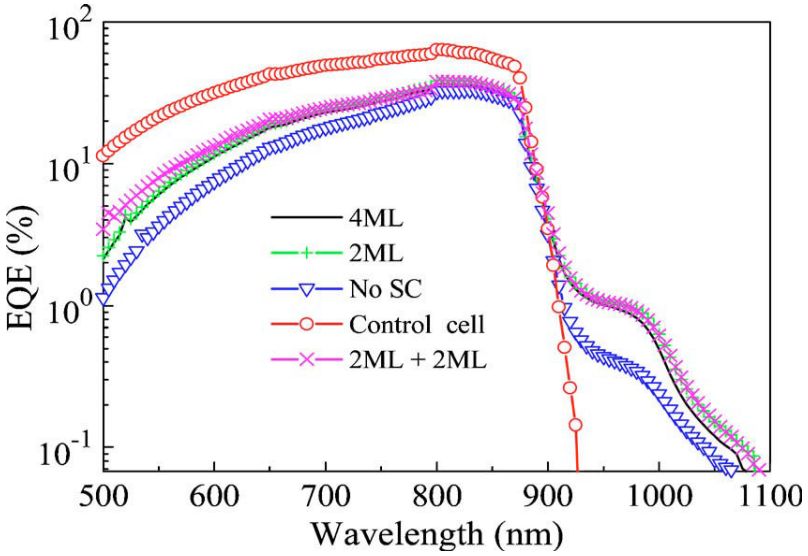

Figure 20. External quantum efficiency characteristics of photovoltaic cells fabricated with and without strain compensation layers. Clearly, the devices with strain compensation outperform the device without compensation.

8. Novel materials for intermediate band solar cells

As noted previously, there have been numerous attempts to use established QD material systems for IBSCs. However, these QD systems have had only limited success because their band alignments do not meet the IBSC requirements. Levy *et al*. and Dahal *et al*. have identified exotic material combinations that are more suitable for IBSCs [40, 41]. These material systems are difficult to grow and very few attempts have been made to realize them. Simmonds *et al*. have reported the growth of InAs(Sb) QDs with $AlAs_{0.56}Sb_{0.44}$ barriers on InP substrates [42]. This system has near ideal bandgaps for IBSCs, and furthermore, InAs(Sb)/AlAsSb QDs exhibit a type II band alignment. This offers strong electron confinement, while the valence band offset at the InAs(Sb)/AlAsSb interface is small (zero for certain As and Sb compositions). Initial attempts were made to develop InAs (no antimony) QDs. However, when InAs was directly grown on AlAsSb barriers, irrespective of good QD morphology, no PL emission was observed. This was attributed to aluminum diffusion into the QDs. The aluminum diffusion issue was solved by introducing very thin layers of $GaAs_xSb_{1-x}$ between the QD and AlAsSb layers. This process resulted in PL emission between 0.7 – 0.9 eV (at 77 K). The $GaAs_xSb_{1-x}$ spacer scheme was further optimized by Sun *et al*. to tune the QD morphology and bandgap [43].

http://dx.doi.org/10.5772/59283

Figure 21 (a) shows the schematic of InAs QD using GaAs and GaAsSb cladding layer scheme. Figure 21 (b) shows the atomic force microscope image of InAs/AlAsSb QDs with 5 ML of GaAs below the QDs. These QDs have an areal density 2×10^{10} cm^{-2} and are 4.1 nm tall and 33 nm in diameter. The average size of these QDs can be easily controlled, and hence the energies of the quantum confined states, simply by changing the InAs coverage. Power-dependent photoluminescence measurements on these QD samples confirm a type II band alignment (Figure 22). In samples containing GaAs/InAs/GaAsSb QDs, carrier lifetimes as long as 7 ns are measured. This is greater than the lifetimes measured in typical type I QD systems. These longer lifetimes are especially beneficial for efficient carrier extraction, leading to higher IBSC efficiency.

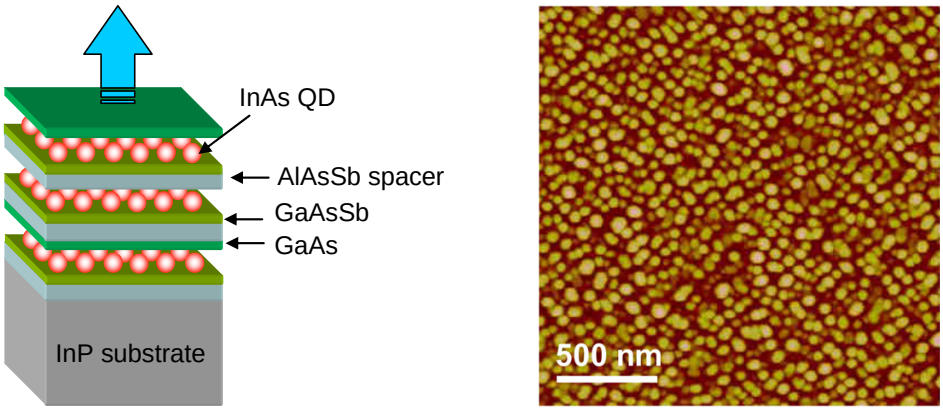

Figure 21. a) Schematic of an InAs QD structure with GaAs and $GaAs_{0.95}Sb_{0.05}$ cladding layers, as well as thin AlAsSb spacers, and b) atomic force microscopy image of InAs QDs on $AlAs_{0.56}Sb_{0.44}$ with a five-monolayer-thick GaAs cladding layer placed beneath the QDs. The QD density is $2\times10^{10}cm^{-2}$, and they are 4.1 nm tall and 33 nm in diameter [42].

To understand the performance and operation of InAs/AlAsSb QD PV cells, an AlAsSb p-i-n solar cell device was fabricated with 10 layers of InAs QDs buried within the optimized cladding layers (similar to schematic in Figure 21(a)). EQE data from an AlAsSb control cell without dots or cladding layers and another cell with cladding layers only is also presented for comparison (Figure 23). The EQE spectra show an extended wavelength response in cases where there are cladding layers and QDs. To date, this is the longest wavelength response reported in any QD PV device. The QD cell shows an extremely broad-band photoresponse up to 1800 nm, consistent with the PL measured from respective devices. Though these results are encouraging, further device optimization will be required to achieve a high efficiency IBSC performance, perhaps including the use of high solar concentrations.

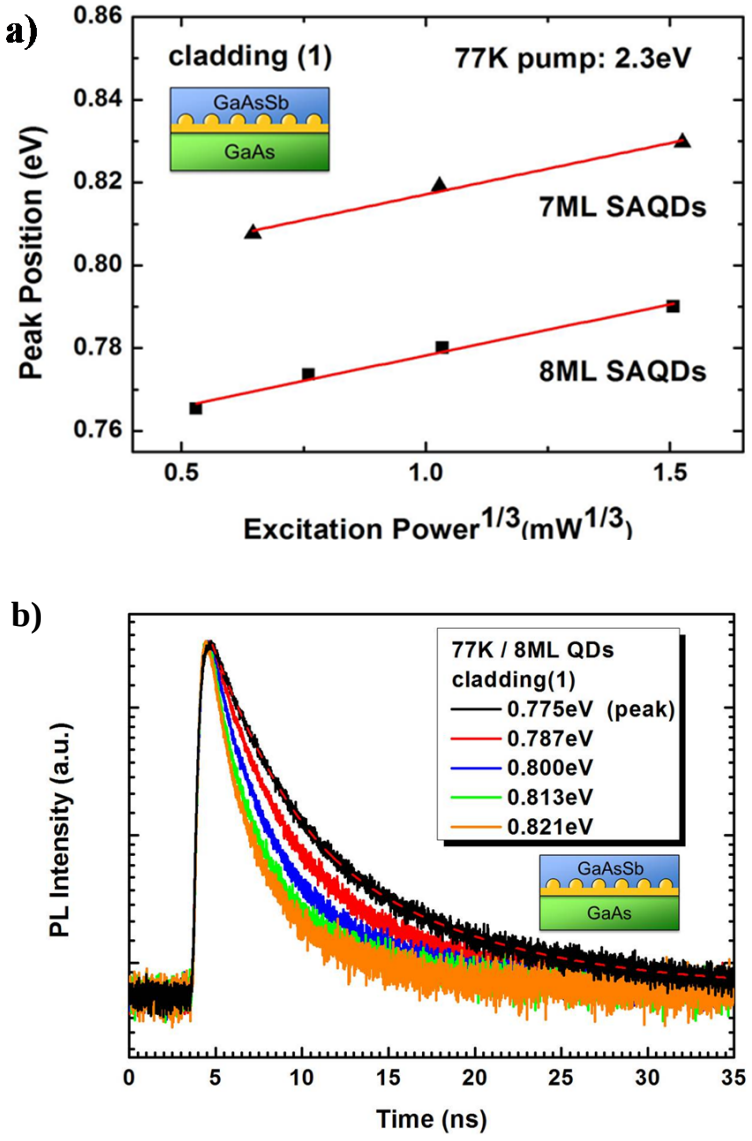

Figure 22. (a) PL peak position at 77 K as a function of the cube root of excitation power for 7 ML and 8 ML InAs QDs with optimized cladding scheme, shown in the inset, and b) time dependent PL decay traces for 8 ML InAs SAQDs at different detection wavelengths. The dashed line is the fitting curve for the decay trace at peak wavelength.

http://dx.doi.org/10.5772/59283

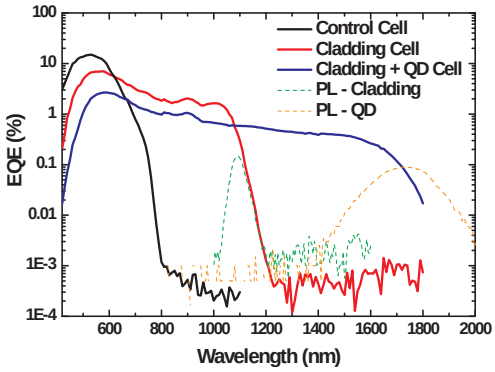

Figure 23. External quantum efficiency measured from an InAs/AlAsSb QD PV cell with GaAs and GaAsSb cladding layers, compared to measurements from a control cell and a cell incorporating only the cladding layers (no QDs). The QD cell shows a response up to 1800 nm, consistent with the PL measurements.

9. Conclusions

While multi-junction III-V devices have achieved record-breaking efficiency under select operating conditions, inherent sensitivity to changes in the spectral conditions and high manufacturing costs preclude their wide-spread usage in energy harvesting applications. On the other hand, thin-film single-junction III-V devices can offer more robust performance at lower costs. Moreover, single-junction III-V cells can potentially match or even exceed the peak efficiency performance levels of present day multi-junction devices by incorporating advanced structures that leverage light trapping, optical up-conversion and/or hot carrier effects.

In this chapter, the theoretical performance of optically-thin solar cells has been described using a generalized detailed balance model, specifically adapted for nano-enhanced absorbers. This model has been employed to assess the impact of both absorber thickness and effective optical path length on the performance of III-V photovoltaic devices, using data from GaAs-based structures to validate the approach. In later sections, recent experimental work focused on reducing the diode dark current (and hence increasing the operating voltage) and boosting the current output of nano-enhanced III-V solar cells has been summarized. In particular, the combination of a thin optical absorber and advanced light trapping structures was shown to provide a means to increase the voltage of operation while maintaining current output in photovoltaic devices. However, if the absorber thickness is reduced too far, two-dimensional carrier confinement will effectively enhance radiative recombination and negate the voltage benefits of thin-absorber cells. In addition, optical losses in the high-doped contact layers and surface regions can limit some of the enhanced voltage benefits of light-trapping in thin absorber structures. There are, however, several other mechanisms for reducing radiative emissions in photovoltaic devices. For example, radiative emissions can be minimized and the voltage increased by embedding thin-absorbers in lower refractive index material or employ-

ing step-graded structures to harness hot carrier effects. Finally, infrared up-conversion has been demonstrated as a pathway to enhance current output in intermediate band solar cells.

Author details

Roger E. Welser[1], Ashok K. Sood[1*], Ramesh B. Laghumavarapu[2], Diana L. Huffaker[2], David M. Wilt[3], Nibir K. Dhar[4] and Kimberly A. Sablon[5]

*Address all correspondence to: aksood@magnoliaoptical.com

1 Magnolia Solar, Inc., 251 Fuller Road, CESTM-B250, Albany, NY, USA

2 Electrical Engineering Department, University of California Los Angeles, CA, USA

3 Space Vehicle Directorate, Air Force Research Laboratory, Kirtland AFB, NM, USA

4 DARPA/MTO, 675 North Randolph Street, Arlington, VA, USA

5 Army Research Laboratory, 2800 Powder Mill Road, Adelphi, MD, USA

References

[1] A. Chirilă, S. Buecheler, F. Pianezzi, P. Bloesch, C. Gretener, A. R. Uhl, C. Fella, L. Kranz, J. Perrenoud, S. Seyrling, R. Verma, S. Nishiwaki, Y. E. Romanyuk, G. Bilger, and A. N. Tiwari, "Highly Efficient Cu(In,Ga)Se_2 Solar Cells Grown on Flexible Polymer Films," *Nature Materials*, vol. 10, pp. 857-861 (September 2011).

[2] C. Youtsey, J. Adams, R. Chan, V. Elarde, G. Hillier, M. Osowski, D. McCallum, H. Miyamoto, N. Pan, C. Stender, R. Tatavarti, F. Tuminello, A. Wibowo, "Epitaxial Lift-Off of Large-Area GaAs Thin-Film Multi-Junction Solar Cells," Proc. of the CS MANTECH Conference (April 2012).

[3] P. Patel, D. Aiken, A. Boca, B. Cho, D. Chumney, M. B. Clevenger, A. Cornfeld, N. Fatemi, Y. Lin, J. McCarty, F. Newman, P. Sharps, J. Spann, M. Stan, J. Steinfeldt, C. Strautin, and T. Varghese, "Experimental Results From Performance Improvement and Radiation Hardening of Inverted Metamorphic Multijunction Solar Cells," IEEE J. of Photovoltaics 2, 377 - 381 (July 2012).

[4] J. Boisvert, D. Law, R. King, E. Rehder, P. Chiu, D. Bhusari, C. Fetzer, X. Liu, W. Hong S. Mesropian, R. Woo, K. Edmondson, H. Cotal, D. Krut, S. Singer, S. Wierman, and N. H. Karam, "High Efficiency Inverted Metamorphic (IMM) Solar Cells," Proceedings of 39th IEEE PVSC Conference, Tampa, pp. 2790 - 2792 (June 2013).

[5] http://www.nrel.gov/ncpv/images/efficiency_chart.jpg

[6] R. E. Welser, G. G. Pethuraja, J. W. Zeller, A. K. Sood, K. A. Sablon, S. R. Tatavarti, and N. K. Dhar, "High-Voltage Thin-Absorber Photovoltaic Device Structures For Efficient Energy Harvesting," Proc. of SPIE, vol. 9115, no. 9115-14 (May 2014).

[7] T. Trupke and P. Wurfel, "Improved Spectral Response of Triple Tandem Solar Cells by Combined Series / Parallel Interconnection," J. Applied Phys., vol. 96, pp. 2347-2351 (August 2004).

[8] L. C. Hirst, H. Fujii, Y. Wang, M. Sygiyama, and N. J. Ekins-Daukes, "Hot Carriers in Quantum Wells for Photovoltaic Efficiency Enhancement," IEEE J. of Photovoltaics 4, 244-252 (January 2014).

[9] W. Shockley and H. J. Queisser, "Detailed Balance Limit of Efficiency of p-n Junction Solar Cells," J. Appl. Phys. 32, 510-519 (March 1961).

[10] T. Tiedje, E. Yablonovitch, G. D. Cody, and B. G. Brooks, "Limiting Efficiency of Silicon Solar Cells," IEEE Trans. Electron Devices 31, 711-716 (May 1984).

[11] A. Marti, J. L. Balenzategui, and R. F. Reyna, "Photon Recycling and Shockley's Diode Equation," J. Appl. Phys. 82, 4067-4075 (June 1997).

[12] U. Rau, "Reciprocity Relation Between Photovoltaic Quantum Efficiency and Electroluminescence Emission of Solar Cells," Phys. Rev. B 76, 085303 (August 2007).

[13] T. Kirchartz and U. Rau, "Electroluminescence Analysis of High Efficiency Cu(In,Ga)Se_2 Solar Cells," J. Appl. Phys. 102, 104510 (November 2007).

[14] S. Roensch, R. Hoheisel, F. Dimroth, and A. W. Bett, "Subcell I-V Characteristic Analysis of GaInP/GaInAs/Ge Solar Cells Using Electroluminescence Measurements," Appl. Phys. Lett. 98, 251113 (June 2011).

[15] T. Trupke, M. A. Green, and P. Wurfel, "Improving Solar Cell Efficiencies by Up-Conversion of Sub-Band-Gap Light," J. Appl. Phys. 92, 4117-4122 (October 2002).

[16] K. A. Sablon, J. W. Little, V. Mitin, A. Sergeev, N. Vagidov, and K. Reinhardt, "Strong Enhancement of Solar Cell Efficiency Due to Quantum Dots with Built-In Charge," Nano Lett. 11, 2311-2317 (May 2011).

[17] M. Sugiyama, Y. Wang, K. Watanabe, T. Morioka, Y. Okada, and Y. Nakano, "Photocurrent Generation by Two-Step Photon Absorption with Quantum-Well Superlattice Cell," IEEE J. Photovoltaics 2, 298-302 (July 2012).

[18] R. B. Laghumavarapu, M. Sun, P. J. Simmonds, B. Liang, S. Hellstroem, Z. Bittner, S. Polly, S. Hubbard, A. G. Norman, J-W. Luo, R. Welser, A. K. Sood, and D. L. Huffaker, "New Quantum Dot Nanomaterials to Boost Solar Energy Harvesting," SPIE Newsroom 10.1117/2.1201401.005315 (January 2014).

[19] R. E. Welser, O. A. Laboutin, M. Chaplin, and V. Un, "Reducing Non-Radiative and Radiative Recombination in InGaAs Quantum Well Solar Cells," Proceedings of the 37th IEEE Photovoltaic Specialists Conference, 002683-002686 (June 2011).

[20] R. Tatavarti, A. Wibowo, G. Martin, F. Tuminello, C. Youtsey, G. Hillier, N. Pan, M.W. Wanlass, and M. Romero, "InGaP/ GaAs / InGaAs Inverted Metamorphic Solar Cells on 4" Epitaxial Lifted Off (ELO) Wafers," Proceedings of 35th IEEE PVSC conference, Honolulu, pp. 002125 - 002128 (June 2010).

[21] O. D. Miller, E. Yablonovitch, and S. R. Kurtz, "Strong Internal and External Luminescence as Solar Cells Approach the Shockley-Queisser Limit," *IEEE J. of Photovoltaics*, vol. 2, pp. 303-311 (July 2012).

[22] S. Kurtz, J. F. Geisz, D. J. Friedman, J. M. Olson, and A. Duda, "Modeling of Electron Diffusion Length in GaInAsN Solar Cells," Proceedings of the 28th IEEE Photovoltaic Specialists Conference, pp. 1210-1212 (September 2000).

[23] G. B. Lush, "B-coefficient in n-type GaAs," *Solar Energy Materials & Solar Cells*, vol. 93, pp. 1225-1229 (March 2009).

[24] P. Asbeck, "Self-Absorption Effects on the Radiative Lifetime in GaAs-GaAlAs Double Heterostructures," *J. Appl. Phys*., vol. 48, pp. 820-822 (February 1977).

[25] A. Alemu, J. A. H. Coaquira, and A. Freundlich, "Dependence of Device Performance on Carrier Escape Sequence in Multi-Quantum-Well p-i-n Solar Cells," J. Appl. Phys. 99, 084506 (May 2006).

[26] P. Blood, "On the Dimensionality of Optical Absorption, Gain, and Recombination in Quantum-Confined Structures," IEEE J. of Quantum Electronics 36, 354-362 (March 2000).

[27] K. W. J. Barnham and G. Duggan, "A New Approach to High-Efficiency Multi-Band-Gap Solar Cells," J. Appl. Phys. 67, 3490-3493 (April 1990).

[28] R. B. Laghumavarapu, A. Moscho, A. Khoshakhlagh, M. El-Emawy, L.F. Lester, and D.L. Huffaker, "GaSb/GaAs Type II Quantum Dot Solar Cells for Enhanced Infrared Spectral Response," Appl. Phys. Lett. 90, 173125 (April 2007).

[29] S. M. Hubbard, C. D. Cress, C. G. Bailey, R. P. Raffaelle, S. G. Bailey, D. M. Wilt, "Effect of Strain Compensation on Quantum Dot Enhanced GaAs Solar Cells," Appl. Phys. Lett. 92, p. 123512, (March 2008).

[30] R. E. Welser, "Thick-Well Quantum-Structured Solar Cells: Design Criteria for Nano-Enhanced Absorbers," Proc. of SPIE, vol. 8620, no. 86201C (February 2013).

[31] J. G. J. Adams, W. Elder, G. Hill, J. S. Roberts, K. W. J. Barnham and N. J. Ekins-Daukes, "Higher Limiting Efficiencies for Nanostructured Solar Cells," Proc. of SPIE Vol. 7597, 759705 (January 2010).

[32] A. Luque and A. Marti, "Increasing the Efficiency of Ideal Solar Cells by Photon Induced Transitions at Intermediate Levels," Phys. Rev. Lett., vol. 76, pp. 5014-5017 (June 1997)

[33] M. Y. Levy, and C. Honsberg, "Solar cell with an intermediate band of finite width," Physical Review B, 78(16), 165122 (2008).

[34] N. Nuntawong, "Strain Compensation Technique in InAs/GaAs SAQD Structure Grown by Metalorganic Chemical Vapor Deposition," Ph.D. Dissertation, University of New Mexico (2007).

[35] A. Kouichi, N. Yamamoto, and M. Tsuchiya. "Highly Stacked Quantum-Dot Laser Fabricated Using a Strain Compensation Technique," Appl. Phys. Lett., 93(4) 041121 (2008).

[36] N. Nuntawong, Y. C.Xin, S. Birudavolu, P. S. Wong, S. Huang, C. P Hains, and D. L. Huffaker, "Quantum Dot Lasers Based on a Stacked and Strain-Compensated Active Region Grown by Metal-Organic Chemical Vapor Deposition," Appl. Phys. Lett., 86(19), 193115-193115 (2005).

[37] R. Oshima, A. Takata, Y. Okada, "Strain-Compensated InAs/GaNAs Quantum Dots for Use in High-Efficiency Solar Cells," Appl. Phys. Lett. 93, 083111, (2008).

[38] R. B. Laghumavarapu, M. El-Emawy, N. Nuntawong, A. Moscho, L. F. Lester, and D. L. Huffaker. "Improved device performance of InAs/GaAs quantum dot solar cells with GaP strain compensation layers," Appl. Phys. Lett. 91, no. 24 243115-243115 (2007).

[39] C. G. Bailey, D. V. Forbes, R. P. Raffaelle, and S. M. Hubbard, "Near 1V open circuit voltage InAs/GaAs quantum dot solar cells", Appl. Phys. Lett., 98(16), 163105 (2011).

[40] M. Y. Levy, C. Honsberg, A. Martí, and A. Luque, "Quantum Dot Intermediate Band Solar Cell Material Systems with Negligible Valence Band Offsets," IEEE 31st Photovoltaic Specialists Conference, pp. 90-93 (2005).

[41] S. N. Dahal, S. P. Bremner, and C. B. Honsberg, "Band Structure Calculation for Quantum Dot Solar Cells using KP Method," IEEE 33rd Photovoltaic Specialists Conference, pp. 1-4, (2008).

[42] P. J. Simmonds, R. B. Laghumavarapu, M. Sun, A. Lin, C. J. Reyner, B. Liang, and D. L. Huffaker, "Structural and Optical Properties of InAs/AlAsSb Quantum Dots with GaAs (Sb) Cladding Layers," Appl. Phys. Lett. 100(24), 243108 (2012).

[43] M. Sun, P. J. Simmonds, R. B. Laghumavarapu, A. Lin, C. J. Reyner, H.-S. Duan, B. Liang, D. L. Huffaker, "Effects of GaAs(Sb) Cladding Layers on InAs/AlAsSb Quantum Dots," Appl. Phys. Lett. 102, p. 023107 (2013).

Chapter 10

Crystalline Silicon Solar Cells with Nickel/Copper Contacts

Atteq ur Rehman and Soo Hong Lee

Additional information is available at the end of the chapter

http://dx.doi.org/10.5772/59008

1. Introduction

In silicon solar cell technology, metallization plays an integral part in outlining the cost and efficiency of solar cells. Indeed, the development of better techniques for the metallization of silicon solar cells is vital for achieving higher efficiencies. Presently, screen-printed contacts are primarily employed in photovoltaic industry as they can be realized easily with high throughputs. However, screen-printing technology has the draw-backs of higher contact resistance and lower aspect ratios, degrading the solar cells' performance. In recent years, an overall decrease in the photovoltaic module price index has occurred, while the higher cost of silver has disturbed this decrease adversely [1]. The future of solar cell technology will involve decreasing the wafer's thickness as well as decreasing the use of silver according to the standards set out by the international technology roadmap for photovoltaics (ITRPV) [2]. Metal contacts with superior electrical performance and lower production costs are vital for photovoltaic industrial production. In short, the pressing process of screen printing technology for thinner silicon wafers, along with expensive silver pastes, needs to be replaced by a fresh metallization technology. A series of workshops have been dedicated to the metallization of crystalline silicon solar cells, where various metallization techniques have already been inquired [3-6]. All of these meetings have helped in understanding and reforming present-day advancements in solar cell metallization techniques.

Among the capable metallization techniques, contacts composed of nickel/copper (Ni/Cu) metal stacks are considered to be one of the most feasible candidates for future metallization technologies. The use of such metal stacks offers precise and low contact resistance and also helps in improving solar cells' efficiency [7]. The most important feature is that the technique can be realized with lower material costs. Ni/Cu contact formations involve two major steps: a Ni seed layer formation followed by a Cu metal deposition as a front electrode. The Cu metal stack over the Ni layer plays the role of the main contact to the front of the cell [7-12]. The Cu

front metals stack is usually formed by an electro-plating process, which is a well-developed plating technique and can only be applied to conductors. Cu has also been deposited by an electroless plating process, but it also requires a seed layer at the silicon surface [13, 14]. An auto-catalytic method of depositing Ni-phosphorus or Ni-boron by electroless plating bath compositions can be adopted to contact the semiconducting surface of silicon [15-17]. The use of a seed layer (i.e., Ni) can help to plate metal stacks on semiconducting or even non-conducting materials. Apart from Ni deposition from a conventional Ni plating bath, it can be plated under illumination (light-induced electroless plating) [18, 19] or by laser-assisted electroless plating [20]. A galvonic deposition method was also adopted to realize thin Ni layers on a textured silicon surface uniformly [21]. The Cu metal is usually electroplated by a light-induced plating (LIP) process developed at the Fraunhofer Institute for Solar Energy (ISE) [22, 23]. The LIP process involves the immersion of a sample composed of an np-junction with aluminium (Al) screen-printed on the back into an illuminated plating bath. The details of the LIP process will be discussed in the following sections.

This chapter deals with issues regarding contact formations using Ni/Cu metal stacks for crystalline silicon solar cells. The key issues for the discussed technology are: (i) an effective Ni seed layer formation, and (ii) the development of Cu metal contacts by the LIP process. In this section, we will give an overview of the process conditions for such metallization schemes and of the current research work as well as the challenges and issues that have emerged. The sections are dedicated to addressing the most important topics in detail.

2. Silver *vs*. copper metallization

Currently, the photovoltaic industry is primarily occupied by metallization schemes composed of silver-based (Ag-based) screen-printed contacts. The key attribution is a simple process control with an attainable mass production on the industrial scale. However, the efficiencies of cells with screen-printed electrodes are degraded by factors such as the finger width and fill-factor (FF). Ag-based screen-printed contacts usually offer high contact resistance and have lower metal conductivity, and junction shunting can occur during the contact firing process. Such issues degrade the FF of the cell, which is why screen-printed contacts typically offer FFs within the range of 75-78%. On the other hand, the FFs of the contacts patterned with the photolithography process lies within the range of 81-82% [24, 25]. Moreover, screen-printed contacts offer higher shading losses because of larger finger widths (usually ≥ 100 μm wide).

The metallization of solar cell has a vital role in contributed to cell performance and it also determines a considerable number of cell processing costs. On average, about 40% of expenses are associated with the pastes used for front-and rear-side metallization [1]. This shows that the overall cost of the solar modules can be reduced drastically if the expensive Ag paste is replaced by relatively cheaper materials, such as copper. The schematics of both the metallization concepts are shown in Figure 1.

Considering the higher cost of Ag and tarnished cell parameters due to shading losses and lower FFs, screen-printed contacts offer an opportunity for replacement by an alternate metallization. Recently, metal contacts composed of Ni/Cu metal stacks have emerged and are

http://dx.doi.org/10.5772/59008

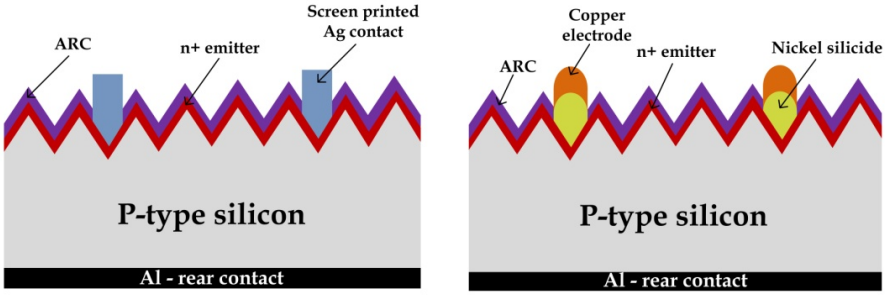

Figure 1. Schematic structures of solar cells composed of metal contacts formed with screen-printed Ag paste (left) and Ni/Cu plating (right).

considered to be a potential candidate for future crystalline silicon photovoltaic cells. Ni/Cu has shown some good results for solar cell performance in terms of improved FFs and higher efficiencies. The overall cost per watt-peak (W_p) can also be decreased as the copper is cheaper than Ag (about 100 times) and is almost equally conductive [26, 27]. It has been reported that Ni/Cu-in comparison to Ag paste-has higher electrical conductivity and lower contact resistance, even at lower doping concentrations (N_s) [28]. Cu is usually deposited by a self-aligned electro-plating process which helps to plate electrodes with finer line widths. The electrodes are plated and processed at lower temperatures (250-450 °C), considerably lower than the temperatures (700-850 °C) required for Ag pastes. The low temperature process is favourable for cell processing, as the degradation of the passivation layers can occur at higher temperatures. Furthermore, the rear side Al contact may be melted as well if Ag pastes are fired at higher temperatures. Although Cu offers certain advantages, it can create highly active generation/recombination centres if diffused in silicon [29]. In order to prevent Cu diffusion in silicon, a barrier layer is required. It has been reported that Ni plays a vital role in reducing the contact resistance as well acting as an effective diffusion barrier between Cu and silicon [30]. In Table 1, both the metallization schemes are compared in terms of the advantages and issues that they offer to crystalline silicon solar cells.

Contacts	Advantages	Challenges
Ag contacted cells	Simple process control High throughputs	Expensive Poor aspect ratios High contact resistance Lower cell efficiency
Ni/Cu plated cells	Lower price Lower shading losses High aspect ratios Low contact resistance Higher efficiency potential	Complex process Back-ground plating Poor adhesion to Si

Table 1. Comparison of the solar cells fabricated with screen-printed Ag contacts and Ni/Cu metallized solar cells.

3. Ni/Cu contacting schemes

Cu metallization offers greater resistance against electron migration and has been implemented widely for ultra-large-scale integrated circuits (ULSIs). However, it has a major weakness as being a deep-level impurity in silicon and can disturb the electrical performance of the device. These impurities tend to generate traps which act as generation/recombination centres and degrade the minority carrier lifetimes in the substrates [31, 32]. To avoid the Cu from being diffused in the silicon, Ni, as a diffusion barrier, has been employed successfully. Ni not only acts as a diffusion barrier but also promotes adhesion between Cu and silicon [9, 33]. Cu along with a Ni seed layer has given some promising results in terms of the efficiency of the crystalline silicon solar cells. The metallization technique using Ni/Cu metal stacks mainly involves two steps:

i. Ni seed layer deposition.

ii. Cu deposition by LIP.

The two step process (seed and plate) for the metallization of solar cells increases the efficiency potential considerably [34]. After depositing Ni/Cu metal stacks, a thin capping layer of silver (Ag) or tin (Sn) is usually electroplated above the Cu. The purpose of this capping layer is to prevent the Cu metal lines from being oxidized. Moreover, these capping layers help to solder the interconnecting tabs and also prevent the Cu interacting with the EVA encapsulant. The processing steps involved in metalizing the Ni/Cu/Ag or Sn metal stacks are shown in Fig. 2. However, the schematics for these steps are shown in Fig. 3.

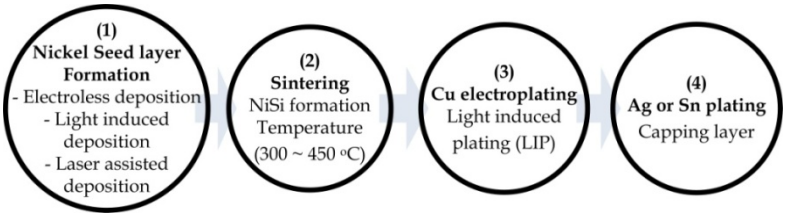

Figure 2. Processing steps involved for depositing Ni/Cu/Ag or Sn metal stacks.

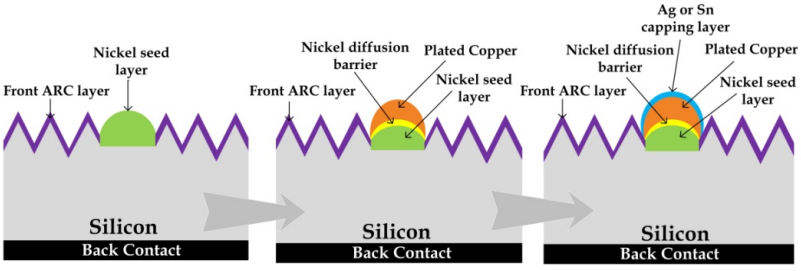

Figure 3. Schematic structures of the steps involved in the formation of Ni/Cu/Ag or Sn-based metallization schemes.

http://dx.doi.org/10.5772/59008

3.1. Ni seed layer deposition

Ni as a seed layer has to be deposited to prevent the diffusion of the Cu in the silicon. There are a number of ways to effect Ni deposition by adopting the mechanism of oxidation reduction reactions. The diffusion barriers used as alternatives to Ni include titanium (Ti) and tungsten (W) [35]. However, Ni has the ability to provide a lower contact resistance to doped silicon and it works well as a diffusion barrier [28, 36]. Low resistivity ohmic contacts can be made by initiating a low temperature sintering process after Ni deposition [8, 11, 36-38]. The basic requirement of the Ni seeding layer formation is a uniform and adequate thickness over the entire front grid. The effectiveness of the Ni barrier layer can be defined by its role in blocking Cu diffusion. In this section, various methods adopted to form a Ni diffusion barrier at various research institutes will be discussed.

3.1.1. Electroless deposition

This type of process is done without the application of any external power source. The process involves autocatalytic chemical reduction reactions to deposit metal layers. The electroless plating deposition principle is shown in Fig.4, where the reduction of metal cations occurs by electrons produced from a reducing agent. The actual electrochemical nature of the process written for the z-valent metal in the form of two half reactions is also shown in Fig. 4 [39]. The final product of the reactions comes in the form of metal deposition on the substrates. The most important feature of the electroless deposition process is that it is capable of metalizing semiconducting or even non-conducting surfaces, such as plastics, ceramics and glass.

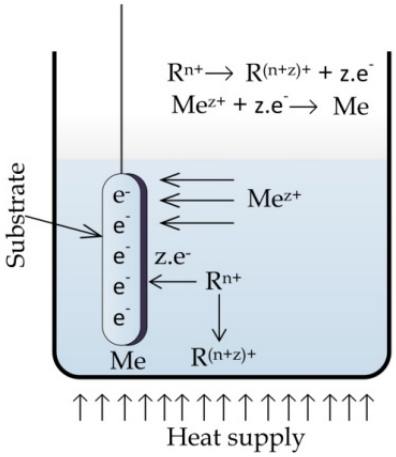

Figure 4. Electroless plating deposition principle for: the oxidation of the reductant and metal layer formation from the reduction of metal ions [39].

The Ni electroless plating bath is composed of the following bath compositions [40]:

- A source of nickel from nickel sulphate ($NiSO_4[H_2O]_6$) or nickel chloride, ($NiCl_2\ 6H_2O$).

- A reducing agent of sodium hypophosphite (NaH_2PO_2 H2O).
- A buffer or mild complex agent of triammonium citrate [$(NH_4)_3C_6H_5O_7$)].

Additionally, a small amount of ammonium hydroxide (NH_4OH) is also added to elevate the pH of the solution. The pH of the plating bath should be maintained at around 8 ~ 10 for bath stability and uniform deposition rates [10, 16, 41]. The chemical reactions based on catalytic oxidation-reduction between hypophosphite ions and Ni can be described as the sum of two simultaneous steps [27]:

$$\text{Step 1}: \ H_2PO_2^- + H_2O \rightarrow \ HPO_3^{2-} + 2H^+ + \ H^- \tag{1}$$

$$\text{Step 2}: \ 2H^- + Ni^{2+} \rightarrow \ Ni + \ H_2 \tag{2}$$

$$\text{Sum}: \ 2H_2PO_2^- + 2H_2O + Ni^{2+} \rightarrow \ Ni + H_2 + 4H^+ + 2HPO_3^{2-} \tag{3}$$

3.1.2. Light-induced deposition

Light source along with an electroless deposition process were used to deposit a Ni barrier layer. The phenomenon of a chemical reaction taking place is the same (catalytic oxidation-reduction) as described in the previous section. However, the light source provided here helps in adjusting the electrochemical potential of the front are rear of the cell and enhances the plating rates [42]. The electron migration at the surface is controlled by the photo-voltage generated from the np-junction and the electronegativity of the substrates. Moreover, higher plating rates can be achieved as these photo-generated electrons enhance the reduction of the Ni^{2+}ions on the silicon surface [15]. The increase in the plating rates due to light inclusion relives in the form of operating the bath at lower temperatures. Although a uniform Ni layer at higher plating rates can be deposited, the process of light-induced electroless plating involves complexity related to the process's characterization. Furthermore, the light-induced current in the LIP process helps to transport electrons only to the n-type surface, which limits the technique in metallizing n-type surfaces [43]. The light-induced nickel plating (LINP) process was also investigated by Yu-Han et al., and uniform Ni surfaces of high intrinsic quality were reported [44].

3.1.3. Laser-assisted deposition

Laser-assisted deposition has also been used to employ the Ni deposition process on a silicon surface. The process is considered to be feasible for industrial applications, as the anti-reflection coating (ARC) layer can be ablated along with the Ni deposition. This can reduce the number of steps involved in cell processing and can help the development of solar cells with mass production on the industrial scale.

http://dx.doi.org/10.5772/59008

Here, an electrolyte solution is used where a cell composed of an np-junction is immersed and a laser beam is applied to pattern the grid at the wafer surface. The application of the laser beam increases the temperature in the solution and at the wafer surface [20]. The ARC is ablated due to the heat generated at the laser-exposed surface and increased temperatures in the electrolyte solution decompose the Ni particles. Furthermore, the light induced in the cell generates an electron-hole pair, the generated electrons support Ni deposition at the sample surface. The use of water containing Ni salts is considered to be useful for depositing the Ni layer on the silicon surface uniformly. There has been some progress reported regarding laser chemical Ni deposition by various research institutes [45-50], although the process still needs to matured. Laser chemical metal deposition (LCMD) is a solution for implementation on the industrial scale since ARC ablation along with Ni deposition can be performed at the same time. The LCMD process was successfully implemented at Fraunhofer ISE to form Ni-based Cu metallization with 17.9% efficient cells on CZ substrates [51]. Röder et al. also reported a laser-based method to deposit a Ni layer with thinner finger widths (< 30 μm) with a low temperature process known as 'laser transfer contact' (LTC) [52].

3.2. Nickel sintering

In order to form a contact between the deposited Ni and silicon, a sintering step is required to form Ni silicide [38, 53, 54]. This sintering process helps to form an alloy of Ni and silicon and it act as a seed layer for the Cu. Furthermore, the sintering process reduces the contact resistance between the metals and the silicon interface [33]. The process involves heat treatment in the ambiance of N_2 gas, and Ni is known to form various phases at different temperatures [55]. Three different phases of Ni_2Si (~300 °C), NiSi (300~700 °C) and $NiSi_2$ (~700 °C) can be realized after the sintering process. The NiSi phase offers the lowest resistivity (~14 $\mu\Omega.cm^2$) among all three phases and is suitable for solar cell applications [10].

3.3. Copper electroplating

Subsequent to the Ni seed layer's formation with the sintering process, the deposition of a suitable metal is required in order to further reduce the line resistance of the front grid. Materials such as Ag and Cu have been deposited by using electroplating arrangements. Cu is under consideration, since it is relatively cheap in comparison to Ag and it can reduce the overall cell costs drastically. To deposit Cu, an electrolytic metal deposition method can be used. Here, a sample composed of a np-junction and a Cu anode is immersed into an admixed solution of copper sulphate ($CuSO_4[H_2O]_5$) and sulphuric acid (H_2SO_4) [56]. The $CuSO_4[H_2O]_5$) supplies, the Cu (positively charged) and SO_4 (negatively charged) ions for the electroplating process. A positive potential is applied at the anode while the sample is kept at the negative terminal. This applied potential attracts the positively charged Cu ions towards the cathode and the negatively charged SO_4 ions towards the anode. According to the reactions shown in Eq. 4, the Cu deposition occurs at the cathode due to the reduction of Cu ions [39].

$$Cu^{2+} + 2e \rightarrow Cu \tag{4}$$

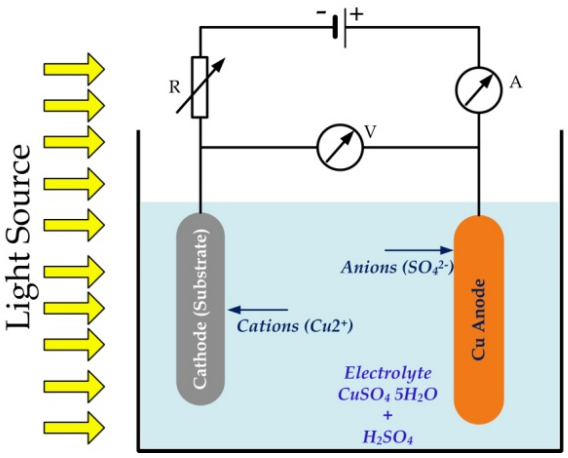

Figure 5. Schematic arrangements of Cu-based light-induced electroplating systems.

The Cu electroplating is mostly done by the approach implementing LIP arrangements as shown in Fig. 5. The LIP process works on the same principle as the conventional electroplating process; however, the inclusion of a light source enables the utilization of the photo-generation property of the solar cell. This process, developed at Fraunhofer ISE, includes the immersion of a patterned cell into the electrolyte plating with the light source arrangements. A protective potential is applied at the sample in order to make the rear-side of the cell more cathodic, which helps in minimizing the corrosion of the aluminium back-electrode. Furthermore, the plating can also be done relatively uniformly, as this potential operates the cell closer to its short-circuit conditions [43]. As to having a uniform voltage distribution across the grid pattern, the LIP process also provides stable baths with no reducing agents. LIP is an encouraging method, particularly for the solar cell metallization since it helps to deposit metal with higher aspect ratios and higher deposition rates.

3.4. Anti-reflection coating (ARC) patterning

The conventional Ag metal contacts are usually formed by screen-printing and firing the Ag pastes through SiN_x passivation layers. However, Ni/Cu-based metallization requires a separate step to open the ARC/passivation layer in order to form the contact grid. A simple example could be a mask and etch sequence [42]. Under this method, the passivated front surface of the cell is patterned with a photolithography process and the unprotected passivated layer is etched away using wet etching. Later on, the photoresist (PR) material is stripped away in an organic solvent solution (the process sequence is described in Fig. 6). For patterning the front contact grids, various approaches have been adopted. These approaches can be categorized as wet etching, direct etching, mechanical scribing and laser-assisted etching. All these etching methods will be discussed in this section of the chapter.

http://dx.doi.org/10.5772/59008

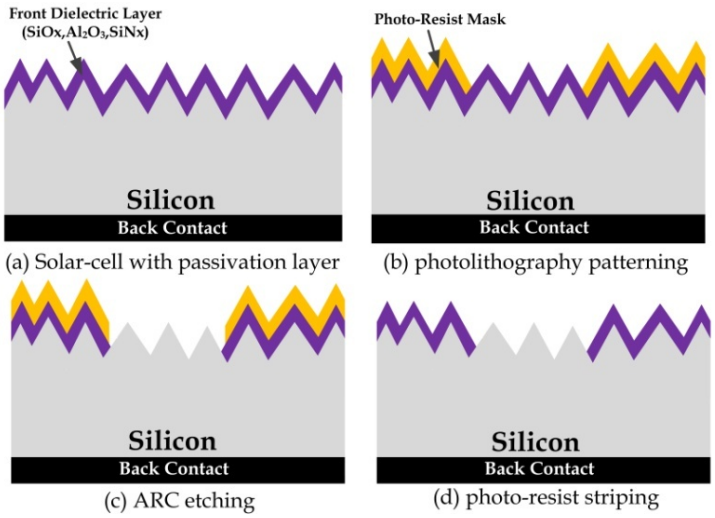

Figure 6. Mask and etch process sequence: (a) solar cell with a passivation layer, (b) front-electrode patterning with a photolithography process, (c) exposed ARC etching, and (d) PR removal.

3.4.1. Wet etching

The process of wet etching involves the front-electrode grid opening in the passivation layers through a wet chemical solution (e.g., hydrofluoric acid). An example of a mask and etch sequence using a photolithography process has already been discussed. The photolithography process has the ability to open finger lines with lower widths (reduced shading losses). Although the photolithography-based grid patterning has shown great results in the form of higher efficiencies, nonetheless the process complexity limits its implementation on the industrial scale. Other methods, such as the use of etch resists deposited by either screen printing or ink-jet printing followed by ARC etching by wet chemical treatment, have also been employed [57, 58]. The ink-jet by aerosol jet printing has also been used to etch away the contact grids by non-contact writing for front metallization [23, 57]. The wet etching methods involve some cleaning steps, which restrict their implementation on the industrial scale.

3.4.2. Direct etching

The application of appropriate etching pastes can also be helpful in etching away the passivation layer directly [59-61]. The process is done by applying phosphoric acid-based etch pastes on the ARC layer followed by temperature curing (at 300~390 °C) to etch away the desired passivation layer. Thinner finger lines (85 μm wide) have been realized by screen printing a phosphoric acid paste and curing at 350 °C for 90 seconds on a textured surface [58]. Another form of the direct etching of the passivation layer was reported which uses a water-soluble acidic polymer with a fluoride-based solution for the etching of SiN_x and SiO_x layers [62]. The method uses the fluoride-based solution-it is safer to handle in comparison to HF-

based etching solutions. Furthermore, lower expenses are involved and the method produces less waste.

3.4.3. Laser ablation

Laser-based front-contact openings and metal deposition are considered to constitute the most appropriate method for fabricating cells with Ni/Cu contacts on the industrial scale. In 1990, laser-based contact patterning was done for EFG polycrystalline silicon solar cells [63]. The laser process was used to fabricate laser-grooved buried contact (LGBC) solar cells at the University of New South Wales (UNSW), Australia [64]. Later on, a BP Solar was involved to produce LGBC solar modules commercially [65].

Laser-based ARC ablation can not only help in patterning the grid more easily with Ni deposition, but can also assist in producing cells with higher efficiencies. Thin-width laser grooves for the LGBC cells and selective emitter doping can be performed with the laser-based process for solar cell applications. Thinner finger lines and selective emitter doping ensure that a high open-circuit voltage (V_{oc}) and higher efficiencies can be realized. Moreover, the heavy diffusion step for selective emitter solar cells can be conducted relatively easily [66, 67]. At Fraunhofer ISE, laser chemical processing (LCP) was demonstrated involving the performance of local etching by the use of phosphorus doping and laser grooving with damage free silicon microstructuring [68]. LCMD and LTC methods were also adopted to pattern the front-contact grid and Ni seed layer deposition simultaneously for solar cell applications [51, 52].

3.4.4. Mechanical scribing

The front and rear contacts of the solar cells can be patterned by a process called 'mechanical scribing'. Here, an artificial diamond tip is used to scribe a uniform and shallow depth over a given surface area. The method has the advantage of process simplicity and it can be helpful in patterning the solar cell surface with high throughputs. A mechanical scribing method was used to make grooves for buried contact solar cells [69]. Passivated emitter rear-cell (PERC) solar cells with a back-contact formed by a mechanical scribing process were also reported [11]. Solar cell efficiencies of more than 20% were achieved for such PERC solar cells. An artificial diamond tip of about 10 μm was used to pattern SiO_x and SiN_x passivation layers, while Si-enriched SiN_x layers were found to be etched away easily. Solarex Corporation, USA, used a diamond blade to form deep grooves with widths within the range of 25-45 μm for solar cell applications [70]. Mechanical V-texturing for buried contact solar cells on multi-crystalline silicon with a record 17.5% efficiency was also reported [71].

4. Potential and commercial aspects

Copper can be the best alternative to silver in the front-electrode formation of crystalline silicon solar cells. The main motivation derives from the fact that it exhibits conductivity almost equal to silver, while its cost is about 100 times lower. The higher efficiency potential of the copper in terms of lower shading losses and higher FFs also provides additional benefits compared

http://dx.doi.org/10.5772/59008

to its counterparts. However, the commercialization of Cu-plated contacts is limited at present. In this portion of the chapter, the potential of Cu plating for crystalline solar cells will be discussed. State-of-the-art research developments in the field of crystalline silicon solar cells composed of Ni/Cu-plated contacts will be addressed.

4.1. High efficiency potential with n-type substrates

In recent years, the growth and increase in efficiency of silicon solar cells have been observed. N-type silicon substrates have emerged as a potential material offering considerable advantages for high efficiency photovoltaic module production on the industrial scale [72]. Based upon n-type silicon substrates, SunPower and Panasonic have already presented 24.4% IBC [73] and 24.7% HIT [74] solar cells, respectively.

Ni is known to form ohmic contacts to both p-and n-type silicon surfaces [75]. However, Ni/Cu metallization schemes for n-type substrates can play an important role in cost reduction and the improvement in the efficiency of cells (improved FF, less shadowing). It has been observed that a base material of n-type against p-type silicon has improved stability in relation to thermal Ni contact formation [76]. For a boron-doped p^+emitter on n-type silicon substrates, contact resistivity of up to 0.6 $m\Omega cm^2$ has been achieved [77]. An efficiency of 20.5% with a FF of 79.2% has already been achieved for a n-type rear-junction cell composed of Ni/Cu/Ag metal contacts [78].

4.2. Current industrial trends

Additional steps for front-contact patterning and Ni seed layer formation with a sintering step followed by Cu electroplating makes the process more complex for Ni/Cu metallized silicon solar cells. At present, Ni/Cu contacts have seen limited implementation on the industrial scale. Modules based on laser-grooved buried grid (LDBG) cells from BP Solar were only produced commercially [79]. However, there has been a lot of progress in terms of increases in solar cell efficiencies. More than 20% efficiencies have already been achieved at Fraunhofer ISE, Interuniversity Microelectronics Centre (IMEC), Kaneka, Roth & Rau Research and Schott Solar [78, 80-83]. Many research institutes have been involved in investigating metallization schemes composed of Ni/Cu metal stacks [8, 10, 13, 42, 84-90].

Thus far, efficiencies of up to 23.5% for a Cu-plated heterojunction-type solar cell have been achieved by Kaneka [80]. Roth & Rau Research also came up with a 22.3% efficient heterojunction cell with Ni/Cu contacts [81]. For a passivated emitter rear cell (PERC), solar cell structure efficiencies above 20% have already been demonstrated by Fraunhofer ISE, Schott Solar and IMEC. Fraunhofer ISE and Schott Solar presented efficiencies of 21.4% [82] and 21.3% [91], respectively. However, at IMEC, an industrially applicable Ni/Cu-plated i-PERC-type solar cell with an average efficiency of 20.5% (more than 100 cells) and a best cell efficiency of 20.79% has been fabricated [83]. IMEC also investigated the application of Ni/Cu contacts for a rear-junction solar cell on a n-type substrate and achieved a best cell efficiency of 20.5% [78]. Ni/Cu metal stacks were also applied to contact laser-doped selective emitter (LDSE) solar cells. LDSE-type solar cells with efficiencies of 19.8% and 19.64% were developed at Hyundai

Heavy Industries and Shinsung Solar, respectively [86, 92]. A 19.33% efficient LDSE-type solar cell with Ni/Cu contacts was presented at the UNSW [93]. More recently, a laser-doped Cu-plated bifacial silicon solar cell exceeding 19% efficiency was developed at UNSW [94]. Solar cells consisting of Cu-plated contacts and exceeding 20% efficiency are presented in Table 2.

Research Centre	Type	V_{oc} (mV)	J_{sc} (mA/cm^2)	Fill Factor (%)	Efficiency (%)	References
Kaneka	Hetero-junction	737	39.97	79.77	23.5	[80]
Roth & Rau	Hetero-junction	734	38.1	79.9	22.3	[81]
Fraunhofer ISE	PERC	679	38.8	81.5	21.4	[82]
Schott Solar	PERC	665	39.9	80.5	21.3	[91]
IMEC	PERC	649.8	39.3	78.3	20.79	[83]
IMEC	Rear Junction	676	38.4	79.2	20.5	[78]
Fraunhofer ISE	-	646.4	38.86	80.8	20.3	[42]

Table 2. Solar cells consisting of Cu-plated contacts exceeding 20% efficiency.

5. Challenges and open research issues

Higher efficiencies for Ni/Cu contacts have been achieved, with a reported cell efficiency as high as 23.5% for a heterojunction solar cell on CZ wafers [80]. The potential high efficiency and lower processing costs of Ni/Cu-based metallization compared to its screen printing counterpart is striking; however, there are certain factors that limit its implementation on the industrial scale. It is assumed that replacing Ag-based metallization by Ni/Cu contacts could reduce the overall cost, yet the cost of ownership for Ni/Cu contacts needs to be reviewed. If it only concerns material costs, Ni/Cu may be beneficial. However, the additional process complexity and the replacement of an Ag screen printer/dryer with equipment comprising a laser, plating arrangements and a sintering furnace should be kept in mind. Apart from the issue of process complexity, in addition contact adhesion, background plating and-more importantly – long-term reliability need to be addressed.

5.1. Process complexity

To realize Ni/Cu metal contact for solar cell applications, a number of processing steps are required. Steps such as ARC opening, Ni deposition/sintering and Cu electroplating are required. These steps make the process more complex and difficult to implement in mass production. To realize such a metallization scheme on the industrial scale, the processing steps need to be minimized. The use of lasers for depositing a Ni seed layer could help to decrease

http://dx.doi.org/10.5772/59008

these processing steps to some extent by combining ARC ablation and the Ni deposition process [45]. The conventional electroless plating techniques might be replaced with light-assisted electroless plating for faster and uniform plating. At IMEC, a simple copper metallization process with higher cell efficiencies and a reliable module was presented [95].

5.2. Contact adhesion

Cu exhibits poor adhesion to silicon and requires a seed layer to form an effective and adhesive metal contact. However, Ni has shown some promising results in providing ohmic contact with good adherence to silicon. Further improvements are required to satisfy the standard heat-quenching and peel force tests. Bath-ageing, acidity and residues on the substrate surface have been found to affect contact adhesion adversely [96, 97]. Various research institutes are currently working to improve the adhesion between Cu and silicon in order to resolve this issue completely. So far, IMEC has presented Ni/Cu metals stacks with adhesions within the range of 1~2.7 N/mm [89]. A research team at Fraunhofer ISE has also presented a two-stage process for etching the back of unreacted Ni and re-plating it [98]. Adhesion strengths of up to 2.5 N/mm were achieved by adopting just such a two-stage process at Fraunhofer ISE.

5.3. Background plating

Background plating-also known as 'ghost plating' or 'parasitic plating'-is an unwated copper plating that occurs at the passivation layers. Inhomogeneities at the SiN_x surface, silicon residuals and cracks are mainly responsible for background plating [99, 100]. The phenomenon may affect cell performance by creating undesirable shading and can divest the solar cell aesthetically. The shading affects cell performance by causing a reduction in the short-circuit current density and can also lead to junction shunting due to metal diffusion [101]. Furthermore, the localized metal silicon contact due to this undesired plating increases the recombination velocity at the surface. The point-like effects and cracks on the samples are the two main types of background plating [99].

An appropriate cleaning step is required before applying the passivation layers to remove forms of silicon residuals. Cleaning in a chemical solution, such as piranha (an admixed solution of H_2O_2 and H_2SO_2) is one way to clean the sample surface properly [99]. Another way to reduce pinholes on the SiN_x surface might be the deposition of thin (10~15 nm) silicon dioxide on diffused silicon before SiN_x deposition [101]. Mechanical stress during the ultrasonic step should be minimized and wafers should be handled carefully to avoid the microcracks which cause the undesired metal plating [99, 102].

5.4. Reliability of Ni/Cu contacts

Long-term reliability for Ni/Cu metal stacks is a very important feature and should be considered while evaluating the solar module lifetime. Cu is known to create deep-level impurities if diffused in silicon. Solar cell modules have to fulfil the criteria defined in the form of the IEC 61215 test [103]. The IEC 61215 requirements are to satisfy the conditions of either

1,000 hours damp-heat exposure at 85 °C with 85% relative humidity or a ≤5% p_{max} loss after 200 thermal cycles between-40 °C and 85 °C.

Limited progress in terms of reliability for the Ni/Cu contacts has been made, with few reports made so far [81-83]. Fraunhofer ISE and IMEC have tested solar modules according to the criteria defined by the IEC 61215 reliability test. Both Fraunhofer ISE and IMEC have come up with satisfactory results after damp heat exposure and thermal cycling tests [82, 83]. In another report, reliable Ni/Cu contacts for a heterojunction solar cell were presented which successfully passed the damp heat test when conducted for 3,000 hours [81]. In a report from RENA GmbH, Germany, modules comprising Ni/Cu/Sn metal stacks successfully passed the module reliability test, confirming that no Cu diffusion had occurred in the silicon [104].

6. Summary and outlook

A detailed overview of research activities in the field of Ni/Cu-based metallization for crystalline silicon solar cells has been presented. Many research groups across the globe have taken on the challenge of working on crystalline silicon solar cells with Ni/Cu contacts. The Ni/Cu plating, which was the topic of this section, has enormous potential in realizing improved solar cell efficiency and low cell and module costs. The generic built-up process for such metallization starts from the deposition of the Ni seed layer, which offers lower contact resistance when sintered at specific temperatures. A Cu metal is electroplated on top of this stack and after confining this layer by a top Ag or Sn capping layer. The Ni seed layer acts as a potential barrier to block Cu diffusion into the silicon and the capping layer prevents the Cu from being oxidized.

Progress has been made with various deposition options available for Ni in promoting adhesion and a diffusion barrier to the Cu. Electroless chemical baths containing Ni salts and a reducing agent of NaH_2PO_2 H_2O offer a cost-effective deposition process. The inclusion of light source in the electroless plating process results in uniform and faster deposition by utilizing the photovoltaic effect of the solar cell. Various new patterning techniques are available, including the use of etching pastes, aerosol jet and laser-based chemical metal deposition. Laser-assisted chemical metal deposition provides an opportunity to pattern the front contact grid and to deposit the Ni seed layer together. Ni deposition and ARC patterning in a single step is the solution to minimizing the processing steps and reducing the process complexity. It can provide the opportunity for cell production on the industrial scale.

Promising results in the form of solar cells with a higher FF and improved efficiency have been reported recent years. FFs of the range approaching 80% and efficiencies above 20% have already been reached at various research institutes. More recently, at IMEC, an industry-feasible Ni/Cu plating scheme for i-PERC-type solar cells with a best cell efficiency of 20.5% has been presented.

If we consider material cost and cell performance, Cu as an electrode seems to be the best alternative to the existing screen-printed Ag contacts. However, its implementation on the

industrial scale is still limited by a number of obstacles. Recent reports suggest that there has been progress in finding a solution to the hurdles of background plating and adhesion. Surface pre-treatment prior to passivation layer deposition and the low stress handling of the samples yielded an ARC surface with decreased background plating. A uniform Ni seed layer covering the contact area resulted in good adhesion strengths of the Cu lines to n-type and p-type emitters. However, the challenge of finding sustainable and reliable contacts is vital in creating viable Ni/Cu contacts for solar cells on the industrial scale.

Acknowledgements

The authors would like to thank all the members of the Green Strategic Energy Research Institute, Sejong University, Seoul, Korea. We gratefully acknowledge the financial support of the Ministry of Trade, Industry and Energy, the New and Renewable Energy Core Technology Programme of the Korea Institute of Energy Technology, Evaluation and Plating (KETEP) (No. 20133010011780) and the Korea Evaluation Institute of Industrial Technology (KEIT) (No. 10043793), Republic of Korea.

Author details

Atteq ur Rehman and Soo Hong Lee*

*Address all correspondence to: shl@sejong.ac.kr

Green Strategic Energy Research Institute, Department of Electronics Engineering, Sejong University, Seoul, Korea

References

[1] Kamp, M., Bartsch, J., Nold, S., Retzlaff, M., Hörteis, M., Glunz, S. Economic evaluation of two-step metallization processes for silicon solar cells. Energy Procedia. 2011, 8, 558-64.

[2] International Technology Roadmap for Photovoltaic (ITRPV) Home Page. Available online: http://www.itrpv.net/ (Accessed on 01 July 2014).

[3] First Work Shop on Metallization. Available online: http://www.metallizationworkshop.eu/previous-workshops/1st-edition/ (Accessed on 01 July 2014)

[4] Beaucarne, G., Hoornstra, J., Schubert, G. Lessons from the 2nd workshop on metallization of crystalline silicon solar cells. Futur. Photovolt. 2010.

[5] Beaucarne, G., Schubert, G., Hoornstra, J., Horzel, J., Glunz, S.W. Summary of the third workshop on metallization for crystalline silicon solar cells. Energy Procedia. 2012, 21, 2-13.

[6] Fourth Workshop on Metallization. Available online: http://www.metallizationworkshop.eu/ (Accessed on 01 July 2014)

[7] Raval, M.C., Solanki, C.S. Review of Ni-Cu Based Front Side Metallization for c-Si Solar Cells. Journal of Solar Energy. 2013, 2013.

[8] Chaudhari, V.A., Solanki, C.S. A novel two step metallization of Ni/Cu for low concentrator c-Si solar cells. Solar Energy Materials and Solar Cells. 2010, 94, 2094-101.

[9] Lee, E., Kim, D., Lee, S. Ni/Cu metallization for low-cost high-efficiency PERC cells. Solar energy materials and solar cells. 2002, 74, 65-70.

[10] Kim, D., Lee, E., Kim, J., Lee, S. Low-cost contact formation of high-efficiency crystalline silicon solar cells by plating. Journal of the Korean Physical Society. 2005, 46, 1208-12.

[11] Lee, S. Cost effective process for high-efficiency solar cells. Solar Energy. 2009, 83, 1285-9.

[12] Rehman, A.U., Lee, S. H. Review of the Potential of the Ni/Cu Plating Technique for Crystalline Silicon Solar Cells. Materials. 2014, 7, 1318-41.

[13] Janušonis, J., Galdikas, A., Juzumas, V., Jaraminė, L., Lukštaraupis, T., Andrijauskas, D., et al. Electroless copper contacts for low concentration silicon solar cells. In: 8th international conference on concentrating photovoltaic systems: cpv-8, AIP Publishing, 2012, Vol. 1477, pp. 53-6.

[14] Kim, A., Lee, S.J., Choi, E., Pyo, S.G. Characterization and Selective Properties of Electroless Deposited All Wet Contact Electrode. Journal of The Electrochemical Society. 2014, 161, D118-D24.

[15] Iwasa, H., Yokozawa, M., Teramoto, I. Electroless nickel plating on silicon. Journal of The Electrochemical Society. 1968, 115, 485-8.

[16] Sullivan, M.V., Eigler, J.H. Electroless nickel plating for making ohmic contacts to silicon. Journal of the electrochemical Society. 1957, 104, 226-30.

[17] Boulord, C., Kaminski, A., Canut, B., Cardinal, S., Lemiti, M. Electrical and structural characterization of electroless nickel–phosphorus contacts for silicon solar cell metallization. Journal of The Electrochemical Society. 2010, 157, H742-H5.

[18] Minsek, D. Light induced electroless plating. US Patent US20110052835 A1, 29 August 2009.

[19] Yao, Y., Sugianto, A., Lennon, A., Tjahjono, B., Wenham, S. Use of inductively coupled plasma measurements to characterise light induced plating for silicon solar cells. Solar Energy Materials and Solar Cells. 2012, 96, 257-65.

[20] Rudolph, D., Alemán, M., Bay, N., Mayer, K., Glunz, S. Laser-induced nickel deposition from an aqueous electrolyte for the front-side metallization of silicon solar cells. In: Proceeding of the 23th European Photovoltaic Solar Energy Conference, Valencia, Spain, 2008.

[21] Yao, Y., Rodriguez, J., Cui, J., Lennon, A., Wenham, S. Uniform plating of thin nickel layers for silicon solar cells. Energy Procedia. 2013, 38, 807-15.

[22] Mette, A., Schetter, C., Wissen, D., Lust, S., Glunz, S., Willeke, G. Increasing the efficiency of screen-printed silicon solar cells by light-induced silver plating. In:, Conference Record of the IEEE 4th World Conference on Photovoltaic Energy Conversion, IEEE, 2006, Vol. 1, pp. 1056-9.

[23] Hörteis, M., Glunz, S.W. Fine line printed silicon solar cells exceeding 20% efficiency. Progress in Photovoltaics: Research and Applications. 2008, 16, 555-60.

[24] Neuhaus, D.-H., Münzer, A. Industrial silicon wafer solar cells. Advances in OptoElectronics. 2008, 2007.

[25] Hilali, M.M., Rohatgi, A., To, B. A review and understanding of screen-printed contacts and selective-emitter formation. In: 14th workshop on crystalline silicon solar cells and modules, Winter Park, Colorado 2004, Vol. 1617, pp. 80401-3393.

[26] Bartsch, J., Mondon, A., Schetter, C., Hörteis, M., Glunz, S. Copper as conducting layer in advanced front side metallization processes for crystalline silicon solar cells, exceeding 20% on printed seed layers. In: 35th IEEE Photovoltaic Specialists Conference (PVSC), 2010, pp. 001299-303.

[27] Rehman, A., Lee, S. Review of the Potential of the Ni/Cu Plating Technique for Crystalline Silicon Solar Cells. Materials. 2014, 7, 1318-41.

[28] Tous, L., Recaman Payo, M., Ngamo, M., Hernandez, J.L., Poortmans, J., Mertens, R.P. Evaluating contact resistance using epitaxially grown phosphorous emitters. In: Proceedings of the 26th European Photovoltaic Solar Energy Conference, Hamburg, Germany, 2011.

[29] Weber, E.R. Transition metals in silicon. Applied Physics A. 1983, 30, 1-22.

[30] Grenon, L., Sakiotis, N., Coleman, M. Reliability of silicon solar cells with a plated nickel-copper metallization system. In: 15th Photovoltaic Specialists Conference, 1981, Vol. 1, pp. 522-6.

[31] Schibli, E., Milnes, A. Deep impurities in silicon. Materials Science and Engineering. 1967, 2, 173-80.

[32] Abd El Rehim, S., Sayyah, S., El Deeb, M. Electroplating of copper films on steel substrates from acidic gluconate baths. Applied surface science. 2000, 165, 249-54.

[33] Schroder, D.K., Meier, D.L. Solar cell contact resistance—a review. Electron Devices, IEEE Transactions on. 1984, 31, 637-47.

[34] Glunz, S., Aleman, M., Bartsch, J., Bay, N., Bayer, K., Bergander, R., et al. Progress in advanced metallization technology at Fraunhofer ISE. In: Photovoltaic Specialists Conference, 2008. PVSC'08. 33rd IEEE, IEEE, 2008, pp. 1-4.

[35] Mulligan, W.P., Cudzinovic, M.J., Pass, T., Smith, D., Swanson, R.M. Metal contact structure for solar cell and method of manufacture. Google Patents, 2008.

[36] Nguyen, A., Rane-Fondacaro, M., Efstathiadis, H., Haldar, P., Michaelson, L., Wang, C., et al. Formation of a low ohmic contact nickel silicide layer on textured silicon wafers using electroless nickel plating. Proc. of the 25th EPVSEC. 2010, 2672-5.

[37] Chaudhari, V.A., Solanki, C.S. Two Step Metallization using Ni/Cu and Ni/Ag front contacts for conversion of commercial C-Si solar cell to low concentrator solar cell. In: Proceedings of the 23rd European Photovoltaic Conference and Exhibition, 2008, pp. 1-5.

[38] Tous, L., van Dorp, D., Russell, R., Das, J., Aleman, M., Bender, H., et al. Electroless nickel deposition and silicide formation for advanced front side metallization of industrial silicon solar cells. Energy Procedia. 2012, 21, 39-46.

[39] Kannan, N. Electroplating: basic principles, processes and practice, Elsevier, 2004.

[40] Schlesinger, M. Electroless deposition of nickel. Modern Electroplating. 2000, 4, 667-84.

[41] Kim, D.H., Lee, S.H. Investigation on plated Ni/Cu contact for mono-crystalline silicon solar cells. Electronic Materials Letters. 2013, 9, 677-81.

[42] Bartsch, J., Mondon, A., Godejohann, B., Hörteis, M., Glunz, S. Advanced front side metallization for crystalline silicon solar cells based on a fully plated contact. In: Proceedings of the 25th European PV Solar Energy Conference and Exhibition, Valencia, Spain, 2010, pp. 6-10.

[43] Lennon, A., Yao, Y., Wenham, S. Evolution of metal plating for silicon solar cell metallisation. Progress in Photovoltaics: Research and Applications. 2013, 21, 1454-68.

[44] Su, Y.-H., Ma, W.-Y., Yang, T.-N., Lan, S.-M. An investigation of the mechanisms of light-induced nickel plating on P-type silicon substrates. Int. J. Electrochem. Sci. 2012, 7, 10711-21.

[45] Ochoa-Martínez, E., Wehkamp, N., Ramos-Barrado, J., Bartsch, J. Progress on Laser Assisted Nickel Seed Layer Deposition for Front Contact Copper Plating. Energy Procedia. 2013, 38, 777-86.

[46] Kordás, K., Remes, J., Leppävuori, S., Nánai, L. Laser-assisted selective deposition of nickel patterns on porous silicon substrates. Applied surface science. 2001, 178, 93-7.

[47] Karlicek, R., Donnelly, V., Collins, G. Laser-induced metal deposition on InP. Journal of Applied Physics. 1982, 53, 1084-90.

[48] Kordás, K., Leppävuori, S., Békési, J., Nánai, L., Remes, J., Vajtai, R., et al. Nickel deposition on porous silicon utilizing lasers. Applied surface science. 2002, 186, 232-6.

[49] Wang, J., Fei, X., Yu, Z., Zhao, G. Laser-induced selective deposition of Ni P alloy on silicon. Applied surface science. 1995, 84, 383-9.

[50] Knorz, A., Peters, M., Grohe, A., Harmel, C., Preu, R. Selective laser ablation of SiNx layers on textured surfaces for low temperature front side metallizations. Progress in Photovoltaics: Research and Applications. 2009, 17, 127-36.

[51] Wehkamp, N., Fell, A., Bartsch, J., Granek, F. Laser chemical metal deposition for silicon solar cell metallization. Energy Procedia. 2012, 21, 47-57.

[52] Röder, T., Hoffmann, E., Konrad, B., Köhler, J. Low temperature laser metallization for silicon solar cells. Energy Procedia. 2011, 8, 552-7.

[53] Foggiato, J., Yoo, W.S., Ouaknine, M., Murakami, T., Fukada, T. Optimizing the formation of nickel silicide. Materials Science and Engineering: B. 2004, 114, 56-60.

[54] Lee, J.D., Kwon, H.Y., Lee, S.H. Analysis of front metal contact for plated Ni/Cu silicon solar cell. Electronic Materials Letters. 2011, 7, 349-52.

[55] Léonard, F., Talin, A.A. Electrical contacts to one-and two-dimensional nanomaterials. Nature nanotechnology. 2011, 6, 773-83.

[56] Oh, W.-J., Lee, S.-H. Investigation of selective emitter in single step diffusion process for plated Ni/Cu metallization crystalline silicon solar cells. Current Applied Physics. 2013, 13, S186-S9.

[57] Mette, A., Richter, P., Hörteis, M., Glunz, S. Metal aerosol jet printing for solar cell metallization. Progress in Photovoltaics: Research and Applications. 2007, 15, 621-7.

[58] Bähr, M., Kim, S., Sridharan, S., Khadilkar, C., Shaikh, A., Köhler, I., et al. A new approach for the front side metallization of industrial type silicon solar cells using a structurization by etching. In: Proceedings of the 22nd European Photovoltaic Solar Energy Conference, Milan, Italy, 2007, pp. 1015-9.

[59] Neckermann, K., Correia, S., Andra, G. Local structuring of dielectric layers on silicon for improved solar cell metallization. Proc. 22nd EPVSEC, Milan. 2007.

[60] Park, S., Cho, E., Kim, D. Toward a High Efficiency Siliocn Solar Cells-Simplified Cell Processing using Paste Contained Phosphorous Compounds. In: Photovoltaic Energy Conversion, Conference Record of the 2006 IEEE 4th World Conference on, IEEE, 2006, Vol. 1, pp. 1231-3.

[61] Book, F., Raabe, B., Hahn, G. Two diffusion step selective emitter: comparison of mask opening by laser or etching paste. In: 23rd EUPVSEC, Valencia, Spain, 2008.

[62] Lennon, A.J., Ho-Baillie, A.W., Wenham, S.R. Direct patterned etching of silicon dioxide and silicon nitride dielectric layers by inkjet printing. Solar Energy Materials and Solar Cells. 2009, 93, 1865-74.

[63] Dubé, C., Gonsiorawski, R. Improved contact metallization for high efficiency EFG polycrystalline silicon solar cells. In: Photovoltaic Specialists Conference, 1990., Conference Record of the Twenty First IEEE, IEEE, 1990, pp. 624-8.

[64] Chong, C.M., Wenham, S.R., Green, M.A. High-efficiency, laser grooved, buried contact silicon solar cells. Applied physics letters. 1988, 52, 407-9.

[65] Jordan, D., Nagle, J. New generation of high-efficiency solar cells: Development, processing and marketing. Progress in Photovoltaics: Research and Applications. 1994, 2, 171-6.

[66] Pirozzi, L., Arabito, G., Artuso, F., Barbarossa, V., Besi-Vetrella, U., Loreti, S., et al. Selective emitters in buried contact silicon solar cells: Some low-cost solutions. Solar energy materials and solar cells. 2001, 65, 287-95.

[67] Colville, F. Laser-assisted selective emitters and the role of laser doping. Photovoltaics International. 2009, 5, 1-7.

[68] Kray, D., Fell, A., Hopman, S., Mayer, K., Willeke, G., Glunz, S. Laser chemical processing (LCP)—a versatile tool for microstructuring applications. Applied Physics A. 2008, 93, 99-103.

[69] Green, M.A., Wenham, S.R. Buried contact solar cell. Google Patents, 1988.

[70] Narayanan, S., Wohlgemuth, J., Creager, J., Roncin, S., Perry, J. Buried contact solar cells. In: Photovoltaic Specialists Conference, 1993., Conference Record of the Twenty Third IEEE, IEEE, 1993, pp. 277-80.

[71] Jooss, W., Fath, P., Bucher, E., Roberts, S., Bruton, T. Large area multicrystalline silicon buried contact solar cells with bulk passivation and an efficiency of 17.5%. In: Photovoltaic Specialists Conference, 2002. Conference Record of the Twenty-Ninth IEEE, IEEE, 2002, pp. 202-5.

[72] Geerligs, L., Romijn, I.G., Burgers, A., Guillevin, N., Weeber, A.W., Bultman, J.H., et al. Progress in low-cost n-type silicon solar cell technology. In: Photovoltaic Specialists Conference (PVSC), 2012 38th IEEE, IEEE, 2012, pp. 001701-4.

[73] Cousins, P., Smith, D., Luan, H.-C., Manning, J., Dennis, T., Waldhauer, A., et al. Generation 3: Improved performance at lower cost. In: Photovoltaic Specialists Conference (PVSC), 2010 35th IEEE, IEEE, 2010, pp. 000275-8.

[74] Taguchi, M., Yano, A., Tohoda, S., Matsuyama, K., Nakamura, Y., Nishiwaki, T., et al. 24.7% record efficiency HIT solar cell on thin silicon wafer. IEEE Journal of Photovoltaics. 2014, 4, 1-4.

[75] Dhar, S., Chakrabarti, S. Electroless Ni plating on n-and p-type porous Si for ohmic and rectifying contacts. Semiconductor science and technology. 1996, 11, 1231.

[76] Rauer, M., Mondon, A., Schmiga, C., Bartsch, J., Glatthaar, M., Glunz, S.W. Nickel-plated front contacts for front and rear emitter silicon solar cells. Energy Procedia. 2013, 38, 449-58.

[77] Seren, S., Braun, S., Schiele, Y., Hahn, G., Terheiden, B. Nickel Plating on P+Silicon: A Characterization of Contact Resistivity and Line Resistance. In: Proceedings of the 27th European Photovoltaic Solar Energy Conference and Exhibition, Frankfurt, Germany, 2012, pp. 24-8.

[78] Aleman, M., Tous, L., Cornagliotti, E., Duerinckx, F., John, J., Posthuma, N., et al. Large-area high-efficiency n-type Si rear junction cells featuring laser ablation and Cu-plated front contacts. In: 28th European Photovoltaic Solar Energy Conference and Exhibition-EUPVSEC, 2013, pp. 731-5.

[79] Bruton, T., Mason, N., Roberts, S., Hartley, O.N., Gledhill, S., Fernandez, J., et al. Towards 20% efficient silicon solar cells manufactured at 60 MWp per annum. In: Photovoltaic Energy Conversion, 2003. Proceedings of 3rd World Conference on, IEEE, 2003, Vol. 1, pp. 899-902.

[80] J.L. Hernández, D.A., K. Yoshikawa, D. Schroos, E. Van Assche, A. Feltrin, N. Valckx, N. Menou, J. Poortmans, M. Yoshimi, T. Uto, H. Uzu, M. Hino, H. Kawasaki, M. Kanematsu, K. Nakano, R. Mishima, T. Kuchiyama, G. Koizumi, C. Allebé, T. Terashita, M. Hiraishi, N. Nakanishi, K. Yamamoto High Efficiency Copper Electroplated Heterojunction Solar Cells. In: 27th European Photovoltaic Solar Energy Conference and Exhibition, 2012, pp. 655-6.

[81] Papet, P., Hermans, J., Söderström, T., Cucinelli, M., Andreetta, L., Bätzner, D., et al. Heterojunction Solar Cells with Electroplated Ni/Cu Front Electrode. In: Proceedings of the 28th European Photovoltaic Solar Energy Conference and Exhibition, Paris, France, Vol. 30.

[82] Bartsch, J., Mondon, A., Kamp, M., Kraft, A., Wendling, M., Mehling, M., et al. Copper as Conducting Layer in the Front Side Metallization of Crystalline Silicon Solar Cells-Challenges, Processes and Characterization. In: Proceedings of the 2nd Workshop on Metallization for Crystalline Silicon Solar Cells—Status, Trends and New Directions, Constance, Germany, Konstanz, Germany, 2010, Vol. 15.

[83] Russell, R., Tous, L., Labie, R., Aleman, M., Duerinckx, F., Bertens, J., et al. Cost-effective and reliable Ni/Cu plating for p-and n-type PERx silicon solar cells yielding efficiencies above 20.5%. Photovolt. Int. 2013, 2013, 62-9.

[84] You, J., Kang, J., Kim, D., Jungho Pak, J., Sik Kang, C. Copper metallization for crystalline Si solar cells. Solar energy materials and solar cells. 2003, 79, 339-45.

[85] Tous, L., Lerat, J.F., Emeraud, T., Negru, R., Huet, K., Uruena, A., et al. Nickel silicide contacts formed by excimer laser annealing for high efficiency solar cells. Progress in Photovoltaics: Research and Applications. 2013, 21, 267-75.

[86] Cho, K.-Y., Kim, J., Lee, E.-J., Hong, K.-k., Lee, H.-W., Shim, J.-M., et al. Shinsung Solar Energy high efficiency commercial crystalline Si solar cells. In: Photovoltaic Specialists Conference (PVSC), 2012 38th IEEE, IEEE, 2012, pp. 002145-8.

[87] You, J., Kang, J., Kim, D., Pak, J.J., Kang, C.S. A study on Cu metallization for crystalline Si solar cells. In: Photovoltaic Specialists Conference, 2002. Conference Record of the Twenty-Ninth IEEE, IEEE, 2002, pp. 277-80.

[88] Michaelson, L., Munoz, K., Wang, J.C., Xi, Y., Tyson, T., Gallegos, A. Improved contact formation for large area solar cells using the alternative seed layer (ASL) process. In: Photovoltaic Specialists Conference (PVSC), 2012 38th IEEE, IEEE, 2012, pp. 002208-12.

[89] Tous, L., Russell, R., Das, J., Labie, R., Ngamo, M., Horzel, J., et al. Large area copper plated silicon solar cell exceeding 19.5% efficiency. Energy Procedia. 2012, 21, 58-65.

[90] Knauss, H., Terheiden, B., Fath, P. Large-area metallisation wrap through solar cells using electroless plating. Solar energy materials and solar cells. 2006, 90, 3232-7.

[91] Metz, A., Adler, D., Bagus, S., Blanke, H., Bothar, M., Brouwer, E., et al. Industrial high performance crystalline silicon solar cells and modules based on rear surface passivation technology. Solar Energy Materials and Solar Cells. 2014, 120, 417-25.

[92] Kyeong, D., Cho, S., Lim, J., Lee, K., Hwang, M., Lee, W. Approaching 20%-efficient selective-emitter solar cells with copper front contacts on industrial 156 mm Cz Si wafers. In: Proc. 27th European Photovoltaic Solar Energy Conference and Exhibition, Frankfurt, 2012, pp. 600-3.

[93] Hallam, B., Wenham, S., Sugianto, A., Mai, L., Chong, C., Edwards, M., et al. Record large-area p-type Cz production cell efficiency of 19.3% based on LDSE technology. Photovoltaics, IEEE Journal of. 2011, 1, 43-8.

[94] Wang, X., Allen, V., Vais, V., Zhao, Y., Tjahjono, B., Yao, Y., et al. Laser-doped metal-plated bifacial silicon solar cells. Solar Energy Materials and Solar Cells. 2014.

[95] Russell, R., Tous, L., Philipsen, H., Horzel, J., Cornagliotti, E., Ngamo Toko, M., et al. A simple copper metallisation process for high cell efficiencies and reliable modules. In: 27th European Photovoltaic Solar Energy Conference and Exhibition-EUPVSEC, 2012, pp. 538-43.

[96] Walker, G.H., Lewis, B.W. A study of the adhesion of copper to nickel. Metallurgical and Materials Transactions B. 1971, 2, 2189-93.

[97] Jacquet, P.A. Adhesion of electrolytic copper deposits. Transactions of The Electrochemical Society. 1934, 66, 393-426.

[98] Mondon, A., Jawaid, M., Bartsch, J., Glatthaar, M., Glunz, S. Microstructure analysis of the interface situation and adhesion of thermally formed nickel silicide for plated nickel–copper contacts on silicon solar cells. Solar Energy Materials and Solar Cells. 2013, 117, 209-13.

[99] Braun, S., Zuschlag, A., Raabe, B., Hahn, G. The origin of background plating. Energy Procedia. 2011, 8, 565-70.

[100] Kray, D., Bay, N., Cimiotti, G., Kleinschmidt, S., Kosterke, N., Losel, A., et al. Industrial LCP selective emitter solar cells with plated contacts. In: Photovoltaic Specialists Conference (PVSC), 2010 35th IEEE, IEEE, 2010, pp. 000667-71.

[101] Wenham, S.R., Tjahjono, B.S., Kuepper, N.B., Lennon, A.J. Metallization method for silicon solar cells. Google Patents, 2010.

[102] Saint-Cast, P., Tanay, F., Alemán, M., Reichel, C., Bartsch, J., Hofmann, M., et al. Relevant pinhole characterisation methods for dielectric layers for silicon solar cells. In: Proceedings of the 24th European Photovoltaic Solar Energy Conference and Exhibition, Hamburg, Germany, 2009, pp. 21-5.

[103] Arndt, R., Puto, R. Basic understanding of IEC standard testing for photovoltaic panels.

[104] Kuehnlein, H., Koesterke, N., Cimiotti, G., Hartmannsgruber, E., Buerger, N., Nussbaumer, H., et al. > 0.4% absolute efficiency gain by fast Ni-Cu-Sn electroplating of solar cells with fine line printed contacts by a single side wet treatment technology. In: Proceedings of the 24th European Photovoltaic Solar Energy Conference and Exhibition (EU PVSEC'09), 2009, pp. 282-4.

Chapter 11

Quantum Dots Solar Cells

Khalil Ebrahim Jasim

Additional information is available at the end of the chapter

http://dx.doi.org/10.5772/59159

1. Introduction

One of the foremost challenges in solar cells industry is reducing the cost/watt of delivered solar electricity. In conventional microstructures (bulk) single junction solar cells, photons with energies less than semiconductor bandgap are not harvested while those with energies much larger than the bandgap produce hot-carries and upon cooling down (thermalization) the excess energyget wasted as heat. Therefore, novel materials or structures with tunable bandgap or intermediate band that can be tuned to match the spectral distribution of solar spectrum arecrucial. Quantum dots (QDs) have the advantage of tunable bandgap as a result of size variation as well as formation of intermediate bands. In contrast to traditional semiconductor materials that are crystalline or amorphous, quantum dots can be molded into a variety of different types, in two-dimensional (sheets) or three-dimensional arrays. They can be processed to create junctions on inexpensive substrates such as plastics, glass or metal sheets.They can easily be combined with organic polymers and dyes.

Quantum dots are a special class of semiconductors, which are nanocrystals, composed of periodic groups of II-VI, III-V, or IV-VI materials and can confine electrons (quantum confinement). When the size of a QD approaches the size of the material's exciton Bohr radius, quantum confinement effect becomes prominentand electron energy levels can no longer be treated as continuous band, they must be treated as discrete energy levels. Hence, QD can be considered as an artificial molecule with energy gap and energy levels spacing dependent on its size (radius). The energy band gap increases with a decrease in size of the quantum dot, as shown in Figure 4. As the size of a QD increases its absorption peak is red shifted due to shrinkage of its bandgap (see Figure 5). The adjustable bandgap of quantum dots allow the construction of nanostructured solar cell that is able to harvest more of the solar spectrum.QDs have large intrinsic dipole moments, which may lead to rapid charge separation. Quantum dots have been found to emit up to three electrons per photon dueto multiple exciton gener-

ation (MEG), as opposed to only one for standard crystalline silicon solar cell.Theoretically, this could boost solar power efficiencyfrom 20 % to as high as 65 %.

Generally speaking, there are three important parameters that characterize the performance of a photovoltaic cell. These are the open-circuit voltage (V_{oc}), the short circuit current (I_{sc}), and the fill factor ($F F$). However, the fill factor is also a function of V_{oc} and I_{sc}. Therefore, these last two parameters are the key factors for determining the cell's power conversion efficiency. Under ideal conditions, each photon incident on the cell with energy greater than the band gap will produce an electron flowing in the external circuit. The fill factor is determined from the maximum area of the I-V characteristics under illumination and the short circuit current and open circuit voltage, or

$$FF = \frac{V_{mp}\ \mathrm{I}_{\mathrm{m}p}}{V_{oc}\ I_{sc}} \tag{1}$$

where V_{mp} and I_{mp} are the operating point that will maximize the power output. In this case, the energy conversion efficiency is given by:

$$\eta = \frac{V_{oc}\ \mathrm{I}_{sc}\ FF}{P_{in}} \tag{2}$$

where P_{in} is the input power.

This chapter main objective is to give an introductory coverage of a more sophisticated subject. After we review the physics, designs, structures, and some growth/synthesis techniques of quantum dots. We will give a comprehensive description of some architectures of QD solar cells (e.g., Schottky cell, p-i-n configuration, depleted heterojunction, and quantum dots sensitized solar cell. Also, challenges and opportunities of quantum dots solar cells will be discussed.

2. Brief history of quantum dots

Since the early days of 1960s colloidal semiconductor crystallites or quantum dots concept has been suggested as a new structure of semiconductor materials. In 1981 Ekimove [1] reported the existence of semiconductor crystallitesin a glass matrix. In 1985 Louis Brus developed a quantum model of spherical quantum dots based on effective mass model [2]. Quantum dot term was coined in 1988 by Reed's group [3]. Smith and his coworkers [4] successfully reported the growth of quantum film by depositing 3D silver Ag islands on gallium arsenide GaAs substrate in a two-step process. By the end of the 1990s, commercial productions of colloidal quantum dots becomefeasible. In 2004 a research group at Los Alamos [5] reported that a quantum dotis capable of emitting up to three electrons per photon, as opposed to onlyone for

http://dx.doi.org/10.5772/59159

standard single crystalline layer semiconductors. It is now well established that absorption of high energy photon ($8\times E_g$) quantum dot is capable of generation seven photo-generated charge carriers due to inverse Auger recombination [6]. Now a days quantum dots are promising nanostructure materials in photonics and biomedical applications.

3. Physics of quantum dots

In a bulk semiconductor, electrons and holes are free to move and there is no confinement and hence they have continuous energy values, where energy levels are so close to each other and packed such that energy bands are formed. Occupied bands called valance band and empty ones called conduction bands. The highest occupied band (valance band) and the lowest unoccupied band (conduction band) are separated by what is called energy bandgap E_g. Exciton is formed when electron hole pair are generated. The bond electron-hole system (exciton) form a hydrogen like atom. The separation of between the electron-hole is called Bohr's radius. Table 1 presents examples of exciton Bohr radius for some semiconductors.

Semiconductor Structure	Exciton Bohr Radius (nm)	Bandgap Energy (eV)
PbS	40.0	0.41
GaAs	28.0	1.43
CdTe	15.0	1.50
CdSe	10.6	1.74
ZnSe	8.4	2.58
CdS	5.6	2.53

Table 1. Exciton Bohr radius and bandgap energy of some common semiconductors.

Dimensionality of a material specifies how many dimensions do the carriers of thematerial act as free carriers. In bulk semiconductor continuous density of states results in both conduction and valence bands. However, when the number of atoms in the lattice is very few, the density of states becomes discrete, and loses the continuous 'band' likefeature. Generally speaking, when a material has one or more dimensions small enough to affect itselectronic density of state as illustrated in Figure 1, then the material is said to be confined. Accordingly we can have quantum wells, quantum wires, and quantum dots. Bulk semiconductor materials are example of three dimensional systems where density of states is proportional to $(E-E_{c/v})^{1/2}$. Quantum well system is a two dimensional system where electrons are confined in one dimension and therefore possess step like density of states. Quantum wire system is a one dimensional systemwhere electrons are confined in two dimensions and therefore possess density of states proportional to $(E-E_{c/v})^{-1/2}$. Quantum dot is a zero dimensional system where electron motion is confined in three dimensions. Therefore, a quantum dot possess atomic like density of states that is described mathematically by a delta function $\delta(E-E_{c/v})$.

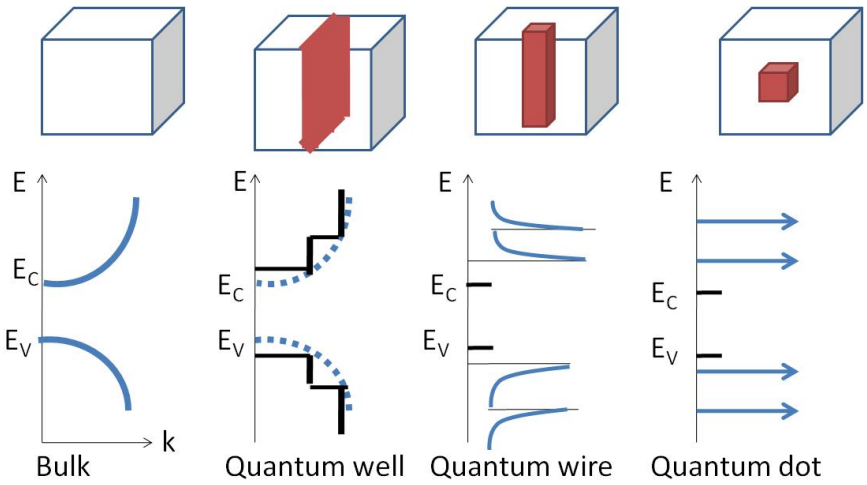

Figure 1. Schematic of density of states as system dimensionality is reduced. The density of states in different confinement configurations: (a) bulk; (b) quantum well; (c) quantum wire; (d) quantum dot. The conduction and valence bands split into overlapping subbands that become successively narrower as the electron motion is restricted in more dimensions. dimension. Adopted from [7].

In fact, quantum confinement is mainlybecause of relatively few atoms presentin a quantum dot (see Figure 2),where excitons get confined to a much smaller space, on the order of the material's exciton Bohr radius. This pronounced confinement leads to discrete, quantized energy levels more like those of an atom than the continuous bands of a bulk semiconductor. For this reason in some literatures, quantum dots have sometimes been referred to as "artificial atoms."

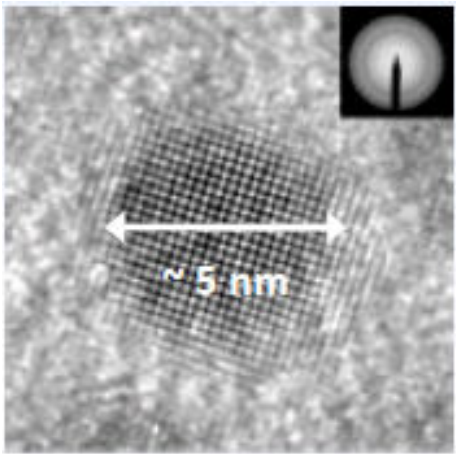

Figure 2. TEM of colloidal lead selenide PbSe quantum dot, from [8].

http://dx.doi.org/10.5772/59159

In order to specify energy eigenvalues of electrons and holes in a quantum dot, a good approximation is the infinite potential well illustrated in Figure 3. Therefore, a quantum dot can be imagined as quantum box. Assuming $\Psi_n(r)$ is the wave function of the n^{th} state. Schrödinger equation for an electron confined in one-dimensional infinite square potential well of size L is:

$$-\frac{\hbar^2}{2m}\frac{d^2\psi_n}{dx^2}+V(x)\psi_n=E_n\psi_n \tag{3}$$

The energy eigenvalues E_n and eigen-wavefunction $\Psi_n(r)$ of the Schrödinger equation are given

$$\psi_n(x)=\sqrt{\frac{2}{L}}\sin\left(\frac{n\pi}{L}x\right)+\sqrt{\frac{2}{L}}\cos\left(\frac{n\pi}{L}x\right) \tag{4}$$

$$E_n=\frac{\pi^2\hbar^2}{2mL^2}n^2,\ n=1,2,3,.... \tag{5}$$

Now if we extend the confinements of electron in three-dimensional potential well (box with dimensions L_x, L_y, and L_z) its momentum and energy will be quantized in all dimensions and we have:

$$E_{n_{x,y,z}}=\frac{\pi^2\hbar^2}{2m}\left(\frac{n_x^2}{L_x^2}+\frac{n_y^2}{L_y^2}+\frac{n_z^2}{L_z^2}\right) \tag{6}$$

With quantum dot (cubic box) of side dimension $L_x=L_y=L_z=L$,then E_n is written as:

$$E_{n_{x,y,z}}=\frac{\pi^2\hbar^2}{2mL^2}\left(n_x^2+n_y^2+n_z^2\right)=\frac{\pi^2\hbar^2}{2mL^2}n^2 \tag{7}$$

Similar energy eigenvalues can be written for holes. One must specify the m_e for electron and m_h for hole. Considering spherical shape of quantum dot with radius R, based on the effective mass model developed by Louis Brus [2] for colloidal quantum dots. The band gap E^{QD} can be approximated by:

$$E^{QD}=E_g^{bulk}+\frac{\hbar^2\pi^2}{2R^2}\left(\frac{1}{m_e}+\frac{1}{m_h}\right)-\frac{1.8e^2}{4\pi\varepsilon\varepsilon_0 R} \tag{8}$$

where ε is the relative permittivity, and $\varepsilon_0 = 8.85410^{-14}$ F.cm^{-1} the permittivity of free space.

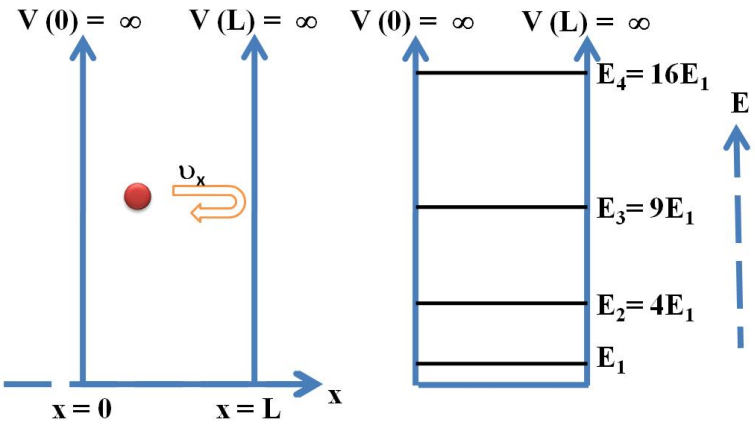

Figure 3. Infinite quantum well model.

In Equation (8), the first term on the right hand side describes the energy bandgap value of the bulk, the second term represents particle in a box quantum confinement model, and the third term details the Coulomb attraction between electron and hole (exciton). As the radius of the quantum dot decreases the Coulomb attraction term could be neglected compared to the second term in calculations. Therefore, Equation (8) indicates that bandgap energy eigenvalues increases as the quantum dot size decreases.

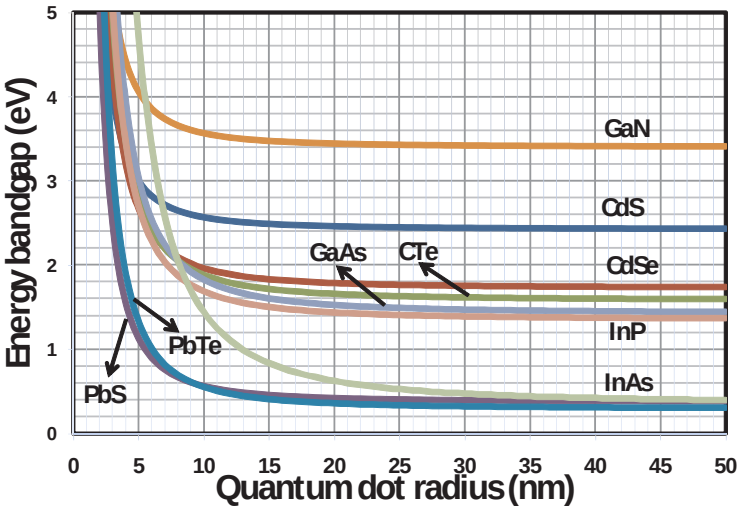

Figure 4. Variation of quantum dot energy bandgap vs. dot size for some common semiconductors. From [9].

http://dx.doi.org/10.5772/59159

Figure 4 presents few examples of well-known quantum dots, only the first and the second terms have been considered. Other detailed models such as the strong confinement model [10] have been adopted in determining the quantum dot sizes such as CdS.

Figure 5 shows the measured absorbance of three different sizes of lead sulfide (PbS) quantum dots suspended in toluene using dual beam spectrophotometer. Since a quantum dot bandgap is tunable depending on its size, the smaller the quantum dot the higher energy is required to confine excitons into its volume. Also, energy levels increase in magnitude and spread out more. Therefore, exciton characteristic peak is blue shifted.

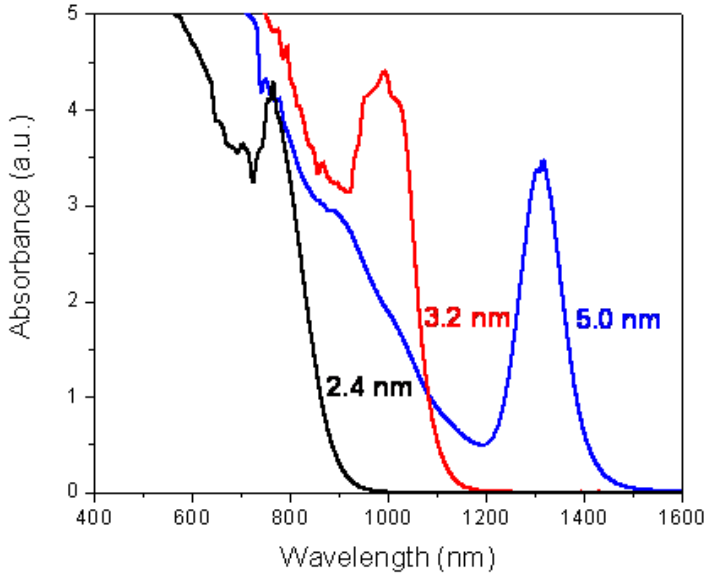

Figure 5. Measured absorbance of three different sizes PbS quantum dot suspended in toluene.

Quantum dot structured materials can be used to create the so called intermediate band. The large intrinsic dipole moments possessed by quantum dots, lead torapid charge separation.Solar cells based on intermediate bandgap materials expected to achieve maximum theoretical efficiency as high as 65%.

Nozik and his coworkwers [11-13] invesitigated Multiple exciton generation in semiconductor quantum dots. As illustrated in Figure 6, unlike bulk semiconductors such as crystalline silicon, quantum dots can generate multiple exciton (electron-hole pairs) after collisionwith one photon of energy exceeding the bandgap.In bulk semiconductor absorption of photon with energy exceeding the bandgap promotes an electron from the valance band to higher level in the conduction band these electrons are called hot carrier. The excited electron (hot carrier) undergoes many nonradiative relaxation (thermalization: multi-phonon emission) before

reaching the bottom of the conduction band. However, in a quantum dot the hot carrier undergoes impact ionization process (carrier multiplication). Therefore, absorption of a single photon generates multiple electron-hole pairs.This phenomena is called multiple exciton generation MEG. Therefore, absorption of UV photons in quantum dots produces more electrons than near infrared photons.

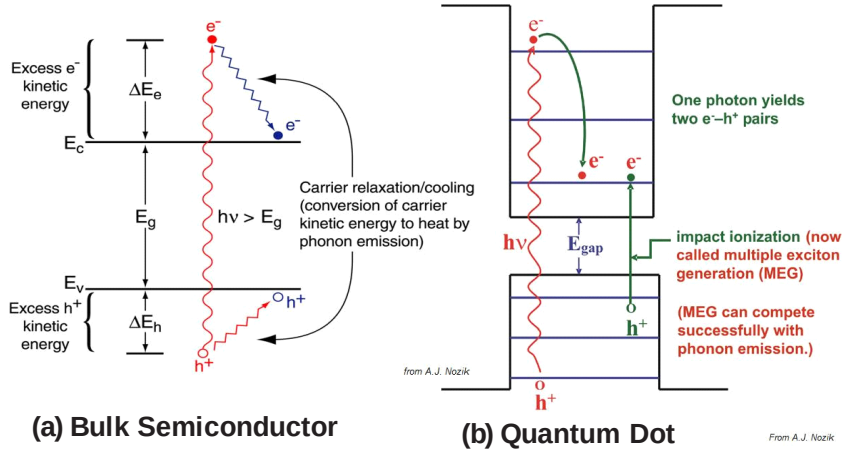

Figure 6. Thermalization of hot carriers in a bulk semiconductor (a) and a quantum dot (b), from [12].

After excitation of charge carriers the timing of the processes leading to generation of multiple charge carriers are detailed in [14] and schematically illustrated in Figure 7. After absorption of photon it takes hot carries 0.1 ps to go for impact ionization, then after 2 ps carries cool down. It takes around 20 ps for Auger recombination and finally 2ps are needed for carries to cool down and become ready for new excitation.

Experimentally carrier multiplication process-one photon generates more than one exciton via impact ionization or inverse of Auger recombination-in quantum dot has been investigated and quantified using the transient absorption spectroscopy technique. In short, [5] laser pulses are directed on the sample one for excitation and another for absorption. Measuring time of relaxation indicates whether there are single excitons recombining radiatively or biexcitons recombining via Auger recombination.

It has been discovered that there is linear proportionality between absorption change for number of generated electron-hole pairs less than 3 and number of generated electron-hole pairs. For example, investigations using PbSe and PbS QDs; confirmed 300% photo-generated carrier density (quantum yield QY)in PbSe QDs by a photon with energy of 4 times the energy spacing between the HOMO and LUMO (E_g) of the quantum dot [5, 15] as shown in Figure 8-a.Further investigations by Schaller and his coworkers [6] reported higher carrier multiplication efficiencies of 700% of photo-generated carrier density at higher photon energy to bandgap

http://dx.doi.org/10.5772/59159

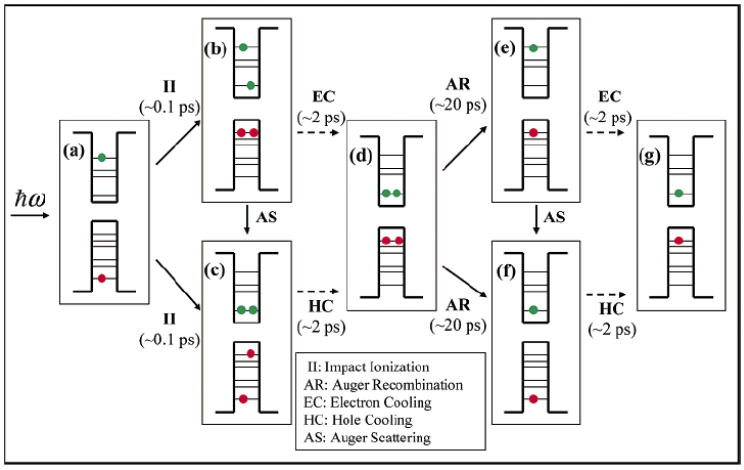

Figure 7. Illustration of the time of the processes leading to generation of multiple charge carriers in a quantum dot, from [14].

(E_g) ratios (photon energy 8×E_g).Multiplication onset starts at photon with energy equals to 3 times E_g as shown in Figure 8-b.

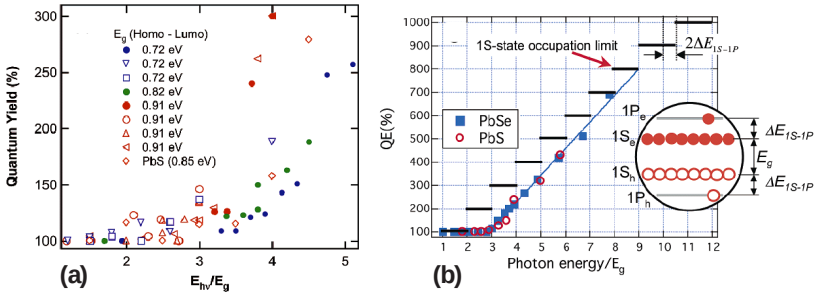

Figure 8. Experimental confirmation of carrier multiplication efficiencies. From(a) [5] and (b) [6].

4. Synthesis of quantum dots

There are many methods or techniques used in fabrication or synthesis of quantum dots that can be classified as top-down (carving large piece of a material to the desired nanostructures) or bottom-up (assembling atoms to form the desired nanostructures) methods. Generally speaking, some of these techniques are practical in solar cells applications. A summary of each synthesis method is given below.

4.1. Electron-beam lithography

Electron-beam lithography is one of the top-down methods. Electron beam system is used to etch well defined patterns on a bulk semiconductorand or superlattice, then a semiconductor layers are grown according to a well-established protocol in micro-technology.

4.2. Self-assembly growth

Self-assembly growth is one of the bottom-up methods. Molecular Beam Epitaxy (MBE) and Metal Organic Chemical Vapor Deposition (MOCVD) are widely used in the growth of the superlattice with different materials of different lattice constants.Semiconducting compound with a smaller lattice constant is grown (deposited atom by atom) on the surface of a compoundwith a larger lattice constant. The relaxation of the grown layer after specific growth thickness due to lattice mismatch results in nucleation of islands of random shapes and controllable size. This growth mode is known as Stranski-Krastanov growth (see Figure 9).MBE method, beside it is sophisticated and slow, it is expensive. However, growth control of quantum dots is precise and multi-layers of quantum dots is possible. MOCVD is used in mass production of sample wafers and in contrast to MBE the growth of crystals is by chemical reaction and not physical deposition. In this approach high vacuum and temperature are required.

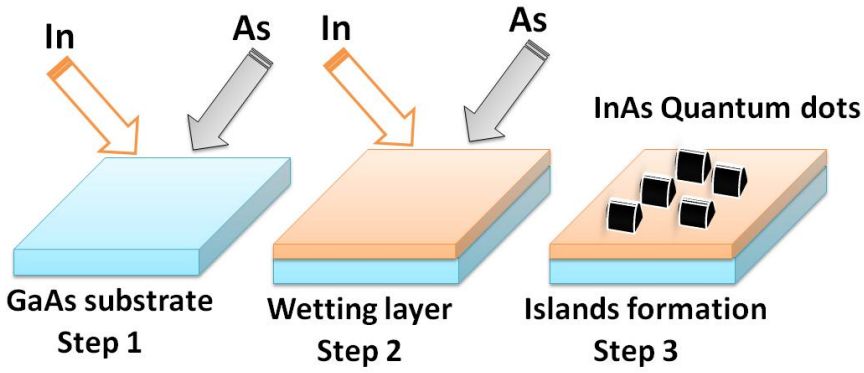

Figure 9. Schematic of InAs island formation on GaAs surface by Stranski-Krastanow growth.

4.3. Organometallic or colloidal (Wet Chemistry) synthesis method

Organometallic or colloidal (Wet Chemistry) synthesis method is one of bottom-up methods. It's also a self-assembly technique. It's relatively inexpensive and fast growth method to synthesis large quantity of quantum dots all at once. The growth could occur at non-extreme conditions. Figure 10 show a schematic of an example of the setup used in synthesis of colloidal quantum dots.

http://dx.doi.org/10.5772/59159

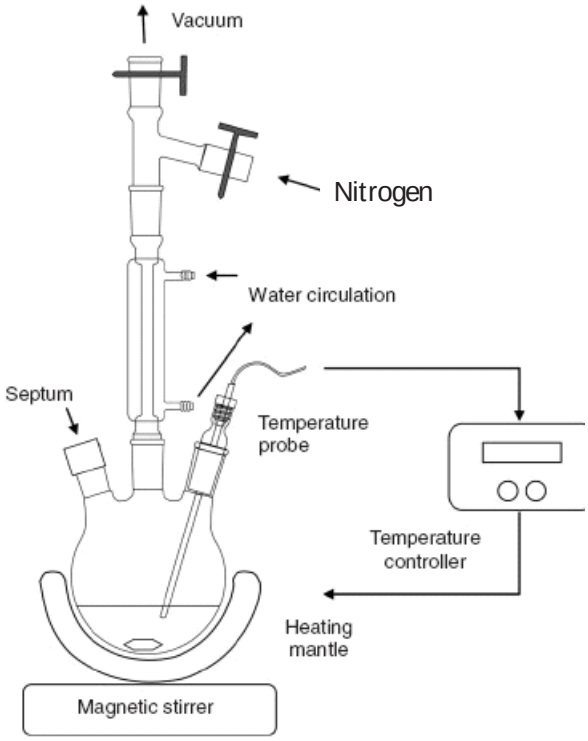

Figure 10. Schematic of a common setup used in synthesis of colloidal quantum dots.

As an example recipe given by [16] to synthesis colloidal Lead Sulfide PdS quantum dots: Heat together in a flask at 150 °C for 1 hr under N_2 flow (to make lead oleate):

- 220 mg lead(II) oxide
- 0.25 ml oleic acid (tech grade)
- 9.75 ml 1-octadecene (ODE, tech grade)

After cooling to 90-100 °C, quickly inject into the reaction flask 5 ml of 0.1 M hexamethyldisilathiane (0.5 mmol) dissolved in ODE. Then immediately cool with an ice bath.

Precipitate (methanol/butanol mixture), centrifuge and resuspend in nonpolar solvent (e.g., toluene, tetrachloroethylene, or hexanes).

$$\mathrm{PbO} + 2\mathrm{C}_{18}H_{34}O_2 - (N_2\ ODE\langle 122\ ^\circ C) \rightarrow Pb(_{ol\,ae}^{et}) + H_2O$$

$$Pb(_{ol\,ae}^{et}) + (_{(\ )_{C^{H_3}}}^{i\,2}S - (N_2\ ODE\langle 122\ ^\circ C) \rightarrow PbS\ quantum\ dots\ capped\ with\ OA$$

To manipulate functionality, alter the charge and reactivity of the surface, synthesized quantum dots usually caped with a shell from different composition. Also, the shell can enhance the stability and dispersability of the colloidal core. Magnetic, optical, or catalytic functions may be readily imparted to the dispersed colloidal core. In fact, encasing colloids in a shell of different composition may perhaps protect the core from extraneous physical and chemical changes.

Generally speaking, colloidal quantum dots could be categorized as Type-I (e.g., CdSe/ZnS) and Type-II QDs (e.g., CdTe/CdSe) as shown in Figure 11:

- In Type-I QDs, all charge carriersare confined in the core material inwhich radiative recombinationoccurs (see Figure 11-a).
- In Type-II QDs, charge carriers aresegregated in the core and shell;radiative recombination occursacross the material interface (see Figure 11-b).

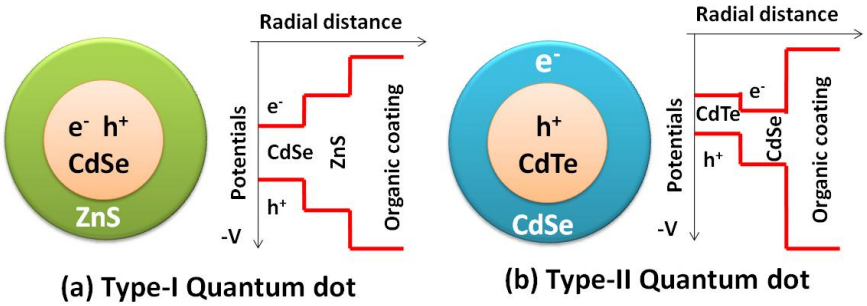

Figure 11. Illustration of (a) Type-I quantum dots (b) and Type-II quantum dots.

In fact, many researchers investigating quantum dot sensitized solar cells adopt other growth strategies to assemble quantum dots on electrode surface. We used the most direct and easiest one, the drop casting (electrode is socked with quantum dots solution drop by drop). Chemical bath deposition CBD has been used by [17], Electrophoritic deposition has been adopted by [18], successive ionic layer adsorption and reaction (SILAR) has been used by [19], and the used of bifunctional linker was demonstrated by Subramanian and coworkers [20].

5. Quantum dots solar cells

There are many realistic quantum dots based solar cells. In this section we classify them in seven strategies just as an approach to fulfill the main objective of this chapter that is introducing quantum dot solar cells. For example, [21] metal-semiconductor junction, polymer-semiconductor, and semiconductor-semiconductor systems are well know strategies of quantum dots based solar cell. Moreover; quantum dots attached to n-C_{60} composite clusters

see [18] or single and multi-walled carbon nanotubes based solar cells have been investigated [22,23].

5.1. Metal-semiconductor junction solar cell

Figure 12-a schematically shows the structure of the metal-semiconductor junctionwhich also called Schottky barrier quantum dotsbased solar cell. Itis basically fabricated from quantum dots layers (Nanocrystals film) sandwiched between metallic electrode and ITO counter electrode deposited on transparent glass substrate to act as photo-electrode.In the band diagram shown in Figure 12-b, a depletion region is due tocharge transfer to QD film. Because of high electron density in metal (~ 10^{22} cm^{-3}), the depletion is negligible on its side of the cell.

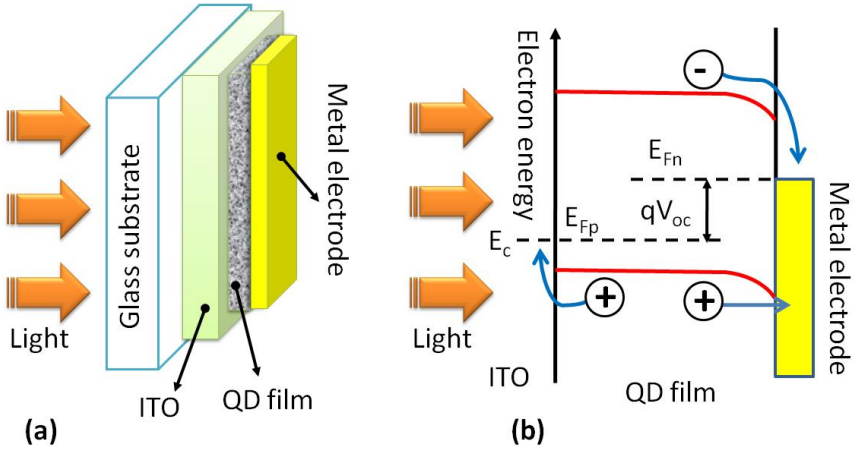

Figure 12. (a) Schematic of Schottky barrier quantum dots based solar cell, (b) band diagram of Schottky solar cell. Adopted from [24].

Layer-by-layer fabrication of quantum dots film is prepared by layer-by-layer dip coating of the substrate. For example, in layer by layer fabrication of PbSe quantum dots films, quantum dots film prepared by dip-coating, alternating between PbSe NCs in hexane and then 0.1 M EDT in anhydrous a cetonitrile, allowing the film to dry between each layer [25]. Device with 140 nm-thick QD film achieved an efficiency of ~2.2 % [26] heterojunction solar cell has been investigated by sputtering 150 nm layer of ZnO and growing layers of PbS quantum dots fabricated in air (4.1 mg/mL concentration of PbS 820 nm NC in hexanes;1 mM solution of 1,2-ethanedithiol in a cetonitrile layer-by-layer deposition for 20 cycles (~ 120nm PbS film thickness). Tested devices showed good air stability over ~1,000 hrs with cell power efficiency of 1.53 %.

It has been found [24] that the open circuit voltage in Schottky cell is constrained due to pinning of Fermi level resulted from the formed defect states at the metal-semiconductor inter-

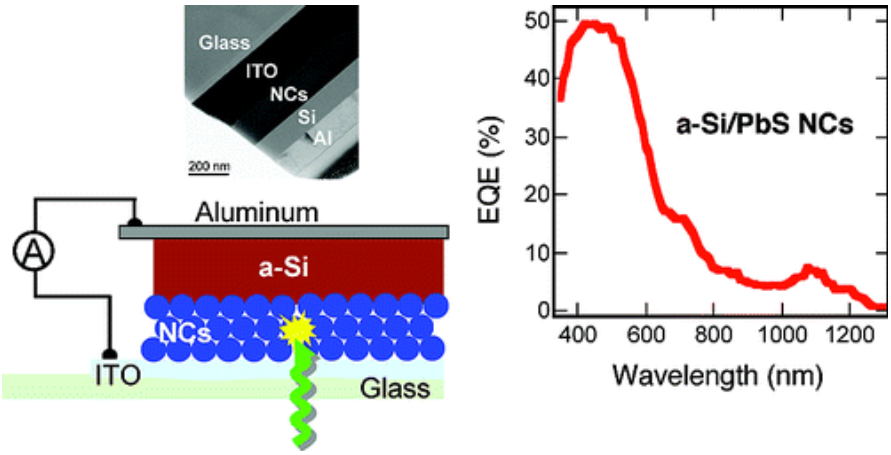

Figure 13. Hybrid silicon/PbS QD film solar cells. From [28].

face.Moreover, as illustrated in Figure 12-a, photoelectrons are firstly generated near the ITO (ohmic contact) and need to pass through long pathwayto the metallic electrode. Hence, many of the photoelectrons are encountering high recombination probability.Also on the onset of photovoltaic action the hole current injection to metallic contact is not reduce because the barrier to hole injection become less effectiveas shown in Figure 12-b. Gao J. et. al. [27] reported a method to eliminate such disadvantage by inserting a layer of a transition metal oxide (TMO) between the quantum dot (QD) layer and metal electrode. An n-Type transition metal oxide such asmolybdenum oxide (MoO_x) and vanadium oxide (V_2O_x) work as a hole extraction layer in PbS quantum dot solar cells resulted in power conversion efficiency =4.4%. The formation of dipole at the interface of MoO_x and PbS enhances the band binding and hence allowing efficient hole extraction from the PbS film valance band by the MoO_x.

5.2. Hybrid silicon/QD film (NCs) solar cells

Kilimov and his coworkers [28] demonstrated the feasibility of hybrid PV devices thatcombine advantages of mature silicon fabrication technologies with the uniqueelectronic properties of semiconductor QD (see Figure 13).The hybrid silicon/PbS QD film (Nanocrystals) solar cells show external quantum efficiencies of 7%at infrared energies and 50% in the visible and a power conversion efficiency ofup to 0.9%.

5.3. P-i-n structure solar cell

The advances in multiple quantum well solar cells [29], see Figure 14, and remarkable efficiency improvement of such p-i--n structure configurations due efficient management of photo-generated carries have encouraged researchers to replace the III-V intrinsic region of semi-conductors quantum wells structures with quantum dots.

http://dx.doi.org/10.5772/59159

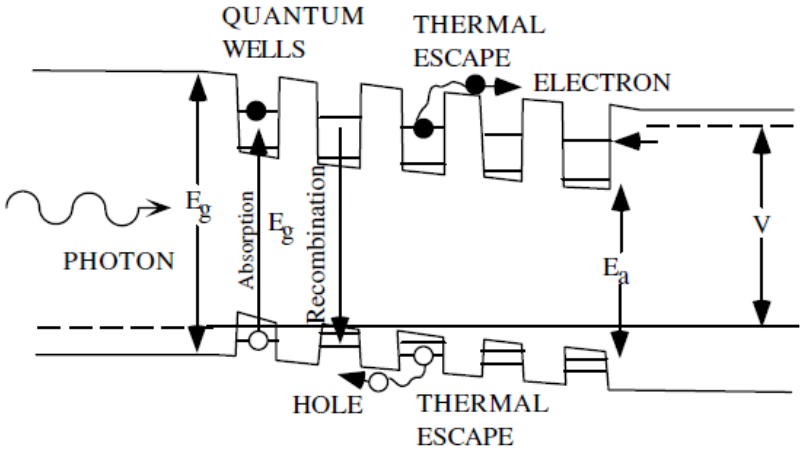

Figure 14. Multiple quantum well solar cell band structure. From [29].

Nozik and his coworkers [11,13] suggested a general p-i-n junction configuration for incorporating array of QDs into solar cells. QDs array forms the active medium of the cell (the intrinsic region). In this arrangement quantum size effects should not beeradicated due to cell architecture, excitons must be separated prior to Auger recombination, and upon absorption of photonsexcitons ought to be separated into free-charge carriers and transported to appropriate electrodes. Figure 15, shows quantum dot layers forming the i-region of a solar cell. The QDs are electronically coupled to each other to sustain electron and hole transport. Also, mini-bands are formed and hence could facilitate intermediate band formation [30]. Intermediate energy band is energy absorbing band which can accept electron excitations from the valance band and then allow transitions tothe conduction band. In quantum dots solar cells with intermediate bands photon of energies lower than the bandgap are basically absorbed and high energy photons produce hot-carries (see Figure 15). Collecting charge-carries while they are hot enhances cell voltage. On the other hand, photocurrent enhancement could be achieved by getting more from the hot-carriers via inverse Auger recombination (impact ionization) leading to multiple exciton generation MEG. One needs to bear in mind electron tunneling mechanism between quantum dots.

Investigation done by Nozik group found that [31] by comparing the performance of GaAs base solar cell to one incorporating InAs/GaAs QDs intrinsic region sandwiched between *p* and *n* GaAs emitters (grown by MBE system in the Stranski–Krastanov growth mod), the cell exhibits an extended response for photon energies lower than the GaAs bandgap. The contribution to the total current of the cell came as a result of harvesting below-bandgap-energy photons is minute (1%).

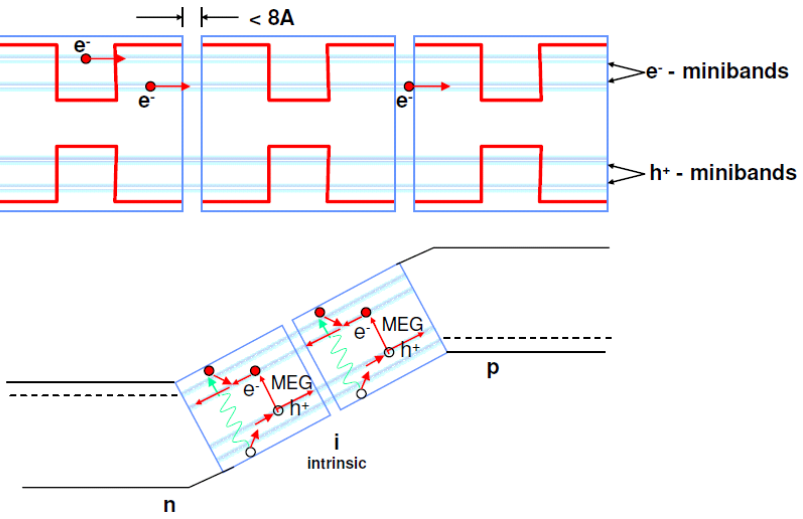

Figure 15. Possible p-i-n QD arrangements for solar cells.From [11].

5.4. Polymer-semiconductor structure configuration

In 2002 Huynh and his coworkers [32] investigated photovoltaic action in hybrid nanorods-polymer solar cells and under Air Mass (A.M.) 1.5 Global solar conditions, a power conversion efficiency of 1.7 % was obtained. This works and others encouraged many groups to investigate incorporation of quantum dots in polymers. Quantum dots are dispersed in organic-semiconductor polymer matrices. For example, in a hole-conducting polymer such as MEH-PPV (poly(2-methoxy,5-(2-ethyl)-hexyloxy-pphenylenevinylene) disordered arrays of CdSe quantum dots are synthesized. When the cell illuminated, the absorbed photons results in photo-generated carriers. As illustrated in Figure 16 [31], the photo-generated holes are injected into the MEH-PPV polymer phase which is in contact with metallic electrode to facilitate their collection.Sun et al., in 2003 reported that solar power conversion efficiencies of 1.8 % were achieved under AM1.5 illumination fora device containing 86 wt % of quantum dots [33].

5.5. Depleted heterojunction quantum dots solar cells

In depleted heterojunction colloidal quantum dot solar cells as detailed in ref. [24] a nano-structured wide bandgap semiconductor such as TiO_2 and quantum dot film are sandwiched between conductive transparent electrode (glass coated with Tin Oxide SnO_2F) and metallic (such as gold) coated electrode (see Figure 17-a).Figure 17-b illustrate the energy band diagram. Although TiO_2 has low carrier density (~10^{16} cm^{-3}) compared to metal, a depletion region in the cells forms due to charge transfer to QD film. And because of high electron density in metal (~ 10^{22} cm^{-3}), the depletion is negligible on its side of the cell. Depleted heterojunction cell overcome the disadvantages encountered with Schottky cell.

http://dx.doi.org/10.5772/59159

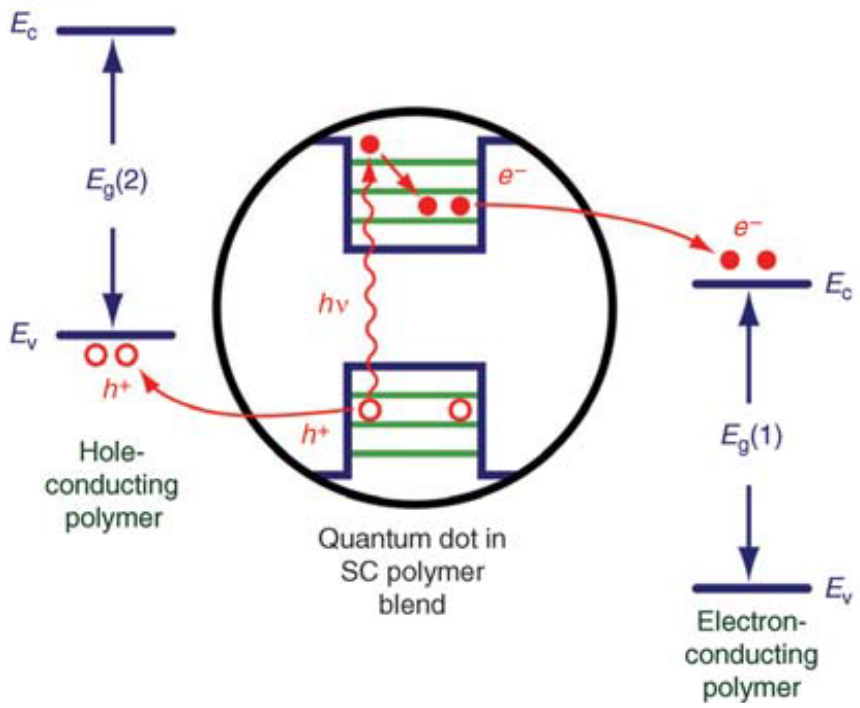

Figure 16. Shows how photo-generated carriers from quantum dots injected in conducting polymers. From [31].

In their work Grätzel and coworkers [24] have reported that the resultant depleted hetero-junction solar cells offer power conversion efficiency of 5.1% at AM1.5 illumination. The devices were capable of harvesting broadband of the solar spectrum as a result of employing infrared-bandgap size-effect-tuned PbS CQD.

5.6. Quantum dot sensitized solar cells

The structure and operation principle of QD sensitized photovoltaic cell is almost identical to dye sensitized cells [9, 34,35] with the exception that now the QDs are the source of current injection. Quantum dots can be produced in situ or more without difficulty adsorbed from a colloidal QD solution. The structure of the photovoltaic cell is shown schematically in Figure 18. In this figure, we distinguish four essential elements of the cell, namely, the conducting and counter conducting electrodes, the nanostructured TiO_2 layer, the quantum dot energy levels, and the electrolyte.

The operation of the cell can be described by the following steps and the corresponding process equations:

1. Upon absorption of a photon, a quantum dot is excited from the ground state (QD_S) to a higher energy state (QD_S^*), as illustrated by Eq.(1) below.

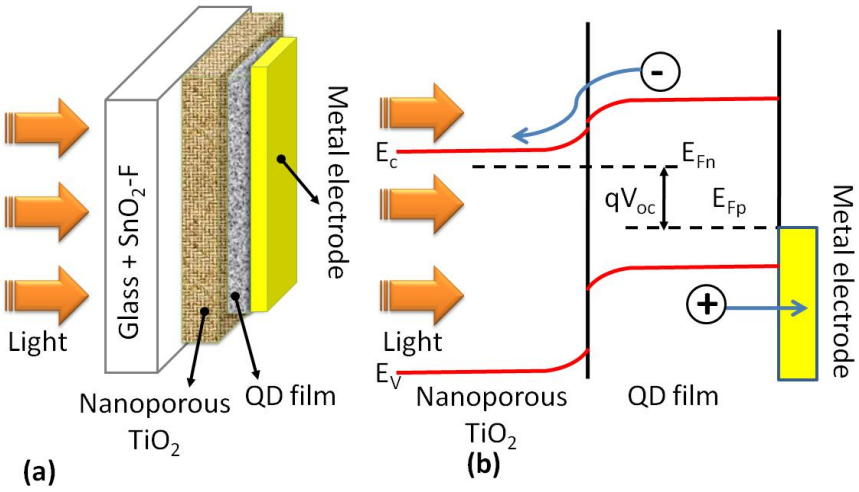

Figure 17. (a) Schematic diagram of Depleted-heterojunction Colloidal Quantum Dots Solar Cells, (b) energy band diagram. From [24].

$$Excitation\ process: QD_S + h\nu \rightarrow QD_S^* \tag{9}$$

Where QD_S and QD_S^* is the quantum dot in its ground state and excited state respectively.

2. The absorption process results in the creation of electron-hole pair in the form of exciton. Dissociation of the exciton occurs if the thermal energy exceeds its binding energy.

$$Exciton\ dissociation: QD_S^* \rightarrow e^{-*} + h^{+*}\left(\text{free carriers}\right) \tag{10}$$

3. The excited electron is then injected in the conduction band of the wide bandgap semiconductor nanostructured TiO_2 thin film. This process will cause the oxidation of the photosensitizer (The QDs).

$$Injection\ process: QD_S^* + TiO_2 \rightarrow TiO_2(e^{-*}) + QD_S^+ \tag{11}$$

4. The injected electron is transported between the TiO_2 nanoparticles, and then gets extracted to a load where the work done is delivered as electrical energy.

$$Energy\ generation: TiO_2(e^{-*}) + C.E. \rightarrow TiO_2 + e^{-*}(C.E.) + elecrical\ energy \tag{12}$$

http://dx.doi.org/10.5772/59159

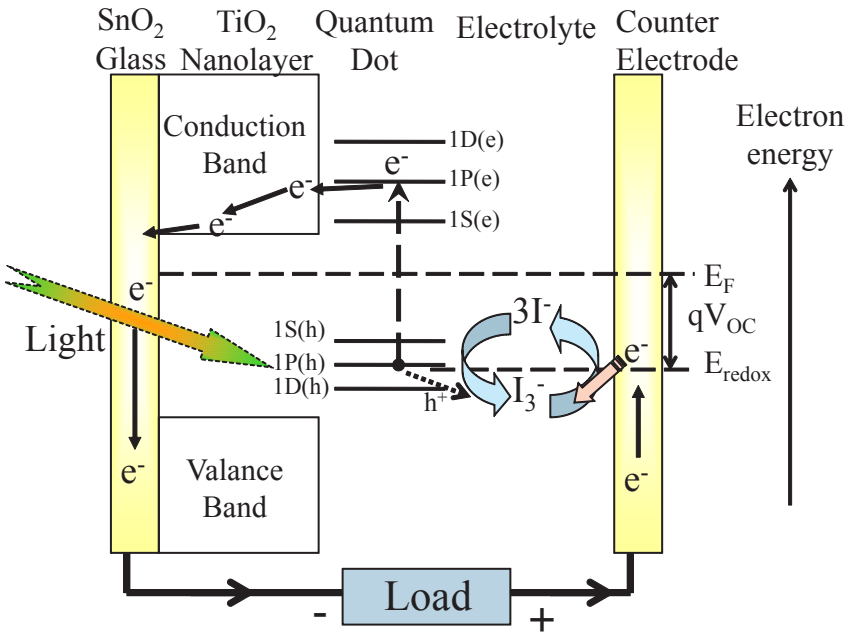

Figure 18. Schematic diagram illustrating the structure and operation of quantum dots-sensitized photovoltaic cell.

Where C.E. stands for counter electrode. The counter electrode is identical to the photoelectrode where the nanostructured TiO_2 is deposited. The counter electrode is usually coated with a catalyst (graphite).

5. Most common electrolytes used in QDSCs are aqueous polysulfide and organic electrolyte with I^-/I_3^--redox couple. In some works the liquid electrolyte has been replacedwith solid-state hole conductors such as spiro-OMeDAT andCuSCN [36]. Assuming electrolyte used in the cell contains I^-/I_3^-redox ions, that play the role of electron mediator between the TiO_2 photoelectrode and the counter electrode [9]. Therefore, the oxidized photosensitizer states (QD_S^+) are regenerated by receiving an electron from the oxidized I^-ion redox mediator, regenerating the ground state (QD_S), and I^-becomes oxidized to the oxidized state I_3^-(triodide ions).

$$Regeneration\ of\ QDs: QD_S^+ + \frac{3}{2}I^- \rightarrow QD_S + \frac{1}{2}I_3^- \tag{13}$$

6. The I_3^-diffuses to the counter electrode and substitutes the internally donated electron with that from the external load and gets reduced back to I^-ion.

$$\textit{Electron capture reaction}: \frac{1}{2}I_3^- + e^-(\text{C.E}) \rightarrow \frac{3}{2}I^- + \text{C.E.} \tag{14}$$

Overall, generation of electric power in this type of cells causes no permanent chemical transformation.

To enhance electron injection into the conduction band of the TiO_2 thin film, one must choose a sensitizer with a proper matching energy gap. Quantum dots can fulfill the necessary energy gap requirement by choosing the ones with the proper size. It is interesting to note that for the QD to effectively accept the donated electron from the redox mediator. Finally, the maximum potential produced by the cell is determined by the energy separation between the electrolyte chemical potential (E_{redox}) and the Fermi level (E_F) of the TiO_2 layer, as shown in Figure 18.

The bulk of many research works done on QD synthesized solar cells focused on CdS, CdSe, and CdTe QD as sensitizers [37-39] The choice of these materials follows the success of earlier studies on identifying the morphological and electrolyte effects on their performance and stability [40-41]. Incident Photon to carriers conversion efficiency IPCE is directly related to the product of light harvesting efficiency = $1\text{-}10^{-A(\lambda)}$ (where $A(\lambda)$ is the spectral absorbance of the quantum dots sample, electron injection efficiency Φ_{inj} (how efficient are electrons injected from excited quantum dot into TiO_2 conduction band), and electron collection efficiency Φ_{coll} (how efficent are electrons are collected by the photoelectrode), hence we have:

$$IPCE = LHE \times \Phi_{inj} \times \Phi_{coll} \tag{15}$$

Light harvesting efficiency could be affected by both the type and size of quantum dots. For example PdS based quantum dots have broader spectral absorbance than CdS quantum dots. Kamat reported that charge injection from excited CdSe quantum dots into nanostructured TiO_2 film can be controlled by varying solution pH as illustrated in Figure 19 "At increasing solution pH, the conduction band of TiO_2 shifts 59 mV/pH unit to a more negative potential, thereby decreasing the driving force and thus decreasing the rate of nonradiative electron transfer from excited CdSe. The emission yield and the average emission lifetime increase with increasing pH, thus providing a way to monitor the variation in medium pH." [42].

Kongkanand and co-workers has investigated the effect of quantum dots size on charge injection rate [43]. They found that smaller-sized CdSe quantum dots show greater charge injection rates and also higher IPCE at the excitonic band.Interestingly, Larger particles have better absorption in the visible region, on the other hand,it cannot inject electrons into TiO_2 as effectivelyas smaller-sized CdSe quantum dots. It has been found that surface treatments can strongly influence charge transfer, recombination, and transport processes of photogenerated electrons and holes in QDSCs [44]. Figure 20 schematically shows that transport of electrons through the nonporous electrode is dominated by diffusion [45]. A path taken by an electron is not simply a straight line. An electron undergoes through a crisscross path before reaching

http://dx.doi.org/10.5772/59159

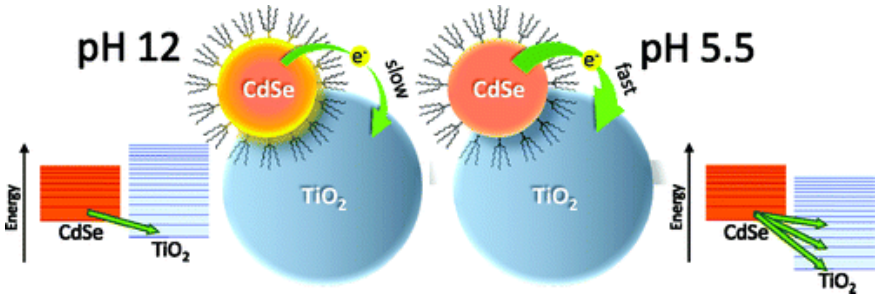

Figure 19. Illustration of how charge injection from excited CdSe quantum dots into nanostructured TiO_2 film can be controlled by varying solution pH. From [42].

the photoelectrode. The electron diffusion length, L_n is related to electron lifetime (τ_n) and diffusion coefficient (D_n) as:

$$L_n = \sqrt{D_n \tau_n} \tag{16}$$

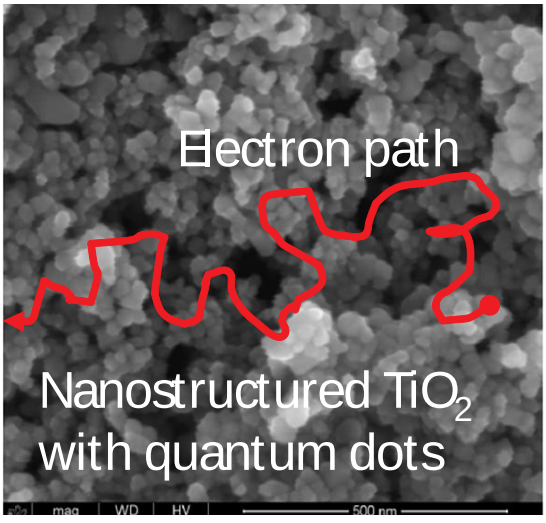

Figure 20. Illustrate a path taken by an electron after being injected into nanoporous TiO_2 layer (Not to scale). The nanoporous TiO_2 layer has been imaged using scanning electron microscope SEM.

Cell conversion efficiency is affect by morphology of the photoelectrode [43]. Tube type is more advantageous to the fast electronic conduction, due to shorter diffusion path comparedwith the particle type. For example, OTE / TiO_2 (Nanoparticles)/CdSe: 0.6 % versus Ti / TiO_2 Nanotubes /CdSe: 0.7 %.

Interesting results have been reported by some investigators who studied the incorporation of a layer of PbS quantum dots in thin film solar cells, by direct growth of PbS quantum dots on nanostructured TiO_2 electrodes [27]. Deposition of a transition metal oxide (n-type) layer on grown layer of PbS quantum dots to act as hole extractor layers [46] or employing a graded recombination layer [47].

Several methods have been employed to prepare TiO_2 thin layer. We prepared nanostructured thin films following the procedure detailed in [9, 34]. In this method, a suspension of TiO_2 is prepared by adding 9 ml of nitric acid solution of PH 3-4 (in ml increment) to 6 g of colloidal P25 TiO_2 powder in mortar and pestle. To get a white free flow-paste, we added 8 ml of distilled water (in 1 ml increment) during the grinding process. Finally, a drop of transparent surfactant is added in 1 ml of distilled water to ensure uniform coating and adhesion to the transparent conducting electrode. It was found that the ratio of the nitric acid solution to the colloidal P25 TiO_2 powder is a critical factor for cell performance. If the ratio exceeds certain threshold value, the resulting film becomes too thick and has a tendency to peel off. On the other hand, a low ratio reduces appreciably the efficiency of light generation.

Doctor blade technique was employed by depositing the TiO_2 suspension uniformly on a cleaned (rinsed with ethanol) conductive plate. The TiO_2 film was allowed to dry for few minutes and then annealed at approximately 450 °C (in a well-ventilated zone) for about 15 minutes to form a nanoporous TiO_2 layer as shown in Figure 20. The conductive plate is then allowed to cool slowly to room temperature. This is a necessary condition to remove stresses and avoid cracking of the glass or peeling off the TiO_2 layer. Once the TiO_2 nanocrystalline layer is prepared, it is coated with colloidal QDs. The counter electrode is coated with graphite that Acts as a catalyst in regenerating quantum dots. Both the photo-and counter electrodes are clamped together and drops of electrolyte are applied to fill the clamped cell. The electrolyte used is iodide electrolyte (0.5 M potassium iodide mixed with 0.05 M iodine in water free ethylene glycol) containing a redox couple (traditionally the iodide/tri-iodide I^-/I^{3-}couple). The measurements of the open circuit voltage and short circuit current have been performed under direct illumination from a solar simulator producing 1 sun illumination. UV or IR cut-off filters have been used to eliminate carrier generation from TiO_2 layer and to impede cell overheating.No antireflection coatings on the photoelectrode have been applied. Figure 21 shows an example of the obtained I-V characteristics of PdS quantum dots (size 3.2 nm) sensitized cell with power conversion efficiency =1.8 %.

As it's the case with dye sensitized solar cells, quantum dots sensitized solar cells light harvesting efficiency could be enhanced via efficient light management [48] by increasing light scattering effect [49]. The distance traveled by transmitted photons in the cell is increases by multiple scattering and hence get highly probable by the sensitizer. Surface plasmons resonance effect in the cell also has been suggested [50]. Another approach that is effective in enhancing photovoltaic effect is the reduction of the charge recombination by controlling transparent-conducting-oxide/electrolyte interface such that injected electrons in photoelectrode are excluded from recombining with the redox couple in electrolyte.

http://dx.doi.org/10.5772/59159

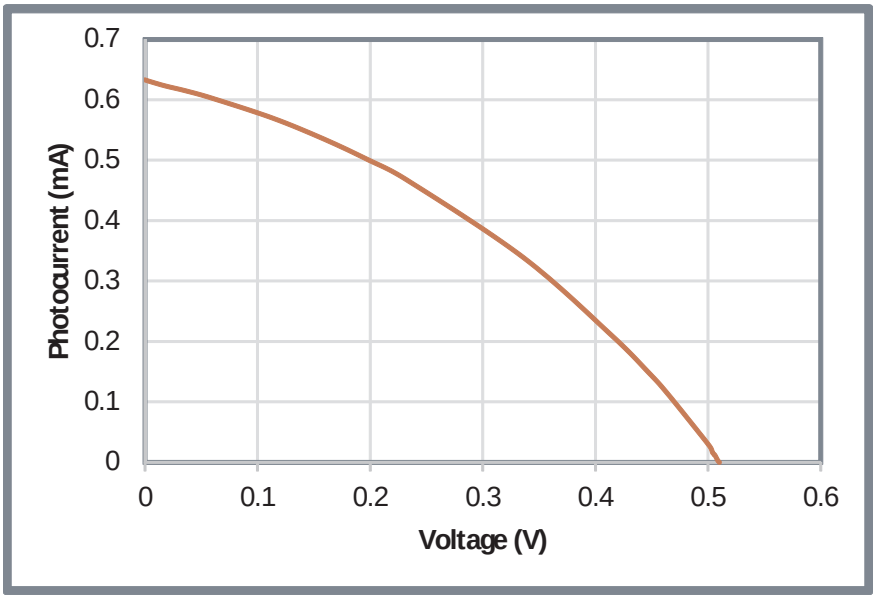

Figure 21. I-V characteristics of PbS quantum dot sensitized solar cell. Quantum dots have on the average radius of 3.2 nm.

5.7. Quantum dot-dye sensitized solar cells

Incorporation of dye with quantum dots as sensitizer of wide bandgap semiconductor has attracted attention of many research groups. For example, we found that some natural dyes are enhancing power conversion efficiency, while some others are not. Figure 22 shows an example of the I-V characteristics of a first round study of assembled cells illuminated with a collimated beam from a hot filament lamp. In cell preparation we followed the same strategy described in section 5.6 such that after coating the photoelectrode with PbS quantum dots it was soaked in dye for an hour. Then, the electrode was rinsed with deionized water and ethanol. After that the cell is assembled and tested. The dye used was extracted from a pomegranate.

New configuration based on quantum dot-dye bilayer-sensitized solar cells has been demonstrated by Zaban and co-workers [51]. The bi-sensitizer layer cell is made up of a nanocrystalline TiO_2/CdS QD+amorphous TiO_2/N719 dye. The main aim was to providea configuration having increased charge-separation efficiency by slowing the interfacial charge recombination processes that resulted in 250% increase in cell efficiency compared to a QD monolayer cell.

The configuration investigated by Zaban and co-workers [52] established on making colloidal quantum dots (CdSe/CdS/ZnS core/shell/shell quantum dots) that serve as antennas. Via nonradiative energy transfer, absorbed light is funneled to the charge separating dye molecules (SQ02 dye molecules). The colloidal quantum dot donors are incorporated into the solid TiO_2 photoelectrode resulting in high energy transfer efficiency as well assubstantial improve-

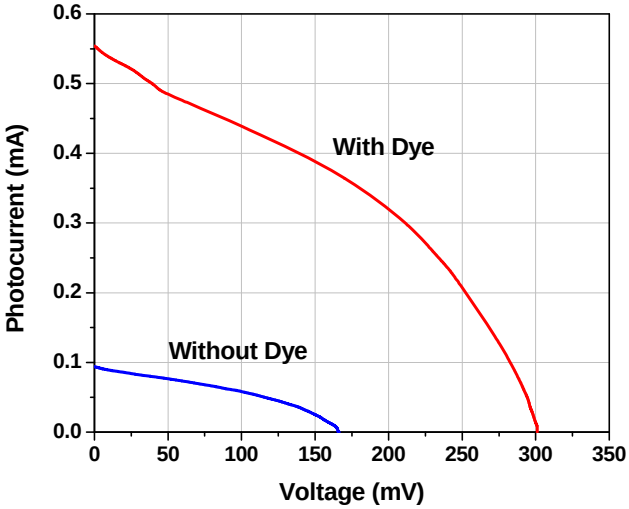

Figure 22. I-V characteristics of typical assembled quantum dot-dye sensitized solar cell. Quantum dots average size of 2.4 nm and pomegranate dye extract used as sensitizers of TiO_2 nanoporous layer.

ment of the cell stability. In this approach the processes of light absorption can be separated from charge carrier injection. Therefore, this approach enablesoptimization of each independently. Time resolved luminescence measurements relate the significant contribution of the QDs to the spectral response of the cell in the presence of the dye to Förster resonance energy transfer from the QDs to the dye molecules.

The efficiency of solar cells can be enhanced by combining quantum dots with some dye and used as a sensitizer. We suggest doing further investigations in order to understand QD-dye system. The performance of dye sensitized or quantum dots solar cells can be increased by optimizing preparation technique, using different types of electrolyte, utilizing different nanostructures (e.g., rods, stars), and replacing TiO_2 with other types of wide bandgap semiconductors such as zinc oxide ZnO.

6. Conclusion

Crystalline semiconductor solar cells besides possessing low efficiency due to their band gab limit (Shockley-Queisser limit)[53] they are expensive in terms of manufacturing cost per generated Watt of delivered electric power. In single junction bulky semiconductor solar cells, photon of energies less than the band gap are wasted since none of them are absorbed. Moreover, excess energy of those photons with energies greater than the bandgap is wasted as heat as a result of hot-carriers thermalization. A quantum dot is a crystalline semiconductor nanoparticles. Examples of well investigated quantum dots structures are CdS, CdSe, PbS, and PbSe. The operation principle of quantum dots sensitized solar cell is similar to that of the dye

http://dx.doi.org/10.5772/59159

sensitized solar cells DSSCs. In a quantum dot, confinement effect arises from size effect when particle size is smaller or comparable to exciton Bohr radius. As the size of the quantum dot decreases its characteristic excitonic beak get blue shifted.

Growth or synthesis methods of quantum dots are well established. In quantum dots, the rate of energy dissipation is significantly reduced, and the charge carriers are confined within a minute volume, thereby increasing their interactions and enhancing the probability for generating multiple excitons due to hot carries mechanism. There are many proposed quantum dot solar cells configurations.

The functional principle of QD-sensitized solar cell is the same as that of DSSC. The difference is that the dye in DSSC is replaced with quantum dots. This class of third generation solar cell is promising and recently attracting considerable attention. Operation principles, and performance limitations are well understood and many solutions have been proposed to enhance cell efficiency.

Acknowledgements

The author is greatly indebted to prof. Dr. Shawqi Aldallal for his kind support and encouragements. His valuable suggestions are highly appreciated. Special thanks to Miss. Fatema Aljaboori for here assistance in obtaining the I-V characteristic presented in Figure 21.

Author details

Khalil Ebrahim Jasim

Department of Physics, College of Science, University of Bahrain, Kingdom of Bahrain

References

[1] Ekimov A.I., and Onushchenko A.A. Quantum size effect in three-dimensional microscopic semiconductor crystals. JETP Lett. 1981; 34 345–349.

[2] Brus L. E. Electronic wave functions in semiconductor clusters: experiment and theory. J. Phys. Chem. 1986; 90 2555-2560.

[3] Reed M.A., Randall J.N., Aggarwal RJ, Matyi R.J., Moore T.M., and Wetsel A.E. Observation of discrete electronic states in a zero-dimensional semiconductor nanostructure. Phys Rev Lett. 1988; 60 (6) 535–537.

[4] Smith A.R., Chao K.-J., Niu Q., and Shih C.-K. Formation of atomically flat silver film on GaAs with a 'silver-mean' quasiperiodicity. Science 1996; 273 226-228.

[5] Schaller R.D., and Klimov V.I. High Efficiency Carrier Multiplication in PbSe Nanocrystals: Implications for Solar Energy Conversion. Phys. Rev. Letts 2004; 92 186601-186614.

[6] Schaller R.D., Sykora M., Pietryga J.M., and Klimov V.I. Seven Excitons at a Cost of One: Redefining the Limits for Conversion Efficiency of Photons into Charge Carriers. Nano Letters 2006; 6 424-429.

[7] Saleh, B., and Teich, M. Fundamentals of Photonics, ch.15. John Wiley & Sons, Inc. ISBNs: 0-471-83965-5 1991.

[8] Sargent E.H. Infrared Quantum Dots. Adv. Mat. 2005; 17 515-522.

[9] Jasim, K.E. Dye Sensitized Solar Cells-Working Principles, Challenges and Opportunities. In: Solar Cells-Dye-Sensitized Devices, Leonid A. Kosyachenko, (Ed),, Book Published by InTech Open Access Publisher, ISBN 978-953-307-735-2. 2011. Chapter 8, pp. 171-204.

[10] Gaponenko S.V. Strong Confinement Approximation in Optical Properties of Semiconductor Nanocrystals. New York: Cambridge University Press; 1998.

[11] Nozik, A.J. Quantum dot solar cells. Physica E 2002;14 115-120.

[12] Nozik A.J. Multiple exciton generation in semiconductor quantum dots. Chemical Physics Letters 2008; 457 3-11.

[13] Nozik A.J. Nanoscience and Nanostructures for Photovoltaics and Solar Fuels. Nano Lett. 2010; 10 2735-2741.

[14] Franceschetti A., An J.M., and Zunger A. Impact ionization can explain carrier multiplication in PbSe quantum dots. Nano Letters 2006; 6 2191-2195.

[15] Ellingson R.J., Beard M.C., Johnson J.C., Yu P., Micic O.I., Nozik A.J., Shabaev A., and Efros, Al. L. Highly Efficient Multiple Exciton Generation in Colloidal PbSe and PbS Quantum Dots. Nano Letters 2005; 5 865-871.

[16] Hines M. A., Scholes G.D. Colloidal PbS nanocrystals with size-tunable near-infrared emission: observation of post-synthesis. Adv. Mater.2003; 15 1844-1849.

[17] Yochelis S., and Hodes G. Nanocrystalline CdSe formation by direct reaction between Cd ions and selenosulfate solution. Chem Mater 2004; 16 2740-2744.

[18] Brown P. & Kamat, P.V. Quantum Dot Solar Cells.Electrophoretic Deposition of CdSe-C_{60} Composite Films and Capture of Photogenerated Electrons with nC_{60} Cluster Shell. J. Am. Chem. Soc. 2008; 130 8890-8891.

[19] Baker D.R. and Kamat P.V. Photosensitization of TiO2 Nanostructures with CdS Quantum Dots: Particulate versus Tubular Support Architectures. Adv. Funct. Mater. 2009; 19 805–811.

[20] Subramanian V, Kuno M, Kamat, V.Quantum dot solar cells. harvesting light energy with CdSe nanocrystals molecularly linked to mesoscopic TiO2 films. J Am Chem Soc 2006; 128 (7) 2385–2393.

[21] Kamat P.V. Quantum Dot Solar Cells. Semiconductor Nanocrystals as Light Harvesters. J. Phys. Chem. C 2008; 112 18737-18753.

[22] Sheeney-Haj-Kia L., Basnar B., Willner I. Efficient Generation of Photocurrents by using CdS/Carbon nanotube Assemblies on Electrodes. Angew. Chem. Int. Ed. 2005; 44 78-83.

[23] Huang Q., and Gao L. Synthesis and Characterization of CdS/multiwalled carbon nanotube heterojunctions. Nanotecnol 2004; 15 1855-1860.

[24] Pattantyus-Abraham A.G., Kramer I.J., Barkhouse A.R., Wang X., Konstantatos G., Debnath R., Levina L., Raabe I., Nazeeruddin M.K., Gratzel M., and Sargent E.H. Depleted-Heterojunction Colloidal Quantum Dot Solar Cells. ACSNano 4 (6) 3374–3380.

[25] Luther J.M., Law M.*et al*. Structural, Optical, and Electrical Properties of Self-Assembled Films of PbSe Nanocrystals Treated with 1,2-Ethanedithiol. ACS Nano. 2008; 2 271.

[26] Luther M., Gao J., Lloyd M.T., Semonin O.E., Beard M.C., and Nozik A.J. Stability... solar cell. Advanced Materials 2010; 22 (33) 3704–3707.

[27] Gao J., Perkins C.L, Luther J.M., Hanna M.C., Chen H-Yu, Semonin O.E., Nozik A.J., Ellingson R.J., and Beard, M.C. n-Type Transition Metal Oxide as a Hole Extraction Layer in PbS Quantum Dot Solar Cells. Nano Letters 2011; 11 3263

[28] Sun, B., Findikoglu A.T., Sykora M., Werder D.J., and Klimov V.I. Hybrid Photovoltaics Based on Semiconductor Nanocrystals and Amorphous Silicon. Nano Lett. 2009; 9 (3) 1235–1241.

[29] Barnham K. and Duggan G. A new approach to high efficiency multibandgap solar cells. J. Appl. Phys. 1990; 67 3490-3493.

[30] Luque A., and Marti A. Increasing the Efficiency of Ideal Solar Cells by Photon Induced Transitions at Intermediate Levels Phys. Rev. Lett. 1997; 78 5014-5017.

[31] Luque A., Martí A., and Nozik A.J. Solar Cells Based on Quantum Dots: Multiple Exciton Generation and Intermediate Bands. MRS BULLETIN 2007, 32, pp: 236-241.

[32] Huynh W.U. Hybrid Nanorod-Polymer Solar Cells. Science 2002; 295 2425.

[33] Sun B., Marx E., and Greenham, N.C. Photovoltaic Devices Using Blends of Branched CdSe Nanoparticles and Conjugated Polymers. Nano-Letters 2003; 3 (7) 961-963.

[34] Hara K., and Arakawa H. Handbook of Photovoltaic Science and Engineering, by A. Luque and S. Hegedus (Eds.), Chapter 15, p.663, John Wiley & Sons, Ltd., ISBN: 0-471-49196-9; 2003.

[35] O'Regan B.; and Grätzel M. A Low-cost High-Efficiency Solar Cell Based on Dye Sensitized Colloidal TiO_2 Films. Nature 1991; 353 737-740.

[36] Rhle S., Shalom, M., and Zaban, A. Quantum-Dot-Sensitized Solar Cells. Chem. Phys, Chem. 2010; 11 2290 –2304.

[37] Peng A., and Peng X. Formation of high-quality CdTe, CdSe, and CdS nanocrystals using CdO as precursor". Journal of the American Chemical Society 2001; 123 (1) 183–184.

[38] Lee H.J., Yum J.H., Leventis H.C. CdSe quantum dot-sensitized solar cells exceeding efficiency 1% at full-sun intensity. Journal of Physical Chemistry C. 2008; 112 (30) 11600 –11608.

[39] Bang J. H. and Kamat, P. V. Quantum dot sensitized solar cells. A tale of two semiconductor nanocrystals: CdSe and CdTe,. ACS Nano. 2009; 3 (6) 1467–1476.

[40] Wang P., Zakeeruddin S. M., Comte P., Exnar I., and Grätzel M. Gelation of Ionic Liquid-Based Electrolytes with Silica Nanoparticles for Quasi-Solid-State Dye-Sensitized Solar Cells. Chem. Commun. 2002; 24 2972-2973.

[41] Wang P., Zakeeruddin S. M., Moser J.E., Nazeeruddin M. K., Sekiguchi T., and Grätzel, M. Molecular-scale interface engineering of TiO_2 nanocrystals: Improving the efficiency and stability of dye-sensitized solar cells. Nat. Mater. 2003; 2 402.

[42] Chakrapani V., Tvrdy K., and Kamat P.V. Modulation of Electron Injection in CdSe –TiO_2 System through Medium Alkalinity", J. Am. Chem. Soc. 2010; 132 (4) 1228-1229.

[43] Kongkanand A., Tvrdy K., Takechi K., Kuno M., and Kamat P.V. Quantum Dot Solar Cells. Tuning Photoresponse through Size and Shape Control of CdSe-TiO2 Architecture. J. Am. Chem. Soc. 2008; 130 (12) 4007-4015.

[44] Mora-Sero I., and Bisquert J. Breakthroughs in the Development of Semiconductor-Sensitized Solar Cells. J. Phys. Chem. Lett. 2010; 1 3046–3052.

[45] Barnes P.R.F, Liu L., Li X., Anderson A.S., Kisserwan H., Ghaddar T.H., James R., Durrant J.S., and O'Regan, B.C. Re-evaluation of Recombination Losses in Dye-Sensitized Cells: The Failure of Dynamic Relaxation Methods to Correctly Predict Diffusion Length in Nanoporous Photoelectrodes. Nano Lett. 2009; 9 (10) 3532–3538.

[46] Braga A., Gimenez S., Concina, I., Vomiero, A., and Mora-Sero, I. Panchromatic sensities solar cells based on metal sulfied quantum dots grown directly on nanostructured TiO_2 electrode. J. Phys. Chem. Lett. 2011; 2 454-460.

[47] W X., Koleilat G.I., Tang J., Liu H., Kramer I.J., Debnath R., Brzozowski L., Barhouse D.A.R., and Levina, L.; and Hoogland, S.; Tandem colloidal quantum dot solar cells employing a graded recombination layer. Nature Photonics 2011 ; 5 480.

[48] Choi H., Nahm C., Kim J., Kim C., Kang S., Hwang T., and Park B.Toward highly efficient quantum-dot-and dye-sensitized solar cells. Current Applied Physics 2003; 13 S2-S13.

[49] Koo H.-J., Park J., Yoo B., Yoo K. Kim K., and Park N.-G. Size-dependent scattering efficiency in dye-sensitized solar cell. Inorg. Chim. Acta. 2008; 361 677-683.

[50] Atwater H.A., and Polman, A. Plasmonics for improved photovoltaic devices. Nat. Mater. 2010; 9 205-213.

[51] Shalom M., Albero J., Tachan Z., Martínez-Ferrero E., Zaban A., and Palomares E. Quantum Dot-Dye Bilayer-Sensitized Solar Cells: Breaking the Limits Imposed by the Low Absorbance of Dye Monolayers. J. Phys. Chem. Lett. 2010; 1 1134–1138.

[52] Buhbut S., Itzhakov S., Tauber E., Shalom M., Hod I., Geiger T., Garini Y., Oron D., and Zaban, A. Built-in Quantum Dot Antennas in Dye-Sensitized Solar Cells. Acs Nano 2010; 4 (3) 1293–1298.

[53] Shockley W., and Queisser H.J. Detailed Balance Limit of Efficiency of p-n Junction Solar Cells", Journal of Applied Physics 1961; 32 510-519.

Chapter 12

Solar Cells with InGaN/GaN and InP/InGaAsP and InGaP/GaAs Multiple Quantum Wells

Shaoguang Dong, Kanghua Chen, Guojie Chen and Xin Chen

Additional information is available at the end of the chapter

http://dx.doi.org/10.5772/58899

1. Introduction

InGaN alloys materials are extensively utilized in light emitting diodes (LEDs) and laser diodes (LDs). In recent years, InGaN alloys materials have also been considered to use in solar cells because of their favorable photovoltaic properties, including a direct band gap, a higher absorption coefficient at the band edge, superior radiation resistance, high carrier mobility, thermal stability and so on. Especially, the band gap of the InGaN alloys materials can even vary from 0.7 eV to 3.4 eV, which covers almost the sun spectrum. [1] Additionally, four-junction tandem solar cells with a theoretical conversion efficiency of over 60% have been designed, but these designs require some junctions that have band gap of greater than 2.4 eV. Very few materials have a band gap of over 2.4 eV but InGaN alloys. Therefore, InGaN alloys are the candidate of using in highly efficient tandem solar cells.

Many challenges must be overcome before InGaN alloys can be used widely photovoltaic devices. A large lattice mismatch between GaN and InN atoms limits InGaN alloys using in photovoltaic devices in which these alloys must incorporate a thick absorb layer with high indium composition for absorbing incident light. Generally, the critical thickness of $In_{0.1}Ga_{0.9}N$ is approximately 100 nm, and this thickness falls rapidly as the indium composition increasing. When the thickness of InGaN alloys layer exceeds a critical value, defects are formed as recombination centers. These recombination centers increase the rate of consumption of photogenerated electron-hole pairs, degrading photovoltaic performance. Owing to the need for high crystalline quality, the thickness of absorb layers in InGaN alloys photovoltaic devices is limited by challenges related to epitaxial deposition such that a compromise of multiple quantum well (MQW) structure is used for the absorb layers in InGaN alloys photovoltaic devices, which results in insufficient light absorption.

Previous studies have utilized several methods for improving the collecting of light in InGaN/GaN MQWs solar cells, such as the use of a ZnO or SiO_2 sub-wavelength structure to realize a graded refractive index interface to reduce Fresnel reflection and simultaneously to increase the light scattering effect. Silver nanoparticles have also been used to exploit the surface plasmon effect to promote the scattering of light. However, because the light absorption is not sufficient, the lower external quantum efficiency and the higher absorption coefficient in the ultraviolet region have not been solved yet. [2]A back reflector that reflects the unused light back to the absorr layer provides a solution and has an important role in thin film solar cells. For this purpose, distributed Bragg reflectors (DBRs) are good candidates for InGaN/GaN MQWs solar cells.

Due to InGaN alloys materials have tunable band gaps and superior photovoltaic characteristics, they would be emerged as promising solar cells materials. [3] The band gap of InGaN alloys materials changed from 0.7 eV to 3.4 eV and these band gaps can be tuned by changing the contents of indium in the InGaN alloys materials. InGaN alloys mateials also have direct band gaps in the entire alloys range. For achieving higher photoelectric conversion efficiency, the multiple quantum wells solar cell structure has been proposed, which exhibits stronger absorption properties than bulk materials. [3] The quantum wells layers of the solar cells extend the absorption spectrum into the infrared region, in the case of radiant energy levels in the semiconductor band gap. The quantum wells similar to the *p–i–n* diode structure may extend the solar cells absorption spectrum, and then results in a higher short circuit current density (J_{sc}). The recombination rate of these quantum wells has been improved, which result in a higher open circuit voltage (V_{oc}). The finally result is that the photoelectric conversion efficiency (η) of the solar cells has been increased.

Group III–Nitride alloys materials solar cells are the better candidates for multiple quantum wells solar cells, because these alloys have direct band gaps and also have the better absorption of the solar spectrum. Recently, multi-junctions solar cells have been used to obtain higher conversion efficiency than single-junction solar cells. [3]However, the properties of lattice-matched quantum wells solar cells with different In content significantly complicate the fabrication process and design of the solar cells device. The average strain is chief when designing strained quantum wells solar cells. In order to maximize the absorption of quantum wells, it is better to maximize the carries concentration of quantum wells, the width and the number of quantum wells. In fact, all these factors increase the average strain, so the solar cells eventually become limited by the critical thickness. So the relative contributions of tunneling and thermionic emission currents of the multiple quantum wells structure are functions of the operation temperature and should provide guidance for the optimized design of multiple quantum wells solar cells tailored for operation in specific temperature ranges.

For the fabrication of InGaN alloys solar cells, there is considerable interest in the growth of GaN and InGaN alloys on Si substrates, because Si substrates have the advantages of low cost and large size. [4] Si substrates have a better thermal conductivity, whereas sapphire and SiC substrates have worse thermal conductivity. However, integration has been hampered by the large density of defects and cracks arising from larger lattice mismatch between GaN and Si.

http://dx.doi.org/10.5772/58899

Some studies have grown GaN on Si (100) or Si (111) substrates by adding buffers to overcome the larger density of defects and cracks. [5]

Recently most reported InGaN alloys solar cells have very low photovoltaic efficiency compared to Si-based solar cells. However, InGaN alloys materials superior resistance against irradiation damage makes themselves very suitable for the applications in photovoltaic devices, and motivates further development. In some investigations, GaN has usually been grown on sapphire or SiC substrates, which are expensive and difficult to integrate into the silicon industry. [3] Therefore, it is desirable to grow GaN on silicon substrate and integrate GaN with the mature silicon fabrication techniques.

The optoelectronic performance of InGaN solar cells devices are researched by preparing InGaN/GaN multiple quantum wells with In composition exceeding 0.3, attempting to alleviate to the phase separation phenomenon of InN and GaN materials at a certain degree by this InGaN/GaN multiple quantum wells structure. The InGaN/GaN multiple quantum wells solar cells have a better optoelectronic performance at wavelengths longer than 430 nm. The InGaN solar cells devices show better open circuit voltage (2.0 V) and external quantum efficiency (45%) and high fill factor (65%) because of the InGaN/GaN multiple quantum wells structure.

Recently, concentrator systems solar cells are becoming a main technology for the large scale electrical power by utilizing high conversion efficiency group III–V multi-junctions solar cells. Sharp's triple-junctions InGaP/GaAs/InGaAs concentrator solar cells have got a high conversion efficiency of 44.4% under about 300 suns. [6] The solar cells will probably to be four or more junction cells with higher conversion efficiency in the future. The ideal highest conversion efficiency is 55% for four-junctions solar cells, which could be achieved by utilizing an optimized band gap combination of 1.9/1.4/1.0/0.7 eV. [6]The four-junctions solar cells is a promising photovoltaic candidate devices because of the bandgap combination of InGaP/GaAs (1.9/1.4 eV) which matched to GaAs in their lattice and that of InGaAsP/ InGaAs (1.0/0.7 eV) which matched to InP in their lattice.

Currently, only a few contributions have been reported on InGaAsP materials solar cells grown by metal organic chemical vapor deposition (MOCVD). In fact, InGaAsP materials solar cells can also be grown by molecular beam epitaxy (MBE), which can give more precise growth control technology. Researcher ever think that the photovoltaic performance of solar cells grown by MBE method is not probably better than MOCVD growth methods, because the growth temperature of MBE methods is very lower, which results in more defect states and deep defect centers in bulk materials. Recently, a high efficiency GaInP/GaAs/GaInAsN triple-junctions solar cell was successfully grown by MBE methods. [6]The experimental results showed that the solar cells containing group III–V materials grown by MBE growth are as good as the MOCVD growth. It has been a challenge to grown a high quality InGaAsP materials which bandgap is only 1.0 eV on an InP substrate by MBE methods. Furthermore, a comprehensive study on the carrier recombination dynamics of InGaAsP material grown by MBE has not been reported.

The solar cells of InP/InGaAsP double hetero-junction (DH) structure have been investigated and compared these solar cells to the InP control cells. [7] The InGaAsP has many band gap values from 0.75 eV to 1.35 eV which very matched to the InP in lattice. The InP/InGaAsP double hetero-junction structure solar cells whose light absorption layer is the InGaAsP has also been investigated. [7] The investigated results are that the InP/InGaAsP double hetero-junction structure solar cells have a lower open-circuit voltage and the short-circuit current improves twice compared to the InP control cells. So the InP/InGaAsP double hetero-junction structure can greatly improve the conversion efficiency of the solar cells.

The photoelectric performance of InP/InGaAsP multiple quantum wells solar cells are improved by light scatter coming from deposited dielectric or metal nanoparticles. [8]The integration of dielectric or metal nanoparticles on the multiple quantum wells solar cells showed that incident light can enter the bulk by lateral optical propagation paths, and the refractive index can provide the optical confinement between the quantum well layers and surrounding materials layers. By the materials surface optimization of silica and Au nanoparticle, short-circuit current density could be increased by 12.9% and photoelectric conversion efficiency also could be increased by 17%, respectively.

Group III–V compound multi-junctions solar cells have the advantage for achieving photoelectric conversion efficiency exceed to 40%, and they are also a promising photovoltaic materials for the space and terrestrial solar cells devices. [9] Among the multi-junctions solar cells technologies, the double-junctions solar cells is the simplest structure and has attracted extensive interesting for further optimizing these solar cells device performance. One of the most trusted materials is the GaInP/GaAs alloys system whose band gap is 1.9 and 1.4 eV respectively. When GaInP materials are acted as the top cell, many problems of bulk defects and crystal quality found existing in other alloy materials such as AlGaAs can even be avoided.

As a result, the researches on the GaInP and GaAs materials property have been become very important, especially the study on the recombination dynamics of carriers in the active layers. For example, surface recombination velocity of the GaInP layer could be measured by the intensity of photoluminescence, and the effective lifetime of minority carriers of the GaInP or GaAs layer could be also measured by the intensity of photoluminescence. On the other hand, the characterization of carrier dynamics and the loss of carriers have been reported little from references. Despite the electroluminescence measurement has been used for modeling the irradiation-induced degradation of the multi-junctions solar cells structures in space conditions, compared with the photoluminescence technique, it is believed that the electroluminescence measurement is also competent in revealing detailed the kinetics of the recombination loss of carriers. InGaP solar cells which have about 1.9 eV band gap and lattice-matched to GaAs, have been used for the top cells of multi-junctions solar cells.

InGaP/GaAs/InGaAs multi-junctions solar cells have been achieved high conversion efficiency of 36.4% under AM1.5. Recently, the intermediate band solar cells have been extensively studied and providing a high conversion efficiency of over 60% under concentrated sunlight conditions. [10]The intermediate band is formed by the quantum dot superlattice in intermediate band solar cells, which located in the bandgap and used to absorb the sub-bandgap photons in the intermediate band state. To achieve a conversion efficiency of more than 60%,

http://dx.doi.org/10.5772/58899

the materials with a bandgap of about 1.9 eV are needed. However, the quantum dot superlattice solar cells have used GaAs semiconductor materials whose bandgap is only 1.4 eV. In order to realize intermediate band solar cells with a conversion efficiency of over 60%, a wide bandgap semiconductor material is needed. In fact, InGaP is a suitable intermediate band material with bandgap of 1.9 eV. [10]

InGaP material is very difficult to grow by the solid-source molecular beam epitaxy technique which is suitable for growing a high quality quantum dot structure. The InGaP epitaxial layers are required to obtain sufficient light absorption in the solar cells devices, a large-scale phosphorus source are needed in the molecular beam epitaxy chamber. In fact, all of most InGaP solar cells are grown by metal organic chemical vapor deposition.

An InGaP/GaAs tandem solar cell of 4 cm^2 larger area is realized, which got a new conversion efficiency record of over 30% under AM 1.5. [11]Those tandem solar cells performances were improved by utilizing InGaP tunnel junction and a double hetero-junctions structure, where the InGaP layers are surrounded by AlInP barrier layers. The double hetero-junctions structure increased the peak current value of InGaP tunnel junction. The AlInP barrier layer takes the part of a back surface field; it is found that the AlInP barrier layer can effectively reflect minority carriers in the InGaP top cells. The AlInP barrier layer has a high potential and can prevent the diffusion of zinc from a doped tunnel junction toward the top cells during growth. Furthermore, the InGaP tunnel junction can also reduce the light absorption loss and increase the photogenerated current in the GaAs bottom cell. [11]

The photoelectric conversion efficiency of InGaP/GaAs/Ge multi-junctions solar cells has been technically improved up to 32% under AM1.5. The InGaP material is on first hetero-junction growth layer, combined with Ge bottom layer and double hetero-junction tunnel junctions, in which Ge substrate is precisely matched with the conventional GaAs in their lattice structure. If the AlInGaP material whose band gap is 1.95 eV is employed in the top cells layer, the conversion efficiency of these solar cells should be improved further. Furthermore, thin film structure of InGaP/GaAs solar cells on metal film has been reported. The thin film solar cells of InGaP/GaAs are founded lightweight, high flexibility, high radiation resistance and high efficiency.

The use of multiple quantum wells is very advantageous in the conventional tandem solar cells, because multiple quantum wells can independently tailor the absorption edge of each cell, which has no such problem of lattice mismatch and relaxation. [12]The InGaP/GaAs solar cells was improved by using strain balanced multiple quantum wells; the multiple quantum wells structure of tandem solar cells has achieved the conversion efficiency of over 30% under AM1.5. This conversion efficiency is a new record for currently photovoltaic devices. The conversion efficiency of over 34% could be realized under AM1.5 by optimizing the solar cells device structure. The possibility and gains are currently researched by introducing multiple quantum wells structure into top cells and bottom cells layer of an InGaP/GaAs solar cells device.

2. InGaN/GaN MQWs solar cells

InGaN alloys semiconductor materials as active layers of light emitting diodes have been widely investigated, which emission wavelengths cover from red to near ultraviolet spectral regions. [13] Recently, InGaN alloys as a new solar cells materials have been interested by their tunable energy band gaps which vary from 0.7 eV to 3.4 eV, covering almost the whole sunlight spectrum, and also their superior photovoltaic characteristics, such as high carrier mobility, direct energy band gap, high optical absorption coefficient near the band edge, high drift velocity and low radiation resistance. [14]

Although InGaN alloys material solar cells offer tremendous potential for photovoltaic applications, there are only a few references on InGaN alloys solar cells. Furthermore, most of reported InGaN alloys solar cells usually have In contents no more than 15% and band gaps about 3.0 eV or larger, therefore, external quantum efficiency is nearly not exist at wavelengths longer than 420 nm. [15] An earlier theoretical calculation has been indicated that the use of a special active material in solar cells can obtain conversion efficiency greater than 50%, that material is InGaN alloys whose In content exceed 40%. [16]Additionally, group III-nitride multi-junction solar cells with ideal band gaps for maximum conversion efficiency must be incorporated InGaN alloys with higher In contents. [13]

In this section, the optoelectronic properties of InGaN alloys solar cells are researched by merging into InGaN/GaN multiple quantum wells (MQWs), attempt to alleviate the phase separation issue of InN and GaN in a certain extent, and demonstrate the photovoltaic performance of solar cells operating in wavelengths longer than 420 nm.

2.1. MQWs solar cells layers structure

The MQWs solar cells layers structure fabricated by InGaN alloys and GaN materials is shown in Figure 1, the light absorption region consists of eight periods of InGaN (3 nm)/GaN (8 nm) MQWs. The MQWs were grown under the established MOCVD growth conditions; InGaN alloys materials with In content about 0.3 or 0.4 work in longer wavelengths in order to obtain better photovoltaic responses. The thickness of *p*-GaN or *n*-GaN is about 150 nm. The device structure was grown on a GaN/Al_2O_3 template. As demonstration, the device fabrication steps are adopted to commercial group III-nitride LEDs and implemented a thin Ni/Au semitransparent current spreading layer to minimize the *p*-contact resistance on the *p*-GaN window layer.

The growth of high quality crystalline structure InGaN alloys materials is highly challenging in all of In composition range. One of the main problems is that the lattice is seriously mismatched between InN and GaN atoms, resulting in low solubility and phase separation between InN and GaN materials. [17]Recently, single crystalline phase InGaN alloys materials with all of In composition range could be grown by metal organic chemical vapor deposition (MOCVD) by directly depositing on GaN templates without using buffer layers. [18] These InGaN alloys characteristics are illustrated in Figure 2, in which X-ray diffraction data of the (002) plane for several InGaN alloys materials for θ-2θ scans are shown. All scanned curves

http://dx.doi.org/10.5772/58899

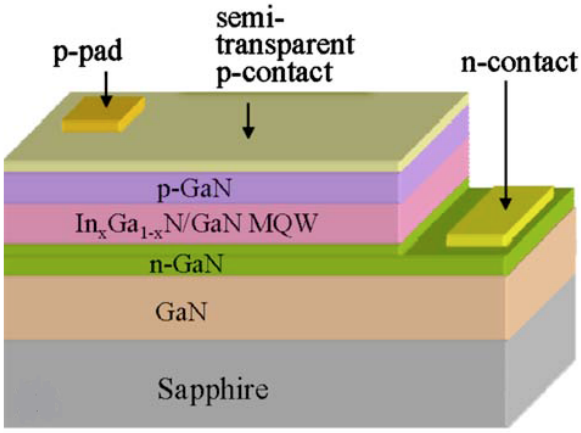

Figure 1. Schematic of layers structure based on InGaN/GaN MQWs solar cells.

exhibit no multiple peaks except for closing the InN peak position, showing that InGaN alloys materials have not been phase separation. The results show a significant growth improvement of InGaN alloys materials by MOCVD. [13]

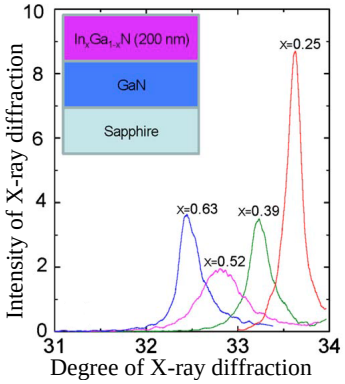

Figure 2. X-ray diffraction data for θ-2θ scan curves of the (002) plane

However, when In composition range exceed to the 0.5, the homogeneity of InGaN alloys materials is pretty poorer. The full width at half maximum of the θ-2θ-scans rocking curves of the (002) plane increases from about 1000 arcsec when In composition is 0.2 to about 3000 arcsec when In content is 0.5 for InGaN alloys materials of 200 nm thickness. The photoluminescence (PL) emission spectrum of InGaN alloys materials also is deteriorated with an increase of In composition, as shown in Figure 3. The intensity of PL emission spectrum of $In_{0.4}Ga_{0.6}N$ alloys is about 100 times lower than that of $In_{0.2}Ga_{0.8}N$. This trend of crystalline

quality reduced with In composition increasing makes the realization of solar cells based on InGaN alloys materials with In content greater than 0.3 highly challenging. Evidence that strain could suppress phase separation in InGaN alloys materials has been reported. [19] It was shown that InGaN alloys materials with In content lower than 0.5 without phase separation can be grown when the alloys is embedded by an InGaN/GaN double heterostructure.

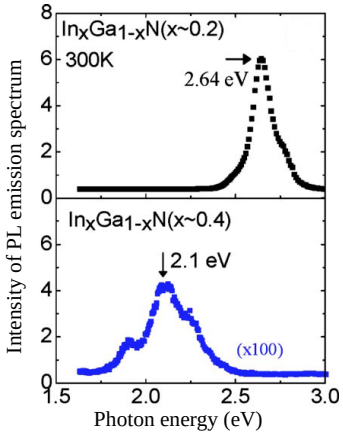

Figure 3. PL emission spectrum of InGaN alloys materials grown on GaN/Al_2O_3 templates.

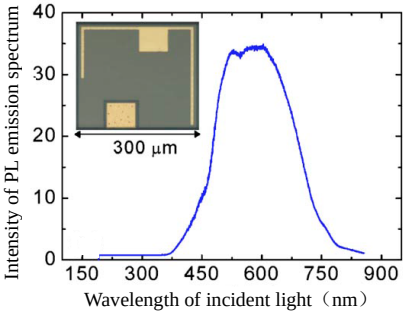

Figure 4. Emission spectrum of the white light source and the inset is the microscopy image of MQWs solar cells.

2.2. MQWs solar cells performance

An optical microscopy image of a MQWs solar cells fabricated by InGaN alloys materials is shown in the inset of Figure 4. The MQWs solar cells were characterized by a microprobe station with a Keithley 2400 source meter. The solar cells were illuminated by a white light source with no optical filters to measure the current versus voltage characteristics, whose PL emission spectrum is shown in Figure 4. The solar cells were illuminated monochromatically

http://dx.doi.org/10.5772/58899

by using the same white light source to achieve the characterization of quantum efficiency versus excitation wavelength.[13]The PL emission spectrum for MQWs solar cells structure fabricated by InGaN alloys materials with In content about 0.3 and GaN is shown in Figure 5, and exhibits an PL emission peak about 472 nm.

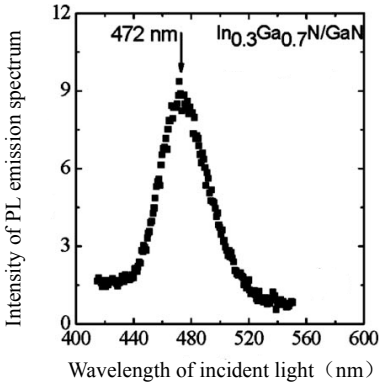

Figure 5. PL emission spectrum of an InGaN/GaN MQWs solar cells structure.

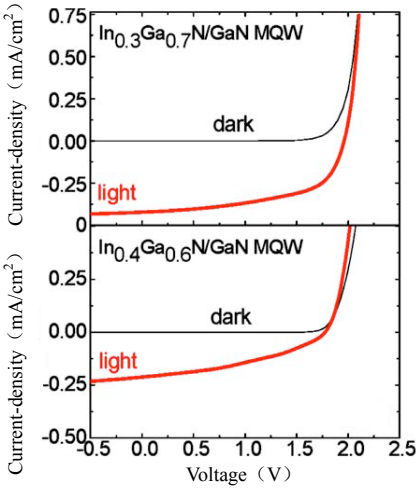

Figure 6. Curves of *I-V* characteristics for $In_xGa_{1-x}N$/GaN MQWs solar cells.

Current versus voltage (*I-V*) characteristics of two MQWs solar cells fabricated by InGaN alloys materials with In composition about 0.3 or 0.4 in the quantum well region and GaN are shown in Figure 6. The open-circuit voltage (V_{oc}) is about 2.0 V or 1.8 V for two MQWs solar cells with In composition about 0.3 or 0.4, respectively. These values are in good agreement with the

band gaps of $In_{0.3}Ga_{0.7}N$ and $In_{0.4}Ga_{0.6}N$. However, the performance of the solar cells with $In_{0.4}Ga_{0.6}N$/GaN MQWs as active region is no more than that of the solar cells with $In_{0.3}Ga_{0.7}N$/GaN MQWs, despite the $In_{0.4}Ga_{0.6}N$/GaN MQWs solar cells active layers are shown to have a much better spectral overlap with the excitation light source. [3]This degradation of these solar cells performance and the X-ray diffraction results are shown in Figure 2 and it is a direct reason of the InGaN alloys materials quality degradation with In composition increasing, which further leads to much loss of the photogenerated carriers. The observed photovoltaic characteristics of these solar cells are consistent with the quantum efficiencies of group III-nitride green LEDs which are much lower than those of blue LEDs. [13]

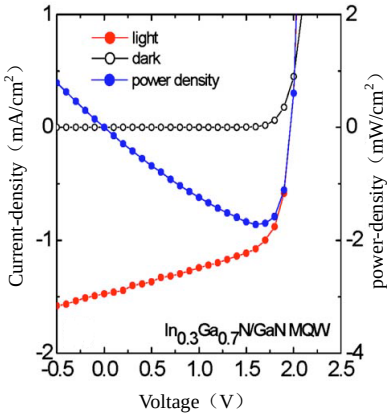

Figure 7. Curves of current-density vs voltage and power-density vs voltage.

Current density versus voltage and power density versus voltage curves of the solar cells with $In_{0.3}Ga_{0.7}N$/GaN MQWs as active layer are shown in Figure 7, a fill factor of over 60% is obtained from the solar cells. The external quantum efficiency as a function of excitation wavelength for the $In_{0.3}Ga_{0.7}N$/GaN MQWs solar cells is shown in Figure 8, from which we can see that the solar cells have an external quantum efficiency of 40% at 420 nm. The spectrum response is limited by using *p*-GaN window in the shorter wavelength region, and it would be improved if the *p*-AlGaN or *p*-InAlGaN material is incorporated. [13]Three major factors limited the external quantum efficiency are the following: (1) Light absorption in the semi-transparent *p*-contact layer. Current spreading in *p*-contact layer was only adopted from LED structure and the *p*-contact layer need to be optimized for solar cells devices. (2) The thickness of light absorption layer is too thin in the $In_{0.3}Ga_{0.7}N$/GaN MQWs structure. The well thickness and period of the $In_{0.3}Ga_{0.7}N$/GaN MQWs active region need to be optimized to maximize light absorption and minimize other detrimental effects, which is incorporated by relatively high In composition InGaN alloys materials in the multiple quantum well region. (3) InGaN alloys materials with relatively high In composition are very low crystalline quality. Nevertheless, the InGaN alloys materials solar cells have good external quantum efficiency working at such long wavelengths, so the MQWs is a effec-

http://dx.doi.org/10.5772/58899

tive method to design MQWs solar cells by InGaN alloys materials with relatively high In compostion for high photoelectric conversion efficiency. [13]

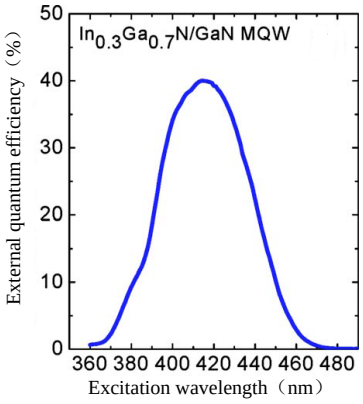

Figure 8. Curves of external quantum efficiency vs excitation wavelength.

3. InP/InGaAsP MQWs solar cells

Currently, there are extensively interests in the application of multiple quantum wells structure in solar cells devices; their optoelectronic conversion efficiency can exceed the single-junction solar cells theoretical efficiency limit of 31%. [20]Theoretically, maximum optoelectronic conversion efficiency range in multiple quantum wells solar cells could be predicted from 50% to 65%. The incorporation of multiple quantum wells structure can ensure high energy photon absorption efficiency and improved short-circuit current density (J_{sc}) and reduced in open-circuit voltage (V_{oc}), because no enough collection efficiency of photogenerated carriers is especially obvious. [21] Regardless of these problems, the maximum power of multiple quantum wells solar cells devices can exceed that of the similar homo-junction solar cells devices by extending the absorption spectrum to longer wavelengths. [22]We have got a conclusion that incident light can be normally got into lateral optical propagation paths in the multiple quantum wells solar cells devices by scattering from metal or dielectric nanoparticles, whose optical confinement is provided by the refractive index contrast between the quantum wells layer and surrounding materials. Substantially, the photogenerated current generation and collection over a large range of incident light wavelengths has been improved, particularly at longer wavelengths. [8]

3.1. MQWs solar cells *p-i-n* structure

The lattice matched InP/InGaAsP multiple quantum wells *p-i-n* structure solar cells is nominally shown in Figure 9. The *n*-type electrode of all *p-i-n* structures solar cells consist of a S

doped InP substrate with doping concentration about 5×10^{18} cm^{-3}, while the intrinsic region consist of 10 nm $In_{0.91}Ga_{0.09}As_{0.2}P_{0.8}$ barriers alternating with 10 nm $In_{0.81}Ga_{0.19}As_{0.4}P_{0.6}$ quantum wells for ten periods with an additional 50 nm or 25 nm $In_{0.91}Ga_{0.09}As_{0.2}P_{0.8}$ barrier on the top quantum wells layer. The *p*-type electrode of all *p-i-n* structures solar cells consist of a Zn doped 50 nm *p*-type InP layer or 25 nm *p*-type InP and 10 nm *p*-type $In_{0.47}Ga_{0.53}As$ with doping concentration about 3×10^{18} cm^{-3}. The *n*-type Ohmic contacts were fabricated by using Ti (40 nm)/Au (200 nm) metal deposited by electron beam evaporation. 2 mm^2 window regions were formed by conventional photolithography, and *p*-type contacts were formed by using Ti (20 nm)/Pd (20 nm)/Au (200 nm) metal deposited by electron beam evaporation. [8]The top $In_{0.47}Ga_{0.53}As$ contact layer was removed from the window region by a selective wet etch (H_2SO_4:H_2O_2:H_2O, 1:10:220) for 15 s, and about 15 nm SiO_2 surface passivation layer was sputter deposited over the window area of all devices.

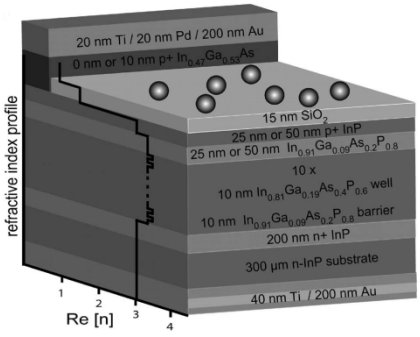

Figure 9. InP-based multiple quantum well solar cells with nanoparticles on the surface

To optimize collection efficiency of photogenerated carriers in the multiple quantum wells and to minimize the reduction of V_{oc}, a sufficiently large electric field across the intrinsic region is definitely required, in which the electric field intensity is 30 kV/cm or so, [23] and the barriers must be thermally or optically excited usually at 200~450 meV or less. [24] The electric field condition requires that the intrinsic region in the *p-i-n* structure should be especially thin, where the intrinsic region is required by choosing appropriate materials for the multiple quantum wells and barrier. [8]For the solar cells device structure with an intrinsic layer thickness of 250 nm, shown in Figure 9, the quantum wells electric field intensity is about 48 kV/cm at equilibrium condition, and 32 kV/cm at a maximum power state when operating voltage is about 0.4 V.

Incorporation of the multiple quantum wells region in solar cells device, not only improves photon absorption efficiency at longer wavelengths, but also increases the refractive index in the intrinsic region relative to the surrounding electrode contact layers, as also shown in Figure 9, which produces a slabby waveguide structure. [25] Waveguide mode accompanied by light scattered from metallic nanoparticles has been demonstrated by metal nanoparticles on silicon-on-insulator photodetectors. [26] The scattering effect is achieved by depositing metal

http://dx.doi.org/10.5772/58899

nanoparticles or dielectric nanoparticles at top of the solar cells device, as shown in Figure 10. The incident light scattered by the nanoparticles not only can improve transmission of photons into the solar cells active layers, but also make normally incident photons into lateral confined paths in the multiple quantum wells waveguide layer, result in photon absorption efficiency increasing, more photocurrent generating and optoelectronic conversion efficiency improving. [8]

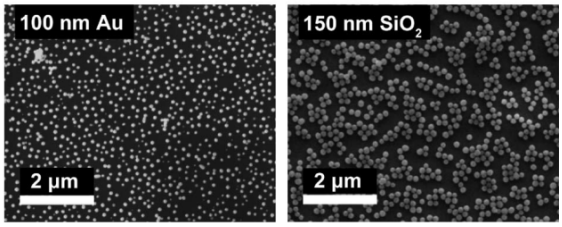

Figure 10. SEM images of 100 nm diameter Au nanoparticles (left) and 150 nm diameter SiO_2 nanoparticles (right).

3.2. MQWs solar cells *p-i-n* performance

The photocurrent response is shown in Figure 11 for an InP homojunction control device, a *p*-InP/ *i*-$In_{0.91}Ga_{0.09}As_{0.2}P_{0.8}$ /*n*-InP barrier control device, and a *p-i-n* multiple quantum wells solar cells device. These epitaxial layer structures for the control device and barrier control device and multiple quantum wells device were grown on 225 nm thicknesses intrinsic layer under identical reactor conditions. The photocurrent response only extends to 950 nm of the InP absorption edge for the InP homojunction control device, which is determined by room temperature photoluminescence measurements, but the photocurrent responses can extend to 1050 nm of the $In_{0.91}Ga_{0.09}As_{0.2}P_{0.8}$ absorption edges and 1150 nm of $In_{0.81}Ga_{0.19}As_{0.4}P_{0.6}$ absorption edges for the barrier control device and multiple quantum wells solar cells device, respectively.

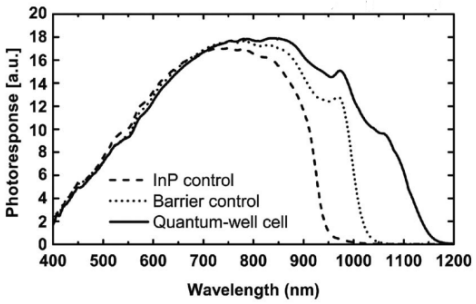

Figure 11. Photocurrent response spectra for InP homojunction device, barrier device and quantum well solar cell device

The maximum power curves are shown in Figure 12 for InP homo-junction control device, *p*-InP/*i*-$In_{0.91}Ga_{0.09}As_{0.2}P_{0.8}$/*n*-InP barrier control device and *p*-*i*-*n* multiple quantum wells solar cells device which all grown on 250 nm intrinsic layer thicknesses. Despite V_{oc} drops to 0.63V for the homo-junction control device and barrier control devices, and drops to 0.53 V for the quantum wells solar cells device, the maximum power output of the quantum wells solar cells device increases 7.4% and 4.6% relative to the homo-junction control device and barrier control device, respectively. [8]

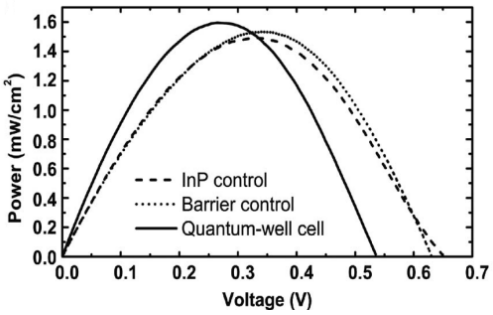

Figure 12. Power output curves for InP control device, barrier control device and quantum wells solar cells device

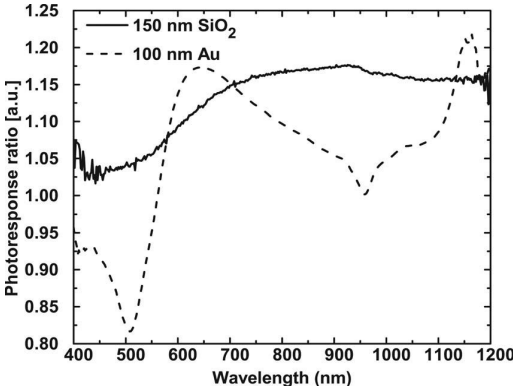

Figure 13. Photocurrent response spectra of quantum well solar cells with Au nanoparticles and SiO_2 nanoparticles

To illustrate the effect of nanoparticle scattering on the solar cells device in improved photocurrent response and optoelectronic conversion efficiency, Figure 13 shows photocurrent response spectra for quantum wells solar cells with either 100 nm diameter Au or 150 nm diameter SiO_2 nanoparticles deposited on these solar cells surface, which plotted by photocurrent response ratios relative to the spectrum for the solar cells device without nanoparticles. Au and SiO_2 nanoparticles densities were employed with about 2.7×10^9 cm^{-2} and 2.1×10^9 cm^{-2},

http://dx.doi.org/10.5772/58899

respectively. The nanoparticles deposition proceeding and photocurrent measurement apparatus are described in reference [27]. The incident light scattered by Au nanoparticles leads to a reduction of photocurrent response at wavelengths about 560 nm, at the same time, a phase shift is accompanied in the scattered wavelength near the nanoparticle plasmon resonance, which results in partially destructive interference between the scattered waves and the transmitted waves. [28] The scattering of incident light by the nanoparticles arise a broad wavelength range increased from 560 nm to 900 nm. But no surface plasmon polarization resonance is present for the SiO_2 nanoparticles, and the transmission and photocurrent response are increased over the range from 400 nm to 1200 nm wavelengths. [29]

The photocurrent response is increased at near 960 nm and cut off at about 1200 nm for the solar cells devices deposited by Au nanoparticles. This phenomenon is attributed to the scattering of incident light into optical propagation path modes, which associated with the slabby waveguide formed by the multiple quantum wells region and surrounding p-layers and n-layers. [8]A standard calculation shows that the slabby waveguide supports two confined modes at 960~1200 nm wavelengths range. [30]Furthermore, the optical waveguide structure mode becomes better confined with increasing wavelength because of the dependence of the wavelength and semiconductor refractive indices, resulting in the waveguide modes efficiency increased. [26]The photocurrent response is improved in these wavelength ranges because of incident light coming into the waveguide mode, and substrate radiation modes leads to photon propagation path lengths increased dramatically within the multiple quantum wells region that associated with lateral photon propagation path rather than vertical path. Consequently, the efficiency of photon absorption is improved greatly. [8]

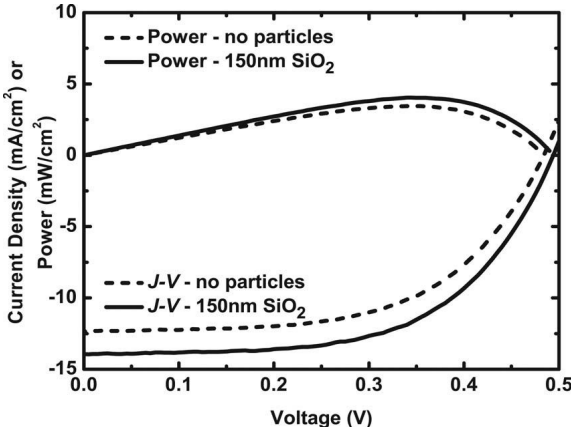

Figure 14. *J-V* and *P-V* curves measured for quantum well solar cell with and without SiO_2 nanoparticles

Previously, some groups have reported that the short circuit current density and optoelectronic conversion efficiency are increased due to optical scattering from metal nanoparticles deposited on Si solar cells [31] and *a*-Si solar cells [32]. The photocurrent response is enhanced on

the surface deposited nanoparticle quantum wells solar cells, which leads to the short circuit current density and optoelectronic conversion efficiency improved greatly under normal illumination incidence provided by a solar simulator with a Xenon arc lamp. The short circuit current density and voltage and the power output and voltage characteristics are shown in Figure 14 for the multiple quantum wells solar cells deposited SiO_2 nanoparticles on the surface before and after. For a SiO_2 nanoparticle surface density about 2.1×10^9 cm^{-2}, the short circuit current density increased 12.9% and maximum power conversion efficiency increased to 17.0%. For Au nanoparticle surface density about 2.7×10^9 cm^{-2}, the short circuit current density increased 7.3% and maximum power conversion efficiency increased only 1%.

The conversion efficiency and photocurrent response are improved substantially for the solar cells device structures whose quantum wells region bound with a lower refractive index substrate. A model developed by Soller and Hall [33] shows that when a horizontal electric dipole is located on a silicon insulator substrate, an excess of 80% of the light emitted by the electric dipole is coupled into the waveguide modes of the high refractive index Si insulator layer. [34]The ratio of the power of the electric dipole into waveguide modes fully to the total power of the electric dipole for the solar cells device structure over 600~1200 nm wavelengths occurs with a maximum efficiency no more than 10% in the course of the emission into waveguide, and leaky modes is in the range of 85~90%. This low efficiency is due to the small refractive index contrast to the solar cells device structure and could be improved with greater refractive index. [8]

4. InGaP/GaAs MQWs solar cells

Concentrators have the advantage to reduce the cost of photovoltaic systems by collecting the direct photon component with inexpensive lenses. The economic benefits of the concentrators demand a lot of high efficiency solar cells and the application of a nanostructure technology to these photovoltaic materials. GaAs materials provide the highest conversation efficiency in single-junction solar cells in all concentrations. However, the bandgap of GaAs is 1.42 eV and higher than the 1.1 eV of optimal efficiency bandgap at the conditions of high concentration. [35]Strain balanced InGaAs quantum wells in the intrinsic region of GaAs single junction solar cells can extend the absorption edge in substrate devices. [36] The result of increasing short circuit current accompanied with drop in open circuit voltage and increasing efficiency prevails over comparable conventional solar cells. [37]

An optimum of similar band gap can also exist in the case of two junction tandem solar cells. The efficiency record is 30.2% for the InGaP/InGaAs tandem solar cells at 300 times concentration. [12] However, as shown in Figure 15, the bandgaps combination of 1.8 eV/1.42 eV of an InGaP/GaAs tandem solar cells is significantly higher than the optimum bandgaps combination under 500 times concentration. Approaches have being actively pursued to lower the bandgaps of tandem solar cells, including lattice mismatched dilute nitrides InGaP/InGaAs grown on a virtual substrate. [38] These introducing dislocations can lower the voltage of the tandem solar cells, though the efficiency record has achieved about 42 % by the virtual

http://dx.doi.org/10.5772/58899

substrate approach. [39] Strain balanced quantum wells in InGaP/InGaAs tandem solar cells may allow the absorption edge of top and bottom cell to be adjusted independently without existing relaxation and lattice mismatch. [40] If there is enough absorption in the strain balanced quantum wells of top and bottom cell, the conversion efficiency of InGaP/InGaAs tandem solar cells device could ascend along the contours in Figure 15 and be adjusted to the solar spectrum. [12]Dark line shows the bandgaps of GaInP and GaAs. The red-cross shows the bandgaps position of the strain balance quantum wells tandem solar cells and the blue star shows a proposed structure with quantum wells in two junction solar cells.

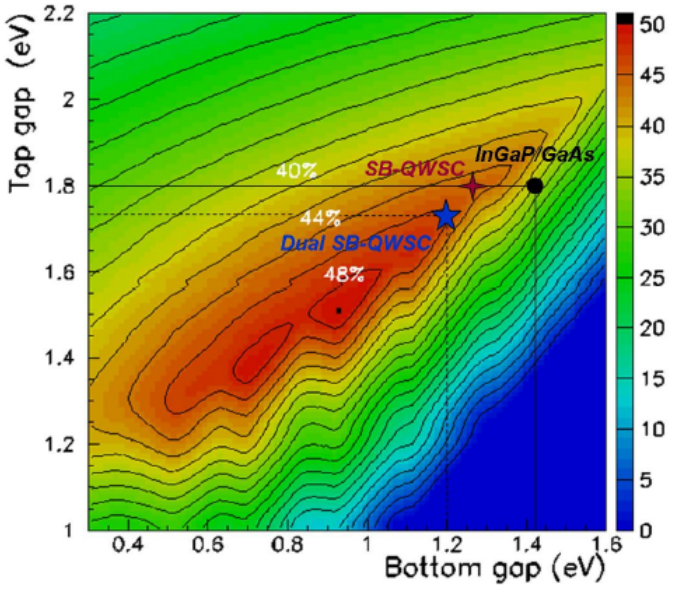

Figure 15. Ideal conversion efficiency contour plot for tandem solar cells under 500 times concentration

4.1. SBQW solar cells layers structure

Many quantum wells can be grown in the intrinsic layers of the *p-i-n* solar cell without dislocations and relaxation [41] by strain balancing the pressure imposed by the lower lattice spacing of InGaAs quantum wells and the higher lattice spacing of GaAsP barrier materials. [42]The strain balancing (SB) method and a resultant energy band diagram are shown in Figure 16.

All the solar cells devices were fabricated by metal organic vapour phase epitaxy (MOVPE). The InGaP/GaAs tandem solar cells were grown on the bottom cell where quantum wells in the intrinsic region of it. The second cell was top cell with higher emitter doping and lower In content in quantum wells. In the two cells, the bottom cell was grown by III-V growing technologies. The top cell was grown on a passive Ge substrate according to a conventional

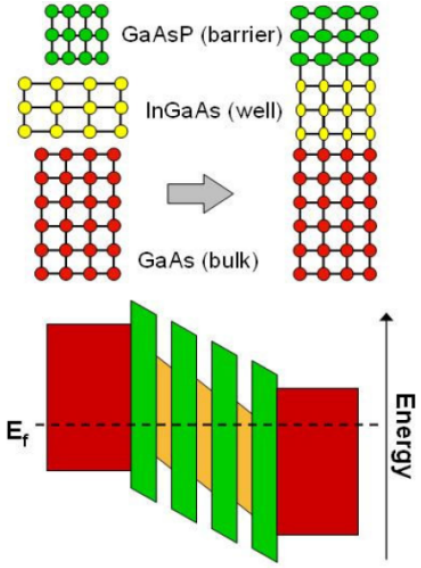

Figure 16. The energy band structure of three strain balanced quantum wells in GaAs solar cells

GaAs cell in order to create a control cell device. The control top cell was grown poorly due to an insufficient thickness of the *p-i-n* top cell. A schematic of the InGaP/GaAs tandem solar cells devices structure is shown in Figure17. [12]

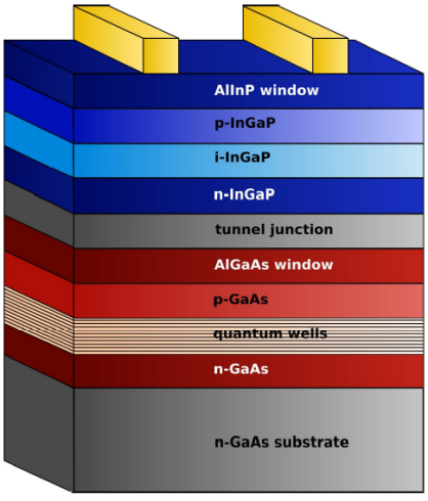

Figure 17. A cross section of the InGaP/GaAs tandem quantum well solar cells devices structure

http://dx.doi.org/10.5772/58899

All solar cells devices were processed for quantum efficiency measurements, fully metalized devices for dark current measurements, and concentrator devices were prepared from each wafer.

4.2. SBQW solar cells simulation results

The external quantum efficiency of the two tandem solar cells devices was characterized as described in [43], their results are shown in Figure 18. Left curves which are from top to bottom in Figure 18 are the top cell of first cell, the control top cell and the top cell of second cell with quantum wells, respectively, right curves which are from top to bottom in Figure 18 are the bottom cell of first cell, the control bottom cell and the bottom cell of second cell with quantum wells, respectively. The lower In content of InGaAs in the second cell with quantum wells improves their band gap. Thus the exciton absorption peaks of the second cell at 922 nm compared to 932 nm for the first cell.

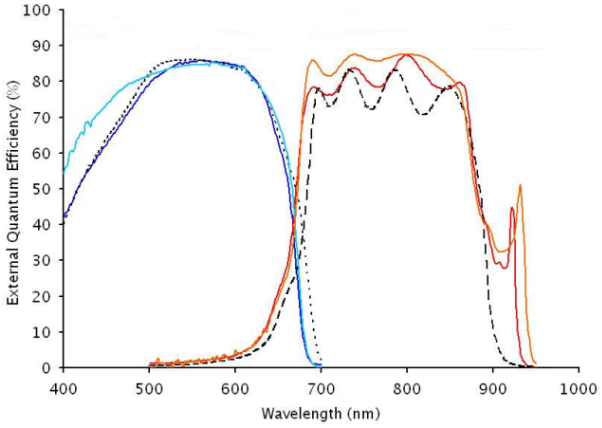

Figure 18. The external quantum efficiency of the tandem control cells and quantum wells cells devices

The Shockley injection currents and Shockley-Read-Hall dark currents of two tandem solar cells devices are simulated using drift diffusion model. The radiative component of the dark currents is calculated from the generalized Planck formula with no free parameters. [44] The conversion efficiency of first cell was independently measured 22.1 ± 0.7 % under low aerosol optical depth, as is shown in Figure 19. The light current curves of top and bottom cell have been constructed by subtracting the dark current of each cell by using the short circuit current measurement at Fraunhofer. These currents weren't mismatch between the top cell and bottom cell calculated by internal quantum conversion efficiency measurement.

Because the top cell emitter doping is lower, the conversion efficiency of first cell is 27.2%. Extrapolating the model for the dark current to higher concentrations, the conversion efficiency of first cell with no series resistance losses would have achieved 29.8% under low aerosol optical depth. The second cell was grown with the higher top cell emitter doping to overcome

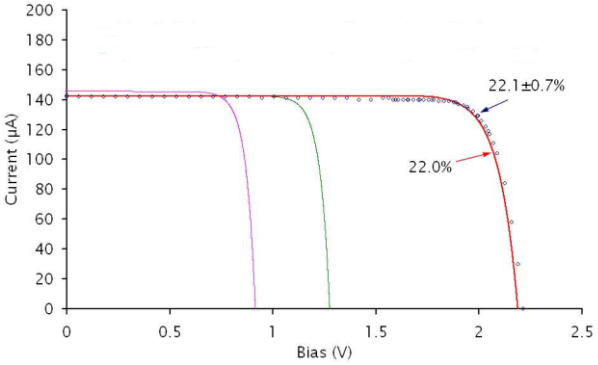

Figure 19. Tandem devices dark current model results relative to the light current curve measured at Fraunhofer

the series resistance of the first cell. The quantum well band gap was increased to counter the production of current in the quantum wells solar cells. Concentrator measurements have been performed on the second solar cells. The results in Table 1 show the conversion efficiencies recorded for both solar cells devices.

The superior photoelectric performance of the quantum wells control solar cells devices in Table 1 could be illustrated by function of the Xenon spectrum wavelengths and the resultant short circuit currents intensity in Figure 20. In the second solar cells devices, the current intensity of limiting bottom cell is improved in the condition of the Xenon spectrum illumination, the current is matched with the control solar cells devices under low aerosol optical depth. The top cell of the second solar cells limited and controlled performs of the quantum wells solar cells devices, because the top cell spectral response can extend to longer wavelengths.

Device	Fill Factor (%)	Efficiency (%)
The second solar cell	81.5	30.4
The control solar cell	81.7	31.6

Table 1. The measured photoelectric performance of the quantum wells control solar cells devices.

Figure 21 shows the quantum wells solar cells could perform over the control solar cells under concentrator spectrum and could perform better over the top solar cells with a larger spectral response. The control solar cells were grown on Ge substrate but the quantum wells solar cells were grown on GaAs substrate. It is known that growth of InGaP would give rise to a higher order degree in the arrangement of In and Ga atoms which could lower the InGaP band gap. [45]The most likely cause is the discrepancy between the top solar cells and optimized design of the InGaP/GaAs quantum wells tandem solar cells.

http://dx.doi.org/10.5772/58899

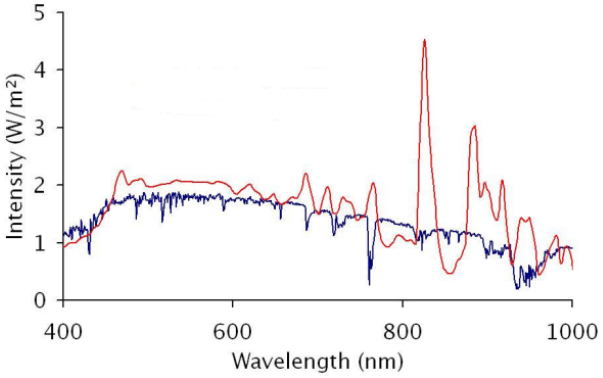

Figure 20. The Xenon spectrum used to characterize the second solar cells alongside a concentrator spectrum

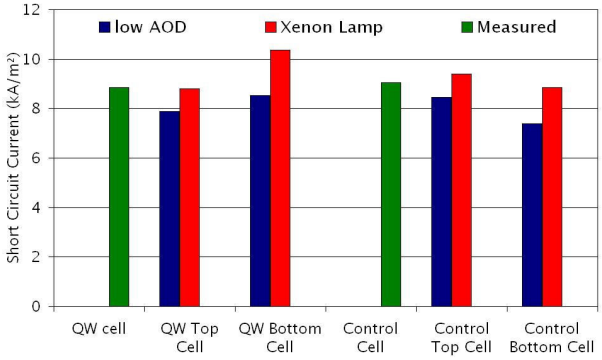

Figure 21. Short circuit currents under a xenon lamp spectrum and calculated from spectral response curves.

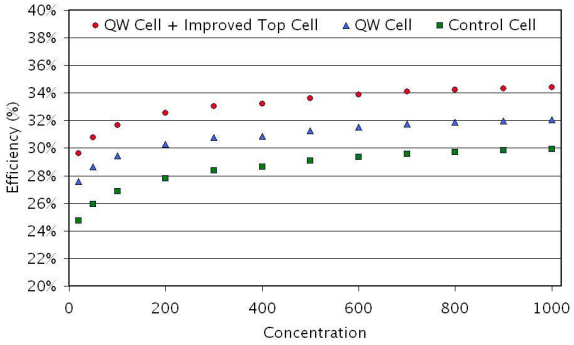

Figure 22. Efficiency predictions under the assumption of additives and a low aerosol optical depth spectrum

To investigate further the performance of the quantum wells solar cells and control solar cells, the conversion efficiency and dark currents have been combined under the assumption of additives and a low aerosol optical depth spectrum, as shown in Figure 22. The red dots show an improved tandem solar cells structure where the top control solar cell with high disorder is grown on the quantum well bottom solar cell. Such solar cells structure should achieve a conversion efficiency of over 34%.

5. Conclusions

In this chapter, the structure characteristics and optoelectronic properties of InGaN/GaN multiple quantum wells solar cells with In content about 0.3 and 0.4 are analyzed and studied, the phase separation of GaN and InN are not observed in the InGaN alloy materials with all kinds of In content when the InGaN alloys materials are packaged by InGaN/GaN multiple quantum wells heterojunction. The open circuit voltage of InGaN/GaN multiple quantum wells solar cells with In content about 0.3 and 0.4 are measured by 2 V and 1.8 V, respectively, when InGaN alloys materials are irradiated by monochromatic light under the same white light source. The InGaN/GaN multiple quantum wells are used as solar cells excitation region, the fill factor of this solar cell is about 0.6. The external quantum efficiency of this solar cell is 40% at the wavelength 420 nm, but external quantum efficiency drops to only 10% at the wavelength of 450 nm.

The performance of InP/InGaAsP quantum wells solar cells can be greatly improved by integration of dielectric or metal nanoparticles into the surface of the tandem solar cells devices structure in order to couple incident light into the lateral propagation paths which can confine the slabby waveguide formed by the multiple quantum wells intrinsic layer. This approach can also improve the inherent conflict in achieving both efficient photon absorption which mandated a thick multiple quantum wells layer and efficient collection of the photo-generate carriers which required a thin multiple quantum wells layer, and could further realize the high optoelectronic conversion efficiency predicted for InP/InGaAsP quantum wells tandem solar cells.

It has been known that quantum wells can tailor bandedges absorption, which also provides the flexibility to currently match InGaP/GaAs tandem solar cells under any defined spectrum. The device conversion efficiency has been achieved to 30.6% under the concentrator spectrum. This is a new record for any nanostructure solar cells devices. Strain balanced quantum wells solar cells with optimized conventional top solar cells should achieve the conversion efficiency of 34%. A new high efficiency consisting of quantum wells tandem solar cells have been proposed in both the GaAs and InGaP solar cells. This solar cells devices structure has the advantage to achieve higher efficiency comparable to the current lattice mismatched multi-junction tandem solar cells.

Acknowledgements

In this chapter, the research was sponsored by the National Nature Science Foundation of China (Project No. 61178030) and Center for Collaborative Innovation of Functional Polymer Materials in Foshan University.

Author details

Shaoguang Dong[1*], Kanghua Chen[1], Guojie Chen[2] and Xin Chen[2]

*Address all correspondence to: dshgfosu@126.com

1 Department of Optoelectronics and Physics, Foshan University, Foshan, China

2 Institute of Science, Foshan University, Foshan, China

References

[1] Neufeld C J, Toledo N G, Cruz S C, Iza M, DenBaars S P and Mishra U K. High quantum efficiency InGaN/GaN solar cells with 2.95 eV band gap. Applied Physics Letters 2008; 93: 143502.

[2] Tsai, Y L, Lin C C, Han H V, Chen H C, Chen K J, Lai W C, Sheu J K, Lai F I and Yu P C. Efficiency enhancement of InGaN/GaN multiple quantum well solar cells using CdS quantum dots and distributed Bragg reflectors, Physics Simulation and Photonic Engineering of Photovoltaic Devices II, 2013.

[3] Liou B W. Design and fabrication of $In_xGa_{1-x}N$/GaN solar cells with a multiple-quantum-well structure on SiCN/Si (111) substrates. Thin Solid Films 2011; 520(3): 1084-1090.

[4] Liou B W. Temperature of $In_xGa_{1-x}N$/GaN solar cells with a multiple-quantum-well structure on SiCN/Si(111) substrates. Solar Energy Materials & Solar Cells 2013; 114: 141–146.

[5] Chang S H, Fang Y K, Ting S F. Poly- and single-crystalline h-GaN grown on SiCN/Si(100) and SiCN/Si(111) substrates by MOCVD. Journal of Electronic Materials 2006; 10: 1837-1841.

[6] Ji L, Lu S L, Wu Y Y, Dai P, Bian L F, Masayuki A, Tomomasa W, Naohiro A, Mitsunori U, Atsushi T, Shiro U and Yang H. Carrier recombination dynamics of MBE grown InGaAsP layers with 1eV bandgap for quadruple-junction solar cells. Solar Energy Materials and Solar Cells 2014; 27: 1-5.

[7] Kwon Y S. InP/InGaAsP/InP double heterojunction solar cells with increased short-circuit current. Conference Record of the Thirty-first IEEE Photovoltaic Specialists Conference, 2005.

[8] Derkacs D, Chen W V, Matheu P M, Lim S H, Yu P K L and Yu E T. Nanoparticle-induced light scattering for improved performance of quantum-well solar cells. Applied Physics Letters 2008; 93: 091107.

[9] Deng Z, Wang R X, Ning J Q, Zheng C C, Bao W, Xu S J, Zhang X D, Lu S L, Dong J R, Zhang B S and Yang H. Radiative recombination of carriers in the $Ga_xIn_{1-x}P$/GaAs double-junction tandem solar cells. Solar Energy Materials and Solar Cells 2013; 111: 102-106.

[10] Sugaya T, Takeda A, Oshima R, Matsubara K, Niki S and Okano Y. InGaP solar cells fabricated using solid-source molecular beam epitaxy. Journal of Crystal Growth 2013; 378: 576-578.

[11] Tatsuya T, Eiji I, Hiroshi K and Masamichi O. Over 30% efficient InGaP/GaAs tandem solar cells. Applied Physics Letters 1997; 70: 381.

[12] Browne B, Andreas I, James C, Barnham K, John R, Robert A, Hill G, Guy S and Begin J V. Tandem Quantum Well Solar Cells. Photovoltaic Specialists Conference, 2008: 1-5.

[13] Lu T, Kao C, Kuo H, Huang G and Wang S. CW lasing of current injection blue GaN-based vertical cavity surface emitting laser. Applied Physics Letters 2008; 92: 141102.

[14] Dahal R. InGaN/GaN multiple quantum well solar cells with long operating wavelengths. Applied Physics Letters 2009; 94: 063505.

[15] Jani O, Ferguson I, Honsberg C and Kurtz S. Design and characterization of GaN/InGaN solar cells. Applied Physics Letters 2007; 91: 132117.

[16] Vos A D. Endoreversible Thermodynamics of Solar Energy Conversion. Oxford: Oxford University Press; 1992.

[17] Ho I and Stringfellow G B. Solid phase immiscibility in GaInN. Applied Physics Letters 1996; 69(18): 2701-2703.

[18] Pantha B N, Li J, Lin J Y and Jiang H X. Single phase $In_xGa_{1-x}N$ ($0.25 \leq x \leq 0.63$) alloys synthesized by metal organic chemical vapor deposition. Applied Physics Letters 2008; 93: 182107.

[19] Tabata A, Teles L K, Scolfaro L M R, Leite J R, Kharchenko A, Frey T, As D J, Schikora D, Lischka K, Furthmuller J and Bechstedt F. Phase separation suppression in InGaN epitaxial layers due to biaxial strain. Applied Physics Letters 2002; 80(5): 769-771.

[20] Wei G, Shiu K T, Giebink N C and Forrest S R. Thermodynamic limits of quantum photovoltaic cell efficiency. Applied Physics Letters 2007; 91: 223507.

[21] Barnham K W J, Braun B, Nelson J, Paxman M, Button C, Roberts J S and Foxon C T. Short -circuit current and energy efficiency enhancement in a low-dimensional structure photovoltaic device. Applied Physics Letters 1991; 59(1): 135-137.

[22] Raisky O Y, Wang W B, Alfano R R, Reynolds C L, Stampone D V and Focht M W. $In_{1-x}Ga_xAs_{1-y}P_y$/InP multiple quantum well solar cell structures. Journal of Applied Physics 1998; 84(10): 5790-5794.

[23] Alemu A, Coaquira J A H and Freundlich A. Dependence of device performance on carrier escape sequence in multi-quantum-well p-i-n solar cells. Journal of Applied Physics 2006; 99: 084506.

[24] Mohaidat J M, Shum K, Wang W B and Alfano R R. Barrier potential design criteria in multiple- quantum-well-based solar cell structures. Journal of Applied Physics 1994; 76(9): 5533-5537.

[25] Adachi S. Optical dispersion relations for GaP, GaAs, GaSb, InP, InAs, InSb, $Al_xGa_{1-x}As$, and $In_{1-x}Ga_xAs_yP_{1-y}$. Journal of Applied Physics 1989; 66 (12): 6030-6040.

[26] Catchpole K R and Pillai S. Absorption enhancement due to scattering by dipoles into silicon waveguides. Journal of Applied Physics 2006; 100: 044504.

[27] Derkacs D, Lim S H. Matheu P. Mar W and Yu E T. Improved performance of amorphous silicon solar cells via scattering from surface plasmon polaritons in nearby metallic nanoparticles. Applied Physics Letters 2006; 89: 093103.

[28] Lim S H, Mar W, Matheu P, Derkacs D and Yu E T. Photocurrent spectroscopy of optical absorption enhancement in silicon photodiodes via scattering from surface plasmon polaritons in gold nanoparticles. Journal of Applied Physics 2007; 101: 104309.

[29] Sundararajan S P, Grady N K, Mirin N and Halas N J. Nanoparticle-induced enhancement and suppression of photocurrent in a silicon photodiode. Nanoparticle Letters 2008; 8(2): 624-630.

[30] Yeh P. Optical Waves in Layered Media. New York: Wiley-Blackwell; 2005.

[31] Pillai S, Catchpole K R, Trupke T and Green M A. Surface plasmon enhanced silicon solar cells. Journal Applied Physics 2007; 101: 093105.

[32] Schaadt D M, Feng B and Yu E T. Enhanced semiconductor optical absorption via surface plasmon excitation in metal nanoparticles. Applied Physics Letters 2005; 86: 063106.

[33] Soller B J and Hall D G. Energy transfer at optical frequencies to silicon-based waveguiding structures. Journal of the Optical Society America A 2001; 18(10): 2577-2584.

[34] Soller B J, Stuart H R and Hall D G. Energy transfer at optical frequencies to silicon on insulator structures. Optics Letters 2001; 26(18): 1421-1423.

[35] Ward J S, Wanlass M W, Emery K A and Coutts T J. GaInAsP solar cells with the ideal band gap for terrestrial concentrator applications. Proceeding of the 23rd IEEE Photovoltaic Specialists Conference, Louisville; 1993.

[36] Barnham K W J, Abbott P, Ballard I M, Bushnell D B, Connolly J, Ekins-Daukes N, Mazzer M, Nelson J, Rohr C, Tibbits T N D, Airey R, Hill G and Roberts J. Recent Results on Quantum Well Solar Cells. World Conference on Photovoltaic Energy Conversion, Osaka, Japan; 2003.

[37] Bushnell D B, Tibbits T N D, Barnham K W J, Connolly J P, Mazzer M, Ekins- Daukes N J, Roberts J S, Hill G and Airey R. Effect of well number on the performance of quantum-well solar cells. Journal of Applied Physics 2005; 97.

[38] Ptak A J, Friedman D J, Kurtz S R. Enhanced-Depletion-Width GaInNas Solar Cells Grown by Molecular-Beam Epitaxy. Proceeding of the 31st IEEE Photovoltaics Specialists Conference and Exhibition, Lake Buena Vista, Florida; 2005.

[39] King R R. 40% efficient metamorphic GaInP/GaInAs/Ge multijunction solar cells. Applied Physics Letters 2007; 90: 183516.

[40] Tibbits T N D, Ballard I M, Barnham K W J, Ekins-Daukes N J, Airey R, Hill G and Roberts J S. The Potential for Strain Balanced Quantum Well Solar Cells in Terrestrial Concentrator Applications. World Conference on Photovoltaic Energy Conversion, Osaka, Japan; 2003.

[41] Lynch M C, Ballard I M, Bushnell D B, Connolly J P, Johnson D C, Tibbits T N D, Barnham K W J, N. Ekins-Daukes J, Roberts J S, Hill G, Airey R and Mazzer M. Spectral response and III-V characteristics of large well number multi quantum well solar cells. Journal of Materials Science 2005; 40: 1445-1449.

[42] Ekins D N J, Kawaguchi K and Zhang J. Strain-Balanced Criteria for Multiple Quantum Well Structures and Its Signature in X-ray Rocking Curves. Crystal Growth & Design 2002; 2: 287-292.

[43] Ioannides A, Tibbits T N D, Connolly J P, Bushnell D B, Barnham K W J, Calder C, Hill G, Roberts J S and Smekens G. Strain Balanced Multi-Quantum Well Dual Junction Monolithic Tandem Solar Cell. Proceeding of the 21st European Photovoltaic Specialists Conference, Dresden; 2006.

[44] Connolly J P. Efficiency Limits of Quantum Well Solar Cells. Proceeding of the 19th European Photovoltaic Solar Energy Conference, Paris; 2004.

[45] Ernst P. Ordering in GaInP studied by optical spectroscopy. Physica status solidi (c) 1996; 193: 213.

Chapter 13

Bulk Heterojunction Solar Cells — Opportunities and Challenges

Qun Ye and Jian Wei Xu

Additional information is available at the end of the chapter

http://dx.doi.org/10.5772/58924

1. Introduction

Due to the rising concerns over the exhaust of fossil fuel and the associated environmental consequence of the carbon emission problem, search for renewable energy has become a hot research topic worldwide. Organic semiconducting materials based photovoltaic (PV) technology developments have attracted tremendous attention from both the academic community and the industry. In principle, the organic solar cells employ organic material based light absorbing functional layer to convert sunlight to electricity. Typically the light absorbing layer is made of a blend of donor material and a fullerene based acceptor material. The observation of photovoltaic effect on organic materials began in 1986 with the "Tang cell" [1], which was a two-layer device with a structure of ITO/copper phthalocyanine/perylene diimide/gold. Later in the early 1990s, the discovery of ultrafast charge transfer from polymer to fullerene [2] initiated the research field of bulk hetero-junction (BHJ) solar cells. Over the past two decades, substantial research progress have been made in the development of more robust light harvesting materials, the further modification of the modelling theory of the OPV physics, better understanding and elucidation of the light-to-electricity process and the continuous optimization of the device fabrication process with new strategies employed. This process can be witnessed by the fast growing efficiency data of the OPV cells (Figure 1) and the vast amount of literatures published annually on the topic of OPV technology. Concurrently, the industrial attention is mainly focused on development of robust materials with long lifetime and good efficiency in large scale application, production technique optimization and market exploration for OPV technology. The fast growing research activity on OPV technology involves the collaborative consolidation of knowledge from synthetic chemistry, especially on π-chemistry, semiconductor physics and device engineering. Figure 1 [3] depicts the certified record PCE data of various types of PV technologies that have been continuously optimized

in the past decade. Compared with inorganic PV technologies, organic solar cells have achieved magnificent improvement in terms of efficiency. Currently the record holder is Mitsubishi Chemicals who has demonstrated a reproducible 10.7 ± 0.3% organic solar cell.

Compared with the existing mature inorganic based photovoltaic technology, a list of proposed advantages of OPV technology should be mentioned which include 1) short energy payback time [4]; 2) lower production cost compared with inorganic PVs; 3) potential fabrication via continuous printing tools; 4) new market opportunities, such as flexible PV, wearable PV, semitransparent PV window, etc.; 5) low weight and easy integration of the organic PV products. Nevertheless, inorganic based PV technologies, such as silicon, cadmium telluride (CdTe), III-V group semiconductors and copper indium gallium selenide (CIGS), are still dominating the PV market.[5] The reasons why the OPV are short of the market are mainly due to the inferior power conversion efficiency (PCE) and the poor stability of the organic solar cell devices compared with their inorganic analogs. As the ultimate goal of materials research is to apply the material based science and technology into material based products, the applicability and the competitiveness of the technology should always be buried in mind. The economic aspects of the OPV technology have attracted more attention as many companies start to step into the OPV market and create opportunities. The optimization of the OPV device, both in terms of device stability and power conversion efficiency, has become a synergistic work between the academia and the industries. Moreover, the industrial production of OPV modules, which is very different from the lab-scale production step, is also being optimized. All these efforts will be highlight in this Chapter.

With both the advantages and existing disadvantages of OPV technology in mind, we plan to give an overview of how to transform a molecule to a material and finally to a product for OPV technology and we organize this Chapter in the following way. Firstly we will summarize the existing strategies to prepare new and better light harvesting materials by synthetic chemists. Due to the limited space, we focus on the most commonly used polymeric donor-acceptor (D-A) type materials. In the following part, we summarize the recently developed device engineering methods to improve the performance of the OPV materials. This part deserves its own merit because the OPV device engineering process is essential to demonstrate the full potential of a new polymer molecule as a functional light harvesting material. Then we will summarize some aspects of OPV materials which are important for the production development, such as the lifetime/stability of the material and production techniques. Finally we will end up our discussion with a summary and perspective on the future research. There have been many excellent summary works dealing with various aspects of OPV technology, such as the working mechanism and physics of the OPV device [6-9], design principles and synthesis of new light absorbing materials [9-19], thin film morphology control and characterization [20-21], new device architecture development [22-24], interface engineering [25], quantum chemical calculations [26], economical aspects [27-29] and many insightful overviews and perspectives [30-42]. There are also a series of *Photovoltaics Literature Survey* papers by Santosh Shrestha [43] in *Progress in Photovoltaics: Research and Applications* which are useful for readers to catch up current research progress in various aspects regarding PV technology.

http://dx.doi.org/10.5772/58924

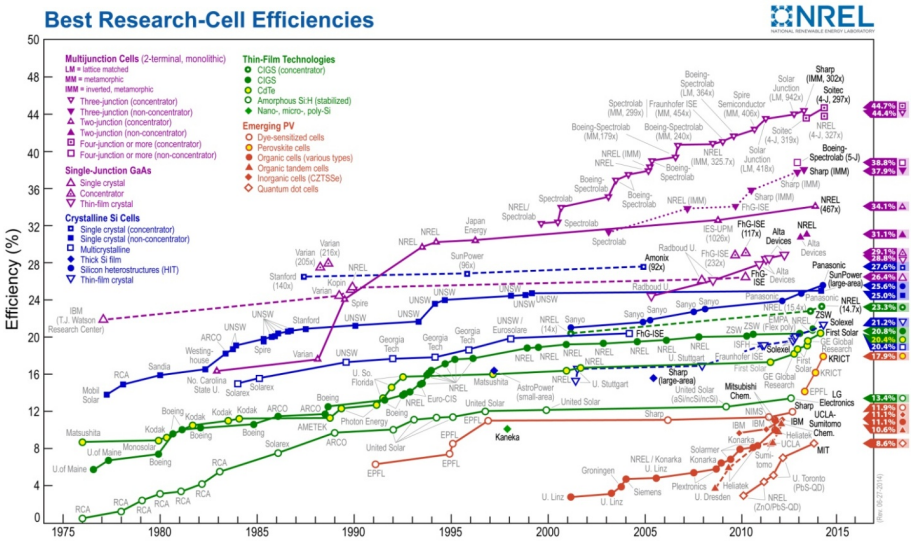

Figure 1. Best Research Cell Efficiencies for all types of PV technology. Data from National Renewable Energy Laboratory (NREL).[3]

2. Development of new materials

2.1. Chromophores with new π-structure

In the concept of BHJ solar cells, the active layer is comprised of a blend of electron-donating material and electron-withdrawing material. The electron-donating material can be small molecules [12, 13] or polymeric materials [10,11,14-19] while polymeric materials are more commonly used in the literature. Both types of materials typically follow a Donor-Acceptor (D-A) design principle, in which the conjugated backbone is constructed by covalent linkage of a series of electron rich moieties and electron deficient moieties in an alternative way. This design strategy is especially useful in tuning the physical properties (absorption, frontier orbital energy levels, etc.) of the final materials due to the vast stock of electron rich and electron deficient building blocks. Guo and co-workers [44] have presented a thorough summary of current prevailing donor and acceptor species, which include about 45 donor and 60 acceptor backbones. Note that there are also variations on the solubilizing chains and spacer groups. Hence the actual number of such building blocks would be much larger than the summarized numbers. Given the wide choice of building blocks, there is no surprise that a huge structural diversity of OPV materials exists and a large amount of new materials are coming out every year in the literature. The design principle of the donor material in the BHJ blend has been summarized [45]. Basic considerations include light absorption range, frontier orbital energy levels, charge carrier mobility, favorable blend morphology, stability and solubility.

Concurrently new building blocks are being synthesized to provide more possibilities to further optimize the optical and electronic properties of the final material. Take benzothiadiazole (BT) as an example (Figure 2). Benzothiadiazole (BT) is one of the most commonly used building blocks for the construction of D-A type conjugated polymers. By carrying out structural modification of the backbone, a series of new electron-deficient moieties with different electronic properties can be prepared. One strategy is to replace the sulfur atom in the thiadiazole hetero-cycle with other elements such as carbon [46], oxygen [47,48], nitrogen [49], selenium [50,51], etc. The new building blocks have various electron withdrawing properties and hence are useful in tuning the properties of the polymer materials. The second strategy is to introduce substitutions on the BT unit, such as fluorine atoms [52-60], alkoxy groups [61-65], or replacement of C-H with imine nitrogen [66-69]. More building blocks can be prepared with the combination of these two strategies [70-75]. The third strategy is to extend the π-conjugation of the BT unit to prepare π-extended moieties [76-81]. Extension of the π-backbone is a versatile route to tune the electronic properties of the BT unit; however, the new building blocks typically exhibit poorer solubility and have to be prepared in longer synthetic steps. For example, by fusion of one more thiadiazole ring to the BT unit, bis-benzothiadiazole (BBT) can be prepared and possess much higher electron deficiency but poorer solubility.

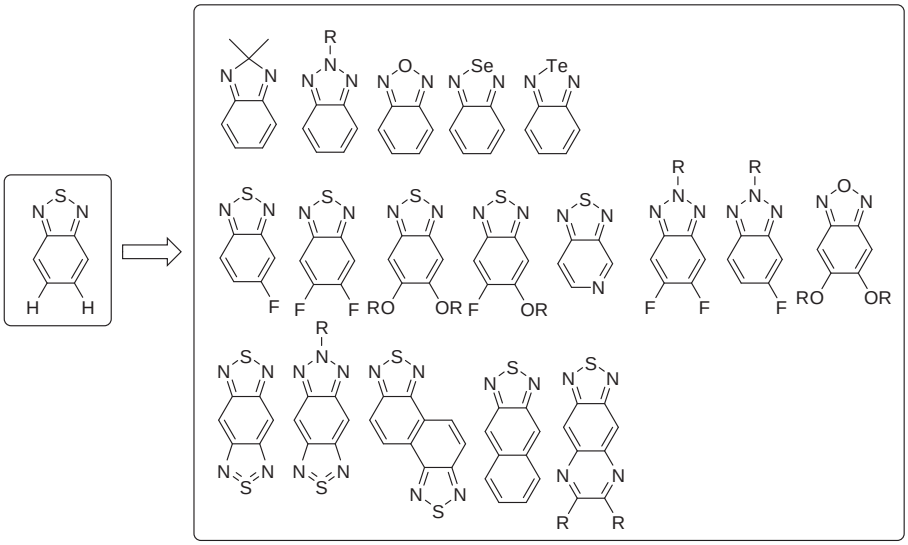

Figure 2. Evolution of benzothiadiazole (BT) based electron withdrawing moieties for the preparation of D-A type light absorbing polymers.

Out of all these strategies, the substitution of fluorine atoms on the aromatic backbone turns out to be a very efficient approach to achieve high-performance OPV materials. Introduction of fluorine substitutions has minor influence on the absorption behavior of the polymer; however, it induces a decrease of the frontier orbital energy levels due to its strong electrone-

http://dx.doi.org/10.5772/58924

gativity and consequently the fluorinated polymers typically exhibit higher open circuit voltage (V_{oc}). The advantages of fluorine in OPV polymer have been demonstrated by Zhou et al. [82] Polymer **PBnDT-DTBT** (Figure 3) exhibits a HOMO and LUMO energy level at-5.20 eV and-2.92 eV, respectively. After addition of two fluorine atoms on the BT unit, the HOMO and LUMO energy level of **PBnDT-DTffBT** decreases to-5.30 eV and-2.97 eV, respectively. **PBnDT-DTBT**/$PC_{61}BM$ based solar cell device exhibits the best PCE=5.0% with J_{sc}=10.03 mA cm^{-2}, V_{oc}=0.87 V and FF=0.57. For **PBnDT-DTffBT**, the best device exhibits PCE=7.2% with J_{sc}=12.91 mA cm^{-2}, V_{oc}=0.91 V and FF=0.61. It is found that after attachment of the fluorine atoms on the repeating unit, the short circuit current, the open circuit voltage and the factor are all enhanced.

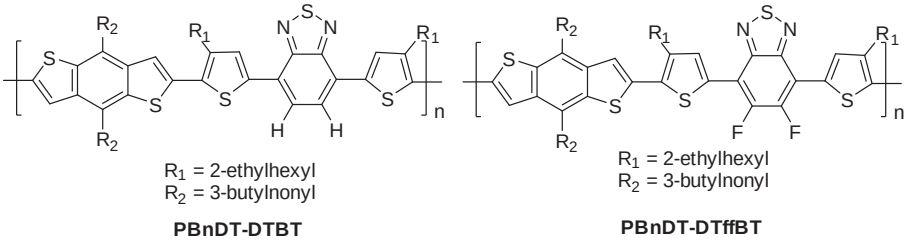

Figure 3. Chemical structures of **PBnDT-DTBT** and **PBnDT-DTffBT**.

The longer synthesis steps for the more complicated building blocks are also a concern if they are to attract industrial attention. Although achieving materials in a cost-effective way is generally neglected in the academic publication and in many cases the complicated synthesis of a monomer is considered as *novelty* of the work, a simple, high yield and easily scalable synthesis of materials is highly desirable in the industry from the application point of view. For example, 4,7-dibromobenzo[c][1,2,5]thiadiazole can be prepared in three steps from 1,2-phenylenediamine (Scheme 1). As this building block is so commonly used nowadays, it has become commercially available by vendors such as Sigma Aldrich. While for alkylated 4,8-dibromo-[1,2,5]thiadiazole[3,4-f]benzotriazole [83], which is a BT unit fused with a triazole hetero-cycle, is prepared with four more synthetic steps from 4,7-dibromobenzo[c] [1,2,5]thiadiazole. According to a recent estimation [84], the cost per gram of the final material increases linearly with the number of synthetic steps needed for the synthesis. The extended synthesis would definitely reduce the potential applicability of the material, as the value of a material is a compromise between the performance and the cost.

A list of D-A type polymers that have demonstrated PCE values > 7% are shown in Figure 4 [85]. It should be highlighted that the high performance of the polymers does not necessarily mean that the embedded building blocks are superior. The power conversion efficiency is determined by a number of factors and the chemical structure of the polymer is just one of them. Even for a classical polymer P3HT, after careful optimization of the device condition, the PCE can also reach 7.4% [86]. Many other factors, like the fabrication conditions, also play

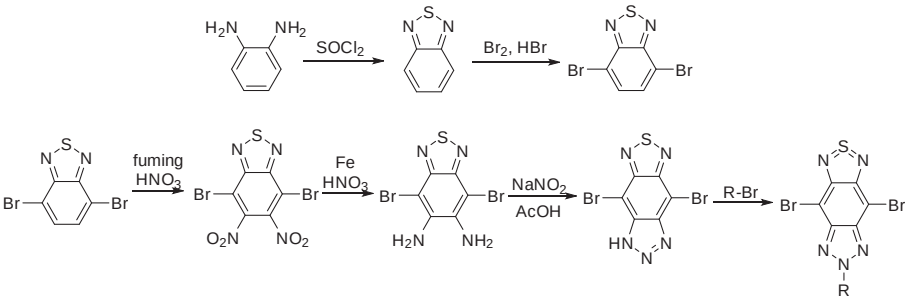

Sheme 1. Synthetic routes of 4,7-dibromobenzo[c][1,2,5]thiadiazole and alkylated 4,8-dibromo-[1,2,5]thiadiazole[3,4-f]benzotriazole.

a significant role in determining the overall efficiency of the cell. These factors will be discussed in the following text.

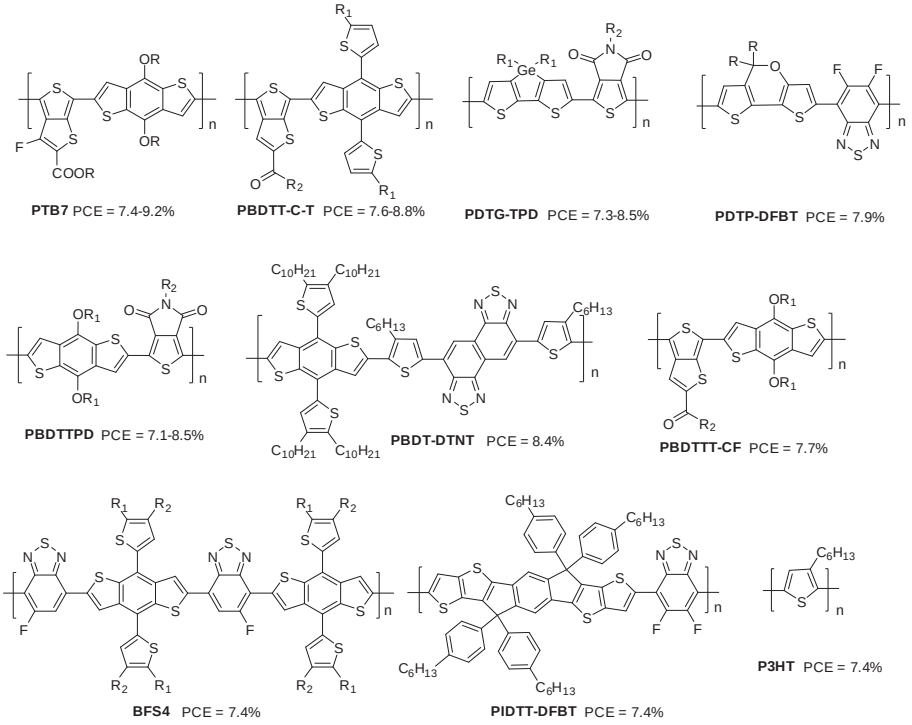

Figure 4. Chemical structures of polymers that exhibit PCE > 7%.

http://dx.doi.org/10.5772/58924

2.2. Side chain engineering

Side chains are attached on the rigid aromatic π-backbones to form "hairy rod" type polymers with suitable solubility to allow solution based processing techniques viable. In fact, the role of the side chains are far beyond the solubility concerns. Other physical properties of the polymer, such as absorption, emission, energy levels, molecular packing, charge transport and the morphology of the thin film are critically affected by the side chains attached in many cases. Commonly used side chains include linear alkyl side chains (n-C_nH_{2n+1}), branched alkyl side chains, electron donating side chains (-OR,-SR,-NHR, etc.), electron withdrawing side chains (-C(=O)R,-SO_2R, etc.), aromatic side chains (4-alkoxyphenyl, etc.), functional side chains (e.g. with cleavable groups on the side chains), ionic side chains, oligoether side chains, fluorinated side chains and so on. A comprehensive discussion on various types of side chains has been presented by Mei and Bao [87]. Side chain engineering has become a routinely used strategy to modify the physical properties, especially the self-assembly of the materials in the thin film, and thus to optimize the light absorbing materials in the OPV device. Given the importance of side chain engineering, it should be noted that as the side chains do not contribute to the light absorption or charge transport in the thin films, a trade-off between the solubility and the performance of the final polymer must be made.

2.3. New synthetic methodology

Currently, the D-A type polymers are typically synthesized via palladium catalyzed cross coupling reactions such as Stille coupling [88] and Suzuki coupling reactions [89]. Stille coupling involves C-C bond formation between trialkylstannyl species and aromatic halide species and has been routinely used for the preparation of a large number of high performance polymers. However, the high toxicity of the tin reagent and the associated environmental issue of the generated tin wastes inhibit its wide industrial applications. Recently, a new polymerization method involving direct heteroarylation polymerization (DHAP) between aryl C-H bond and aromatic halides has been developed as a promising greener alternative of Stille coupling for the preparation of conjugated polymers (Scheme 2). Berrouard et al. [90] has demonstrated that the DHAP reaction between 5-alkyl[3,4-c]thienopyrrole-4,6-dione and 5,5′-dibromo-4,4′-dioctyl-2,2′-bithiophene is as efficient as the corresponding Stille approach. As in this direct coupling reaction no organo-tin or organo boron reagents are needed, it shortens the synthesis of final polymer by at least two steps. This strategy has been successfully implemented for the synthesis of OPV polymers [91,92], OFET polymers [92] and EC polymers [93] with reasonable molecular weight and polydispersity after judicious optimization of the coupling condition. Nevertheless, as this polymerization technique is still in its infancy, the reaction is still difficult to control for some substrates and the final polymer might be branched due to unselective C-H activation in the substrate [94,95]. The reaction conditions of the reaction including the catalyst, ligand, base, additive, solvent, temperature and duration have to be carefully controlled and optimized in order to achieve the highest molecular weight.

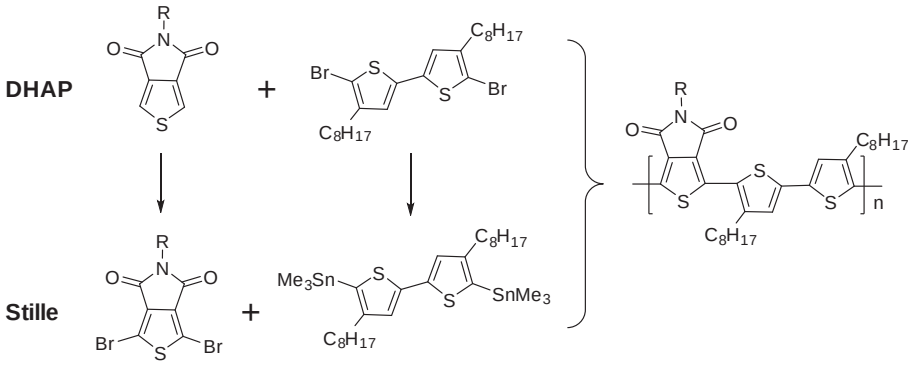

Sheme 2. Synthetic approaches of direct heteroarylation polymerization (DHAP) and conventional Stille coupling reaction.

2.4. Molecular weight and purity of the polymer

The molecular weight and the purity of the polymers are issues beyond the molecular architecture of the semiconducting polymers. But both factors have been demonstrated as essential parameters to ensure the good performance of the prepared polymers within the device. A high molecular weight increases the regularity of thin film and in many cases induces enhanced charge carrier transport in the transistor device [96,97] and power conversion efficiency in the BHJ solar cell device [98]. For instance, **P1** (Figure 5) [99,100] with a low molecular weight (M_n < 10 kg mol^{-1}) exhibits a charge carrier mobility of μ=5.2 × 10^{-5} cm^2 V^{-1} s^{-1} and power conversion efficiency of η=2.7% with J_{sc}=4.2 mA cm^{-2}, V_{oc}=0.64 V, and FF=0.35. For **P1** with high molecular weight (M_n > 34 kg mol^{-1}), it exhibits an enhanced mobility of μ=3.6 × 10^{-2} cm^2 V^{-1} s^{-1} and power conversion efficiency of η=5.9% with J_{sc}=17.3 mA cm^{-2}, V_{oc}=0.57 V, and FF=0.61. Similar phenomenon is also observed for **P2** [98]. **P2** with a low molecular weight (M_n ~ 46 kg mol^{-1}) exhibits an ambipolar behavior with μ_h=2 × 10^{-3} cm^2 V^{-1} s^{-1} and μ_e=5.2 × 10^{-5} cm^2 V^{-1} s^{-1} and a PCE η=5.48% with J_{sc}=12.1 mA cm^{-2}, V_{oc}=0.90 V, and FF=0.50. For **P2** with high molecular weight (M_n ~ 61.8 kg mol^{-1}), the mobility increases to μ_h=0.15 cm^2 V^{-1} s^{-1} and μ_e=0.064 cm^2 V^{-1} s^{-1} and an enhanced PCE η=6.79% with J_{sc}=13.7 mA cm^{-2}, V_{oc}=0.89 V, and FF=0.56. The improved mobility for high molecular weight samples is ascribed to improved π-π stacking, thin-film formation properties and increased inter-chain interactions. The increased J_{sc} and fill factor are mainly because of the improved hole mobility of the polymer, which facilitates the charge collection and inhibit charge recombination in the blend.

The purity [101-103] and the end group effect [104-106] on the performance of transistor materials and OPV materials have also been investigated. However, as the exact determination of "contaminant" or "purity level" of a given material, especially for polymers, is very difficult to achieve, the attempts to correlate the performance of an "impure" material to the existence of some extrinsic impurity would be questionable. Even though the end capping strategy has been found efficient to improve the performance of the polymer [104-106], it is still not

http://dx.doi.org/10.5772/58924

commonly adopted by research groups, even not routinely used by the groups who claimed the positive effect. Questions such as how the end group influences the performance of the polymer, what kinds of impurities are detrimental to the performance and what kinds of impurities serve as friendly dopants still remain unaddressed. More research effort, for example, intentional doping [107,108], is in need to solve the impurity issue of organic semiconductors in both the theoretical aspect and the practical aspect. But it is commonly believed that tedious and labor-intensive purification processes, such as Soxhlet extraction and silica gel column chromatography is always necessary to ensure sufficient purity of the sample for characterization.

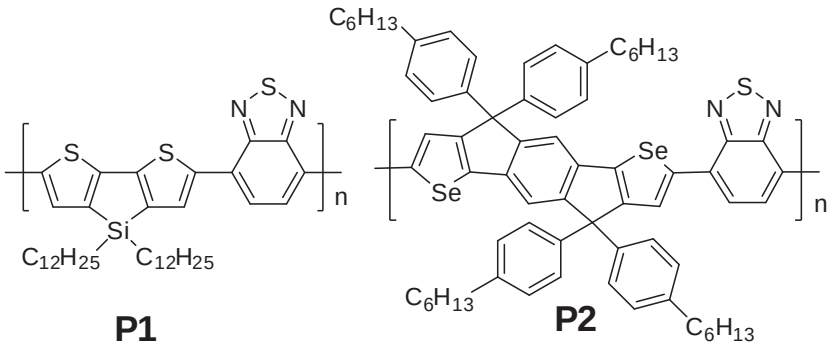

Figure 5. Chemical structures of **P1** and **P2**.

2.5. Acceptor

The other important active species in the BHJ blend is the acceptor. The benchmark acceptors are fullerene based derivatives, mainly [6,6]-phenyl-C_{61}-butyric acid methyl ester ($PC_{61}BM$) and [6,6]-phenyl-C_{71}-butyric acid methyl ester ($PC_{71}BM$) (Figure 6) [109,110]. The key features of these sphere-shaped acceptors are their low internal reorganization energy, high polarizability, relatively high dielectric constant, favorable LUMO energy level, reversible redox properties, good electron transport properties and anisotropic charge transport behavior [109,110]. The superior performance of these two acceptors in the BHJ devices renders them as the first choice for most of the newly developed donor materials. Whereas $PC_{61}BM$ absorbs minimal amount of light in the visible region, $PC_{71}BM$ is strongly blue and green light absorbing acceptor and is more useful when the absorption of it is complementary to that of the donor so that more sunlight can be captured [111]. Nevertheless, some drawbacks of these fullerene derivatives would hamper their wide application in the industrial production. One is the high production energy cost of these fullerene based acceptors. For $PC_{71}BM$, the production energy is approximately 90 GJ kg^{-1} [112]. For comparison, the production energy of P3HT is only about 1.9 GJ kg^{-1}[113]. The other concern is the relative high price of these fullerene derivatives. A recent analysis by Lewis and Nocera [114] indicates that the OPV system should cost no more than \$10 per m^2 to compete with fossil fuels for energy production. The cost of

PCBM at roughly $500-1000 per m^2 [42] makes the BHJ based PV technology with PCBM problematic for commercialization. Use of technical grade PCBM (~80% $PC_{61}BM$ and 20% $PC_{71}BM$) [115] might help relieve the stress but is far away from the desired price range. In fact, various types of small molecule based [116] or polymer based [117] acceptors have been tested to replace fullerene derivatives in OPV cells. But yet the efficiency of these acceptors still cannot surpass that of fullerene based derivatives.

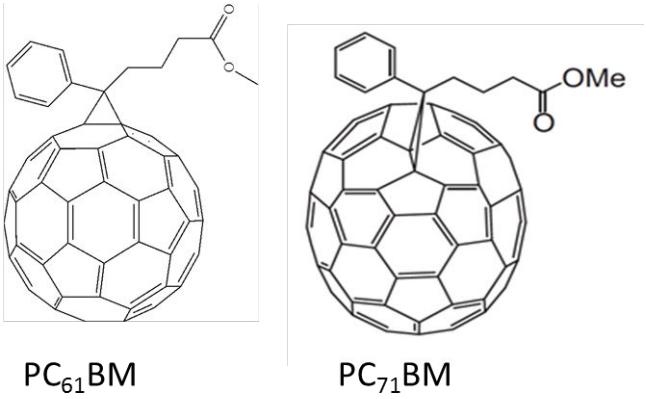

Figure 6. Chemical structures of $PC_{61}BM$ and $PC_{71}BM$.

3. Morphology and device engineering

3.1. Characterization of morphology

Along with the research effort to prepare D-A type conjugated polymers in BHJ solar cells to achieve the world record efficiency value, studies revealing the importance of the morphology of the polymer/fullerene blend have been carried out and the experience gained on controlling the morphology has become a valuable tool to explore the full potential of a new polymer as light harvesting materials. The thin film morphology characterization tools include grazing incidence wide-angle X-ray scattering, grazing incidence small angle X-ray scattering, resonant soft X-ray scattering, small-angle neutron scattering, transmission electron microscopy, atomic force microscopy, solid-state nuclear magnetic resonance, dynamic secondary ion mass spectrometry, near-edge X-ray absorption fine structure and scanning transmission X-ray microscopy. These analysis techniques are comprehensively summarized by Huang et al. [21]. As so much work has been done to investigate the morphology of the thin film, a rational question to ask is: *what is the best morphology?* Unfortunately, so far a precise answer to this question has not been achieved. One reason is because every characterization technique only sees the film from one aspect and a thorough mapping of the material distribution in the film still remains a challenge [118-119]. Another reason may be due to the fact that the reported

polymers with the highest power conversion efficiency values do not really share exactly the same morphology profile. As a result, the *optimal* morphology and the engineering method to achieve the best performance are case-by-case and mostly obtained in a trial-and-error approach. General descriptions like *homogeneous* and *interpenetrating networks* with *nanoscale phase-separated domains* are routinely used to describe the morphology in the cells with distinct performance.

3.2. Morphology optimization by device engineering

A series of parameters that will influence the morphology of the polymer/fullerene thin film are listed in Figure 7. The physical properties of the polymer such as the π-backbone, side-chains, the molecular weight, the identity of the fullerene acceptors used and the mass ratio between the two etc., are factors related to the materials. The determination of the ideal D:A ratio for a new polymer material has been a matter of trial and error, with the ratio 1:1 to 1:4 most commonly used. The solubility of the polymer and the fullerene derivative should be sufficient in the processing solvent. Halogenated solvents (chloroform, chlorobenzene, 1,2-dichlorobenzene, 1,2,4-trichlorobenzene) are routinely used as they possess high solubility for both the donor polymer and the fullerene acceptors. For many reported polymers [20,21], judicious choice of the processing solvent has to be made in order to achieve the optimal morphology and power conversion efficiency. For a specific new polymer, or a new polymer/fullerene blend, the choice of optimal processing solvent is not trivial, normally based on trial-and-error investigations. Recently, more research has been focused on the replacement of halogenated processing solvents with more environmentally friendly solvents, such as toluene, xylenes and long alkanes [120]. This is especially important for the industrial production of OPV modules [121].

Processing additives with low vapor pressure and high boiling point are commonly added in the solvent to optimize the morphology of the polymer/fullerene blend [85]. Commonly used additives include 1,8-diiodooctane, 1,8-octanedithiol and 1-chloronaphthalene (Figure 8). General guideline for selection of the additive is that the solvent additive should be less volatile with higher boiling points than the host solvents. The mechanism how the additive influence the morphology and the overall performance of the device has been discussed by Lee et al. [122]. It should be noted that solvent additives added during the fabrication process might remain in the solar cell and behave as contaminants to hamper the performance of the solar cell. In some case, addition of additives shows no effect [123,124] while in some case the addition of additives is detrimental to the performance [125]. These results indicate that the solvent additive is not an elixir to enhance the PCE performance of all polymers and the detailed effect and mechanism should be made case by case. Moreover, a specific process step must be added to remove the residual deleterious compounds which are obviously unfavorable in the industrial application. Hence, it is more desirable to design high performance polymer/fullerene system with no such additives needed to achieve the good performance. During the production of OPV modules, some other additives, such as rheology modifiers, anti-foaming agents and surface tension modifiers would be added into the ink formulation to make it more suitable for printing technology. The effect of these additives on the solar cell

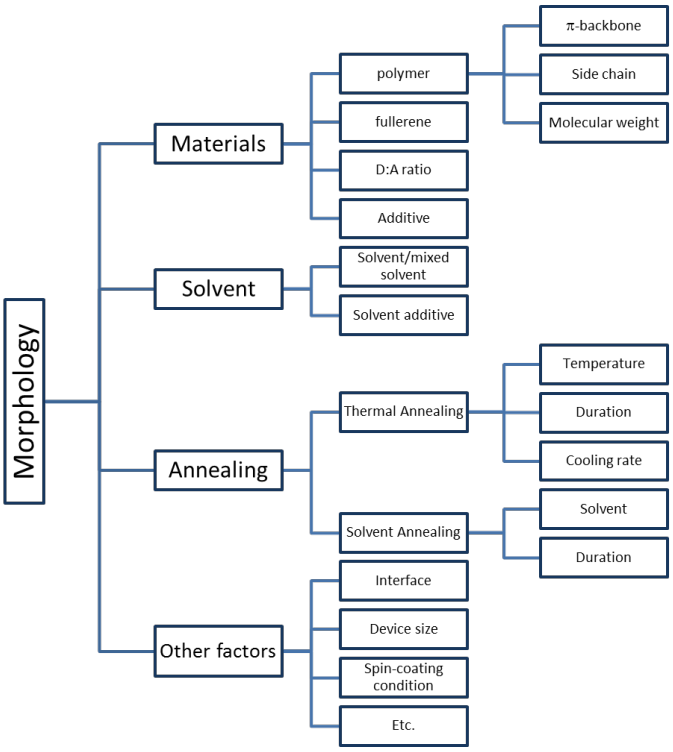

Figure 7. Summary of parameters that influence the morphology of the BHJ active thin film.

performance has not yet been well studied. There are research attempts to incorporate various non-solvent additives, such as nanoparticles [126], carbon nanotubes [127], small molecules [128] and polymers [129], to create a ternary blend BHJ solar cell. These strategies have demonstrated how a third component in the polymer/fullerene blend influences the overall morphology and performance of the solar cell, which could be used as a potent routine method to enhance the performance of the device [130].

Thermal annealing is an alternative method for controlling the BHJ morphology and improving the PCEs. By applying thermal energy to the thin film, it helps the reorganization of the polymer/fullerene blends and increases the crystallinity of the film [131]. This processing method has been routinely used to optimize the thin films for transistors [132] and BHJ solar cells [20,21]. The annealing temperature, the annealing duration and the cooling rate are key parameters to optimize the performance of the device and the optimal combination of the thermal treatment is material-dependent. Even for the same material, e.g., P3HT/PCBM blend, the optimal annealing condition differs from lab to lab [20], presumably due to different device structure, different solvent, different purity, different molecular weight, or even different operator. So far there is no general guideline to predict the optimal condition for a new OPV material and the optimal condition is obtained via a tedious trial-and-error approach.

http://dx.doi.org/10.5772/58924

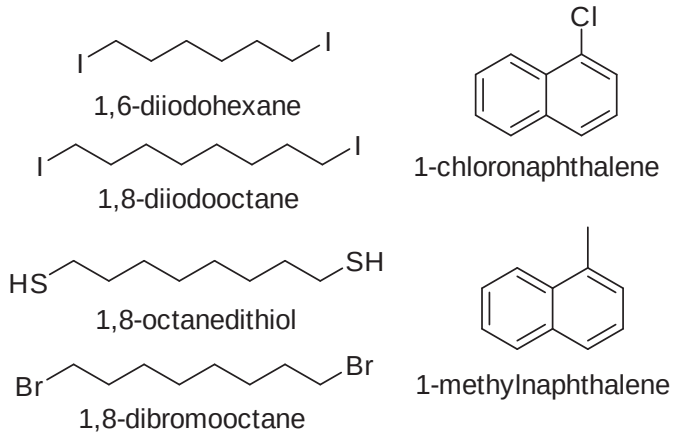

Figure 8. Chemical structures of solvent additives for BHJ solar cells.

Solvent annealing refers to the treatment of the BHJ thin film with solvent vapor, typically in a petri dish contained with the solvent. Parameters to optimize include the solvent type and the treatment duration. By exposing the coated thin film with solvent vapors, there is reorganization and further morphological evolution over time. This method has been demonstrated to enhance the morphology, the hole mobility of P3HT [133] and the PCE performance of the P3HT/PCBM solar cell [134]. Treatment of the thin film with polar solvents, such as methanol and ethanol, is also found to improve the morphology and render higher PCE values for P3HT/PCBM [135].

In summary, the morphology of the active polymer/fullerene blend in the BHJ solar cell can be tuned by a number of factors, such as the materials, choice of solvent, solvent additives, annealing condition, etc. The optimal condition to achieve the best device performance is typically material dependent and achieved in a trial-and-error approach. Sometimes, a minor modification of the processing condition can introduce magnificent enhancement of the device performance, for example, addition of processing additives. The complexity of the morphology control and the tedious optimization process would account for the phenomenon that why so many promising polymer materials in the literature with suitable absorption, energy level and solubility possess inferior device performance. Even for the same polymer motif, the OPV performance would vary significantly by different processing methods [136]. This again highlights the importance of device engineering work to explore the full potential of a new polymer in the BHJ solar cell.

4. Industrial concerns

As the ultimate goal of any material related research and technology development is to apply the material and to fulfill the promises of the material, such stress on the large scale manufac-

turing and product development has also been witnessed for OPV technology. With the fast performance improvement of OPV cells in research labs, the application of OPV technology as a renewable energy source has become more appealing. However, it is never trivial to translate a lab-based technology into a large volume production process. A large number of difficulties and problems have to be overcome to ensure the successful commercialization of the technology. In this session, we will highlight some aspects related to the industrialization of OPV technology.

4.1. The stability and the lifetime issue

The stability issue of the light harvesting material in the solar cell device should be brought into discussion as the OPV technology is aimed to generate electricity from sunlight for a long period of service time. The materials used to construct the OPV module, which include the active layer, the electrode materials and the encapsulating materials, should be robust under the outdoor condition and the performance of the OPV module should be maintained to ensure the power generation efficiency of the technology. The currently known degradation mechanisms of the solar cell device, including morphology degradation, photo-oxidation, interface degradation, physical and mechanical degradation, have been well discussed in a number of review articles [137-139]. It should be highlighted that the active layers and the metal electrode materials are especially prone to degrade upon contact with water and oxygen. Therefore, in real practice the encapsulation of the device is mandatory to guarantee the long-term stability of the device. The water and oxygen transmission properties of the encapsulant materials are thus essential to ensure the stability of the OPV module [29]. The growing concerns over the stability issue on OPV technology and fulfillment of the promise of OPV as a renewable energy technology has initiated the "International Summits on Organic Photovoltaic Stability" (ISOS) [140] to stimulate the research effort to address these issues.

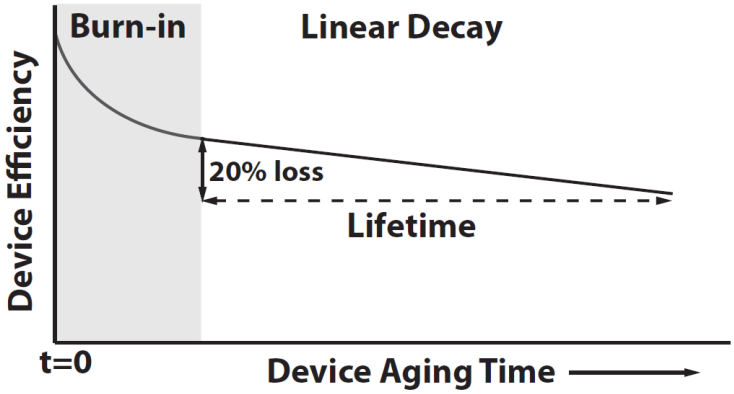

Figure 9. Typical decay curve of a polymer solar cell employing a standard device architecture. The lifetime is defined by the point at which the efficiency has dropped by 20% from the start of the linear decay period. [141] Copyright 2011 WILEY-VCH Verlag GmbH & Co. KGaA, Weinheim.

The degradation profile of an OPV module typically follows a trend shown in Figure 9 [141]. The device suffers a *burn-in* degradation process at the early working life which is characterized by an exponential loss in efficiency and then a linear decay process. The lifetime of the device is defined as the time at which the efficiency drops to 80% of the efficiency after *burn-in* process. By appropriate encapsulation, solar cell devices based on poly[9′-hepta-decanyl-2,7-carbazole-alt-5,5-(4′,7′-di-thienyl-2′,1′,3′-benzothiadiazole)] and $PC_{71}BM$ blend have demonstrated a lifetime of ca. six years [141]. This lifetime is marvelous in reported lifetime of OPV solar cells [142]. However, such lifetime is still considered insufficient if OPV technology is aimed to compete with the mainstream Si-based PV technology. A silicon based solar cells typically lasts on the order of 25 years and much higher PCE (Figure 1). In this regard, there is still a huge space for OPV technology to improve in order to survive in the PV market.

4.2. Processing technique

As one of the potential advantages, solution based processing methods, such as roll-to-roll printing and ink-jet printing, are suitable for organic solar cell materials [143-145]. So far in the lab scale, the BHJ solar cells are typically fabricated by spin-coating method. As spin-coating turns out to be suitable for the reproducible formation of homogeneous thin films, it is difficult to scale up and a large amount of inks is wasted during the spin-coating process. Wet-printing with a roll to roll production process is a more favorable processing technique for large scale OPV module fabrication. These printing techniques include gravure printing, flexographic printing, screen printing, rotary screen-printing, knife coating, slot die coating, and so on. More details regarding these printing techniques can be found in [144, 145]. Demonstration of large scale printing of OPV modules has been done by Krebs et al. [146] and currently OPV based solar parks have been established to explore the potential this new energy technology. One issue related to the printing technology is the uniformity and reproducibility of the final OPV module since the OPV performance of BHJ blend is very sensitive to the morphology of the thin film whereas the morphology is very sensitive to the processing condition. The materials used and the processing technique should be able to provide an OPV module with lifetime > 10 years with an average power conversion efficiency > 10% to compete with the mature inorganic PV products in the mainstream market. Even though the current start-of-the-art efficiency can reach >10% for small devices in the research lab, the efficiencies of the large area devices by solution processing methods are still low (< 3.5%) [144]. Further optimization of both the materials and the processing methods is urgently needed to fulfill all the advantageous claims of OPV technology.

4.3. The economic potential of OPV technology

One concern regarding the OPV technology is that how cheap the electricity generated by this renewable technology can be. More anxiety appears after the business failures of endeavors in the OPV market [147,148]. As a matter of fact, in the past years only a number of companies (Solarmer Energy Inc., Ossila, DyeSol, Heliatek, G24 Power, Eight19, Mitsubishi, Plextronics, Sharp Solar, Solaronix, SolarPrint, etc.) have ventured into the OPV technology related business, and are struggling to survive in the market. A number of articles have addressed the

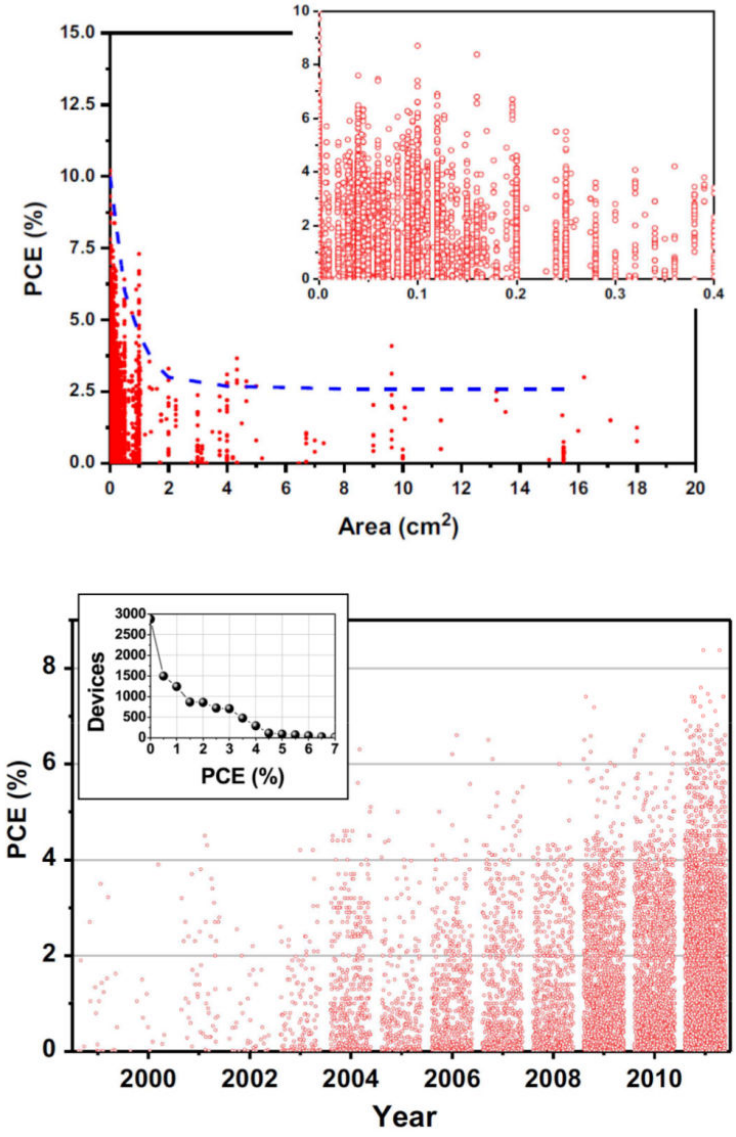

Figure 10. Top: A plot of the power conversion efficiency versus the active area. Bottom: The PCE values obtained versus the publication year. [30] Copyright Elsevier 2013.

economic potential of OPV technology to estimate the cost of the OPV electricity [4, 27-29, 149-150]. One key factor that dominates the cost is definitely the power conversion efficiency. Figure 10 shows the PCE values of the reported OPV devices vs. the area (top) and the year (bottom) by Krebs et al.[30] It is found that most of the highly promising efficiency data are

only achievable with a device area < 1 cm^2. Furthermore, even though there are promising efficiency data (~7-10%) of some hero polymers, the majority of the research work exhibits a power conversion efficiency of less than 3%. As the area of the solar cell device increases, the efficiency is expected to be lower. With the current efficiency number for large scale OPV modules (< 3.5%), the applicability as mainstream power generation technology is rather dim. Some potential market and niche products for OPV technology include portable, low weight charger for electronics, PV covered uniforms, backpacks and tents for military usage and OPV integrated windows and walls. One intriguing idea about OPV usage is to serve as top cell in a tandem device with an inorganic bottom cell [151]. The tandem cell design strategy for all organic based materials has been proven efficient to improve the power conversion efficiency [22,24]. Key to the success of this tandem organic/inorganic strategy is the development of OPV modules with comparable lifetimes so that the technology can be used in a time of 5-10 years range. Another aspect is the energy pay-back time. For crystalline silicone PV technology, the energy pay-back time is estimated to be 4.12-2.38 year while for OPV it is about 2.02 to 0.79 year [28]. An even more optimistic estimation of the energy pay-back time of OPV technology is only 1 day [4]. As currently all promising data about OPV technology come from research labs and theoretical work, it is still difficult to conclude on the future and fate of OPV technology. Efficiency and stability are two major obstacles, but may also become opportunities for new business players.

5. Summary and outlook

The concept of bulk hetero junction solar cells has been continuously developed over the past two decades. Enormous achievements have been witnessed over the journey and currently the record efficiency of BHJ solar cells has reached over 10% (Figure 1). New materials, especially the donor materials in the blend, have been developed in an expanding rate, with new design strategies, new building blocks and new polymerization methods at the same time. For the acceptor part, fullerene based derivatives, $PC_{61}BM$ and $PC_{71}BM$, are still the first choice for researchers. As the energy conversion process involves charge transfer over the donor/acceptor interface, the morphology of the donor/acceptor is therefore essential for an efficient power conversion process. The morphology of the thin film, however, is very sensitive to the processing conditions, such as the materials used, solvent, solvent additives, annealing, spin-coating conditions, etc. A tedious but worthwhile optimization process of all these parameters has to be carried out to explore the full potential of any newly synthesized polymer donor material or any new acceptor material. So far, the choice of the best condition is still based on a trial-and-error approach. Furthermore, problems arise as the OPV technology is translated from the lab-scale to industrial scale, e.g., how to achieve the optimal morphology of a cm^2 device in the industrial scale, how to optimally process the OPV module, and how to improve the device stability by suitable encapsulation. The solutions to these questions are by no means trivial. Most probably a rediscovery process has to be carried out to optimize all the parameters associated with the industrial scale production.

As the OPV technology has gradually become business relevant and quite a number of companies are currently active in the OPV market to cash the promises of OPV researchers, more creative breakthroughs are in urgent need to solve the intrinsic efficiency and stability issues of current OPV technology. Other than further development of more efficient light harvesting materials, some new concepts such as ternary solar cell [23, 130], and modification of the solar cell structures [22,24], e.g., inverted solar cells, tandem solar cells, or tandem organic/inorganic solar cells would pave new ways to improve the efficiency of the solar cell. Further development of encapsulant materials with lower water/oxygen transmission rate would help the solar cells survive longer under ambient conditions [29]. The continuous optimization effort on the industrial roll-to-roll printing techniques would help minimize the gap between the best efficiency data from lab devices and the large scale OPV modules. These developments have to be fast, as tremendous work is spent to optimize current inorganic PV technology as well (Figure 1). Furthermore, BHJ based solar cells also have to compete with other organic material based PV technology, such as dye-sensitized solar cells [152] and perovskite solar cells [153]. There are also issues regarding the marketing of OPV based technology. As it is envisaged that OPV will not be able to compete with inorganic PV technology in the mainstream energy production market in the coming 5 to 10 years [28], niche markets, such as portable electronics chargers, flexible PV and wearable PV, are therefore sought in the short term. The light weight and the flexibility of OPV technology would become advantageous to survive in the market.

To end up our discussion, we will emphasize the nature of OPV research and related materials development. Any science and technology development, if it is aimed at large scale application, it should be robust, reproducible, affordable and efficient in its claimed function. The materials used in the device should be accessed in an easy and cheap way and the production process should be cost-effective. And more importantly, the commercial products should have attractive features to survive in the market. There are still a lot of obstacles for OPV researchers to conquer, but more opportunities in the future.

Acknowledgements

The authors would like to acknowledge the financial support from the Institute of Materials Research and Engineering (IMRE), Agency for Science, Technology and Research (A*STAR).

Author details

Qun Ye and Jian Wei Xu*

Institute of Materials Research and Engineering, Agency for Science, Technology and Research (ASTAR), Singapore

References

[1] Tang CW. Two-layer organic photovoltaic cell. Applied Physics Letters 1986; 48 (2) 183-185.

[2] Yu G, Gao J, Hummelen JC, Wudl F, Heeger AJ. Polymer Photovoltaic Cells: Enhanced Efficiencies via a Network of Internal Donor-Acceptor Heterojunctions. Science 1995; 270 (5243) 1789-1791.

[3] NREL efficiency chart. http://www.nrel.gov/ncpv/images/efficiency_chart.jpg (accessed 01 July 2014).

[4] Espinosa N, Hösel M, Angmo D, Krebs FC. Solar cells with one-day energy payback for the factories of the future. Energy &Environmental Science 2012; 5 (1) 5117-5132.

[5] Green MA, Emery K, Hishikawa Y, Warta W, Dunlops ED. Solar cell efficiency tables (version 44). Progress in Photovoltaics: Research and Applications 2014; 22 (7) 701-710.

[6] Dou L, You J, Hong Z, Xu Z, Li G, Street RA, Yang Y. 25th Anniversary Article: A Decade of Organic/Polymeric Photovoltaic Research. Advanced Materials 2013; 25 (46) 6642-6671.

[7] Schlenker CW, Thompson ME. The molecular nature of photovoltage losses in organic solar cells. Chemical Communications 2011; 47 (13) 3702-3716.

[8] Proctor CM, Kuik M, Nguyen TQ. Charge carrier recombination in organic solar cells. Progress in Polymer Science 2013; 38 (12) 1941-1960.

[9] Clarke TM, Durrant JR. Charge Photogeneration in Organic Solar Cells. Chemical Reviews 2010; 110 (11) 6736-6767.

[10] Bian L, Zhu E, Tang J, Tang W, Zhang F. Recent progress in the design of narrow bandgap conjugated polymers for high-efficiency organic solar cells. Progress in Polymer Science 2012; 37 (9) 1292-1331.

[11] Rasmussen SC, Evenson SJ. Dithieno[3,2-b:2′,3′-d]pyrrolo-based materials: Synthesis and application to organic electronics. Progress in Polymer Science 2013; 38 (12) 1773-1804.

[12] Coughlin JE, Henson ZB, Welch GC, Bazan GC. Design and Synthesis of Molecular Donors for Solution-Processed High-Efficiency Organic Solar Cells. Accounts of Chemical Research 2014; 47 (1) 257-270.

[13] Chen Y, Wan X, Long G. High Performance Photovoltaic Applications Using Solution-Processed Small Molecules. Accounts of Chemical Research 2013; 46 (11) 2645-2655.

[14] Boudreault PLT, Najari A, Leclerc M. Processable Low-Bandgap Polymers for Photovoltaic Applications. Chemistry of Materials 2011; 23 (3) 456-469.

[15] Cheng YJ, Yang SH, Hsu CS. Synthesis of Conjugated Polymers for Organic Solar Cell Applications. Chemical Reviews 2009; 109 (11) 5868-5923.

[16] Li Y. Molecular Design of Photovoltaic Materials for Polymer Solar Cells: Toward Suitable Electronic Energy Levels and Broad Absorption. Accounts of Chemical Research 2012; 45 (5) 723-733.

[17] Duan C, Huang F, Cao Y. Recent development of push-pull conjugated polymers for bulk-heterojunction photovoltaics: rational design and fine tailoring of molecular structures. Journal of Materials Chemistry 2012; 22 (21) 10416-10434.

[18] Son HJ, He F, Carsten B, Yu L. Are we there yet? Design of better conjugated polymers for polymer solar cells. Journal of Materials Chemistry 2011; 21 (47) 18934-18945.

[19] Kularatne RS, Magurudeniya HD, Sista P, Biewer MC, Stefan MC. Donor-Acceptor Semiconducting Polymers for Organic Solar Cells. Journal of Polymer Science Part A: Polymer Chemistry 2013; 51 (4) 743-768.

[20] Dang MT, Hirsch L, Wantz G, Wuest JD. Controlling the Morphology and Performance of Bulk Heterojunctions in Solar Cells. Lessons Learned from the Benchmark Poly(3-hexylthiophene):[6,6]-Phenyl-C_{61}-Butyric Acid Methyl Ester System. Chemical Reviews 2013; 113 (5) 3734-3765.

[21] Huang Y, Kramer EJ, Heeger AJ, Bazan GC. Bulk Heterojunction Solar Cells: Morphology and Performance Relationships. Chemical Reviews 2014 DOI: 10.1021/cr400353v.

[22] Sista S, Hong Z, Chen LM, Yang Y. Tandem polymer photovoltaic cells-current status, challenges and future outlook. Energy & Environmental Science 2011; 4 (5) 1606-1620.

[23] Ameri T, Khoram P, Min J, Brabec CJ. Organic Ternary Solar Cell: A Review. Advanced Materials 2013; 25 (31) 4245-4266.

[24] You J, Dou L, Hong Z, Li G, Yang Y. Recent trends in polymer tandem solar cells research. Progress in Polymer Science 2013; 38 (12) 1909-1928.

[25] Po R, Carbonera C, Bernardi A, Camaioni N. The role of buffer layers in polymer solar cells. Energy & Environmental Science 2011; 4 285-310.

[26] Risko C, McGehee MD, Brédas JL. A quantum-chemical perspective into low optical-gap polymers for highly-efficient organic solar cells. Chemical Science 2011; 2 (7) 1200-1218.

[27] Dennler G, Scharber MC, Brabec CJ. Polymer-Fullerene Bulk-Heterojunction Solar Cells. Advanced Materials 2009; 21 (34) 1323-1338.

[28] Darling SB, You F. The case for organic photovoltaics. RSC Advances 2013; 3 (39) 17633-17648.

[29] Po R, Bernardi A, Calabrese A, Carbonera C, Corso G, Pellegrino A. From lab to lab: how must the polymer solar cell materials design change? – an industrial perspective. Energy & Environmental Science 2014; 7 (3) 925-943.

[30] Jørgensen M, et al. The state of organic solar cells – A meta analysis. Solar Energy Materials & Solar Cells 2013; 119 (1) 84-93.

[31] Dennler G and co-signatories. The value of values. Materials Today 2007; 10 (11) 56.

[32] Krebs FC, Espinosa N, Hösel M, Søndergaard RR, Jørgensen M. 25th Anniversary Article: Rise to Power – OPV-Based Solar Parks. Advanced Materials 2013; 26 (1) 29-39.

[33] Krebs FC, Jorgensen M. Polymer and organic solar cells viewed as thin film technologies: What it will take for them to become a success outside academia. Solar Energy Materials & Solar Cells 2013; 119 (1) 73-76.

[34] Henson ZB, Müllen K, Bazan GC. Design strategies for organic semiconductors beyond the molecular formula. Nature Chemistry 2012; 4 (9) 699-704.

[35] Janssen RAJ, Nelson J. Factors Limiting Device Efficiency in Organic Photovoltaics. Advanced Materials 2013; 25 (13) 1847-1858.

[36] Thompson BC, Fréchet JMJ. Polymer-Fullerene Composite Solar Cells. Angewandte Chemie International Edition 2008; 47 (1) 58-77.

[37] Helgesen M, Søndergaard R, Krebs FC. Advanced materials and processes for polymer solar cell devices. Journal of Materials Chemistry 2010; 20 (1) 36-60.

[38] Brabec CJ, Gowrisanker S, Halls JJM, Laird D, Jia S, Williams SP. Polymer-Fullerene Bulk-Heterojunction Solar Cells. Advanced Materials 2010; 22 (34) 3839-3856.

[39] Beaujuge PM, Fréchet JMJ. Molecular Design and Ordering Effects in π-Functional Materials for Transistor and Solar Cell Applications. Journal of the American Chemical Society 2011; 133 (50) 20009-20029.

[40] Brunetti FG, Kumar R, Wudl F. Organic electronics from perylene to organic photovoltaics: painting a brief history with a broad brush. Journal of Materials Chemistry 2010; 20 (15) 2934-2948.

[41] Chiechi RC, Havenith RWA, Hummelen JC, Koster LJA, Loi MA. Modern plastic solar cells: materials, mechanisms and modeling. Materials Today 2013; 16(7/8) 281-289.

[42] Scharber MC, Sariciftci NS. Efficiency of bulk-heterojunction organic solar cells. Progress in Polymer Science 2013; 38 (12) 1929-1940.

[43] Burke DJ, Lipomi DJ. Green Chemistry for organic solar cells. Energy & Environmental Science 2013; 6 (7) 2053-2066.

[44] Shrestha S. Literature Survey Photovoltaics Literature Survey (No. 112). Progress in Photovoltaics: Research and Applications 2014; 22 (8) 933-936.

[45] Guo X, Baumgarten M, Müllen K. Designing π-conjugated polymers for organic electronics. Progress in Polymer Science 2013; 38 (12) 1773-2070.

[46] Ye Q., Chi C. Conjugated Polymers for Organic Solar Cells. In: Kosyachenko LA. (ed.) Solar Cells – New Aspects and Solutions. Rijeka: InTech; 2011. P453-474.

[47] Song S, Kim J, Shim JY, Kim G, Lee BH, Jin Y, Park SH, Kim I, Lee K, Suh H. Synthesis and characterization of dimethyl-benzimidazole based low bandgap copolymers for OPVs. Synthetic Metals 2012; 162 (11-12) 988-994.

[48] Hoven CV, Dang XD, Coffin RC, Peet J, Nguyen TQ, Bazan GC. Improved Performance of Polymer Bulk Heterojunction Solar Cells Through the Reduction of Phase Separation via Solvent Additives. Advanced Materials 2010; 22 (8) E63-E66.

[49] Bijleveld JC, Shahid M, Gilot J, Wienk MM, Janssen RAJ. Copolymers of Cyclopentadithiophene and Electron-Deficient Aromatic Units Designed for Photovoltaic Applications. Advanced Functional Materials 2009; 19 (20) 3262-3270.

[50] Balan A, Baran D, Toppare L. Benzotriazole containing conjugated polymers for multipurpose organic electronic applications. Polymer Chemistry 2011; 2 (5) 1029-1043.

[51] Hou J, Park MH, Zhang S, Yao Y, Chen LM, Li JH, Yang Y. Bandgap and Molecular Energy Level Control of Conjugated Polymer Photovoltaic Materials Based on Benzo[1,2-b:4,5-b′]dithiophene. Macromolecules 2008; 41(16) 6012-6018.

[52] Zhao W, Cai W, Xu R, Yang W, Gong X, Wu H, Cao Y. Novel conjugated alternating copolymer based on 2,7-carbazole and 2,1,3-benzoselenadiazole. Polymer 2010; 51 (14) 3196-3202.

[53] Qin T, Zajaczkowski W, Pisula W, Baumgarten M, Chen M, Gao M, Wilson G, Easton CD, Müllen K, Watkins SE. Tailored Donor-Acceptor Polymers with an A-D1-A-D2 Structure: Controlling Intermolecular Interactions to Enable Enhanced Polymer Photovoltaic Devices. Journal of the American Chemical Society 2014; 136 (16) 6049-6055.

[54] Xu YX, Chueh CC, Yip HL, Ding FZ, Li YX, Li CZ, Li X, Chen WC, Jen AKY. Improved Charge Transport and Absorption Coefficient in Indacenodithieno[3,2-b]thiophene-based Ladder-Type Polymer Leading to Highly Efficient Polymer Solar Cells. Advanced Materials 2012; 24 (47) 6356-6361.

[55] Kim J, Yun MH, Kin GH, Lee J, Lee SM, Ko SJ, Kim Y, Dutta GK, Moon M, Park SY, Kim DS, Kim JY, Yang C. Synthesis of PCDTBT-Based Fluorinated Polymers for High Open-Circuit Voltage in Organic Photovoltaics: Towards an Understanding of Relationships between Polymer Energy Levels Engineering and Ideal Morphology Control. ACS Applied Materials & Interfaces 2014; 6 (10) 7523-7534.

[56] Albrecht, Janietz S, Schindler W, Frisch J, Kurpiers J, Kniepert J, Inal S, Pingel P, Fostiropoulos K, Koch N, Neher D. Fluorinated Copolymer PCPDTBT with Enhanced

Open-Circuit Voltage and Reduced Recombination for Highly Efficient Polymer Solar Cells. Journal of the American Chemical Society 2012; 134 (36) 14932-14944.

[57] Chang HH, Tsai CE, Lai YY, Chiou DY, Hsu SL, Hsu CS, Cheng YJ. Synthesis, Molecular and Photovoltaic Properties of Donor-Acceptor Conjugated Polymers Incorporating a New Heptacyclic Indacenodithieno[3,2-b]thiophene Arene. Macromolecules 2012; 45 (23) 9282-9291.

[58] Li Y, Zou J, Yip HL, Li CZ, Zhang Y, Chueh CC, Intemann J, Xu Y, Liang PW, Chen Y, Jen AKY. Side-chain effect on cyclopentadithiophene/fluorobenzothiadiazole-based low band gap polymers and their application for polymer solar cells. Macromolecules 2013; 46 (14) 5497-5503.

[59] Dou L, Chen CC, Yoshimura K, Ohya K, Chang WH, Gao J, Liu Y, Richard E, Yang Y. Synthesis of 5H-Dithieno[3,2-b:2′,3′-d]pyran as an electron rich building block for donor-acceptor type low bandgap polymers. Macromolecules 2013; 46 (9) 3384-3390.

[60] Bronstein H, Frost JM, Hadipour A, Kim Y, Nielsen CB, Ashraf RS, Rand BP, Watkins S, McCulloch I. Effect of Fluorination on the Properties of a Donor-Acceptor Copolymer for Use in Photovoltaic Cells and Transistors. Chemistry of Materials 2013; 25 (3) 277-285.

[61] Zhang Y, Chien SC, Chen KS, Yip HL, Sun Y, Davies JA, Chen FC, Jen AKY. Increased open circuit voltage in fluorinated benzothiadiazole-based alternating conjugated polymers. Chemical Communications 2011; 47 (39) 11026-11028.

[62] Almeataq MS, Yi H, Al-Faifi S, Alghamdi AAB, Iraqi A, Scarratt MW, Wang T, Lidzey DG. Anthracene-based donor-acceptor low bandgap polymers for applications in solar cells. Chemical Communications 2013; 49 (22) 2252-2254.

[63] Alghamdi AAB, Watters DC, Yi H, Al-Faifi S, Almeataq MS, Coles D, Kingsley J, Lidzey DG, Iraqi A. Selenophene vs. thiophene in benzothiadiazole-based low energy gap donor-acceptor polymers for photovoltaic applications. Journal of Materials Chemistry A 2013; 1 (16) 5165-5171.

[64] Gong X, Li C, Lu Z, Li G, Mei Q, Fang T, Bo Z. Anthracene-containing Wide-Band-Gap Conjugated Polymers for High-Open-Circuit-Voltage Polymer Solar Cells. Macromolecular Rapid Communications 2013; 34 (14) 1163-1168.

[65] Liu X, Wen W, Bazan GC. Post-Deposition Treatment of an Arylated-Carbazole Conjugated Polymer for Solar Cell Fabrication. Advanced Materials 2012; 24 (33) 4505-4510.

[66] Ku SY, Liman CD, Burke DJ, Treat ND, Cochran JE, Amir E, Perez LA, Chabinyc ML, Hawker CJ. A Facile Synthesis of Low-Band-Gap Donor-Acceptor Copolymers Based on Dithieno[3,2-b:2′,3′-d]thiophene. Macromolecules 2011, 44 (24) 9533-9538.

[67] Zhou H, Yang L, Price SC, Knight KJ, You W. Enhanced Photovoltaic Performance of Low-Bandgap Polymers with Deep LUMO levels. Angewandte Chemie International Edition 2010; 49 (43) 7992-7995.

[68] Tseng HR, Phan H, Luo C, Wang M, Perez LA, Patel SN, Ying L, Kramer EJ, Nguyen TQ, Bazan GC, Heeger AJ. High-Mobility Field-Effect Transistors Fabricated with Macroscopic Aligned Semiconducting Polymers. Advanced Materials 2014; 26 (19) 2993-2998.

[69] Sun Y, Chien SC, Yip HL, Zhang Y, Chen KS, Zeigler DF, Chen FC, Lin B, Jen AKY. High-mobility low-bandgap conjugated copolymers based on indacenodithiophene and thiadiazole[3,4-c]pyridine units for thin film transistor and photovoltaic applications. Journal of Materials Chemistry 2011; 21 (35) 13247-13255.

[70] Wen W, Ying L, Hsu BBY, Zhang Y, Nguyen TQ, Bazan GC. Regioregular pyridyl[2,1,3]thiadiazole-co-indacenodithiophene conjugated polymers. Chemical Communications 2013; 49 (65) 7192-7194.

[71] Wang Y, Liu Y, Chen S, Peng R, Ge Z. Significant Enhancement of Polymer Solar Cell Performance via Side-Chain Engineering and Simple Solvent Treatment. Chemistry of Materials 2013; 25 (15) 3196-3204.

[72] Tumbleston JR, Stuart AC, Gann E, You W, Ade H. Fluorinated Polymer Yields High Organic Solar Cell Performance for a Wide Range of Morphologies. Advanced Functional Materials 2013; 23 (27) 3463-3470.

[73] Uy RL, Yan L, Li W, You W. Tuning Fluorinated Benzotriazole Polymers through Alkylthio Substitution and Selenophene Incorporation for Bulk Heterojunction Solar Cells. Macromolecules 2014; 47 (7) 2289-2295.

[74] Price SC, Stuart AC, Yang L, Zhou H, You W. Fluorine Substituted Conjugated Polymer of Medium Band Gap Yields 7% Efficiency in Polymer-Fullerene Solar Cells. Journal of the American Chemical Society 2011; 133 (12) 4625-4631.

[75] Jiang JM, Yang PA, Hsieh TH, Wei KH. Crystalline Low-Band Gap Polymers Comprising Thiophene and 2,1,3-benzooxadiazole Units for Bulk Heterojunction Solar Cells. Macromolecules 2011; 44 (23) 9155-9163.

[76] Min J, Zhang ZG, Zhang M, Li Y. Synthesis and photovoltaic properties of a D-A copolymer of dithienosilole and fluorinated-benzotriazole. Polymer Chemistry 2013; 4 (5) 1467-1473.

[77] Fan J, Yuen JD, Wang M, Seifter J, Seo JH, Mohebbi AR, Zakhidov D, Heeger AJ, Wudl F. High-Performance Ambipolar Transistors and Inverters from an Ultralow Bandgap Polymer. Advanced Materials 2012; 23 (16) 2186-2190.

[78] Keshtov ML, Marochkin DV, Kochurov VS, Khokhlov AR, Koukaras EN, Sharma GD. Synthesis and characterization of a low band gap quinoxaline based D-A copoly-

mer and its application as a donor for bulk heterojunction polymer solar cells. Polymer Chemistry 2013; 4 (14) 4033-4044.

[79] Zha D, Chen L, Wu F, Wang H, Chen Y. Modulation of the molecular geometry of carbazolebis[thiadiazole]-based conjugated polymers for photovoltaic applications. Polymer Chemistry 2013; 4 (8) 2480-2488.

[80] Zhou P, Zhang ZG, Li Y, Chen X, Qin J. Thiophene-Fused Benzothiadiazole: A Strong Electron-Acceptor Unit to Build D-A Copolymer for Highly Efficient Polymer Solar Cells. Chemistry of Materials 2014; 26 (11) 3495-3501.

[81] Wang M, Hu X, Liu P, Li W, Gong X, Huang F, Cao Y. Donor-Acceptor Conjugated Polymer Based on Naphtho[1,2-c:5,6-c]bis[1,2,5]thiadiazole for High-Performance Polymer Solar Cells. Journal of the American Chemical Society 2011; 133 (25) 9638-9641.

[82] Wang M, Hu X, Liu L, Duan C, Liu P, Ying L, Huang F, Cao Y. Design and Synthesis of Copolymers of Indacenodithiophene and Naphtho[1,2-c:5,6-c]bis(1,2,5-thiadiazole) for Polymer Solar Cells. Macromolecules 2013; 46 (10) 3950-3958.

[83] Zhou H, Yang L, Stuart AC, Price SC, Liu S, You W. Development of Fluorinated Benzothiadiazole as a Structural Unit for a Polymer Solar Cell of 7% Efficiency. Angewandte Chemie International Edition 2011; 50 (13) 2995-2998.

[84] Dong Y, Cai W, Wang M, Li Q, Ying L, Huang F, Cao Y. [1,2,5]Thiadiazolo[3,4-f]benzotriazole based narrow band gap conjugated polymers with photocurrent response up to 1.1 μm. Organic Electronics 2013; 14 (10) 2459-2467.

[85] Osedach TP, Andrew TL, Bulović V. Effect of synthetic accessibility on the commercial viability of organic photovoltaics. Energy & Environmental Science 2013; 6 (3) 711-718.

[86] Liao HC, Ho CC, Chang CY, Jao MH, Darling SB, Su WF. Additives for morphology control in high-efficiency organic solar cells. Materials Today 2013; 16 (9) 326-336.

[87] Gao X, Cui C, Zhang M, Huo L, Huang Y, Hou J, Li Y. High efficiency polymer solar cells based on poly(3-hexylthiophene)/indene-C_{70} bisadduct with solvent additive. Energy & Environmental Science 2012; 5 (7) 7943-7949.

[88] Mei J, Bao Z. Side Chain Engineering in Solution-Processable Conjugated Polymers. Chemistry of Materials 2014; 26 (1) 604-615.

[89] Carsten B, He F, Son HJ, Xu T, Yu L. Stille Polycondensation for Synthesis of Functional Materials. Chemical Reviews 2011; 111 (3) 1493-1528.

[90] Miyaura N, Suzuki A. Palladium-catalysed cross-coupling reactions of organoboron compounds. Chemical Reviews 1995; 95 (7) 2457-2483.

[91] Berrouard P, Najari A, Pron A, Gendron D, Morin PO, Pouliot JR, Veilleux J, Leclerc M. Synthesis of 5-Alkyl[3,4-c]thienopyrrole-4,6-dione-Based Polymers by Direct Heteroarylation. Angewandte Chemie International Edition 2012; 51 (9) 2068-2071.

[92] Rudenko AE, Khlyabich PP, Thompson BC. Random Poly(3-hexylthiophene-co-3-cyanothiophene) Copolymers via Direct Arylation Polymerization (DArP) for Organic Solar Cells with High Open-Circuit Voltage. ACS Macro Letters 2014; 3 (4) 387-392.

[93] Kuwabara J, Yasuda T, Choi SJ, Lu W, Yamazaki K, Kagaya S, Han L, Kanbara T. Direct Arylation Polycondensation: A Promising Method for the Synthesis of Highly Pure, High-Molecular-Weight Conjugated Polymers Needed for Improving the Performance of Organic Photovoltaics. Advanced Functional Materials 2014; 24 (21) 3226-3233.

[94] Estrada LA, Deininger JJ, Kamenov GD, Reynolds JR. Direct (Hetero)arylation Polymerization: An Effective Route to 3,4-Propylenedioxythiophene-Based Polymers with Low Residual Metal Content. ACS Macro Letters 2013; 2 (10) 869-873.

[95] Okamoto K, Zhang J, Housekeeper JB, Marder SR, Luscombe CK. C-H Arylation Reaction: Atom Efficient and Greener Syntheses of π-Conjugated Small Molecules and Macromolecules for Organic Electronic Materials. Macromolecules 2013; 46 (20) 8059-8078.

[96] Mercier LG, Leclerc M. Direct (Hetero)Arylation: A New Tool for Polymer Chemists. Accounts of Chemical Research 2013; 46 (7) 1597-1605.

[97] Kline RJ, McGehee MD, Kadnikova EN, Liu J, Fréchet JMJ. Controlling the Field-Effect Mobility of Regioregular Polythiophene by Changing the Molecular Weight. Advanced Materials 2003; 15 (18) 1519-1522.

[98] Tsao HN, Cho DM, Park I, Hansen MR, Mavrinskiy A, Yoon DY, Graf R, Pisula W, Spiess HW, Müllen K. Ultrahigh Mobility in Polymer Field-Effect Transistors by Design. Journal of the American Chemical Society 2011; 133 (8) 2605-2612.

[99] Intemann JJ, Yao K, Yip HL, Xu YX, Li YX, Liang PW, Ding FZ, Li X, Jen AKY. Molecular Weight Effect on the Absorption, Charge Carrier Mobility, and Photovoltaic Performance of an Indacenodiselenophene-Based Ladder-Type Polymer. Chemistry of Materials 2013; 25 (15) 3188-3195.

[100] Coffin RC, Peet J, Rogers J, Bazan GC. Streamlined microwave-assisted preparation of narrow-bandgap conjugated polymers for high-performance bulk heterojunction solar cells. Nature Chemistry 2009; 1 (8) 657-661.

[101] Tong M, Cho S, Rogers JT, Schmidt K, Hsu BBY, Moses D, Coffin RC, Kramer EJ, Bazan GC, Heeger AJ. Higher Molecular Weight Leads to Improved Photoresponsivity, Charge Transport and Interfacial Ordering in a Narrow Bandgap Semiconducting Polymer. Advanced Functional Materials 2010; 20 (22) 3959-3965.

[102] Nikiforov MP, Lai B, Chen W, Chen S, Schaller RD, Strzalka J, Maser J, Darling SB. Detection and role of trace impurities in high-performance organic solar cells. Energy & Environmental Science 2013; 6 (5) 1513-1520.

[103] Nielsen KT, Bechgaard K, Krebs FC. Removal of Palladium Nanoparticles from Polymer Materials. Macromolecules 2005; 38 (3) 658-659.

[104] Leong WL, Welch GC, Kaake LG, Takacs CJ, Sun Y, Bazan GC, Heeger AJ. Role of trace impurities in the photovoltaic performance of solution processed small-molecule bulk heterojunction solar cells. Chemical Science 2012; 3 (6) 2103-2109.

[105] Park JK, Jo J, Seo JH, Moon JS, Park YD, Lee K, Heeger AJ, Bazan GC. End-Capping Effect of a Narrow Bandgap Conjugated Polymer on Bulk Heterojunction Solar Cells. Advanced Materials 2011; 23 (21) 2430-2435.

[106] Kim JS, Lee Y, Lee JH, Park JH, Kim JK, Cho K. High-Efficiency Organic Solar Cells Based on End-Functional Group Modified Poly(3-hexylthiophene). Advanced Materials 2010; 22 (12) 1355-1360.

[107] Kim Y, Cook S, Kirkpatrick J, Nelson J, Durrant JR, Bradley DDC, Giles M, Heeney M, Hamilton R, McCulloch I. Effect of the End Group of Regioregular Poly(3-hexylthiophene) Polymers on the Performance of Polymer/Fullerene Solar Cells. The Journal of Physical Chemistry C 2007; 111 (23) 8137-8141.

[108] Kaake L, Dang XD, Leong WL, Zhang Y, Heeger AJ, Nguyen TQ. Effects of Impurities on Operational Mechanism of Organic Bulk Heterojunction Solar Cells. Advanced Materials 2013; 23 (12) 1706-1712.

[109] Cowan SR, Leong WL, Banerji N, Dennler G, Heeger AJ. Identifying a Threshold Impurity Level for Organic Solar Cells: Enhanced First-Order Recombination Via Well-Defined $PC_{84}BM$ Traps in Organic Bulk Heterojunction Solar Cells. Advanced Functional Materials 2011; 21 (16) 3083-3092.

[110] He Y, Li Y. Fullerene derivatives acceptors for high performance polymer solar cells. Physical Chemistry Chemical Physics 2011; 13 (6) 1970-1983.

[111] Li CZ, Yip HL, Jen AKY. Functional fullerenes for organic photovoltaics. Journal of Materials Chemistry 2012; 22 (10) 4161-4177.

[112] Wienk MM, Kroon JM, Verhees WJH, Knol J, Hummelen JC, Hal PA, Janssen RAJ. Efficient Methano[70]fullerene/MDMO-PPV Bulk Heterojunction Photovoltaic Cells. Angewandte Chemie International Edition 2003; 42 (29) 3371-3375.

[113] Anctil A, Babbitt CW, Raffaelle RP, Landi BJ. Material and Energy Intensity of Fullerene Production. Environmental Science & Technology 2011; 45 (6) 2353-2359.

[114] Anctil A, Babbitt CW, Raffaelle RP, Landi BJ. Cumulative energy demand for small molecule and polymer photovoltaics. Progress in Photovoltaics: Research and Applications 2013; 21 (7) 1541-1554.

[115] Lewis NS, Nocera DG. Powering the planet: Chemical challenges in solar energy utilization. Proceedings of the National Academy of Sciences of the United States of America 2006; 103 (43) 15729-15735.

[116] Solaris: http://www.solarischem.com (access 1 July 2014).

[117] Anthony JE. Small-Molecule, Nonfullerene Acceptors for Polymer Bulk Heterojunction Organic Photovoltaics. Chemistry of Materials 2011; 23 (3) 583-590.

[118] Facchetti A. Polymer donor-polymer acceptor (all-polymer) solar cells. Materials Today 2013; 16 (4) 123-132.

[119] Kouijzer S, Michels JJ, Berg M, Gevaerts VS, Turbiez M, Wienk MM, Janssen RAJ. Predicting Morphologies of Solution Processed Polymer:Fullerene Blends. Journal of the American Chemical Society 2013; 135 (32) 12057-12067.

[120] Meng L, Shang Y, Li Q, Li Y, Zhan X, Shuai Z, Kimber RGE, Walker AB. Dynamic Monte Carlo Simulation for Highly Efficient Polymer Blend Photovoltaics. The Journal of Physical Chemistry B 2010; 114 (1) 36-41.

[121] Chueh CC, Yao K, Yip HL, Chang CY, Xu YX, Chen KS, Li CZ, Liu P, Huang F, Chen Y, Chen WC, Jen AKY. Non-halogenated solvents for environmentally friendly processing of high-performance bulk-heterojunction polymer solar cells. Energy & Environmental Science 2013; 6 (11) 3241-3248.

[122] Schmidt-Hansberg B, Sanyal M, Grossiord N, Galagan Y, Baunach M, Klein MFG, Colsmann A, Scharfer P, Lemmer U, Dosch H, Michels J, Barrena E, Schabel W. Investigation of non-halogenated solvent mixtures for high throughput fabrication of polymer-fullerene solar cells. Solar Energy Materials & Solar Cells 2012; 96 (1) 195-201.

[123] Lee JK, Ma WL, Brabec CJ, Yuen J, Moon JS, Kim JY, Lee K, Bazan GC, Heeger AJ. Processing Additives for Improved Efficiency from Bulk Heterojunction Solar Cells. Journal of the American Chemical Society 2008; 130 (11) 3619-3623.

[124] Hammond MR, Kline RJ, Herzing AA, Richter LJ, Germack DS, Ro HW, Soles CL, Fischer DA, Xu T, Yu L, Toney MF, DeLongchamp DM. Molecular Order in High-Efficiency Polymer/Fullerene Bulk Heterojunction Solar Cells. ACS Nano 2011; 5 (10) 8248-8257.

[125] Collins BA, Li Z, Tumbleston JR, Gann E, McNeill CR, Ade H. Absolute Measurement of Domain Composition and Nanoscale Size Distribution Explains Performance in PTB7:$PC_{71}BM$ Solar Cells. Advanced Energy Materials 2013; 3 (1) 65-74.

[126] Guo X, Cui C, Zhang M, Huo L, Huang Y, Hou J, Li Y. High efficiency polymer solar cells based on poly(3-hexylthiophene)/indene-C_{70} bisadduct with solvent additive. Energy & Environmental Science 2012; 5 (7) 7943-7949.

[127] Kim K, Carroll DL. Roles of Au and Ag nanoparticles in efficiency enhancement of poly(3-octylthiophene)/C_{60} bulk heterojunction photovoltaics. Applied Physics Letters 2005; 87 (20) 203113.

[128] Berson S, Bettignies R de, Bailly S, Guillerez S, Jousselme B. Elaboration of P3HT/CNT/PCBM Composites for Organic Photovoltaic Cells. Advanced Functional Materials 2007; 17 (16) 3363-3370.

[129] Burke KB, Belcher WJ, Thomsen L, Watts B, McNeill CR, Ade H, Dastoor PC. Role of Solvent Trapping Effects in Determining the Structure and Morphology of Ternary Blend Organic Devices. Macromolecules 2009; 42 (8) 3098-3103.

[130] Tsai JH, Lai YC, Higashihara T, Lin CJ, Ueda M, Chen WC. Enhancement of P3HT/PCBM Photovoltaic Efficiency Using the Surfactant of Triblock Copolymer Containing Poly(3-hexylthiophene) and Poly(4-vinyltriphenylamine) Segments. Macromolecules 2010; 43 (14) 6085-6091.

[131] Yang L, Yan L, You W. Organic Solar Cells beyond One Pair of Donor-Acceptor: Ternary Blends and More. Journal of Physical Chemistry Letters 2013; 4 (11) 1802-1810.

[132] Yang X, Loos J, Veenstra SC, Verhees WJH, Wienk MM, Kroon JM, Michels MAJ, Janssen RAJ. Nanoscale Morphology of High-Performance Polymer Solar Cells. Nano Letters 2005; 5 (4) 579-583.

[133] Dong H, Fu X, Liu J, Wang Z, Hu W. 25th Anniversary Article: Key Points for High-Mobility Organic Field-Effect Transistors. Advanced Materials 2013; 25 (43) 6158-6183.

[134] Mihailetchi VD, Xie H, Boer B, Popescu LM, Hummelen JC, Blom PWM, Koster LJA. Origin of the enhanced performance in poly(3-hexylthiophene):[6,6]-phenyl C_{61}-butyric acid methyl ester solar cells upon slow drying of the active layer. Applied Physics Letters 2006; 89 (1) 012107.

[135] Li G, Shrotriya V, Huang J, Yao Y, Moriarty T, Emery K, Yang Y. High-efficiency solution processable polymer photovoltaic cells by self-organization of polymer blends. Nature Materials 2005; 4 (11) 864-868.

[136] Nam S, Jang J, Cha H, Hwang J, An TK, Park S, Park CE. Effects of direct solvent exposure on the nanoscale morphologies and electrical characteristics of PCBM-based transistors and photovoltaics. Journal of Materials Chemistry 2012; 22 (12) 5543-5549.

[137] Beaupré S, Leclerc M. PCDTBT: en route for low cost plastic solar cells. Journal of Materials Chemistry A 2013; 1 (37) 11097-11105.

[138] Jørgensen M, Norrman K, Krebs FC. Stability/degradation of polymer solar cells. Solar Energy Materials & Solar Cells 2008; 92 (7) 686-714.

[139] . Jørgensen M, Norrman K, Gevorgyan SA, Tromholt T, Andreasen B, Krebs FC. Stability of Polymer Solar Cells Advanced Materials. 2012; 24 (5) 580-612.

[140] Lee JU, Jung JW, Jo JW, Jo WH. Degradation and stability of polymer-based solar cells. Journal of Materials Chemistry 2012; 22 (46) 24265-24283.

[141] ISOS: http://www.ines-solaire.org/anglais/DT1366880015/page/ISOS-6-6th-International-Summit-on-Organic-Photovoltaic-Stability.html (access 10 July 2014).

[142] Peters CH, Sachs-Quintana IT, Kastrop JP, Beaupré S, Leclerc M, McGehee MD. High Efficiency Polymer Solar Cells with Long Operating Lifetimes. Advanced Energy Materials 2011; 1 (4) 491-494.

[143] Hauch JA, Schilinsky P, Choulis SA, Childers R, Biele M, Brabec CJ. Flexible organic P3HT:PCBM bulk-heterojunction modules with more than 1 year outdoor lifetime. Solar Energy Materials & Solar Cells 2008; 92 (7) 727-731.

[144] Arias AC, MacKenzie JD, McCulloch I, Rivnay J, Salleo A. Materials and Applications for Large Area Electronics: Solution-Based Approaches. Chemical Reviews. 2010; 110 (1) 3-24.

[145] Søndergaard R, Hösel M, Angmo D, Larsen-Olsen TT, Krebs FC. Roll-to-roll fabrication of polymer solar cells. Materials Today 2012; 12 (1-2) 36-49.

[146] Krebs FC. Fabrication and processing of polymer solar cells: A review of printing and coating techniques. Solar Energy Materials & Solar Cells 2009; 93 (4) 394-412.

[147] Krebs FC, Espinosa N, Hösel M, Søndergaard RR, Jørgensen M. 25th Anniversary Article: Rise to Power – OPV-Based Solar Parks. Advanced Materials 2014; 26 (1) 29-39.

[148] Konarka Technology: http://en.wikipedia.org/wiki/Konarka_Technologies (access 15 July 2014).

[149] Solyndra: http://en.wikipedia.org/wiki/Solyndra (access 15 July 2014)

[150] Yue D, Khatav P, You F, Darling SB. Deciphering the uncertainties in life cycle energy and environmental analysis of organic photovoltaics. Energy & Environmental Science 2012; 5 (11) 9163-9172.

[151] Lizin S, Passel SV, Schepper ED, Maes W, Lutsen L, Manca J, Vanderzande D. Life cycle analyses of organic photovoltaics: a review. Energy & Environmental Science 2013; 6 (11) 3136-3149.

[152] Beiley ZM, McGehee MD. Modelling low cost hybrid tandem photovoltaics with the potential for efficiencies exceeding 20%. Energy & Environmental Science 2012; 5 (11) 9173-9179.

[153] Hagfeldt A, Boschloo G, Sun L, Kloo L, Pettersson H. Dye-Sensitized Solar Cells. Chemical Reviews 2010; 110 (11) 6595-6663.

[154] Snaith HJ. Perovskites: The Emergence of a New Era for Low-Cost, High-Efficiency Solar Cells. The Journal of Physical Chemistry Letters 2013; 4 (21) 3623-3630.